Environmental Engineering

Jaime Klapp
Anne Cros
Oscar Velasco Fuentes
Catalina Stern
Mario Alberto Rodríguez Meza *Editors*

Experimental and Theoretical Advances in Fluid Dynamics

Springer

Environmental Science and Engineering

Environmental Engineering

For further volumes:
http://www.springer.com/series/7487

Jaime Klapp · Anne Cros
Oscar Velasco Fuentes · Catalina Stern
Mario Alberto Rodríguez Meza
Editors

Experimental and Theoretical Advances in Fluid Dynamics

Springer

Jaime Klapp
Instituto Nacional des Investigaciones Nucleares
Carretera Mexico-Toluca S/N
La Marquesa
Ocoyoacac
52750 Mexico City
Mexico
e-mail: jaime.klapp@inin.gob.mx

Anne Cros
Instituto de Astronomia y Meteorologia
Vallarta 2602
44100 Guadalajara
Mexico
e-mail: anne_cros@yahoo.com

Oscar Velasco Fuentes
CICESE
Carretera Ensenada-Tijuana 3918
Ensenada
Mexico
e-mail: ovelasco@cicese.mx

Catalina Stern
Departamento de Fisica
UNAM
Cuidad Universitaria D.F.
04360 Mexico City
Mexico
e-mail: catalina@ciencias.unam.mx

Mario Alberto Rodríguez Meza
Instituto Nacional de Investigaciones Nucleares
Carretera Mexico-Toluca S/N
La Marquesa
52750 Mexico City
Mexico
e-mail: marioalberto.rodriguez@inin.gob.mx

ISSN 1863-5520

Sponsoring Organizations
Consejo Mexiquense de Ciencia y Tecnología (COMECYT), Consejo Nacional de Ciencia y Tecnología (CONACYT), Instituto Nacional de Investigaciones Nucleares (ININ), Universidad Nacional Autónoma de México (UNAM), and Sociedad Mexicana de Física (SMF).

ISBN 978-3-642-17957-0 e-ISBN 978-3-642-17958-7
DOI 10.1007/978-3-642-17958-7
Springer Heidelberg Dordrecht London New York
Library of Congress Control Number: 2011936142

Cover design: deblik, Berlin

Printed on acid-free paper

Springer is part of Springer Science+Business Media (www.springer.com)

Preface

This book presents recent experimental and theoretical advances in fluid dynamics and contains invited lectures and contributions presented at the International Enzo Levi Spring School 2011 held in the Instituto Nacional de Investigaciones Nucleares, 6–7 May 2011, and the XVI National Congress of the Fluid Dynamics Division of the Mexican Physical Society, held in Boca del Rio, Veracruz, Mexico, 25–29 October 2011.

The Spring School is organized every year in honour of Prof. Enzo Levi, a well known Mexican scientist that dedicated his research to the study of fluids. He was one of the founders of the Instituto de Ingeniería (Engineering Institute) of the Universidad Nacional Autónoma de México (UNAM), and of the Instituto de Tecnología del Agua (Institute for Water Technology) of the UNAM. He was the mentor of several generations of Mexican Engineers.

During the two day school, lectures are given by well known national and international scientists. In 2010 a wide variety of topics were presented, ranging from nonlinear dynamics and multiphase flow to star formation. About 50 researchers and a 100 graduate and undergraduate students, mostly from Mexican universities and institutes, attended the meeting.

The Annual Fluid Dynamics Congress has a different format. It lasts 5 days and has invited contributions and short oral presentations on original research. There is also a Gallery of Fluid Motion where photographs of special beauty and scientific interest compete. In 2010, the XV Meeting had about 70 attendees. The scope of this congress is very wide. It is traditionally held in parallel with the National Congress of Physics, with which we share one of the invited lectures. This year Prof. Nadine Aubry from Carnegie Melon University gave the main lecture on microfuidics. At the moment of the congress there was a large spill of oil in the Gulf of Mexico so one of the invited lectures was offered by an expert on the subject, Dr. Hermilo Ramírez from The Mexican Oil Institute. Dr. Luis Manuel Farfán from CICESE gave a talk on Tropical Cyclones in the Pacific Ocean and their impact in Mexico. The last invited lecture was given by Dr. Tereza Cavazos also from CICESE, on the challenges Mexico has to face due to the change of climate.

The short oral presentations are organized by themes: CFD, Geophysics, Astrophysics, Multiphase Flow, Porous Media, Viscous Flow, Heat Transfer, Rheology, Granular Flow and Viscous Flow.

The book is aimed to 4th year undergraduate and graduate students, and to scientists in the field of physics, engineering and chemistry that have interest in fluid dynamics from the experimental and theoretical point of view. The material includes recent advances in experimental and theoretical fluid dynamics and is adequate for both teaching and research. The invited lectures are introductory and avoid the use of complicated mathematics. The other selected contributions are also adequate to fourth year undergraduate and graduate students.

The editors are very grateful to the Institutions that made possible the realization of the International Enzo Levi Spring School and the XVI National Congress of the Fluid Dynamics Division of the Mexican Physical Society, especially the Consejo Mexiquense de Ciencia y Tecnología (COMECYT), the Consejo Nacional de Ciencia y Tecnología (CONACYT), the Sociedad Mexicana de Física, and the Instituto Nacional de Investigaciones Nucleares (ININ). We thank the support of Elías Micha Zaga and Jorge Antonio Villegas Rodríguez of the COMECYT, and José Raúl Ortiz Magaña and Luis Carlos Longoria Gándara of the ININ.

We acknowledge the help of the Edition Committee: Estela Mayoral Villa, Elizabeth Teresita Romero Gúzman, Eduardo de la Cruz Sánchez, Roberto Zenit, Sergio Cuevas, Abraham Medina, Fernando Gómez Ramírez, Marcos José Solache Ríos, Edmundo del Valle Gallegos, Arturo Olvera, Carlos Málaga and in particular Nora Isabel Pérez Quezadas, Roberto González Galán, and Salvador Galindo Uribarri for their important contribution to the final manuscript.

Mexico City, April 2011

Jaime Klapp
Anne Cros
Oscar Velasco Fuentes
Catalina Stern
Mario A. Rodríguez-Meza

Contents

Part III Multiphase Flow and Porous Media

Contributors

R. M. Aceves-Pérez Departamento de Ingeniería Mecatrónica, Universidad Politécnica de Puebla, Tercer Carril del Ejido Serrano S/N, San Mateo Cuanalá, Juan C. Bonilla, C.P. 72640 Puebla, Mexico

A. Aguilar-Corona Facultad de Ingeniería Mecánica, Universidad Michoacana de San Nicolás de Hidalgo, Francisco J. Mujica s/n, C.P. 58040 Morelia-Michoacan, Mexico

C. Aguilar-Espinosa UNAM, Colegio de Ciencias Humanidades, Cataratas y Llanura S/N, Jardines del Pedregal, C.P. 04500 Coyoacan, México D.F., Mexico

C. E. Alvarado-Rodríguez Campus Guanajuato, División de Ciencias Naturales y Exactas, Universidad de Guanajuato, Noria Alta S/N Guanajuato, Mexico

R. F. Arellano Castro Departamento de Física, Universidad de Guadalajara, Av. Revolución 1500, Col. Olímpica, 44430 Guadalajara, Jalisco, Mexico

G. Arreaga-García Centro de Investigación en Física, Universidad de Sonora, Blvd. Rosales y Blvd. Encinas, s/n, Col. Centro, 83000 Hermosillo, Sonora, Mexico, e-mail: garreaga@cajeme.cifus.uson.mx

G. Ascanio Instituto de Investigaciones en Materiales, Universidad Nacional Autónoma de México, Ciudad Universitaria, C. Exterior s/n, 04510 Coyoacan, México D.F., Mexico

A. C. Barbosa-Aguiar Faculdade de Ciências da Universidade de Lisboa, Instituto de Oceanografia, Campo Grande, 1749-016 Lisboa, Portugal

S. A. Baz-Rodríguez Process and Hydraulics Engineering Department, Universidad Autónoma Metropolitana – Iztapalapa, San Rafael Atlixco 186, Col. Vicentina, C.P. 09340 Mexico City, Mexico, e-mail: bazrodriguez@gmail.com

O. C. Benítez-Centeno Centro Nacional de Investigación y Desarrollo Tecnológico, Prolongación Av. Palmira esq. Apatzingan, Col. Palmira, 62490 Cuernavaca, Morelos, Mexico, e-mail: omarcbc@gmail.com

Instituto Tecnológico de Zacatepec, Calzada del Tecnológico No. 27, 62780 Zacatepec, Morelos, Mexico

I. Camarillo-R Departamento de Física, Laboratorio de Crecimiento de Cristales, Universidad Autónoma Metropolitana, Iztapalapa, Mexico

E. Cañeda-Guzmán Departamento de Física, Universidad Autónoma Metropolitana, 09340 Iztapalapa, Mexico D.F., Mexico

J. A. Castillo Centro de Investigación en Energía, Universidad Nacional Autónoma de México, Privada Xochicalco S/N Col. Centro, AP 34, C.P. 62580 Temixco, Morelos, Mexico

F. Castillo-Flores Departamento de Física, Universidad de Guadalajara, Av. Revolución 1500, Col. Olímpica, 44430 Guadalajara, Jalisco, Mexico

T. Cavazos Departamento de Oceanografía Física, Centro de Investigación Científica y de Educación Superior de Ensenada Ensenada, Baja California, Mexico, e-mail: tcavazos@cicese.mx

O. Cazarez-Candia Instituto Mexicano del Petróleo, Eje Central Lázaro Cárdenas, Norte 152 San Bartolo Atepehuacan, C.P. 07730 Gustavo A. Madero, Distrito Federal, Mexico, e-mail: ocazarez@imp.mx

Instituto Tecnológico de Zacatepec, Calzada del Tecnológico No. 27, 62780 Zacatepec, Morelos, Mexico

C. Centeno-Reyes Eje Central Lázaro Cárdenas, Instituto Mexicano del Petróleo, Norte 152 San Bartolo Atepehuacan, C.P. 07730 Gustavo A. Madero, Distrito Federal, Mexico, e-mail: ccenteno@imp.mx

O. Cortés-Aburto Departamento de Ingeniería Mecatrónica, Universidad Politécnica de Puebla, Tercer Carril del Ejido Serrano S/N, San Mateo Cuanalá, Juan C. Bonilla, C.P. 72640 Puebla, Mexico, e-mail: obedca@uppuebla.edu.mx

A. J. C. Crespo Grupo de Física de la Atmósfera, Universidad de Vigo Ourense, Spain

A. Cros Departamento de Física, Universidad de Guadalajara, Av. Revolución 1500, Col. Olímpica, 44430 Guadalajara, Jalisco, Mexico, e-mail: anne@astro.iam.udg.mx

R. Chicharro-S Departamento de Física, Laboratorio de Fluidos Zacatecas, Mexico

E. de la Cruz-Sánchez Instituto Nacional de Investigaciones Nucleares, Carretera México-Toluca s/n, La Marquesa, 52750 Ocoyoacac, Estado de México, Mexico, e-mail: eduardo.delacruz@inin.gob.mx

E. Díaz-Herrera Departamento de Física, Universidad Autónoma Metropolitana, 09340 Iztapalapa, México D.F., Mexico, e-mail: diaz@xanum.uam.mx

A. B. Domínguez-Gómez Instituto Tecnológico de Ciudad Madero Tamaulipas, Mexico

R. Duarte-Pérez Instituto Nacional de Investigaciones Nucleares, Carretera México-Toluca s/n, La Marquesa, 52750 Ocoyoacac, Estado de México, Mexico, e-mail: ricardo.duarte@inin.gob.mx

C. Eloy Institut de Recherche sur les phénomènes Hors Equilibre, UMR 6594 CNRS – Aix-Marseille Université, 49 rue Joliot Curie, 13384 Marseille Cedex 13, France

L. M. Farfán Centro de Investigación Científica y de Educación Superior de Ensenada B.C., Unidad La Paz, Miraflores 334, B.C.S. 23050 La Paz, Mexico, e-mail: farfan@cicese.mx

B. Figueroa-Espinoza LIPC-Instituto de Ingeniería, Universidad Nacional Autónoma de México campus Sisal Yucatan, Mexico

S. Galindo Instituto Nacional de Investigaciones Nucleares, Carretera México-Toluca s/n, 52750 Ocoyoacac, Estado de México, Mexico, e-mail: salvador.galindo@inin.gob.mx

M. Gómez-Gesteira Grupo de Física de la Atmósfera, Universidad de Vigo Ourense, Spain

F. Gómez-Ramírez Facultad de Ciencias, Universidad Autónoma del Estado de México El cerrillo Piedras Blancas, Mexico

Z. I. González-Acevedo Instituto Nacional de Investigaciones Nucleares, Carretera México-Toluca s/n, 52750 Ocoyoacac, Estado de México, Mexico

R. González-Galán Facultad de Ciencias, Universidad Autónoma del Estado de México, 50200 El cerrillo Piedras Blancas, Estado de México, Mexico, e-mail: rgonzalez470@yahoo.com.mx

A. Guerrero-Zuñiga Petroleum Mexican Institute Mexico City, Mexico, e-mail: aguerrer@imp.mx

J. E. V. Guzmán Instituto de Investigaciones en Materiales, Universidad Nacional Autónoma de México, Ciudad Universitaria, C. Exterior s/n, 04510 Coyoacan, México D.F., Mexico, e-mail: eguzman@iim.unam.mx

A. Hernández-Almada Departamento de Física, Centro de Investigación y de Estudios Avanzados del IPN, A.P. 14-740, 07000 Mexico City, Mexico

J. Hernández-Cordero UNAM, Instituto de Investigaciones en Materiales, Ciudad Universitaria, Apartado Postal 70-360, 04510 Delegación Coyocán, Mexico D.F., Mexico, e-mail: jhcordero@iim.unam.mx

S. Hernández-Zapata Facultad de Ciencias, UNAM, Ciudad Universitaria, Circuito exterior s/n, 04520 Coyoacan, México D.F., Mexico

J. Klapp Instituto Nacional de Investigaciones Nucleares, Carretera México-Toluca s/n, La Marquesa, 52750 Ocoyoacac, Estado de México, Mexico, e-mail: jaime.klapp@inin.gob.mx

T. K. Levy-C UNAM, Colegio de Ciencias Humanidades, Cataratas y Llanura S/N, Jardines del Pedregal, C.P. 04500 Coyoacan, México D.F., Mexico

L. C. Longoria-Gandara Instituto Nacional de Investigaciones Nucleares, Carretera México-Toluca s/n, La Marquesa, 52750 Ocoyoacac, Estado de México, Mexico

E. J. López-Sánchez Facultad de Ciencias, UNAM, Ciudad Universitaria, Circuito exterior s/n, 04520 Coyoacan, México D.F., Mexico, e-mail: lsej@ciencias.unam.mx

A. López-Villa SEPI ESIME Azcapotzalco, Instituto Politécnico Nacional, Av. de las Granjas 682, Col. Sta. Catarina, C.P. 02250 Azcapotzalco, México D.F., Mexico

T. Matos Departamento de Física, Centro de Investigación y de Estudios Avanzados del IPN, A.P. 14-740, 07000 Mexico City, Mexico

O. Masbernat Laboratoire de Génie Chimique, UMR CNRS/INP/UPS 5503, 5 rue Paulin Talabot BP1301, 31106 Toulouse, France

Ma. De J. Marín Allende Universidad Autónoma del Estado de México, Paseo Tollocan esq, Paseo Colon Toluca, Estado de México, Mexico, e-mail: q_l_o@hotmail.com

B. M. Marín-Santibáñez Escuela Superior de Ingeniería Química e Industrias Extractivas, Instituto Politécnico Nacional, U.P.A.L.M., Col. S. P. Zacatenco, C.P. 07738 Del. Gustavo A. Madero, México D.F., Mexico, e-mail: bmarin@ipn.mx

B. Marino Instituto de Física Arroyo Seco, Facultad de Ciencias Exactas, Universidad Nacional del Centro de la Pcia, de Buenos Aires, Pinto 399, B7000GHG Tandil, Argentina

E. Mayoral-Villa Instituto Nacional de Investigaciones Nucleares, Carretera México-Toluca s/n, La Marquesa, 52750 Ocoyoacac, Estado de México, Mexico, e-mail: estela.mayoral@inin.gob.mx

A. Medina Departamento de Ciencias Básicas, UAM Azcapotzalco, Laboratorio de Sistemas Complejos, Av. San Pablo 180, C.P. 02200 Azcapotzalco, México D.F., Mexico, e-mail: abraham_medina_ovando@yahoo.com

M. E. Mejía-Marín Departamento de Física, Universidad de Guadalajara, Av. Revolución 1500, Col. Olímpica, 44430 Guadalajara, Jalisco, Mexico

L. Molina-Ezpinoza Instituto Mexicano del Petróleo, Eje Central Lázaro Cárdenas, Norte 152 San Bartolo Atepehuacan, C.P. 07730 Gustavo A. Madero, Distrito Federal, Mexico, e-mail: lmespino@imp.mx

D. J. Montoya-Hernández Instituto Mexicano del Petróleo, Eje Central Lázaro Cárdenas, Norte 152 San Bartolo Atepehuacan, C.P. 07730 Gustavo A. Madero, Distrito Federal, Mexico, e-mail: djmontoy@imp.mx

J. A. Moreno-Razo Departamento de Física, Universidad Autónoma Metropolitana, 09340 Iztapalapa, México D.F., Mexico

S. L. Moya-Acosta Centro Nacional de Investigación y Desarrollo Tecnológico., Prolongación Av. Palmira esq. Apatzingan, Col. Palmira, 62490 Cuernavac, Morelos, Mexico

J. E. Ochoa Facultad de Ciencias, Universidad Nacional Autónoma de México, Ciudad Universitaria, C. Exterior s/n, 04510 Coyoacan, Mexico D.F., Mexico

G. E. Ovando Chacón Instituto Tecnológico de Veracruz, Depto. de Metal Mecánica y Mecatrónica, Calzada Miguel A. de Quevedo 2779, Col. Formando Hogar, 91860 Veracruz, Mexico, e-mail: geoc@itver.edu.mx

S. L. Ovando Chacón Instituto Tecnológico de Tuxtla Gutierrez, Depto. de Química y Bioquímica, Carretera Panamericana Km. 1080, Tuxtla Gutierrez, 29000 Chiapas, Mexico, e-mail: ovansandy@hotmail.com

F. Peña-Polo Instituto de Venezolano de Investigaciones Científicas (IVIC), Centro de Física, Apartado Postal, 20632 Caracas 1020-A, Venezuel, e-mail: franklin.pena@gmail.com

A. C. Pérez-Guerrero-N Área de Mecánica Estadística, Departamento de Física, Universidad Autónoma Metropolitana, Iztapalapa, Mexico, e-mail: acpgn@yahoo.com

J. Pérez-González Laboratorio de Reología, Escuela Superior de Física y Matemáticas, Instituto Politécnico Nacional, U.P.A.L.M, Col. S. P. Zacatenco, C.P. 07730 Del. Gustavo A. Madero, México D.F., Mexico, e-mail: jpg@esfm.ipn.mx

S. Piedra Center for Energy Research, Universidad Nacional Autónoma de México, 62580 Temixco, Morelos, Mexico, e-mail: sapig@cie.unam.mx

R. Pimentel-Domínguez Instituto de Investigaciones en Materiales, UNAM, Ciudad Universitaria, Apartado Postal 70-360, 04510 Coyoacan, México D.F., Mexico, e-mail: vetuasaber@ciencias.unam.mx

J. C. Prince-Avelin Instituto Tecnológico de Tuxtla Gutierrez, Depto. de Química y Bioquímica, Carretera Panamericana Km. 1080, 29000 Tuxtla Gutierrez, Chiapas, Mexico, e-mail: jcpa@itv.edu.mx

M. A. Ramírez-C Center for Energy Research, Universidad Nacional Autónoma de México, 62580 Temixco, Morelos, Mexico, e-mail: marac@cie.unam.mx

H. Ramírez-León Petroleum Mexican Institute Mexico, Mexico, e-mail: hrleon@imp.mx

C. Ramírez-Guerra Facultad de Ciencias, Universidad Nacional Autónoma de México, Ciudad Universitaria, C. Exterior s/n, 04510 Coyoacan, México D.F., Mexico

E. Ramos Center for Energy Research, Universidad Nacional Autónoma de México, 62580 Temixco, Morelos, Mexico, e-mail: erm@cie.unam.mx

J. L. Reyes-de la Cruz Departamento de Ingeniería Mecánica, Instituto Superior Minero Metalúrgico Moa, Cuba

L. R. Reyes-Gutiérrez Instituto Potosino de Investigación Científica y Tecnológica (IPICYT), 78216 San Luis Potosí S.L.P., Mexico, e-mail: raymundo.reyes@ipicyt.edu.mx

R. Rodríguez-Castillo Instituto de Geofísica, Universidad Nacional Autónoma de México Mexico City, Mexico

F. Rodríguez-González Escuela Superior de Ingeniería Química e Industrias Extractivas, Instituto Politécnico Nacional, U.P.A.L.M., Col. S. P. Zacatenco, C.P. 07738 Del. Gustavo A. Madero, México D.F., Mexico

M. A. Rodríguez-Meza Departamento de Física, Instituto Nacional de Investigaciones Nucleares, Km 36.5 Carretera México-Toluca, 52750 Ocoyoacac, Estado de México, Mexico, e-mail: marioalberto.rodriguez@inin.gob.mx

J. A. Rodríguez-Romero Departamento de Física, Universidad de Guadalajara, Av. Revolución 1500, Col. Olímpica, 44430 Guadalajara, Jalisco, Mexico

J. C. Rodríguez-Sierra Departamento de IPH Av. San Rafael Atlixco No. 186, Universidad Autónoma Metropolitana-Iztapalapa, Col. Vicentina, 09430 Mexico City, México D.F., Mexico, e-mail: jcrs@xanum.uam.mx

J. Rojas Centro de Investigación en Energía, Universidad Nacional Autónoma de México, Privada Xochicalco S/N Col. Centro, AP 34, C.P. 62580 Temixco, Morelos, Mexico

R. Rojas-Rodríguez Departamento de Ingeniería Mecatrónica, Universidad Politécnica de Puebla, Tercer Carril del Ejido Serrano S/N, San Mateo Cuanalá, Juan C. Bonilla, C.P. 72640 Puebla, Mexico

A. Romero-Arteaga CICESE Ensenada, Mexico, e-mail: anromero@cicese.mx

E. T. Romero-Guzmán Departamento de Química, Instituto Nacional de Investigaciones Nucleares, Carretera México-Toluca s/n, La Marquesa, 52750 Ocoyoacac, Estado de México, Mexico

J. C. Romero-Sierra Departamento de IPH Av. San Rafael Atlixco No. 186, Universidad Autónoma Metropolitana – Iztapalapa, Col. Vicentina, 09430 Mexico City, México D.F., Mexico, e-mail: jcrs@xanum.uam.mx

G. Ruíz Chavarría Facultad de Ciencias, UNAM, Ciudad Universitaria, Circuito exterior s/n, 04520 Coyoacan, México D.F., Mexico, e-mail: gruiz@servidor.unam.mx

D. A. Salas de León Instituto de Ciencias del Mar y Limnología, UNAM, Avenida Universidad 3000, Circuito exterior s/n, Ciudad Universitaria, 04510 Coyoacan, Mexico, e-mail: dsalas@servidor.unam.mx

M. Y. Salazar-Romero Facultad de Ciencias, Universidad Nacional Autónoma de México, Ciudad Universitaria, C. Exterior s/n, 04510 Coyoacan, México D.F., Mexico, e-mail: yayafisica@gmail.com

E. J. Sambriski Department of Chemistry and Biochemistry, Delaware Valley College, Doylestown Pennsylvania, 18901, USA, e-mail: Edward.Sambriski@delval.edu

D. Sámano Instituto de Investigaciones en Materiales, Universidad Nacional Autónoma de México, Ciudad Universitaria, C. Exterior s/n, 04510 Coyoacan, México D.F., Mexico

R. Sánchez Laboratorio de Reología, Escuela Superior de Física y Matemáticas, Instituto Politécnico Nacional, U.P.A.L.M., Col. S. P. Zacatenco, C.P. 07730 Del. Gustavo A. Madero, Mexico

R. Sanjuan-Galindo Centro de Ciencias Aplicadas y Desarrollo Tecnológico, Universidad Nacional Autónoma de México, Apdo. Postal 70-186, 04510 Mexico City, México D.F., Mexico

T. Santiago-Arce Posgrado en Ciencias del Mar y Limnología, UNAM Avenida Universidad 3000, Circuito exterior s/n, Ciudad Universitaria, 04510 Coyoacan, Mexico, e-mail: arcesant@gmail.com

L. Schouveile Institut de Recherche sur les phénomènes Hors Equilibre, UMR 6594 CNRS – Aix-Marseille Université, 49 rue Joliot Curie, 13384 Marseille, Cedex 13, France, e-mail: schouveiler@irphe.univ-mrs.fr

A. Servin-Martínez Instituto Tecnológico de Tuxtla Gutierrez, Depto. de Química y Bioquímica, Carretera Panamericana Km. 1080, 29000 Tuxtla Gutierrez, Chiapas, Mexico, e-mail: alser@hotmail.com

L. G. Di Sigalotti Instituto de Venezolano de Investigaciones Científicas (IVIC), Centro de Física, Apartado Postal 20632 Caracas 1020-A, Venezuela, e-mail: leonardo.sigalotti@gmail.com

C. Stern Facultad de Ciencias, Universidad Nacional Autónoma de México, Ciudad Universitaria, C. Exterior s/n, 04510 Coyoacan, México D.F., Mexico, e-mail: catalina@ciencias.unam.mx

A. Soria Universidad Autónoma Metropolitana – Iztapalapa, Departamento de IPH Av. San Rafael Atlixco No. 186, Col. Vicentina, 09430 Iztapalapa, México D.F., Mexico, e-mail: asor@xanum.uam.mx

E. Soto Centro de Ciencias Aplicadas y Desarrollo Tecnológico, Universidad Nacional Autónoma de México, Apartado Postal 70-186, 04510 Mexico D.F., Mexico

L. Thomas Instituto de Física Arroyo Seco, Facultad de Ciencias Exactas, Universidad Nacional del Centro de la Pcia, de Buenos Aires, Pinto 399, B7000GHG Tandil, Argentina

R. Tovar Centro de Investigación en Energía, Universidad Nacional Autónoma de México, Privada Xochicalco S/N Col. Centro, AP 34, C.P. 62580 Temixco, Morelos, Mexico

L. Trujillo Instituto de Venezolano de Investigaciones Científicas (IVIC), Centro de Física, Apartado Postal 20632, Caracas 1020-A, Venezuela, e-mail: leonardo.trujillo@gmail.com

C. A. Vargas Laboratorio de Sistemas Complejos, Departamento de Ciencias Básicas, UAM Azcapotzalco, Av. San Pablo 180, C.P. 02200 Azcapotzalco, Mexico D.F., Mexico

E. Vázquez-L Laboratorio de Fluidos, Departamento de Física San Luis, Argentina

O. Velasco-Fuentes CICESE Ensenada, Mexico, e-mail: ovelasco@cicese.mx

J. R. Vélez-Cordero Instituto de Investigaciones en Materiales, Universidad Nacional Autónoma de México, Ciudad Universitaria, C. Exterior s/n, 04510 Coyoacan, México D.F., Mexico

C. Verde-Rodarte Instituto de ingeniería, UNAM, C.P. 04510 Coyoacan, México D.F., Mexico, e-mail: cverder@iingen.unam.mx

A. G. Vital-Ocampo Centro Nacional de Investigación y Desarrollo Tecnológico, Depto. de Mecánica, Interior Internado Palmira s/n, Col. Palmira, C.P. 62490 Cuernavaca, Morelos, Mexico, e-mail: agvital@yahoo.com

J. M. Zavala-Ake Instituto de Física, Universidad Nacional Autónoma de México Mexico City, Mexico

L. Zavala-Sansón Departamento de Oceanografía Física, Centro de Investigación Científica y de Educación Superior de Ensenada, Carretera Ensenada-Tijuana 3918, 22860 Ensenada, Baja California, Mexico

R. Zenit Instituto de Investigaciones en Materiales, Universidad Nacional Autónoma de México, Ciudad Universitaria, C. Exterior s/n, 04510 Coyoacan, México D.F., Mexico, e-mail: zenit@servidor.unam.mx

Part I
Invited Lectures

Flapping Plate(s)

Lionel Schouveiler and Christophe Eloy

Abstract The flutter that spontaneously appears when a flexible plate is immersed in a parallel flow is addressed both experimentally and theoretically. Linear stability of the plate is analyzed using a model of one-dimensional flutter coupled with a three-dimensional potential flow. The analysis leads to results in quantitative agreement with the experiments. The coupled flutter of parallel plates is also considered. A similar, but simplified, model shows that the problem is then reduced to a system of linearly coupled oscillators which is in agreement with the coupled flutter modes observed in the experiments.

1 Introduction

The flutter instability of flexible bodies due to their interaction with a fluid flow is encountered in many applications in domains as different as aeronautics (wing flutter), papermaking industry (where the continuous sheet of paper can undergoes flutter when traveling through drying cylinders leading to its breaking and then to a stop of the production) or biology, for example the snoring that is caused by the vibration of the soft palate interacting with the inspiratory flow. The flapping of a plate immersed in a parallel flow appears as a canonical example of such flow-induced vibrations whose simplicity allows to conduct well-controlled experiments as well as theoretical approaches. For these reasons this system has motivated numerous stability studies.

L. Schouveiler (✉) · C. Eloy
Institut de Recherche sur les phénomènes Hors Equilibre,
UMR 6594 CNRS—Aix-Marseille Université, 49 rue Joliot Curie,
13384 Marseille Cedex 13, France
e-mail: lionel.schouveiler@irphe.univ-mrs.fr

J. Klapp et al. (eds.), *Experimental and Theoretical Advances in Fluid Dynamics*, Environmental Science and Engineering, DOI: 10.1007/978-3-642-17958-7_1,

To our knowledge, Rayleigh (1879) was the first to mention this problem in his study devoted to jet instabilities. In his paper, the "plate" is an infinite discontinuity surface between two parallel inviscid flows, that is a zero mass–zero rigidity plate and it appears to be always unstable. Effect of finite chord L on the linear stability of a plate of infinite span H immersed in a parallel potential flow has been considered one century later, first by Kornecki et al. (1976), using the airfoil theory of Theodorsen (1935), then followed by numerous studies in which the plate is treated as an Euler–Bernoulli beam. Note that with the assumption of infinite span, the flow can be regarded as two-dimensional and is described by vortex lines parallel to the span distributed in the plate and possibly in the wake. The various theories mainly differ by the way they deal with the pressure boundary conditions at the plate leading and trailing edges. They all conclude that finite chord results in the existence of a critical velocity for the appearance of flutter. These two-dimensional flow studies (referred hereafter to as 2D theories) have been reviewed by Païdoussis (2004) or more recently by Eloy et al. (2007) and Shelley and Zhang (2011). In addition to these 2D theories devoted to finite chord–infinite span plates ($H \gg L$), the limit $H \ll L$ has also been considered (see e.g. the experimental and theoretical work by Lemaitre et al. 2005). In this limit case, the fluid force on the plate can be expressed by applying the slender body theory developed by Lighthill (1960) in the context of the swimming of elongated fish.

The first extensive experimental works have been performed by Taneda (1968) using flags made of different kind of fabrics. He presented visualizations of the flow around the flags using smoke, and visualizations of the flutter modes performed with a stroboscope and a camera. Most of the studies cited above present also experimental results in parallel to the linear stability analyses.

Results of the different two-dimensional flow analyses have been compiled by Watanabe et al. (2002) and compared with those of various experimental studies. The compilation shows that all the 2D flow theories lead to predicted critical velocities close to each other. However, the comparison with experiments shows that such 2D flow approaches tend to strongly underestimate this velocity. This is one of the motivations for developing three-dimensional (3D) flow theories.

In the next section we shall present a linear stability analysis with a 3D flow approach in order to take into account the finite span of the plate and we will compare the results with those of experiments. We will show that the 3D flow description allows to explain the underestimate of the critical velocity by the 2D theories and to recover the threshold measured in the experiments. Before the concluding section, we will also investigate a system consisting in an assembly of parallel plates. Depending of the separation distance between flags, coupling of plate flutter can be observed.

2 Single Plate Flutter

2.1 Theoretical Approach

The mechanism of the flutter instability of a plate immersed in a parallel flow of velocity U is illustrated in Fig. 1. As soon as the plate undergoes a small lateral deflection a pressure difference appears between its two sides which tends to increase this deflection while the plate rigidity acts to return the plate to planar state.

In agreement with experimental observations the flapping is considered as one-dimensional, and the plate (of length L) is modeled by an Euler–Bernoulli beam. The flow is assumed to be potential in such a way that the flow load on the plate is only due to pressure. Then, according to the instability mechanism described above and neglecting effects of tension (due to viscosity or gravity for plate hanging vertically in a vertical descending flow) and fluid and material damping, the governing equation for the plate writes, using the coordinate system defined in Fig. 1

$$m\partial_t^2 h + D\partial_x^4 h + \Delta p = 0 \tag{1}$$

where $h(x, t)$ is the plate deflection, m is the mass per unit area of the plate, D its flexural rigidity per unit span and $\Delta p(x, y = 0, t)$ the pressure jump across the plate. Because of the flow antisymmetry with respect to the plate plane $y = 0$, $\Delta p = 2\ p(x, y = 0^+, t)$ where $p(x, y = 0^+, t)$ is the pressure perturbation on the plate on the side $y > 0$.

It should be pointed out that for the 2D flow theories that concern infinite span plates, the flow depends on the two space variables x and y and then the pressure jump Δp depends indeed only on x (and t), it will be noted in the following Δp_{2D}. But in the study presented here we are interested to investigate the effects of finite span, the flow can no longer be regarded as two dimensional and a three dimensional flow theory is presented. This means that the pressure field on the plate depends not only on x but also on the variable along the span direction z and in this case Δp in Eq. 1 stands for $\Delta p(x, t) = \langle \Delta p \rangle_z$ the pressure jump across the plate averaged along the span H.

In this study we consider a plate clamped at the leading edge ($x = 0$) and free at the trailing edge ($x = L$) such that the boundary conditions for the deflection h are $h(0) = \partial_x h(0) = 0$ and $\partial_x^2 h(L) = \partial_x^3 h(L) = 0$.

The pressure term Δp has now to be determined. For this purpose, the fluid problem is considered and we recall that we are concerned here with the potential flow limit. Then the flow perturbation due to the plate can be fully described by a vorticity distribution γ. In the framework of the linear theory we consider vortex lines that lie in the plane $y = 0$, in the plate and in the wake. For the 2D flow theories these vortex lines are parallel to the z-axis whereas they have a Π-shape in the 3D theory as shown in Fig. 1. The pressure jump Δp is

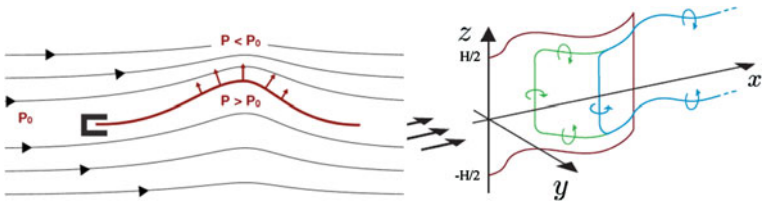

Fig. 1 Mechanism of the flutter instability (*left*) and flow description (*right*)

deduced from the vorticity distribution $\gamma(x, z, t)$ by means of the unsteady Bernoulli equation

$$\partial_x \Delta p = \rho(\partial_t + U\partial_x)\gamma \tag{2}$$

where ρ is the fluid density. In the wake, the vorticity distribution is of the form of a progressive wake $\gamma_0(z)e^{i(kx-\omega t)}$ with wave velocity $\omega/k = U$ that is the wake is constituted of vortex lines advected at the flow velocity. From Eq. 2 it is seen that this vorticity distribution ensures the continuity of the pressure $\Delta p = 0$ outside of the plate in the plane $y = 0$.

In order to determine the vorticity distribution in the plate, we consider the kinematic condition of continuity of the normal velocity on the plate that can be written under the following form

$$\int \langle\gamma(\xi)\rangle K(x-\xi)d\xi = (\partial_t + U\partial_x)h \tag{3}$$

where $(\partial_t + U\partial_x)h$ is the normal plate velocity in the fluid frame. In order to have a unique solution this equation is completed by the Kutta condition at the trailing edge $\Delta p(L) = 0$.

The kernel function K in Eq. 3 gives the influence of the vorticity line parallel to z and located at ξ on the fluid velocity component parallel to y at x. We have shown that slender body theory results in $K(X) = \mathrm{sgn}(X)/(\pi H)$ whereas if we return to infinite span plates ($H/L \gg 1$) that is 2D flow theories with a distribution of vortex lines parallel to the span, the kernel function writes $K(X) = 1/(2\pi X)$. And for any H, the approximate kernel $K(X) = 1/(2\pi X) + [1/(\pi H) - (1/\pi - 1/8)/(H + |H|)]$ $\mathrm{sgn}(X)$ is valid.

The linear stability of the plate is then analyzed using a Galerkin decomposition for the plate deflection h:

$$h(x,t) = \sum_{n=1}^{\infty} a_n y_n(x) e^{i\omega t} \tag{4}$$

where $(y_n)_{n\,=\,1\ldots\infty}$ is the orthogonal basis formed by the eigenmodes of a clamped-free beam (in order to satisfy the proper boundary conditions) in vacuo, and ω is the complex frequency.

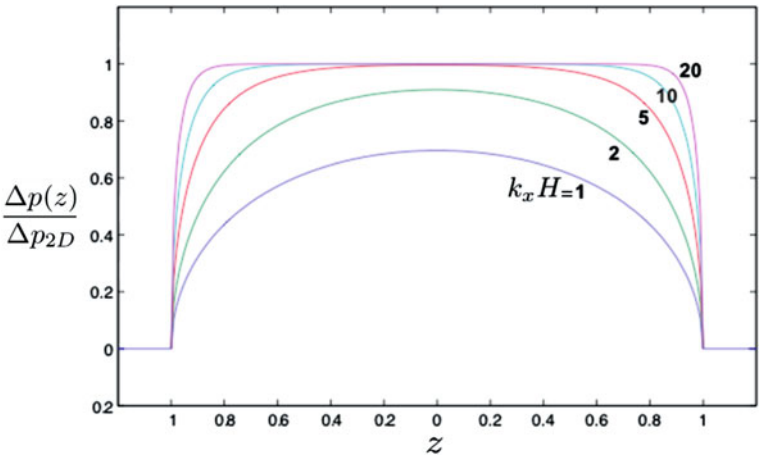

Fig. 2 Repartition of the pressure jump along the span calculated with the 3D flow theory for different values of k_xH (z is nondimensionalized by the half-span $H/2$)

The problem being linear, we can process mode by mode. For a given Galerkin mode, Eq. 3 is inverted and the result is inserted into Eq. 2 to deduce the corresponding pressure jump that is itself inserted into the governing equation for the plate deflection (Eq. 1). This latter yields then to an eigenvalue problem for the complex frequency ω where the eigenmodes are the the flutter instability modes of the plate.

All the technical details of this 3D flow approach, and in particular the deduction of the approximate kernel function and of the integral equation for the vorticity distribution (Eq. 3) can be found in Eloy et al. (2007). In Eloy et al. (2008) an asymptotic form of this model valid for large, but finite, span has also been presented.

The plate becomes unstable at the critical value of the flow velocity U for which one of the instability modes has a positive growth rate (a negative imaginary part of the frequency ω).

The results of the linear stability analysis that gives the critical velocity for the appearance of flutter, the flutter modes and their frequency (real part of ω) will be presented together with experimental results in the next section.

Figure 2 shows the repartition of the pressure jump $\Delta p(z)$ across the plate as calculated with the present 3D flow theories for different values of the span H nondimensionalized with $\lambda_x/(2\pi) = k_x^{-1}$ (where λ_x is the wavelength of the flutter mode). For comparison, the pressure jump is scaled with its value for infinite span that is obtained with the 2D flow approach. For long spans, $\Delta p(z)$ tends towards a uniform repartition with a value of one, that is tends towards the value calculated with the 2D flow approach. For smaller spans the pressure jump repartition is elliptic with a maximum always smaller than 1. This shows the tendency of the 2D flow theories to overestimate the pressure jump. Recalling that the pressure jump is the destabilizing term this should result in an underestimate

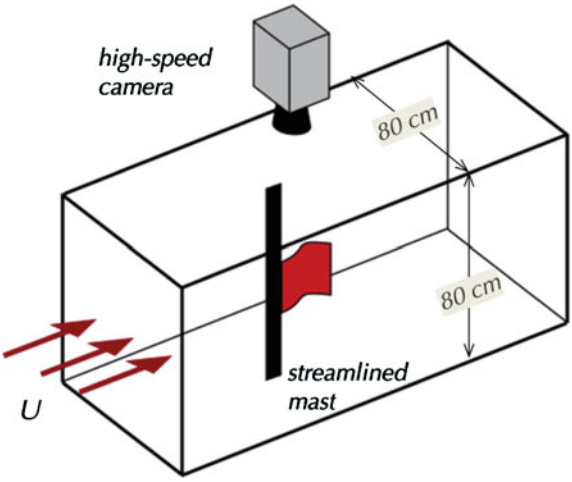

Fig. 3 Experimental setup

of the plate stability as it is emphasized in the results of the stability analysis presented in parallel with the experiments.

For the presentation of these results L and L/U are used as characteristic length and time in such a way that the system parameters reduce to the three following dimensionless numbers:

- the reduced velocity $U^* = UL\sqrt{m/D}$,
- the mass ratio $M^* = \rho L/m$,
- the aspect ratio $H^* = H/L$.

2.2 Experiments and Comparison with Theory

For comparison and validation of the model described above, experiments are performed in the setup schematically shown on Fig. 3. They are conducted in a low turbulence wind tunnel with a horizontal square test section of 80×80 cm^2. The flow velocity can be continuously varied and is measured by means of a Pitot tube. The plates are clamped inside a vertical streamlined mast. The experiments are performed with plates of different length L and span H and made of paper or polypropylene of different thickness resulting in a variety of mass per unit area m and rigidity D.

The successive positions of the upper plate edge during flutter are recorded with a high speed camera. The flutter frequency being moderate and always less than 50 Hz, the camera is operating at a maximum of 300 images per second.

For a given plate (L, H, m and D fixed), an experiment consists in increase slowly from 0 the flow velocity U. The plate is stable at small velocity and flutter takes place spontaneously at a critical value. We continue to increase U well above

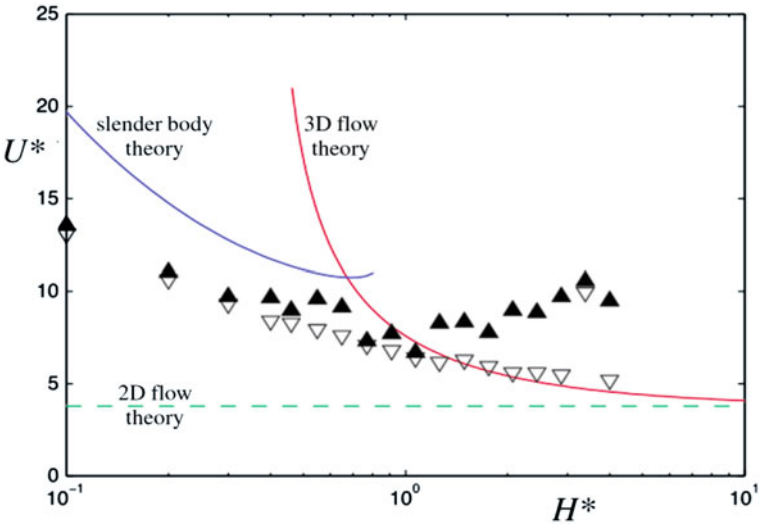

Fig. 4 Critical velocities as function of H^* for $M^* = 0.645$: experimental results for increasing (▲) and decreasing (▽) velocity and comparison with theories

this critical value, recording the flutter with the camera at each step. In order to detect a possible hysteresis cycle, U is then decreased until to the plate returns to the stable state. A difference between the critical values obtained increasing and decreasing the flow velocity is observed which is indicative of a hysteretical behavior. This point is still a subject of investigation and will be briefly discussed in the concluding section.

The values of the critical velocity are plotted in Fig. 4 for plates of mass ratio $M^* = 0.645$ and various aspect ratios H^*. The value of M^* is kept constant meaning that the plate length L is constant while the span H is varied to change H^*. For comparison, the theoretical values calculated with the 3D and 2D flow approaches and with the slender body approximation are also plotted. The 3D flow theory is clearly the missing link between the 2D and the slender body theories. The critical velocity appears as a monotonically decreasing function of H^* and, in agreement with the discussion concluding the previous section, the thresholds calculated with 3D flow theory are always larger than the values computed from 2D flow theories. The experimental values obtained for decreasing flow velocity appears to be well predicted by the present 3D flow linear stability analysis.

For a given material, the flutter modes at the threshold depend on the plate length L. Figure 5 shows superimposed views of the plate during one flutter period for the two modes we can observe in the experiments.

The experiments, in agreement with the analysis, show that for small lengths, the loss of stability of the plate leads to a single-neck flutter mode (the necks are marked by the arrows in Fig. 5), and when L is increased a double-neck mode is first destabilized. Experimental and theoretical modes are calculated for the same

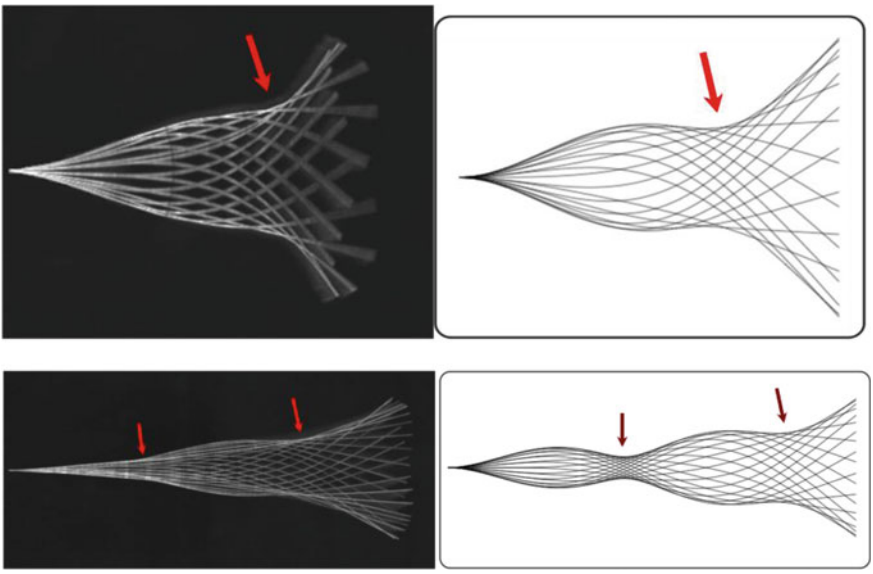

Fig. 5 Flutter modes at the threshold: comparison experiment (*left*)/theory (*right*) for $M^* = 0.74$, $H^* = 1$, $U^* = 8.1$ (*top*) and $M^* = 1.94$, $H^* = 1$, $U^* = 10.9$ (*bottom*)

parameters, the corresponding flutter frequencies (non-dimensionalized with U/L) are found to be, for the single-neck mode $\omega^* = 1.8$ and 2.0 in the experiment and in the theory respectively, and $\omega^* = 2.5$ and 3.5 for the double-neck mode.

It should be pointed out first that, the analysis being linear, the amplitude of the calculated flutter modes is arbitrary, and second, that the zero neck mode is never observed in the experiments and similarly never unstable in the analysis. Observation of higher order flutter modes (with three or more necks) would require longer plate or lighter material. But this would result in the plate sagging owing to its weight due to gravity, and thus a non-planar plate as a basic state.

3 Coupled Flutter of Parallel Plates

The coupling of plate flutter that can occur when a number of parallel plates are immersed in an axial flow has been studied. Such a situation is encountered in plate heat exchangers that consist in fluid flow passing through an assembly of parallel plates, this allows to get large surface of exchange between the plates and the fluid and thus to increase the heat transfer.

The case of two plates has been the object of numerous studies which report different coupling modes that mainly depend on the separation distance between the two plates. When the separation distance is increased, the plates flap first in

phase then out of phase, while there is no coupling when the separation distance is large enough. These kinds of interactions have been observed in the experiments of Zhang et al. (2000) performed with filaments in a flowing soap film, and confirmed by the numerical simulations of Zhu and Peskin (2003); Farnell et al. (2004); Huang et al. (2007) or, more recently, Wang and Yin (2010). Jia et al. (2007) have analyzed the linear stability of the two-plate system assuming infinite plates in a potential flow, while in their analysis Guo and Païdoussis (2000) and Michelin and Llewellyn Smith (2009) have considered the finite size of the plates.

In the present study we perform experiments with two, three and four plates and compare the results with a linear stability analysis that generalizes the approach of Jia et al. (2007).

The experiments are performed in the same wind tunnel with the high-speed camera as previously described. The plates are clamped in vertical parallel masts separated by a distance d that can be changed. In order to limit three-dimensional flow (especially when two neighbor plates flap out-of-phase) the plate assembly is confined between two horizontal plates, made of transparent material for the visualizations, with a gap between the plate edge and these confinement plates smaller than 1 mm.

In addition to the three parameters of the single plate problem U^*, M^* and H^*, the dimensionless separation $d^* = d/L$ defined a fourth parameter for the plate assembly. For this study we only use plates made of polypropylene of mass per unit area $m = 0.44$ kg/m^2 and flexural rigidity $D = 9.7 \times 10^{-3}$ N m and the plate span H is fixed to 0.1 m. The plate length L is varied from 0.1 to 0.25 m and the separation distance d can be changed by step of 0.02 m.

A very simplified analysis is conducted to study the linear stability of an assembly of n plates. It consists in considering the plates as infinite both in span and length. With this latter assumption, the one-dimensional plate deflections can be assumed to be propagative waves, thus for the ith plate (see the sketch of the system in Fig. 6) the deflection reads

$$y_i(x,t) = Y_i e^{i(kx-\omega t)} \tag{5}$$

and is governed by the Euler–Bernoulli equation (Eq. 1) in which the pressure jump Δp_i is deduced from the perturbation potentials ϕ_i and ϕ_{i+1} on both side of the plate through the unsteady Bernoulli equation. The potential ϕ_i being solution of the Laplace equation with appropriate kinematic conditions on the ith and $(i-1)$th plates.

Details of this analysis can be found in Schouveiler and Eloy (2009), we show that the n-plate problem is then reduced to the following linear system for the complex amplitude vector $\boldsymbol{Y} = (Y_i)_{i=1,\ldots,n}$

$$\mathcal{M}\boldsymbol{Y} = 0 \tag{6}$$

where $\mathcal{M}$ is a $n \times n$ tridiagonal matrix

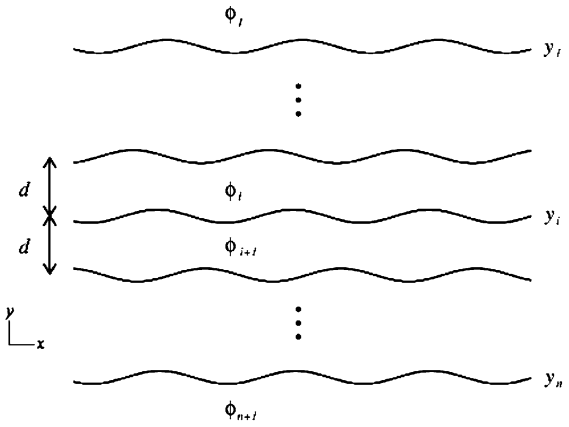

Fig. 6 Schema of the plate assembly

$$\mathcal{M} = \begin{pmatrix} \alpha & b & 0 & \cdots & & 0 \\ b & a & b & & & \vdots \\ 0 & \ddots & \ddots & \ddots & & 0 \\ \vdots & & & b & a & b \\ 0 & & \cdots & 0 & b & \alpha \end{pmatrix} \tag{7}$$

where α, a and b depend on the problem parameters ω, k, m, D, ρ, U and d.

Thus this approach reduces the problem of the coupled flutter of parallel plates to a system of oscillators linearly coupled to their first neighbors.

This very simplified analysis does not allow quantitative comparisons but in agreement with the result above the experiments with two, three and four plates have shown the different coupling modes of linear oscillators (Fig. 7). For each mode, we present a snapshot and a space–time diagram to illustrate the dynamics. These diagrams are built by stacking a video line, transverse to the flow at one-half of the plate length, extracted from the successive video frames. For all these diagrams we plot a period of 1 s.

It should be pointed out that in all cases the first mode to be destabilized is the fastest mode for which two adjacent plates flap out-of-phase. The other coupled modes are observed for larger flow velocities and thus are a result of a non linear selection that cannot be captured by a linear model.

4 Conclusions and Perspectives

We have studied the flapping of one or more plates due to the interaction with a parallel fluid flow. We developed simple models that take into account the physical mechanisms involved in the appearance of flutter of a plate immersed in an axial flow. In these models, the plate is considered as an Euler–Bernoulli beam and the flow as

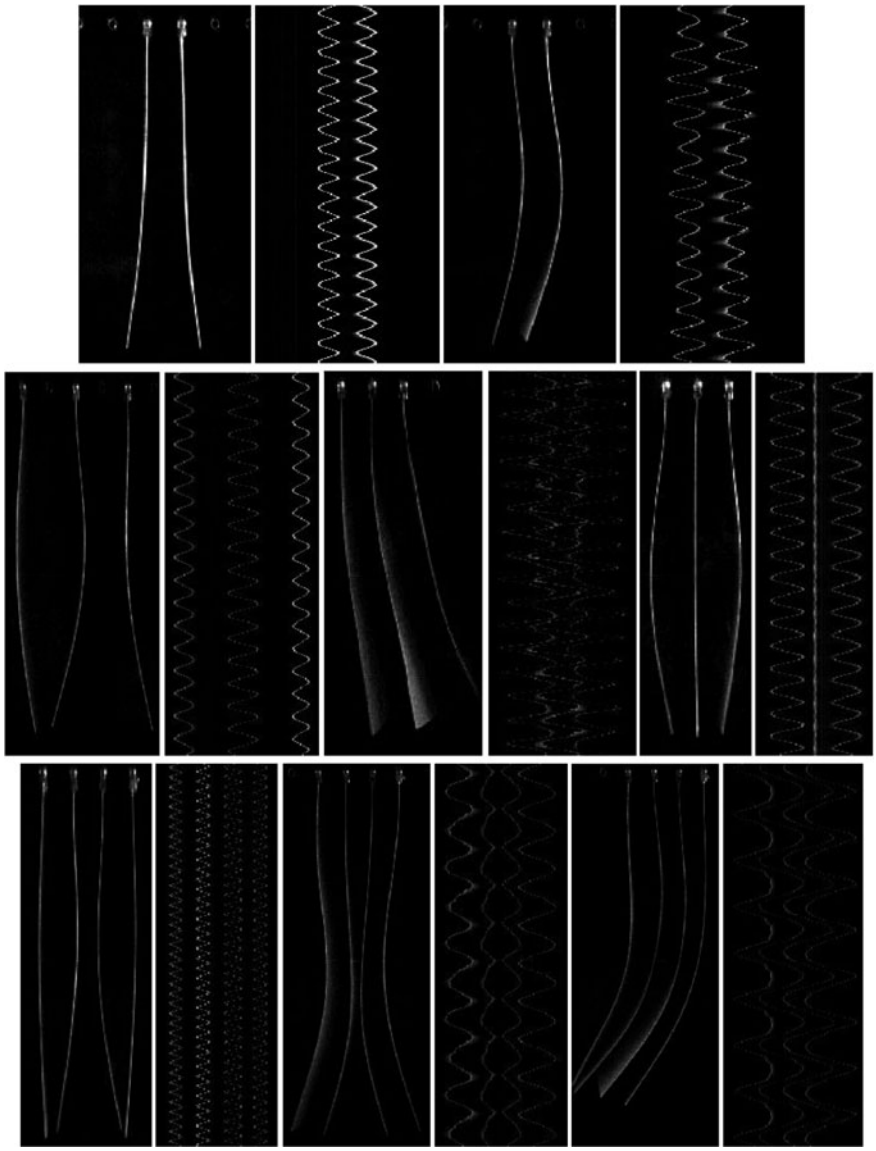

Fig. 7 Experimental coupling modes for two (*top*), three (*middle*) and four (*bottom*) plates

potential. In agreement with our experimental observations at (or close to) threshold the flutter is treated as one-dimensional while the flow is three-dimensional. We showed that this later point allows to reconcile experimental and theoretical results. In spite of their simplicity these models allow to predict with a good accuracy the instability threshold and the resulting flutter modes at low cost when compared to direct numerical simulations.

In spite of the large number of studies that have addressed the plate flutter instability, the nature of the bifurcation giving rise to this instability is still a controversial subject. Indeed in all experiments a large hysteresis is reported that could be indicative of a subcritical bifurcation, as mentioned in Sect. 2.2, while two-dimensional simulations exhibit either a supercritical bifurcation or a much smaller hysteretic cycle. We presently perform experiments to show that these hysteric cycles are mainly due to planarity defects of the plates inherent to all experimental works. Undesired plate deflections are also driven by gravity (specially for long or light plates) for experiments conducted in horizontal wind tunnel as it is the case for the present study. Such defects can result in a plate curvature along the span and then lead to a drastic increase of the flexural rigidity and thus of the stabilizing term.

References

Eloy C, Souilliez C, Schouveiler L (2007) Flutter of a rectangular plate. J Fluids Struct 23:904–919

Eloy C, Lagrange R, Souilliez C, Schouveiler L (2008) Aeroelastic instability of cantilevered flexible plates in uniform flow. J Fluid Mech 611:97–106

Farnell DJJ, David T, Barton DC (2004) Coupled states of flapping flags. J Fluids Struct 19:29–36

Guo CQ, Païdoussis MP (2000) Analysis of hydroelastic instabilities of rectangular parallel-plate assemblies. ASME J Press Vessel Technol 122:502–508

Huang WX, Shin SJ, Sung HJ (2007) Simulation of flexible filaments in a uniform flow by the immersed boundary method. J Comput Phys 226:2206–2228

Jia LB, Li F, Yin XZ, Yin XY (2007) Coupling modes between two flapping filaments. J Fluid Mech 581:199–220

Kornecki A, Dowell EH, O'Brien J (1976) On the aeroelastic instability of two-dimensional panels in uniform incompressible flow. J Sound Vib 47:163–178

Lemaitre C, Hémon P, de Langre E (2005) Instability of a long ribbon hanging in axial air flow. J Fluids Struct 20:913–925

Lighthill MJ (1960) Note on the swimming of slender fish. J Fluid Mech 9:305–317

Michelin S, Llewellyn SG (2009) Linear stability analysis of coupled parallel flexible plates in an axial flow. J Fluids Struct 25:1136–1157

Païdoussis MP (2004) Fluid-structure interaction: slender structures and axial flow, vol 2. Elsevier Academic Press, New York

Rayleigh L (1879) On the instability of jets. Proc London Math Soc 10:4–13

Schouveiler L, Eloy C (2009) Coupled flutter of parallel plates. Phys Fluids 21:08703

Shelley MJ, Zhang J (2011) Flapping and bending bodies interacting with fluid flows. Annu Rev Fluid Mech 43:449–465

Taneda S (1968) Waving motions of flags. J Phys Soc Jpn 24:392–401

Theodorsen T (1935) General theory of aerodynamics instability and the mechanism of flutter. NACA Report 496

Wang SY, Yin XZ (2010) A numerical method to simulate the coupled oscillations of flexible structures in flowing fluids. Chin Sci Bull 55:3880–3888

Watanabe Y, Isogai K, Suzuki S, Sugihara M (2002) A theoretical study of paper flutter. J Fluids Struct 16:543–560

Zhang J, Childress S, Libchaber A, Shelley M (2000) Flexible filaments in a flowing soap film as a model for one-dimensional flags in a two-dimensional wind. Nature 408:835–839

Zhu LD, Peskin CS (2003) Interaction of two flapping filaments in a flowing soap film. Phys Fluids 15:1954–1960

Sky Dancer: A Complex Fluid-Structure Interaction

Anne Cros, Jesse Alexander Rodríguez Romero and Fernando Castillo Flores

Abstract Sky dancers are long vertical flexible tubes which fluctuate above an air blower. These systems involve fluid-structure interactions that can give rise to complex dynamics. Air flow which passes through the tube deforms the tube wall which in turn modifies the flow hydrodynamical properties, and so on. We present in this article an experiment which models a sky dancer. The blown air speed can be varied and tubes of low rigidity and of different dimensions are used. The critical values of the flow velocity for which each tube begins "dancing" are measured. Comparisons with previous theoretical studies conducted for much more rigid tubes (Païdoussis, J Sound Vib 33:267–294, 1970) allow us to show that for tubes of low rigidity, the mechanism of destabilization is different.

1 Introduction

One of the first studies about the instability of pipes conducting flows was published by Ashley and Haviland (1950) in an attempt to explain vibrations which appear in pipelines. For half a century, studies about this kind of system have become more and more numerous (Païdoussis 1998). Indeed, many practical applications can be modeled by this kind of system as, for example, pipelines or heat transfer systems used in aircraft engines and nuclear reactors. Other typical examples can be found in biomechanics as blood flows in veins or air flow in pulmonary alveolus. This kind of instability can also be observed in everyday life

A. Cros (✉) · J. A. R. Romero · F. C. Flores
Departamento de Física, Universidad de Guadalajara, Av. Revolución 1500 Col., Olímpica, 44430 Guadalajara, Jalisco, México
e-mail: anne@astro.iam.udg.mx

J. Klapp et al. (eds.), *Experimental and Theoretical Advances in Fluid Dynamics*, Environmental Science and Engineering, DOI: 10.1007/978-3-642-17958-7_2,

when we water the garden and let the pipe loose: if the flow is sufficient, the garden-hose will fluctuate, making snake-like undulations.

The sky dancers are another example of such an instability. Sky dancers are long flexible tubes, made with ripstop fabrics, which fluctuate in streets as advertising. They "dance" above an air blower to advertise a product.

Previous works about slender structures and axial flow interaction are extensively reviewed by Paidoussis (1998). We present here theoretical and experimental results related to the present work.

1.1 Theoretical Studies

Let consider a tube with mass per unit length m_t (kg/m) and flexural rigidity EI (N.m^2), where E is the Young's modulus of the material and I the second moment of inertia of the tube section. This pipe conducts a fluid and the mass of fluid contained per unit length of pipe is noted m_f. This fluid flows with velocity v in the pipe. Now let us call $w(x, t)$ the transversal displacement of the pipe from its vertical position, where x is the longitudinal coordinate (vertical ascending in the present study) and t is the time. If gravity, dissipation and pressurization effects are neglected and if air velocity v is considered as being constant, the governing equation for the pipe motion writes:

$$EI\frac{\partial^4 w}{\partial x^4} + m_f v^2 \frac{\partial^2 w}{\partial x^2} + 2m_f v \frac{\partial^2 w}{\partial x \partial t} + (m_f + m_t)\frac{\partial^2 w}{\partial t^2} = 0 \tag{1}$$

The first term corresponds to internal forces in the tube generated by the pipe flexural rigidity. These forces tend to make the tube return to its straight vertical position. The second term corresponds to the centrifugal force. Indeed $\partial^2 w/\partial X^2 \sim 1/R$, where R is the local curvature radius. This force is the same as the reaction generated by the flow on a curved rigid surface. It is directed towards the tube convex curvature and is destabilizing. The third term corresponds to the Coriolis force. Indeed $\partial w/\partial X \sim \theta$, where θ is the tube angle with respect to vertical, so that $\partial^2 w/\partial X \partial t \sim \Omega$, where $\Omega = \partial\theta/\partial t$ is the angular velocity of a tube element. The Coriolis force is always opposing the tube movement. The last term represents the inertial forces of the system pipe and fluid.

Theoretical studies (Gregory and Païdoussis 1966a; Païdoussis 1966, 1969; Païdoussis and Issid 1974) show that in case of cantilevers, the system is governed by three nondimensional parameters, the nondimensional velocity

$$u = \left(\frac{m_f}{EI}\right)^{1/2} Lv \tag{2}$$

the gravity parameter

$$\gamma = \frac{(m_f + m_t)L^3}{EI} g \tag{3}$$

and the mass ratio

$$\beta = \frac{m_f}{m_f + m_t} \tag{4}$$

Païdoussis (1970) takes the convention $\gamma > 0$ when the tube hangs and $\gamma < 0$ when the tube stands up. In this theoretical work, Païdoussis finds that for $0 < |\gamma| < 7.83$, the tube is stable for low values of flow velocities v and unstable above a threshold which depends upon β and γ. Nevertheless if the tube length is such that $7.83 < |\gamma| < 55.9$, the tube falls down because of its own weight for low velocity values. If velocity is increased the tube stands up for short enough tubes, then it fluctuates at higher velocities. For the longest tubes, the rising-up regime never happens and the air flow makes the tube fluctuate when the velocity is large enough.

The thresholds between the different regimes depend upon β and γ. The threshold u_{cf} for "fluttering" region is higher if β is greater. That is to say that it is more difficult to destabilize a slighter tube. Moreover, the stability curves delimiting the fluctuating region from the other ones are such that u_{cf} is a decreasing function of $|\gamma|$: a long tube is easier to destabilize than a short one.

1.2 Experimental Works

Experiments were conducted by Païdoussis (1963) and Gregory and Païdoussis (1966b) with horizontal pipes. Those authors used rubber and metal pipes, conveying air or water. Pipes of internal diameter from 1 to 13 mm and of thickness extending from 0.8 to about 3 mm were used. The pipe length was varied from 20 to 76 cm. We will see that our tubes have roughly the same lengths but have a greater diameter, a thinner wall, and a very low rigidity (very low Young modulus).

Those authors reported, particularly in the case of rubber pipes, hysteresis behavior: the pipe persisted oscillating below the threshold value when flow intensity was decreased. This suggests that the Hopf bifurcation is subcritical (Paidoussis 1998, p. 134).

We can also mention the experimental works with hanging pipes of Greenwald and Dugundji (1967) or Doaré and de Langre (2002). Nevertheless, results of the present study can only be compared to those of Païdoussis (1970) since this last study includes experiments with hanging and standing pipes. Only this last configuration is similar to the case investigated in this paper.

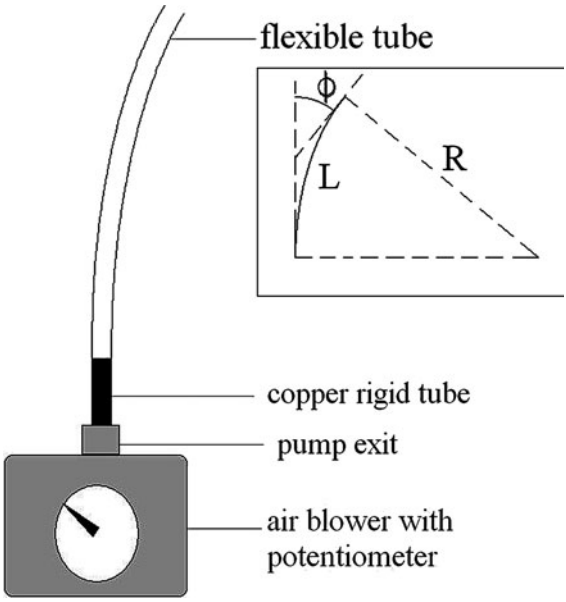

Fig. 1 Experimental system: the air blower is connected to 110 V, and a potentiometer permits variation of the air velocity. Copper cylinders of different diameters can be connected to the pump exit and the flexible tubes are made to adapt the copper tubes. The insert shows tube length L, deviation angle ϕ and curvature radius R

2 Experimental Device

The set-up used in the present experiments is schematically shown in Fig. 1. It consists in a centrifugal air blower coupled to a potentiometer to allow the variation of the pump power and thus of the air flow velocity. This velocity can be varied from 0 to 40 m/s if no charge is connected at the pump. The blower exit diameter is 4 cm and various copper connections are used to adjust to flexible tubes of different diameters. Tubes of diameters $d = 4.0$, 2.9, 2.2 and 1.5 cm have been used, their length L was varied from 0.35 to 1.0 m.

Flexible tubes are made with a plastic membrane. The measured characteristics for this material were a thickness e of 0.1 mm, a surface density ϱ_s of 0.083 kg/m^2 and a Young modulus E of 4.5 MPa. The tubes were made sealing the plastic membrane with heat, so that membrane was superimposed along the tube over less than 1 mm. In comparison to the sticking technique described in Castillo Flores and Cros (2009), the heat-sealing technique presently used allows to avoid a rigid band formation along the tube and the formation of a slight curvature effect. We found in our experiments that tubes as long as 1 m and as slim as 1.5 cm diameter could stand up with an adequate air speed. This shows that the tubes we made were straight enough.

The experimental procedure was the following. A flexible tube was connected to the pump exit, then the flow velocity was quasi-statically increased from 0.

The tube was first observed to be stable (did not fall down because of its own weight). Then at a critical value of the flow velocity, the tube began oscillating. At this value, we introduce in the free end of the flexible tube two thin pipes, each one connected to a manometer, in order to measure the dynamical pressure p_d and the static pressure p. The critical velocity v could then be estimated from these measurements by means of the following relation:

$$v = \sqrt{\frac{2(p_d - p)}{\rho}} \tag{5}$$

where ρ is the air density.

3 Results

3.1 Observations

For each tube length and each critical air velocity value, at the threshold of the instability, we record the transient dynamics with a video camera. So we visualize how the tube evolves from a raised, immobile state, to the instant when the tube falls down and "breaks". Figure 2 illustrates the tube transient dynamics.

Figure 2 shows the tube position only for the last oscillation cycle. We counted for this video four cycles before the first picture of Fig. 2. The tube begins oscillating with very small amplitude which increases with time. For the last oscillation cycle, amplitude is so great that the tube breaks (that is, a singularity appears along the tube), as shown in the tenth and last pictures.

This transient dynamics was not observed by Castillo Flores and Cros (2009). In this previous study, we saw that the tube collapsed locally at its basis (that is, where it is fixed to the pump exit) and that the constriction point climbed upwards to the free extreme of the tube. It is suspected that this difference is due to the tube manufacture previously used. This later resulted in a slight curvature defect that has been strongly reduced with the manufacture process described above (see Sect. 2).

So we observe that in the transient dynamics, the tube is destabilized in the same way as the tubes with higher rigidity: it fluctuates with a certain periodicity and with a continuous spatial shape, until it breaks. From these observations, we can deduce that the instability which appears in our slim flexible tubes is of the same nature as that described by previous studies (Païdoussis 1970). Nevertheless, the threshold values do not agree with this theory, as it is shown in the next section.

3.2 Thresholds

Experiments have been performed with four different diameters $d = 1.5$, 2.2, 2.9 and 4.0 cm. Nevertheless we have not been able to observe any instability for the

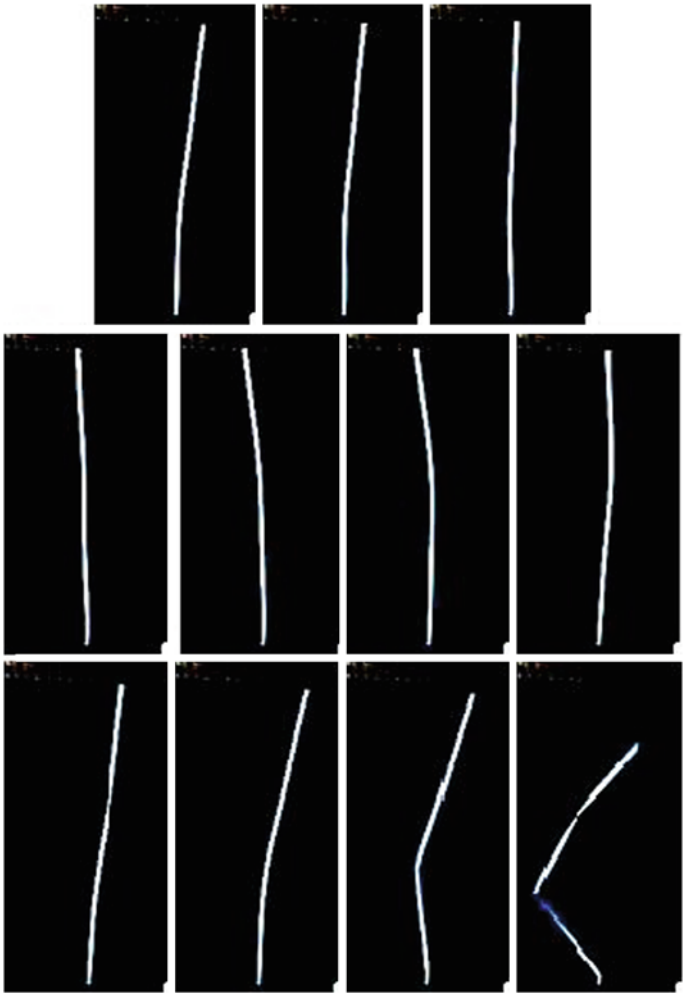

Fig. 2 Tube transient dynamics just at the threshold, before it breaks (*final picture*). Those pictures are extracted from a video corresponding to a 1 m-long, 1.5 cm-diameter tube. There is a lapse of 230 ms between each picture

tubes of diameter $d = 4.0$ cm because of the air speed values that can be reached by our air blower.

Figure 3 shows the thresholds v_c measured in our system for tubes of different diameters and lengths. Firstly, we observe that tubes of greater diameter are more stable than slim tubes. For example, for tubes of length $L = 0.95$ m, the critical velocity is $v_c = 32.8$ m/s for a diameter $d = 2.9$ cm, whereas it is of 27.7 m/s for $d = 2.2$ cm and of 20.9 m/s for $d = 1.5$ cm. This result is in agreement with Païdoussis's observations (see Sect. 1.1). Indeed as diameter d is increased,

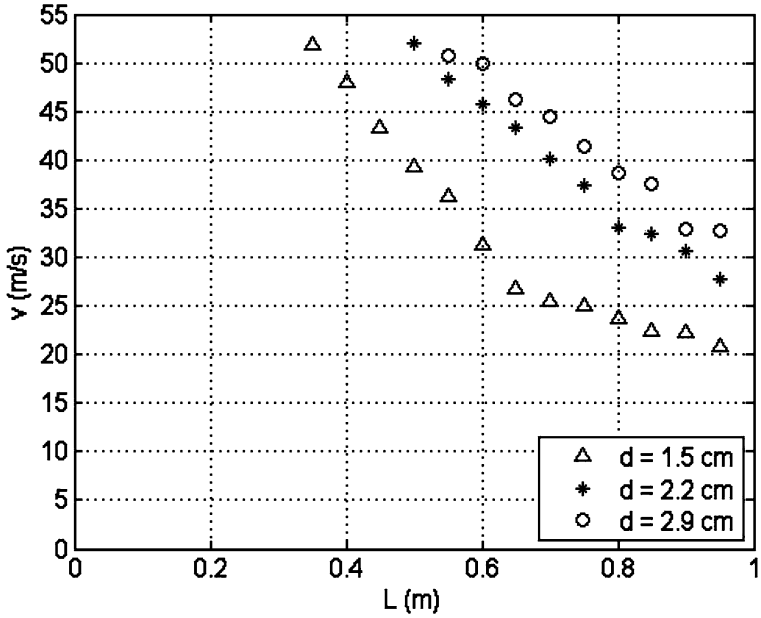

Fig. 3 Threshold values for tubes with different diameters: (Δ) 1.5 cm, (*) 2.2 cm, (o) 2.9 cm. *x-axis*: tube length L (m), *y-axis*: air velocity v_c (m/s) at instability threshold

parameter β (Eq. 4) increases, as seen in Table 1, and the instability threshold is greater.

Moreover, Fig. 3 shows that shorter tubes are more stable since they need higher air speeds to be destabilized. It should be pointed out that our air blower did not allow to reach threshold values for tubes shorter than 0.35 m. These observations are also in agreement with Païdoussis's results.

4 Analysis

In this section, a scaling analysis is conducted in order to emphasize the predominant stabilizing and destabilizing effects involved in the observed instability.

As described in the introduction (Sect. 1.1), destabilization is caused by centrifugal effects. Let us imagine a curved rigid tube conveying air flow. If air flow is deviated by an angle ϕ as shown in Fig. 1, momentum conservation leads to a horizontal force F which acts on the tube and is given by:

$$F = A\rho v^2 \sin\phi \tag{6}$$

where A is the tube cross-section and ρ the fluid density. This force component always acts in the convex direction: for example in Fig. 1, F is leftwards directed.

Table 1 Flexural rigidity values EI for the three different diameters and values for β (Eq. 4)

d (cm)	1.5	2.2	2.9
EI (10^{-4} Nm^2)	6	21	42
β	0.052	0.076	0.095

On the other hand tube stiffness makes the tube return to its straight position. Internal moment M generated by a radius R-curved tube can be written as:

$$M = \frac{EI}{R} \tag{7}$$

where EI is the tube flexural rigidity. For small Φ angles, that is to say large R curvature radius, we can show geometrically that:

$$\frac{1}{R} = \frac{\phi}{L} \tag{8}$$

Therefore, a characteristic force F_{EI} for flexural rigidity is given by:

$$F_{EI} = \frac{EI\phi}{L^2} \tag{9}$$

Finally the ratio Q between the destabilizing force (Eq. 6) and the stabilizing force (Eq. 9) for small tube deviations can be written as:

$$Q = \frac{A\rho v^2 L^2}{EI} \tag{10}$$

Remembering that $m_f = \varrho A$, this ratio appears to be the squared value of the nondimensional velocity u defined in Eq. 2.

The nondimensional critical values of the flow velocity are plotted in Fig. 4 as function of the nondimensional parameter γ introduced by Païdoussis (1998).

For these results, the flexural rigidity EI was determined with the measured value of the Young modulus $E = 4.5$ MPa and with the following formula for the second moment of inertia

$$I = \frac{\pi}{4}(r^4 - (r - e)^4) \tag{11}$$

where r is the tube radius and e the membrane thickness. Table 1 shows the corresponding values for EI and β for the three different diameters.

We can see in Fig. 4 that the points for $d = 2.2$ and 2.9 cm collapse on a single curve. The values for $d = 1.5$ cm are close to but smaller than both the other series. Nevertheless it is not expected theoretically that the three point series strictly superimpose since they correspond to different β values. It is expected that series relatively close together have similar β values, and this is observed experimentally.

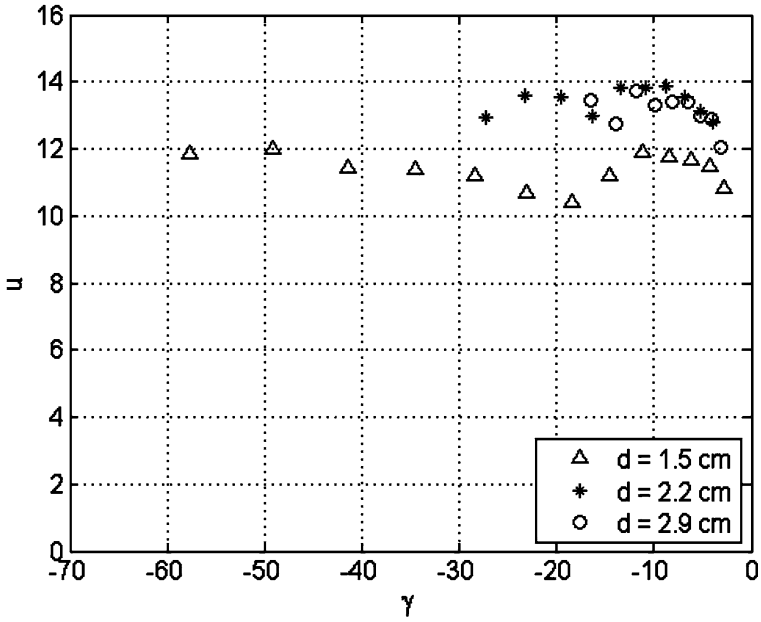

Fig. 4 Nondimensional critical flow velocities u as function of the nondimensional parameter γ for different tubes

Even so, the results found by Païdoussis (1970) are different. For our β experimental values shown in Table 1, theoretical nondimensional thresholds u vary between 0 and 4 and increase as $|\gamma|$ decreases. We can see that the thresholds in our case are three times higher than the predicted values. Moreover u is roughly constant in our experiment. We do not know yet how to explain these discrepancies.

5 Conclusion and Perspectives

In this work, we have experimentally measured the instability thresholds for a reduced "sky dancer" model. The measurements have been performed for various tube lengths and three different diameters. We have plotted the nondimensional critical velocities as function of the nondimensional parameter γ introduced by Païdoussis (1970) in a study concerning more rigid tubes. This allowed to show that the results strongly differ when much less rigid tubes are considered.

In order to characterize the instability mechanism which makes the tube "break", we should in future take into account the following considerations:

1. We will measure thresholds with a more precise apparatus like a hot-wire anemometer. This will reduce the uncertainty on measured thresholds.

2. We also want to measure pressure values on the tube base at the instability thresholds. This experimental system appears cheap and simple at first sight, but it is also more complex because both pressure and air speed vary simultaneously.
3. On the other hand we want to determine the flexural rigidity *EI* in a completely experimental way. A method is given by Païdoussis (1998). Indeed the slight overlapped membrane region along the tube may make *EI* values higher than the calculated ones in Table 1. This could change values on the *x*-axis.
4. We will also perform new experiments with another membrane to check the influence of Young modulus.
5. Another parameter we could compare with Païdoussis' theoretical work is oscillation frequency in the transient regime. This could help us to explain discrepancies and similarities between our experiment and the previous studies.
6. Finally we should also characterize the thresholds which delimit other two regimes: when the tube falls down because of its own weight (large tubes, small air speed values) and when the tube stands up. In the present study we were only interested in the thresholds delimiting the raised-tube regime from the "instability" regime, where the flow makes the tube "dance".

References

Ashley H, Haviland G (1950) Bending vibrations of a pipe line containing flowing fluid. J Appl Mech 17:229–232

Castillo Flores F, Cros A (2009) Transition to chaos of a vertical collapsible tubeconveying air flow. J Phys Conf Ser 166:012017

Doaré O, de Langre E (2002) The flow-induced instability of long hanging pipes. Eur J Mech A Solids 21:857–867

Greenwald AS, Dugundji J (1967) Static and dynamic instabilities of a propellant line. MIT Aeroelastic and Structures Research Lab, AFOSR Sci Report: AFOSR 67-1395

Gregory RW, Païdoussis MP (1966a) Unstable oscillation of tubular cantilevers conveying fluid. I. Theory. Proc R Soc (London) A 293:512–527

Gregory RW, Païdoussis MP (1966b) Unstable oscillation of tubular cantilevers conveying fluid. II. Experiments. Proc R Soc (London) A 293:528–542

Païdoussis MP (1963) Oscillations of liquid-filled flexible tubes. Ph. D. Thesis, University of Cambridge

Païdoussis MP (1966) Dynamics of flexible slender cylinders in axial flow. Part 1: theory. J Fluid Mech 26:717–736

Païdoussis MP (1969) Dynamics of vertical tubular cantilevers conveying fluid. Mechanical engineering research laboratories report MERL, Department of Mechanical Engineering, McGill University, Montreal, Québec, Canada, pp 69–73

Païdoussis MP (1970) Dynamics of tubular cantilevers conveying fluid. Int J Mech Eng Sci 12:85–103

Païdoussis MP, Issid NT (1974) Dynamic stability of pipes conveying fluid. J Sound Vib 33:267–294

Païdoussis MP (1998) Fluid-Structure interactions. Slender structures and axial flow, vol 1. Academic Press, London

Structure and Translational Diffusion in Liquid Crystalline Phases of a Gay-Berne Mesogen: A Molecular Dynamics Study

Enrique Cañeda-Guzmán, José Antonio Moreno-Razo, Enrique Díaz-Herrera and Edward John Sambriski

Abstract Structures and self-diffusion coefficients of Gay-Berne (GB) mesogens with parameterizations GB(3.0, 5.0, 2.0, 1.0) and GB(4.4, 20.0, 1.0, 1.0) were extracted from *NVT* Molecular Dynamics simulations. These parameterizations are commonly used in the study of mesogenic systems. Structural features of accessible phases were characterized through translational $[g_{\parallel}(r_{\parallel})]$ and positional $[g_{\perp}(r_{\perp})]$ radial distribution functions. Translational self-diffusion coefficients parallel ($D_{\parallel}$) and perpendicular ($D_{\perp}$) to the global director were determined. Upon cooling a mesogenic system with parameterization GB(3.0, 5.0, 2.0, 1.0), a solid-like phase forms (as deduced from diffusivity) without attaining a smectic phase. Instead, the GB(4.4, 20.0, 1.0, 1.0) parameterization yields a range of liquid crystalline phases that follows the sequence isotropic → nematic → smectic A → smectic B, for which the smectic B phase exhibits small, but measurable diffusivity. Collectively, results point to the GB(4.4, 20.0, 1.0, 1.0) parameterization as being a better candidate in capturing the typical gamut of liquid crystalline phases.

E. Cañeda-Guzmán · J. A. Moreno-Razo · E. Díaz-Herrera (✉)
Departamento de Física, Universidad Autónoma Metropolitana,
09340, Iztapalapa, D.F., México
e-mail: diaz@xanum.uam.mx

E. J. Sambriski
Department of Chemistry and Biochemistry, Delaware Valley College,
18901, Doylestown, Pennsylvania, USA
e-mail: Edward.Sambriski@delval.edu

J. Klapp et al. (eds.), *Experimental and Theoretical Advances in Fluid Dynamics*, Environmental Science and Engineering, DOI: 10.1007/978-3-642-17958-7_3,

1 Introduction

Since their discovery (Reinitzer 1888; Lehmann 1889) liquid crystals (LCs) have been a subject of intense experimental and theoretical research (de Gennes and Prost 1995). Moreover, LCs have stimulated a wide range of device applications. Liquid crystal displays (LCDs) represent one of the many tangible applications of liquid crystalline phases. From a statistical physics point of view, LC phase behavior exemplifies, in a salient manner, entropically-driven phase transitions. As shown by Onsager (1949), the isotropic-nematic transition in systems of infinitely long and thin rods can be explained as a result of the competition between translational and rotational entropy. In a complementary manner, computer simulations have played an important role in understanding the complex phase behavior of LC systems (Allen et al. 1993; Pasini et al. 2005). Specifically, LCs exhibit varying extents of translational and orientational order between an isotropic fluid and a crystalline phase (de Gennes and Prost 1995; Pershan 1988; Demus et al. 1999). The Gay-Berne (GB) potential has proven to be a useful model in the study of thermotropic phase transitions in LCs by computer simulation.

Accessible thermotropic phases and their associated stability become prerequisite information for an LC application. With a judicious choice of model parameters, it is possible to mimic chemical behavior with a mesogen, the rigid unit of an LC with axial symmetry. The GB interaction potential, coupled with computer simulations, can be used to describe the origin of short- and long-range order, phase stability, interfacial properties, and dynamic behavior arising from the microscopic structure of a mesogen. The GB potential allows for anisotropy in attractive and repulsive interactions given by the parameter set GB(κ, κ', μ, ν). While many GB parameterizations are possible, only a limited number have been investigated (Bates and Luckhurst 1999; Adams et al. 1987; Luckhurst et al. 1990; Luckhurst and Simmonds 1993; Berardi et al. 1993; de Miguel et al.1996). An oft-cited parameterization is GB(3.0, 5.0, 2.0, 1.0), originally constructed to mimic anisotropic interactions in an equivalent linear-site Lennard-Jones potential (Gay and Berne 1981), though this system is not unique (Luckhurst et al. 1990; Berardi et al. 1993). Computer simulations (Luckhurst et al. 1990; de Miguel et al. 1991, 1996; Hashim et al. 1995; de Miguel 2002), and theoretical studies (Velasco et al. 1995; Velasco and Mederos 1998), have focused on phase behavior as well as liquid crystalline properties.

A parameterization inspired by a chemical system is GB(4.4, 20.0, 1.0, 1.0), formulated to model the mesogenic domain of *p*-terphenyl. Studies have focused on phase behavior (Luckhurst and Simmonds 1993), pair distribution functions (Luckhurst and Simmonds 1993), rotational dynamics (Bates and Luckhurst 2001), structure of various phases, and calculations of X-ray scattering patterns (Bates and Luckhurst 2003). It is of interest to compare GB(3.0, 5.0, 2.0, 1.0) and GB(4.4, 20.0, 1.0, 1.0) mesogens, not only on the basis of previous work, but also because these parameterizations capture LC phases to varying extents. For example, the

parameterization GB(3.0, 5.0, 2.0, 1.0) cannot describe a smectic A phase, while the smectic B phase arising in this system has been suggested to be a solid phase (de Miguel and Vega 2002). Prior simulation studies suggest that the occurrence of the smectic B phase is not very sensitive to GB parameterizations, but the formation of the smectic A phase requires a sufficiently large molecular aspect ratio κ (Bates and Luckhurst 1999; Luckhurst and Simmonds 1993; Brown et al. 1998; Allen et al. 1996). As κ increases, so does the smectic A region of the phase diagram, though the region is bounded at high and low temperatures (Brown et al. 1998). The parameterization GB(4.4, 20.0, 1.0, 1.0) was recently employed to study translational self-diffusion in nematic, smectic A, and smectic B phases (Luckhurst and Simmonds 1993; Bates and Luckhurst 2004).

In the present work, a comparison is made between mesogens with parameterizations GB(3.0, 5.0, 2.0, 1.0) and GB(4.4, 20.0, 1.0, 1.0), in the context of structural and dynamical properties. In particular, translational $[g_{\parallel}(r_{\parallel})]$ and positional $[g_{\perp}(r_{\perp})]$ radial distribution functions, as well as parallel $(D_{\parallel})$ and perpendicular $(D_{\perp})$ translational diffusion coefficients, are calculated and compared for different phases. The paper is organized as follows: In Sect. 2, the molecular model is presented, while in Sect. 3, details are given for Molecular Dynamics simulations. In Sect. 4, structural properties of liquid crystalline phases are treated as a function of temperature. In Sect. 5, mean-square displacements are presented and discussed. Finally, conclusions are offered in Sect. 6.

2 Molecular Model

The GB interaction potential between two mesogens (labeled i and j), with center-of-mass positions $\{\mathbf{r}_i, \mathbf{r}_j\}$ and orientation unit vectors $\{\hat{\mathbf{u}}_i, \hat{\mathbf{u}}_j\}$, is characterized by attractive and repulsive contributions. At the mesogenic level, each molecule is represented as an ellipsoid of revolution separated by an intermolecular vector $\mathbf{r}_{ij}$. Given the separation $r_{ij} = |\mathbf{r}_i - \mathbf{r}_j|$ between mesogens, *attractive* and *repulsive* contributions vanish as r_{ij}^{-6} and r_{ij}^{-12}, respectively, for $r_{ij} \to \infty$. Anisotropy in the interaction enters through $\hat{\mathbf{u}}_i$ and $\hat{\mathbf{u}}_j$, which are defined along the symmetry axis of the ith and jth molecules, respectively. All contributions for the interaction between two mesogens are collectively expressed through the GB potential energy function,

$$U(\hat{\mathbf{u}}_i, \hat{\mathbf{u}}_j, \hat{\mathbf{r}}_{ij}) = 4\varepsilon_0 \varepsilon(\hat{\mathbf{u}}_i, \hat{\mathbf{u}}_j, \hat{\mathbf{r}}_{ij}) \left(\Xi_{ij}^{-12} - \Xi_{ij}^{-6} \right), \tag{1}$$

where $\hat{\mathbf{r}}_{ij} = \mathbf{r}_{ij}/r_{ij}$ is the unit vector along the center-to-center vector $\mathbf{r}_{ij}$ and

$$\Xi_{ij} = \frac{r_{ij} - \sigma(\hat{\mathbf{u}}_i, \hat{\mathbf{u}}_j, \hat{\mathbf{r}}_{ij}) + \sigma_0}{\sigma_0}. \tag{2}$$

In this arrangement, σ_0 and ε_0 are the contact distance and potential energy well depth, respectively, for a pair of mesogens perpendicularly oriented with respect to

each other ($\hat{\mathbf{u}}_i \cdot \hat{\mathbf{u}}_j = 0$) and with respect to the intermolecular vector ($\hat{\mathbf{u}}_i \cdot \hat{\mathbf{r}}_{ij} = \hat{\mathbf{u}}_j \cdot \hat{\mathbf{r}}_{ij} = 0$). Molecular shape information enters through

$$\sigma(\hat{\mathbf{u}}_i, \hat{\mathbf{u}}_j, \hat{\mathbf{r}}_{ij}) = \sigma_0[\Gamma(\omega = \chi)]^{-1/2}. \tag{3}$$

The molecular anisotropy parameter χ is defined by

$$\chi = \frac{\kappa^2 - 1}{\kappa^2 + 1}, \tag{4}$$

where $\kappa = \sigma_e/\sigma_s$ is the aspect ratio between major (σ_e) and minor (σ_s) length scales, defined in terms of contact distances for the ellipsoid. In a physical sense, κ influences the formation of orientationally ordered phases. Now, $\Gamma(\omega)$ is a fully specified function of a general variable ω and reads

$$\Gamma(\omega) = 1 - \omega \left[\frac{\left(\hat{\mathbf{u}}_i \cdot \hat{\mathbf{r}}_{ij}\right)^2 + \left(\hat{\mathbf{u}}_j \cdot \hat{\mathbf{r}}_{ij}\right)^2 - 2\omega\left(\hat{\mathbf{u}}_i \cdot \hat{\mathbf{r}}_{ij}\right)\left(\hat{\mathbf{u}}_j \cdot \hat{\mathbf{r}}_{ij}\right)\left(\hat{\mathbf{u}}_i \cdot \hat{\mathbf{u}}_j\right)}{1 - \omega^2\left(\hat{\mathbf{u}}_i \cdot \hat{\mathbf{u}}_j\right)^2} \right]. \tag{5}$$

The potential energy well depth anisotropy, $\varepsilon(\hat{\mathbf{u}}_i, \hat{\mathbf{u}}_j, \hat{\mathbf{r}}_{ij})$, is expressed as a product of two functions, and reads

$$\varepsilon(\hat{\mathbf{u}}_i, \hat{\mathbf{u}}_j, \hat{\mathbf{r}}_{ij}) = \left[\varepsilon_1\left(\hat{\mathbf{u}}_i, \hat{\mathbf{u}}_j\right)\right]^{\nu}\left[\varepsilon_2\left(\hat{\mathbf{u}}_i, \hat{\mathbf{u}}_j, \hat{\mathbf{r}}_{ij}\right)\right]^{\mu}. \tag{6}$$

The first function, $\varepsilon_1\left(\hat{\mathbf{u}}_i, \hat{\mathbf{u}}_j\right)$, favors parallel alignment and promotes liquid crystalline formation through

$$\varepsilon_1\left(\hat{\mathbf{u}}_i, \hat{\mathbf{u}}_j\right) = \left[1 - \chi^2\left(\hat{\mathbf{u}}_i \cdot \hat{\mathbf{u}}_j\right)^2\right]^{-1/2}. \tag{7}$$

The second function, $\varepsilon_2\left(\hat{\mathbf{u}}_i, \hat{\mathbf{u}}_j, \hat{\mathbf{r}}_{ij}\right)$, favors side-to-side over end-to-end molecular alignments and promotes the smectic phase through

$$\varepsilon_2\left(\hat{\mathbf{u}}_i, \hat{\mathbf{u}}_j, \hat{\mathbf{r}}_{ij}\right) = \Gamma(\omega = \chi'), \tag{8}$$

where $\Gamma(\omega)$ is given by Eq. 5. The potential energy well depth anisotropy parameter is defined as

$$\chi' = \frac{(\kappa')^{1/\mu} - 1}{(\kappa')^{1/\mu} + 1}, \tag{9}$$

where $\kappa' = \varepsilon_s/\varepsilon_e$ governs the competition of molecular alignments through the ratio between side-to-side (ε_s) and end-to-end (ε_e) energy well depths. Physically, the anisotropy in attractive forces is controlled by κ' and influences the tendency of the system to form smectic phases. Moreover, μ and ν influence attractive and repulsive forces in the GB potential, thus affecting formation and stability of ordered phases.

The previous development establishes that the GB interaction energy function is fully defined by four adjustable parameters (κ, κ', μ, ν) that tune the anisotropy of interactions and by two scaling parameters (σ_0 and ε_0) for length and energy. It is customary to express mesogenic parameterizations using the notation introduced

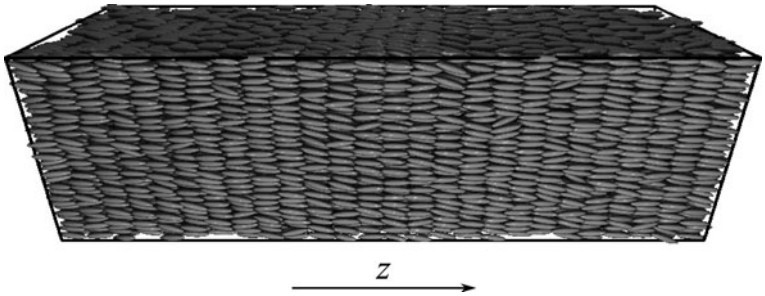

Fig. 1 Simulation snapshot (in perspective) of a smectic phase in a parallelepiped box

by Luckhurst (Bates and Luckhurst 1999), as GB(κ, κ', μ, ν). The parameterizations investigated and compared in this work are GB(3.0, 5.0, 2.0, 1.0) and GB(4.4, 20.0, 1.0, 1.0).

3 Details of Simulations

All state variables and quantities in this study are in reduced units and appear with an asterisk. Thus, distance is $r^* = r/\sigma_0$, time is $t^* = t[\varepsilon_0/(m\sigma_0^2)]^{1/2}$, temperature is $T^* = k_B T/\varepsilon_0$, density is $\rho^* = \rho\sigma_0^3$, pressure is $P^* = P\sigma_0^3/\varepsilon_0$, moment of inertia is $I^* = I/(m\sigma_0^2)$, and diffusion coefficient is $D^* = D[m/(\sigma_0^2\varepsilon_0)]^{1/2}$. For all parameterizations considered in this work, the particle mass m is set to unity ($m = 1$).

Molecular Dynamics simulations were carried out in the *NVT* ensemble, in which the temperature T was fixed with a Nosé-Hoover thermostat. The particle number N was set to 2×10^4, corresponding to an order of magnitude larger than that of previous studies. Simulations were started from orientationally isotropic configurations. Low-temperature states were typically obtained by stepwise cooling of the system. Initial molecular velocities were pooled from a Maxwell-Boltzmann distribution and moments of inertia were set to $I^* = (1/20)(1 + \kappa^2)$ (Gruhn and Schoen 1997). Translational and orientational equations of motion were integrated using the velocity-Verlet algorithm (Allen and Tildesley 1987; Ilnytskyi and Wilson 2002) with a reduced time step $\delta t^* = 1.5 \times 10^{-3}$. Tetragonal boxes were used with (mutually orthogonal) box sides L_x, L_y, and L_z. The simulation box was periodically replicated along the x-, y-, and z-directions. In the present simulations, a computational box with a cross section $L_x = L_y = 30\sigma_0$ was used. The length L_z of the simulation box was adjusted to obtain the desired average density. It is particularly useful in the case of the smectic phase to perform simulations in a parallelepiped so as to separate, in a simple manner, parallel and perpendicular contributions of the diffusivity. In a parallelepiped, the nematic director of the smectic A phase or smectic B phase is induced to bear the same direction as the direction of the longest dimension of the simulation box, i.e., L_z in this work (Fig. 1).

4 Results: Structure of Liquid Crystalline Phases

A starting point for the presentation of results rests on the structural features of accessible LC mesophases. Thermodynamic properties of simulated systems are summarized in Table 1, which lists temperature T^*, density ρ^*, nematic orientational order parameter P_2, and corresponding LC mesophase. In particular, P_2 quantifies the extent of orientational ordering of a phase and is the second-rank order parameter defined in the usual way (Allen and Tildesley 1987), monitored as the largest eigenvalue of the ordering matrix $\mathbf{Q} = (1/N)\sum_{i=j}^{N}(3\hat{\mathbf{u}}_i \otimes \hat{\mathbf{u}}_i - \mathbf{I})/2$, where $\mathbf{I}$ is the identity matrix. The corresponding normalized eigenvector is the global director $\mathbf{n}$.

The sole characterization of P_2 does not enable a distinction between smectic A and B phases. Smectic phases can be thought of as two-dimensional liquid layers stacked upon one another, with a well-defined interlayer spacing (de Gennes and Prost 1995). In the smectic A phase, there are no in-layer positional correlations. In the smectic B phase, the centers of mass are distributed in each layer in a hexagonal pattern. Although the orientationally-averaged pair distribution function $g(r)$ provides some structural information about smectic phases, the radial character of this function does not discern between smectic A or smectic B phases. To differentiate between these phases, it is necessary to calculate a distribution sensitive to the underlying material structure. Thus, aside from determining $g(r)$, translational and positional pair correlation functions are calculated. Specifically, smectic ordering is probed with the quasi two-dimensional translational (parallel) radial distribution function and reads

$$g_{\parallel}(r_{\parallel}) = \frac{\left\langle \sum_{i\neq j}^{N} \delta\left[\left(r_{\parallel} \pm dR/2\right) - r_{ij,\parallel}\right]\theta\left(\sigma_0/2 - r_{ij,\perp}\right)\right\rangle}{2N\rho\pi(\sigma_0/2)^2 dR}. \tag{10}$$

Here, $\theta(x)$ is a step function, in which $\theta(x) = 1$ when $x \geq 0$ and $\theta(x) = 0$ otherwise. Also, $r_{ij,\parallel} = |\mathbf{r}_{ij,\parallel}| = |\mathbf{r}_{ij} \cdot \mathbf{n}|$ is the separation between centers of mass along the global director $\mathbf{n}$ and $r_{ij,\perp} = |\mathbf{r}_{ij,\perp}| = |\mathbf{r}_{ij} - \mathbf{r}_{ij,\parallel}|$ is the corresponding transversal separation from $\mathbf{n}$. Moreover, $dR = 0.05\sigma_0$ is a tolerance and the factor of two in the denominator arises due to the symmetry $\mathbf{r}_{ij,\parallel} \rightarrow -\mathbf{r}_{ij,\parallel}$. Smectic layering is signaled by (essentially undamped) oscillations in $g_{\parallel}(r_{\parallel})$, the period of which indicates the interlayer spacing. If translational correlations are lacking (as in the case of isotropic or nematic phases), then $g_{\parallel}(r_{\parallel})$ has rather liquid-like (i.e., short-ranged) structure.

The positional (perpendicular) radial distribution $g_{\perp}(r_{\perp})$ accounts for particles in a disk of height L around a given particle, corresponding to a pairwise distribution of molecules in the same layer perpendicular to the phase director $\mathbf{n}$ and reads

Table 1 Thermodynamic properties of simulated phases for a GB(4.4, 20.0, 1.0, 1.0) model

T^*	ρ^*	P_2	Phase
1.8	0.156	0.02	Isotropic
1.5	0.181	0.77	Nematic
1.3	0.200	0.92	Smectic A
1.1	0.220	0.97	Smectic B

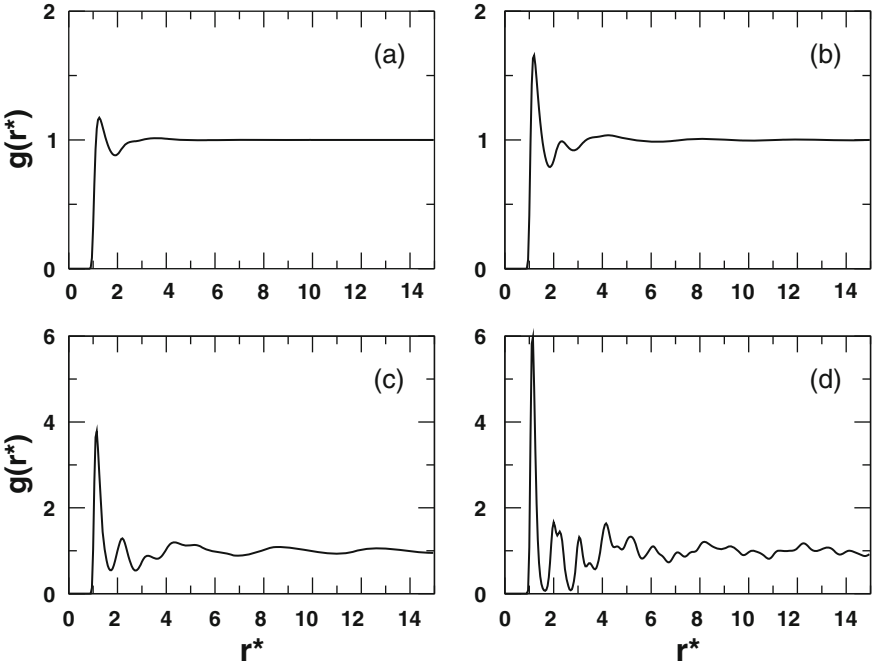

Fig. 2 Pair correlation function $g(r^*)$ for a GB(4.4, 20.0, 1.0, 1.0) mesogen in: **a** isotropic ($T^* = 1.8$, $\rho^* = 0.156$), **b** nematic ($T^* = 1.5$, $\rho^* = 0.181$), **c** smectic A ($T^* = 1.3$, $\rho^* = 0.200$), and **d** smectic B ($T^* = 1.1$, $\rho^* = 0.220$) phases

$$g_{\perp}(r_{\perp}) = \frac{\left\langle \sum_{i \neq j}^{N} \delta\left[(r_{\perp} \pm dR/2) - r_{ij,\perp}\right] \theta\left(\sigma_{\mathrm{e}}/2 - r_{ij,\parallel}\right) \right\rangle}{2N\rho\pi r_{\perp} LdR}. \tag{11}$$

In a smectic A phase, $g_{\perp}(r_{\perp})$ has only short-ranged structure, indicating a liquid-like distribution of particles within the layer. On the other hand, a smectic B phase is characterized by a pronounced and rather long-ranged structure, resembling that observed in crystalline configurations with hexagonal packing. A diagnostic feature of such arrangements is the splitting of the second peak of nearest neighbors into two sub-peaks.

In Fig. 2, the radial distribution function $g(r^*)$ for the four phases studied is shown and described in Table 1. In isotropic and nematic phases, only structure due to nearest neighbors can be observed at distances on the order of particle size,

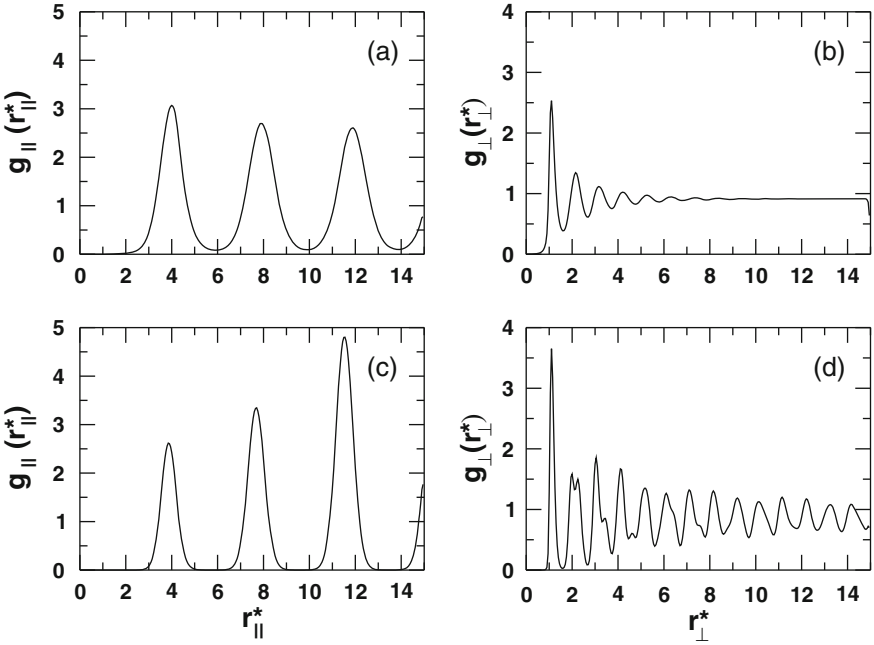

Fig. 3 Pair correlation functions $g_{\parallel}(r^*_{\parallel})$ (**a** and **c**) and $g_{\perp}(r^*_{\perp})$ (**b** and **d**) for a GB(4.4, 20.0, 1.0, 1.0) mesogen, for smectic A (*top*) and smectic B (*bottom*) phases, with corresponding conditions indicated in Fig. 2

indicating lack of long-range translational order. In the smectic A phase, the peak due to nearest neighbors is quite pronounced (Fig. 2c), as plausibly expected from the layered packing of particles. The shell of next nearest neighbors is apparent from the peak at $r^* = 2\sigma_0$. However, the new feature in $g(r^*)$, at least in comparison with that of the nematic phase, is a slight, long-range oscillation with periodicity of$\approx 4\sigma_0$. This is associated with a layering structure of the smectic A phase. In the smectic B phase, peaks in $g(r^*)$ become sharper and fine structure appears through long-range oscillations (Fig. 2d). The separation between adjacent peaks constituting the fine structure at $r^* \approx 2\sigma_0$ is attributed to hexagonal packing within smectic B layers.

To classify the type of smectic phase, it is more appropriate to use translational and positional distribution functions, as previously defined. As expected, $g_{\parallel}(r^*_{\parallel})$ shows no long-range structure for isotropic or nematic phases (not shown), due to translational disorder characterizing these LC phases. However, for the smectic A phase (Fig. 3a), $g_{\parallel}(r^*_{\parallel})$ exhibits strong oscillatory behavior, indicating the tendency for particles to yield a layered arrangement. A pronounced regularity in oscillation amplitude of $g_{\parallel}(r^*_{\parallel})$ is expected for a smectic A phase, manifesting a highly probable end-to-end configuration between layers. On cooling the system to obtain the smectic B phase, peaks become sharper and more distinct (Fig. 3c). However,

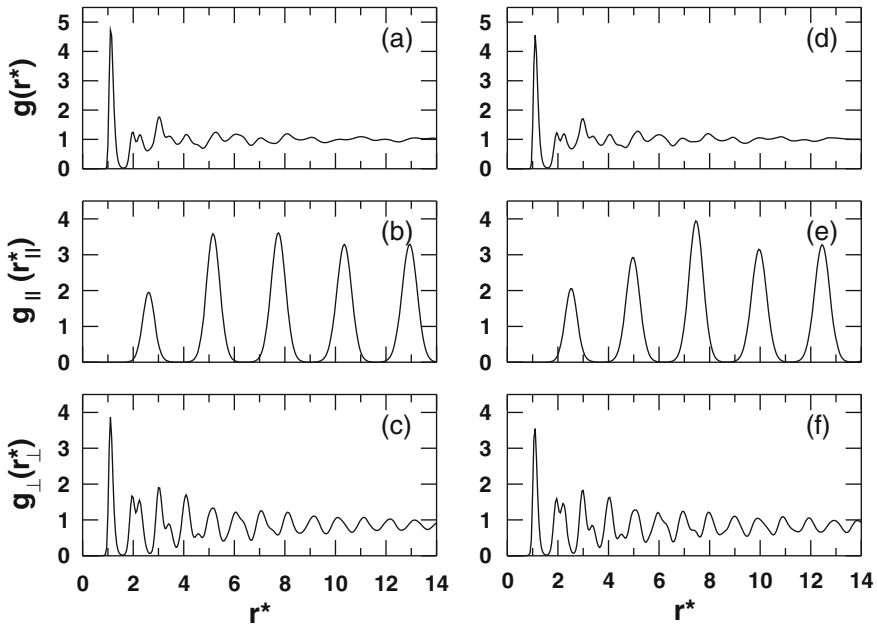

Fig. 4 Pair correlation functions $g(r^*)$ (**a** and **d**), $g_{\parallel}(r^*_{\parallel})$ (**b** and **e**), and $g_{\perp}(r^*_{\perp})$ [(**c**) and (**f**)] for a GB(3.0, 5.0, 2.0, 1.0) mesogen, for $P^* = 2.0$ and $T^* = 0.70$ (*left*), as well as $P^* = 5.0$ and $T^* = 0.95$ (*right*)

irregularity is detected in the amplitude of $g_{\parallel}(r^*_{\parallel})$. The origin of this irregularity can be explained by particles being regularly shifted from **n** and between adjacent layers. Thus, the first maximum is expected to have a lower amplitude than the second maximum. This behavior of $g_{\parallel}(r^*_{\parallel})$ is derived from hexagonal packing of layers, characteristic of the smectic B phase.

Positional order within smectic layers is given by $g_{\perp}(r^*_{\perp})$, the results of which are shown in Fig. 3b and Fig. 3d. In the smectic A phase (Fig. 3b), it is apparent that in-layer order is liquid-like: the function does not show long-range structure. This in-layer order extends to larger separations in the smectic B phase (Fig. 3d), and $g_{\perp}(r^*_{\perp})$ does not monotonically tend to unity at large distances, indicative of long-range positional order within layers. Also, the first peak in $g_{\perp}(r^*_{\perp})$ for the smectic B phase is narrower and better differentiated than for the smectic A phase, signifying that the nearest neighbor cluster is more ordered at lower temperatures. The structure of $g_{\perp}(r^*_{\perp})$ is qualitatively different in the two smectic phases for the shell of next nearest neighbors. In the smectic A phase, the second peak is rather weak and broad in comparison to the first peak. In the smectic B phase, the distribution at $r^* \approx 2\sigma_0$ shows two peaks, characteristic of hexagonal, in-layer order.

Correlation functions for the GB(3.0, 5.0, 2.0, 1.0) parameterization are shown in Fig. 4. Profiles obtained for the two thermodynamic states points in each class of

pair correlation functions are very similar and resemble the smectic B phase. When comparing this system with the GB(4.4, 20.0, 1.0, 1.0) parameterization, similar profiles are obtained in each case. Given the likeness between the two parameterizations on structural grounds at low temperatures, it is not possible to discern whether either parameterization is prone to form a solid phase. In this regard, it is useful to study the diffusivity of the system as a means of probing dynamical behavior and stability of a solid phase, the results of which are presented in Sect. 5.

5 Results: Translational Diffusion of Liquid Crystalline Phases

A complementary assessment on the nature of LC mesophases is particle diffusivity in the mesogenic system. This information is readily obtained from the self-diffusion coefficient, determined from

$$\langle \Delta r_{\alpha}^{2}(t^{*}) \rangle = \lim_{t^{*} \to \infty} 2dD^{*}t^{*}, \tag{12}$$

where $\langle \Delta r_{\alpha}^{2}(t^{*}) \rangle$ is the mean-square displacement (MSD) for an orientation component $\alpha \in \{\parallel, \perp\}$ with respect to the director $\mathbf{n}$, d is the dimensionality with respect to α (for $\alpha = \parallel$ then $d = 1$, while for $\alpha = \perp$ then $d = 2$), D^{*} is the self-diffusion coefficient, and t^{*} is time. More specifically,

$$\langle \Delta r_{\alpha}^{2}(t^{*}) \rangle = \frac{1}{N} \sum_{i=1}^{N} \left| \mathbf{r}_{i,\alpha}(t^{*}) - \mathbf{r}_{i,\alpha}(0) \right|^{2} \tag{13}$$

is the canonical average over all time intervals of the simulation trajectory given by t^{*}. In Eq. 13, N is the total number of particles and $\mathbf{r}_{i}$ is the position vector of the ith particle, extracted from two frames separated by an interval t^{*}. When $\alpha = \parallel$, $\Delta r_{\parallel}(t^{*}) = |\mathbf{r}_{\parallel}(t^{*}) - \mathbf{r}_{\parallel}(0)|$ is the distance traveled in a time interval t^{*} along a particular direction *parallel* to the director $\mathbf{n}$, and *not* the total distance traveled in the parallel plane. When $\alpha = \perp$, $\Delta r_{\perp} = |\mathbf{r}_{\perp}(t^{*}) - \mathbf{r}_{\perp}(0)|$ is the distance traveled in a time interval t^{*} along a particular direction *perpendicular* to $\mathbf{n}$, and *not* the total distance traveled in the perpendicular plane.

Diffusion coefficients were determined from a linear regression analysis of the long-time MSD behavior, between $t^{*} = 25$ and $t^{*} = 38$. Results for $D_{\parallel}$ and $D_{\perp}$ are summarized in Table 2. When comparing nematic to isotropic phases, $D_{\parallel}$ is $\sim$2.7-fold larger, an effect linked to the extent of orientational order in the nematic phase (Bates and Luckhurst 2004). As the system undergoes cooling, side-to-side attractive interactions become important for surrounding mesogenic molecules in the same layer. In effect, this promotes the formation of layers in smectic phases, resulting in decreased diffusion when compared to the nematic phase (Bates and Luckhurst 2004) (refer to Table 2). Moreover, excluded volume interactions in adjacent layers counteracts diffusion parallel to the director in smectic

Table 2 Diffusion coefficients $D_{\parallel}^{*}$ and $D_{\perp}^{*}$ for a GB(4.4, 20.0, 1.0, 1.0) mesogen

T^{*}	$D_{\parallel}^{*}$	$D_{\perp}^{*}$	Phase
1.8	0.40	0.40	Isotropic
1.5	1.07	0.34	Nematic
1.3	0.07	0.08	Smectic A
1.1	0.00	0.0015	Smectic B

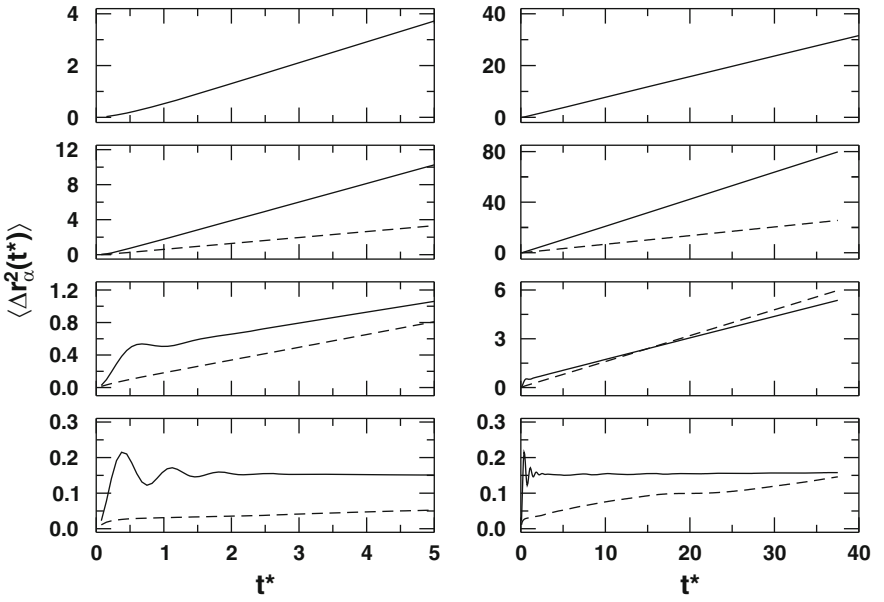

Fig. 5 Short- (*left*) and long-time (*right*) behavior of the MSD for a GB(4.4, 20.0, 1.0, 1.0) mesogen at $P^{*} = 2.0$ and $T^{*} = 1.8$ (isotropic), $T^{*} = 1.5$ (nematic), $T^{*} = 1.3$ (smectic A), $T^{*} = 1.1$ (smectic B) phases (*top* to *bottom*), resolved into $\langle \Delta r_{\parallel}^{2}(t^{*}) \rangle$ (*full line*) and $\langle \Delta r_{\perp}^{2}(t^{*}) \rangle$ (*dashed line*)

phases, and the effect is stronger in the smectic B phase due to an increased layered structure when compared to the smectic A phase in the long-time regime. In agreement with experiments (Kruger 1982), diffusion coefficients (in the case of $D_{\perp}$) of the smectic B phase are an order of magnitude smaller than those of the smectic A phase, indicating high translational order in the former system.

The temporal behavior of the MSD for the four phases is shown in Fig. 5. For the isotropic phase, the MSD is linear above $t^{*} = 2.0$. The anisotropy in the diffusion tensor is already evident in the nematic phase, for which the slope of the parallel component is larger than that of the perpendicular component, as shown previously (Bates and Luckhurst 2004). However, for the smectic A phase, the slope of the perpendicular component is reduced approximately four-fold when compared to the nematic phase. In the smectic A phase, $\langle \Delta r_{\parallel}^{2}(t^{*}) \rangle$ is different from the nematic phase. The short-time behavior of the parallel component is weakly oscillatory for the time interval between $t^{*} = 1.5$ and $t^{*} = 2.5$, an effect linked to the layered structure of the smectic A phase. At short times, the smectic B phase

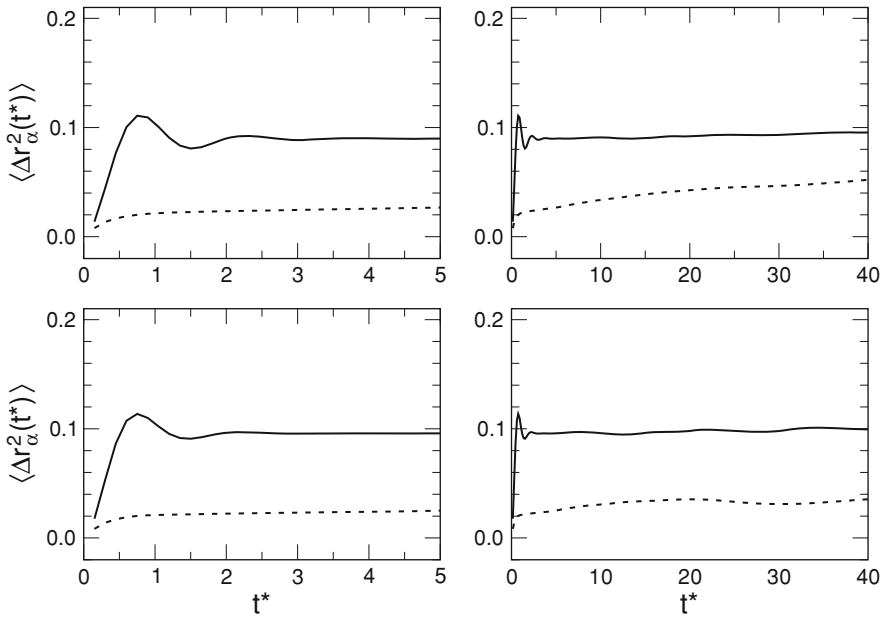

Fig. 6 Short- (*left*) and long-time (*right*) behavior of the MSD for a GB(3.0, 5.0, 2.0, 1.0) mesogen in the smectic B phase at $P^* = 2.0$ and $T^* = 0.70$ (*top*) as well as $P^* = 5.0$ and $T^* = 0.95$ (*bottom*), resolved into $\langle \Delta r_\parallel^2(t^*) \rangle$ (*full line*) and $\langle \Delta r_\perp^2(t^*) \rangle$ (*dashed line*)

shows strong oscillatory behavior for $\langle \Delta r_\parallel^2(t^*) \rangle$. Oscillations in $\langle \Delta r_\parallel^2(t^*) \rangle$ decay to zero on a time scale greater than that of the smectic A phase. As expected, higher translational and positional order of the smectic B phase leads to a long-time limit of $\langle \Delta r_\parallel^2(t^*) \rangle$ tending toward a constant value, and as a result,

$$2D_\parallel^* = \lim_{t \to \infty} \frac{\partial}{\partial t^*} \langle \Delta r_\parallel^2(t^*) \rangle \to 0. \tag{14}$$

Thus, translational motion along the director **n** is arrested and only $D_\perp^*$ persists (Bates and Luckhurst 2004). Corresponding MSD data for the GB(3.0, 5.0, 2.0, 1.0) parameterization are displayed in Fig. 6. For this latter case, the dynamical long-time behavior for the two thermodynamic state points investigated shows that $\langle \Delta r_\parallel^2(t^*) \rangle$ tends toward a constant value, thus yielding motion arrest through $D_\parallel^* \to 0$ and $D_\perp^* \to 0$. Whereas these conditions are diagnostic of a solid-like phase for a GB(3.0, 5.0, 2.0, 1.0) mesogen at low temperatures, a GB(4.4, 20.0, 1.0, 1.0) mesogen sustains transversal diffusivity ($D_\perp \neq 0$) for the range of low temperatures considered.

6 Conclusions

In this work, *NVT* MD simulations were used to explore the phase behavior of dense, liquid crystals of prolate GB ellipsoids characterized by two different molecular models, i.e., GB(3.0, 5.0, 2.0, 1.0) and GB(4.4, 20.0, 1.0, 1.0) parameterizations. Phase structures were investigated with systems larger (10-fold) than previously used, making it possible to track positional and translational correlations over relatively larger length and time scales. Correlation functions perpendicular to the director were used to characterize the spatial structure of smectic phases, allowing a distinction between smectic A and smectic B phases. Mean-square displacements were calculated to uncover differences in dynamical behavior in the two parameterizations. Our key results are summarized as follows:

- the structural analysis of the mesogenic system corroborates previous findings that the GB(3.0, 5.0, 2.0, 1.0) parameterization has no stable smectic A phase,
- the phase previously identified as smectic B for the GB(3.0, 5.0, 2.0, 1.0) parameterization is solid-like, based on mean-square displacements for $P^* > 2.0$,
- the solid-like phase observed for a GB(3.0, 5.0, 2.0, 1.0) parameterization is attained with no accessible smectic phase, at least for $P^* > 2.0$,
- the GB(3.0, 5.0, 2.0, 1.0) and GB(4.4, 20.0, 1.0, 1.0) parameterizations, while yielding very similar pairwise distributions at low temperatures, exhibit different (long-time) dynamical behaviors, and
- the GB(4.4, 20.0, 1.0, 1.0) parameterization displays the typical gamut of LC mesophases (isotropic, nematic, smectic A, and smectic B) and is thus a valuable molecular model of liquid crystals formed from rod-like particles.

References

Adams DJ, Luckhurst GR, Phippen RW (1987) Computer simulation studies of anisotropic systems XVII. The Gay-Berne model nematogen. Mol Phys 61:1575–1580

Allen MP, Tildesley DJ (1987) Computer simulation of liquids. Academic Press, London

Allen MP, Evans GT, Frenkel D, Mulder BM (1993) Hard convex body fluids. Adv Chem Phys 86:1–166

Allen MP, Brown JT, Warren MA (1996) Computer simulation of liquid crystals. J Phys Condens Matter 8:9433–9437

Bates MA, Luckhurst GR (1999) Computer simulation studies of anisotropic systems XXX. The phase behavior and structure of a Gay-Berne mesogen. J Chem Phys 110:7087–7108

Bates MA, Luckhurst GR (2001) Determination of the Maier-Saupe strength parameter from dielectric relaxation experiments: a Molecular Dynamics simulation study. Mol Phys 99: 1365–1371

Bates MA, Luckhurst GR (2003) X-ray scattering patterns of model liquid crystals from computer simulation: calculation and analysis. J Chem Phys 118:6605–6614

Bates MA, Luckhurst GR (2004) Studies of translational diffusion in the smectic A phase of a Gay-Berne mesogen using Molecular Dynamics computer simulation. J Chem Phys 120: 394–403

Berardi R, Emerson APJ, Zannoni C (1993) Monte Carlo investigations of a Gay-Berne liquid crystal. J Chem Soc Faraday Trans 89:4069–4078

Brown JT, Allen MP, Martín del Río E, de Miguel E (1998) Effects of elongation on the phase behavior of the Gay-Berne fluid. Phys Rev E 57:6685–6699

Demus D et al (eds) (1999) Physical properties of liquid crystals. Wiley-VCH, New York

de Gennes PG, Prost J (1995) The physics of liquid crystals, 2nd edn. Oxford University Press, Oxford

de Miguel E, Rull LF, Chalam MK, Gubbins KE (1991) Liquid crystal phase diagram of the Gay-Berne fluid. Mol Phys 74:405–424

de Miguel E, Martín del Río E, Brown JT, Allen MP (1996) Effect of the attractive interactions on the phase behavior of the Gay-Berne liquid crystal model. J Chem Phys 105:4234–4249

de Miguel E (2002) Reexamining the phase diagram of the Gay-Berne fluid. Mol Phys 100: 2449–2459

de Miguel E, Vega C (2002) The global phase diagram of the Gay-Berne model. J Chem Phys 117:6313–6322

Gay JG, Berne BJ (1981) Modification of the overlap potential to mimic a linear site-site potential. J Chem Phys 74:3316–3319

Gruhn T, Schoen M (1997) Microscopic structure of molecularly thin confined liquid-crystal films. Phys Rev E 55:2861–2875

Hashim R, Luckhurst GR, Romano S (1995) Computer-simulation studies of anisotropic systems XXIV. Constant-pressure investigations of the smectic B phase of the Gay-Berne mesogen. J Chem Soc Faraday Trans 91:2141–2148

Ilnytskyi JM, Wilson MR (2002) A domain decomposition Molecular Dynamics program for the simulation of flexible molecules of spherically-symmetrical and nonspherical sites. II. Extension to NVT and NPT ensembles. Comp Phys Comm 148:43–58

Krüger GR (1982) Diffusion in thermotropic liquid crystals. Phys Rep 82:229–269

Lehmann O (1889) Ueber fliessende Krystalle. Z Phys Chem 4:462–472

Luckhurst GR, Stephens RA, Phippen RW (1990) Computer simulation studies of anisotropic systems XIX. Mesophases formed by the Gay-Berne model mesogen. Liq Cryst 8:451–464

Luckhurst GR, Simmonds PS (1993) Computer simulation studies of anisotropic systems XXI. Parametrization of the Gay-Berne potential for model mesogens. Mol Phys 80:233–252

Onsager L (1949) The effects of shape on the interaction of colloidal particles. Ann NY Acad Sci 51:627–659

Pasini P, Zannoni C, Žumer S (2005) Computer simulations of liquid crystals and polymers. Kluwer, Dordrecht

Pershan PS (eds) (1988) Physical properties of liquid crystals. World Scientific, New York

Reinitzer F (1888) Beitraege zur Kenntiss des Cholesterins. Monatshefte für Chemie (Wien) 9:421–441

Velasco E, Somoza AM, Mederos L (1995) Liquid-crystal phase diagram of the Gay-Berne fluid by perturbation theory. J Chem Phys 102:8107–8113

Velasco E, Mederos L (1998) A theory for the liquid-crystalline phase behavior of the Gay-Berne model. J Chem Phys 109:2361–2370

Agitation in a Liquid Fluidized Bed

Alicia Aguilar-Corona, Olivier Masbernat, Roberto Zenit-Camacho and Bernardo Figueroa-Espinoza

Abstract The random motion of mono-dispersed particles in a liquid fluidized bed was measured and processed from video recordings, using a refractive index matching method. 3D trajectories of coloured particles have been collected in a wide range of solid fraction, and statistical quantities have been derived in the range of high particle Reynolds number ($O(10) < Re_p < O(10^3)$) and intermediate Stokes number ($O(1) < St < O(10)$). The evolution of the particle velocity variance as a function of solid fraction has been determined for different concentrations.

1 Introduction

The liquid fluidized beds span a large variety of operations (Epstein 2003). In order to design and control these processes, it is necessary to understand fundamental mechanisms like the inter-particle and fluid-particle interactions. The liquid fluidization is relevant from the academic viewpoint as a bench mark

A. Aguilar-Corona (✉)
Facultad de Ingeniería Mecánica, Universidad Michoacana de San Nicolás de Hidalgo, Francisco J. Mujica s/n, C.P. 58040 Morelia, Michoacán, Mexico

O. Masbernat
Laboratoire de Génie Chimique, UMR CNRS/INP/UPS 5503, 5 rue Paulin Talabot BP1301, 31106 Toulouse, France

R. Zenit-Camacho
Instituto de Investigaciones en Materiales, Universidad Nacional Autónoma de México, 04510 México City, D.F., Mexico

B. Figueroa-Espinoza
LIPC-Instituto de Ingeniería, Universidad Nacional Autónoma de México Campus, Sisal, Yucatán, Mexico

J. Klapp et al. (eds.), *Experimental and Theoretical Advances in Fluid Dynamics*, Environmental Science and Engineering, DOI: 10.1007/978-3-642-17958-7_4,

case for two-fluid modelling. The solid phase agitation is induced by the collisional and hydrodynamic inter-particle interactions, and the contribution due to the continuous phase turbulence is negligible (in general). Even if a fluidized bed is not the host of chaotic mixing or sharp regime transitions (as would be the case of bubbly flows), it cannot be considered as homogeneous fluidization. Low frequency fluctuations, at large scale, have been indeed observed experimentally and consequently studied (El-Kaissy and Homsy 1980).

The Eulerian two-fluid and the statistical models developed from the kinetic theory face the problem of the lack of experimental data for validation. The validation of macroscopic models (Buyevich 1999; Wang and Ge 2005) or numerical simulations in liquid fluidization (De Wilde 2005; Gevrin et al. 2008; Gevrin 2002) use nowadays the results of Zenit et al. (1997) and Zenit and Hunt (2000), consisting of granular pressure and fluctuations of the solid fraction in a wide range of Stokes numbers. A key variable for validating models is the velocity variance; yet, experimental data of this type is rather rare. The major measuring problem in a fluidized bed is common in the context of dense media. It is difficult to implement local properties measuring techniques, intrusive (optical probe, electrochemical or capacitive) or not (video, impedance, spectroscopic or acoustic, light diffusion, radioactive tracers).

The problem of insufficient experimental data is not limited only by the difficulties in measurement techniques. The absence of dimensional analyses of the statistical parameters and the lack of scaling laws make the basic understanding of the fluctuating motion in a liquid fluidized bed very difficult. A comparison with the experimental and theoretical procedures developed for the case of solid–liquid suspensions (low Reynolds and Stokes) in homogeneous shear of sedimentation revealed the experimental data analysis weaknesses in a fluidized bed. Even if the spatio-temporal scaling is very different, the experimental details of the velocity fluctuations and auto-diffusion in sedimentation (Ham and Homsy 1988; Nicolai et al. 1995), or induced by the constraint (Leighton and Acrivos 1987; Breedveld et al. 1998), constitute a good example to follow to characterize the fluctuating movement in a fluidized bed.

This work is devoted to the study of particles random motion within a liquid fluidized bed. In addition to the procedure by itself, this study was primarily motivated by the lack of detailed experimental data of the hydrodynamic field of both phases in fluidized beds; in particular, we focused on the determination of velocity fluctuations. The lack of a robust experimental base limits the validation of numerical schemes and hinders the advance of a more profound understanding of the scaling in liquid fluidized bed.

2 Experimental Set-Up

The experimental device is shown in Fig. 1. The fluidization section is composed of a 60 cm high cylindrical glass column of 8 cm inner diameter. The column was equipped with a glass square section box to reduce optical distortion. A fixed bed of packed beads covered by a layer of synthetic foam layers is mounted at the

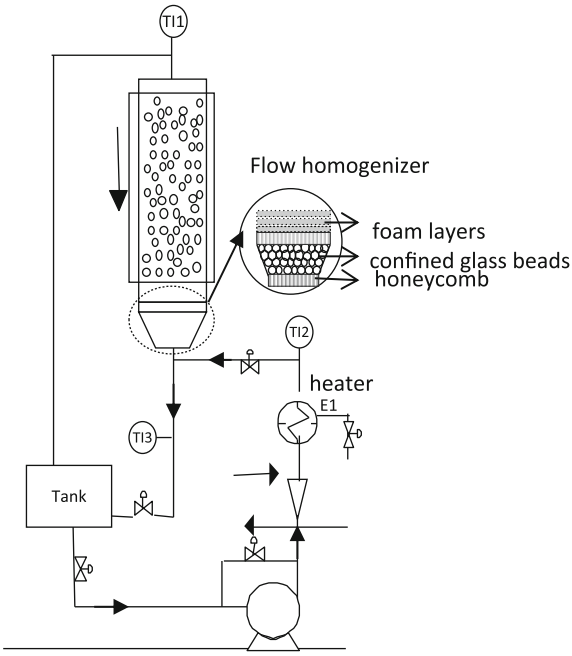

Fig. 1 Sketch of the liquid fluidized bed

bottom of the column to ensure a homogeneous flow entry. The flow temperature is maintained at 20°C.

Calibrated Pyrex beads and a concentrated aqueous solution of Potassium Thiocyanate (KSCN, 64% *w/w*) were used as dispersed and continuous phase, respectively. The fluid and the particles have a very similar refractive index ($\sim$1.474), so that a tagged particle can be tracked individually in a nearly transparent suspension. Particle and fluid properties are reported in Table 1.

For all experiments the mean solid fraction is calculated as follows,

$$\langle \alpha_p \rangle = \alpha_{pm} \frac{h_0}{h_b} \tag{1}$$

where α_{pm} is the experimental maximal compaction of solid fraction ($\sim$0.57), h_b fluidized bed height and h_0 bed height at maximal compaction.

The fluidization velocity evolution (U_o) as function of the mean liquid fraction ($\langle \alpha_l \rangle = 1 - \langle \alpha_p \rangle$) is shown in Fig. 2.

Clearly, for both particle diameters the fluidization velocity agrees well with the Richardson-Zaki relation:

$$U_0 = U_t (1 - \langle \alpha_p \rangle)^n \tag{2}$$

where U_0 is the fluidization velocity; U_t is terminal velocity and n is the exponent of Richardson-Zaki relation.

Table 1 Fluid and particle properties at 20°C

Pyrex beads	$d_p = 6$ mm	$\rho_p = 2{,}230$ kg m^{-3}	$n_D = 1.474$
	$d_p = 3$ mm		
KSCN Solution 64%	$\mu_f = 3.8 \times 10^{-3}$ Pas	$\rho_f = 1{,}400$ kg m^{-3}	$n_D = 1.4744$

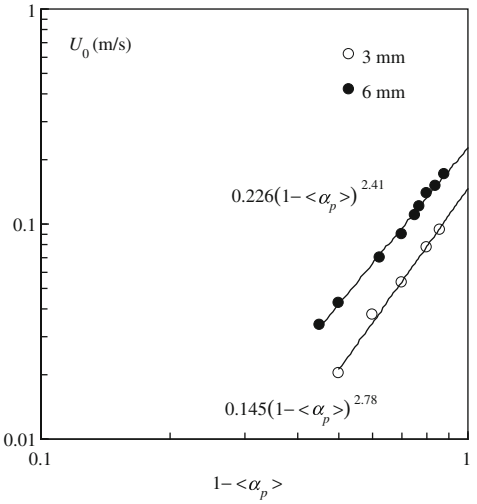

Fig. 2 Fluidization velocity evolution as a function of liquid fraction for the glass particles

Table 2 Fluidization parameters of the glass particles

d_p (mm)	Re_t	St_t	n	U_t (m s^{-1})
3	160	4.8	2.78	0.145
6	500	7.6	2.41	0.226

Due to the moderate values of the density difference and of the fluid viscosity, the particle Reynolds number at terminal velocity (Re_t) is high but the Stokes number, defined in Eq. 3 as

$$St = \frac{8\rho_p}{3\rho_f C_{Dt}} \tag{3}$$

is of the order of 10. These fluidization parameters are also shown in the Table 2.

3 Particle Trajectories

The analysis of particle movement was performed by 3D trajectography, for two particle sizes (6 and 3 mm) and solid fractions in the range of 0.10–0.60. A mirror was mounted in a vertical plane at 45° with respect to the wall of the visualization

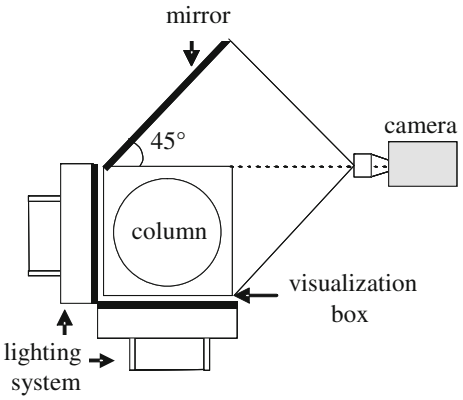

Fig. 3 Trajectography 3D system. View to *top*

(Fig. 3) to obtain the image of the particle from two perpendicular views. A high frequency lighting system was mounted in the both sides of the column. The camera is placed in face, in such a way that the visualization zone is composed by left (x, z) and right side (y, z) of the column in the same frame.

A single black colored particle (with the same properties) was introduced in the bed. Its trajectory was recorded using a high speed camera (APX Photon). The memory capacity of the camera allows for long time recording of the particle position. In this manner it is possible to capture a wide range of frequencies of the particle motion within the bed, in particular the low frequencies. In our case, a framing rate of 30 fps was used, and the corresponding duration of an experiment was 204 s.

The particle position was determined on each image by means of a particle tracking program, developed in Matlab®. A gray level thresholding followed by a binarization was applied and the center of mass of the tracer particle was determined. The Fig. 4a–d show the typical image obtained from experiments (512 pixel by 1,024 pixel), as well as the image processing steps for the black particle in plane (x, z) and (y, z).

Finally, the instantaneous velocity of the center of mass of the particle is derived from its displacement between two consecutive images. The vertical (x, z) and transversal (x, y) plane projections of eight trajectories are represented in Fig. 5, for a particle size of 6 mm at $\langle \alpha_p \rangle = 0.20$. Note that the bed domain is covered completely by these trajectories; the particle motion is approximately axially symmetric. A toroidal-shape motion is observed in the lower section of the bed for all the solid fractions and for both bead sizes. This motion is more pronounced for the case of 3 mm particles at large concentrations. The movement is characterized by an ascending and slightly accelerated upwards motion at the centre of the column and descendant flow at the vicinity of the walls. A similar structure was also observed by Handley et al. (1966); Carlos and Richardson (1968) and Latif and Richardson (1972). The visualization of 3D trajectories in the liquid fluidized bed clearly shows the role of large scale that result from confinement (height and diameter of the bed), on the random particle motion.

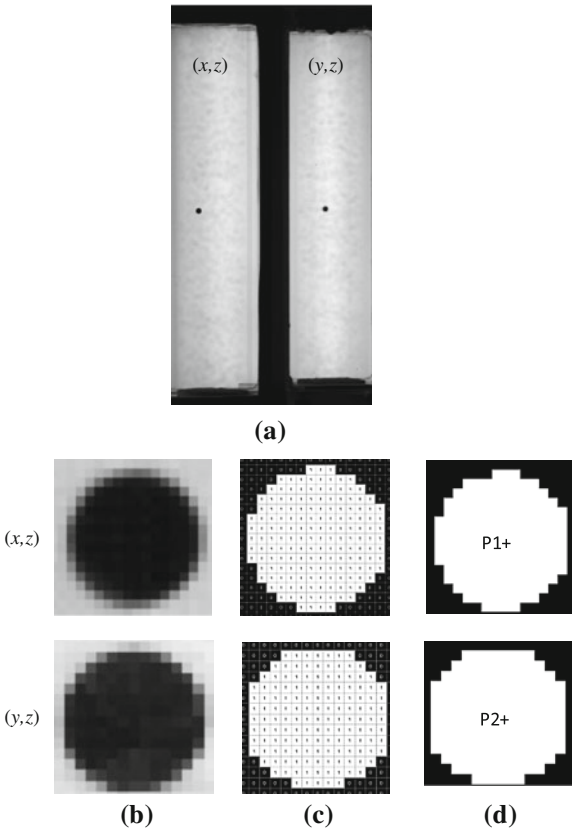

Fig. 4 **a** Raw image of experiments for 6 mm at $\langle\ \alpha_p\ \rangle = 0.14$, **b** zoom on *black* particles in both planes, **c** binarization and **d** center of mass determination (P1, P2)

It also allows understanding the difficulties and scattering that arise on the interpretation of the observed results in the literature when dealing with the characterization of the random motion.

4 Solid Phase Velocity and Variance

In order to determine the necessary number of trajectories to attain the statistical convergence of the second order moments, the cumulative mean velocity components (referred to as $(\overline{u_{pi}})_{\text{cum}}$) and variances (referred to as $(\overline{u_{pi}'^2})_{\text{cum}}$) were calculated as function of the number of trajectories N. An example of these quantities is shown in Fig. 6. It can be observed that the mean velocity cumulative component is less to 1×10^{-4} m s^{-1} in absolute value, an order of magnitude smaller than the absolute error on the instantaneous particle velocity measurement (around

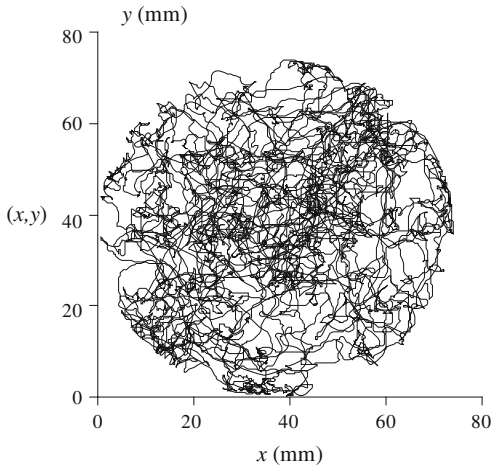

Fig. 5 Trajectories projections $d_p = 6$ mm, $\langle \alpha_p \rangle; = 0.20$

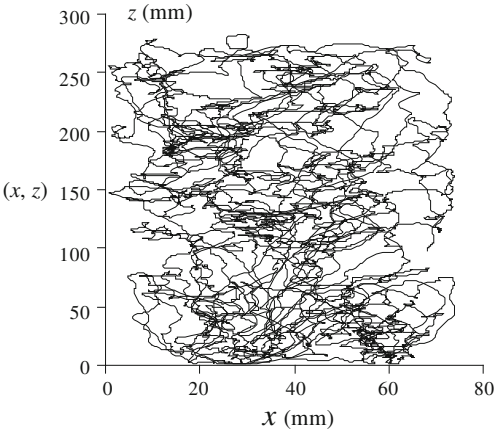

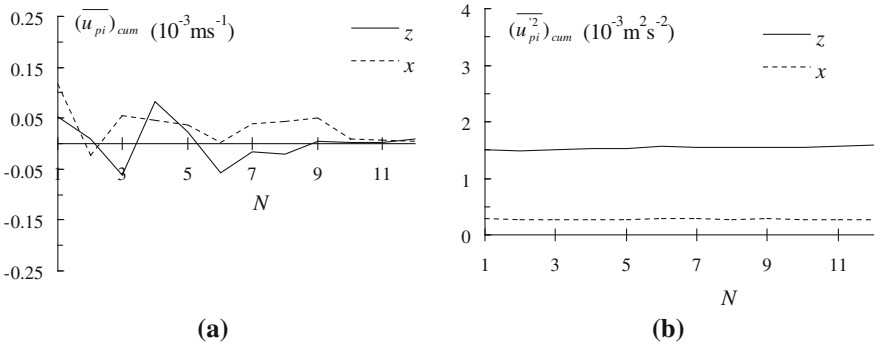

Fig. 6 Cumulative mean velocity components $(\overline{u_{pi}})_{\text{cum}}$ and variances $(\overline{u_{pi}'^2})_{\text{cum}}$ as a function of the number of trajectories for $d_p = 3$ mm at $\langle \alpha_p \rangle = 0.3$

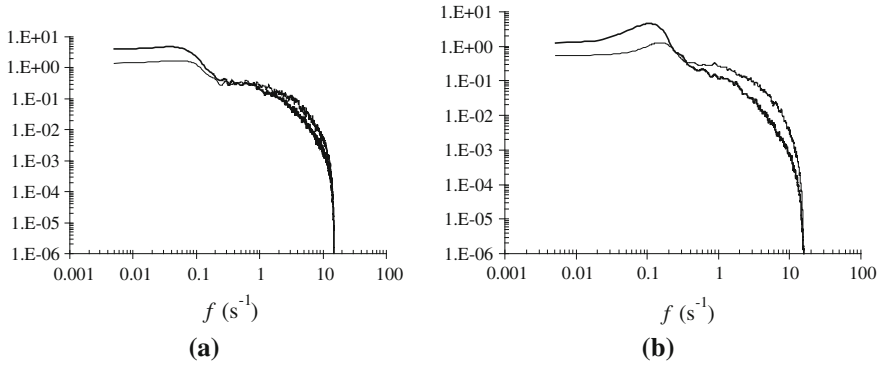

Fig. 7 Power spectral density in (—) *vertical* axis and (—) *transversal* axis for $\langle \alpha_p \rangle = 0.50$. **a** $d_p = 3$ mm, **b** $d_p = 6$ mm

2.5×10^{-3}m s^{-1}). Twelve trajectories were necessary to reach statistical convergence of the velocity distributions for the solid fraction agitation analysis.

The axial velocity components (z) are larger in magnitude than the horizontal axis projections (x). The velocity signals are composed by high and low frequency components. The mean FFT of 12 trajectories of velocity signals (Fig. 7), shows a peak in the low frequency range that can be related to the mean particle trajectory along the whole vertical axis. This effect is more important at high concentrations. These low frequency fluctuations are a consequence of the large scale motion induced by the presence of the walls. Additionally, this motion coexists with small scale hydrodynamic interactions and collisions between particles and also particle/wall collisions.

5 Particle Velocity Distribution

The PDF of the particle velocity components are reported in Fig. 8 for different solid fraction and for both particle diameters. It is clear that these distributions are anisotropic, since the axial component of the PDF is always larger than its horizontal counterpart. On each of these graphs, the experimental PDF's are compared to a Gaussian distribution of the same standard deviation. The velocity distributions are centered around zero and symmetrical. For each velocity component, the agreement with the Gaussian distribution is reasonable for small solid concentration ($\alpha_p \leq 0.2$). However, for larger concentrations (between 0.3 and 0.4) a velocity peak near the origin can be observed. Such characteristic has been observed in the past by Carlos and Richardson (1968) for a similar range of concentrations. The peak is larger for 3 mm particles than for the 6 mm case. This could be interpreted as a result of experimental uncertainty, which would tend to increase for the smallest particle displacements. If this were the case, the

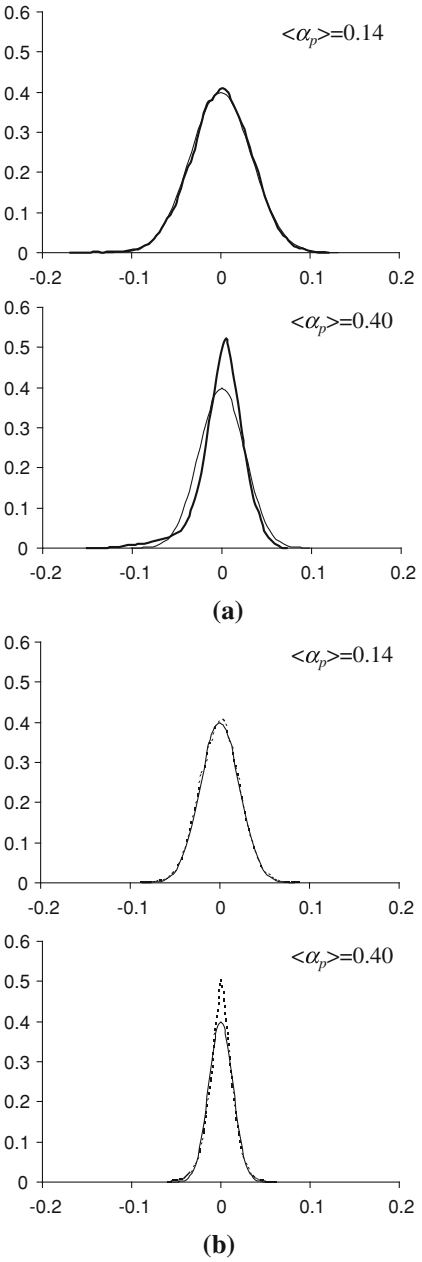

Fig. 8 Probability density function for $d_p = 3$ mm. **a** *axial velocity* (—), **b** *transversal velocity* (···). Best fit for Gaussian distribution presented as *solid line* (—)

peak would be more pronounced on the horizontal velocity distributions. It is clear that this is not the case. As the concentration increases, the collision frequency also increases, but the relative velocity between particles decreases.

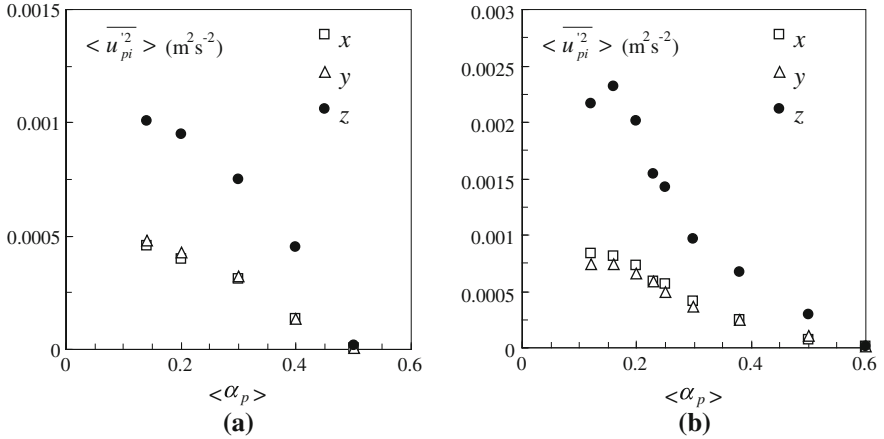

Fig. 9 Velocity variance as a function of the solid fraction. **a** $d_p = 3$ mm, **b** $d_p = 6$ mm

This could result in the dampening of the relative motion, having as a consequence a reduction of the collisional motion (zero restitution coefficient). Moreover, this explanation is supported by the existence of a critical Stokes number (based on the relative impact velocity, i.e. the standard deviation of the measured velocities). Below this critical value restitution coefficient vanishes (see Yang and Hunt 2006).

The qualitative analysis of the velocity distributions and instantaneous signal components suggests, in view of the scale decomposition analysis on one hand, and on the Maxwellian distribution hypothesis on the other, that Eulerian models coming from the kinetic theory of granular media provide a plausible description of liquid fluidization (Gevrin et al. 2008).

6 Velocity Variance

The variance for the three particle velocity components $\langle \overline{u'^2_{pi}} \rangle$ is shown as function of the solid fraction in Fig. 9, for both particle diameters. The two horizontal measurements are very similar, a fact that validates the experimental technique. For both axial and horizontal cases and particle diameters, the variance decreases with concentration, with a slight axial component maximum at $\langle \alpha_p \rangle = 0.16$ for the 6 mm beads.

The velocity variance in the vertical direction is larger than the horizontal component, for all concentrations and both particle diameters. This anisotropy is characterized by the coefficient $k_{anis} = \sqrt{\langle u'^2_{pz} \rangle} \Big/ \sqrt{\langle u'^2_{px} \rangle} = \sigma_{pz}/\sigma_{px}$, represented in Fig. 10 as function of the concentration and for both bead diameters.

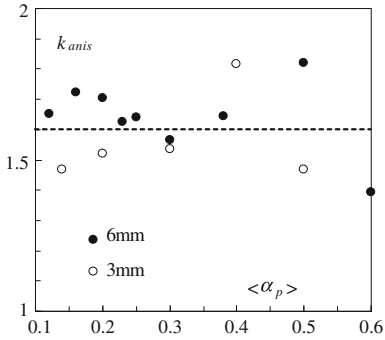

Fig. 10 Anisotropy coefficient as a function of concentration

The numerical value of this ratio is about 1.6 for both types of beads, and seems to be independent of the concentration. Note that this value is smaller than the ones reported by Carlos and Richardson (1968) of approx. 2.1, by Handley et al. (1966) of about 2.5 and by Latif and Richardson (1972) of about 2.3. This result shows, on the other hand, a difference with the value of K_{anis} obtained in low Re (sedimentation phenomena), where velocity anisotropy tends to decrease with concentration (Nicolai et al. 1995). If we admit that the fluctuating small scale motion (granular temperature) is represented by the horizontal variance velocity component. This proportionality relation between large scale motion and granular temperature (independently of the solid fraction) is interesting from the modeling viewpoint.

From these experimental measurements, the evolution of the energy of the fluctuating motion as a function of the concentration can be studied. The total fluctuating kinetic energy E_p, and the kinetic energy of small scale motion $\langle \overline{q_p^2} \rangle$ are represented as:

$$E_p = \frac{1}{2}\left(\langle \overline{u_{px}'^2} \rangle + \langle \overline{u_{py}'^2} \rangle + \langle \overline{u_{pz}'^2} \rangle\right), \qquad \langle \overline{q_p^2} \rangle \equiv \frac{3}{2}\langle \overline{u_{pT}'^2} \rangle \tag{4}$$

with

$$\langle \overline{u_{pT}'^2} \rangle = \frac{1}{2}\left(\langle \overline{u_{px}'^2} \rangle + \langle \overline{u_{py}'^2} \rangle\right), \tag{5}$$

where $\langle \overline{u_{pT}'^2} \rangle$ is the velocity variance on the horizontal direction. The evolution of both quantities as a function of the solid fraction is presented in Fig. 11 for both bead diameters. In all cases the total kinetic energy is larger than q_p^2 by a factor of two.

The effect of bead diameter on the agitation is important. For a given concentration, the velocity variance is larger for the particles with larger diameter.

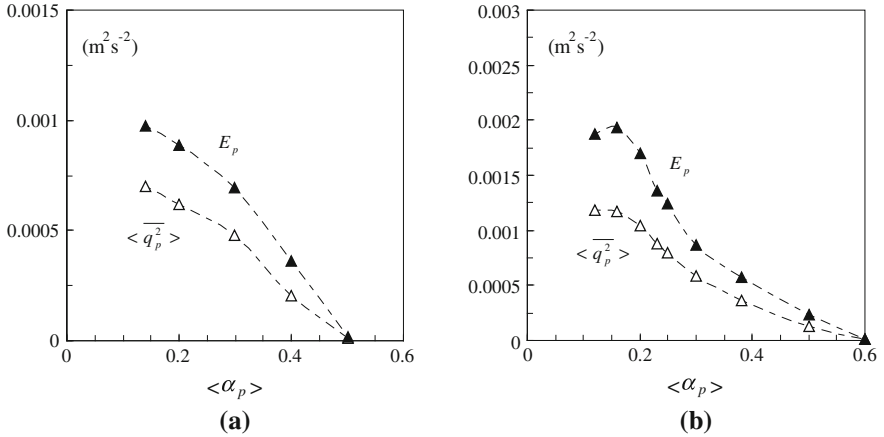

Fig. 11 Total fluctuating kinetic energy E_p, and the small scale motion kinetic energy $\langle\overline{q_p^2}\rangle$ as a function of *solid* fraction. **a** $d_p = 3$ mm, **b** $d_p = 6$ mm

7 Conclusions

Experimental results characterizing the mean level of agitation for the solid phase within a fluidized bed were presented.

The particle velocity signal is formed by a low frequency component of large amplitude and a high frequency component having less energy. The velocity distributions can be well fitted by Gaussian curves. However, a peak appears for large solid concentrations around zero velocity: in our opinion this can be explained by the restitution coefficient vanishing at low velocities and large concentrations.

The velocity components variance was determined for the case of homogeneous fluidization, for two bead diameters and for a large concentration range of values. The kinetic energy decreases monotonically with concentration, and its squared root varies approximately between both diameters as the ratio between their terminal speeds. It has been observed that the fluctuating particle motion is anisotropic, and the ratio between the standard deviation of the axial and horizontal components is close to 1.6 for this particular geometry**,** independent of concentration. The fluctuating kinetic energy decreases with concentration, for solid fractions in the range between 0.1 and 0.3.

References

Breedveld V, Van den Ende D, Tripathi A, Acrivos A (1998) The measurement of the shear-induced particle and fluid tracer diffusivities in concentrated suspensions by a novel method. J Fluid Mech 375:297–318

Buyevich YA (1999) Particulate stress in dense dispersed flow. Ind Eng Chem Res 38:731–743

Carlos CR, Richardson JF (1968) Solids movements in liquid fluidised beds-I particle velocity distribution. Chem Eng Sci 23(8):813–824
De Wilde J (2005) Reformulating and quantifying the generalized added mass in filtered gas-solid flow models. Phys Fluids 17(113304):1–14
El-Kaissy MM, Homsy GM (1980) Instability waves and the origin of bubbles in fluidized beds Part 2: experiments. Int J Multiphase Flow 2:379–395
Epstein N (2003) Applications of liquid–solid fluidization. Int J Chem Reactor Eng 1(R1):1–16
Gevrin F (2002) Modelisation dynamique de la fluidisation solide–liquide. PhD thesis, Institut National Polytechnique de Toulouse, Toulouse, France
Gevrin F, Masbernat O, Simonin O (2008) Granular pressure and particle velocity fluctuations prediction in liquid fluidized beds. Chem Eng Sci 63:2450–2464
Ham JM, Homsy GM (1988) Hindered settling and hydrodynamic dispersion in quiescent sedimenting suspensions. Int J Multiphase flow 14(5):533–546
Handley D, Doraisamy A, Butcher KL, Franklin NL (1966) A study of the fluid and particle mechanics in liquid-fluidised beds. Trans Inst Chem Eng 44:T260–T273
Latif BAJ, Richardson JF (1972) Circulation patterns and velocity distribution for particles in a liquid fluidised bed. Chem Eng Sci 27:1933–1949
Leighton D, Acrivos A (1987) Measurement of shear-induced self-diffusion in concentrated suspensions of spheres. J Fluid Mech 177:109–131
Nicolai H, Herzhaft B, Hinch EJ, Oger L, Guazzelli E (1995) Particle velocity fluctuations and hydrodynamic self-diffusion of sedimenting non-Brownian spheres. Phys Fluids 7(1):12–23
Wang J, Ge W (2005) Collisional particle-phase pressure in particle-fluid flows at high particle inertia. Phys Fluids 17(128103):1–3
Yang FL, Hunt ML (2006) Dynamics of particle-particle collision in a viscous liquid. Phys Fluids 18(12):1–11 121506
Zenit R, Hunt ML (2000) Solid fraction fluctuations in solid–liquid flows. Int J Multiphase Flow 26:763–781
Zenit R, Hunt ML, Brennen CE (1997) Collisional particle pressure measurements in solid–liquid flows. J Fluid Mech 353:261–283

Formation of Massive Stars by Runaway Accretion

Leonardo Di G. Sigalotti and Jaime Klapp

Abstract Although massive stars play a dominant role in shaping galactic structure and evolution, their origin and early evolution are not well understood mainly because of the lack of a good observational guidance. One major conceptual problem in massive star formation arises from the radiation pressure they exert on the surrounding dust and gas, which could be strong enough to halt further accretion and impose a limit to the mass of a star. Radiation hydrodynamic collapse calculations of massive protostars have suggested an upper limit of $\sim 40\ M_{\odot}$ before radiation pressure can exceed the star's gravitational pull and block the infall of dusty gas. However, observational evidence for an upper mass limit near to $150\ M_{\odot}$ has been found in young massive clusters ($>10^4\ M_{\odot}$) in the Galactic Center. This cut-off seems to be unrelated to the heavy-element content of the star-forming gas, implying that radiation pressure may not be the physical mechanism that determines how massive stars can become. Here we find using frequency-dependent radiation transfer calculations, coupled to a frequency-dependent dust model, that stellar masses in excess of $100\ M_{\odot}$ may well form by runaway accretion in a collapsing, pressure-bounded logatrope. The radii and bolometric luminosities ($\sim 10^6 L_{\odot}$) of the produced stars are in good agreement with the figures reported for known candidates of massive stars.

L. D. G. Sigalotti (✉)
Centro de Física, Instituto de Venezolano de Investigaciones Científicas (IVIC), Apartado Postal 20632, Caracas, 1020-A, Venezuela
e-mail: leonardo.sigalotti@gmail.com

J. Klapp
Instituto Nacional de Investigaciones Nucleares (ININ), Km. 36.5, Carretera México-Toluca, La Marquesa, 52750, Estado de México, México
e-mail: jaime.klapp@inin.gob.mx

J. Klapp et al. (eds.), *Experimental and Theoretical Advances in Fluid Dynamics*, Environmental Science and Engineering, DOI: 10.1007/978-3-642-17958-7_5,

1 Introduction

The study of the origin of massive stars is a relatively new and increasingly important field of research in astrophysics. It is known that stars form from interstellar gas and that they synthesize elements heavier than helium by means of nuclear fusion reactions in their cores. Stars around the mass of our Sun can only produce helium, carbon, and oxygen, while stars more massive than about 8 $M_\odot$ can synthesize heavier elements up to iron and nickel. Atoms heavier than these are made in supernova explosions from the rapid combination of neutrons with heavy nuclei. Therefore the exact knowledge of how massive stars can be is a key point to understand how galaxies evolve and are enriched in these elements. Most of the stellar content of galaxies is locked up in long-lived dwarf stars (Reid et al. 2002; Kroupa 2002), which return hardly any of their mass back to their local environs, whereas stars weighing more than $\sim 20\ M_\odot$ are rarely found. The three young stellar clusters in the Galactic Center, namely the Quintuplet, the Arches, and the Central clusters (Figer et al. 1999; Figer 2003) represent the closest examples of massive starbursts and provide unique places where a number (~ 360) of stars with initial masses $>20\ M_\odot$ can be found, including Luminous Blue Variable (LBV) and Wolf-Rayet (WR) stars (Figer 2004, 2005). In particular, the Quintuplet cluster provides a view of the most massive stars that are known, the Pistol star and FMM362 both with an estimated mass of $\sim 200\ M_\odot$ (Figer et al. 1998; Geballe et al. 2000).

Despite the importance of massive stars, there is no known firm upper limit to the maximum stellar mass. Such a basic quantity escapes both theory, because of the complex interplay between radiation pressure and opacity, and observation, first, because high dust extinction makes it difficult to resolve massive stars individually and second, because they evolve so quickly (a few Myr) that important evolutionary phases are short-lived and may elude observations. However, the Arches cluster is massive enough ($>10^4\ M_\odot$) to expect the presence of high-mass stars, young enough (2.5 ± 0.5 Myr) for its most massive members to still be visible, and close enough for us to discern its individual stars (Serabyn et al. 1998; Figer et al. 2002). Figer (2005) has analyzed the stellar content of this cluster and found no stars with initial masses $>130\ M_\odot$, suggesting an upper mass cut-off of $\sim 150\ M_\odot$. A similar limit was found for the cluster R136 in the low-metallicity, Large Magellanic Cloud (Weidner and Kroupa 2003), implying that the upper mass limit is independent of the heavy-element content of the star-forming gas. Whereas theory suggests that radiation pressure, and/or ionizing flux, may inhibit accretion for stellar masses $>60\ M_\odot$ (Eddington barrier; Wolfire and Cassinelli 1987; Yorke and Sonnhalter 2002), the observations suggest that radiation pressure is not the physical mechanism that limits the stellar mass.

Theories have been proposed that invoke other mechanisms as increasing accretion rates of $\sim 10^{-4}$–$10^{-3}\ M_\odot\ \mathrm{yr}^{-1}$ compared to $\sim 10^{-6}\ M_\odot\ \mathrm{yr}^{-1}$ for low-mass star formation (e.g., Norberg and Maeder 2000; McKee and Tan 2003), accretion via disks (e.g., Jijina and Adams 1996; Yorke and Sonnhalter 2002),

accretion through hypercompact HII regions (Keto 2003; Keto and Wood 2006), the escape of radiation through wind-blown cavities (Krumholz et al. 2005a), and radiatively driven Rayleigh–Taylor instabilities (Krumholz et al. 2005b). All these variations suggest that massive stars can form within an accretion-based picture of star formation. Contrary to this, the coalescence scenario has also been proposed based on the observation that massive stars always form at the dense centers of stellar clusters. In this picture, the protostellar and stellar densities of a forming massive cluster are high enough ($\sim 10^8$ pc^{-3}) that protostars may undergo collisions and merge, thereby avoiding the effects of radiation pressure (Bonnell et al. 1998; Bally and Zinnecker 2005). Reviews on the current status of observational and theoretical research in massive star formation are given by Beuther et al. (2007) and Zinnecker and Yorke (2007).

In an attempt to model the hot molecular core (HMC) phase of early massive star formation, Osorio et al. (1999) calculated the accretion of a spherically symmetric dusty envelope onto a central OB star. They found that the best fits between the derived spectra and the observed fluxes of several internally heated HMCs were obtained from the collapse of a singular logatropic sphere (McLaughlin and Pudritz 1997), instead of a singular isothermal sphere (SIS, Shu 1977). Based on these findings, here we describe the results of further collapse calculations of massive logatropic spheres, using frequency-dependent radiation transfer coupled to the frequency-dependent dust model of Preibisch et al. (1993). We follow the early gravitational collapse, the formation of the central protostar, and its subsequent accretion phase to investigate the upper limit to the stellar mass that can be formed in a logatrope. The initial masses and sizes of the cores are consistent with those of compact cores detected in infrared dark clouds (Rathborne et al. 2007), which are thought to be the precursors of HMCs (Cesaroni 2005) within which high-mass star formation is suspected to occur (Garay and Lizano 1999; Churchwell 2002).

2 Observable Stages and Theory

2.1 Observational Results

Star formation typically begins with a collapsing gas condensation (*core*) inside a larger subunit (*clump*) of a molecular cloud (Williams et al. 2000). The term *clump* is used for condensations associated with cluster formation and the term *core* is used for much smaller condensations that form single or multiple massive protostars. Massive dense clumps have masses between a few 100 and a few 1,000 $M_\odot$, sizes of the order of 0.25–1.0 pc, mean densities of 10^5 cm^{-3}, and temperatures of 10–16 K (Beuther et al. 2007). Peak densities (cores) in such dense clumps can easily reach 10^6 cm^{-3} and are the main location where high-mass star formation is taking place. A massive protostar (i.e., a hydrostatic object

of mass >8 $M_{\odot}$ that has not yet begun hydrogen burning) forms from collapse and increases its mass by accretion (i.e., accumulation) of neighboring gas and dust, while at the same time mass loss occurs through a bipolar flow and/or a collimated jet (Zinnecker and Yorke 2007). When hydrogen burning commences, a Zero-Age-Main-Sequence (ZAMS) star is born and as long as hydrogen burning occurs at the stellar core, we speak of a main-sequence (MS) star.

Infrared dark clouds (IRDCs) are suspected to represent the earliest stages of massive star formation prior to cloud collapse (Pillai et al. 2006; Rathborne et al. 2007). They are in turn expected to harbor various evolutionary stages, from genuine high-mass starless cores to the youngest high-mass protostellar objects (HMPOs). Another class of objects termed hot molecular cores (HMCs), which were first detected at centimeter and millimeter wavelengths, have been identified as sites of massive star formation (Cesaroni 2005). These are compact (<0.1 pc) and dense ($\sim 10^6$–10^8 cm^{-3}) pockets of molecular gas, which are about 10 times less massive than their associated clumps. They have temperatures of $\sim$100–300 K and luminosities $>10^4$ $L_{\odot}$, implying that they are regions enlightened by newly born high-mass stars embedded in the cores themselves (Kurtz et al. 2000; van der Tak 2004). Therefore it has been suggested that the HMC phase presumably begins with the creation of an HMPO via free-fall collapse (De Buizer 2004). Accretion of gas and dust onto the protostar allows the HMPO to evolve later into a hot core and enter the HMC phase. HMCs are in all cases associated with H_2O masers and $\sim$50% of them also with one or more ultra-compact HII (UC HII) regions (Churchwell 2002). In contrast to earlier claims that the density distributions ($n \propto r^{-p}$) of massive star-forming clumps may have power-law indices p around 1.0, several other studies have derived density distributions with mean power-law indices around 1.5–2.5 (Fontani et al. 2002; Hatchell and van der Tak 2003; Williams et al. 2004). The end of the HMC phase is probably determined by the onset of powerful molecular outflows and the subsequent development of UC H_{II} regions, whose estimated expansion time ($\sim 10^5$ yr) is comparable to the clump life time (Wood and Churchwell 1989). This also marks the end of the accretion phase on HMCs, setting a limit of a few 100 $M_{\odot}$ on their mass. Direct observational evidence in favor of the high-mass star formation scenario proposed above is given by the region G24.78 + 0.08 (Cesaroni et al. 2003; Cesaroni 2005; Beltrán et al. 2004).

2.2 Theoretical Background

In the last two decades an ever growing effort has been made to image HMCs in the near- and mid-infrared, where information on the embedded stellar component may be obtained. This has motivated theoretical studies to take the HMC phenomenon into consideration as a fundamental ingredient in the process leading to the formation of massive stars (Osorio et al. 1999, 2009; Behrend and Maeder 2001; Yorke and Sonnhalter 2002; McKee and Tan 2003; Pascucci

et al. 2004; Krumholz et al. 2005a; Sigalotti et al. 2009). Notwithstanding the interest in the topic of HMCs, some confusion still remains on their nature and the role played by them in the context of massive star formation.

In particular, self-consistent models of the HMC phase of massive star formation were first conducted by Osorio et al. (1999), who calculated the spectral energy distribution (SED) from infrared (IR) to radio wavelengths for a spherically symmetric dusty envelope infalling onto a central OB-type star with accretion rates $\dot{M}$ from 6×10^{-4} to $10^{-3}\ M_\odot\ \mathrm{yr}^{-1}$. They found that the observed spectra of several HMCs were better reproduced using an envelope with the density distribution resulting from the collapse of a singular logatropic sphere (SLS; McLaughlin and Pudritz 1996). Isothermal envelopes were found to require much higher accretion rates ($>10^{-3}\ M_\odot\ \mathrm{yr}^{-1}$) than the logatropic ones to fit the observed SEDs of HMCs. This is expected because the SLS collapse tends to produce more massive envelopes, where inside the radius of the expansion wave only 3% of the mass is in the central star, while 97% of it resides in the collapsing envelope. However, calculations of pre-main-sequence (PMS) evolution of stars from 1 to 85 $M_\odot$ with growing accretion rates have shown that, at 85 $M_\odot$, the accretion rate may be as high as $\sim 8 \times 10^{-3}\ M_\odot\ \mathrm{yr}^{-1}$ (Behrend and Maeder 2001). Self-consistent calculations of the hydrodynamic collapse of axisymmetric massive clumps, with wavelength-dependent radiation transfer, were carried out by Yorke and Sonnhalter (2002). Their calculations, which included the effects of rotation and started with a $\rho \propto r^{-2}$ density configuration, corresponding to that of the SIS, produced central stars of 33.6 and 42.9 $M_\odot$ in clumps of 60 and 120 $M_\odot$, respectively. In particular, a maximum value of the accretion rate of $\sim 2 \times 10^{-3}\ M_\odot\ \mathrm{yr}^{-1}$ was obtained in the collapse of the 60 $M_\odot$ clump. Despite this high rate, accretion was impeded by the Eddington barrier, yielding final stellar masses which in all cases were a fraction of the initial clump mass. Evidently, in these models the outward radiative acceleration per gram of gas exceeded the inward gravitational acceleration, producing a rapid decay of the accretion luminosity and setting an upper limit to the stellar mass.

A model for the dust spectrum and ammonia (4,4) line emission of the G1.41 + 0.31 HMC was recently proposed by Osorio et al. (2009), using an envelope profile resulting from the collapse of a SLS. They predicted (2,2), (4,4), and (5,5) line transitions which were in reasonable agreement with the single-dish ammonia data. The best fit of the calculated SED with the ammonia emission for this core was obtained for a model with a central star of $\sim 25\ M_\odot$, a mass accretion rate of $\sim 3 \times 10^{-3}\ M_\odot\ \mathrm{yr}^{-1}$, and a total luminosity of $\sim 2 \times 10^5\ L_\odot$. On the other hand, radiation transfer calculations that include the effects of outflows have shown that the presence of outflows can modify the radiation field and reduce the radiation pressure around a massive protostar (Krumholz et al. 2005a), providing a mechanism for circumventing the Eddington limit and increasing rather than decreasing the final stellar mass.

3 Numerical Methods and Initial Conditions

3.1 The Clump Model

Following Sigalotti et al. (2009), we calculate the spherical gravitational collapse and subsequent accretion phase of massive nonsingular logatropes, but this time with much increased spatial resolution. The hydrodynamics couples with a radiation transfer module capable of calculating the absorption and emission of dust simultaneously with the radiation density at each frequency and the equilibrium dust temperatures. The details of the code are fully described in Sigalotti et al. (2009) and so here we shall only mention the salient aspects of the numerical scheme.

The hydrodynamics equations are the same as in Sigalotti et al. (2002), except that the gas pressure and self-gravitational acceleration term in the momentum equation has been modified to add the radiation acceleration of the grains

$$\frac{\mathrm{d}\mathbf{v}}{\mathrm{d}t} = \frac{1}{\rho c}\int_0^\infty \kappa(\nu)F(\nu)\mathrm{d}\nu, \tag{1}$$

where ν is the frequency, c is the speed of light, $\kappa(\nu)$ is the frequency-dependent extinction coefficient, and $F(\nu)$ is the frequency-dependent flux. The equation of state, relating the pressure to the density, is given by the logatropic relation (McLaughlin and Pudritz 1997):

$$p = p_c\left[1 + A\ln\left(\frac{\rho}{\rho_c}\right)\right], \tag{2}$$

here p_c and ρ_c are, respectively, the pressure and density at the center of the cloud clump and $A = 0.2$. Considering that high-mass stars may have formed from a massive starless core through an evolutionary sequence involving a HMPO stage followed by a HMC phase as a result of intense accretion of the free-falling envelope of gas and dust, we start the collapse from a marginally stable (starless), pressure-bounded logatrope, where the initial density profile is nonsingular, i.e., the clump structure consists of a central (finite) density plateau surrounded by an outer envelope, where the density varies as $\rho \propto r^{-1}$. The clump properties are completely determined by specifying the central temperature T_c, the surface pressure p_s, and the truncation radius R at which the internal pressure equals the external one (McLaughlin and Pudritz 1997). For all models we choose $T_c = 10$ K and assume solar composition ($\mu = 2.33$).

We use the frequency-dependent dust opacity model of Preibisch et al. (1993), where the dust is composed of a mixture of small amorphous carbon (aC) grains with radii between 7 and 30 nm for temperatures $\leq$2,000 K and large silicate (Si) particles with radii between 40 nm and 1 μm for temperatures in the range of 125 K $\leq T_{\mathrm{grain}} \leq$ 1,500 K (Draine 1985). At grain temperatures lower than 125 K

the silicate particles are coated with a thin mantle of dirty ice of thickness equal to 1.62 times the radius of the bare silicate cores. The optical constants of the ice mantles are valid for a mixture of H_2O- and NH_3-ice with a volume ratio of 3:1 that is polluted with aC grains. The size distribution of the grains is assumed to obey an MRN-type power law (Mathis et al. 1977). The quantities of interest in radiation transfer are the frequency-dependent absorption and scattering cross sections of the grains $\sigma_{\rm abs}$ and $\sigma_{\rm sca}$, respectively, so that the extinction cross section, or gram opacity, is given by $\sigma(\nu) = \sigma_{\rm abs} + \sigma_{\rm sca.}$ The dust opacity $\kappa(\nu)$ is finally calculated as the product $\rho\sigma(\nu)$, where ρ is the total density of the gas and dust.

We use the flux-limited diffusion (FLD) approximation proposed by Levermore and Pomraning (1981) to deal with the effects of radiation transfer. In this approximation we solve the zeroth-order moment equation

$$\nabla \cdot H(\nu) = j(\nu) + \sum_k \kappa_k^{\rm abs}(\nu)[B(\nu, T_k) - J(\nu)], \tag{3}$$

where the summation is over all dust components k, $J(\nu)$ is the mean intensity of the radiation field, B is the frequency-dependent Planck function, $j(\nu)$ is the emissivity from the central star, T_k is the grain temperature of component k, $\kappa^{\rm abs}(\nu) = \rho\sigma_{\rm abs}$ is the absorption coefficient, and $\boldsymbol{H}(\nu) = \boldsymbol{F}(\nu)/4\pi$ is the monochromatic radiation flux. The FLD approximation consists of enforcing the closure relation between the radiation flux and the radiation energy density

$$H(\nu) = -\frac{\lambda(\nu)}{\omega(\nu)\kappa(\nu)}\nabla J(\nu), \tag{4}$$

where $\omega(\nu)$ is the effective albedo and $\lambda(\nu)$ is the flux limiter, which are defined by Eqs. 15 and 16 of Sigalotti et al. (2009). Equations 3 and 4 must be solved simultaneously for all frequencies together with the condition for radiative equilibrium for each of the absorbing species:

$$\int_0^\infty \kappa_k^{\rm abs}[B(\nu, T_k) - J(\nu)]d\nu = 0. \tag{5}$$

This integral equation defines the temperature of grains of type k. The solution of these three equations gives a self-consistent description of the dust continuum emission.

During the phase of early collapse, the code works in a Lagrangian mode up to the point where the density profile becomes approximately singular everywhere. Immediately after singularity formation a spherical sink cell is activated around the center $r = 0$ and the collapse is continued in an Eulerian mode. An inflow/outflow boundary condition is enforced at the surface of the sink cell (Foster and Chevalier 1993). The mass which crosses this surface and enters the sink cell condenses at $r = 0$ and interacts with the rest of the grid gravitationally via a point mass potential and through its own radiation, heating the clump envelope from

inside. The mass of the central protostar, M_*, is given by the mass of the sink cell and is calculated at any time as the time integral of the mass accretion rate, $\dot{M}$, over the time interval dt. For a spherically symmetric accreting star, the total, or bolometric, luminosity is given by the sum of the intrinsic luminosity and the accretion luminosity

$$L_{\rm bol} = L_* + L_{\rm acc} = L_* + GM_*\dot{M}/R_*, \tag{6}$$

where R_* is the stellar radius. From the star's mass and age we can fix its position in the Hertzsprung-Russell (HR) diagram and determine its intrinsic luminosity L_*, effective temperature $T_{\rm eff}$, and radius R_*. When the mass of the central protostar is less than 0.02 $M_\odot$, the stellar radius is determined using a mass-radius relation consistent with a polytrope of degree $n = 3/2$ (Kippenhahn and Weigert 1990), which is a fairly good approximation for fully convective protostars of low mass in the PMS. For masses $> 0.02\ M_\odot$, we use published PMS and MS tracks of Population I stars to determine L_* and $T_{\rm eff}$. In particular, when $0.02\ M_\odot \leq M_* \leq 1.10\ M_\odot$, we employ the PMS tracks for nonaccreting stars calculated by D'Antona and Mazzitelli (1994), which incorporate deuterium and lithium burning in detail. For $1.188\ M_\odot \leq M_* \leq 15.74\ M_\odot$, we use the tracks published by Behrend and Maeder (2001) for stars leaving the birthline after their accretion phase, while for higher masses we use the MS tracks of Schaller et al. (1992), which apply to stars starting their evolution from the ZAMS at the beginning of the H-burning phase.

The emergent flux of the embedded star for wavelengths between 3 and 30 μm is one observable in the course of the evolution that we can use to constrain the models. If we assume that the star radiates as a blackbody, the emergent flux (or SED) at a distance d from the source can be calculated as (Wolfire and Cassinelli 1987)

$$\nu F(\nu) = \pi R_{\rm ph}^2 \nu B(\nu, T_k)/d^2, \tag{7}$$

where $R_{\rm ph}$ is the photospheric radius, which separates the optically thick regions from the optically thin ones, and $T_{\rm ph}$ is the photospheric temperature, i.e., the temperature at the radius where the optical depth $\tau = 2/3$. If the accretion rate is high enough, the flow becomes optically thick prior to reaching the central star.

3.2 Initial Conditions and Parameters

We choose a sequence of clump models with initial masses ranging from 20 to 150 $M_\odot$. Table 1 lists the initial conditions, where the entries, starting from the first column, are, respectively, the initial clump mass, the central density, the surface pressure, the clump radius, the mean free-fall time in terms of the average clump density, and the total mass contained by the growing protostar at the time when the accretion rate achieves its maximum value (see Sect. 4 below). In all models, the collapse of the clumps is initiated by enhancing everywhere the

Table 1 Initial conditions for collapse of the massive clumps

Clump mass ($M_\odot$)	ρ_c(g cm^{-3})	p_s(k cm^{-3}K)	R(pc)	t_{ff}(10^5yr)	$M_*(M_\odot)$
20	2.15(−17)	2.753(6)	0.105	1.262	8.04
50	3.44(−18)	4.406(5)	0.263	3.155	20.18
92	1.01(−18)	1.300(5)	0.483	5.808	36.91
120	5.97(−19)	7.649(4)	0.630	7.572	48.09
150	3.82(−19)	4.895(4)	0.788	9.465	61.07

equilibrium density profile by a small fraction $\delta = 0.008$ so that the mass and pressure are also increased by the same fractional amount.

The temperature of the gas and dust is set initially equal to 10 K everywhere and the initial mean intensity $J(\nu)$ is defined as the frequency-dependent Planck function at this temperature, implying that there is no radiation flux at $t = 0$ since according to Eq. 4 $H(\nu) = 0$. Solution of Eq. 3 demands fixing the mean intensity at the outer clump boundary to a constant value equal to the Planck function at $T = 10$ K for all times ($t > 0$). Equation 3 is discretized using finite differences on a spherical radial grid consisting of 1,000 concentric shells of uniform width initially. In comparison, the calculations of Sigalotti et al. (2009) employed only 400 shells. The resolution of the frequency mesh was also increased from 128 to 256 logarithmically equidistant points covering the range between $\nu_{min} = 6.0 \times 10^{10}$ Hz ($\lambda = 5{,}000$ μm) and $\nu_{max} = 3.0 \times 10^{15}$ Hz ($\lambda = 0.1$ μm). After discretization of Eq. 3, the mean intensity is obtained by means of a tridiagonal matrix solver and the grain temperature is calculated simultaneously with the mean intensity by means of an iterative procedure on Eq. 5. A typical run took from 20 to 25 million steps to complete the evolution, corresponding to more than a week of CPU time on a DELL Precision 670 computer equipped with 4 processors of 3.6 GHz each.

4 Results

In this section we describe the results obtained for a set of massive clump collapse calculations with initial conditions similar to those reported by Sigalotti et al. (2009), but with much improved spatial resolution. With this provision, the new models are designed to provide a much better description of the central flow close to the point of singularity formation and across the sink cell where mass accretion is being tracked.

Prior to singularity formation the effects of radiation are not important and the collapse is entirely dominated by gravity. The details of the early collapse are very similar to those described by Sigalotti et al. (2002) for nonradiative clumps. In Fig. 1, we display the evolution of the central protostar in terms of the mass

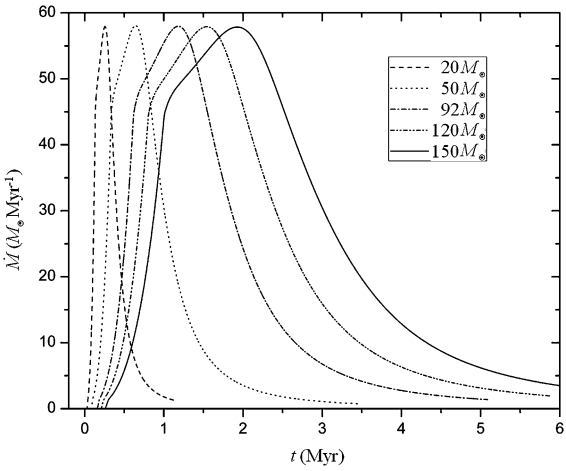

Fig. 1 Time variation of the mass accretion rate for all models

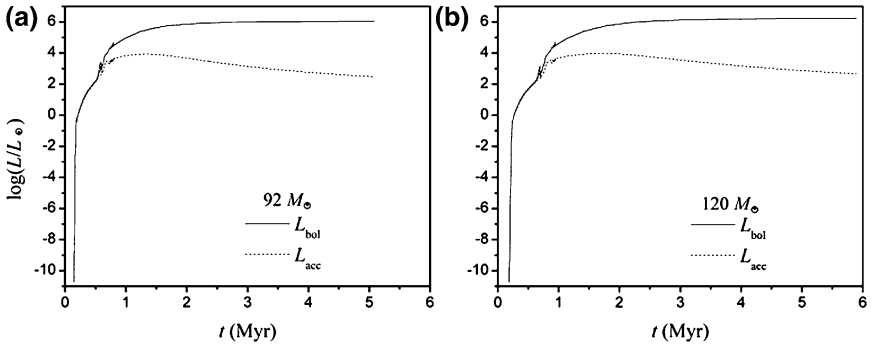

Fig. 2 Time variation of the bolometric (*solid line*) and accretion (*dashed line*) luminosities for a clump with **a** 92.05 $M_\odot$ and **b** 120 $M_\odot$

accretion rate. In a logatrope, the accretion timescale increases with the clump mass. After singularity formation, the speed at which mass is accreted into the protostar rises rapidly and steepens for clumps of lower mass. This also causes a rapid rise of the luminosity, which at this stage is almost entirely given by the accretion luminosity as shown in Fig. 2, where the evolution of the bolometric (solid line) and accretion (dotted line) luminosities is depicted for the 92 and 120 $M_\odot$ clumps. Thereafter, the accretion rate slows down and reaches a peak of $\sim 5.82 \times 10^{-5}\,M_\odot\,\mathrm{yr}^{-1}$, which shifts toward longer times for higher envelope masses. At this point nearly 42% of the envelope mass has been accreted by the central protostar. The accretion rate attains its maximum value when the collapse

expansion wave reaches the outer surface of the clump and is the same for all clumps independently of their initial mass.

This is true because for critically stable logatropes, the accretion rate varies as $p_s^{3/2}t^3$. The surface pressure decreases and the time of the peak increases with increasing mass in such a way that the product $p_s^{3/2}t^3$ remains constant for all masses. Once the expansion wave reaches the clump surface, the accretion rate declines slowly because of the finite mass reservoir. We note that the SIS models of Yorke and Sonnhalter (2002) and the SLS models of Osorio et al. (1999) have predicted much higher peaks of the accretion rate ($\sim 10^{-3}$–$10^{-4}\ M_\odot\ \mathrm{yr}^{-1}$) compared to our nonsingular logatropes. Evidently the radiation pressure does not halt the collapse and stars with masses higher than 100 $M_\odot$ may well form by runaway accretion in a nonsingular logatrope. When the accretion rate has dropped to $\sim 1.0 \times 10^{-5}\ M_\odot\ \mathrm{yr}^{-1}$ more than 90% of the envelope mass has condensed into the central star, while the remaining 10% does it very slowly. When the accretion rate peaks, the bolometric luminosity exceeds the accretion luminosity by about two orders of magnitude because of the intrinsic luminosity of the central star (Fig. 2). By the time when more than 98% of the envelope mass has been accreted into the central star, our models predict stellar radii of ~ 9.5, 13.6, 15.4, and 43.8 $R_\odot$ and luminosities of $\sim 3.7 \times 10^5$, 1.2×10^6, 1.9×10^6, and $5.1 \times 10^6\ L_\odot$ for the 50, 92, 120, and 150 $M_\odot$ clumps, respectively.

These values are very close to those obtained in the lower resolution runs by Sigalotti et al. (2009) and are not too far from those inferred for stars with initial masses in excess of 100 $M_\odot$ (Figer 2005; Barniske et al. 2008). In particular, Barniske et al. (2008) reported an analysis of the K-band spectra of WR 102c and WR 102 ka, two of the most luminous WN stars in the Galaxy, inferring initial masses in excess of 100 and 150 $M_\odot$, radii of 20 and 92 R, and luminosities of $\sim 2.0 \times 10^6$ and $3.2 \times 10^6\ L_\odot$, respectively, which are in fairly good agreement with the predictions of our models.

In Fig. 3 we show the emergent flux distribution (SED) from the stellar photosphere at different stages during accretion for the 20, 92, and 120 $M_\odot$ cores. All the spectra are measured at a reference distance $d = 4.9$ kpc from the source (see Eq. 7). During rapid accretion (solid lines), the peaks of emission occurs at a frequency of ~ 260 GHz in the microwave region for the 20 $M_\odot$ core, while the more massive clumps exhibit stronger emission peaks toward the far-infrared (FIR). During declination of the accretion rate (dashed lines) and at the end of accretion (dot-dashed lines) the peaks of emission shift toward the FIR and the lower frequency extreme of the mid-infrared (MIR) for the 20 $M_\odot$ clump and toward the MIR for the more massive clumps (Fig. 3b and c). At the late stages of accretion, substantial radiation is being emitted in the microwave and FIR bands, with the more massive stars showing also significant NIR emission. Only little radiation escapes the photosphere in the radio wavelengths and essentially no visible and ultraviolet radiation is emitted. These results are also in fair agreement with observations of HMCs, which display not only microwave and MIR luminosities, but NIR emission as well (Persi et al. 2003).

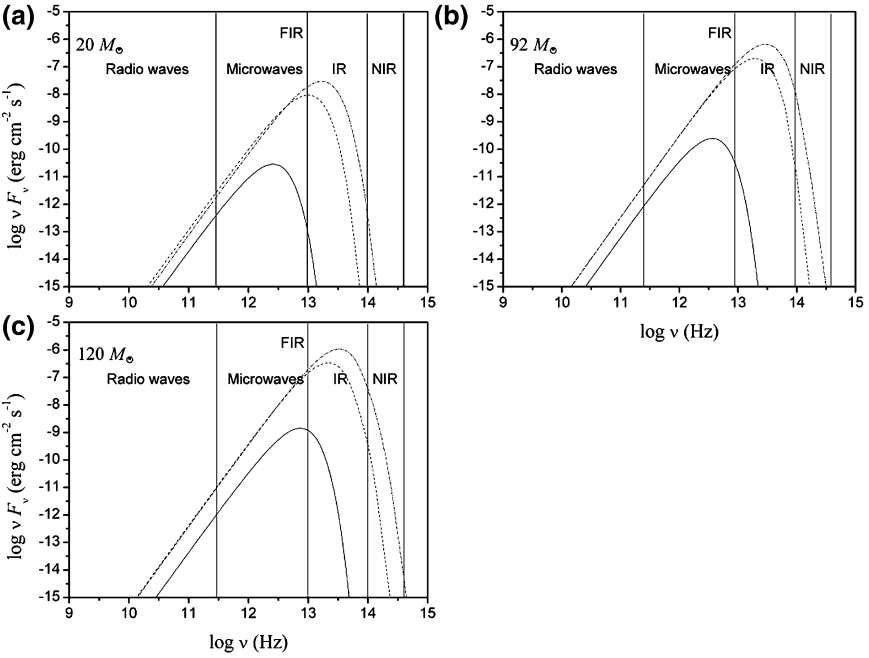

Fig. 3 Derived SEDs at three distinct times during collapse of the **a** 20 $M_\odot$, **b** 92 $M_\odot$, and **c** 120 $M_\odot$ clumps. The *solid line* displays the spectrum during the stage of rapid accretion, while the *dashed* and *dot-dashed lines* depict the emission at late stages of accretion. The radio wave, microwave, IR, and NIR bands are shown

5 Conclusions

We have carried out further numerical calculations of the radiation hydrodynamic collapse of massive $(20\,M_\odot \leq M_{\rm clump} \leq 150\,M_\odot)$, pressure-bounded logatropes, starting with much improved spatial resolution and initial conditions close to radiative and hydrostatic equilibrium. We find that there is no an apparent upper mass cut-off in a logatrope due to grain deceleration as induced by the radiation pressure gradient of the infrared field. In all models, runaway accretion is maintained because the inward gravitational acceleration per gram always exceeds the outward radiative acceleration. Therefore, stars as massive as the initial core can form via continued accretion.

Although the use of a central sink oversimplifies the physics in the innermost regions, the logatropic collapse models predict reasonably well the microwave to MIR to NIR emission detected for massive protostars in the HMC phase of evolution. A more detailed treatment of the central flow accompanied by the inclusion of rotation and stellar outflow mechanisms, will certainly improve the physics and produce the observed dust thermal spectrum from radio wavelengths to infrared as well as the expected NIR to ultraviolet emission for massive stars.

References

Bally J, Zinnecker H (2005) The birth of high-mass stars: accretion and/or mergers? Astron J 129:2281–2293

Barniske A, Oskinova LM, Hamann W-R (2008) Two extremely luminous WN stars in the galactic center with circumstellar emission from dust and gas. Astron Astrophys 486:971–984

Behrend R, Maeder A (2001) Formation of massive stars by growing accretion rate. Astron Astrophys 373:190–198

Beltrán MT, Cesaroni R, Neri R, Codella C, Furuya RS, Testi L, Olmi L (2004) Rotating disks in high-mass young stellar objects. Astrophys J 601:L187–L190

Beuther H, Churchwell EB, McKee CF, Tan JC (2007) The formation of massive stars. In: Reipurth B, Jewitt D, Keil K (eds) Protostars and planets V. University of Arizona Press, Tucson, pp 165–180

Bonnell IA, Bate MR, Zinnecker H (1998) On the formation of massive stars. Mon Not R Astron Soc 298:93–102

Cesaroni R (2005) Hot molecular cores. In: Cesaroni R, Felli M, Churchwell E, Walmsley M (eds) Massive star birth: a crossroads of astrophysics. Proceedings of IAU Symposium 227, Florence, Italy, 16–20 May 2004, pp 59–69

Cesaroni R, Codella C, Furuya RS, Testi L (2003) Anatomy of a high-mass star forming cloud: the G24.78 + 0.08 (proto)stellar cluster. Astron Astrophys 401:227–242

Churchwell E (2002) Ultra-compact H_{II} regions and massive star formation. Annu Rev Astron Astrophys 40:27–62

D'Antona F, Mazzitelli I (1994) New pre-main-sequence tracks for $M \leq 2.5\ M_{\odot}$ as tests of opacities and convection model. Astrophys J Suppl Ser 90:467–500

De Buizer JM (2004) High-resolution mid-infrared observations of high mass protostellar objects. In: Burton M, Jayawardhana R, Bourke T (eds) Star formation at high angular resolution. Proceedings of IAU Symposium 221, Sydney, Australia, 22–25 July 2003, pp 181–189

Draine BT (1985) Tabulated optical properties of graphite and silicate grains. Astrophys J Suppl Ser 57:587–594

Figer DF (2003) Massive stars and the creation of our galactic center. In: van der Hucht K, Herrero A, Esteban C (eds) A massive star odyssey: From main sequence to supernova. Proceeings of IAU Symposium 212, Canary Island, Spain, 24–28 June 2001, pp 487–496

Figer DF (2004) Young massive clusters in the galactic center. In: Lamers HJGLM, Smith LJ, Nota A (eds) The formation and evolution of massive young clusters. ASP Conference Series, San Francisco: ASP, 322:49–58

Figer DF (2005) An upper limit to the masses of stars. Nature 434:192–194

Figer DF, Najarro F, Morris M, McLean IS, Geballe TR, Ghez AM, Langer N (1998) The Pistol star. Astrophys J 506:384–404

Figer DF, Kim SS, Morris M, Serabyn E, Rich RM, McLean IS (1999) Hubble space telescope/NICMOS observations of massive stellar clusters near the galactic center. Astrophys J 525:750–758

Figer DF, Najarro F, Gilmore D, Morris M, Kim SS, Serabyn E, McLean IS, Gilbert AM, Graham JR, Larkin JE, Levenson NA, Teplitz HI (2002) Massive stars in the Arches cluster. Astrophys J 581:258–275

Fontani F, Cesaroni R, Caselli P, Olmi L (2002) The structure of molecular clumps around high-mass young stellar objects. Astron Astrophys 389:603–617

Foster PN, Chevalier RA (1993) Gravitational collapse of an isothermal sphere. Astrophys J 416:303–311

Garay G, Lizano S (1999) Massive stars: their environment and formation. Publ Astron Soc Pac 111:1049–1087

Geballe TR, Najarro F, Figer DF (2000) A second luminous blue variable in the Quintuplet cluster. Astrophys J 530:L97–L101

Hatchell J, van der Tak FFS (2003) The physical structure of high-mass star-forming cores. Astron Astrophys 409:589–598

Jijina J, Adams FC (1996) Infall collapse solutions in the inner limit: radiation pressure and its effects on star formation. Astrophys J 462:874–887

Keto E (2003) The formation of massive stars by accretion through trapped hypercompact H_{II} regions. Astrophys J 599:1196–1206

Keto E, Wood K (2006) Observations on the formation of massive stars by accretion. Astrophys J 637:850–859

Kippenhahn R, Weigert A (1990) Stellar structure and evolution. Springer, Heidelberg

Kroupa P (2002) The initial mass function of stars: evidence for uniformity in variable systems. Science 295:82–91

Krumholz MR, McKee CF, Klein RI (2005a) Bondi accretion in the presence of vorticity. Astrophys J 618:757–768

Krumholz MR, Klein RI, McKee CF (2005b) Radiation pressure in massive star formation. In: Cesaroni R, Felli M, Churchwell E, Walmsley M (eds) Massive star birth: A crossroads of astrophysics. Proceedings of IAU Symposium 227, Florence, Italy, 16–20 May 2004, pp 231–236

Kurtz S, Cesaroni R, Churchwell E, Hofner P, Walmsley CM (2000) Hot molecular cores and the earliest phases of high-mass star formation. In: Mannings V, Boss AP, Russell SS (eds) Protostars and planets IV. University of Arizona Press, Tucson, pp 299–326

Levermore CD, Pomraning GC (1981) A flux-limited diffusion theory. Astrophys J 248:321–334

Mathis JS, Rumpl W, Nordsieck KH (1977) The size distribution of interstellar grains. Astrophys J 217:425–433

McKee CF, Tan JC (2003) The formation of massive stars from turbulent cores. Astrophys J 585:850–871

McLaughlin DE, Pudritz RE (1996) A model for the internal structure of molecular cloud cores. Astrophys J 469:194–208

McLaughlin DE, Pudritz RE (1997) Gravitational collapse and star formation in logotropic and nonisothermal spheres. Astrophys J 476:750–765

Norberg P, Maeder A (2000) On the formation of massive stars by accretion. Astron Astrophys 359:1025–1034

Osorio M, Lizano S, D'Alessio P (1999) Hot molecular cores and the formation of massive stars. Astrophys J 525:808–820

Osorio M, Anglada G, Lizano S, D'Alessio P (2009) Collapsing hot molecular cores: a model for the dust spectrum and ammonia line emission of the G31.41 + 0.31 hot core. Astrophys J 694:29–45

Pascucci I, Apai D, Henning T, Stecklum B, Brandl B (2004) The hot core-ultracompact H_{II} connection in G10.47 + 0.03. Astron Astrophys 426:523–534

Persi P, Tapia M, Roth M, Marenzi AR, Testi L, Vanzi L (2003) Near and mid-infrared images of the massive star forming complex G9.62 + 0.19. Astron Astrophys 397:227–236

Pillai T, Wyrowski F, Menten KM, Krügel E (2006) High mass star formation in the infrared dark cloud G11.11-0.12. Astron Astrophys 447:929–936

Preibisch T, Ossenkopf V, Yorke HW, Henning T (1993) The influence of ice-coated grains on protostellar spectra. Astron Astrophys 279:577–588

Rathborne JM, Simon R, Jackson JM (2007) The detection of protostellar condensations in infrared dark cloud cores. Astrophys J 662:1082–1092

Reid IN, Gizis JE, Hawley SL (2002) The Palomar/MSU nearby star spectroscopy survey. IV. The luminosity function in the solar neighborhood and M dwarf kinematics. Astron J 124:2721–2738

Schaller G, Schaerer D, Meynet G, Maeder A (1992) New grids of stellar models from 0.8 to 120 $M_{\odot}$ at $Z = 0.020$ and $Z = 0.001$. Astron Astrophys Suppl Ser 96:269–331

Serabyn E, Shupe D, Figer DF (1998) An extraordinary cluster of massive stars near the centre of the Milky Way. Nature 394:448–451

Shu FH (1977) Self-similar collapse of isothermal spheres and star formation. Astrophys J 214:488–497
Sigalotti L Di G, de Felice F, Sira E (2002) Gravitational collapse of nonsingular logatropic spheres. Astron Astrophys 395:321–338
Sigalotti L Di G, de Felice F, Daza-Montero J (2009) Collapse of molecular cloud cores with radiation transfer: formation of massive stars by accretion. Astrophys J 707:1438–1448
van der Tak FFS (2004) Hot molecular cores and high mass star formation. In: Burton M, Jayawardhana R, Bourke T (eds) Star formation at high angular resolution. Proceeings of IAU Symposium 221, Sydney, Australia, 22–25 May 2003, pp 59–66
Weidner C, Kroupa P (2003) Evidence for a fundamental stellar upper mass limit from clustered star formation. Mon Not R Astron Soc 348:187–191
Williams JP, Blitz L, McKee CF (2000) The structure and evolution of molecular clouds: from clumps to cores to the IMF. In: Mannings V, Boss AP, Russell SS (eds) Protostars and planets IV. University of Arizona Press, Tucson, pp 97–120
Williams SJ, Fuller GA, Sridharan TK (2004) The circumstellar environments of high-mass protostellar objects. I. Submillimetre continuum emission. Astron Astrophys 417:115–133
Wolfire MG, Cassinelli JP (1987) Conditions for the formation of massive stars. Astrophys J 319:850–867
Wood DOS, Churchwell E (1989) Massive stars embedded in molecular clouds—their population and distribution in the galaxy. Astrophys J 340:265–272
Yorke HW, Sonnhalter C (2002) On the formation of massive stars. Astrophys J 569:846–862
Zinnecker H, Yorke HW (2007) Toward understanding massive star formation. Annu Rev Astron Astrophys 45:481–563

Strong Shocks with Smoothed Particle Hydrodynamics

Jaime Klapp, Leonardo Di G. Sigalotti, Franklin Peña-Polo and Leonardo Trujillo

Abstract Godunov-type methods relying on Riemann solvers have performed spectacularly well on supersonic compressible flows with sharp discontinuities as in the case of strong shocks. In contrast, the method of standard smoothed particle hydrodynamics (SPH) has been known to give a rather poor description of strong shock phenomena. Here we focus on the one-dimensional Euler equations of gas dynamics and show that the accuracy and stability of standard SPH can be significantly improved near sharp discontinuities if the bandwidth (or smoothing length, h) of the interpolating kernel is calculated by means of an *adaptive density estimation* procedure. Unlike existing adaptive SPH formulations, this class of estimates introduces less broad kernels in regions where the density is low, implying that the minimum necessary smoothing is applied in these regions. The resolving power of the method is tested against the strong shock-tube problem and the interaction of two blast waves. The quality of the solutions is comparable to that obtained using Godunov-type schemes and, in general, superior to that obtained from Riemann-based SPH formulations.

J. Klapp (✉)
Instituto Nacional de Investigaciones Nucleares (ININ), Km. 36.5,
Carretera México-Toluca, La Marquesa, 52750 Estado de México, Mexico
e-mail: jaime.klapp@inin.gob.mx

L. D. G. Sigalotti · F. Peña-Polo · L. Trujillo
Centro de Física, Instituto Venezolano de Investigaciones Científicas (IVIC),
Apartado Postal 20632, Caracas 1020-A, Venezuela
e-mail: leonardo.sigalotti@gmail.com

F. Peña-Polo
e-mail: franklin.pena@gmail.com

L. Trujillo
e-mail: leonardo.trujillo@gmail.com

J. Klapp et al. (eds.), *Experimental and Theoretical Advances in Fluid Dynamics*, Environmental Science and Engineering, DOI: 10.1007/978-3-642-17958-7_6,

1 Introduction

The dynamical evolution of a fluid is determined by the principles of conservation of mass, momentum, and energy supplemented by constitutive relations that characterize the material properties of the fluid. Since the pioneering work of Riemann (1860), this set of conservation laws has motivated many of the central ideas in both the analysis of hyperbolic partial differential equations and the development of numerical methods for solving them.

A Riemann problem for a system of conservation laws is an initial value problem such that the initial data is scale-invariant (Menikoff and Plohr 1989). In one dimension (1D), the initial data consist of different constant states on the left and right of a jump discontinuity. In particular, the solution of the Riemann problem for the 1D Euler equations of gas dynamics admits three types of elementary waves, namely: shock waves, rarefaction waves, and contact discontinuities (Toro 1997). Contact discontinuities are linear waves across which both the pressure and velocity are constant but the density jumps discontinuously. The other two waves are nonlinear and arise from sharp changes in density, pressure, and velocity. Shock waves accompany compression of the fluid, whereas rarefactions are associated to expansions of the fluid. In particular, a shock wave is a thin transition layer propagating with supersonic speed in a fluid and can form from the steepening of ordinary compression waves. The transition layer for a strong shock is of the same order of magnitude as the mean-free path for elastic collisions of the fluid molecules. Therefore, at a microscopic level, a shock wave has a finite thickness which decreases as the Mach number, $M = v/c$, increases, where v is the fluid velocity and c is the speed of sound in the fluid. However, on macroscopic scales, a shock front can be defined as an infinitely thin discontinuity (or jump) with a reasonably good approximation.

Riemann problems have played a key role in the framework of Godunov-type methods (Godunov 1959) for solving the equations of gas dynamics in the presence of sharp discontinuities (e.g., van Leer 1979; Colella and Woodward 1984; Woodward and Colella 1984; Colella and Glaz 1985; Fryxell et al. 1986; Munz 1994; Miller and Puckett 1996; Rider 1999; Shashkov and Wendroff 1999). A drawback of Riemann-based solutions is that the Riemann problem must be solved anew when the equation of state (EOS) is changed. However, they display low dissipative errors and present favourable stability and robustness properties due to the inherent upwind treatment of the flow, resulting in unrivalled shock-capturing abilities. In contrast, conventional smoothed particle hydrodynamics (SPH) is known to suffer from either excessive post-shock oscillations and/or excessive smearing of the shock front, resulting in a poor description of shock phenomena compared to high-quality Godunov-type schemes (Monaghan and Gingold 1983).

This technical difficulty has been partly solved with the advent of SPH reformulations based on Riemann solutions (Monaghan 1997; Inutsuka 2002; Cha and Whitworth 2003; Ferrari et al. 2007). In particular, Monaghan (1997) focused on modifying the artificial viscous terms in the SPH equations according to Riemann

solver prescriptions, while Inutsuka (2002) and Cha and Whitworth (2003) relied on solutions of the Riemann problem to evaluate the force between each pair of interacting particles. A similar approach was also employed by Ferrari et al. (2007) but solving the Riemann problem in Lagrangian coordinates. Alternative SPH formulations for handling strong shocks and that do not rely on Riemann solvers have also started to appear (Børve et al. 2001; Sigalotti et al. 2006). A common feature of these latter methods is that the particle distribution is used to shape the smoothing length (h) profile and not vice versa which has normally been the case. In the method proposed by Børve et al. (2001), a strategy of particle regularization is employed to improve the estimation of gradients by redefining the particle distribution after a number of time steps in accordance with a previous update of h, whereas the scheme proposed by Sigalotti et al. (2006) combines ordinary SPH with an adaptive density kernel estimation (ADKE) as described by Silverman (1996). In this approach, the density is estimated at the location of particles to derive a locally variable h that minimizes the amount of smoothing, and therefore the broadness of the kernel, in regions of low density. This feature results in a significant reduction of the rates of numerical dissipation and diffusion, while the adaptive character of the kernel improves the accuracy and stability near sharp discontinuities. Here we focus on SPH solutions of the 1D Euler equations for an ideal gas and show that the SPH ADKE method can be used to calculate difficult test cases, involving strong shocks as well as multiple interactions of strong shocks and rarefactions with each other and with contact discontinuities.

2 Gas Dynamic Equations

A stream of gas moving along the x-axis of a Cartesian coordinate system can be described by the set of conservation laws:

$$\frac{1}{\rho}\frac{d\rho}{dt} = -\frac{\partial v}{\partial x}, \tag{1}$$

$$\frac{dv}{dt} = -\frac{1}{\rho}\frac{\partial p}{\partial x}, \tag{2}$$

$$\frac{dU}{dt} = -\frac{p}{\rho}\frac{\partial v}{\partial x}, \tag{3}$$

where d/dt is the substantial time derivative, ρ is the gas density, v is the velocity, U is the specific internal energy, and p is the pressure. For an ideal gas, the EOS is given by

$$p = (\gamma - 1)\rho U, \tag{4}$$

where γ is the adiabatic index.

3 Discrete SPH Equations

For numerical work, the stream of gas is represented by N particles, of equal mass m, linearly distributed along the x-axis, which act as interpolation centers to determine the fluid properties. It is common use in SPH to calculate the smoothed estimate of the density at the position x_a of particle a by the summation interpolant

$$\rho_a = \sum_{b=1}^{N} m_b W_{ab}, \tag{5}$$

where $W_{ab} = W(|x_a - x_b|, h)$ is the kernel function giving different weights to the information provided by particle a and h is the smoothing length, or bandwidth of the kernel, specifying the extension of the interpolation associated to particle a. In practice, smoothing kernels with compact supports are almost always used, so that a fix number $N_n \ll N$ of particles, or neighbors, around particle a contribute to the density summation in Eq. 5.

If Eq. 5 is used to calculate the density, variational consistency of the SPH scheme will demand using standard symmetrized SPH representations for Eqs. 2 and 3 (Bonet and Lok 1999). In particular, we use the symmetrized SPH discretizations:

$$\frac{dv_a}{dt} = -\sum_{b=1}^{N} m_b \left(\frac{p_a}{\rho_a^2} + \frac{p_b}{\rho_b^2} + \Pi_{ab} \right) \frac{\partial W_{ab}}{\partial x_a}, \tag{6}$$

$$\frac{dU_a}{dt} = -\frac{1}{2} \sum_{b=1}^{N} m_b \left[\left(\frac{p_a}{\rho_a^2} + \frac{p_b}{\rho_b^2} + \Pi_{ab} \right) (v_b - v_a) + 2H_{ab}(x_b - x_a) \right] \frac{\partial W_{ab}}{\partial x_a}, \tag{7}$$

for Eqs. 2 and 3, respectively. Here Π_{ab} is an artificial viscous term, which is used to dissipate post-shock oscillations in the solution and avoid interparticle penetration in high Mach number collisions (Monaghan and Gingold 1983; Monaghan 1988), and H_{ab} is an artificial heat conduction term, which is added to reduce the wall-heating errors that may arise in applications to infinite strength shocks (Noh 1987), as may occur when two streams of gas collide supersonically, or when a stream of gas is brought to rest against a fixed solid wall. For the artificial viscosity we use the following prescription (Monaghan and Gingold 1983):

$$\Pi_{ab} = \frac{-\alpha c_{ab} \mu_{ab} + \beta \mu_{ab}^2}{\rho_{ab}}, \tag{8}$$

which must be applied only when $(v_a - v_b)(x_a - x_b) < 0$. In the above expression

$$\mu_{ab} = \frac{(v_a - v_b)(x_a - x_b)}{h_{ab}(x_{ab}^2/h_{ab}^2 + \epsilon^2)}, \tag{9}$$

where c_{ab}, ρ_{ab} and h_{ab} are, respectively, the average sound speed, density, and smoothing length between particles a and b and $x_{ab} = |x_a - x_b|$. The values of α and β are of order unity and $\varepsilon^2 = 0.01$, so that smoothing of the velocity will only take place when the particle spacing is less than 0.1 h. We note that the linear term in Eq. 8 produces a shear and bulk viscosity, whereas the quadratic term is introduced to handle high Mach number shocks. Since the use of Eq. 8 in Lagrangian methods may induce errors in the form of excessive heating, we use for the artificial heat conduction term the form:

$$H_{ab} = \frac{2\hbar_{ab}(U_a - U_b)}{\rho_{ab} h_{ab}^2 \left(x_{ab}^2/h_{ab}^2 + \epsilon^2\right)}, \tag{10}$$

where $\hbar_{ab}$ is the average artificial conduction coefficient (normalized to the density) between particles a and b, with

$$\hbar_a = g_1 h_a c_a + g_2 h_a^2 [\,|\partial v_a/\partial x_a| - \partial v_a/\partial x_a\,], \tag{11}$$

where g_1 and g_2 are numbers of order unity. The artificial heat flux is activated only when the artificial viscosity is nonzero. In addition, the second term on the right-hand side of Eq. 11 takes a finite positive value only when there is a compression ($\nabla . \boldsymbol{v} < 0$) and vanishes otherwise.

Equations 5, 6, and 7 are solved simultaneously together with the equation

$$\frac{dx_a}{dt} = v_a, \tag{12}$$

for the instantaneous position of particles.

4 Adaptive Density Kernel Estimation

In order to solve sharp discontinuities in the flow in an accurate and stable manner we must device an adaptive procedure that guarantees accurate evaluation of the kernel gradients near such discontinuities. We find that one simple way to do so is by using the density distribution of particles to estimate the bandwidth, h, of the interpolating kernel function. Among the several existing procedures, one which works surprisingly well for strong gradients and jumps is the estimation procedure proposed by Silverman (1996). In the first step, the method consists of calculating after each time step a *pilot* density estimate from the actual particle distribution using the summation interpolant

$$\overline{\rho_a} = \sum_{b=1}^{N} m_b W(x_{ab}, h_{0,a}), \tag{13}$$

where $h_{0,a}$ is the smoothing length of particle a at the beginning of the new time step. Note that at the beginning of the calculation ($t = 0$), $h_{0,a} = D\Delta x_0$, where D is some dilation factor of the initial uniform interparticle separation Δx_0. In the second step, local bandwidth factors, λ_a, are calculated for each particle a from the pilot estimates according to the formula

$$\lambda_a = k\left(\frac{\overline{\rho_a}}{q}\right)^{-\varepsilon}, \tag{14}$$

where q is a geometric mean of the pilot density given by

$$\log q = \frac{1}{N}\sum_{b=1}^{N} \log \overline{\rho_a}, \tag{15}$$

k is a scaling factor of order unity, and ε is a sensitivity parameter defined in the interval $0 \leq \varepsilon \leq 1$. If we set $\varepsilon = 0$ in Eq. 14, the method reduces to the fixed width kernel approach of standard SPH since $\lambda_a = 1$. On the other hand, if $\varepsilon \to 1$ we get the largest possible sensitivity of λ_a with the density profile, implying the greatest difference between the smoothing lengths in different parts of the sample. In the third step, the adaptive estimator is obtained by redefining the width of the kernel around particle a as $h_a = \lambda_a h_{0,a}$ and recalculating the density with $h_{0,a}$ replaced by h_a in Eq. 13. According to Eq. 14, the adaptive character of h_a is reflected by the length of influence of the kernel being small in regions of high density (high concentration of particles), while it will be larger in zones of low density (low concentration of particles). The amount of smoothing (i.e., broadness of the kernel) will be regulated by the free parameter ε, which must be chosen according to stability considerations. A von Neumann stability analysis of Eqs. 5, 6, and 7 for an ideal gas has shown that the method is stable for a wide range of the free parameters k and ε provided that the linear contribution of the artificial heat conduction coefficient in Eq. 11 is always kept at a sufficiently low value (Sigalotti et al. 2009). This is usually the case near a strong shock, where the quadratic term in Eq. 11 overwhelms the linear one. Values of $\varepsilon \gtrsim 0.5$ are enough to guarantee a minimum smoothing in regions of low density, resulting in a significant reduction of the rates of numerical dissipation and diffusion compared to other existing adaptive SPH formulations. As a final remark, the actual kernel estimate that is employed in Eqs. 5, 6, and 7 is based on the symmetrized form (Hernquist and Katz 1989)

$$W_{ab} = \frac{1}{2}[W(x_{ab},\ h_a) + W(x_{ab},\ h_b)], \tag{16}$$

in order to ensure conservation of linear momentum and total energy.

5 Numerical Tests

For the numerical tests of this section, we shall assume that at the beginning of the calculation the particles are uniformly spaced along the x-axis. We use the cubic B-spline function of Monaghan and Lattanzio (1985) as the interpolating kernel. With this form of the kernel, the particle interactions are exactly zero at distances from the peak of the distribution greater than $2h$.

5.1 Modified Shock-Tube Problem

As a first difficult test, we consider the modified shock-tube problem containing a very strong (Mach 771) shock as proposed by Fryxell et al. (1986). The Riemann problem for this test consists of an ideal gas with adiabatic index $\gamma = 5/3$, left state ($x < 0.6$) given by $\rho_L = 1$, $p_L = 10^6$, $v_L = 0$, and right state ($x \geq 0.6$) given by $\rho_R = 1$, $p_R = 1$, $v_R = 0$. Even with the use of high-quality Godunov-type schemes, an accurate description of this test requires starting the calculation with an initial high spatial resolution. To do so we use 1,000 equidistant particles of equal mass within the interval $0 \leq x \leq 1$. We set $\alpha = \beta = 1$ in Eq. 8 for the artificial viscosity, $g_1 = 0.2$ and $g_2 = 1$ in Eq. 11 for the artificial heat conduction coefficient, $k = 1$ and $\varepsilon = 0.8$ for the ADKE parameters in Eq. 14, and use a constant time step $\Delta t = 5 \times 10^{-6}$ units. Initially, the smoothing length was chosen to be the same for all particles with $h_0 = 1.5\Delta x_0$.

In Fig. 1 we show the numerical solution (dots) as compared with the exact one (solid lines) at $t = 4 \times 10^{-4}$ units. When the diaphragm is broken, the initial discontinuity splits up into three regions. The first region consists of a rarefaction wave to the left where all fluid variables change continuously. To the right of the rarefaction tail there is a second region extending up to the location of a contact discontinuity across which the pressure and velocity are continuous, while the density and thermal energy are discontinuous. To the right of the contact discontinuity there is a post-shock region bordered by a strong shock wave moving to the right. We see that the numerical solution overlaps the exact one in most regions, except for the small roundings at the foot and top of the contact discontinuity, which are in turn responsible for the very small wiggles present in the pressure and velocity profiles at the borders of the post-shocked region.

The post-shock profiles and the shock position are reproduced with relative errors of better than 0.3 and 0.1%, respectively. The smooth profiles at the foot and top of the contact discontinuity can be sharpened by reducing the value of g_1 at the expense of a slight increase of the wiggling amplitude in the velocity and pressure. The quality of the SPH solution for this test is as good as that obtained by Fryxell et al. (1986) using an implicit-explicit Godunov-type scheme on a grid of 1,000 zones of equal width and a time step of 4×10^{-7} units (see their Fig. 10). The good performance of SPH on this test is a clear evidence of the resolving

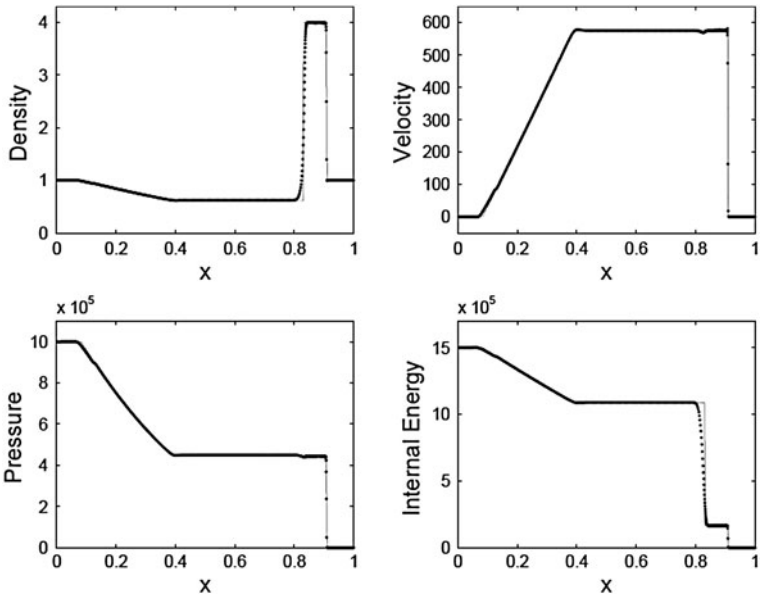

Fig. 1 Numerical solution (*dots*) compared to the exact one (*solid line*) for the modified shock-tube problem containing a Mach 771 shock at $t = 4 \times 10^{-4}$ units

power of the ADKE method. Different choices of $h_0/\Delta x_0$ result essentially in the same numerical profiles of Fig. 1.

5.2 Interaction of Two Blast Waves

As a second test problem, we consider the interaction of two blast waves as described by Woodward and Colella (1984). This test is extremely difficult and was originally calculated to illustrate the strong relationship between the accuracy of the overall flow and the thinness of the discontinuities on the grid for high-performing Godunov-type methods.

For this test the Riemann problem consists of a $\gamma = 1.4$ gas at rest between reflecting walls separated by a distance of unity and with three constant states given by $(\rho_L = 1, v_L = 0, p_L = 10^3)$ for $0 \leq x < 0.1$, $(\rho_M = 1, v_M = 0, p_M = 10^{-2})$ for $0.1 \leq x < 0.9$, and $(\rho_R = 1, v_R = 0, p_R = 10^2)$ for $0.9 \leq x \leq 1$ Since there is no known analytical solution for this problem, we compare our numerical results with an accurate solution obtained with the ADKE method using 5,000 equally spaced particles over the range $0 \leq x \leq 1$ (Sigalotti et al. 2009). We employ the same parameters as for the accurate solution, namely $\alpha = \beta = 1$, $g_1 = 0.2$, $g_2 = 1$, and $k = 1$, and differ only in the value of the sensitivity parameter which for this run we

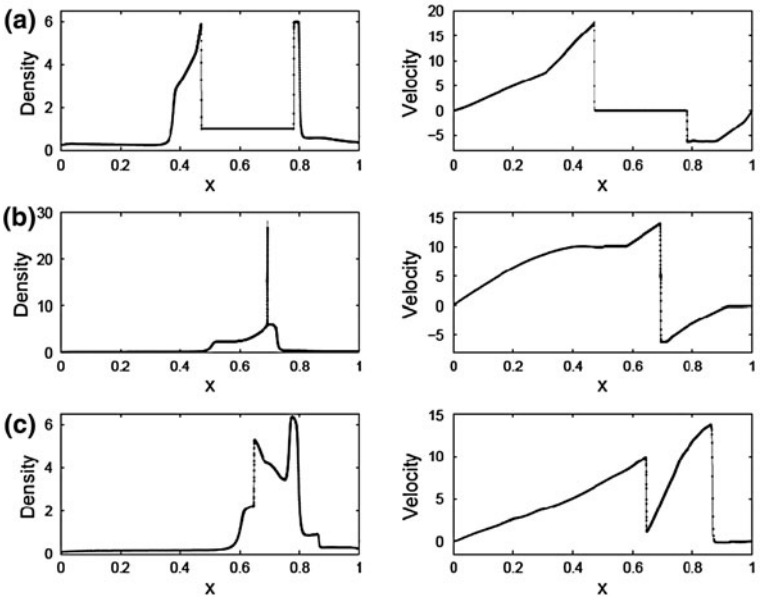

Fig. 2 Density and velocity profiles for two interacting blast waves at three distinct times during the evolution: **a**$t = 0.016$. **b**$t = 0.028$. **c**$t = 0.038$. The calculated profiles with 2,000 particles (*dots*) are compared with a highly-resolved solution with 5,000 particles (*solid lines*)

set to $\varepsilon = 0.7$ against $\varepsilon = 0.8$ for Sigalotti et al. (2009). In this way, we reduce the sensitivity of the bandwidth factors to variations in the density. We use 2,000 equidistant particles, $h_0/\Delta x_0 = 2$, and a variable time stepping. The resulting density and velocity profiles are shown in Fig. 2 (dots) as compared to the highly-resolved ADKE solution (solid line) at $t = 0.016$, 0.028, and 0.038 units. For comparison the reference grid for this test as was originally calculated by Woodward and Colella (1984) with a special version of their Piecewise Parabolic Method (PPM) contained 3,096 equidistant zones (see their Fig. 2).

At $t = 0.016$ units (Fig. 2a), we see that, on the right, the initial pressure jump has split up into a strong shock travelling into the cold gas and a strong rarefaction wave running into the hot gas and reflecting from the wall at $x = 1$. Between the strong shock and the rarefaction near this wall are two constant states separated by a strong contact discontinuity. On the left, near the wall at $x = 0$, a rarefaction has already reflected off this wall and is moving to the right. This has overtaken the strong shock and weakened it. The two blast waves approach each other and collide by $t = 0.028$ units (Fig. 2b), giving rise to a sharp density spike which is indeed well resolved by the calculation. In the next evolution, a rarefaction between the two reflected shocks emerges, bringing the peak density down and giving rise to a lot of structure as the result of multiple interactions of strong nonlinear waves and discontinuities of various kinds. The bottom panels (Fig. 2c), at $t = 0.038$ units, show the final flow pattern obtained. Although a broader kernel

has been used for this run compared to the highly-resolved solution, the profiles almost entirely overlap, apart from a slight reduction of the density spike (Fig. 2b). If we compare the results to those of Woodward and Colella (1984) in their Fig. 2, we shall see that the ADKE method has been quite successful at reproducing the complex details of their PPM solution.

6 Conclusions

We have presented an alternative SPH formulation to usual schemes based on Riemann solvers for evolving compressible flows with sharp discontinuities. The method converts ordinary SPH into a shock-capturing scheme through the use of an adaptive density kernel estimation (ADKE) procedure. In brief, the method consists of using the particle density distribution to calculate local smoothing lengths that minimize both the broadness of the kernel and the amount of smoothing that is effectively applied to the data in regions of low density. While, in general, this feature improves the accuracy of SPH, it becomes particularly important near sharp discontinuities as in the case of phenomena involving strong shocks and rarefactions.

The resolving power of the method has been demonstrated for two difficult tests, namely the modified shock-tube problem containing a strong shock of Fryxell et al. (1986) and the interaction of two blast waves as originally described by Woodward and Colella (1984). In both cases, the ADKE procedure has produced high-quality solutions that are comparable to those from Godunov-type methods and in most cases superior to existing SPH formulations relying on Riemann solvers. In addition, the ADKE procedure is easy to implement and can be generalized to two and three dimensions in a very straightforward manner.

References

Bonet J, Lok T-SL (1999) Variational and momentum preservation aspects of smoothed particle hydrodynamic formulations. Comput Methods Appl Mech Eng 180:97–115

Børve S, Omang M, Trulsen J (2001) Regularized smoothed particle hydrodynamics: a new approach to simulating magnetohydrodynamics shocks. Astrophys J 561:82–93

Cha S-H, Whitworth AP (2003) Implementations and tests of Godunov-type particle hydrodynamics. Mon Not R Astron Soc 340:73–90

Colella P, Glaz HM (1985) Efficient solution algorithms for the Riemann problem for real gases. J Comput Phys 59:264–289

Colella P, Woodward PR (1984) The piecewise parabolic method (PPM) for gas dynamical simulations. J Comput Phys 54:174–201

Ferrari A, Dumbser M, Toro EF, Armanini A (2007) A new stable and consistent version of the SPH method in Lagrangian coordinates. SPHERIC: smoothed particle hydrodynamics european research interest community, 2nd international workshop, Universidad Politécnica de Madrid, Madrid, Spain, 18–23 May 2007, pp 79–82

Fryxell BA, Woodward PR, Colella P, Winkler K-H (1986) An implicit-explicit hybrid method for Lagrangian hydrodynamics. J Comput Phys 63:283–310
Godunov SK (1959) A difference method for numerical calculation of discontinuous solutions of the equations of hydrodynamics. Matematicheskii Sbornik 47:271–306
Hernquist L, Katz N (1989) TREESPH-A unification of SPH with the hierarchical tree method. Astrophys J Suppl Ser 70:419–446
Inutsuka S (2002) Reformulation of smoothed particle hydrodynamics with Riemann solver. J Comput Phys 179:238–267
Menikoff R, Plohr BJ (1989) The Riemann problem for fluid flow of real materials. Rev Mod Phys 61:75–130
Miller GH, Puckett EG (1996) A high-order Godunov method for multiple condensed phases. J Comput Phys 128:134–164
Monaghan JJ (1988) An introduction to SPH. Comput Phys Commun 48:89–96
Monaghan JJ (1997) SPH and Riemann solvers. J Comput Phys 136:298–307
Monaghan JJ, Gingold RA (1983) Shock simulation by the particle method SPH. J Comput Phys 52:374–389
Monaghan JJ, Lattanzio JC (1985) A refined particle method for astrophysical problems. Astron Astrophys 149:135–143
Munz CD (1994) On Godunov-type schemes for Lagrangian gas dynamics. SIAM J Numer Anal 31:17–42
Noh WF (1987) Errors for calculations of strong shocks using an artificial viscosity and an artificial heat flux. J Comput Phys 72:78–120
Rider WJ (1999) An adaptive Riemann solver using a two-shock approximation. Comput Fluids 28:741–777
Riemann B (1860) Uber die Forpflanzung ebener Luftwellen von endlicher Schwingungsweite. In Weber H (ed) Collected Works of Bernhard Riemann, 1953, Dover, New York, p 157
Shashkov M, Wendroff B (1999) A composite scheme for gas dynamics in Lagrangian coordinates. J Comput Phys 150:502–517
Sigalotti LDG, López H, Donoso A, Sira E, Klapp J (2006) A shock-capturing SPH scheme based on adaptive kernel estimation. J Comput Phys 212:124–149
Sigalotti LDG, López H, Trujillo L (2009) An adaptive SPH method for strong shocks. J Comput Phys 228:5888–5907
Silverman BW (1996) Density Estimation for Statistics and Data Analysis. Chapman and Hall, London
Toro EF (1997) Riemann solvers and numerical methods for fluid dynamics: a practical introduction. Springer-Verlag, Berlin
van Leer B (1979) Towards the ultimate conservative difference scheme. V. A second-order sequel to Godunov's method. J Comput Phys 32:101–136
Woodward P, Colella P (1984) The numerical simulation of two-dimensional fluid flow with strong shocks. J Comput Phys 54:115–173

The Role of a Scalar Dark Matter Model in the Large Scale Structure Formation in the Universe

M. A. Rodríguez-Meza

Abstract We study the large scale structure formation in the Universe using a dark matter model steaming from a scalar–tensor theory of gravitation. We present the equations that govern the evolution of the scale factor of the Universe and also the appropriate Newtonian equations to follow the non-linear evolution of the structures. Results are given in terms of the power spectrum that gives quantitative information on the structure formation. The initial conditions we have used are consistent with the so called concordance ΛCDM model.

1 Introduction

Modern cosmological observations establish that the Universe behaves as dominated by dark matter (DM) and dark energy. However, the direct evidence for the existence of these invisible components remains lacking. Several theories that would modify our understanding of gravity have been proposed in order to explain the large scale structure formation in the Universe and the galactic dynamics. The best model we have to explain the observations is the ΛCMD model, i.e., the model of cold dark matter (CDM)—non-relativistic particles at the epoch of last scattering of unknown origin—with cosmological constant (Λ), in particular, this model explains very well the Universe on scales of galaxy clusters and up Bretón et al. (2004).

M. A. Rodríguez-Meza (✉)
Depto. de Física, Instituto Nacional de Investigaciones Nucleares,
Apdo. Postal 18-1027, 11801 México D.F., Mexico
e-mail: marioalberto.rodriguez@inin.gob.mx

J. Klapp et al. (eds.), *Experimental and Theoretical Advances in Fluid Dynamics*,
Environmental Science and Engineering, DOI: 10.1007/978-3-642-17958-7_7,

The ΛCDM model has become the theoretical paradigm leading the models of the Universe to explain the large scale structure (LSS) formation and several other observations. Where "large" means scales larger than 1 Mpc—about the size of the group of galaxies that our Milky Way belongs. Together with the cosmic inflation theory, this model makes a clear prediction about the necessary initial conditions that the Universe has to have in order to have the structures we observe and that those structures build hierarchically due to a gravitational instability. One of its main predictions is that the density profile of galaxies, clusters of galaxies, and so on, is of the form (Navarro et al. 1996, 1997),

$$\rho_{NFW}(r) = \frac{\rho_0}{(r/r_0)(1 + r/r_0)^2},$$

a density profile known as Navarro–Frenk–White profile (NFW). Parameters ρ_0 and r_0 must be fitted, for example, using rotation curves of galaxies.

The ΛCDM model and its success in explaining several observations—this is why this model is also known as the concordance model—yields the following conclusions: on large scales, the Universe is homogeneous and isotropic, as described by the Friedmann–Lamaitre–Robertson–Walker (FLRW) metric. The geometry of the Universe is flat, as predicted by inflation. The dark matter is cold (non-relativistic at decoupling epoch). The initial density fluctuations were small and described by a Gaussian random field. The initial power spectrum of the density fluctuations was approximately the Harrison–Zeldovich spectrum ($P(k) \propto k^n$, $n = 1$) (Zeldovich 1970; Binney and Tremaine 2008).

In terms of the composition of the Universe, the above conclusions can be summarized as follows: Hubble's constant (expansion rate of the Universe at the present epoch): $H_0 = 73.2 \pm 3.1$ km/s/Mpc. Parameter of density (combined mass density of all kind of mass and energy in the Universe, divided by the critical density): $\Omega_0 = 1.02 \pm 0.02$. Matter density parameter (combined mass density of all forms of matter in the Universe, divided by the critical density): $\Omega_m = 0.241 \pm 0.034$. Ordinary matter parameter density (density of mass of ordinary atomic matter in the Universe divided by the critical density): $\Omega_b = 0.0416 \pm 0.001$. Density parameter of dark energy (mass density of dark energy in the Universe divided by the critical density): $\Omega_\Lambda = 0.759 \pm 0.034$ (Komatsu 2011).

Even though of all successes of the ΛCDM, this model has several problems. Some of them are: the number of satellites in a galaxy such as the Milky Way is predicted to be an order of magnitude larger than is observed. Cuspy halo density profiles. The number of superclusters observed in surveys of galaxies (like SDSS) data appears to be an order of magnitude larger than predicted by ΛCDM simulations. The lack of evidence in the Milky Way for a major merger is hard to reconcile with the amount of accretion predicted by ΛCDM.

Also, almost a decade ago a bow shock in the merging cluster 1E0657-56, known as the "bullet cluster", observed by satellite Chandra indicates that the subcluster—found by Barrena et al. (2002)—moving through this massive (10^{15} h^{-1} $M_\odot$) main cluster creates a shock with a velocity as high as 4700 km s^{-1}

(Markevitch 2006; Markevitch et al. 2002). A significant offset between the distribution of X-ray emission and the mass distribution has been observed (Clowe 2004, 2006), also indicating a high-velocity merger with gas stripped by ram pressure. Several authors have done detailed numerical non-cosmological simulations (Takizawa 2005, 2006; Milosavljevic 2007; Springel and Farrar 2007; Mastropietro 2008). One of the key input parameters for the simulations is to set the initial velocity of the subcluster, which is usually given at somewhere near the virial radius of the main cluster. Lee and Komatsu (2011) have run cosmological N-body simulation using a large box ($27\,h^{-3}\,\mathrm{Gpc}^3$) to calculate the distribution of infall velocities of subclusters around massive main clusters. The infall velocity distribution were given at 1–3 R_{200}—similar to the virial radius—and thus it gives the distribution of realistic initial velocities of subclusters just before collision. This distribution of infall velocities must be compared with the best initial velocity used by Mastropietro and Burkert (2008) of 3,000 km s^{-1} at about $2R_{200}$ to be in agreement with observations. Lee and Komatsu (2011) have found that such a high infall velocity is incompatible with the prediction of the ΛCDM.

Therefore, there are plenty of problems that the concordance model have to solve and finally, it does not tell us what is dark matter and dark energy.

The program to study the large scale structure formation should be to start with primordial initial conditions which means give the initial relevant fields, such as for example, density and velocity fields at the epoch of last scattering ($\sim z = 1{,}100$, the value of the redshift at that epoch, i.e., a photon emitted at that epoch is redshifted as $1 + z = \lambda_r/\lambda_e$, with λ_e the wavelength of the photon when emitted, and λ_r is the wavelength of the same photon when observed; the expansion factor for a universe with a flat geometry is related to the redshift as $1 + z = 1/a$). Then, evolve this initial condition using an N-body scheme up to the present epoch ($z = 0$).

Some questions we have to answer are: What are the distribution of the LSS sizes? What is the amount of mass and its distribution at large scales? How are the voids distributed through the space? Are these voids devoid of any matter? How the LSS evolve with time? What is the DM equation of state? What is its role in the LSS formation processes and galactic dynamics? What are the implications of the observed LSS on the cosmological model of our Universe? And on the structure formation? And of course, what is the nature of the dark energy and matter?

During the last decades there have been several proposals to explain DM, for example: massive compact halo objects (Machos), weakly interacting massive particles (WIMPs), supersymmetric particle like the neutralino. Other models propose that there is no dark matter and use general relativity with an appropriate equation of state. Or we can use scalar fields, minimally or non minimally coupled to the geometry.

In this work we are mainly concern with the problem of dark matter and its consequences on the large scale structure formation process. Our DM model is based on using a scalar field (SF) that is coupled non-minimally with the geometry

in the Einstein field equations. A scalar field is the most simple field of nature. Nordstrom proposed a gravity theory by 1912, before Einstein (Faraoni 2004). Scalar fields have been around for so many years since pioneering work of Jordan, Brans, and Dicke. Nowadays, they are considered as: (a) inflation mechanism; (b) the dark matter component of galaxies; (c) the quintessence field to explain dark energy; and so on. Therefore, is natural to consider dark matter model based on modifications of Einstein's general relativity that include scalar fields.

So we organize our work in the following form: in the next section we present the general theory of a typical scalar–tensor theory (STT), i.e., a theory that generalizes Einstein's general relativity by including the contribution of a scalar field that couples non-minimally to the metric. In Sect. 3 we show how the Friedmann equations becomes within a STT and present our model for the evolution of the Universe expansion factor $a(t)$. In Sect. 4, we present the N-body method which we will use to obtain the evolution of the large scale structures. Our results for an initial condition of the fields that is consistent with the observations is given in Sect. 5 Finally, our conclusions are given in Sect. 6.

2 General Scalar–Tensor Theory and Its Newtonian Limit

The Lagrangian that gives us the Einstein equations of general relativity is

$$\mathscr{L} = \frac{\sqrt{-g}}{16\pi G} R \tag{1}$$

The Einstein field equations that are obtained from the above Lagrangian, in the limit of small velocities as compared with the speed of light and small forces, limit known as the Newtonian limit, give us the standard Newtonian potential due to a body of mass m

$$\Phi_N = -G\frac{m}{r} \tag{2}$$

where G is the gravitational constant. What we intend to do in this work is to obtain the consequences in the LSS formation processes when we rise the constant G to a scalar field, $1/G \rightarrow \phi$. But we go beyond this approach and include in the Lagrangian two additional terms that depend on this field, a kinetic and potential terms. We will show, in particular, that the Newtonian limit of this theory gives for the Newtonian potential due to a mass m (Rodríguez-Meza and Cervantes-Cota 2004),

$$\Phi_N = -G\frac{m}{r}\left(1 + \alpha e^{-r/\lambda}\right) \tag{3}$$

i.e., the standard Newtonian potential is modified by an additional term that has the form of a Yukawa potential.

Then, we start with the Lagrangian of a general scalar–tensor theory

$$\mathscr{L} = \frac{\sqrt{-g}}{16\pi}\left[-\phi R + \frac{\omega(\phi)}{\phi}(\partial\phi)^2 - V(\phi)\right] + \mathscr{L}_M(g_{\mu\nu}). \tag{4}$$

Here $g_{\mu\nu}$ is the metric, $\mathscr{L}_M(g_{\mu\nu})$ is the matter Lagrangian and $\omega(\phi)$ and $V(\phi)$ are arbitrary functions of the scalar field. The fact that we have a potential term $V(\phi)$ tells us that we are dealing with a massive scalar field. Also, the first term in the brackets, ϕR, is the one that gives the name of non-minimally coupled scalar field.

When we make the variations of the action, $S = \int d^4x\mathscr{L}$, with respect to the metric and the scalar field we obtain the Einstein field equations (Faraoni 2004)

$$R_{\mu\nu} - \frac{1}{2}g_{\mu\nu}R = \frac{1}{\phi}\left[8\pi T_{\mu\nu} + \frac{1}{2}Vg_{\mu\nu} + \frac{\omega}{\phi}\partial_\mu\phi\partial_\nu\phi - \frac{1\omega}{2\phi}(\partial\phi)^2 g_{\mu\nu} + \phi_{;\mu\nu} - g_{\mu\nu}\Box\phi\right], \tag{5}$$

for the metric $g_{\mu\nu}$ and for the massive SF ϕ we have

$$\Box\phi = \frac{1}{3+2\omega}\left[8\pi T - \omega'(\partial\phi)^2 + \phi V' - 2V\right], \tag{6}$$

where $()' \equiv \frac{\partial}{\partial\phi}$. Here $T_{\mu\nu}$ is the energy–momentum tensor with trace T, $\omega(\phi)$ and $V(\phi)$ are in general arbitrary functions that govern kinetic and potential contribution of the SF. If in Lagrangian (Eq. 4) we set $V(\phi) = 0$ we get the Bergmann–Wagoner theory. If we further set $\omega(\phi) =$ constant the Jordan–Brans–Dicke theory is recovered. The gravitational constant is now contained in $V(\phi)$. Also, the potential contribution, $V(\phi)$, provides mass to the SF, denoted here by m_{SF}.

2.1 Newtonian Limit of a STT

The study of large-scale structure formation in the Universe is greatly simplified by the fact that a limiting approximation of general relativity, the Newtonian mechanics, applies in a region small compared to the Hubble length cH^{-1} ($cH_0^{-1} \approx 3,000\,\mathrm{h}^{-1}$ Mpc, where c is the speed of light, $H_0 = 100\,\mathrm{h}$ km/s/Mpc, is Hubble's constant and $h \approx (0.5-1)$), and large compared to the Schwarzschild radii of any collapsed objects. The rest of the Universe affect the region only through a tidal field. The length scale cH_0^{-1} is of the order of the largest scales currently accessible in cosmological observations and $H_0^{-1} \approx 10^{10}\ \mathrm{h}^{-1}$ year characterizes the evolutionary time scale of the Universe.

Therefore, in the present study, we need to consider the influence of SF in the limit of a static STT, and then we need to describe the theory in its Newtonian approximation, that is, where gravity and the SF are weak (and time independent)

and velocities of dark matter particles are non-relativistic. We expect to have small deviations of the SF around the background field, defined here as $\langle\phi\rangle$ and can be understood as the scalar field beyond all matter. Accordingly we assume that the SF oscillates around the constant background field

$$\phi = \langle\phi\rangle + \bar{\phi}$$

and

$$g_{\mu\nu} = \eta_{\mu\nu} + h_{\mu\nu},$$

where $\eta_{\mu\nu}$ is the Minkowski metric. Then, Newtonian approximation gives (Pimentel and Obregón 1986; Salgado 2002; Helbig 1991; Rodríguez-Meza and Cervantes-Cota 2004)

$$R_{00} = \frac{1}{2}\nabla^2 h_{00} = \frac{G_N}{1+\alpha}4\pi\rho - \frac{1}{2}\nabla^2\bar{\phi}\ , \tag{7}$$

$$\nabla^2\bar{\phi} - m_{\rm SF}^2\bar{\phi} = -8\pi\alpha\rho\ , \tag{8}$$

we have set $\langle\phi\rangle = (1+\alpha)/G_N$ and $\alpha \equiv 1/(3+2\omega)$. In the above expansion we have set the cosmological constant term equal to zero, since on small galactic scales its influence should be negligible. However, at cosmological scales we do take into account the cosmological constant contribution, see below.

Note that Eq. 7 can be cast as a Poisson equation for $\psi \equiv (1/2)(h_{00} + \bar{\phi}/\langle\phi\rangle)$,

$$\nabla^2\psi = 4\pi\frac{G_N}{1+\alpha}\rho \tag{9}$$

and the new Newtonian potential is given by $\Phi_N \equiv (1/2)h_{00} = \psi - (1/2)\bar{\phi}/\langle\phi\rangle$. Above equation together with

$$\nabla^2\bar{\phi} - \lambda^{-2}\bar{\phi} = -8\pi\alpha\rho\ , \tag{10}$$

form a Poisson–Helmholtz equation and gives

$$\Phi_N = \psi - \frac{1}{2}\frac{G_N}{1+\alpha}\bar{\phi}$$

which represents the Newtonian limit of the STT with arbitrary potential $V(\phi)$ and function $\omega(\phi)$ that where Taylor expanded around $\langle\phi\rangle$. The resulting equations are then distinguished by the constants G_N, α, and $\lambda = h_P/m_{\rm SF}c$. Here h_P is Planck's constant.

The next step is to find solutions for this new Newtonian potential given a density profile, that is, to find the so-called potential–density pairs. General solutions to Eqs. 9 and 10 can be found in terms of the corresponding Green functions, and the new Newtonian potential is (Rodríguez-Meza and Cervantes-Cota 2004; Rodríguez-Meza et al. 2005)

$$\Phi_N \equiv \frac{1}{2}h_{00} = -\frac{G_N}{1+\alpha}\int d\mathbf{r}_s \frac{\rho(\mathbf{r}_s)}{|\mathbf{r}-\mathbf{r}_s|} - \alpha\frac{G_N}{1+\alpha}\int d\mathbf{r}_s \frac{\rho(\mathbf{r}_s)\mathrm{e}^{-|\mathbf{r}-\mathbf{r}_s|/\lambda}}{|\mathbf{r}-\mathbf{r}_s|} + \text{B.C.} \tag{11}$$

The first term of Eq. 11, is the contribution of the usual Newtonian gravitation (without SF), while information about the SF is contained in the second term, that is, arising from the influence function determined by the modified Helmholtz Green function, where the coupling ω (α) enters as part of a source factor.

The potential of a single particle of mass m can be easily obtained from Eq. 11 and is given by

$$\Phi_N = -\frac{G_N}{1+\alpha}\frac{m}{r}\left(1+\alpha e^{-r/\lambda}\right) \tag{12}$$

For local scales, $r \ll \lambda$, deviations from the Newtonian theory are exponentially suppressed, and for $r \gg \lambda$ the Newtonian constant diminishes (augments) to $G_N/(1+\alpha)$ for positive (negative) α. This means that Eq. 12 fulfills all local tests of the Newtonian dynamics, and it is only constrained by experiments or tests on scales larger than—or of the order of—λ, which in our case is of the order of galactic scales. In contrast, the potential in the form of Eq. 3 with the gravitational constant defined as usual does not fulfills the local tests of the Newtonian dynamics (Fischback and Talmadge 1999).

It is appropriate to give some additional details on the Newtonian limit for the Einstein equations without scalar fields (see Peebles 1980). We are considering a small region compared to the Hubble length cH^{-1} but large compared to the Schwarzschild radii of any collapsed object. In this small region the metric tensor was written as $g_{\mu\nu} = \eta_{\mu\nu} + h_{\mu\nu}$ where $h_{\mu\nu}$ is small as compared to the Minkowski metric $\eta_{\mu\nu}$. In this region Einstein's field equations are simple because the standard weak field linear approximation applies. One finds,

$$R_{00} = -\frac{1}{2}\eta^{\mu\nu}(h_{\mu\nu,00} - h_{\mu 0,\nu 0} - h_{\nu 0,\mu 0} + h_{00,\mu\nu}) = \nabla_r^2\Phi \tag{13}$$

$$g_{00} = c^2 + 2\Phi \tag{14}$$

Then, the zero–zero component of the field equations for an ideal fluid with density ρ, pressure p, and velocity $v \ll c$ becomes

$$\nabla_r^2\Phi = 4\pi G_N\left(\rho + 3\frac{p}{c^2}\right) - \Lambda \tag{15}$$

For completeness the cosmological constant has been added. The geodesic equations, in the limit $v \ll c$, $h \ll 1$, are

$$\frac{d^2 r^i}{\mathrm{d}t^2} = -\Phi_{,i} \tag{16}$$

Equations 15 and 16 are the standard equations of Newtonian mechanics, except that if there is an appreciable radiation background, one must take into account the active gravitational mass associated with the pressure, and of course if $\Lambda \neq 0$, there is the cosmic force $\Lambda \mathbf{r}/3$ between particles at separation $\mathbf{r}$.

Equations 15 and 16 apply to any observer outside a singularity, though depending on the situation, the region within which these equations apply need not contain much matter. The region can be extended by giving the observer an acceleration g_i to bring the observer to rest relative to distant matter, which adds the term $g_i r^i$ to Φ, and then by patching together the results from neighboring observers. This works (the acceleration and potentials can be added) as long as relative velocities of observers and observed matter are $\ll c$ and $\Phi \ll c^2$ (Eq. 14). For a region of size R containing mass $M \sim \rho R^3$ with density ρ roughly uniform, this second condition is

$$G_N \rho R^2 \ll c^2 \tag{17}$$

In the Friedmann–Lamaître models Hubble's constant is

$$H \sim (G_N \rho)^{1/2} \tag{18}$$

If one assumes Λ is negligible and the density parameter $\Omega \sim 1$, so Eq. 17 indicates

$$R \ll cH^{-1} \sim 3{,}000\,\mathrm{Mpc} \sim 10^{28}\,\mathrm{cm} \tag{19}$$

That is, the region must be small compared to the Hubble length. Since the expansion velocity is $v = Hr$, this condition also says $v \ll c$.

The Newtonian approximation can fail at much smaller R if the region includes a compact object like a neutron star or black hole, but one can deal with this by noting that at distances large compared to the Schwarzschild radius the object acts like an ordinary Newtonian point mass. It is speculated that in nuclei of galaxies there might be black holes as massive as $10^9\,\mathrm{M}_\odot$, Schwarzschild radius $\sim 10^{14}$ cm. If this is an upper limit, Newtonian mechanics is a good approximation over a substantial range of scales, 10^{14} cm $\ll r \ll 10^{28}$ cm.

2.2 Multipole Expansion of the Poisson–Helmholtz Equations

The Poisson's Green function can be expanded in terms of the spherical harmonics, $Y_{ln}(\theta, \varphi)$,

$$\frac{1}{|\mathbf{r} - \mathbf{r}_s|} = 4\pi \sum_{l=0}^{\infty} \sum_{n=-l}^{l} \frac{1}{2l+1} \frac{r_<^l}{r_>^{l+1}} Y_{ln}^*(\theta', \varphi') Y_{ln}(\theta, \varphi),$$

where $r_<$ is the smaller of $|\mathbf{r}|$ and $|\mathbf{r}_s|$, and $r_>$ is the larger of $|\mathbf{r}|$ and $|\mathbf{r}_s|$ and it allows us that the standard gravitational potential due to a distribution of

mass $\rho(\mathbf{r})$, without considering the boundary condition, can be written as (Jackson 1975)

$$\psi(\mathbf{r}) = \psi^{(i)} + \psi^{(e)}$$

where $\psi^{(i)}$ ($\psi^{(e)}$) are the internal (external) multipole expansion of ψ,

$$\psi^{(i)} = -\sum_{l=0}^{\infty}\sum_{n=-l}^{l}\frac{\sqrt{4\pi}}{2l+1}q_{ln}^{(i)}Y_{ln}(\theta,\varphi)r^{l},$$
$$\psi^{(e)} = -\sum_{l=0}^{\infty}\sum_{n=-l}^{l}\frac{\sqrt{4\pi}}{2l+1}q_{ln}^{(e)}\frac{Y_{ln}(\theta,\varphi)}{r^{l+1}},$$

Here, the coefficients of the expansions $\psi^{(i)}$ and $\psi^{(e)}$, known as internal and external multipoles, respectively, are given by

$$q_{ln}^{(i)} = \sqrt{4\pi}\int\limits_{V(r\le r')} d\mathbf{r}'\frac{1}{r'^{l+1}}Y_{ln}^{*}(\theta',\varphi')\rho(\mathbf{r}'),$$
$$q_{ln}^{(e)} = \sqrt{4\pi}\int\limits_{V(r> r')} d\mathbf{r}'Y_{ln}^{*}(\theta',\varphi')r'^{l}\rho(\mathbf{r}').$$

The integrals are done in a region V where $r \le r'$ for the internal multipoles and in a region V where $r > r'$ for the external multipoles. They have the property

$$\begin{aligned} q_{l(-n)}^{(i)} &= (-1)^{n}\left(q_{ln}^{(i)}\right)^{*} \\ q_{l(-n)}^{(e)} &= (-1)^{n}\left(q_{ln}^{(e)}\right)^{*} \end{aligned} \tag{20}$$

We may write expansions above in cartesian coordinates up to quadrupoles. For the internal multipole expansion we have

$$\psi^{(i)} = -M^{(i)} - \mathbf{r}\cdot\mathbf{p}^{(i)} - \frac{1}{2}\mathbf{r}\cdot\mathbf{Q}^{(i)}\cdot\mathbf{r}, \tag{21}$$

and its force is

$$\mathbf{F}_{\psi}^{(i)} = \mathbf{p}^{(i)} + \mathbf{Q}^{(i)}\cdot\mathbf{r}, \tag{22}$$

where

$$M^{(i)} \equiv \int\limits_{V(r\le r')} d\mathbf{r}'\frac{1}{r'}\rho(\mathbf{r}'), \tag{23}$$

$$p_{i}^{(i)} \equiv \int\limits_{V(r\le r')} d\mathbf{r}'x_{i}'\frac{1}{r'^{3}}\rho(\mathbf{r}'), \tag{24}$$

$$Q_{ij}^{(i)} \equiv \int\limits_{V(r \leq r')} d\mathbf{r}' \left(3x_i' x_j' - r'^2 \delta_{ij}\right) \frac{1}{r'^5} \rho(\mathbf{r}'). \tag{25}$$

For the external multipoles we have

$$\psi^{(e)} = -\frac{M^{(e)}}{r} - \frac{\mathbf{r} \cdot \mathbf{p}^{(e)}}{r^3} - \frac{1}{2} \frac{\mathbf{r} \cdot \mathbf{Q}^{(e)} \cdot \mathbf{r}}{r^5}, \tag{26}$$

and its force is

$$\begin{aligned} \mathbf{F}_{\psi}^{(e)} = &- \frac{M^{(e)}}{r^3} \mathbf{r} + \frac{\mathbf{p}^{(e)}}{r^3} - 3 \frac{\mathbf{p}^{(e)} \cdot \mathbf{r}}{r^5} \mathbf{r} \\ &+ \frac{\mathbf{Q}^{(e)} \cdot \mathbf{r}}{r^5} - \frac{5}{2} \frac{\mathbf{r} \cdot \mathbf{Q}^{(e)} \cdot \mathbf{r}}{r^7} \mathbf{r}, \end{aligned} \tag{27}$$

where

$$M^{(e)} \equiv \int\limits_{V(r > r')} d\mathbf{r}' \rho(\mathbf{r}'), \tag{28}$$

$$p_i^{(e)} \equiv \int\limits_{V(r > r')} d\mathbf{r}' x_i' \rho(\mathbf{r}'), \tag{29}$$

$$Q_{ij}^{(e)} \equiv \int\limits_{V(r > r')} d\mathbf{r}' (3x_i' x_j' - r'^2 \delta_{ij}) \rho(\mathbf{r}'). \tag{30}$$

The external multipoles have the usual meaning, i.e., $M^{(e)}$ is the mass, $\mathbf{p}^{(e)}$ is the dipole moment, and $\mathbf{Q}^{(e)}$ is the traceless quadrupole tensor, of the volume $V(r > r')$. We may attach to the internal multipoles similar meaning, i.e., $M^{(i)}$ is the internal "mass", $\mathbf{p}^{(i)}$ is the internal "dipole" moment, and $\mathbf{Q}^{(i)}$ is the traceless internal "quadrupole" tensor, of the volume $V(r \leq r')$.

In the case of the scalar field, with the expansion

$$\begin{aligned} \frac{\exp(-\mathrm{m}|\mathbf{r} - \mathbf{r}_\mathrm{s}|)}{|\mathbf{r} - \mathbf{r}_s|} = &4\pi m \sum_{l=0}^{\infty} \sum_{n=-l}^{l} i_l(m r_<) k_l(m r_>) \\ &\times Y_{ln}^*(\theta', \varphi') Y_{ln}(\theta, \varphi), \end{aligned}$$

the contribution of the scalar field to the Newtonian gravitational potential can be written as

$$\bar{\phi}(\mathbf{r}) = \bar{\phi}^{(i)} + \bar{\phi}^{(e)}$$

where, for simplicity of notation, we are using $m = m_{\mathrm{SF}} = h_P/(c\lambda)$ and

$$\frac{1}{2\alpha}\bar{\phi}^{(i)} = \sqrt{4\pi}\sum_{l=0}^{\infty}\sum_{n=-l}^{l}\frac{i_l(mr)}{(mr)^l}\bar{q}_{ln}^{(i)}r^l Y_{ln}(\theta,\varphi),$$

$$\frac{1}{2\alpha}\bar{\phi}^{(e)} = \sqrt{4\pi}\sum_{l=0}^{\infty}\sum_{n=-l}^{l}(mr)^{l+1}k_l(mr)\bar{q}_{ln}^{(e)}\frac{Y_{ln}(\theta,\varphi)}{r^{l+1}},$$

$i_l(x)$ and $k_l(x)$ are the modified spherical Bessel functions.

We have defined the multipoles for the scalar field as

$$\bar{q}_{ln}^{(i)} = \sqrt{4\pi}\int\limits_{V(r\le r')} d\mathbf{r}'\,\frac{Y_{ln}^*(\theta',\varphi')}{r'^{l+1}}(mr')^{l+1}k_l(mr')\rho(\mathbf{r}'),$$

$$\bar{q}_{ln}^{(e)} = \sqrt{4\pi}\int\limits_{V(r>r')} d\mathbf{r}'\,Y_{ln}^*(\theta',\varphi')\frac{i_l(mr')}{(mr')^l}r'^l\rho(\mathbf{r}').$$

They, also, have the property

$$\bar{q}_{l(-n)}^{(i)} = (-1)^n\left(\bar{q}_{ln}^{(i)}\right)^*$$

$$\bar{q}_{l(-n)}^{(e)} = (-1)^n\left(\bar{q}_{ln}^{(e)}\right)^* \tag{31}$$

The above expansions of SF contribution to the Newtonian potential can be written in cartesian coordinates. The internal multipole expansion of the SF contribution, up to quadrupoles is

$$\begin{aligned}\frac{1}{2\alpha}\bar{\phi}^{(i)} =& i_0(mr)\bar{M}^{(i)} + 3\frac{i_1(mr)}{mr}\mathbf{r}\cdot\bar{\mathbf{p}}^{(i)}\\ &+ 5\frac{1}{2}\frac{i_2(mr)}{(mr)^2}\mathbf{r}\cdot\bar{\mathbf{Q}}^{(i)}\cdot\mathbf{r}\end{aligned} \tag{32}$$

and its force is

$$\begin{aligned}\frac{1}{2\alpha}\mathbf{F}_{\phi}^{(i)} =& -m^2\frac{i_1(mr)}{mr}\bar{M}^{(i)}\mathbf{r} - 3\frac{i_1(mr)}{mr}\bar{\mathbf{p}}^{(i)}\\ &- 3m^2\frac{i_2(mr)}{(mr)^2}(\bar{\mathbf{p}}^{(i)}\cdot\mathbf{r})\mathbf{r} - 5\frac{i_2(mr)}{(mr)^2}\bar{\mathbf{Q}}^{(i)}\cdot\mathbf{r}\\ &+ 5\frac{1}{2r^2}[5\frac{i_2(mr)}{(mr)^2} - \frac{i_1(mr)}{mr}](\mathbf{r}\cdot\bar{\mathbf{Q}}^{(i)}\cdot\mathbf{r})\mathbf{r},\end{aligned} \tag{33}$$

where

$$\bar{M}^{(i)} \equiv \int\limits_{V(r\le r')} d\mathbf{r}'(mr')k_0(mr')\frac{1}{r'}\rho(\mathbf{r}'), \tag{34}$$

$$\bar{p}_i^{(i)} \equiv \int\limits_{V(r \le r')} d\mathbf{r}'(mr'^{)2} k_1(mr') x_i' \frac{1}{r'^3} \rho(\mathbf{r}'), \tag{35}$$

$$\bar{Q}_{ij}^{(i)} \equiv \int\limits_{V(r \le r')} d\mathbf{r}'(mr'^{)3} k_2(mr')(3x_i' x_j' - r'^2 \delta_{ij}) \frac{1}{r'^5} \rho(\mathbf{r}'). \tag{36}$$

In the exterior region the SF multipole contribution to the potential is

$$\begin{aligned} \frac{1}{2\alpha}\bar{\phi}^{(e)} =& mrk_0(mr)\frac{\bar{M}^{(e)}}{r} + 3(mr)^2 k_1(mr)\frac{\mathbf{r}\cdot\bar{\mathbf{p}}^{(e)}}{r^3} \\ &+ 5\frac{1}{2}(mr)^3 k_2(mr)\frac{\mathbf{r}\cdot\bar{\mathbf{Q}}^{(e)}\cdot\mathbf{r}}{r^5} \end{aligned} \tag{37}$$

and its force is

$$\begin{aligned} \frac{1}{2\alpha}\mathbf{F}_\phi^{(e)} =& (mr)^2 k_1(mr)\frac{\bar{M}^{(e)}}{r^3}\mathbf{r} - 3(mr)^2 k_1(mr)\frac{\bar{\mathbf{p}}^{(e)}}{r^3} \\ &+ 3\Big[(mr)k_0(mr) + (2+mr)(mr)^2 k_1(mr)\Big]\frac{(\bar{\mathbf{p}}^{(e)}\cdot\mathbf{r})}{r^5}\mathbf{r} \\ &- 5(mr)^3 k_2(mr)\frac{\bar{\mathbf{Q}}^{(e)}\cdot\mathbf{r}}{r^5} \\ &+ \frac{5}{2}\Big[3(mr)k_0(mr) + 3(mr)^2 k_1(mr) \\ &+ (3+mr)(mr)^3 k_2(mr)\Big]\frac{(\mathbf{r}\cdot\bar{\mathbf{Q}}^{(e)}\cdot\mathbf{r})}{r^7}\mathbf{r}, \end{aligned} \tag{38}$$

where

$$\bar{M}^{(e)} \equiv \int\limits_{V(r > r')} d\mathbf{r}' i_0(mr')\rho(\mathbf{r}'), \tag{39}$$

$$\bar{p}_i^{(e)} \equiv \int\limits_{V(r > r')} d\mathbf{r}' \frac{i_1(mr')}{mr'} x_i' \rho(\mathbf{r}'), \tag{40}$$

$$\bar{Q}_{ij}^{(e)} \equiv \int\limits_{V(r > r')} d\mathbf{r}' \frac{i_2(mr')}{(mr')^2}(3x_i' x_j' - r'^2\delta_{ij})\rho(\mathbf{r}'). \tag{41}$$

In the limit when $m \to 0$ we recover the standard Newtonian potential and force expressions.

Up to here the formulation is general, i.e., mass distribution may have any symmetry or none at all. In order to take advantage of the symmetry of the spherical harmonics, the mass distribution must be spherically symmetric.

3 Cosmological Evolution Equations Using a Static STT

To simulate cosmological systems, the expansion of the Universe has to be taken into account. Also, to determine the nature of the cosmological model we need to determine the composition of the Universe, i. e., we need to give the values of $\Omega_i \equiv \rho_i/\rho_c$, with $\rho_c = 3H^2/8\pi G_N$, for each component i, taking into account in this way all forms of energy densities that exist at present. If a particular kind of energy density is described by an equation of state of the form $p = w\rho$, where p is the pressure and w is a constant, then the equation for energy conservation in an expanding background, $d(\rho a^3) = -pd(a^3)$, can be integrated to give $\rho \propto a^{-3(1+w)}$.

Then, the Friedmann equation for the expansion factor $a(t)$ is written as

$$\frac{\dot{a}^2}{a^2} = H_0^2 \sum_i \Omega_i \left(\frac{a_0}{a}\right)^{3(1+w_i)} - \frac{k}{a^2} \tag{42}$$

where w_i characterizes equation of state of species i.

The most familiar forms of energy densities are those due to pressureless matter with $w_i = 0$ (that is, nonrelativistic matter with rest-mass–energy density ρc^2 dominating over the kinetic-energy density $\rho v^2/2$) and radiation with $w_i = 1/3$. The density parameter contributed today by visible, nonrelativistic, baryonic matter in the Universe is $\Omega_B \approx (0.01 - 0.2)$ and the density parameter that is due to radiation is $\Omega_R \approx 2 \times 10^{-5}$.

In this work we will consider a model with only two energy density contribution. One which is a pressureless and nonbaryonic dark matter with $\Omega_{DM} \approx 0.3$ that does not couple with radiation. Although in the numerical simulations we may include in Ω_{DM} the baryonic matter. Other, that will be a cosmological constant contribution $\Omega_\Lambda \approx 0.7$ with and equation of state $p = -\rho$. The above equation for $a(t)$ becomes

$$\frac{\dot{a}^2}{a^2} = H_0^2 \left[\Omega_{DM}\left(\frac{a_0}{a}\right)^3 + \Omega_\Lambda\right] - \frac{k}{a^2} \tag{43}$$

The above discussion gives us the standard cosmological model with cosmological constant, i.e., ΛCDM model.

In the framework of a scalar–tensor theory the cosmology is given as follows. If we use the Friedmann metric (Faraoni 2004)

$$ds^2 = -dt^2 + a^2(t)\left[\frac{dr^2}{1-\kappa r^2} + r^2(d\theta^2 + \sin^2\theta d\varphi^2)\right]$$

in the time–time component of the Einstein field equations (Hamiltonian constraint) gives

$$H^2 = \frac{8\pi}{3\phi}\rho - H\frac{\dot{\phi}}{\phi} + \frac{\omega(\phi)}{6}\left(\frac{\dot{\phi}}{\phi}\right)^2 - \frac{\kappa}{a^2} + \frac{V}{6\phi}$$

while the equation for the scalar field is

$$\ddot{\phi} + \left(3H + \frac{\dot{\omega}}{2\omega+3}\right)\dot{\phi} = \frac{1}{2\omega+3}\left[8\pi(\rho - 3P) - \phi\frac{dV}{d\phi} + 2V\right]$$

and the equation of the fluid is

$$\dot{\rho} + 3H(\rho + P)$$

The cosmological evolution of the initial perturbed fields should be computed using the above equations for the expansion factor. However, here, we will employ a cosmological model with a static SF which is consistent with the Newtonian limit given above. Thus, the scale factor, $a(t)$, is given by the following Friedman model,

$$a^3H^2 = H_0^2\left[\frac{\Omega_{DM0} + \Omega_{\Lambda 0}a^3}{1+\alpha} + \left(1 - \frac{\Omega_{DM0} + \Omega_{\Lambda 0}}{1+\alpha}\right)a\right] \tag{44}$$

where $H = \dot{a}/a$, Ω_{DM0} and $\Omega_{\Lambda 0}$ are the matter and energy density evaluated at present, respectively.

We notice that the source of the cosmic evolution is deviated by the term $1+\alpha$ when compared to the standard Friedman–Lemaitre model. Therefore, it is convenient to define a new density parameter by $\Omega_i^{(\alpha)} \equiv \Omega_i/(1+\alpha)$. This new density parameter is such that $\Omega_{DM}^{(\alpha)} + \Omega_\Lambda^{(\alpha)} = 1$, which implies a flat Universe, and this shall be assumed in the following computations, where we consider $(\Omega_m^{(\alpha)}, \Omega_\Lambda^{(\alpha)}) = (0.3, 0.7)$.

For positive values of α, a flat cosmological model demands to have a factor $(1+\alpha)$ more energy content (Ω_m and Ω_Λ) than in standard cosmology. On the other hand, for negative values of α one needs a factor $(1+\alpha)$ less Ω_m and Ω_Λ to have a flat Universe. To be consistent with the CMB spectrum and structure formation numerical experiments, cosmological constraints must be applied on α in order for it to be within the range $(-1, 1)$ (Nagata et al. 2002, 2004; Shirata et al. 2005; Umezu et al. 2005).

4 Vlasov–Poisson–Helmholtz Equations and the *N*-body Method

The Vlasov–Poisson equation in an expanding Universe describes the evolution of the six-dimensional, one-particle distribution function, $f(\mathbf{x}, \mathbf{p})$. The Vlasov equation is,

$$\frac{\partial f}{\partial t} + \frac{\mathbf{p}}{ma^2}\cdot\frac{\partial f}{\partial \mathbf{x}} - m\nabla\Phi_N(\mathbf{x})\cdot\frac{\partial f}{\partial \mathbf{p}} = 0 \tag{45}$$

where $\mathbf{x}$ is the comoving coordinate, $\mathbf{p} = ma^2\dot{\mathbf{x}}$, m is the particle mass, and Φ_N is the self-consistent gravitational potential given by the Poisson equation,

$$\nabla^2\Phi_N(\mathbf{x}) = 4\pi G_N a^2[\rho(\mathbf{x}) - \rho_b(t)] \tag{46}$$

where ρ_b is the background mass density. The Vlasov–Poisson system, Eqs. 46 and 49 form the Vlasov–Poisson equation, constitutes a collisionless, mean-field approximation to the evolution of the full N-body distribution.

An N-body code attempts to solve the Vlasov–Poisson system of equations by representing the one-particle distribution function as

$$f(\mathbf{x}, \mathbf{p}) = \sum_{i=1}^{N} \delta(\mathbf{x} - \mathbf{x}_i)\delta(\mathbf{p} - \mathbf{p}_i) \tag{47}$$

Substitution of Eq. 47 in the Vlasov–Poisson system of equations yields the exact Newton's equations for a system of N gravitating particles (See Bertschinger 1998 for details),

$$\ddot{\mathbf{x}}_i + 2H\mathbf{x}_i = -\frac{1}{a^3}G_N \sum_{j\neq i} \frac{m_j(\mathbf{x}_i - \mathbf{x}_j)}{|\mathbf{x}_i - \mathbf{x}_j|^3} \tag{48}$$

where the sum includes all periodic images of particle j and numerically is done using the Ewald method, see (Hernquist et al. 1991). It is important to keep in mind, however, that we are not really interested in solving the exact N-body problem for a finite number of particles, N. The actual problem of interest is the exact N-body problem in the fluid limit, i.e., as $N \to \infty$. For this reason, one important aspect of the numerical fidelity of N-body codes lies in controlling errors due to the discrete nature of the particle representation of $f(\mathbf{r}, \mathbf{p})$.

In the Newtonian limit of STT of gravity to describe the evolution of the six-dimensional, one-particle distribution function, $f(\mathbf{x}, \mathbf{p}, t)$ we need to solve the Vlasov–Poisson–Helmholtz equation in an expanding Universe (Rodriguez-Meza et al. 2007; Rodríguez-Meza 2008, 2009a, b, 2010). The Vlasov equation is given by

$$\frac{\partial f}{\partial t} + \frac{\mathbf{p}}{ma^2} \cdot \frac{\partial f}{\partial \mathbf{x}} - m\nabla\Phi_N(\mathbf{x}) \cdot \frac{\partial f}{\partial \mathbf{p}} = 0 \tag{49}$$

where $\Phi_N = (1/2)h_{00} = \psi - \frac{1}{2}\frac{G_N}{1+\alpha}\bar{\phi}$ with ψ satisfying Poisson equation

$$\nabla^2\psi(\mathbf{x}) = 4\pi G_N a^2[\rho(\mathbf{x}) - \rho_b(t)]$$

and $\bar{\phi}$ satisfying the Helmholtz equation

$$\nabla^2\bar{\phi} - \lambda^{-2}\bar{\phi} = -8\pi\alpha a^2[\rho(\mathbf{x}) - \rho_b(t)],$$

Above equations form the Vlasov–Poisson–Helmholtz system of equations, constitutes a collisionless, mean-field approximation to the evolution of the full N-body distribution in the framework of the Newtonian limit of a scalar–tensor theory.

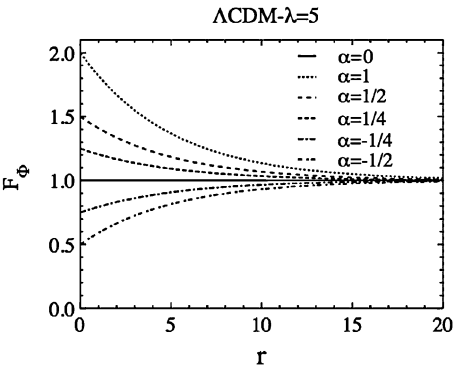

Fig. 1 Function $F_{SF}(r, \alpha, \lambda)$ for $\lambda = 5$ Mpc/h and several values of parameter α

Using the representation of the one-particle distribution function Eq. 47 the Newtonian motion equation for a particle i, is written as (Rodríguez-Meza 2008)

$$\ddot{\mathbf{x}}_i + 2H\mathbf{x}_i = -\frac{1}{a^3}\frac{G_N}{1+\alpha}\sum_{j\neq i}\frac{m_j(\mathbf{x}_i - \mathbf{x}_j)}{|\mathbf{x}_i - \mathbf{x}_j|^3}\, F_{\rm SF}(|\mathbf{x}_i - \mathbf{x}_j|, \alpha, \lambda) \tag{50}$$

where the sum includes all periodic images of particle j, and $F_{\rm SF}(r, \alpha, \lambda)$ is

$$F_{\rm SF}(r, \alpha, \lambda) = 1 + \alpha\left(1 + \frac{r}{\lambda}\right)e^{-r/\lambda} \tag{51}$$

which, for small distances compared to λ, is $F_{\rm SF}(r<\lambda, \alpha, \lambda) \approx 1 + \alpha\left(1 + \frac{r}{\lambda}\right)$ and, for long distances, is $F_{\rm SF}(r > \lambda, \alpha, \lambda) \approx 1$, as in Newtonian physics.

The function $F_{\rm SF}(r, \alpha, \lambda)$ is shown in Fig. 1 for several values of parameter α. We should notice that even though $\lambda = 5$ Mpc/h, $F_{\rm SF}$ gives an important contribution to the force between particles for $r > \lambda$.

5 Results: Large Scale Structure Formation

In this section, we present results of cosmological simulations of a ΛCDM Universe with and without SF contribution.

We use the standard Zel'dovich approximation (Zel'dovich 1970) to provide the initial 256^3 particles displacement off a uniform grid and to assign their initial velocities in a 64 h^{-1} Mpc box. In this approximation the comoving and the lagrangian coordinates are related by

$$\mathbf{x} = \mathbf{q} - \alpha_Z \sum_{\mathbf{k}} b_{|\mathbf{k}|}(t)\mathbf{S}_{|\mathbf{k}|}(\mathbf{q}), \qquad \mathbf{p} = -\alpha_Z a^2 \sum_{\mathbf{k}} b_{|\mathbf{k}|}(t)\left(\frac{\dot{b}_{|\mathbf{k}|}(t)}{b_{|\mathbf{k}|}(t)}\right)\mathbf{S}_{|\mathbf{k}|}(\mathbf{q}), \tag{52}$$

where the displacement vector $\mathbf{S}$ is related to the velocity potential Φ and the power spectrum of fluctuations $P(|k|)$:

$$\mathbf{S}_{|\mathbf{k}|}(\mathbf{q}) = \nabla_q \Phi_{|\mathbf{k}|}(q), \qquad \Phi_{|\mathbf{k}|} = \sum_{\mathbf{k}} (a_{\mathbf{k}} \cos(\mathbf{k}\cdot\mathbf{q}) + b_{\mathbf{k}} \sin(\mathbf{k}\cdot\mathbf{q})) \tag{53}$$

where a and b are gaussian random numbers with the mean zero and dispersion $\sigma^2 = P(k)/k^4$,

$$a_{\mathbf{k}} = \frac{\sqrt{P(|k|)}}{|k|^2} G(0,1), \quad b_{\mathbf{k}} = \frac{\sqrt{P(|k|)}}{|k|^2} G(0,1) \tag{54}$$

where $G(0,1)$ is a gaussian number with mean zero and dispersion 1.

The parameter α_Z together with the power spectrum $P(k)$, define the normalization of the fluctuations. The initial power spectrum was generated using the fitting formula by Klypin and Holtzman (1997) for the transfer function. This formula is a slight variation of the common BBKS fit (Bardeen et al. 1986).

The starting redshift is $z_{in} = 50$ and we choose the following cosmology: $\Omega_{DM} = 0.314$ (where Ω_{DM} includes cold dark matter and baryons), $\Omega_B = 0.044$, $\Omega_\Lambda = 0.686$, $H_0 = 71$ km/s/Mpc, $\sigma_8 = 0.84$, and $n = 0.99$. Particle masses are in the order of $1.0 \times 10^{10}\,\mathrm{M}_\odot$. The individual softening length was 50 kpc/h. This choice of softening length is consistent with the mass resolution set by the number of particles. All these values are in concordance with measurements of cosmological parameters by WMAP (Spergel et al. 2003). The initial condition—called the small box case—is in the Cosmic Data Bank web page: (http://t8web.lanl.gov/people/heitmann/test3.html). See Heitmann et al. (2005) for more details.

Because the visible component is the smaller one and given our interest to test the consequences of including a SF contribution to the evolution equations, our model excludes gas particles, but all its mass has been added to the dark matter. We restrict the values of α to the interval $(-1, 1)$ (Nagata et al. 2002, 2004; Shirata et al. 2005; Umezu et al. 2005) and use $\lambda = 1, 5, 10, 20$ Mpc/h, since these values sweep the scale lengths present in the simulations.

In Fig. 2 we show how the above initial condition evolve and gives us the LSS formation process without SF and with SF. In (a) without SF. In (b) with SF: $\alpha = 1$ and $\lambda = 5$ Mpc/h. In (c) With SF: $\alpha = -1/2$ and $\lambda = 5$ Mpc/h. In (d) With SF: $\alpha = -1/4$ and $\lambda = 5$ Mpc/h.

To study the structure formation in the Universe we follow the evolution of the overdensity,

$$\delta(\mathbf{x}) \equiv \frac{\rho(\mathbf{x})}{\rho_0} - 1$$

where ρ_0 is the average density over a volume V and $\mathbf{x}$ is the commoving distance related to the physical density by $\mathbf{r} = a(t)\mathbf{x}$. In the linear regime $\delta \ll 1$.

The correlation function tell us how δ is correlated in two nearby points $\mathbf{x}'$ and $\mathbf{x}' + \mathbf{x}$,

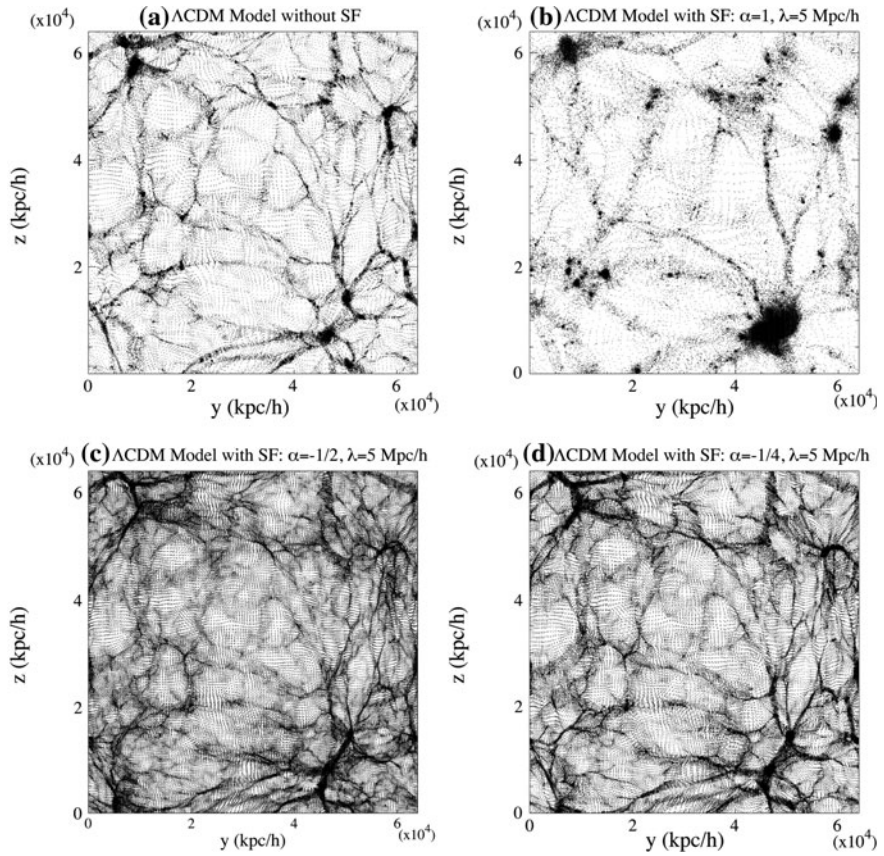

Fig. 2 LSS formation process with and without SF. See text for details

$$\xi(\mathbf{x}) \equiv \langle \delta(\mathbf{x}')\delta(\mathbf{x}' + \mathbf{x}) \rangle$$

and the power spectrum is the Fourier transform of the correlation function,

$$\xi(x) = \frac{1}{V} \sum_{\mathbf{k}} P(\mathbf{k}) e^{i\mathbf{k}\cdot\mathbf{x}}$$

In Fig. 3a we show the evolution of the power spectrum for the small box $L = 64\,\mathrm{Mpc}/h$ without SF, for several values of the redshift z. In this figure we can appreciate how it is forming structures, upper curve of the power spectrum for the present epoch, $z = 0$. Figure 3b shows the power spectrum for the same values as in Fig. 2. Continuous line is without SF. Upper curve (dotted line) is with SF: $\alpha = 1$ and $\lambda = 5\,\mathrm{Mpc/h}$. Lower curve (dashed line) is with SF: $\alpha = -1/4$ and $\lambda = 5\,\mathrm{Mpc/h}$. The curve that is just below the continuous line is with SF: $\alpha = -1/2$ and $\lambda = 5\,\mathrm{Mpc/h}$. More greater values of the power spectrum means more structure formation. Therefore, the inclusion of a SF modifies the structure

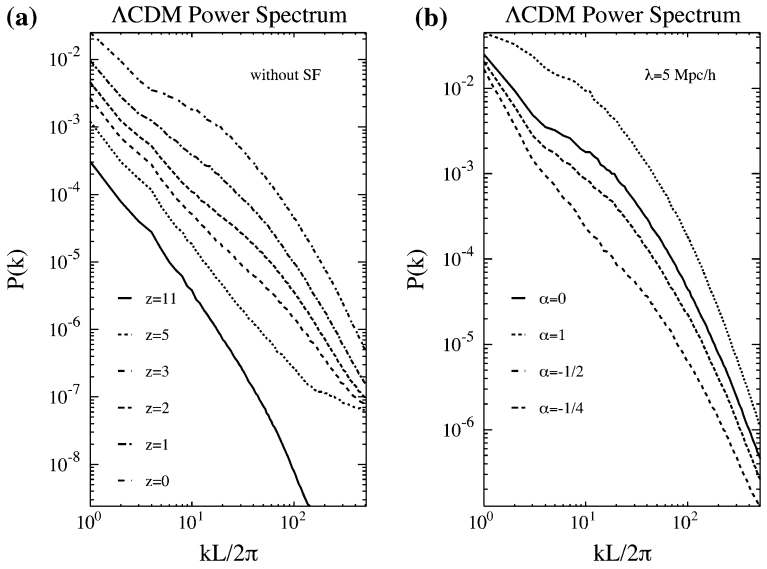

Fig. 3 **a** Evolution of the power spectrum for the case which there is no SF. **b** The power spectrum including SF for several values of parameter α and with $\lambda = 5\,\text{Mpc/h}$

formation process. Depending of the values of its parameters, α and λ we can obtain more structure or less structure at the present epoch, $z = 0$.

In our results as shown in Figs. 2, 3 we have used a fix value of $\lambda = 5\,\text{Mpc/h}$. For a given λ the role of SF parameter α on the structure formation can be inferred by looking at Eqs. 50, 51 and Fig. 1 where we show the behavior of F_{SF} as a function of distance for several values of α. The factor F_{SF} augments (diminishes) for positive (negative) values of α for small distances compared to λ, resulting in more (less) structure formation for positive (negative) values of α compared to the ΛCDM model. In the case of the upper curve in Fig. 3b, for $r \ll \lambda$, the effective gravitational pull has been augmented by a factor of 2, in contrast to the case shown with the lower line in Fig. 3b where it has been diminished by a factor of 1/2. That is why we observe for $r < \lambda$ more structure formation in the case of the upper curve in Fig. 3b and lesser in the case of the lower curve in the same figure. The effect is then, for a growing positive α, to speed up the growth of perturbations, the the halos, and then the clusters, whereas negative values of $\alpha(\alpha \to -1)$ tend to slow down the growth.

6 Conclusions and Final Comments

We have used a general, static STT, that is compatible with local observations by the appropriate definition of the background field constant, i.e., $\langle\phi\rangle = (1+\alpha)/G_N$, to study the LSS formation process. The initial condition for the several cases

(different values of parameter α) was built in such a way that the geometry of the model universe were flat. Quantitatively, this demands that our models have $\Omega/(1+\alpha) = 1$ and this changes the amount of dark matter and energy of the models in order to have a flat cosmology.

Using the resulting modified dynamical equations, we have studied the LSS formation process of a ΛCDM universe. We varied the amplitude and sign of the strength of the SF (parameter α) in the inverval $(-1, 1)$ and performed several 3D-simulations with the same initial conditions. From our simulations we have found that the inclusion of the SF changes the local dynamical properties of the most massive groups, however, the overall structure is very similar, as can be seen in Fig. 2.

The general gravitational effect is that the interaction between dark matter particles given by the potential Φ_N (see Eq. 12) changes by a factor $F_{\rm SF}$, Eq. 51, in comparison with the purely Newtonian case. Thus, for $\alpha > 0$ the growth of structures speeds up in comparison with the Newtonian case (without SF). For the $\alpha < 0$ case the effect is to diminish the formation of structures.

It is important to note that particles in our model are gravitating particles and that the SF acts as a mechanism that modifies gravity. The effective mass of the SF ($m_{\rm SF} = 1/\lambda$) only sets an interaction length scale for the Yukawa term.

In this work we only varied the amplitude of the SF—parameter α—leaving the scale length, λ, of the SF unchanged. However, in other studies we have done (Rodríguez-Meza 2009b) we have found that increasing λ enhances the structure formation process for α positive, and decreasing λ makes the structures grow at a slower rate.

We have computed the mass power spectrum in order to study the LSS formation process. The theoretical scheme we have used is compatible with local observations because we have defined the background field constant $\langle\phi\rangle = G_N^{-1}(1+\alpha)$ or equivalently that the local gravitational constant is given by $(1+\alpha)\langle\phi\rangle^{-1}$, instead of being given by $\langle\phi\rangle^{-1}$. A direct consequence of the approach is that the amount of matter (energy) has to be increased for positive values of α and diminished for negative values of α with respect to the standard ΛCDM model in order to have a flat cosmological model. Quantitatively, our model demands to have $\Omega/(1+\alpha) = 1$ and this changes the amount of dark matter and energy of the model for a flat cosmological model, as assumed. The general gravitational effect is that the interaction including the SF changes by a factor $F_{\rm SF}(r, \alpha, \lambda) \approx 1 + \alpha\left(1 + \frac{r}{\lambda}\right)$ for $r < \lambda$ in comparison with the Newtonian case. Thus, for $\alpha > 0$ the growth of structures speeds up in comparison with the Newtonian case. For the $\alpha < 0$ case the effect is to diminish the formation of structures. For $r > \lambda$ the dynamics is essentially Newtonian.

References

Bardeen JM, Bond JR, Kaiser N, Szalay AS (1986) Astrophys J 304:15
Barrena R, Biviano A, Ramella M, FalcoEE Steitz S (2002) A & A 386:816
Bertschinger E (1998) Annu Rev Astronomy Astrophys 36:599

Binney J, Tremaine S (2008) Galactic dynamics, 2nd edn. Princeton University Press, Princeton
Bretón N, Cervantes-Cota JL, Salgado M (eds) (2004) The early universe and observational cosmology. Springer, Berlin
Clowe D et al (2004) ApJ 604:596
Clowe D et al (2006) ApJ 648:L109
Faraoni V (2004) Cosmology in scalar–tensor gravity. Kluwer, Dordrecht
Fischbach E, Talmadge CL (1999) The search for non-Newtonian gravity. Springer, New York
Heitmann K, Ricker PM, Warren MS, Habib S (2005) Astrophys J Suppl 160:28
Helbig T (1991) Astrophys J 382:223
Hernquist L, Bouchet FR, Suto Y (1991) ApJS 75:231
Jackson JD (1975) Classical electrodynamics, 2nd edn. Wiley, New York
Klypin AA, Holtzman J (1997) arXiv:astro-ph/9712217
Komatsu E et al (2011) Astrophys J Suppl 192:18
Lee J, Komatsu E (2011) Astrophys J 718:60
Markevitch M (2006) In: Wilson (ed) Pro. X-Ray universe 2005. ESA SP-604. ESA, Noordwijk, p 723
Markevitch M, Gonzalez AH, David L, Vikhlinin A, Murray S, Forman W, Jones C, Tucker W (2002) ApJ 567:L27
Mastropietro C, Burkert A (2008) MNRAS 389:967
Milosavljevic et al (2007) ApJ 661:L131
Nagata R, Chiba T, Sugiyama N (2002) Phys Rev D 66:103510
Nagata R, Chiba T, Sugiyama N (2004) Phys Rev D 69:083512
Navarro JF et al (1996) Astrophys J 462:563
Navarro JF et al (1997) Astrophys J 490:493
Peebles PJE (1980) The large-scale structure of the universe. Princeton University Press, Princeton
Pimentel LO, Obregón O (1986) Astrophys Space Sci 126:231
Rodríguez-Meza MA (2008) AIP conference proceedings, 977:302. arXiv:0802.1170
Rodríguez-Meza MA (2009a) AIP conference proceedings, 1083:190. astro-ph: 0810.0491
Rodríguez-Meza MA (2009b) AIP conference proceedings, 1116:171. astro-ph: 0907.2898
Rodríguez-Meza MA (2010) J Phys Conf Series 229:0120663. arXiv: [astro-ph.CO] 1002.4988
Rodríguez-Meza MA, Cervantes-Cota JL (2004) Mon Not Roy Astron Soc 350:671
Rodríguez-Meza MA, Cervantes-Cota JL, Pedraza MI, Tlapanco JF, Dela Calleja EM (2005) Gen Relativ Grav 37:823
Rodríguez-Meza MA, González-Morales AX, Gabbasov RF, Cervantes-Cota JL (2007) J Phys Conf Series 91:012012. arXiv:0708.3605
Salgado M (2002) arXiv: gr-qc/0202082
Shirata A, Shiromizu T, Yoshida N, Suto Y (2005) Phys Rev D 71:064030
Spergel DN et al (2003) Astrophys J Suppl 148:175
Springel V, Farrar G (2007) MNRAS 380:911
Takizawa M (2005) ApJ 629:791
Takizawa M (2006) PASJ 58:925
Umezu K, Ichiki K, Yahiro M (2005) Phys Rev D 72:044010
Zel'dovich YB (1970) Astron & Astrophys 5:84

The Oil Spill in the Gulf of Mexico

Hermilo Ramírez-León

Abstract The present review is intended to give a general background of the main issues involving the oil spill that occurred on April 20, 2010 in the Deepwater Horizon platform owned by British Petroleum. A general description of the zone is provided, as well as the chronology of the facts that occurred since the spill began, including the different attempts to stop it, until the date of its complete control which occurred on July 15. Beside the efforts to stop the spill (on the surface and in deep waters), there were many governmental organizations, universities and scientific societies which contributed with diverse proposal of control, mitigation and prevention activities, such as, retaining and diminishing the amount of oil which could arrive to the coast, forecasting and tracking the behavior of the slick by means of satellite imagery, measurements and models. Finally, this work includes a brief description of possibilities of some influence on the Mexican coasts.

1 Introduction

These notes are the result of the analysis of information collected in the main international sources that followed the British Petroleum (BP) oil spill in the North of the Gulf of Mexico (GOM); in this way, is a review of principal events. Several images and comments are taken from internet sources and several seminars where the author has participated or the information has been put on the web. For this reason some images describing a success sequences are not cited in the text. All the consulted sources are in the references at the end of this document. Some of these images are reproduced in color in the image gallery section.

H. Ramírez-León (✉)
Mexican Petroleum Institute, Mexico City, Mexico
e-mail: hrleon@imp.mx

J. Klapp et al. (eds.), *Experimental and Theoretical Advances in Fluid Dynamics*, Environmental Science and Engineering, DOI: 10.1007/978-3-642-17958-7_8,

Fig. 1 The Deepwater horizon platform (taken from www.deepwater.com, referred hereafter as DW)

On April 20, 2010 the Deepwater Horizon platform (Fig. 1) was in the stage of completion of the well Macondo-252 at block 262, cementing pipe exploitation of 9 7/8 ″× 7″, had a blast, the platform was on fire for 2 days, to complete sinking two days later and collapsed to the seabed at a depth of 1,569 m and 400 m northeast of the drilling well, and located 64 km southeast of Louisiana, starting the oil spill and the biggest environmental disaster in the history. The explosion occurred Tuesday night, around 10 p.m., and on Wednesday afternoon crews were still fighting the fire, which was largely contained to the rig but in photographs provided by the Coast Guard appeared to be shooting enormous plumes of flame into the air. In this time Admiral Landry estimated that 13,000 gallons of crude were pouring out per hour. After the explosion and fire, eleven people were missing, 17 injured workers, who were airlifted to a naval air station in New Orleans and from there, they were taken to the hospital and 1,19 were rescued. Several support ships were sent to release water to the platform in an attempt to extinguish the flames.

The great strategic and technological deployments to contain the spill on the bottom and on surface are mentioned to the date of final control which occurred on July 15 (Fig. 2) later activities of containment, mitigation, and removal of the spill on the surface from the date of the accident are analyzed and continue yet for an indefinite time. Metocean conditions at the time of the spill favored the dispersion of the stain of oil towards coastal Mississippi, Louisiana, Alabama, and Florida.

Several authorities and Government Agencies, Universities and Research Centers in United States have followed the oil spill closely and contributed to the definition of security strategies. In Mexico, National Entities, Universities and Research Institutions created different groups of discussion, to estimate the potential impact in Mexican waters.

From these meetings, it was determined that several models of ocean circulation were not sufficiently validated in GOM, given various forecasts of the currents behavior in the area and, consequently, different patterns of oil dispersion.

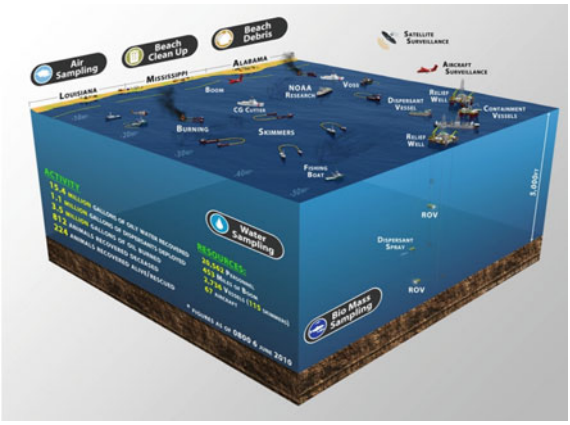

Fig. 2 Deepwater horizon spill control strategies (DW)

Fig. 3 The first photographs, April 21, 2010 (DW)

The National Oceanographic and Atmospheric Administration (NOAA) adopted the HYCOM as a circulation model to predict de currents. With the arrival of the rains and the hurricanes season, the control tasks in bottom and in surface were complicated. These hydro-meteorological phenomena, according to their behavior in recent years, will favor the dispersion of oil into the deep sea and in lower probably towards the Mexican waters.

Finally some comments about implications that the oil spill have and will have on the environment; as well as the potential impact of oil allocated deep waters and the use of dispersants on the bottom. Some possibilities of the arrival of pollution associated with the oil spill in Mexican waters are mentioned.

2 Chronology of Success

April 20 Blowout and fire, blowout preventer fails: the Deepwater Horizon, exploded into flames (Figs. 3 , 4).

April 22 Two days later the rig sank, causing the 5,000 foot pipe that connected the wellhead to the drilling platform to bend (Figs. 5 , 6).

April 24 Robotic devices discovered two leaks in the bent pipe, nearly a mile below the ocean surface.

Fig. 4 Horizon platform on fire (DW)

Fig. 5 The collapse

Fig. 6 The smoke plume after the collapse

April 25 Repairing the blowout preventer. Officials use remotely operated submersibles to try to activate the blowout preventer, a stack of valves at the wellhead meant to seal the well in the event of a sudden pressure increase (Fig. 7). A crucial valve had never fully deployed, and efforts to activate the device after the explosion are unsuccessful (taken from The New York Times: www.nytimes.com, referred hereafter as NYT).

April 29 Just after estimates of the size of the spill were increased from 1,000 barrels a day to 5,000 (they eventually reached 60,000), President Obama announced that the federal government would get involved more aggressively in fighting the spill, and Homeland Security Secretary Janet Napolitano designated the spill as "of national significance" (NYT).

April 30 Injection of chemical dispersant into the oil as it flows from the main leak underwater (Fig. 8). The dispersant, conventionally used on the water

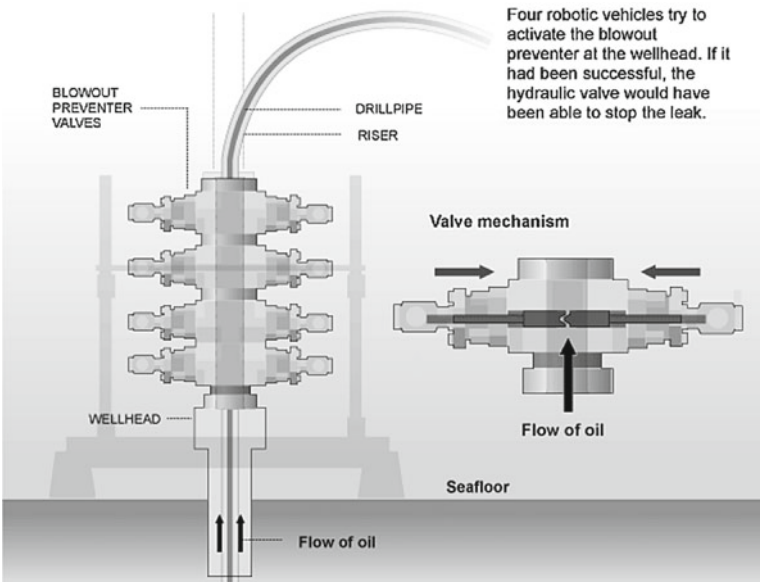

Fig. 7 The wellhead was equipped with a blowout preventer, a 40-foot stack of devices designed to rapidly seal the well. But the preventer failed (NYT)

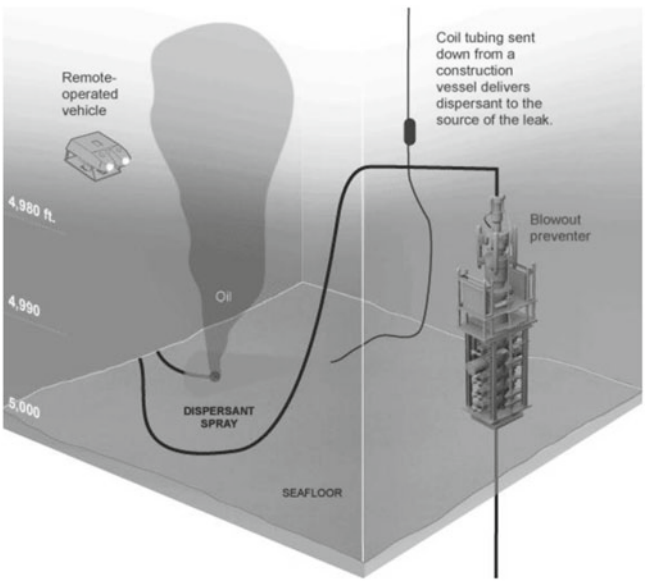

Fig. 8 Chemical dispersants at the bottom (NYT)

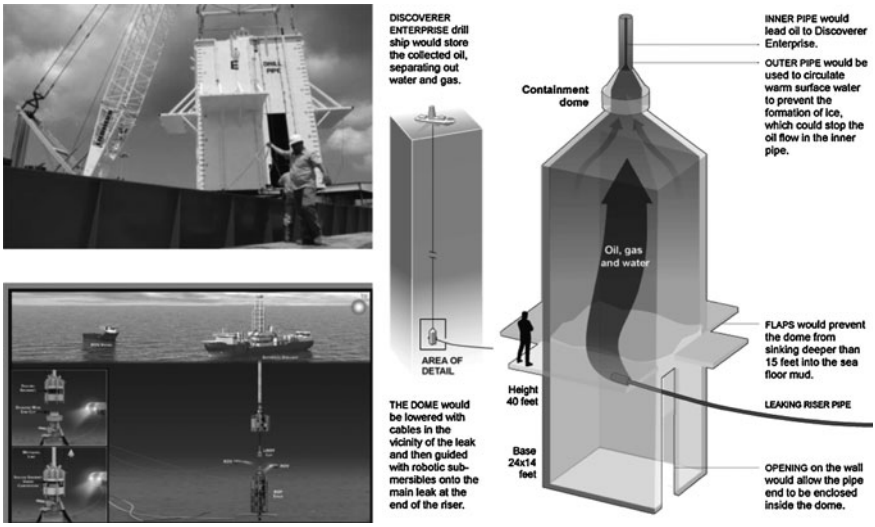

Fig. 9 Transport and installation of containment dome (Figures on the left hand was taken from DW and Figure on the right hand from NYT)

surface, is intended to break the oil into small droplets, reducing its buoyancy. The full impact of chemical dispersants on the underwater ecology is unknown. The Environmental Protection Agency (EPA) later orders BP to change to a less toxic chemical than originally used (NYT).

May 2 First relief well initiated. BP begins drilling the first of two relief wells that may later be used to inject mud and cement into the existing well.

May 7 Containment dome put in place and fails due to hydrate formation (Fig. 9). Workers lower a four-story steel box over the larger leak. But when crews discover that the dome's opening is becoming clogged with an icy mix of gas and water, it is set aside on the seabed.

May 16 Attaching a tube. After two false starts, BP engineers successfully insert a mile-long tube into the broken riser pipe to divert some of the oil to a drill ship on the surface (Fig. 10). Over nine days, the tube siphons off about 22,000 barrels of oil, which is just a fraction of the total spill (NYT).

May 26 BP tries top kill and junk shot, it fails. In a procedure called the top kill, engineers pump heavy drilling mud into the well with hopes that the weight of the fluid overcomes the pressure of the rising oil (Fig. 11). In another technique called the junk shot, objects including golf balls and pieces of rubber are injected into the blowout preventer. Both techniques fail to plug the leak.

May 31 Another Attempt to Cap the Well. Engineers position submarine robots to shear the collapsed riser pipe so that a domeline cap could be placed over the blowout preventer to funnel some of the leaking oil to a tanker on the

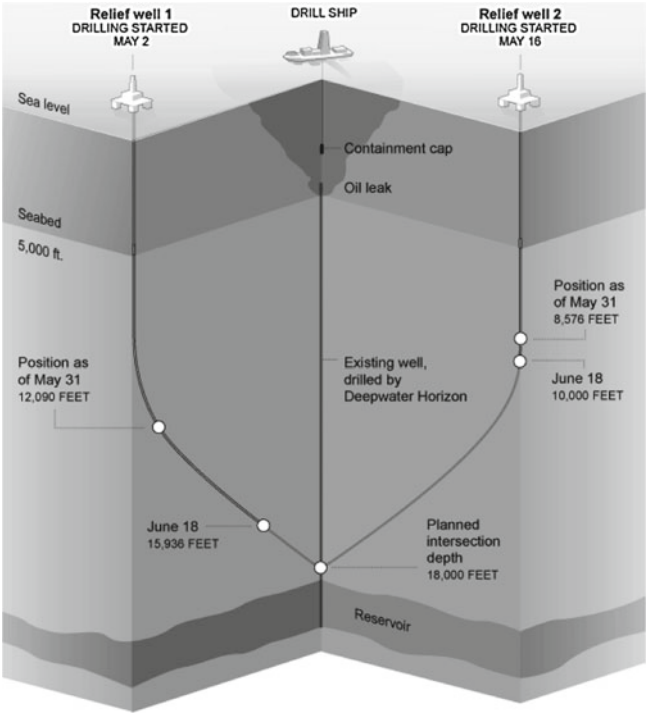

Fig. 10 Tube attached to the broken riser pipe (NYT)

surface. The new riser pipe has a 6.625-inch internal pipe to capture leaking oil and gas. Methanol and warm seawater is pumped down the riser to insulate the smaller pipe and prevent the formation of ice crystals (Fig. 12), which caused the earlier containment dome to fail (NYT).

June 3 Beginning to Capture Some Oil. A cap is placed over the top of the blowout preventer to funnel oil and gas to a surface ship. Methanol is pumped into the cap to prevent the formation of icy hydrates that could block the mile-long pipe rising from the cap (Fig. 13). Oil continues to billow from under the lip and through four open vents on top of the device. Engineers are unable to close all the vents as originally planned (NYT).

June 16 Capturing More Oil. A second containment system begins siphoning oil and gas from the leaking well (Fig. 14). BP estimates the system will carry 5,000–10,000 barrels a day to the surface, supplementing the roughly 15,000 barrels collected daily by a containment cap on top of the blowout preventer. Using equipment originally put in place to inject heavy drilling mud during the failed top kill procedure last month, the new system extracts oil and gas directly from the blowout preventer, passes it through a manifold on the seafloor and pipes it up to the Q4000 surface vessel (NYT).

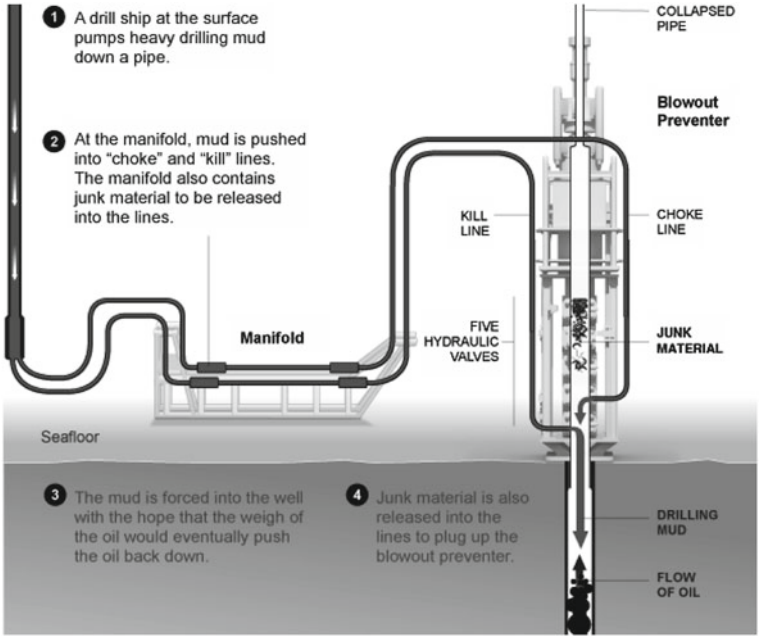

Fig. 11 The Top Kill and Junk Shot (NYT)

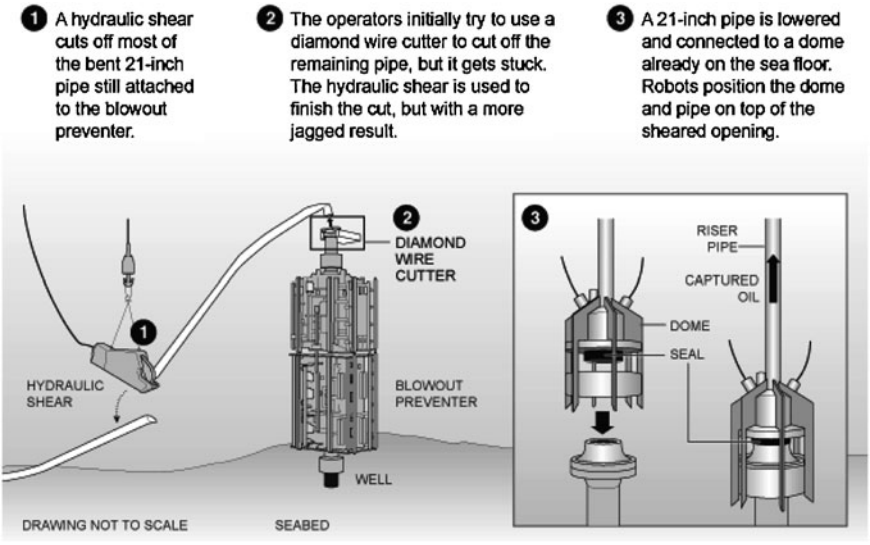

Fig. 12 Another attempt to cap the well (NYT)

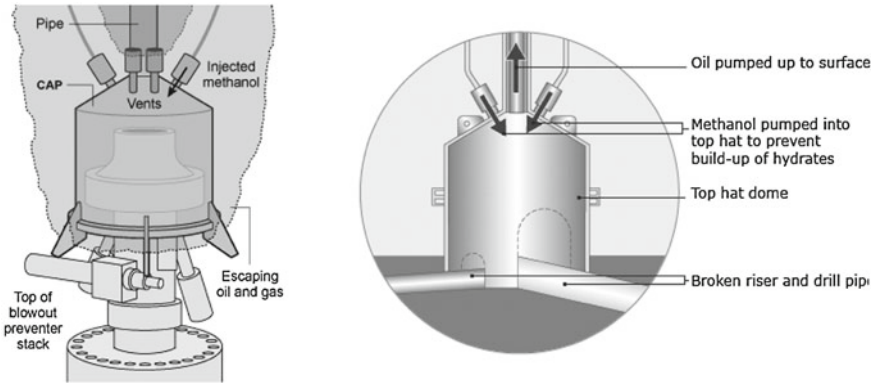

Fig. 13 Top hat placed over blowout preventer, some oil recovered (NYT)

Fig. 14 The Q4000 has no storage capacity and burns the oil and gas (NYT)

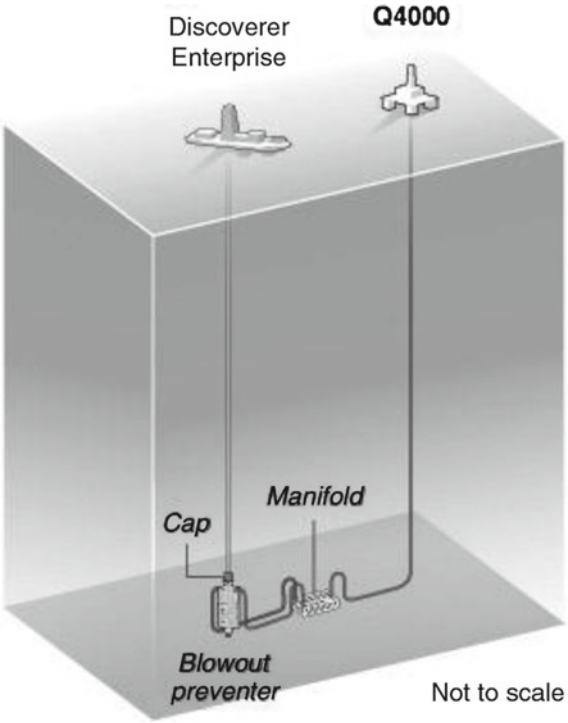

June Tar balls and oil mousse had reached the shores of Mississippi, Alabama and Florida (Fig. 15). Shortly thereafter, it spread on shore, smearing tourist beaches, washing onto the shorelines of sleepy coastal communities and oozing into marshy bays that fishermen have worked for generations.

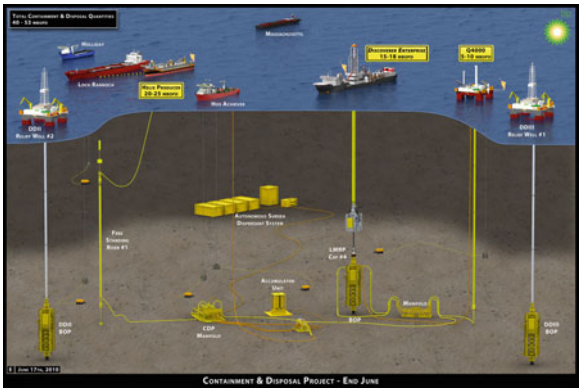

Fig. 15 The three recovery systems at end of June, 2010 (taken from British Petroleum: www.bp.com, referred hereafter as BP)

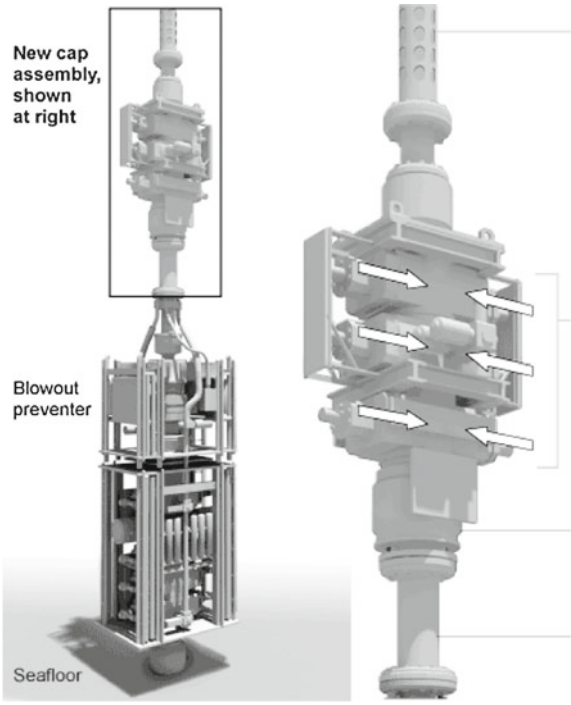

Fig. 16 A better cap (NYT)

July 10 BP replaces the cap put in place on June 3 with a tighter one that could potentially stop the flow of oil from the well. The new cap has some of the same types of components as the blowout preventer (NYT). Three stack ram cap installed and tested (Lower Marine Riser Package, LMRP (Fig. 16).

July 12 After days of delays due to weather, the Helix Producer, a production vessel on the surface, begins collecting oil. BP officials say that they

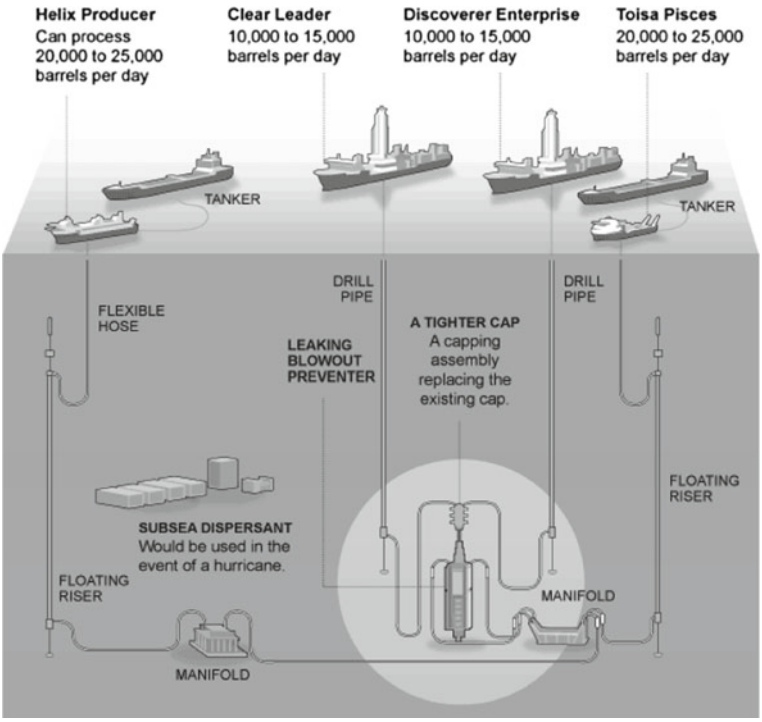

Fig. 17 Adding more capacity (NYT)

eventually expect to have a total of four vessels on site to collect and process oil and gas. The Q4000 will be replaced by another vessel, Toisa Pisces, which will be connected to one of two floating risers that can be disconnected in the event of a hurricane (Fig. 17) (NYT).

July 15 Testing to See if the Well Is Intact. A new capping assembly stops the flow of oil for the first time (Fig. 18). Engineers begin monitoring pressure in the well to determine its integrity (NYT).

August 3–4 Engineers successfully pump mud through a valve on the blowout preventer and into the existing well's metal casing pipe in a procedure similar to the failed top kill. They are able to pump mud slower and at lower pressure because a new cap atop the well has stemmed the flow of oil. Mud forces the oil and gas back down into the reservoir. Cement is also pumped into seal the well (Fig. 19) (NYT).

August 14 BP engineers continue developing a more specific plan on how to complete the bottom kill with minimal risk. When engineers pumped cement into the Macondo well's metal casing pipe during the static kill last month, it is possible that cement also entered the annulus, the space between the pipe and the bore hole (Fig. 20) (NYT).

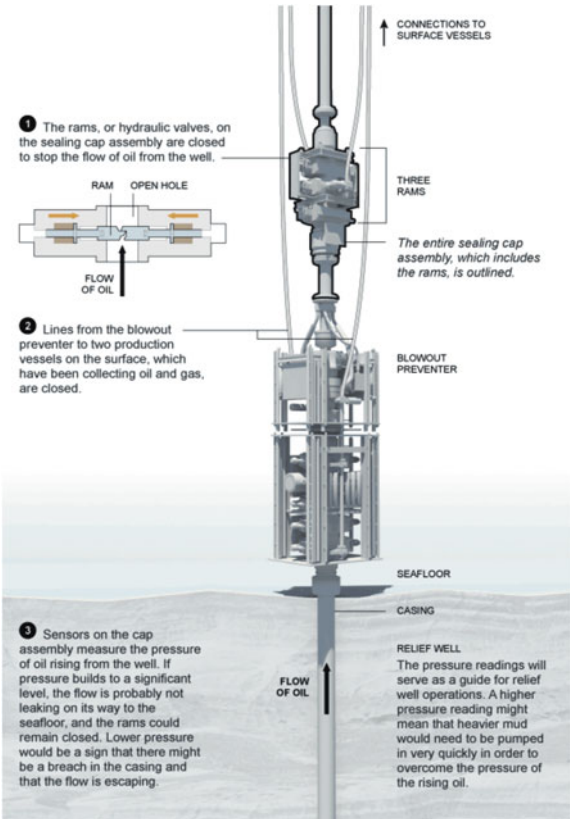

Fig. 18 Oil release is stopped (NYT)

August

- The slick appeared to be dissolving far more rapidly than anticipated. The long term damage caused by the spill, however, is still uncertain, in part because large amounts of oil spread underwater rather than surfacing. A new study published in the journal Science confirmed the existence of a huge plume of dispersed oil deep in the GOM and suggested that it had not broken down, raising the possibility that it might pose a threat to wildlife for months or even years.
- The administration announced that it would revise the process used for granting deepwater drilling permits to require more extensive review. White House officials recommended that the Interior Department suspend use of so-called categorical exclusions, which allow oil companies to sink offshore wells based on environmental impact statements for supposedly similar areas, while the department reviews the environmental impact.
- Top administration officials said that 75% of the oil had evaporated, dissolved or been collected. But the presidential commission said in October that the government's own data did not support such

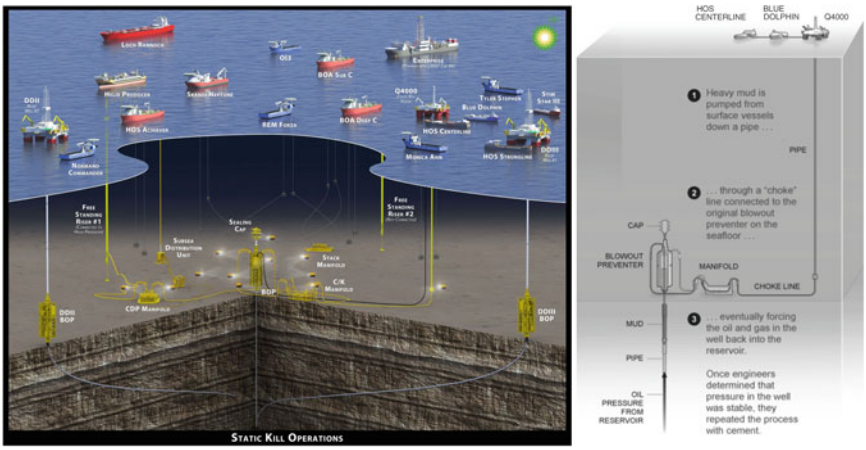

Fig. 19 Static kill completed (cementing) (Figure on the left hand was taken from BP and Figure on the right hand from NYT)

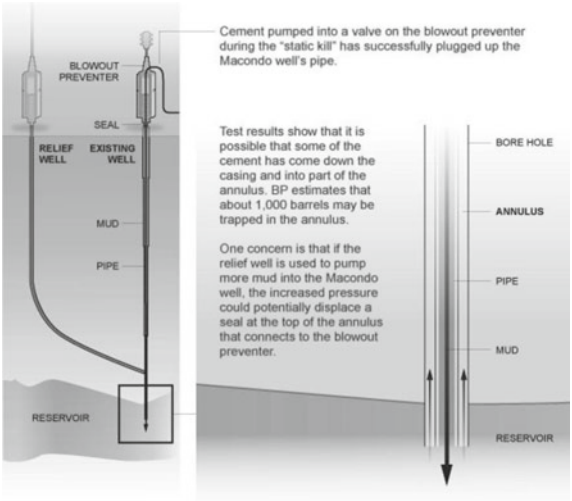

Fig. 20 Making progress on the relief well (NYT)

sweeping conclusions, which were later scaled back. A number of respected independent researchers have concluded that as much as half of the spilled oil remains suspended in the water or buried on the seafloor and in coastal sludge, and that it will be some time before scientists can paint an accurate picture of the ecological damage.

September 4 Cap and original BOP removed, new BOP installed. Original BOP taken as evidence.

September 8 BP releases its accident report, chain of human and mechanical errors.

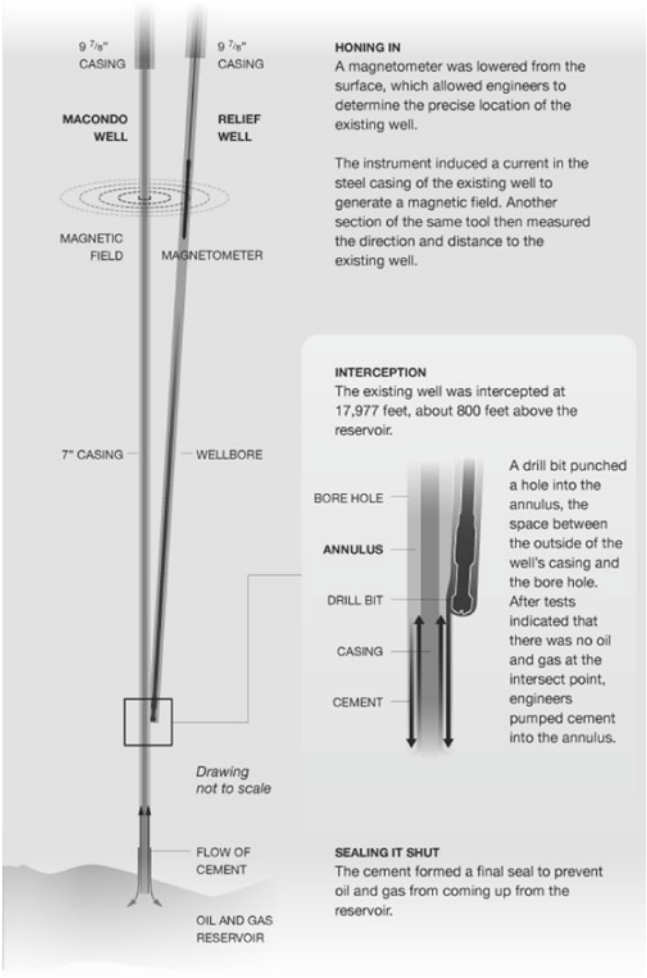

Fig. 21 The Bottom kill (NYT)

September 19 Relief well complete, cap in place.

September 20 Declared sealed by USCG.

September 21 The federal government has finally declared the Macondo well dead after nearly five months of failed attempts and semi-successes by BP engineers to permanently plug the leaking well in the GOM (Fig. 21) (NYT).

September
- Government scientists estimated that nearly five million barrels of oil flowed from BP's well, an amount outstripping the estimated 3.3 million barrels spilled into the Bay of Campeche by the Mexican rig Ixtoc I in 1979.

- In an internal report released in early September, BP claimed that it was a series of failures involving a number of companies that ultimately led to the spill. Citing "a complex and interlinked series of mechanical failures, human judgments, engineering design, operational implementation and team interfaces," the 193-page report deflected attention away from BP and back onto its contractors, especially Transocean and Halliburton.

September–November Underwater plume mapping continues.

November 24 An emergency program had ended and the settlement phase began. Hundreds of thousands of people and businesses have filed for emergency payments from the $20 billion BP fund administered by Kenneth R. Feinberg. More than $2.2 billion is being paid to some 150,000 individuals and businesses with documented claims, according to fund estimates. The rules for those settlements were to be announced on November 24 by Mr. Feinberg, after consulting with lawyers, state attorneys general, the Department of Justice and BP.

December The Department of Justice filed a civil lawsuit in New Orleans against BP and eight other companies over the GOM oil spill. Although the complaint does not specify the damages that the administration is seeking, the fines and penalties under the laws that are cited in the complaint could reach into the tens of billions of dollars.

3 Control Strategies on the Surface

Emergency teams used several methods in diverse attempts to deal with the oil at the surface, which created a slick covering about 2,000 sq miles (5,200 sq km). More than 275 vessels, including skimmers, tugs, barges and recovery vessels were used. Skimmers, which skate over the water, brushing up the oil were also employed and more than 90,000 barrels of oil–water mix were removed. Besides, there was an attempt to remove the oil that has arrived to the shore (Fig. 22).

Around 190 miles of floating boom are being used as a part of the efforts to stop oil reaching the coast. A US charity is even making booms out of nylon tights, animal fur and human hair. Hair donations have been sent from around the world to help make the special booms, which will be laid on beaches to soak up any oil that washes ashore (Figs. 23 and 24).

Dispersant chemicals, rather like soap, are being sprayed from ships and aircraft in an effort to help break down the oil–which is also degraded by wind and waves (Figs. 23 and 25).

Fig. 22 Removing oil in shorelines (taken from Deep Water Horizon response: www.deepwaterhorizonresponse.com, referred hereafter as DWHR)

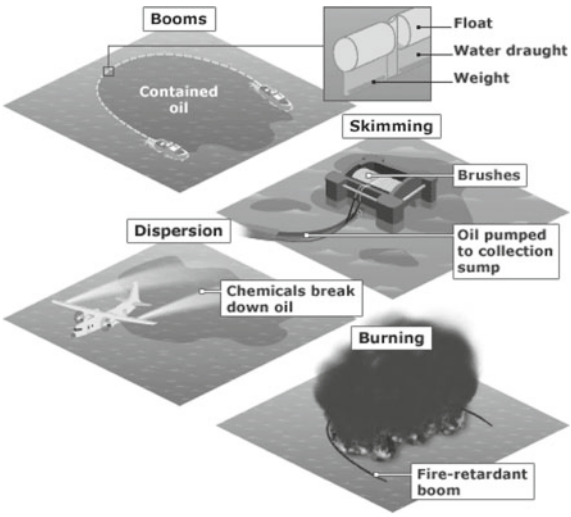

Fig. 23 Surface measures used to contain oil spillage (taken from The British Broadcasting Corporation: www.bbc.co.uk, referred hereafter as BBC)

Burning is another method used to tackle oil spills (Figs. 23 and 26)—although it can be tricky to carry out and has associated environmental risks such as toxic smoke. Controlled burning was coordinated by the U.S. Coast Guard, BP, and other federal agencies to aid in preventing the spread of oil.

So far emergency crews have had little success in containing the spill using those methods. New underwater technology aimed at stopping crude oil rising to the surface at the site of the leak has had some success.

4 Tracking the Gulf Oil Spill

The estimated extent of the oil slick was estimated by the NOAA, by means of wind and ocean current forecasts, as well as analysis of aerial photographs and satellite imagery (Figs. 27, 28, 29 and 30). The "surveyed extent" shows areas where oil was visible on the water surface during aerial and satellite surveys on the

Fig. 24 Protection works around shores and islands (DWHR)

Fig. 25 Aerial dispersant applications (DWHR)

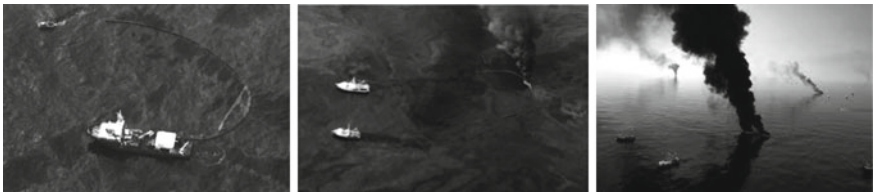

Fig. 26 Controlled burning (DWHR)

GOM. The locations where oil has made landfall are based on reports from federal, state and local officials (Figs. 31 and 32). They are placed on the map on the day of the earliest report, and may change as better reports became available.

On the other hand, the Real Time Ocean Forecast System (RTOFS) for the North Atlantic (Mehra and Rivin 2010) is the ocean forecast system based on the HYbrid Coordinate Ocean Model (HYCOM) and was used to show the circulation patterns of the GOM during the oil spill (Figs. 33 and 34). The RTOFS-Atlantic is an operational real time ocean nowcast/forecast system for the North Atlantic running daily at National Centers for Environmental Prediction (NCEP).

Fig. 27 Main page of NOOA during the oil spill

Fig. 28 Aerial view of the black oil tide

Prediction of oil spill dispersion was simulated using particles as tracers; in the literature almost all modelers used this kind of approximation to simulate the BP oil spill dispersion patterns. In Fig. 35 i.e., we can see historical simulations of how spill might have played out (over 120 days) if it occurred on April 15, 1993 (Fig. 35a) and if it occurred on April 6, 1996 (Fig. 35b). Combined hundred of these scenarios together can help us predict what might happen to the oil in coming months.

The EPA and NOAA were in charge to follow the environmental consequences of oil spill; and together implemented several strategies in sea, in coast, sediments and air. They implemented several measurements campaigns in defined regions. In Fig. 36 for example the evolution of restricted area implemented by EPA and NOAA; inside the closure zone fishery was forbidden.

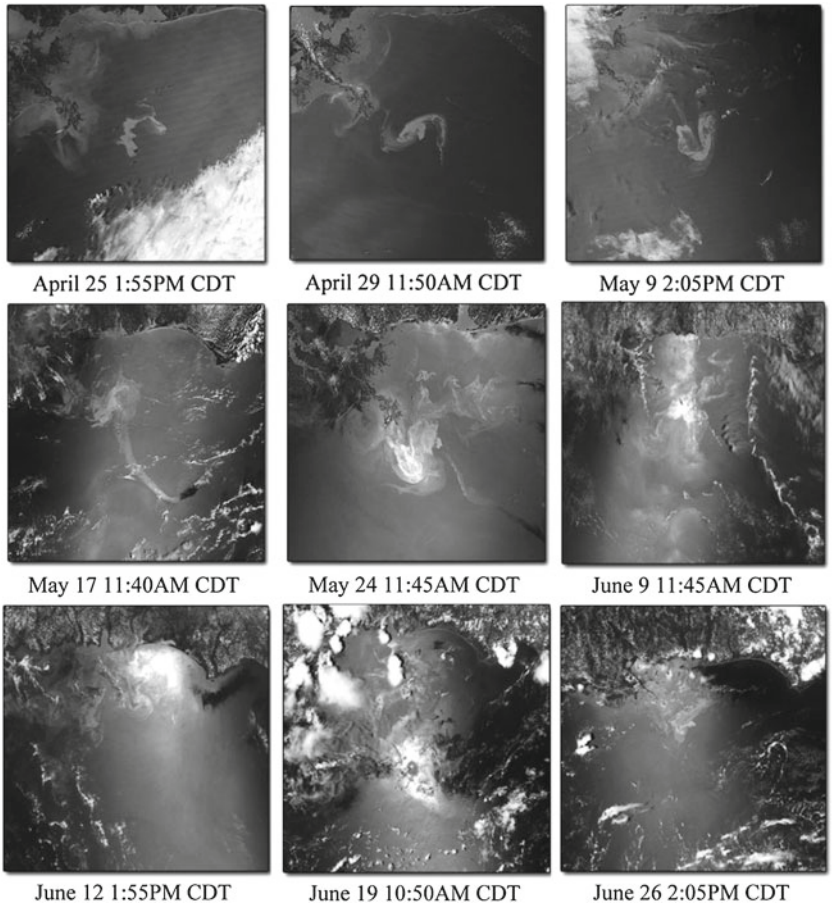

Fig. 29 Sequences taken from a satellite. All images are taken from MODIS rapid response system

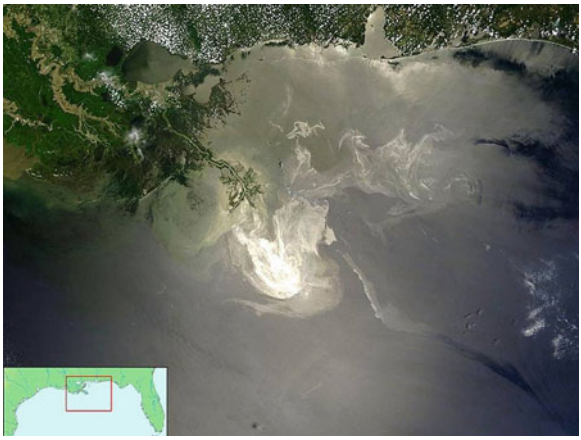

Fig. 30 Black oil tide at August 25

Fig. 31 Oil arriving on the coast

Fig. 32 The black oil tide at the end of the Mississippi delta from International Space Station (May 4)

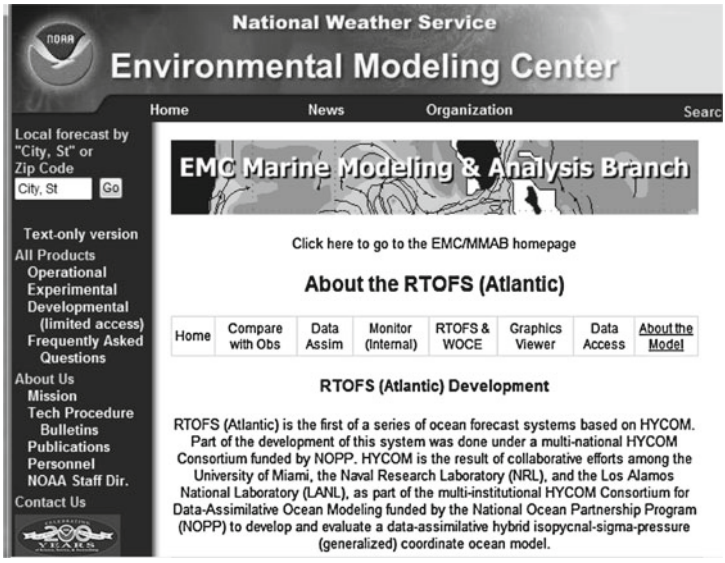

Fig. 33 Main page of RTOFS during the oil spill

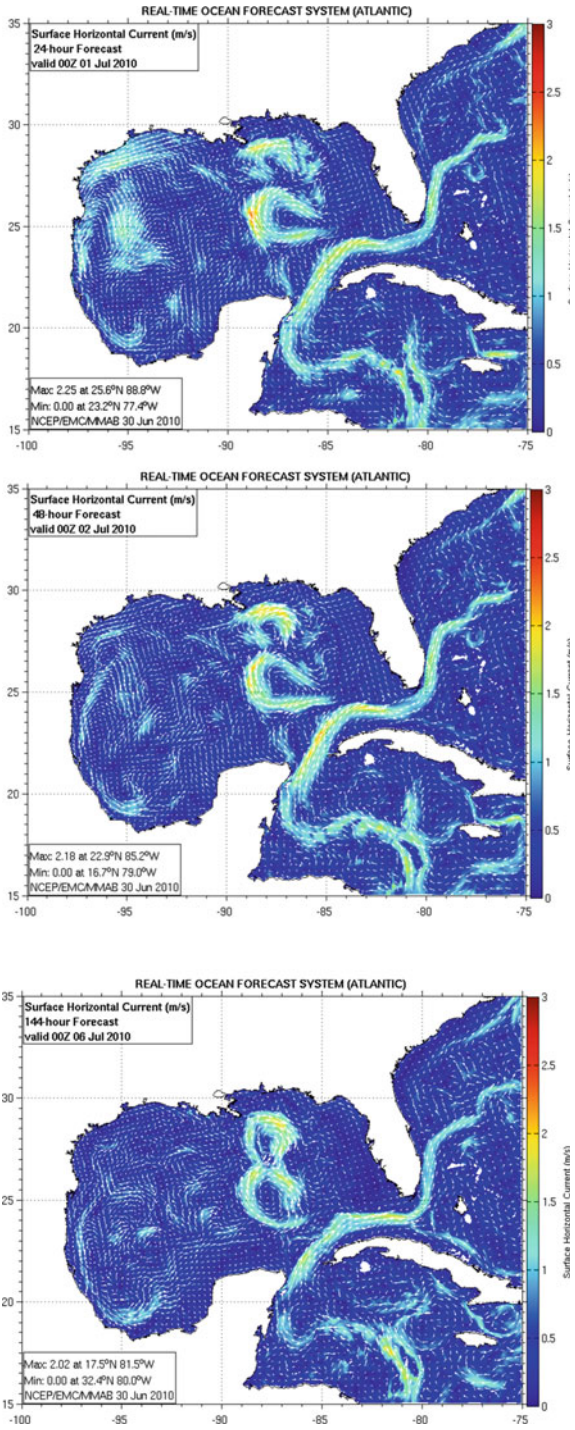

Fig. 34 Circulation estimated and predicted with de HYCOM model

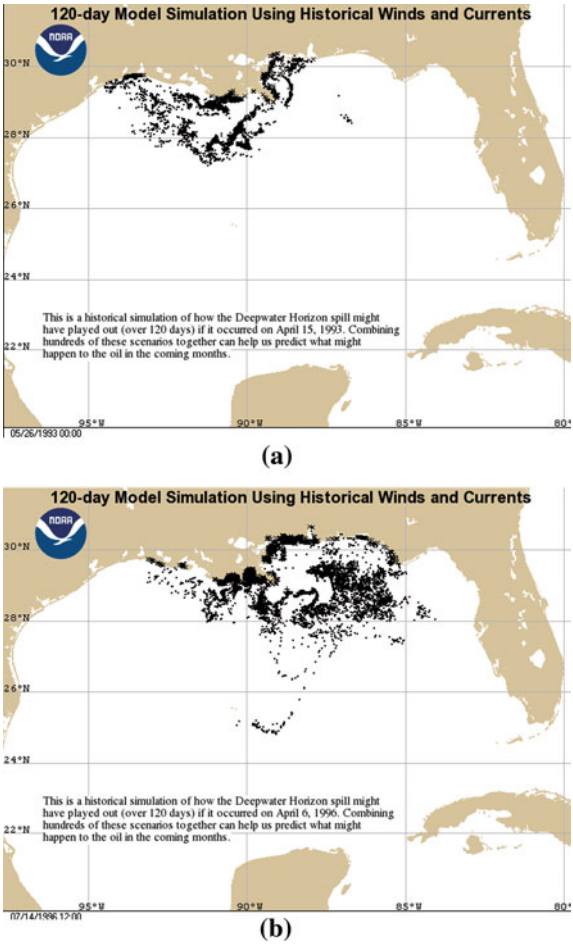

Fig. 35 Dispersion patterns using particles as tracers

In Fig. 37 shows National Center for Atmospheric Research (NCAR) and University Corporation for Atmospheric Research (UCAR) images of how the released oil may move in the upper 20 meters of the ocean. This is not a forecast, but rather, it illustrates a likely dispersal pathway of the oil for roughly four months following the spill. It assumes oil spilling continuously from April 20 to June 20. Simulation shows a passive dye injected at the location of the oil leak and advected by an ocean model for different run times for one likely ensemble. The colors represent a dilution factor ranging from red (most concentrated) to beige (most diluted).

Applied Science Associates (ASA) show some results supported in their own models and databases; they shown three kinds of simulations: using satellite derived currents (Altimeter); using current meters; and using hydrodynamic model (from UK Met Office).The results show considerable differences between them and biggest differences when they are compared with the evolution of oil slick (Fig. 38).

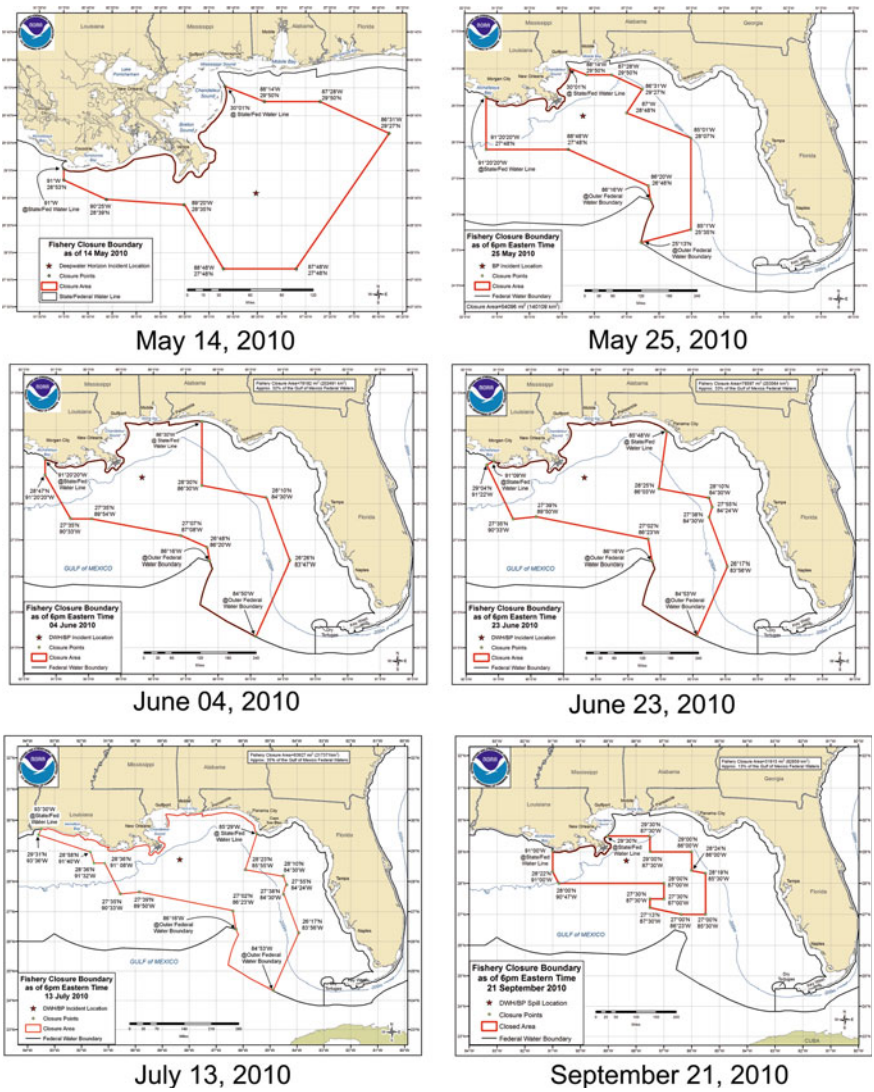

Fig. 36 Restricted area implemented by EPA/NOAA

Recently in The New York times internet page abundant information appeared on the behavior of the oil slick, for example in Fig. 39 we can see the evolution of oil spill from April 22 to August 2; Figure 40 shows the sequence from June 4 to 5 when the Loop Current broke to generate a clock vortex named Franklin and affecting the dispersion of oil slick.

Many other groups in the USA and Mexico showed some simulations of both currents and oil spill dispersion, supported in their own databases and their own

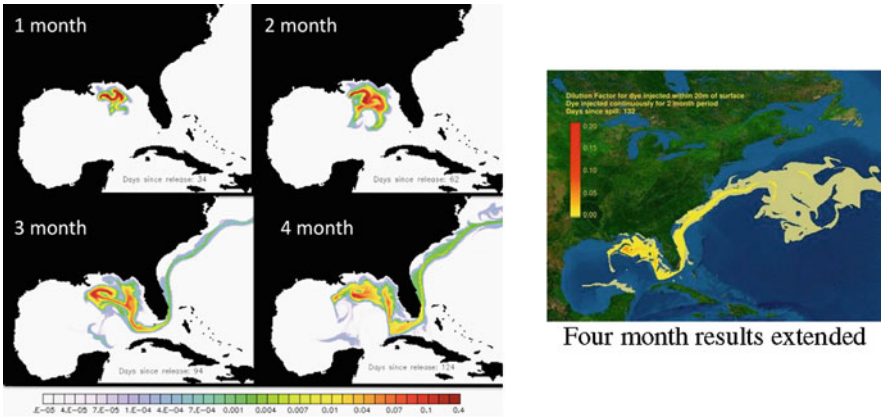

Fig. 37 NCAR simulations

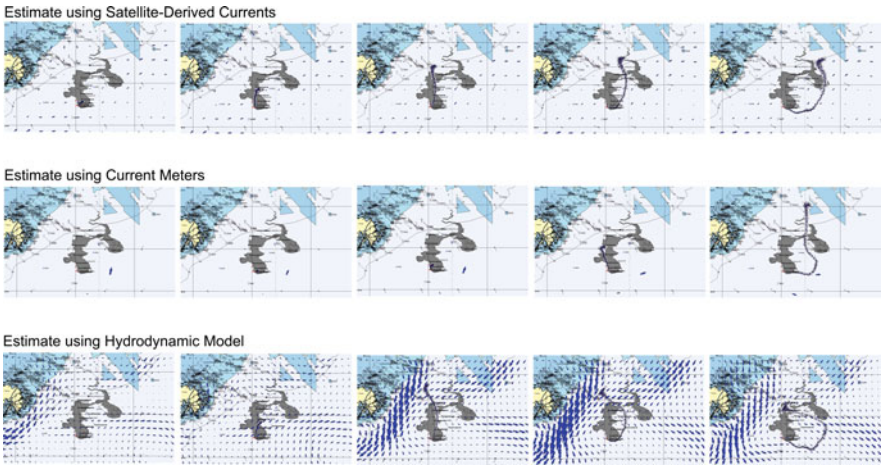

Fig. 38 Results obtained by ASA

experiences. The results are interesting and show a complementary approach to this one.

One of the greatest concerns is how much oil will reach or is contained in the coasts: Fig. 41 shows some predictions made by NOAA supported on satellite images, modeling results and measurement campaigns.

The amount of oil on sections of the coastline often changes day by day because of many factors, including recent efforts by cleanup teams or tides washing-in new oil. For the first month of the spill, the oil stayed mostly in the GOM. But in the last week of May, waves of oil began washing into Louisiana's fragile wetlands

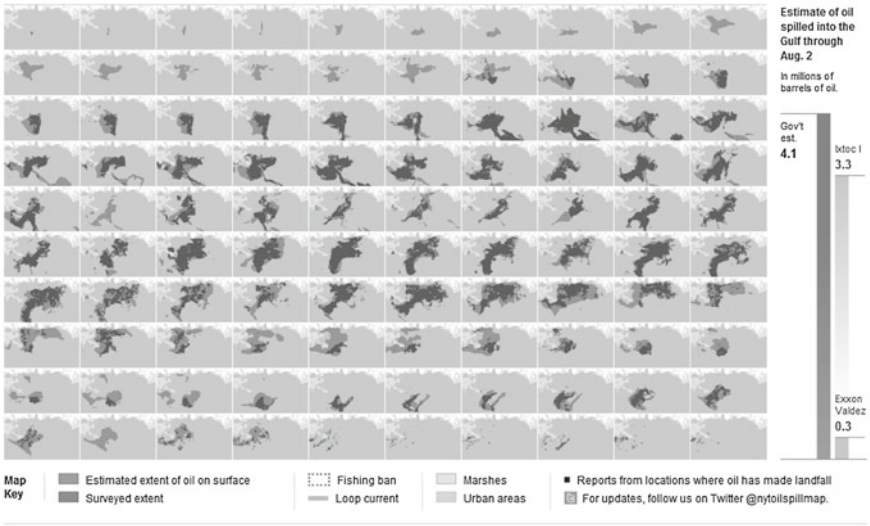

Fig. 39 Oil spill behavior from April 20 to August 2

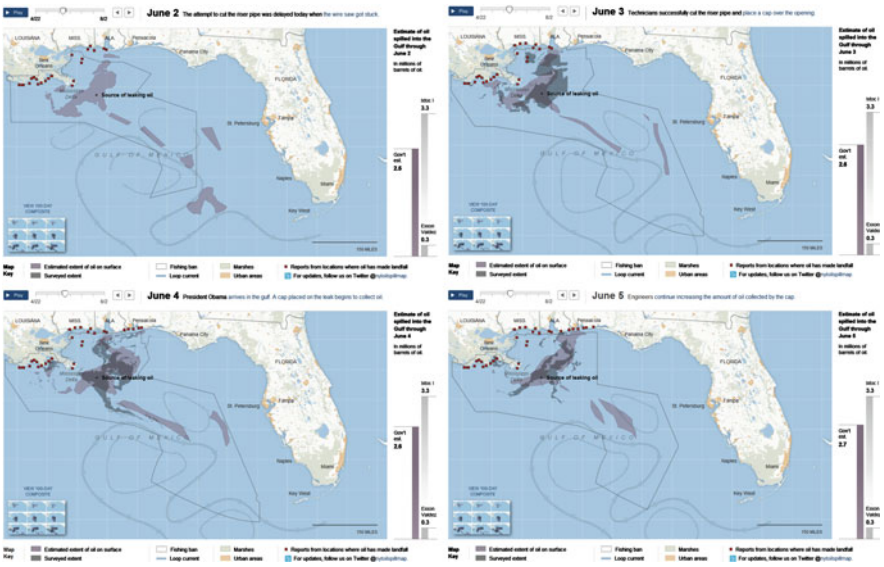

Fig. 40 Sequence of June 2–5, after NYT

and beaches. In June, oil landings began to be reported more frequently in the states to the east. Survey areas for Louisiana were first released on May 24 and for Mississippi, Alabama and Florida beginning on June 12. Survey data were not available for some days.

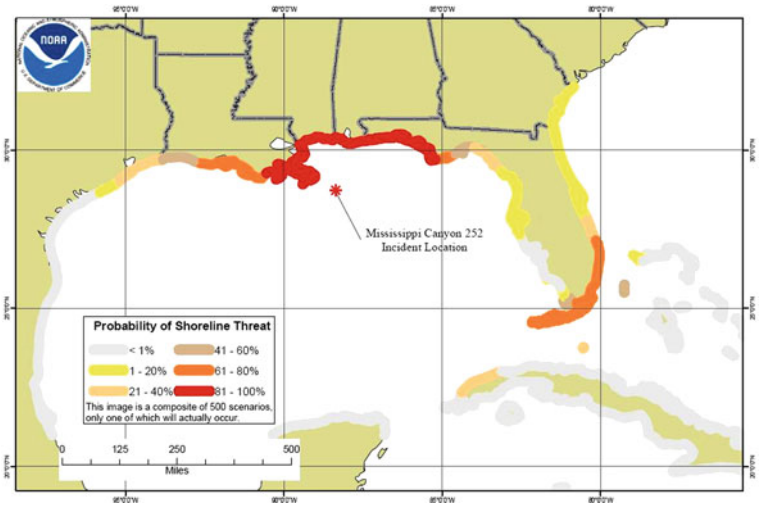

Fig. 41 Impact forecast on coastal zone

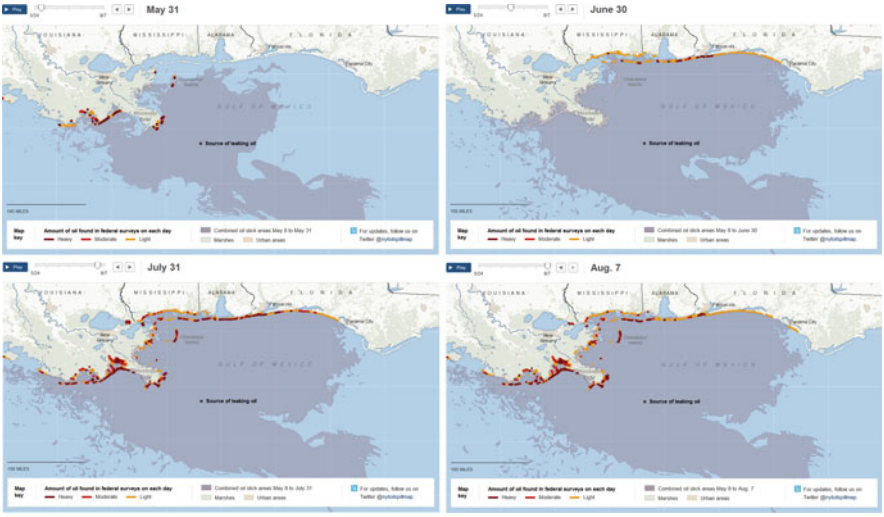

Fig. 42 Sequence of oil arriving on the coast (NYT)

In the same way The New York Times (NYT) website show similar images which represent the amount of oil on the coastline as reported each day by the federal government based on information from air and ground surveys (Fig. 42).

5 Potential Impacts of the Deepwater Horizon Oil Spill[1]

Text reproduced from ASA Oil Spill Workshop, 2010. Natural resources of the GOM (i.e., birds, sea turtles, marine mammals, fish, shellfish, plankton; and a wide variety of habitats along the shoreline, such as salt marshes, mangroves, sea grasses, oyster flats; and at the sea bottom, such as salt marshes and submerged aquatic vegetation) are currently being exposed to and impacted by oil from the Deepwater Horizon oil spill; as well as potentially by other materials being added to the marine environment during the response that might be toxic or change biological or chemical conditions. In addition there will be impacts on water quality near beaches, shellfish (e.g., oyster) beds, and fishery nursery grounds.

In general, the most vulnerable species to oil spills are birds and fur-bearing marine mammals. These animals depend on their feathers or fur to maintain body heat and keep their skin relatively dry. They preen daily, and so will ingest toxic components present in oil that covers any portion of their bodies. Sea turtles, all species of which are threatened or endangered, are also highly susceptible to oil's effects.

Because fish and invertebrates are the most part under the water surface, and much of the oil is not soluble, their exposure to oil hydrocarbons is subject to (1) the degree to which the oil is mixed by turbulence or other means (i.e., dispersed) into the water column, (2) the degree to which the dispersed oil still contains the toxic compounds (which otherwise evaporate), and (3) the rate of dissolution of soluble aromatics into the water. Oil dispersion rate is highest in storm conditions and when large amounts of dispersants are applied to the oil. Mortality is a function of duration of exposure—the longer the duration of exposure, the lower the effects concentration. Thus, a situation where oil is largely dispersed into the water while fresh is that where the highest impacts to fish and invertebrates would be expected.

Figure 43 shows a spatial distribution of a number of marine species in the GOM. Numbers represent all plant and animal species reported for that area. Sizes of circles are proportional to species numbers with each depth range.

The open water environment, the ongoing release of oil and the ongoing response efforts all contribute to complex, constantly-changing exposure conditions for biological resources in the offshore and near-shore environments of the northeastern of GOM. Contributing factors to the complexity of the situation include:

1. Characteristics of released oil and other materials, which change with time due to weathering and response activities; also, there may be changes in the released material at the discharge site due to changes in materials leaving the well;
2. Volume and duration of the continued release of oil, with the oil release rate varying in time;
3. Location and nature of the release (i.e., while burning at the sea surface, from various pipe breaks on the sea floor);

[1] Part of this section has been taken from May 18, 2010 Testimony of Deborah French McCay before the US Senate Committee on Commerce, Science and Transportation.

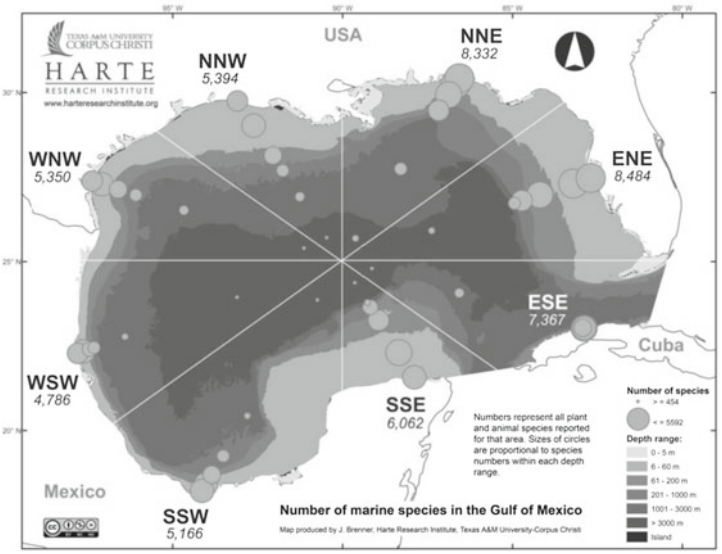

Fig. 43 Spatial distribution of number of marine species in the GOM

4. Physical oceanographic conditions (currents, temperature, etc.), which vary in space and time;
5. Weather (winds, light exposure, air temperature), affecting the oil's chemistry;
6. Response effectiveness to stop or slow the release of oil, as well as changes in the location, nature, and volume of the release;
7. Dispersant type, application methods (i.e., injected versus aerial or boat), volumes, effectiveness, locations and timing;
8. Exposure scenarios for biological resources (i.e. exposure duration, species, life history stages involved):
9. Location of critical habitats (live bottom, deep water corals, cold seeps; fishing grounds); and
10. Impacts of oil hydrocarbon/dispersant/contaminant mixes over time, resulting from short duration and long exposures, delayed and indirect impacts, etc.

The socioeconomic impacts of the spill will include disruption of fisheries and dependant businesses, effects on tourism and recreational uses, and potentially changes in oil industry practices.

The purpose of using dispersants on the oil is to lessen the potential impact to wildlife (birds, mammals, and sea turtles) and shoreline habitats. However, to some degree there is a tradeoff, in that the contamination in the water is increased by dispersant application. The objective is to achieve a net environmental benefit: to disperse the oil sufficiently to reduce the impact to wildlife and shorelines, but to do so in deep water where the dilution potential is high to minimize adverse effects on fisheries resources.

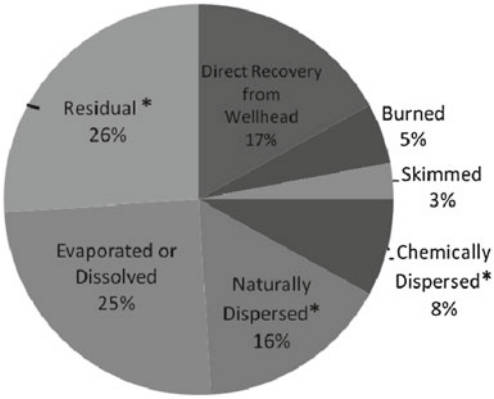

Fig. 44 Response estimate: Percentage of total (Oil Budget Calculator. Deepwater Horizon 2010)

6 Final Comments

6.1 Where is the Oil Spilled?

The BP oil spill is the largest accidental oil release on marine waters according to flow estimates announced on August 2 by a federal panel of scientists, known as Flow Rate Technical Group. The panel said that about 4.9 million barrels of oil have come out of the well and only around 800,000 barrels, or 17%, was captured by BP's containment efforts. From the remaining 4.1 million barrels of oil that were released into the waters of the GOM, more than half had been burned or skimmed, or had already evaporated or dispersed by the beginning of August. This meant that about 1.3 million barrels of oil were still onshore as tar balls, buried under sand and sediment or floating on the ocean surface as a light sheen (FISG and OIB 2010) the amounts shown in Fig. 44 were calculated from the initial explosion at 10 p.m. on April 20 until the flow was stopped on July 15. Totals are adjusted from May 17–25 for oil diverted through a narrow tube that was inserted into the well's damaged pipe and from June 3–15 for oil captured after a cap was successfully placed over the leak. While both oil and gas are leaking from the well, the estimates here are only for the amount of oil. BP said in May that the fluid leaking was roughly half oil, half natural gas.

6.2 Possible Consequences on the Mexican Side

When the BP oil spill occurred, Metocean conditions favored the oil slick dispersion toward the USA coast. Nevertheless with the arrival of hurricanes season (Fig. 45) and "Norths" (wings coming from the USA to Mexican side) the patterns coastal currents can be reversed (Zavala et al. 2002). Consequently the slick oil

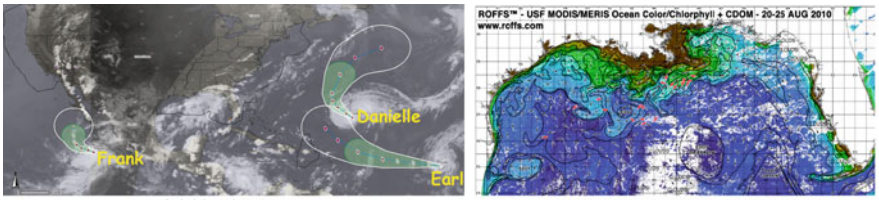

Fig. 45 Hydrometeorological intensity at the end of August. **a** Hurricane, **b** Eddy Fraklin Separation

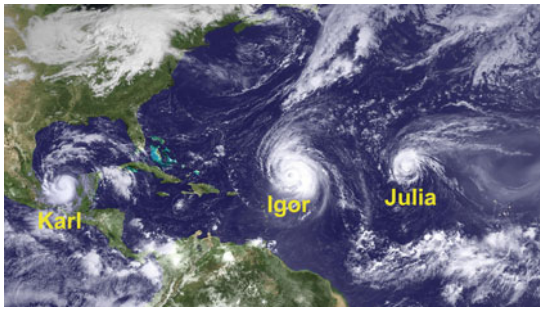

Fig. 46 Hydrometeorological intensity by September 15

dispersion could be reversed too. Fortunately the spill was controlled before this

Fig. 47 Possible affectation of areas in Mexican coast (adapted from SEMARNAT Seminars 2010)

environmental Metocean conditions.

At the end of August the hydro-meteorological conditions were very intense on the zone: for example we had the presence of three hurricanes (Fig. 45a) and in other hand, on the sea surface the eddy Franklin clearly separate from the Loop Current and drift westward while it is rotating in a clockwise direction (Fig. 45b). The Yucatan current water is being pulled around the Loop Current and also around Eddy Franklin. It has been a surprise to us and many others, that over the period since the end of April until now that the majority of the water and the water–oil–dispersant mixture in the northern GOM has not been pulled into the Loop Current and into the Gulf Stream system.

In September 15, for second time on record (Fig. 46), two simultaneous Category 4 hurricanes prowled the Atlantic on—Igor and Julia (far right). Meanwhile, Karl (far left), a Category 3 storm, became the strongest hurricane ever recorded in the Bay of Campeche. Data from NOAA GOES.

Figure 47 shows some possible impacts on the Mexican coasts after some possibilities of dispersion pattern of BP oil spill. Fortunately until now several groups in Mexico searching traces in offshore and onshore of oil spill they have not found any evidence on surface, water column or sediments. These expeditions were coordinated by SEMARNAT with collaboration of UNAM, UABC, IMP, and others.

References

Mehra A, Rivin I (2010) A real time ocean forecast system for the North Atlantic Ocean. Terr Atmos Ocean Sci 21(1):211–228

Oil Budget Calculator. Deepwater Horizon. TECHNICAL DOCUMENTATION. November 2010. A Report by: The Federal Interagency Solutions Group, Oil Budget Calculator Science and Engineering Team Poojitha D, Yapa, Hao Xie Modeling Underwater Oil/Gas Jets and Plumes: Comparison with Field Data

Zavala J, Morey S, O'Brien J (2002) Seasonal circulation on the western shelf of the Gulf of Mexico using a high-resolution numerical model. J Hydr Engrg 128(9):855–860

Seminars and Communications

SEMARNAT Seminars: Resumen del accidente de derrame de petróleo en el Golfo de México. Large Marine Ecosystem: Gulf of Mexico

Seminar CICESE Derrame de Petróleo en el Golfo de México. Perspectivas oceanográficas y ecológicas

UNAM, personal communications from several Researchers Working in the missions commanded by SEMARNAT

IMP, personal communications from several Researchers Working in the missions commanded by SEMARNAT

IMP (2010) weekly reports of PECAP team. 23 Reports

Websites

http://www.app.restorethegulf.gov/go/doc/2931/832251/
ASA Oil Spill Workshop (2010) http://asascience.com/news/bulletins/clean-gulf-2010.shtml
http://www.aoml.noaa.gov/phod/dhos/drifters.php http://www.horizonmarine.com/bp_buoys
BBC: The British Broadcasting Corporation: http://www.bbc.co.uk
BP: British Petroleum: http://www.bp.com
DW: http://www.deepwater.com
DWHR: http://www.deepwaterhorizonresponse.com
EPA: Environmental Protection Agency: http://www.epa.gov
http://www.guardian.com
http://www.industrialaccidentlawyerblog.com
http://www.ndbc.noaa.gov/maps/ADCP_WestGulf.shtml
http://www.nytimes.com
http://www.sciencedaily.com/news/earth_climate/oil_spills/
CONABIO: Comisión Nacional para el Conocimiento y Uso de la Biodiversidad. Comisión nacional para el conocimiento y uso de la biodiversidad. Estructura, objetivos e información sobre especies y monitoreo Estructura, objetivos e información sobre especies y monitoreo: http://www.conabio.gob.mx
CSTARS: cstars.rsmas.miami.edu/cstars-comsat. Center for Southeastern Tropical Advanced Remote Sensing. Universidad de Miami Rosenstiel School of Marine & Atmospheric Science. University of Miami.
ENVISAT: Environmental Satellite envisat.esa.int/earth/www/area/index.cfm
IMP: Instituto Mexicano del Petróleo: http://www.imp.mx
INE: Instituto Nacional de Ecología: http://www.ine.gob.mx
MODIS Rapid Response System: lance.nasa.gov/imagery/rapid-response
NASA-GSFC: http://www.gsfc.nasa.gov
NCAR. National Center for Atmospheric Research: ncar.ucar.edu
NYT: New York Times: http://www.nytimes.com
NOAA: Nationalt Oceanic and Atmospheric Administration: http://www.noaa.gov/
NOAA GOES: http://www.goes.noaa.gov
rapidfire.sci.gsfc.nasa.gov/subsets
SEMARNAT: Secretaria del Medio Ambiente y Recursos Naturales: http://www.semarnat.gob.mx
Texas A&M University: http://www.harteresearchinstitute.org
UCAR. University Corporation for Atmospheric Research: http://www2.ucar.edu/
UNAM-CCA: Universidad Nacional Autónoma de México-Centro de Ciencias de la Atmosfera: http://www.atmosfera.unam.mx
UNAM-ICMyL: Universidad Nacional Autónoma de México-Instituto de Ciencias del Mar y Limnología: http://www.icmyl.unam.mx

Eastern Pacific Tropical Cyclones and Their Impact Over Western Mexico

Luis M. Farfán

Abstract This article documents long-term characteristics of tropical cyclones (TCs) in the eastern Pacific Ocean from 1970 through 2009. This basin is relatively active during the summer and the presence of TCs may result in significant changes in atmospheric moisture and convective activity over populated areas along the west coast of Mexico. Because of its length and geographical location, the Baja California Peninsula received more than 30 landfalls during the period considered. To demonstrate their impact, four case studies from recent seasons were selected for further analysis. The analysis includes examination of TC position and intensity records, satellite imagery, meteorological gridded fields, and surface rainfall observations that are used to illustrate the evolution of these cyclones prior to and during landfall.

1 Introduction

Tropical cyclones (TCs) are atmospheric vortices that form at low latitudes, over relatively warm oceans. They start as loosely organized cloud clusters and go through several stages to become intense circulation systems whose diameter is typically in the range of 500–1,000 km. The activity is confined to certain seasons of the year and regional basins, with the eastern Pacific Ocean being the most productive of any basin per unit area worldwide (McBride 1995). This basin is located north of the Equator, bounded by 140° W as well as the west coast of Central and North America (Fig. 1), and it is active from late spring through the fall.

L. M. Farfán (✉)
Centro de Investigación Científica y de Educación Superior de Ensenada B.C., Unidad La Paz, Miraflores 334, La Paz, B.C.S. 23050, Mexico
e-mail: farfan@cicese.mx

J. Klapp et al. (eds.), *Experimental and Theoretical Advances in Fluid Dynamics*, Environmental Science and Engineering, DOI: 10.1007/978-3-642-17958-7_9,

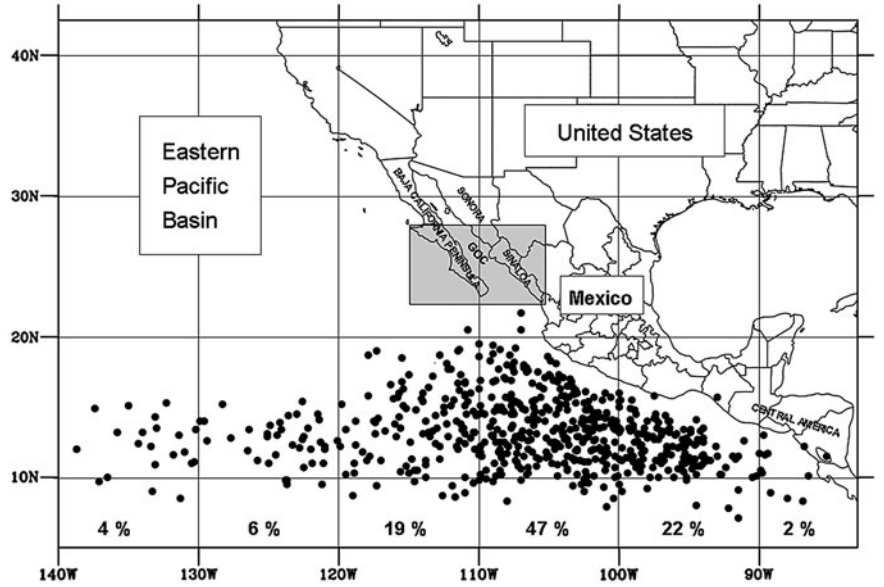

Fig. 1 Initial locations (*dots*) of TCs from 1970 to 2009. *Numbers* indicate percentage for locations inside 10°-longitude bins. The *shadedbox* is the main landfall area and GOC is the Gulf of California

From May through October, an average of 15 named TCs form every summer season and their development provides changes in moisture content to western Mexico. A feature that creates a unique meteorological situation is a pool of warm seawater that extends several hundred kilometers off the southwestern coast of Mexico through the Gulf of California (e.g., Corbosiero et al. 2009). This fact combines with humid air to support deep convection and heavy rainfall that are characteristic of well-organized circulations. In contrast, cooler water and drier air are found west of the Baja California Peninsula, which provide favorable conditions for TC decay.

Sometimes, TCs become a source of adverse weather conditions over populated areas. The west coast of Mexico has a length of 12,500 km, approximately 68% of the country's shoreline, including the Gulf of Mexico and the Caribbean Sea. The peninsula is 1,200 km, it has mountain ranges with maximum elevations above 2,000 m, it has 31% of the nation's shoreline and is located in the northwestern part of the country. These facts suggest that this region requires special attention with respect to research studies of the impact of TCs.

Early studies by Rosendal (1962) and DeAngelis (1967) used in situ observations to examine data from a few decades. These observations included ship reports and aircraft data that helped to identify general patterns of formation, intensification, and impact over land. Serra (1971) examined TCs that affected western Mexico from 1921 through 1969; he concluded that not only landfalling systems affected coastal areas, but systems having a center within 370 km of the

Table 1 Tropical cyclone classification and intensities ($m\ s^{-1}$)

Tropical depression	<17.0
Tropical storm	17.0–32.9
Hurricane, category 1	33.0–43.0
Hurricane, category 2	43.1–49.9
Hurricane, category 3	50.1–58.0
Hurricane, category 4	58.1–69.5
Hurricane, category 5	>69.5

coast were important too. In particular, this study stated that Baja California was the most affected area, with 97% probability of being affected by at least one TC each season and 46% probability of having least one TC move inland.

Landfall, defined as the passage of the circulation center across the coastline, is associated with strong winds, storm surges, and substantial rainfall. Frequently, there is extensive property damage. By documenting several cases and assessing damage and casualties, an analysis of regional impact was performed by Allard (1984) covering 1966 through 1980. In terms of fatalities, the worst TC on record is linked to heavy rainfall during Hurricane Liza in 1976, which caused a dam to fail and flash flood that killed more than 400 people (Gunther 1977).

The purpose of this article is to document development of TCs over the eastern Pacific during the 40 years from 1970 through 2009. This period was chosen because it best represents the basin TCs in terms of continuous detection and reliability of the available data. The TCs of particular interest are those that made landfall in Baja California. Section 2 reviews the datasets and Sect. 3 presents the results from TC activity in the basin. Section 4 examines the evolution of four TCs that made landfall on the peninsula during the seasons of 2006 through 2009. Finally, a summary and conclusion appear in Sect. 5.

2 Data and Methodology

The best-track database of TCs in the eastern Pacific offers the best estimate of the circulation center during their development (Rappaport et al. 2009). A careful post-analysis of all available sources of information, including aircraft fixes, ship reports, radar and satellite data, results in a smoothed, representation at 6-h intervals (Davis et al. 1984). Because of the limitations associated with in situ observations, satellite imagery has been the primary data source to define TC positions and intensities. The database is provided by the United States National Hurricane Center (NHC) and, based on maximum wind speeds, intensities are assigned according to the criteria provided in Table 1 (the Saffir-Simpson Scale; Simpson 2003).

In the present study, digital imagery from the *Geostationary Operational Environmental Satellite-11* (GOES-11) allows identification of humidity patterns in the atmosphere and cloud-cover structure. This includes water vapor and infrared images with spatial resolutions of 8 and 4 km, respectively. The imagery

was provided by the Space Science and Engineering Center of the University of Wisconsin-Madison, it has coverage from 0–70°N to 100–177°W, as well as recording every 30 min.

Additional information to study large-scale flow during development of selected TCs is derived from gridded data from the National Centers for Environmental Prediction-National Center for Atmospheric Research re-analysis (Kalnay et al. 1996). These are three-dimensional, global fields identifies mid- and upper-level circulations present over the Pacific Ocean and Gulf of Mexico, as well as over continental areas in Central and North America.

To determine the intensity of major rainfall events, data from the Mexican network of rain gauges were used. This network is managed by the Mexican Meteorological Service (Servicio Meteorológico Nacional, SMN) and the records are available as 24-h totals ending at 1500 UTC, corresponding 0900 AM local time during the daylight-saving season. Over 100 daily measurements of storm-total rainfall were examined to determine TC impact over the southern part of the peninsula (south of 28°N), known as the State of Baja California Sur (BCS). Following the observations from previous events in BCS, rainfall totals are defined as: extraordinary accumulations (>500 mm), large accumulations (250–500 mm), and moderate amounts (<250 mm).

3 Results

Figure 1 also shows the spatial distribution of initial detection of TCs for 1970 through 2009. Each dot represents the first position of the NHC dataset, which can have an intensity of tropical depression or tropical storm. Most of these locations are confined to the band within 5 and 20°N, 69% of them located south of Mexico between 90 and 110°W. Few TCs formed south of 10°N or north of 20°N. According to the annual summaries published by the NHC in *Monthly Weather Review* (http://journals.ametsoc.org/loi/mwre), three initial positions over land are from TCs that came from the Caribbean Sea, crossed Central America, and then regenerated in the Pacific Ocean.

The examination of best-track records from the eastern Pacific reveals development of 612 named TCs. This implies, for the period of interest, a long-term annual average of 15.3 cases per season. Figure 2 shows the seasonal variation. Minimum activity occurred in 1977 and 1996 (eight cases, each), compared with 24 in 1992. The latter was active from early June to late October, with three TCs making landfall in western Mexico. The frequency of TCs making landfall varies, with a maximum of six TCs occurring in 1981. No landfalls occurred in 1980, 1988, 1991, and 2005, but all years had TCs approaching within 300 km and some passed within 50 km.

The length of seasons, defined by the number of days between the initial and final detection of TCs, is also shown as part of Fig. 2 (thick line). The annual average is 152 days (∼5 months), which is comparable to the 148 days average

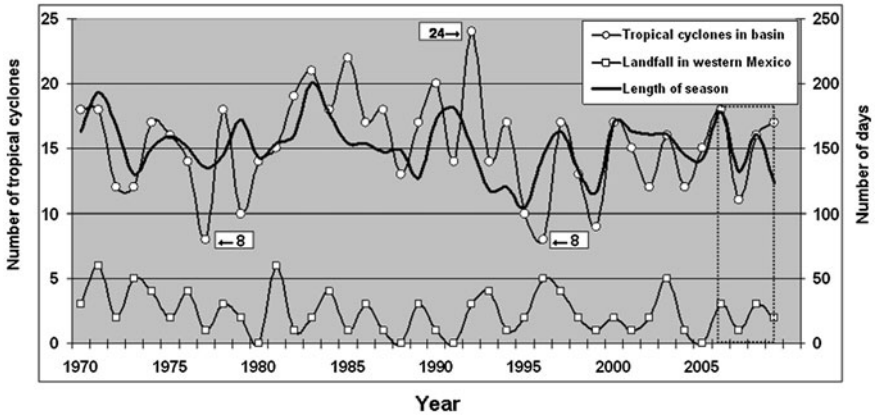

Fig. 2 Frequency of TCs that developed from 1970 through 2009. *Labeledboxes* are maximum and minima mentioned in the text. The *thickline* represents number of days in each season. *Dotted* area is the 2006–2009 period

found by Allard (1984) for 1966–1980. In the present analysis, there are extremes of 104 days in 1995 and 201 days in 1983. The earliest start was May 12, 1990 while the latest starting date was June 21, 2009. The extremely active season of 1992 was right on the average (June 1–October 30) lasting 152 days. A supplementary survey, based on 10 days (or 11 days) periods, indicates that 64% of the starting dates occur between May 21 and June 10.

The TC tracks were partitioned into monthly groups and Fig. 3 displays their distribution. The most active groups are July, August, and September with more than 100 TCs in each month, being September the month with the highest rate (33%) of landfalls in Mexico. These facts are in agreement with the results of Rosengaus et al. (2002) for 1951–2000. Tracks have a significant component of westward motion, although late in the season and associated with seasonal changes in the environmental flow, some of them acquired northward tracks. A recurving track is one that has an eastward component of motion (Renard and Bowman 1976). According to Allard (1984), more than 15% of TCs recurve and the mean coordinates for recurving are 18.5°N and 110.9°W. Note that a TC acquiring a northeast track is likely to hit land across northwestern Mexico.

During these seasons, there were 96 landfalls in western Mexico. The majority was over the states of Baja California Sur (31) and Sinaloa (20). Hence, nearly half of the TCs had direct impact in the landfall area from 22.5 to 28.0°N (shaded box in Fig. 1). Figure 4 shows the summer season's distribution of TCs that make landfall. Note the large frequency (77%) from mid-August to early November and a secondary period from late May through July. In contrast, there were no landfalls prior to May 20, from August 1 to 10, and after November 10. Intensity levels at landfall are mostly tropical storms (31%) followed by tropical depressions and category 1 hurricanes (23% each). The rest includes some category 2 hurricanes, a few category 3 hurricanes, and a single category 4 hurricane.

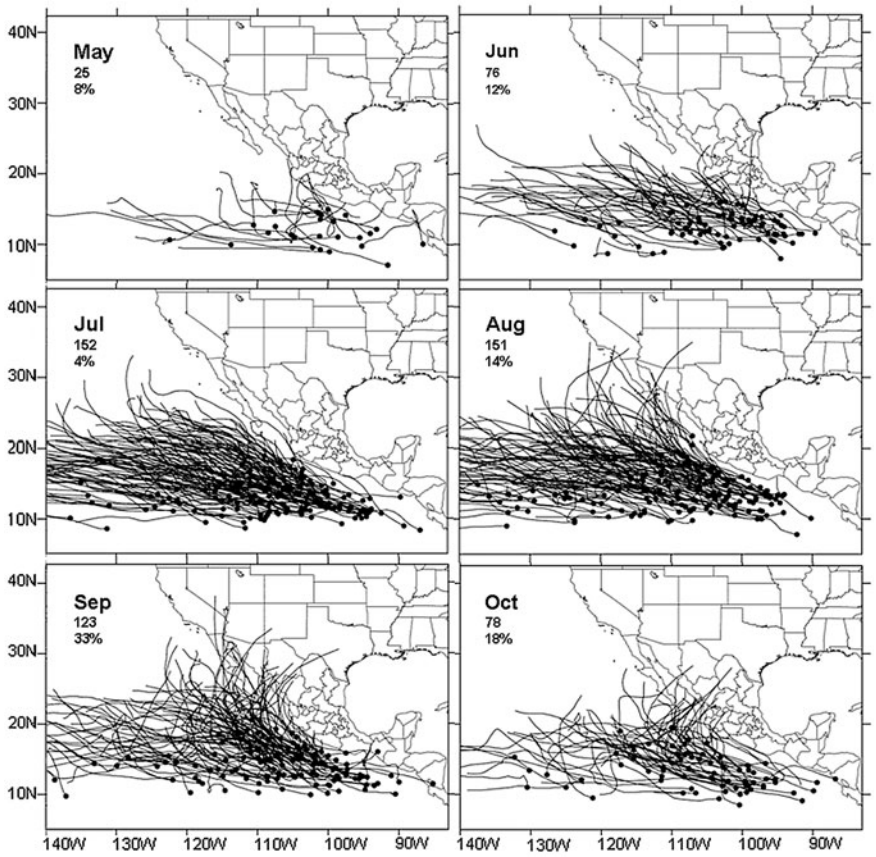

Fig. 3 Tracks of TCs that developed in the eastern Pacific Basin from 1970 to 2009. *Dots* are initial locations. *Numbers* represent total frequency (*middle*) and percentage (*bottom*) of landfall in western Mexico

4 Case Studies

Figure 5 depicts position and evolution of intensity of four events that, from the 2006 to 2009 seasons, made first landfall over the Baja California Peninsula. During these seasons, ten TCs made landfall in Mexico and nine of them were in the northwest. For discussion, only four TCs that moved onshore with hurricane strength are discussed. In order to supply an additional source of display, a set of satellite imagery animations are available at http://met-bcs.cicese.mx/SMF. Animation of this imagery provides an excellent technique to examine changes during TC approach and landfall.

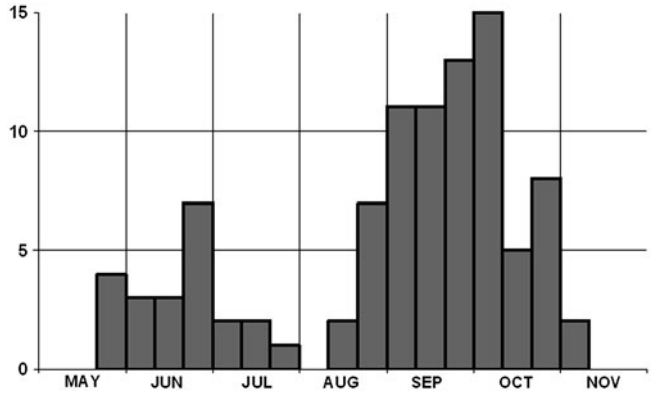

Fig. 4 Distribution of 96 TCs making landfall in western Mexico during summer storm seasons, with each month divided by 10- or 11-day periods

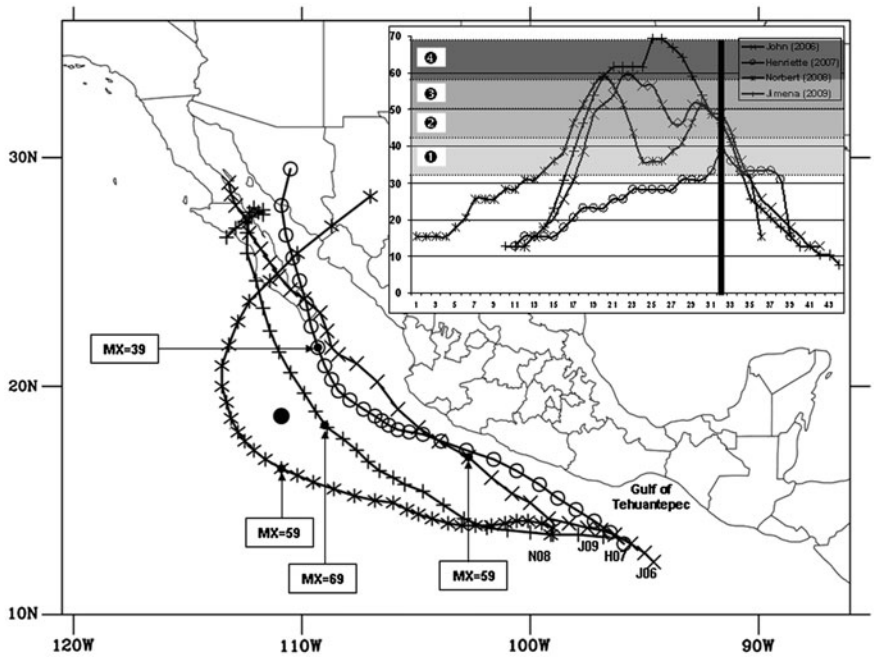

Fig. 5 Tracks of TCs making landfall in BCS. Initial positions are identified with name initial and two-digit day. MX indicates maximum intensity (m s^{-1}). Inset shows wind speeds with respect to the time of landfall (*vertical bar*) and shaded bands are hurricane categories

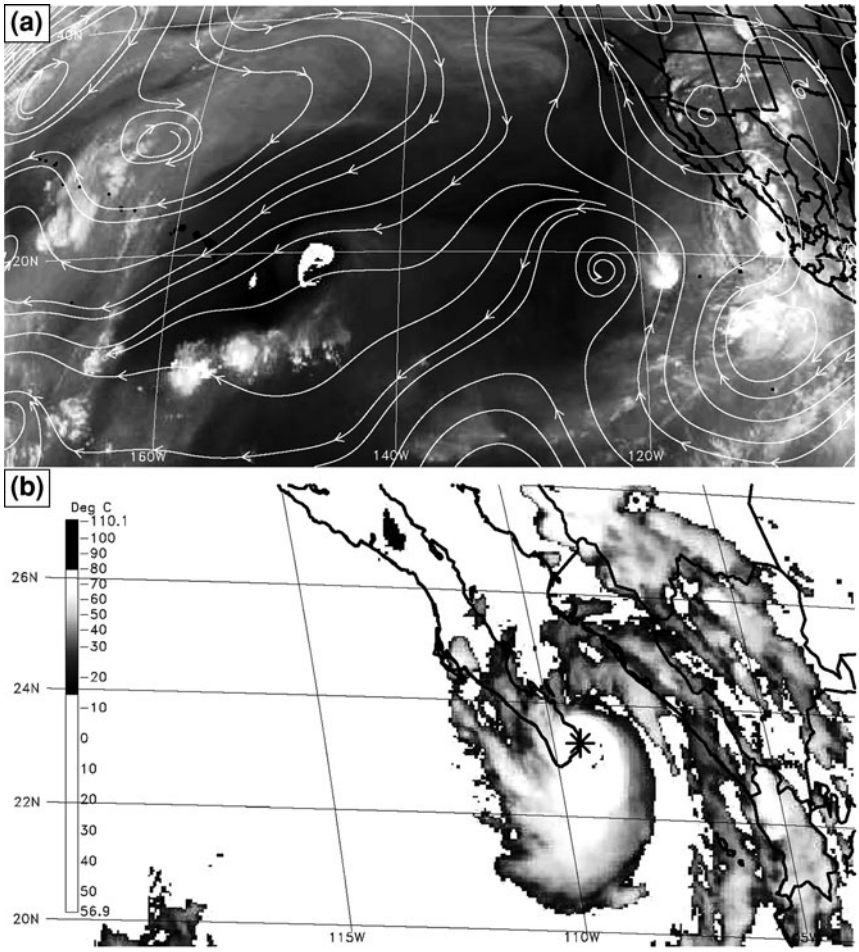

Fig. 6 Satellite imagery from the GOES-11 **a** water vapor channel at 0000 UTC September 1 and **b** infrared channel at 0000 UTC September 2, 2006. *Streamlines* are at the 3-km level. *Blackdot* is the hurricane position and *asterisk* is the landfall site

4.1 (a) John (August 28–September 4, 2006)

During the 2006 season, 18 named TCs developed and three made landfall over northwestern Mexico. In early September, John moved over BCS as a category- 2 hurricane and passed close to major population centers. The tropical depression that eventually became Hurricane John originated south of the Gulf of Tehuantepec and moved parallel to the coast.

One day prior to landfall, GOES-11 water vapor imagery (Fig. 6a) indicated a large mass of moist air east of 120°W. This type of image provides an estimate of atmospheric humidity in the 7–8 km layer, with relatively dry areas displayed in

dark tones, more humid areas in light tones, and clouds in white. Streamlines at the 3 km level indicate that the large-scale flow was controlled by the anticyclonic circulation that covered most of northern Mexico and southwestern United States. The anticyclone's western flank provided a steering current from the southeast, which is consistent with the TC displacement parallel to the Pacific Ocean coastline.

John approached the southern tip of Baja California and, at landfall, was a category-2 hurricane. Infrared imagery (Fig. 6b) showed well-defined areas of high cloud tops around the circulation center with minimum temperatures below −60°C which, in general, are above 13 km. This imagery is calibrated against blackbody temperatures between −90°C and 50°C (Menzel and Purdom 1994) to supply a measure of cloud top temperature with the coldest (highest) tops appearing in black and warmer (lower) tops in gray tones. Cumulus clouds associated with deep convection around the TC core are likely to generate heavy precipitation over localized regions.

In a composite of infrared images, the pattern of cloud tops is shown in the accompanying article by Farfán (2011, this volume). This image displays the highest cloud tops and is derived from all infrared images from September 1 to 3, when John was approaching and moving over the area of interest. Deep convection occurred around the TC core and along the southwestern coast of the peninsula; however, lower tops (> −15°C) were over the northwestern coast. Precipitation data collected by SMN rain gauges reveal lack of rainfall over this area, which is consistent with the composite image. An extraordinary contribution of 506 mm was recorded at one station in the south (23.8°N, 109.8°W) with terrain elevation close to 400 m.

4.2 (b) Henriette (August 30–September 6, 2007)

This was the only landfall event during a relatively inactive 2007. During this season, only 11 named TCs developed (Fig. 2) and the corresponding storm track shows two landfall strikes in northwestern Mexico (Fig. 5). The first strike was over the southeastern part of the peninsula as a category-1 hurricane and another hit over the mainland coast, in the State of Sonora. After initial landfall and while moving across the Gulf of California, Henriette had a relatively constant intensity and this is likely due to the relatively warm gulf below the circulation core.

While the TC was heading toward northwestern Mexico, the re-analysis fields display an anticyclonic circulation centered over the northern Gulf of Mexico (not shown). This configuration is consistent with Henriette's northward motion and enhanced humidity from the tropics (Fig. 7a). Another anticyclone was located off the northern peninsula; however, this circulation vanished just prior to the landfall event.

Figure 7b shows an infrared image at the TC landfall, in which the highest cloud tops were located at the east flank of the circulation center; its curved, spiral bands were present south of the peninsula. The first landfall was associated with heavy rainfall during a couple of days over southeastern BCS. Observations provided by the rain gauge network measured maximum accumulations

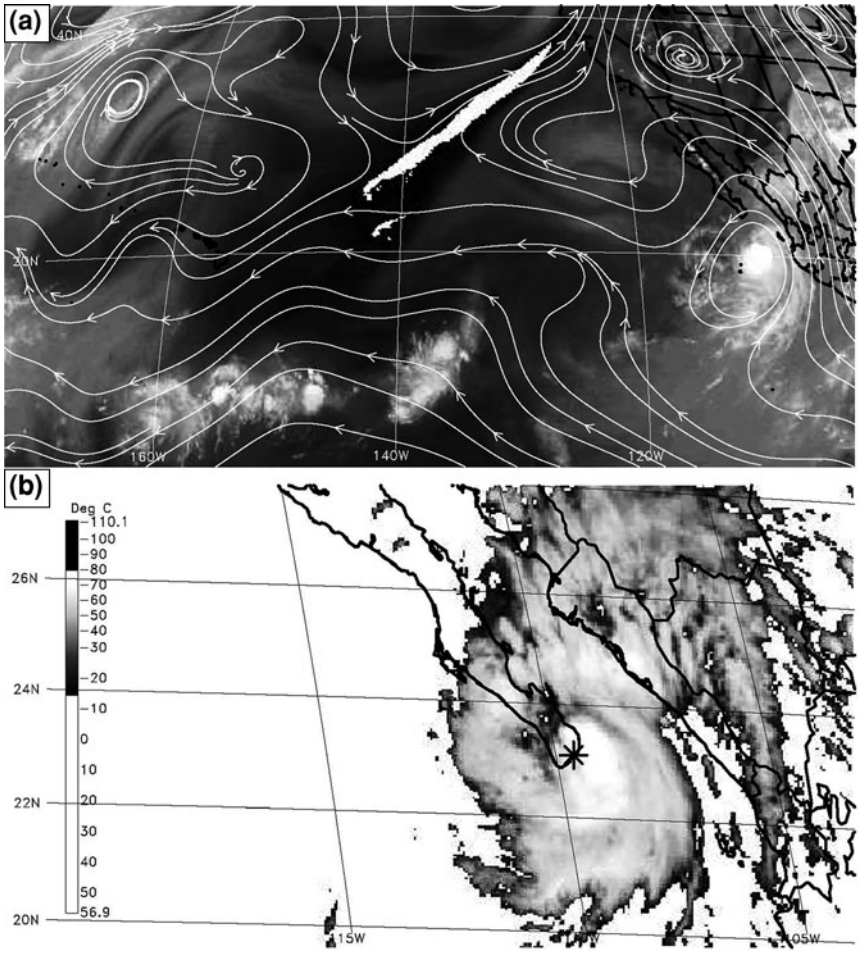

Fig. 7 Satellite imagery from GOES-11 **a** water vapor channel at 0000 UTC September 1 and **b** Infrared channel at 2100 UTC September 2, 2007. *Streamlines* are at the 3 km level. *Black dot* is the hurricane position and the *asterisk* is the landfall site

$\sim$150 mm at the coast and 545 mm over the mountains. These facts are in agreement with the composite image in which the highest cloud tops are south of 24°N and over the central gulf (Farfán 2011).

4.3 (c) Norbert (October 4–12, 2008)

There were 16 named TCs in the eastern Pacific during the 2008 season, eight of them between July and September. Most of the TCs remained at sea; three moved across Baja California; only Norbert remained strong enough to reach the

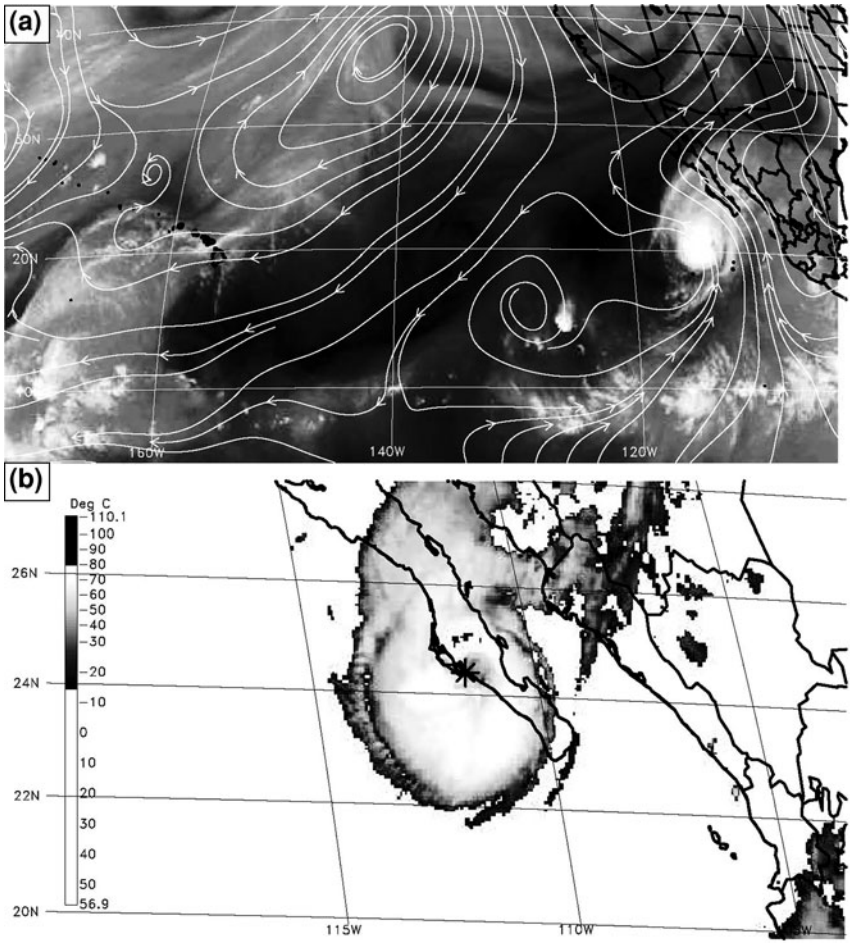

Fig. 8 Satellite imagery from GOES-11 **a** water vapor channel at 1630 UTC October 10 and **b** infrared channel at 1630 UTC October 11, 2008. *Streamlines* are at the 3 km level. *Black dot* is the hurricane position and the *asterisk* is the landfall site

mainland. Eastward deflection started at 20°N and resulted in recurvature and eventual landfall as a category-2 hurricane over the peninsula (Fig. 8b). Extensive property damage and power outages resulted from strong, sustained winds, along with flooding that affected communities around the landfall site (Blake and Pasch 2010).

Prior to landfall, the hurricane was steered by moist, southerly flow associated with an anticyclonic circulation centered over the Gulf of Mexico. A mid-latitude system associated with drier air was present over the southwestern United States (Fig. 8a); this may have influenced the recurved track of Norbert.

High cloud tops to the left of the storm core are shown in the composite of infrared images by Farfán (2011). Several rain gauge stations around the landfall

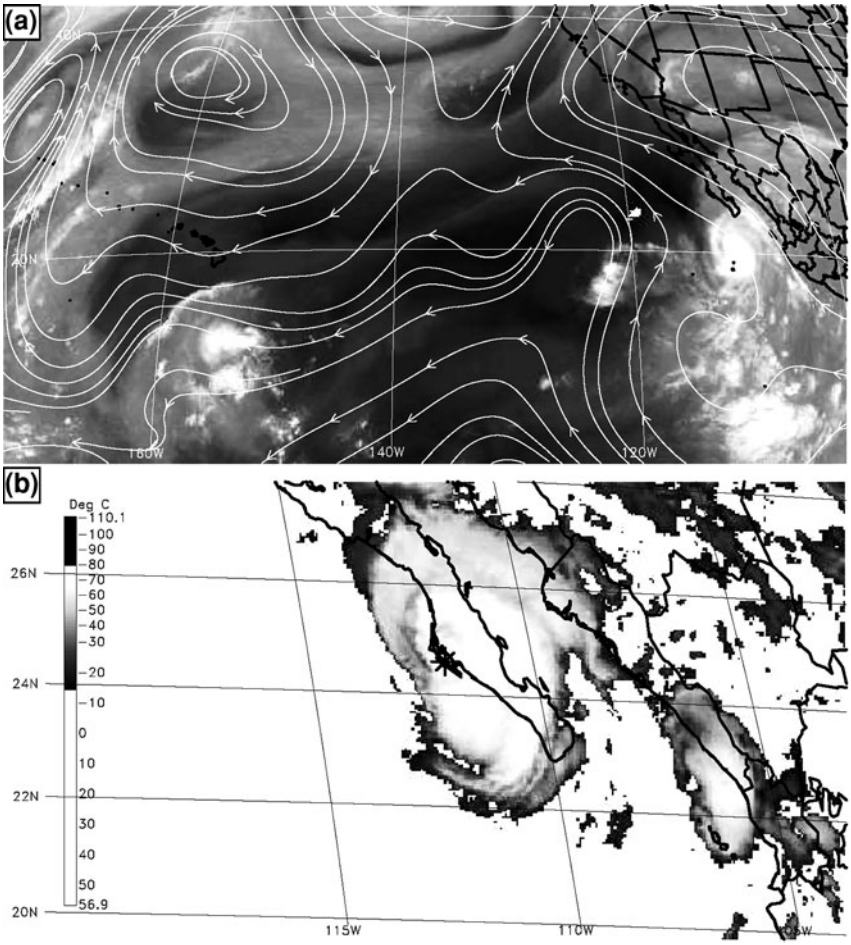

Fig. 9 Satellite imagery from the GOES-11 **a** water vapor channel at 1200 UTC September 1, 2009 and **b** Infrared channel at 1230 UTC 02 September. *Streamlines* are at the 3 km level. *Black dot* is the hurricane position and the *asterisk* is the landfall site

area reported total accumulations of 120 mm while the overall maximum was 235 mm in a site close to the gulf's shoreline (24.8°N, 111.0°W). Flooding occurred in several communities that were 50–100 km west from this site.

4.4 (d) Jimena (August 28–September 4, 2009)

The 2009 season had a late start, yet there were 17 systems, most of them developed west of Isla Socorro (dot in Fig. 5). Five TCs passed within 300 km of the coast and two made landfall in northwestern Mexico. Jimena moved across the

southern part of the peninsula when it reached category-4 strength, remaining at this intensity for more than 48 h (Fig. 5). Just prior to landfall over the western coastline, it was downgraded to a category 2 hurricane.

The storm track was controlled by a mid-level, anticyclonic circulation over northeastern Mexico with steering flow from the southeast (Fig. 9a). As in the landfall of Norbert, Jimena affected the central peninsula (Fig. 9b). The composite image displays areas of high cloud tops (Farfán 2011) between 20 and 26°N. In addition, this image shows a distinct area around 20°N where highest cloud tops were colder than −80°C; this is consistent with the maximum intensity reached near Isla Socorro. Rainfall maximum of 496 mm was collected at one station (26.9°N, 112.4°W; 496 m elevation). According to the NHC (Kimberlain and Brennan 2010), one death was related to flooding in a coastal community located 50 km east of this station.

5 Summary and Conclusion

This article summarizes characteristics of TCs that developed in the eastern Pacific Ocean during the last 40 years. Based on the NHC best-track database, the author was able to provide updated climatology on storm formation track, as well as time, frequency, and intensity at landfall. In general, results agree with previous research studies. Emphasis is given TCs that made landfall in the southern part of the Baja California Peninsula.

Four TCs were selected for further analysis: John (2006), Henriette (2007), Norbert (2008), and Jimena (2009). They moved ashore as late-season hurricanes (early September to mid-October). Strong winds and heavy rainfall affected communities in the southern peninsula and mainland Mexico. Geostationary satellite data was used to display structures of cloud tops as well as humidity patterns as part of the large-scale environment. Gridded fields were a useful tool to identify relevant features in the 3 km level flow during the approach of each event.

Since the peninsula has a coastal length covering almost one-third of the country's coastline and frequently experiences TC landfalls, the area requires special attention. The most recent landfalls justify continued studies of summer regional storms. The monitoring capabilities offered by satellite and in situ observations allow more accurate assessments of structure and motion. Therefore, for real-time observations, these are valuable tools for operational (NHC and SMN) forecasters who are responsible for providing advance warning to the populations in western Mexico.

Acknowledgments This work was carried out with the support of the Inter-American Institute for Global Change Research (IAI) CRN II #2048, which was funded by the U.S. National Science Foundation (NSF grant GEO-0452325), and support of the National Council on Science and Technology of Mexico (CONACYT grant 23448).

References

Allard RA (1984) A climatology of the characteristics of tropical cyclones in the northeast Pacific during the period 1966–1980. M.S. Thesis, Department of Geosciences, Texas Tech University. Lubbock, Texas, p 106

Blake ES, Pasch RJ (2010) Eastern North Pacific hurricane season of 2008. Mon Weather Rev 138:705–721

Corbosiero KL, Dickinson MJ, Bosart LF (2009) The contribution of eastern North Pacific tropical cyclones to the rainfall climatology of the southwest United States. Mon Weather Rev 137:2415–2435

Davis MAS, Brown GM, Leftwich P (1984) A tropical cyclone data Tape for the eastern and central North Pacific basins, 1949–1983: Contents, Limitations, and Uses NOAA Technical Memorandum NWS NHC 25

DeAngelis RM (1967) North Pacific hurricanes: timid or treacherous? Mar Wea Log 11:193–200

Farfán LM (2011) Hurricanes at landfall over the Baja California Peninsula. Experimental and theoretical advances in fluid dynamics. In: Klapp J, Cros A, Velasco O, Stern C, Rodríguez-Meza MA (eds) Proceedings of the XVI annual and Enzo Levi meetings of the fluid dynamics division of the Mexican Physical Society, Environmental Science and Engineering, Environmental Science Subseries, Springer, Heidelberg. ISBN-10: 3642179576; ISBN-13: 978-3-642-17957-0

Gunther EB (1977) Eastern Pacific tropical cyclones of 1976. Mon Weather Rev 105:508–522

Kalnay E, Kanamitsu M, Kistler R, Collins W, Deaven D, Gandin L, Iredell M, Saha S, White G, Woollen J, Zhu Y, Leetmaa A, Reynolds R, Chelliah M, Ebisuzaki W, Higgins W, Janowiak J, Mo KC, Ropelewski C, Wang J, Jenne R, Joseph D (1996) The NCEP/NCAR 40-year reanalysis project. Bull Am Meteor Soc 77:437–471

Kimberlain TB, Brennan MJ (2010) The 2009 eastern North Pacific hurricane season: a return to normal activity. Weatherwise May/June 2010:50–58

McBride JL (1995) Tropical cyclone formation, global perspectives on tropical cyclones. Elsberry RL (ed) World Meteorological Organization, Geneva, Switzerland, pp 106–197

Menzel WP, Purdom JFW (1994) Introducing GOES-I: the first of a new generation of geostationary operational environmental satellites. Bull Am Meteor Soc 75:757–781

Rappaport EN, Franklin JL, Avila LA, Baig SR, Beven JL, Blake ES, Burr CA, Jiing JG, Juckins CA, Knabb RD, Landsea CW, Mainelli M, Mayfield M, McAdie CJ, Pasch RJ, Sisko C, Stewart SR, Tribble AN (2009) Advances and challenges at the National Hurricane Center. Weather Forecast 24:395–419

Renard RJ, Bowman WN (1976) The climatology and forecasting of eastern North Pacific Ocean tropical cyclones, NEPRF Technical paper 7–76, p 79

Rosendal HE (1962) Eastern North Pacific tropical cyclones, 1947–1961. Mar Wea Log 6:195–201

Rosengaus M, Jiménez M, Vázquez MT (2002) Atlas climatológico de ciclones tropicales en Mexico, Centro Nacional de Prevención de Desastres, p 106. ISBN 970-628-633-0

Serra S (1971) Hurricanes and tropical storms of the west coast of Mexico. Mon Wea Rev 99:302–308

Simpson R (2003) Communicating damage potentials and minimizing hurricane damage. In: Simpson R (ed) Hurricane! Coping with disaster. AGU Publications, Washington, D.C., pp 249–891

Challenges of Mexico to Face Climate Change

Tereza Cavazos

Abstract This article discusses some of the challenges that Mexico is facing on climate change issues. Mexico's leadership on the United Nations Framework Convention on Climate Change (UNFCCC) and Conference of the Parties 16 (COP16) celebrated in Cancun, Mexico on December 2010 was a real challenge. In spite of the low expectations of this climate summit, a multilateral agreement was signed by the Parties. The major outcomes of the Cancun Agreement are described here. Funding derived from this agreement is expected to flow (hopefully) soon to underdeveloped countries to support mitigation and adaptation strategies. However, even if Mexico receives international funding through the Cancun Agreement, there are some major challenges that need to be resolved: (1) to understand the causes and impacts of climate change at regional scale and in different sectors, (2) to be able to identify adequate and feasible adaptation and mitigation strategies to build a more resilient country, and (3) to the have the financial support and the political will to implement them at regional scale by order of social importance.

1 Introduction

The recent global warming and associated climate change have emerged as great challenges for modern society for their sudden appearance in the life of our planet. Earth's climate has continuously oscillated from glacial to warm periods due to

T. Cavazos (✉)
Departamento de Oceanografía Física, Centro de Investigación Científica y de Educación Superior de Ensenada. Ensenada, Baja California, Mexico
e-mail: tcavazos@cicese.mx

J. Klapp et al. (eds.), *Experimental and Theoretical Advances in Fluid Dynamics*, Environmental Science and Engineering, DOI: 10.1007/978-3-642-17958-7_10,

natural external forcings, such as volcanic activity, plate tectonics, and the orbital cycles (or Milankovich cycles 1920) of the Earth's movements that modulate the amount of incoming solar radiation on time scales of thousands of years. The Fourth Assessment Report of the Intergovernmental Panel on Climate Change (AR4; IPCC 2007) shows that in the last 100–150 years there has been a rapid and unprecedented increase in the concentration of greenhouse gases (GHG) such as carbon dioxide (CO_2), methane (CH_4), and nitrous oxide (N_2O), that has resulted in a global temperature increase of approximately 0.7°C; the current mean global surface temperature is approximately 15.2°C (Keenlyside et al. 2008). The Earth's climate is very sensitive to small variations in the global temperature; for example at the end of the Renaissance, during 1600–1650 there was a decrease in the number of sunspots and more frequent volcanic eruptions, which resulted in less incoming solar radiation and a decrease of few tenths of degree in the global temperature; this period is known as the *Little Ice Age*. In contrast, at the end of the twentieth century we have seen a sudden increase in global temperature that is not due to natural variations of the incoming solar radiation. The IPCC (2007) report shows scientific evidence from global circulation models (GCMs) and observations that attribute the increase of GHG and current global warming mainly to anthropogenic causes, such as economic development, rapid population growth, and land-use change. The Earth's atmosphere has a particular composition of gases; it is the only planet in our Solar System that has an air with the right combination of GHG that allows the life as we know it. These gases absorb outgoing longwave radiation, the radiation that is emitted by the Earth's surface. This process is known as greenhouse effect. Without the natural greenhouse effect, the global temperature would be −17°C. However, increasing too much the concentration of such gases in the atmosphere could be also lethal for some ecosystems. For example, ocean acidification is produced by an increased uptake of atmospheric CO_2. In the past 200 years the oceans have absorbed approximately half of the CO_2 produced by fossil fuel burning and cement production (Raven et al. 2005). Ridgwell and Schmidt (2010) show that the current rate of ocean acidification is ten times the rate that preceded the mass extinction 55 million years ago. It seems that the present rate of acidification could potentially endanger calcifying organisms, challenge the ability of plankton to adapt (Ridgwell and Schmidt 2010) and therefore, threaten the marine food chain. Since Mexico has an extensive coastline and a vast marine territory, several scientific institutions are collaborating towards the understanding of the carbon cycle in marine ecosystems (Hernandez and Gaxiola 2007).

Petit et al. (1999) in a study of atmospheric CO_2 and CH_4 concentrations from the Vostok ice core, Antarctica, found that present-day atmospheric increase of these two GHG seem to have been unprecedented during the past 420,000 years. In this long term period the CO_2 concentrations varied from 180 ppm (during glacial periods) to 300 ppm (during warm periods), while in the last 150 years the CO_2 concentrations increased from 300 to 385 ppm! The increased levels of GHG in the atmosphere are also partially responsible for the observed warming of the

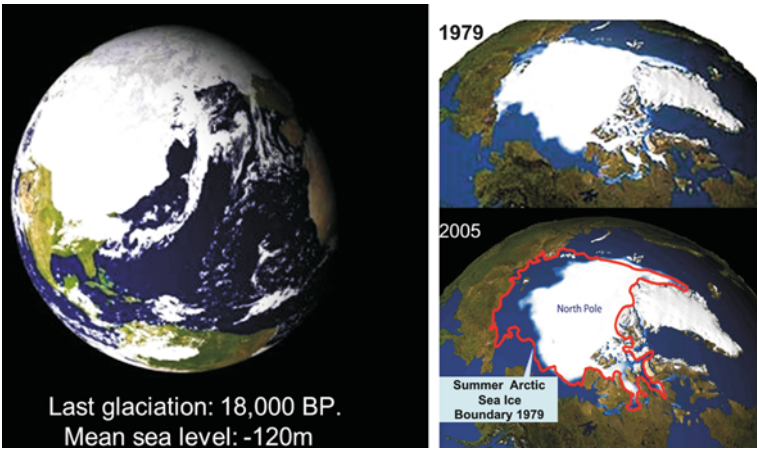

Fig. 1 *Left*: Possible ice sheet extension during the last glacial maximum 18,000 year BP. *Right*: North Pole satellite pictures from NASA for the summers of 1979 and 2005. (*Left* figure is from http://www.johnstonsarchive.net/spaceart/art-e.html)

oceans and the global sea level rise during the second half of the twentieth century (IPCC 2007).

At the end of the last glaciation, 18,000 year. BP, when the surface temperature in Antarctica was 16°C cooler than today and the CO_2 concentrations were 180 ppm (Petit et al. 1999), the sea level was about 120 m below the current mean sea level. Figure 1 shows the possible extension of the ice sheets 18,000 years BP and, as a comparison, the observed North Pole glaciers from NOAA satellite pictures for the summers of 1979 and 2005. Considering the mass of water in major ice sheets, melting of the entire Greenland ice sheet would raise sea level by approximately 7.3 m and that of Antarctic would raise sea level by approximately 56.6 m (e.g., Landerer et al. 2007; see Wallace and Hobbs 2006, p. 39 for the calculations). This is a very extreme scenario, but possible in the Earth's history; for this reason there is a genuine preoccupation around the world from scientists to politicians, and from media to social networks to understand what is happening and what could happen in the near future. Knowledge of the possible causes and impacts is fundamental to be able to take responsible actions.

A study of sea level in several cities located on the Mexican coasts (INE 2008) shows that in the 1953–2003 period sea level rose from 1.13 mm/year in Salina Cruz, Oaxaca in southern Mexico to 9.16 mm/year in Cd. Madero, Tamaulipas in the northern Gulf of Mexico. An independent work shows increases of 2 mm/year in several locations of Baja California (Ortiz and Navarro 2008). The climate change scenarios for the twenty first century warn of the great impact that sea level rise could have on the socio-ecosystems of the Mexican coasts, especially along the Gulf of Mexico and the Caribbean (INE 2008). Moreover, several studies (Allen and Ingram 2002; Kharin and Zwiers 2005; IPCC 2007) show that the impact of climate change will be felt most strongly through increases in the number of weather and climate

extremes rather than changes in mean values. Thus, it is expected that Mexico will be also affected by a larger number of heavy precipitation events (i.e. more intense hurricanes), more intense heat waves (Tejeda-Martínez et al. 2008), and more droughts especially in northern Mexico (CICC 2010). Some of these events have been already documented for several parts of the country (e.g. Arriaga-Ramirez and Cavazos 2010; Tejeda-Martínez et al. 2010).

The actions that Mexico needs to develop to reduce its vulnerability to the impacts of climate change are explained in Sect. 3 in the context of the international agenda on climate change. Thus, a brief background of the United Nations Framework Convention on Climate Change (UNFCCC) is presented first in the next section, as well as the major outcomes of the Cancun Agreement in the Conference of the Parties 16 (COP16). Section 3 describes the Mexican public policy on climate change and discusses some of the climate change challenges that Mexico's government, academia, and Mexican society in general need to face and resolve to build a more resilient country.

2 The International Agenda on Climate Change

2.1 The UNFCCC

Basic scientific knowledge and assessments that discuss the possible causes, impacts, and uncertainties of climate change, such as the Intergovernmental Panel on Climate Change (IPCC) reports, have served as a reference for international climate change negotiations between developed and underdeveloped countries. The UNFCCC (UN 1992) was created in the Earth Summit of Rio de Janeiro in 1992. The conference established commitments for developed (Annex I Parties) and developing (non-Annex I Parties) countries to produce periodical inventories of GHG emissions with the objective to return individually or collectively to the emissions of 1990 (∼350 ppm global emissions). An update of the Rio de Janeiro agreements occurred in the Third Conference of the Parties (COP3) of the UNFCCC in 1997, which resulted in what is known as the Kyoto Protocol. The Protocol, among other things, confirmed the obligations of the Annex I Parties to reduce their emissions by 5% relative to 1990 levels in the period of 2008–2012. However, the non-Annex I country Parties, like the G5 (Mexico, China, South Africa, Brazil, and India), are not obliged to reduce their emissions under the Kyoto Protocol. The Protocol was officially confirmed in 2005 in the COP11 in Montreal, when 55% of the Parties had ratified it. As of 2011, the United States has not ratified the Protocol yet. Figure 2 shows the per capita emissions of GHG (CO_2-equivalent) by country in 2009.

In the 1990–2006 period Mexico contributed 709 Mton CO_2-eq/year or 7.1 ton CO_2-eq/capita/year, 40% above the 1990 levels. The energy sector alone

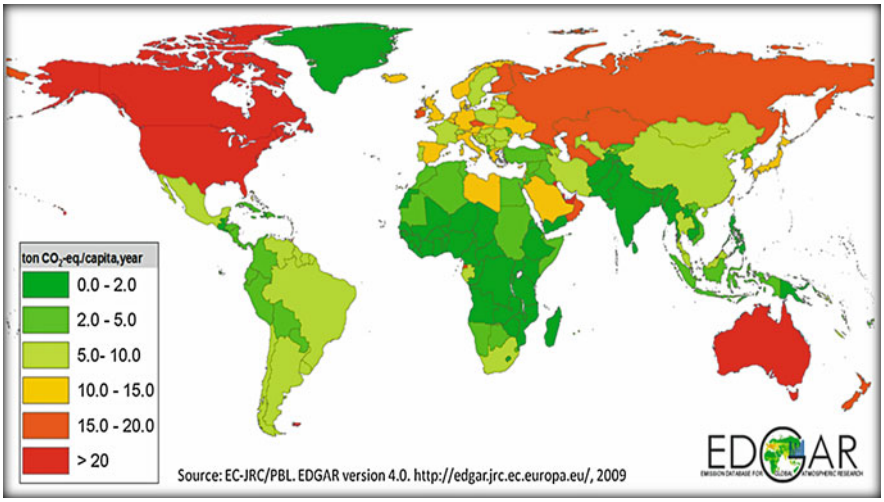

Fig. 2 Per capita emissions of CO_2-eq in 2009 (ton/year). The countries with emissions greater than ten ton CO_2-eq/year are part of the UNFCCC Annex I Parties. Source: http://edgar.jrc.ec.europa.eu/

(production of energy and transport) contributed 60.7% to the total GHG emissions in Mexico (CICC 2010).

2.2 The COP16 and the Cancun Agreement

The COP15 in Copenhagen in 2009 failed to produce a consensual agreement because the climate change agenda was too ambitious, and also because the President of the Convention (the Denmark minister) was unable to mediate the enormous differences among all the Parties (192 countries). The result was a non-binding Copenhagen Accord, which was not compulsory to the Parties of the Convention, but provided the basis for the discussions in the COP16. Based on the Copenhagen experience, there were very low expectations for the results of the COP16 in Cancun, Mexico in 2010. The very influential Lula Da Silva, then President of Brazil, decided not to attend the summit because he doubted of any significant results (Otero 2010). In my view, Lula's negative criticism published at the middle of the negotiations motivated the leaders of the COP16 to work out some of the Parties differences and to reach consensus on at at least few issues.

The agenda of the COP16 was less ambitious, but more realistic than that of the COP15. As president of the summit, one of Mexico's objectives was to restore the confidence on the negotiations. In order to have some success, one topic that was left aside from the discussions, because it produced great divisions in Copenhagen, was the future of the Kyoto Protocol after 2012. The strategic reason to keep it

aside was that the United States, one of the top two emitters of the world, has not signed the protocol yet, and China, the other top emitter, is not obliged to reduce their emissions under the Kyoto Protocol for being an underdeveloped country. According to Japan, it is necessary to create a new and more inclusive mechanism (or protocol) with commitments and responsibilities from all countries.

The topics that were expected to be discussed in Cancun were the 5 lines of the Bali Action Plan, which were also discussed in the COP15:

- Mitigation: To define goals of reduction of emissions from deforestation and forest degradation, what is known as REDD+
- Financial support: To define mechanisms and commitments for long term support from the Annex-I to non-Annex I Parties
- Adaptation: To define financial support for climate action plans and regional scale projects
- Technology transfer: To transfer clean technologies and capacity building
- Long term vision: To advance in the negotiations to define collective goals to reduce emissions to avoid increases of temperature greater than 2°C in the near future.

After two weeks of discussions the international negotiators arrived to a multilateral Cancun Agreement that covers four of the five major topics of the agenda. The long term vision, as well as the future of the Kyoto Protocol, was postponed until the negotiations of the COP17 that will take place in Durban, South Africa in December 2011. The Cancun Agreement was signed by all parties (192 countries) including Japan, the United States, and China that initially had large differences. The only country that did not sign the agreement was Bolivia, which wanted concrete discussions about the future of the Kyoto Protocol. The four major accords of the Cancun Agreement are:

- *Deforestation Accord*: its objectives are to establish a financial framework and to reinforce bilateral and multilateral efforts for forest protection and prevent clear-cutting. The framework would allow developed countries to finance others for reducing emissions from deforestation and degradation (REDD+). The agreement requires developing countries to create national climate change action plans, establish a baseline for historic emissions from forest loss and create a system for monitoring their forest (Tollefson 2010).
- *Green Climate Fund*: This fund was proposed by Mexico in Copenhagen; it was rescued in the COP16 and accepted by the Parties. This fund will be managed by developed and underdeveloped countries to support adaptation and mitigation strategies.
- *Cancun Adaptation Framework*: This framework is a guide for the decisions to support adaptation strategies in underdeveloped countries. The Convention established an Adaptation Committee to provide coherence in the implementation of the adaptation plans, to provide advice on financial mechanisms and elgibility for the new fund, to carry out reviews of portfolios of adaptation projects, and to facilitate the full implementation of these programs in

underdeveloped countries (AWGLCA 2010). The Global Environmental Facility (GEF) will act as interim ministry of the Adaptation Fund Board and the World Bank will act as the interim trustee for the Adaptation Fund and the Adaptation Fund Board (COP16 2010a, 2010b).

- *Technology Transfer*: To support developing countries with clean energies, green technologies and capacity building.

The Convention reached historic agreements on forest protection, and adaptation and technology frameworks to help the developing countries adopt clean energy and to adapt to climate change. The Cancun Agreement, as the Copenhagen Accord, recognized the gravity of global warming and set a goal of limiting average warming to 2°C above preindustrial levels, and pledged to periodically review the goal on the basis of the best available scientific knowledge, such as the IPCC reports. The agreement stated that in future negotiations it should be considered a lower limit of 1.5°C, as small insular countries of the Pacific requested due to their great vulnerability to sea-level rise.

The Ad-Hoc Working Group on Long-term Cooperative Action under the Convention (AWG-LCA) stated that in order to limit global warming to 2°C, Parties should take urgent action to reduce their emissions, but unfortunately there was not a concrete agreement on how to implement this urgent action immediately. The UN Climate Change Secretariat said that "existing pledges for curbs on greenhouse gas emissions are only 60% of those needed to limit a rise in temperatures to below 2°C" (Reuters 2010). Current pledges still puts us on a warming trajectory of about 3.2°C above pre-industrial levels by 2100 and a CO_2 concentration of about 650 ppm (Chen et al. 2011). The failure to resolve the central problem of emissions dismayed environmental groups (Doyle and Wynn 2010).

However, an important resolution of the Cancun Agreement was that both developed and developing countries will have common, but differentiated commitments and responsibilities and will act to reduce GHG emissions. These actions will be registered through a system of monitoring, report, and international verification (MRV). Parties agreed to reduce emissions according to their own capabilities while new international reporting system tracks their progress.

Another milestone was that both China and the United States were able to agree on some basic requirements for the MRV climate pledges. MRV is currently carried out through two processes: National Inventories and and National Communications. Under the Kyoto Protocol countries are required to submit standardized MRV reports based on IPCC measurement criteria; in particular, developing countries will need to carry out the MRV to be able to request and to receive financial support through the four major Cancun accords. It was agreed that a total of US$30 billion in fast start finance from developed countries will be available to support climate action in the developing world up to 2012, and the intention to raise US$100 billion in long term fund by 2020. The resolutions signed in the Cancun Agreement made significant progress from COP15 in Copenhagen and will be the basis to continue the negotiations this year in South Africa.

The AWG-LAC of the COP16 recognized that addressing climate change requires a paradigm shift towards building a low-carbon society based on innovative technologies, sustainable development, and green jobs. In this respect, climate analyst David Kroodsma (2010) interviewed Lord Nicholas Stern at the COP16. Stern said that the new paradigm should be based on investement and innovations "when the electric light came in, the whalers and the candle makers had to adjust." We shouldn't try to save the jobs of the old economy; we should instead celebrate innovative solutions (Kroodsma 2010). A clean energy revolution is a major scientific and technological challenge of the twenty first century that need to be pursued by both developed and developing countries.

3 Challenges of Mexico in Climate Change Issues

3.1 Mexican Public Policy on Climate Change

Mexico as part of the G5 countries has been very active in the international negotiations of climate change. In 2005, the Mexican government created the Inter-Secretariat Council on Climate Change (CICC) as the federal organism responsible to formulate and implement public policy and transversal strategies for the mitigation and adaptation to climate change. The Secretariat of Environment and Natural Resources (SEMARNAT) through the National Institute of Ecology (INE) has coordinated these actions; INE is also the focal point of connection with the IPCC. The CICC has published four National Communications of Mexico to the UNFCCC that report the progress in climate change made by the country. The fourth National Communication was published in 2010 (CICC 2010); it includes the latest GHG inventory, some observed changes in different sectors (which may or may not be associated to climate change), the progress of the State Climate Change Action Plans (PEACCs), and the programs and institutions responsible to implement different mitigation and adaptation strategies in Mexico.

The National Development Program (2007–2012) is the first to address public policy on climate change. The Environmental Sustainability axis includes the National Strategy on Climate Change (2007), the Special Program of Climate Change (2009–2012), and the PEACCs at the lower end.

At the state level, some State Development Programs have begun to include similar policies in the environmental sustainability axis, thus supporting projects and programs on sustainability and climate change. An example is the Government of Baja California that in 2008 had the initiative to financially support the development of the Baja California PEACC (http://peac-bc.cicese.mx). Of the 32 states and a Federal District in Mexico, only the governments of Baja California and Mexico City have financially supported the development of their PEACCs. In 2010, 15 states received sectoral support from SEMARNAT-CONACYT to continue or to begin their PEACCs.

The sustainable development theory offers a conceptual framework that includes the economic, environmental, and social components that could be used in integrated assessments of climate change, such as those supposed to be carried out by the PEACCs. According to the Brundtland Report (UN 1987) sustainability means meeting the needs of the present without compromising the ability of future generations to meet their own needs. Thus, a sustainable development plan is a process that local governments can follow to improve social equity and environmental and economic conditions.

Integrated assessments of climate change, such as those of the PEACCs, are based on the UN framework on Climate Change, whose premise or hypothesis is that socio-economic development, land degradation, and population growth are the main causes of the increase of GHGs and global warming. Therefore, it is necessary to (1) mitigate (decrease) the GHGs, (2) understand the environmental changes, and (3) adapt to the new conditions through different strategies. This framework is in fact derived from the ideas proposed in the Brundtland Report, but it is more simplistic that the sustainable development framework.

3.2 The Challenges

As mentioned in Sect. 2.2, the Cancun Agreement will be a mean to eventually receive international funding toward the implementation of mitigation and adaptation actions and technological innovations in Mexico and other developing countries. Even if Mexico receives some international funding (which may not be enough and may not reach the state level), there are some major challenges that need to be resolved (among others):

- To understand the causes and impacts of climate change at regional scale and in different sectors
- To be able to identify adequate and feasible mitigation and adaptation strategies to build a more resilient country, and
- To have the financial support and the political will to implement the strategies at regional scale by order of social importance.

The first challenge "To understand the causes and impacts of climate change at regional scale and in different sectors" needs to be addressed by the scientific community (that leads the PEACCs for example). It is important to have a strong connection with local stakeholders and users in different sectors to better understand the impacts of climate change and to devise possible lines of action at regional scale. This is an interdisciplinary work that requires capacity building and large financial support from state and federal funds, which some may come from international sources. Moreover, not all states have a scientific community to develop the diagnostic analyses and climate change scenarios or the knowledge to transfer that information to different sectors and to society. Therefore, this challenge should consider the improvement and support of education at different levels

(through workshops, training, and new educational programs). It should also reinforce continuous climate monitoring and the creation of a national environmental monitoring network to support the diagnostic and modeling studies that will help understanding the processes associated with the observed changes, as well as in the development of preventive actions.

The second challenge is "To be able to identify adequate and feasible mitigation and adaptation strategies to build a more resilient country". Having a considerable advance in the first challenge would serve as the basis to prioritize the adaptation actions according to vulnerability studies and local needs, and to identify possible technological opportunities to develop mitigation actions. The planning process to determine the list of priority actions at regional scale requires a strong communication among the scientific community, the stakeholders/private sector, and the government institutions (the decision makers) that eventually may implement the actions.

The last challenge "To the have the financial support and the political will to implement the mitigation and adaptation strategies at regional scale by order of social importance" is the most difficult of all. Adaptation is a challenge by itself for two reasons: (1) in contrast to mitigation that can be tracked by the evolution of quantifiable metrics, adaptation is a subjective process and (2) adequate adaptation planning to reduce the vulnerability of the socio-ecosystems requires a long-term vision (cost-benefit) that transcends the usual temporality of the programs and governments. The scientific and sectoral communities may do their jobs in the first two challenges, but if there is not a continuity from one government to the next, and if there is not the political will to carry out the strategies, nothing will be done. Therefore, it is advisable to have a strong connection with the local government during the whole evolution of the integrated climate assessments (i.e. PEACCs) in order to have some influence during the last stage of the process, which includes the development and implementation of long-term public policy to benefit society and the ecosystems. The interaction with social networks should be also pursued at all stages for their role on informal education and the decision making process.

Acknowledgments I appreciate very much the comments and suggestions of a reviewer, which help improve the manuscript.

References

Allen MR, Ingram WJ (2002) Constraints on future changes in climate and the hydrologic cycle. Nature 419:224–232. doi:10.1038/nature01092

Arriaga-Ramirez S, Cavazos T (2010) Regional trends of daily precipitation indices in northwest Mexico and southwest United States. J Geophys Res 115:D14111. doi:10.1029/2009JD013248

AWGLCA (2010) Enhanced action on adaptation, Ad Hoc Working Group on long-term Cooperative Action under the Convention, Revision of FCCC/AWGLCA/2010/14, Chapter II

Chen C, Hare B, Hagemann M, Höhne N, Moltmann S, Schaeffer M (2011) Cancun climate talks—Keeping options open to close the gap, Climate action tracker, 10 Jan 2011. http://www.climateactiontracker.org

CICC (2010) México, Cuarta Comunicación Nacional ante la Convención Marco de las Naciones Unidas sobre el Cambio Climático, Consejo Intersecretarial de Cambio Climático, SEMARNAT, México, p 274

COP16 (2010a) Financial mechanisms of the convention: fourth review of the financial mechanism, Draft decision -/CP.16. UNFCCC, available online: 20101204_cop16_fm.pdf

COP16 (2010b) Review of the adaptation fund. Draft decision -/CMP.6. UNFCCC, available online: 20101204_cop16_cmp_review_afb.pdf

Doyle A and Wynn G (2010) Climate talks end with modest steps but no Kyoto deal, Reuters, Cancun, 11 Dec 2010

Hernández B, Gaxiola G (eds) (2007) Carbono en ecosistemas acuáticos en México. Instituto Nacional de Ecología, México, p 510

INE (2008) Evaluación regional de la vulnerabilidad actual y futura de la zona costera mexicana y los deltas más impactados ante el incremento del nivel del mar debido al calentamiento global y fenómenos hidrometeorológicos extremos. Vázquez BA (ed), Instituto de Ciencias del Mar y Limnología, UNAM, Instituto Nacional de Ecología, p 330. http://www.ine.gob.mx

Intergovernmental Panel on Climate Change (IPCC) (2007) Climate change 2007, synthesis report, contribution of the working groups I, II, and III to the fourth assessment report of the intergovernmental panel on climate change, Pachauri RK and Reisinger A (eds), IPCC, Geneva, Switzerland

Keenlyside NS, Latif M, Jungclaus JH, Kornblueh L, Roeckner E (2008) Advancing decadal-scale climate prediction in the North Atlantic sector. Nature 453:84–88. doi:10.1038/nature06921 (1 May 2008)

Kharin VV, Zwiers FW (2005) Estimating extremes in transient climate change simulations. J Clim 18:1156–1173. doi:10.1175/JCLI3320.1

Kroodsma D (2010) Lord Stern: not a singing and dancing agreement, but progress, Huffington Post, 15 Dec 2010

Landerer FW, Jungclaus JH, Marotzke J (2007) Regional dynamic and steric sea level change in response to the IPCC-A1B scenario. J Phys Oceanogr 37(2):296–312

Milankovitch M (1920) Théorie Mathématique de phénomenès thermiques produits par la radiation solaire, Gauthiers-Volars, Paris

Ortiz M, González JI (2008) El nivel del mar como indicador del cambio climático global: historia, tendencias regionales y perspectivas en México. In: Martínez PF, Aguilar A (eds) Efectos del cambio climático en los recursos hídricos en México. IMTA, México, pp 59–72

Otero S (2010) La COP16 terminará sin nada: Lula da Silva, El Universal, 2 dic 2010, México. http://www.eluniversal.com.mx/nacion/182207.html

Petit JR, Jouzel J, Raynaud D, Barkov NI, Barnola J-M, Basile I, Bender M, Chappellaz J, Davis M, Delaygue G, Delmotte M, Kotlyakov VM, Legrand M, Lipenkov VY, Lorius C, PÉpin L, Ritz C, Saltzman C, Stievenard M (1999) Climate and atmospheric history of the past 420,000 years from the Vostok ice core, Antarctica. Nature 399:429–436. doi:10.1038/20859

Raven J, Caldeira K, Elderfield H, Hoegh-Guldberg O, Liss P, Riebesell U, Shepherd J, Turley C, Watson A (2005) Ocean acidification due to increasing atmospheric carbon dioxide. The Royal Society, London, p 68. http://www.royalsoc.ac.uk

Reuters (2010) U.N. urges more climate cuts to match Cancun pledges, Oslo, 20 Dec 2010. http://af.reuters.com/article/worldNews/idAFTRE6BJ30820101220

Ridgwell A, Schmidt DN (2010) Past constraints on the vulnerability of marine calcifers to massive carbón dioxide release. Nature Geos 3:196–200. doi:10.1038/ngeo755

Tejeda-Martínez A, Conde-Álvarez C, Valencia-Treviso LE (2008) Climate change scenarios of extreme temperature and atmospheric humidity. Atmosfera 21(4):357–372

Tejeda-Martínez A, Castillo NI, Garcia-Cueto RO (2010) Impactos urbanos: ondas de calor en tres ciudades de Mexico. En: México ante el Cambio Climatico: Evidencias, Impactos, Vulnerabilidad y Adaptacion, MJ Cardenas (ed), Greenpeace, Mexico, p 72

Tollefson J (2010) Last-minute climate deal saves climate talks. Nature 468:875–876. doi:10.1038/468875a, 13 Dec 2010

UN (1987) Our common future, Report of the world commission on environment and development, Annex to UN General Assembly document A/42/427, 11 Dec 1987
UN (1992) United nations framework convention on climate change (UNFCCC), FCCC/INFORMAL/84, Rio de Janeiro
Wallace JM, Hobbs PV (2006) Atmospheric science: an introductory survey, 2nd edn. Elsevier, Amsterdam, p 483

Part II
Geophysics and Astrophysics

Vorticity and Internal Waves in the Campeche Canyon, Gulf of Mexico

Tania Santiago Arce and David Alberto Salas de León

Abstract The hydrographic and hydrodynamic structure of the Campeche Canyon (Southern Gulf of Mexico), was studied using oceanographic data obtained from PROMEBIO 3 on board of the R/V Justo Sierra of the UNAM. The sampling was performed during 24 days, in spring 2000. The hydrographic analysis was based on temperature, conductivity and pressure data obtained with a CTD profiler. Current speeds were recorder with a 75 kHz Acoustic Doppler Current Profiler (ADCP). The vertical velocity component (w) and the vertical component of the vorticity (ς_z) were calculated using the horizontal velocity field registered by the ADCP. An objective analysis was applied to obtain homogeneous fields of hydrodynamic parameters such as currents, vorticity, and the Froude and Rossby numbers. Results shows horizontal speeds of the order of 3×10^{-1} ms^{-1}; positive vorticity to the Southwest of the study area and negative vorticity toward the Western side of the domain with a magnitude of the order of 10^{-6} s^{-1}. An upward and downward flow pattern was observed over the canyon in agreement with the positive and negative vorticity values, at different deeps. Finally, the Froude number with values below one indicated the existence of internal waves and a hydraulic jump within the Campeche Canyon.

T. Santiago Arce (✉)
Posgrado en Ciencias del Mar y Limnología, UNAM, Avenida Universidad 3000, Circuito exterior s/n, Ciudad Universitaria, 04510 México City, D.F., México
e-mail: arcesant@gmail.com

D. A. Salas de León
Instituto de Ciencias del Mar y Limnología, UNAM, Avenida Universidad 3000, Circuito exterior s/n, Ciudad Universitaria, 04510 México City, D.F., México
e-mail: dsalas@servidor.unam.mx

J. Klapp et al. (eds.), *Experimental and Theoretical Advances in Fluid Dynamics*, Environmental Science and Engineering, DOI: 10.1007/978-3-642-17958-7_11,

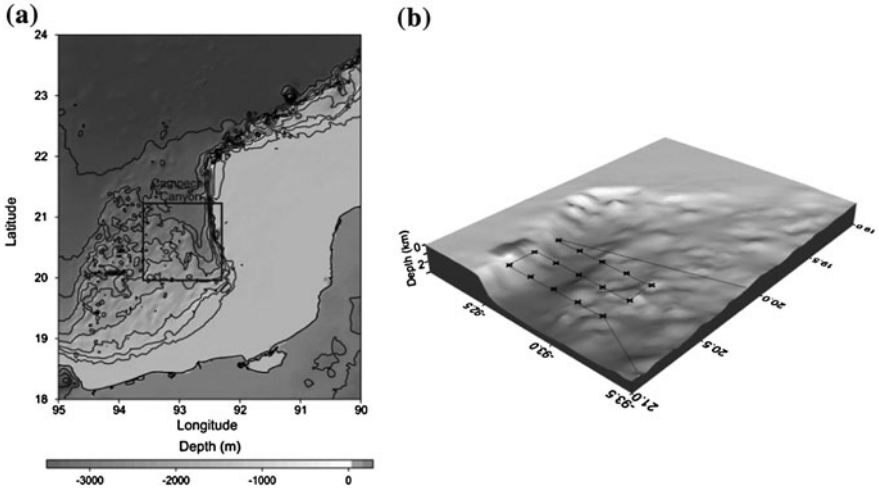

Fig. 1 **a** Geographical location of the study area, **b** *upper view* of the Campeche Canyon with bathymetry (km) and (*dots*) CTD stations, the *line* is the trajectory ship

1 Introduction

Vorticity is a physical quantity widely used to characterize fluid rotation. In the ocean sciences this type of study is important because it is associated with the presence of upward and downward flows, which are of interest in oceanography because they transport energy, momentum, salt and chemicals, like oxygen, suspended sediments, and nutrients (Cruz Gómez et al. 2008). When an ocean current passes over a submarine canyon, it tends to form eddies (Klinck 1996) due to vorticity conservation effect; however, the direct analysis of this property in the study of flows in submarine canyons is not currently described, instead an indirect analysis is used for the field of relative movements. To apply this analysis to the vertical component of the movement may not be very accurate since it is very small, leaving the vertical movements inferred by the horizontal distributions of the different hydrographic parameters such as the temperature, salinity and density. It is known that when the flow passes over the submarine canyon it may generate cyclonic and anticyclonic eddies, upwelling and flow convergence, and internal waves (Klinck 1996); for this reason it is important to study canyon dynamics.

2 Study Area

The Campeche Canyon is located between 20° 12′ N and 21° 36′ N, and 92° 24′ W and 93° 24′ W, in the Southern Gulf of México (Fig. 1a), at the western side of the Yucatan peninsula. With a maximum depth of 160 m at the shelf break and up to

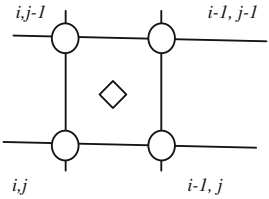

Fig. 2 Arakawa-B grid used in the numerical vorticity solution

2,800 m in its deepest area, the canyon is 125 km long by 55 km wide in the deeper part, and 30 km wide in its head (Fig. 1b). Classified as dynamically wide (Rosales Navarro 2007), because of its internal deformation Rossby radius which is less than the wide of the canyon at the center. The canyon area is of approximately 2,700 km^2, its characteristic slopes vary from less than 1° up to 3° (Mendoza and Ortiz Pérez 2000).

This study area does not present a direct influence of the river, nor a haline front and is mainly affected by the loop current, which is stronger in summer, and by the Yucatan current (Salas de León et al. 2004). It is also influenced by an intrusion current with a southward component (Monreal Gómez et al. 2004).

3 Data Analysis

Data were obtained during the oceanographic cruise PROMEBIO 3 (Oceanic Processes and Biological Production Mechanisms in the Southern Gulf of Mexico, in Spanish) carried out on board the R/V "Justo Sierra" of the Universidad Nacional Autónoma de México (UNAM), from April 17 to May 1st, 2000. Current velocities were obtained with a 75 kHz (RD Instruments) Acoustical Doppler Current Profile (ADCP). On the other hand, the conductivity, temperature and pressure data were recorded with a CTD for characterizing the water column.

The vertical component of the relative vorticity was obtained solving numerically the following equation:

$$\varsigma_Z = (\nabla \times \vec{v})_Z = \frac{\partial u}{\partial y} - \frac{\partial v}{\partial x}$$

where u and v are the horizontal velocity components.

The partial derivatives $\frac{\partial v}{\partial x}$ and $\frac{\partial u}{\partial y}$ can be approximated in finite differences as

$$\frac{\partial v}{\partial x} \approx \frac{v_1 - v_0}{x_1 - x_0}, \text{ and } \frac{\partial u}{\partial y} \approx \frac{u_1 - u_0}{y_1 - y_0},$$

in a regular Arakawa-B grid (Fig. 2).

Using the continuity equation

$$\nabla \cdot \vec{v} = \frac{\partial u}{\partial x} + \frac{\partial v}{\partial y} + \frac{\partial w}{\partial z} = 0,$$

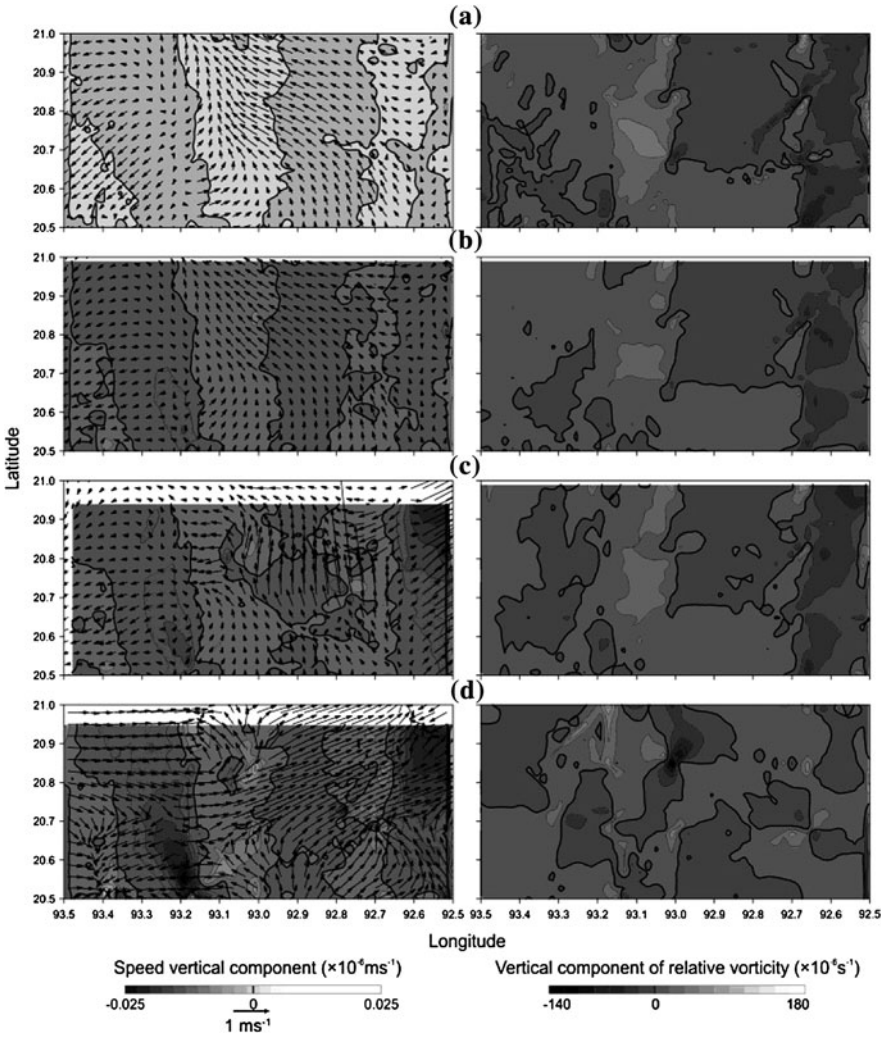

Fig. 3 A current pattern (ms^{-1}), vectors shows the horizontal speeds and in gray tones the vertical component of the speed ($\times 10^{-6}$ ms^{-1}). The vertical component of the relative vorticity ($\times 10^{-6}$ s^{-1}) is also shown at the *right* of the current patterns fields. Figures at **a** 20, **b** 68, **c** 100, **d** 244 m depth, from *up* to *down*

it was determined the vertical component of the velocity current, leaving

$$\frac{\partial w}{\partial z} = -\left(\frac{\partial u}{\partial x} + \frac{\partial v}{\partial y}\right).$$

In the same way as the vorticity calculation it can be approximated $\frac{\partial w}{\partial z}$ in finite differences

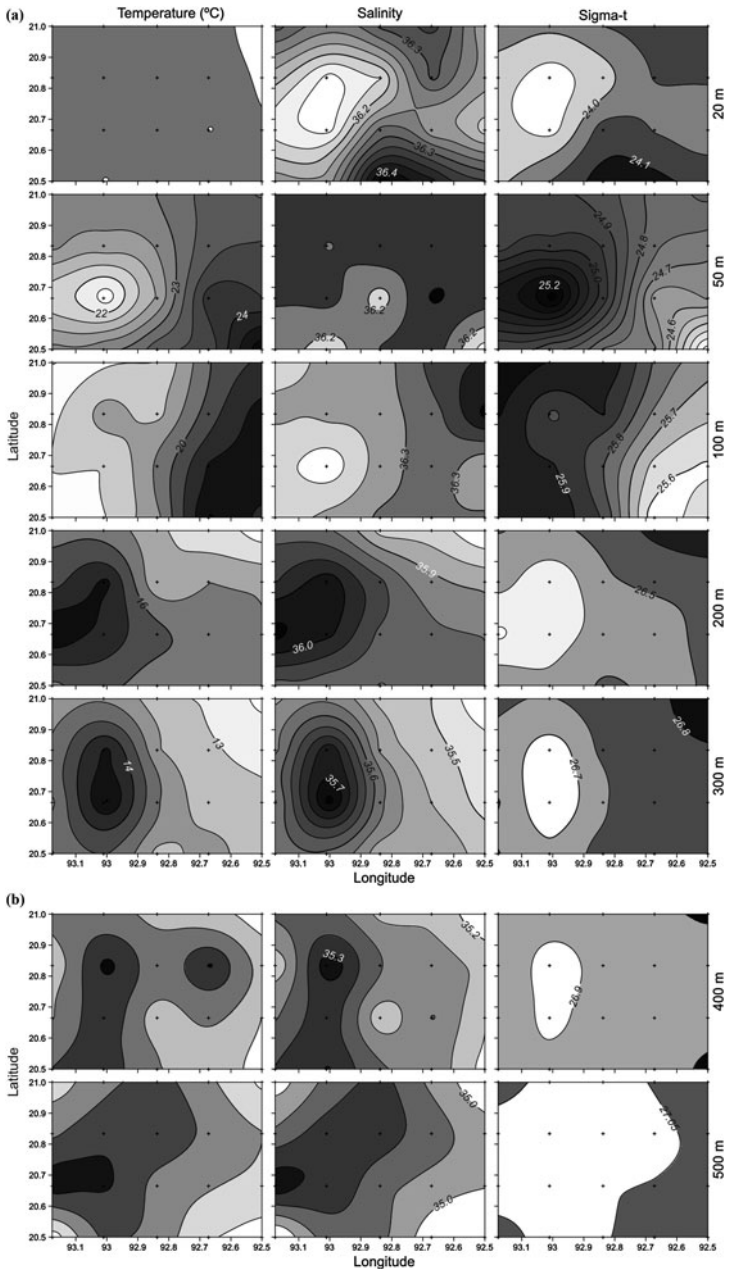

Fig. 4 **a** Temperature (°C), salinity and potential density (kg m^{-3}) at 20, 50, 100, 200 and 300 m depth from *left* to *right* **b** Temperature (°C), salinity and potential density (kg m^{-3}) at 400 and 500 m depth from *left* to *right*

$$\frac{\partial w}{\partial z} \approx \frac{w_1 - w_0}{z_1 - z_0},$$

so

$$w_1 \approx w_0 - \Delta z\left(\frac{\Delta u}{\Delta x} + \frac{\Delta v}{\Delta y}\right),$$

considering that at the sea surface ($z = 0$) we have that $w_0 = 0$.

4 Results and Discussion

The current that falls in the Campeche Canyon formed meanders, and cyclonic and anticyclonic eddies (Fig. 3). The slope of the Campeche Canyon caused a deflection of the marine current forcing it to go up or down. The Canyon presented a water column rising in the head; this was observed at 20, 50 and 100 m depth; with dense, cold and saline water (Fig. 4a, b). At 452 m depth a cyclonic eddy was located at the center and in the southern part of the study area, with 21 km of diameter.

Campeche Canyon had negative and positive vorticity values of the order of 10^{-6} s^{-1}, this is positive vorticity within the cyclonic eddies while the negative values were observed in the anticyclones (Fig. 3).

The Rossby ($R_o = 0.06$) and Froude ($F_o = 0.012$) numbers for all the study region have shown that the interaction of the marine current with the canyon topography is important in the formation of the eddies as well as the influence of the Earth rotation.

5 Conclusions

The Canyon of Campeche showed wavy hydraulic jumps, suggesting internal waves generated by stratification and by strong bathymetric changes. The observed eddies were generated by conservation of potential vorticity induced by topographic effects and the Earth rotation (Coriolis).

References

Cruz Gómez RC, Monreal Gómez MA, Bulgakov NS (2008) Efectos de los vórtices en sistemas acuáticos y su relación con la química, biología y geología. Interciencia 33(10):741–746

Klinck JM (1996) Circulation near submarine canyons: a modeling study. J Geophys Res 101:1211–1223

Mendoza M, Ortiz Pérez MA (2000) Caracterización geomorfológica del talud y la plataforma continentales de Campeche-Yucatán, México. Investigaciones Geográficas. Boletín del Instituto de Geografía, UNAM 43:7–31

Monreal Gómez MA, Salas de León DA, Velasco Mendoza H (2004) La hidrodinámica del Golfo de México. Diagnóstico Ambiental del Golfo de México, Caso M, Pisantry I, Ezcurra E (compiladores), Primera Edición, México, vol I, p 626

Rosales Navarro IS (2007) Hidrografía y Corrientes geostróficas en la región del Cañón de Campeche, Tesis de Maestría. UNAM: Posgrado en Ciencias del Mar y Limnología, Ciudad Universitaria México, D.F., p 89

Salas de León DA, Monreal Gómez MA, Signoret M, Aldeco J (2004) Anticyclonic-cyclonic eddies and their impacto near-surface chlorophyll stocks and oxygen supersaturation over the Campeche Canyon, Gulf of México. J Geophys Res 109:1–10

Linked Toroidal Vortices

Romero Arteaga and Velasco Fuentes

Abstract This paper deals with the dynamics of two or more toroidal filamentary vortices—i.e. thin tubular vortices coiled on an immaterial torus—in an otherwise quiescent, ideal fluid. If the vortices are identical and equally spaced on a meridional section of the torus, the flow evolution depends on the torus aspect ratio (r_1/r_0, where r_0 is the radius of the centreline and r_1 is the radius of the cross section), the number of vortices (N), and the vortex topology ($V_{p,q}$, denoting a vortex that winds p times round the torus symmetry axis and q times round the torus centreline). The evolution of sets of $NV_{1,2}$ vortices was computed using the Rosenhead–Moore approximation to the Biot–Savart law to evaluate the velocity field and a fourth-order Runge–Kutta scheme to advance in time. It was found that when a small number of vortices is coiled on a thin torus the system progressed along and rotated around the torus symmetry axis in an almost steady manner, with each vortex approximately preserving its shape.

1 Introduction

Ring vortices move through the surrounding fluid along a straight line while preserving their shape. They have the important dynamic property of transporting mass and momentum in an efficient manner. This kind of vortices can be observed

R. Arteaga (✉) · V. Fuentes
Departamento de Oceanografía Física, CICESE, Ensenada,
Baja California, Mexico
e-mail: anromero@cicese.mx

V. Fuentes
e-mail: ovelasco@cicese.mx

J. Klapp et al. (eds.), *Experimental and Theoretical Advances in Fluid Dynamics*,
Environmental Science and Engineering, DOI: 10.1007/978-3-642-17958-7_12,

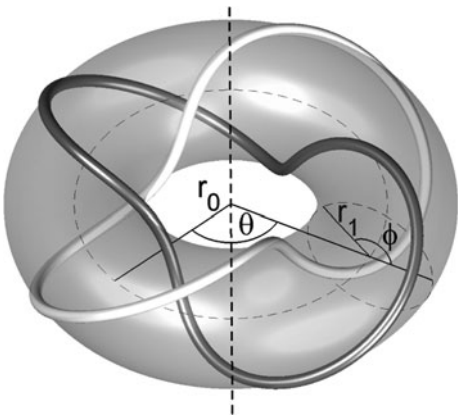

Fig. 1 Two linked vortices represented by *light* and *dark grey* tubes. Each vortex is uniformly coiled on the surface of an immaterial torus of radii r_0 (*centreline*) and r_1 (*cross section*)

at a variety of scales, from the drops falling in a quiescent liquid to the exhalations of volcanoes.

Kelvin (1875), motivated by his desire to construct a theory of matter based on the vortex atom, started the study of elaborate variations of the ring vortex, namely, toroidal vortices. These are tubular vortices coiled on the surface of a torus; according to Kelvin (1875), they are steady and stable if sufficiently thin. This hypothesis has been confirmed numerically in the case of a single vortex (Ricca et al. 1999; Velasco Fuentes 2010). Thomson (1883), also motivated by the misguided theory of the vortex atom, studied the motion of multiple toroidal vortices which are mutually linked. By considering the limiting case of infinitely thin vortices lying on the surface of a torus of infinite aperture radius as compared with its cross-section radius, Thomson (1883) obtained his celebrated result about the stability of a regular polygon of N point vortices when $N \leq 6$.

The purpose of this paper is to present results about Kelvin original problem. That is to say, the motion of a system of linked vortices coiled on the surface of a torus of finite aspect ratio. In particular we present results about the vortices' uniformity of motion and permanence of form.

2 Methods

In the initial condition N filamentary vortices of equal strength, Γ, lie on the surface of an immaterial torus of radius r_0 and cross-section πr_1^2 (see Fig. 1). They are uniformly coiled on the torus in such a way that, before closing on itself, each vortex $V_{p,q}$ winds p times around the torus' symmetry axis and q times around the torus' centreline. Furthermore, they intersect any meridional section of the torus on the vertices of a regular polygon.

Therefore each vortex is given, in Cartesian coordinates, as follows:

$$x_i = (r_0 + r_1 \cos\phi)\cos\theta,$$
$$y_i = (r_0 + r_1 \cos\phi)\sin\theta,$$
$$z_i = r_1 \sin\phi.$$

where $i = 1, \ldots, N$ denotes the vortex being described, $\theta = ps$ is the angle around the torus' symmetry axis, $\phi = qs - 2(N - i)\pi/N$ is the angle around the torus' centreline, and s is a real number in the range $(0, 2\pi)$.

We assume that the vortices evolve in an inviscid, incompressible, homogeneous fluid which is unbounded and acted on by conservative forces only. Therefore we compute the induced velocities with the Rosenhead–Moore approximation to the Biot–Savart law (see Saffman 1995):

$$\mathbf{u}(\mathbf{x}) = -\frac{\Gamma}{4\pi}\sum\nolimits_i \oint \frac{[\mathbf{x} - \mathbf{r}_i(s)] \times \mathrm{d}\mathbf{s}}{\left(|\mathbf{x} - \mathbf{r}_i(s)|^2 + \mu^2 a^2\right)^{3/2}}, \tag{1}$$

where $\mathbf{x}$ is the point in space where the induced velocity is computed, $\mathbf{r}_i(s)$ denotes the position along the ith filament, a is the radius of the filaments' cross sections and μ is a constant with value $e^{-3/4}$. The use of the Rosenhead–Moore approximation implies that the vortices are no longer infinitely thin: they now have a small but finite cross section. This, however, is assumed to be undeformable. The value of μ depends on the vorticity distribution across the vortex; the particular value used here corresponds to uniform vorticity on the vortex cross section (Saffman 1995).

The numerical computation of Eq. 1 requires the discretization of the vortices. Therefore each filament is represented by a finite number of material markers, say n, whose value depends on a and the filaments's length L. We found that for $n \approx 2L/a$ the speed of a circular ring is computed within 0.5 % of the analytical value (see Eq. 2). We assume the same criterion to represent a toroidal vortex and thus n varies in the range 300–500 in the simulations discussed here. Once chosen, the value of n remains constant during the evolution because the filaments approximately preserve their length.

We use a fourth-order Runge–Kutta scheme with fixed time step to integrate the evolution equation

$$\frac{\mathrm{d}\mathbf{x}_\mathrm{k}}{\mathrm{d}t} = \mathbf{u}(\mathbf{x}_k),$$

where $\mathbf{x}_k$ is the position of the node and $\mathbf{u}(\mathbf{x}_k)$ is its velocity, computed with Eq. 1. Note that k runs through all nodes ($j = 1, \ldots, n$) of all filaments ($i = 1, \ldots, N$).

3 Steadiness of Motion

A typical example of the motion of a system of linked toroidal vortices is shown in Fig. 2. The motion of the vortices may be divided into the following three components: (a) progression along the torus' symmetry axis, (b) rotation around the

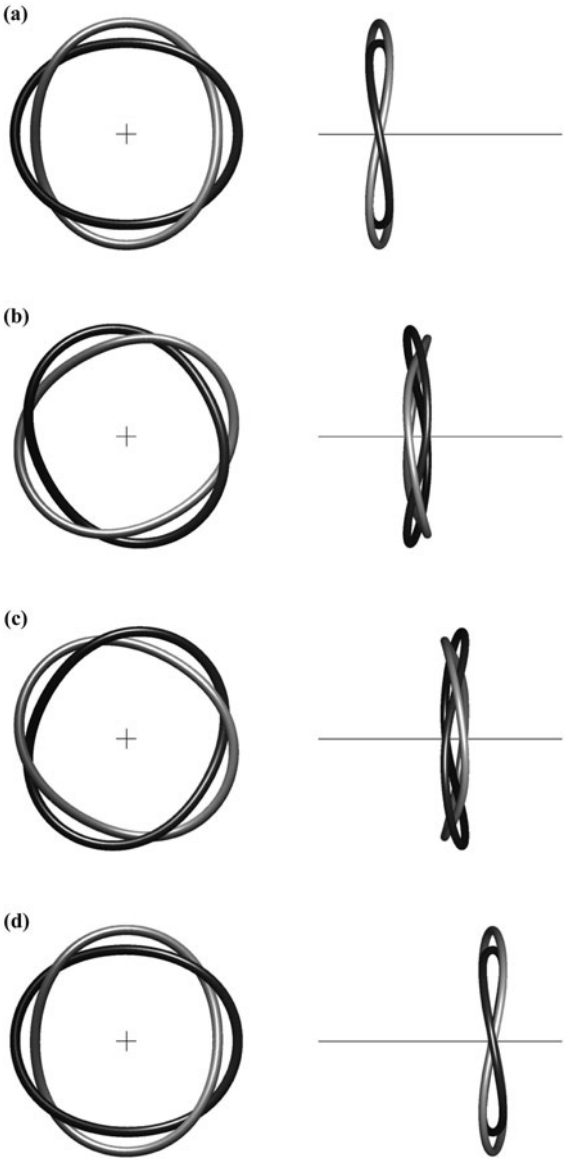

Fig. 2 Time evolution of the set of vortices $2V_{1,2}$ with aspect ratio $r_1/r_0 = 0.1$. A frontal view of the vortices (*left column*) shows the rotation of the set around the torus' symmetry axis (represented here by a cross); a lateral view (*right column*) shows the progression of the set along the same axis (represented here by a *straight line*). The stages depicted are the following: (**a**) $t = 0$, (**b**) $t = 0.23T$, (**c**) $t = 0.46T$, (**d**) $t = 0.69T$, where T is the time required by a ring vortex of radius r_0 and cross section πa^2 to advance a distance equal to r_0 (Eq. 2)

torus symmetry axis, and (c) rotation around the torus' centreline. Since all of these components are approximately uniform (see Fig. 3), each will be characterised by a constant speed, respectively U, Ω_1, and Ω_2.

The speed U grows proportionally with the number of vortices N and decreases marginally with growing aspect ratio r_1/r_0 (Fig. 4a). This behaviour is explained as follows: since $r_1/r_0 << 1$ the progression speed behaves as if there was a single ring with circulation $N\Gamma$ instead of N rings with circulation Γ. In the parameter

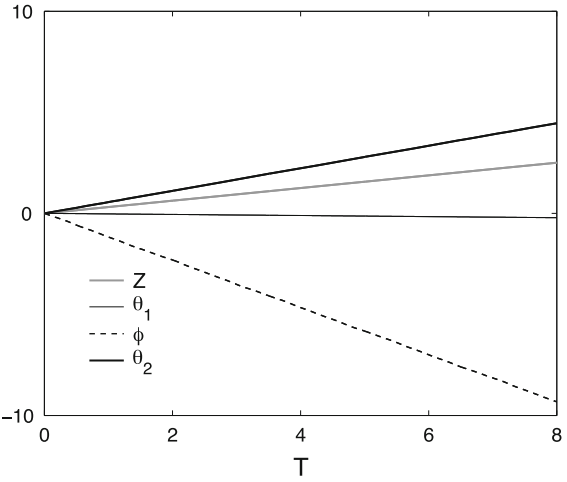

Fig. 3 Uniformity of the vortex motion as shown by the linear displacement along the symmetry axis (Z), the material angular displacement round the symmetry axis (θ_1) the material angular displacement round the torus centreline (ϕ) the phase angular displacement round the symmetry axis (θ_2)

region presented in the figure $U \approx 0.74NU_0$, where U_0 is the speed of a circular ring of strength Γ and radius r_0 Kelvin (1867):

$$U_0 = \frac{\Gamma}{4\pi r_0}\left[\log\frac{8r_0}{a} - \frac{1}{4}\right] \tag{2}$$

The angular speed Ω_1 grows proportionally with the number of vortices N and increases marginally with growing aspect ratio r_1/r_0 (Fig. 4b). An analogy with the motion of a set of straight helical vortices explains this behaviour: these progress uniformly along their axis with a speed that increases as the number of vortices increases (Wood and Boersma 2001). Similarly, the uniform progression of toroidal helical vortices along the torus' azimuthal direction increases in speed with increasing N.

The angular speed Ω_2 increases with N and decreases with r_1/r_0 (Fig. 4c). This behaviour is explained as follows: since the vortices are thin and $r_1/r_0 \ll 1$ they can be locally considered as being straight, that is to say, as a set of point vortices on a plane. In the parameter region shown in the figure $\Omega_2 \approx 0.94\,\Omega_0$, where Ω_0 is the angular speed of a set of N point vortices of circulation Γ placed on the vertices of a regular polygon inscribed in a circle of radius r_1 (Thomson 1883):

$$\Omega_0 = (N-1)\frac{\Gamma}{4\pi {r_1}^2} \tag{3}$$

The combination of the rotations Ω_1 and Ω_2, which involve material elements, gives rise to a rotation of the vortex shape around the torus' symmetry axis. This travelling wave has a phase angular speed, Ω_3, which is approximately equal to $\Omega_2/2$. The rotating wave is particularly important because the vortex is quasi-steady (i.e. almost stationary and of fixed shape) when observed in a system that translates with speed U and rotates with angular speed Ω_3. This fact has been fruitfully applied in the study of advection and transport by toroidal vortices (see Velasco Fuentes 2010; Velasco Fuentes and Romero Arteaga 2011).

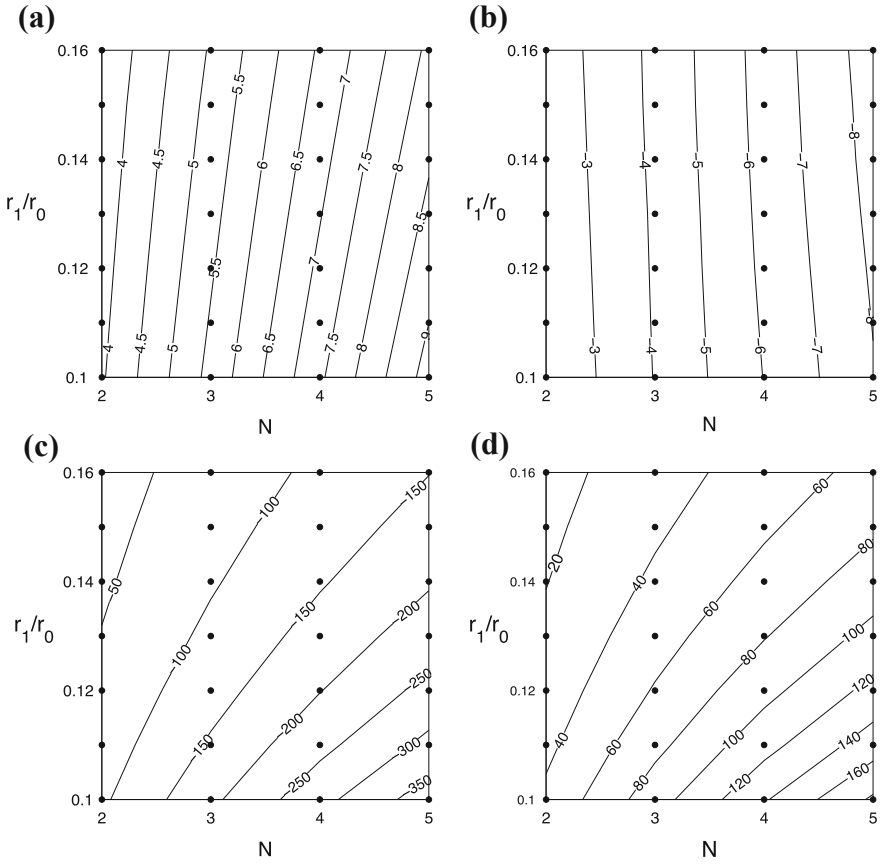

Fig. 4 Properties of the vortex motion as functions of the number of linked vortices (N) and the torus aspect ratio (r_1/r_0.) **a** Linear speed (U), **b** Material angular speed round the symmetry axis (Ω_1,) **c** Material angular speed round the centreline (Ω_2,) **d** Phase angular speed round the symmetry axis (Ω_3)

4 Permanence of Form

We applied several diagnostics to test whether or not the vortices preserve their shape throughout the flow evolution. The simplest one was the time evolution of the vortex length (Fig. 5a). This was observed to vary within 5% of its initial value in the region of the parameter space studied here ($2 \leq N \leq 5,\ 0.1 \leq r_1/r_0 \leq 0.16$).

A second diagnostic consisted in finding the torus that best fitted the vortices at every stage of the flow evolution. For symmetry reasons we assumed that the fitting tori would have the same symmetry axis as the initial one, therefore each fitting torus is uniquely determined by the radii $r_0(t)$ and $r_1(t)$. The value of $r_0(t)$ was found to remain within 1% of its initial value, whereas the value of $r_1(t)$ was found to remain within 5% of its initial value (Fig. 5a).

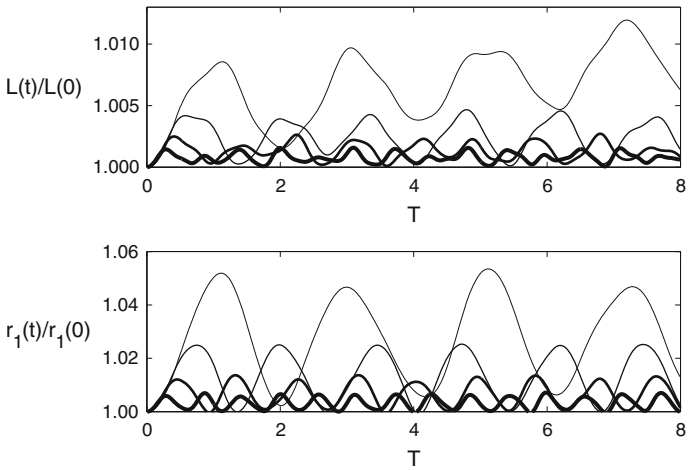

Fig. 5 Variation of the vortex shape for the set $2V_{1,2}$ as illustrated by the time evolution of the following parameters: **a** the length of the vortices, and **b** the cross-sectional radius of the best-fitting torus (see text). Each curve represents a different initial value of the torus aspect ratio; this is, from thicker to thinner line, $r_1/r_0 = 0.10, 0.12, 0.14$, and 0.16

5 Concluding Remarks

Sets of linked toroidal vortices with topology $V_{1,2}$ uniformly progress along and rotate around the torus' symmetry axis. The vortices' shapes of the sets $2V_{1,2}$ and $3V_{1,2}$ are approximately preserved when the aspect ratio $r_1/r_0 < 0.17$. The vortices' shapes of the sets $4V_{1,2}$ and $5V_{1,2}$ are approximately preserved when the aspect ratio $r_1/r_0 < 0.13$.

Acknowledgments This research was supported by CONACyT (México) through a post-graduate scholarship to ARA.

References

Ricca R, Samuels D, Barenghi C (1999) Evolution of vortex knots. J Fluid Mech 391:29–44
Saffman P (1995) Vortex dynamics. Cambridge University Press, Cambridge
Thomson JJ (1883) A treatise on the motion of vortex rings. MacMillan, London
Kelvin (W Thomson) (1875) Vortex statics. Proc R Soc Edinburgh 9:59–73
Kelvin (W Thomson) (1867) The translatory velocity of a circular vortex ring. Philos Mag 33:511–512
Velasco Fuentes O (2010) Chaotic streamlines in the flow of knotted and unknotted vortices. Theor Comput Fluid Dyn 24:189–193
Velasco Fuentes O, Romero Arteaga A (2011) Quasi-steady linked vortices with chaotic streamlines. J Fluid Mech (Submitted for Publication)
Wood DH, Boersma J (2001) On the motion of multiple helical vortices. J Fluid Mech 447:149–171

Remediation Strategy for a Cr(VI) Polluted Aquifer Using Numerical Simulation

Lázaro Raymundo Reyes-Gutiérrez, Ramiro Rodríguez-Castillo and Elizabeth Teresita Romero-Guzmán

Abstract The Buenavista shallow aquifer, in Leon central Mexico is polluted with hexavalent chromium, Cr(VI). The soil and groundwater contamination by it has a significant problem in this area, which must be studied given the importance that represents the shallow aquifer for the drinking water supply at the local level. The real system state of the wells and piezometers in the Buenavista shallow aquifer was revised to design a scheme of P&T and select the sites, wells number and pumping flow most appropriate for the system. The best well location and pumping flow was chosen to capture and reduce the Cr(VI) groundwater concentration. A remediation strategy based on P&T system has been designed by the mathematical approximation optimization simulation (O/S) and a single period of planning, it was used as a tool to identify the sites appropriate to extract Cr(VI) contaminated groundwater, they have the potential to reduce Cr(VI) concentrations with an actual cost for remediation. The strategy was built using a simulation-optimization tool, combining the answer function with a genetic algorithm.

L. R. Reyes-Gutiérrez (✉)
Instituto Potosino de Investigación Científica y Tecnológica (IPICYT),
San Luis Potosí SLP, 78216 México city, Mexico
e-mail: raymundo.reyes@ipicyt.edu.mx

R. Rodríguez-Castillo
Instituto de Geofísica, Universidad Nacional Autónoma de México,
México city, Mexico

E. T. Romero-Guzmán
Departamento de Química, Instituto Nacional de Investigaciones Nucleares,
Carretera México-Toluca s/n, La Marquesa,
Ocoyoacac, 52750 Estado de México, Mexico

J. Klapp et al. (eds.), *Experimental and Theoretical Advances in Fluid Dynamics*,
Environmental Science and Engineering, DOI: 10.1007/978-3-642-17958-7_13,

1 Introduction

In the middle of the last century many industries worked without proper management of their waste. As a result of such practices, and many sites were contaminated. Actually, there is evidence of groundwater contamination for these reasons are necessary realized remediation work in situ to mitigate the contaminations. The limitations of in situ treatments propitiated this research. Different scenarios for reducing and containing the plume were considered: number of wells, pumping rates, cost. The Pump and Treat (P&T), remediation systems based on optimization systems look for the aquifer cleaning (contaminant remotion) or the plume containment (controlling the groundwater hydraulics). The more common way for both goals is pumping the water and treated it. The basic design parameters (decision variables) are the wells location and the pumping rates respect to the hydraulic head and/or the contaminant concentration (state variables) (Aly and Peralta 1999). The remediation schemes by means of optimization techniques maximize the contaminant removal whereas the costs are minimized (Andricevic and Kitanidis 1990; Ahlfeld and Heidari 1994). But in this study the fixed cost are omitted. The process is evaluated with the existent wells. The space decision for this search problem grows as a 2^n function, where n is the total number of the sites of available wells. As the number of wells increases more than three, the space of decision grows rapidly of million to trillions of unique designs of positions of the wells that can be considered.

For this study the simple Genetic Algorithm (GA) with the MGO code (Zheng and Wang 2003) was chosen. This algorithm looks effectively for large decision spaces using a process similar to the Darwinian natural selection. The simulation-optimization modeling (S/O) requires predictive modeling in combination with optimization techniques (Peralta 2001). For the numerical solution the balance equations are discretized using finite differences. Time is discretized as totally implicit by means of backward first order finite differences (Narasimhan and Witherspoon 1976). The resulting group of coupled no lineal algebraic equations are simultaneously solved by means of Gauss-Seidel iterations. An algorithm of conjugate gradient is used to solve the linear equations that result in every step of the iteration (Moridis and Pruess 1995). A chromium compounds factory has operated for more than 30 years in Buenavista, a few kilometers from Leon City in Guanajuato state, central Mexico. The factory deposited its Cr(III) and Cr(VI) solid wastes in its own lands. More than 17,000 tons of wastes were confined in a landfill (an excavated container) over its design capacity. Cr(VI) leakages, coming from the broken container, contaminated the local aquifer. The aquifer was the only water supply source for the Buenavista inhabitants. The wastes were taken out from the landfill in 1994. The presence of the plume 10 years later indicates the persistence of chromium in the sediments. The generated contamination plume is been confined in the area due to the pumping effect an industrial well. The Turbio River also acts as a hydraulic barrier to the south. The study area, remediation domain, with the well field is showed in the Fig. 1.

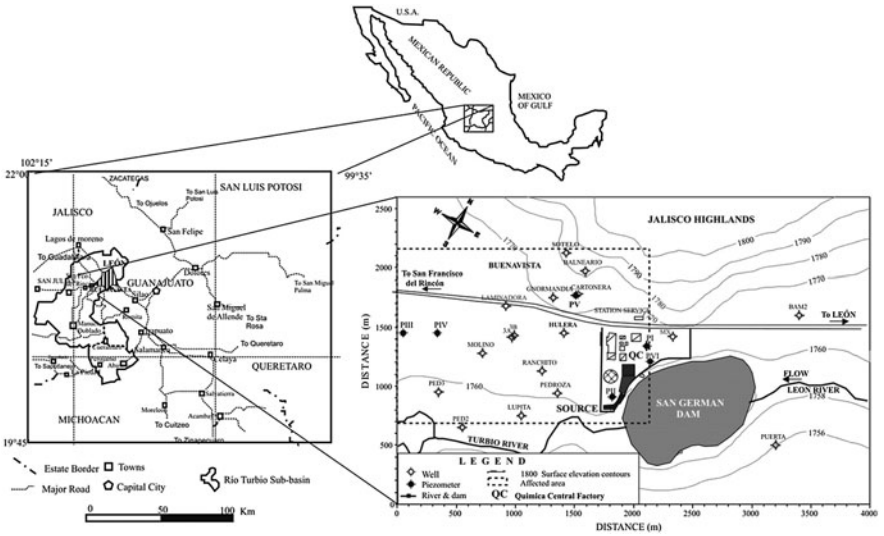

Fig. 1 Domain and well field of the modeled area

2 Experimental

2.1 Local Hydrogeological Framework

The shallow aquifer is conformed by a sedimentary unit (semi-consolidated tuffs), covered by Recent alluvial deposits. Subsoil consists of a layer of clay material at the base; this unit is over a horizon of sand and gravel of 4 m in thickness which is covered by a package loamy sand of 20 m thick. Another 10 m thick loamy sand deposit is located at the top. Finally, a thin layer of loamy clay works as molten surface.

The aquifer thickness is 24–18 m. Clay and clayey sand formed the discontinuous upper confining layer. The thickness of the clayey semi-confining layer is 6–0.5 m (Reyes 1998). In the past, the aquifer was used for urban supply. At present is only used for irrigation and industrial processes. The water table is located to 10 m depth. The three hydroestructures that formed the shallow unconfined aquifer are (Fig. 2): an upper discontinuous impermeable layer ($K_x = 0.26$ m/d); the aquifer unit ($K_x = 100$ m/d) and a semiconfined layer ($K_x = 0.26$ m/d).

The hydraulic conductivity (K) varies from 6.1×10^{-4} to 1.52×10^{-1} m/day for the clayey layer and 45.72–120.2 m/day for the aquifer unit. For modeling purposes precipitation was considered constant, 482 mm/year. The regional flow direction is NE–SW. Locally the flow presents a N–S direction with a mean gradient of 0.007, but the local abstraction alters the flow direction.

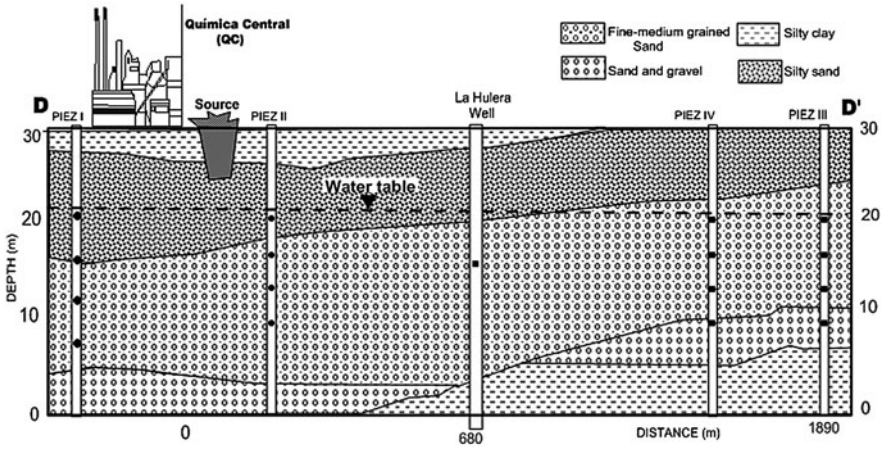

Fig. 2 Geological profile and piezometers I–IV and well La Hulera

2.2 Mathematical Modeling

The equation for the 3D groundwater flow, assuming constant density is:

$$\frac{\partial}{\partial x}\left(K_x \frac{\partial h}{\partial x}\right) + \frac{\partial}{\partial y}\left(K_y \frac{\partial h}{\partial y}\right) + \frac{\partial}{\partial z}\left(K_z \frac{\partial h}{\partial z}\right) + q_z = S_s K_x \frac{\partial h}{\partial t} \tag{1}$$

where h is the hydraulic head [L]; t is time [T]; K_x, K_y, y K_z are the mean components of the hydraulic conductivity along the axis x, y, and z [LT^{-1}]; and, S_s is the specific storage [L^{-1}]. The partial equation that describes the 3D solute transport in the groundwater flow is:

$$\frac{\partial}{\partial x_i}\left(\theta D_{ij} \frac{\partial C}{\partial x_j}\right) - \frac{\partial}{\partial x_j}(q_i C) + q_s C_s + \sum_{k=1}^{N} R_k = \frac{\partial(\theta C)}{\partial t} \tag{2}$$

where C is the solute concentration [ML^{-3}]; D_{ij} is the hydrodynamic dispersion coefficient [L^2T^{-1}]; C_s is the sink/source concentration [ML^{-3}]; θ is the porosity [−]; q_s is the specific discharge or Darcian flow [LT^{-1}]; and R_k is the chemical reaction term [$ML^{-3}T^{-1}$].

The Eq. 1 was solved using MODFLOW 98/96 (McDonald and Harbaugh 1988; Harbaugh and McDonald 1996a) and the Eq. 2 with the 3D solute transport model MT3DMS (Zheng 1990; Zheng and Wang 1999), with finite differences method. In both simulation models was used the graphic interphase preprocessor/postprocessor Groundwater Vistas V.4 (GWV) (Environmental Solutions Inc. 2003). MODPATH (Pollock 1989) is a 3D model of particle trace that works with MODFLOW.

3 Results and Discussion

3.1 The Cr(VI) Contamination Process

The waste leakages generated a well defined contamination plume in the aquifer. The Fig. 3 shown the Cr(VI) chemical analyses (2003–2004). The defined plume has an approximate area of 2.5 km^2. This concentration distribution is obtained from vertical sampling in the piezometer network. The results of the mathematical modeling carried out (Reyes 1998) and the groundwater monthly sampling proved that the source of the plume is the container (Rodríguez et al. 1991; Armienta 1992; Armienta and Rodríguez 1992; Armienta et al. 1996). Nevertheless, although a remediation scheme started with the waste removal in 1994, the plume persists as is showed by the continuous high concentrations of Cr(VI), 0.02–40 mg/L, after the waste removal.

3.2 Simulation Results

The described modeling process was applied in Buenavista, considered the domain and characteristics showed in Fig. 1. The area is 4 × 2.6 km (dash line). A network of 40 × 26 elements of 100 m was created. The chosen well for the P&T scheme was La Hulera. This well has maintained a continuous operation whereas the rest was closed or partially operated alter the contamination detection. Two points of water injection (recharge) was chosen, the piezometer II, located near of the source and the well La Hulera, where the highest Cr concentrations have been detected. The pumping rate was varied between $Q_{min} = 0.0$ and $Q_{máx} = 872$ m^3/d. To evaluate some constant pumping scenarios, the flow modeling in steady state was used. The goal was to identify the minimum pumping rate to contain the plume. It was assumed that the simulations in steady state offer the best representation of the site conditions, as a consequence of the constant pumping for long periods of time, and they can be taken as representatives of a P&T system.

The best obtained simulation with pumping, in transitory state, for 10 years was an alternated pumping of wells La Hulera and La Cartonera with a rate of 3,257.7 and 1,362.7 m^3/d respectively. The plume is minimized and contained in the domain (Fig. 4a). The Fig. 4b shows the distribution of the plume in the shallow aquifer of Buenavista obtained in the model revised starting from the recalibration of the model base.

3.3 Pumping Schemes Evaluation Using the Brute Force Technique

The optimization technique Brute Force is a new way to optimize the P&T systems (Rumbaugh and Rumbaugh 2003). In contrast to other most classic techniques (AQMAN, MODMAN, MODOFC, SOMOS y MGO), Brute Force used the

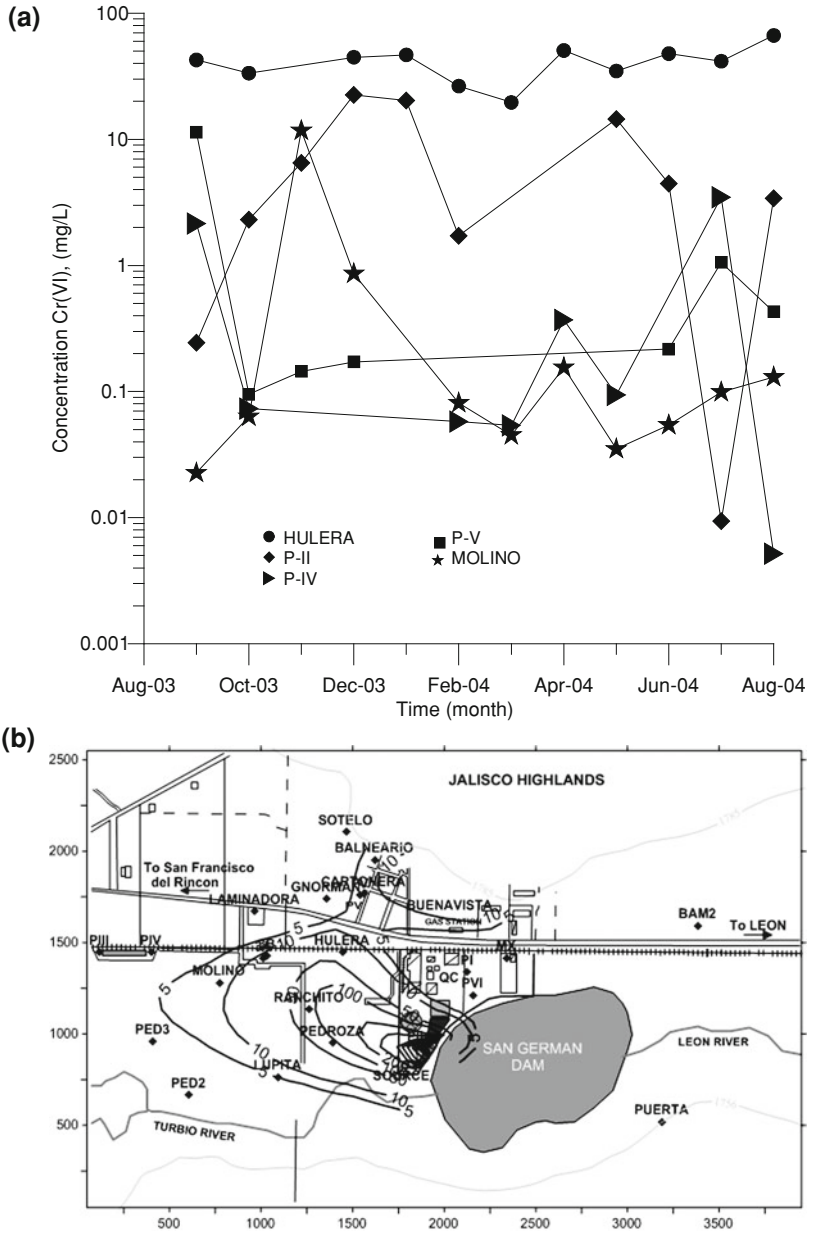

Fig. 3 **a** Cr(VI) [mg/L], concentration variations in the piezometers P-II, P-IV, P-V, well La Hulera and well La Cartonera, from September 2003 to August 2004. **b** Cr(VI) [mg/L] concentration isolines, September 2003. Concentration intervals of 5 mg/L

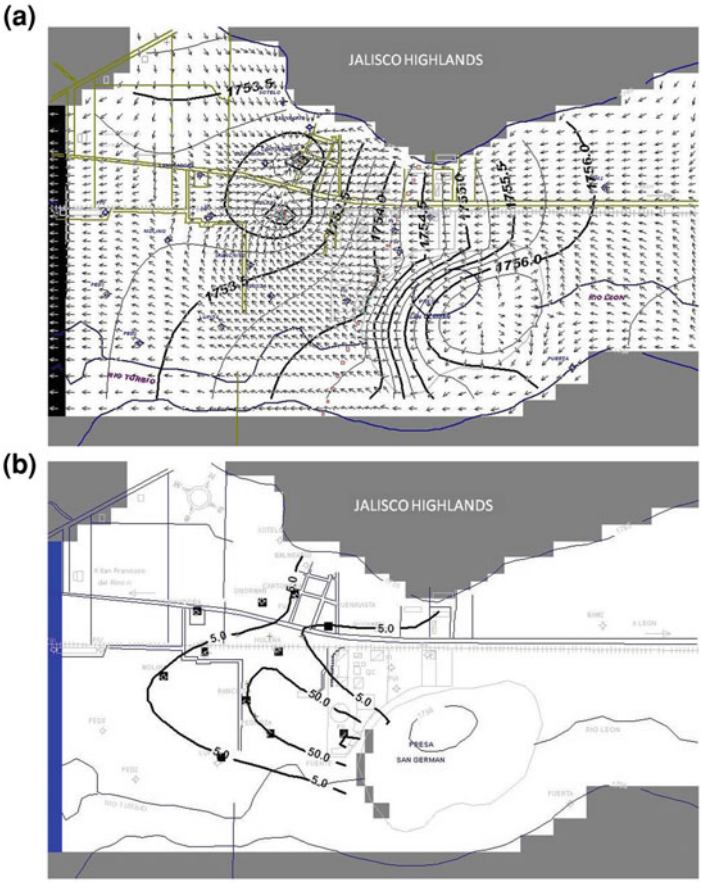

Fig. 4 **a** Hydraulic head isolines obtained with the mathematical modeling. **b** Distribution of the Cr(VI) plume obtained by the alternated pumping of the wells La Hulera and La Cartonera. Values in mg/L

particle trace method to determine if the system is successful and to evaluate different pumping scenarios. This technique works using MODFLOW and MODPATH. The module Brute Force is included in GroundWater Vistas, GWV (ESI 2003).

The optimization considered a maximum withdrawal of 13 m in the pumping rates analyzed. The particles were placed in the plume zone. A single well, La Hulera, was considered in the initial case. Although its pumping rate is relatively low, 162 m^3/d (approximately 9 L/d), it has contained the plume, limiting its migration. Some no polluted areas as the well Molino could be affected. The modeled optimal rate was 3,814.7 m^3/d (Fig. 5a). Alter these results; the pumping stresses ranged from −200 to −5,000 m^3/d. These values were obtained from the flow modeling. Using two wells, La Hulera and La Cartonera, the plume is

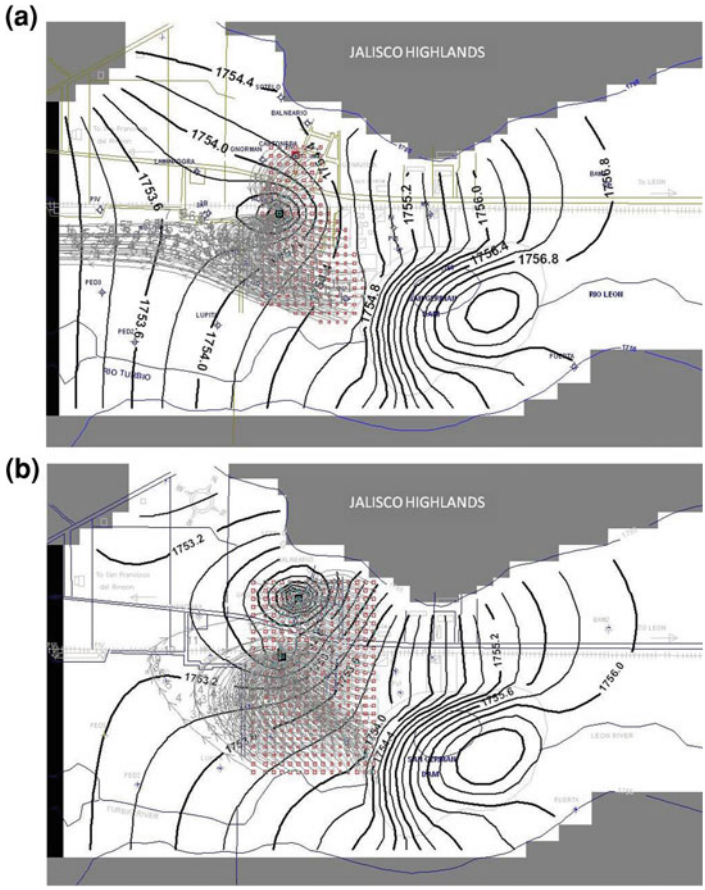

Fig. 5 **a** Capture zone obtained by La Hulera well. **b** Particle capture obtained by the La Hulera and La Cartonera wells

contained with the optimal pumping rates −3,442.76 m^3/d and −2,319.34 m^3/d, respectively. The maximum arrival time of the particles was 313.2 days. All the particles are captured with the total pumping rate, 5,762.1 m^3/d (Fig. 5b).

3.4 Optimization Problem Formulation Using MGO

An optimization method with the genetic algorithm (GA) was used to obtain an optimal pumping strategy and consequently to avoid the dowgradient plume migration. Zhen and Wang (2003) develop a model (MGO) for the design of P&T systems. The model can be applied to problems formulated for minimizing a restricted objective function (Peralta 2001; Zheng and Wang 2002). The goal is

minimize the total pumping for the remediation strategy including the binary variable of the *on/off* well status. Three abstraction wells are considered as well as the hydraulic head limits and the specific well location. For this problem, the objective function was formulated considering that the total pumping only depends of the number of wells, their position and the pumping rate of the active wells. This formulation supposes that any existing well can be used in the remediation, consequently their drilling was not considered. The objective function has the form:

$$\text{Min } J(q) = \sum_{i=1}^{11} y_i |Q_i| \Delta t_i \tag{3}$$

and the constraints:

$$\sum_{i=1}^{11} y_i \leq 3 \tag{4}$$

$$0 \leq Q_i \leq 5000 \tag{5}$$

$$h_w \leq 1728 \tag{6}$$

$$Q_{iny} = -0.5 \sum_{i=1}^{3} Q_i \tag{7}$$

Equation 3 is the absolute sum of all the pumping rates multiplied by the simulation period used in the flow model, Δt. The flow model was run in steady state with one time period, then by simplicity Δt is 1. The Eq. 4 requires that the permitted active wells must be less zero equal than three. The binary variable, y_i, is equal to one for active wells (*on*) and equal to zero for inactive wells (*off*). The remediation considered long terms results, then the well installation costs are negligible in comparison with the pump and treat costs. The Eq. 5 specifies the pumping rate to optimize. The maximum value, 5,000 was determined with Brute Force. The Eq. 6 is the head restriction: water table, h_w, must be located up the aquifer bottom in any pumping well. In this case h_w, is located 1,728 masl. Equation 7 expresses a constraint to the balance injection/abstraction rate. It requires that the injection rate (if apply) is half of the total pumping. The genetic algorithm, GA, can determine the position and optimal pumping rate for a set of remediation wells considering the above mentioned constraints. The Fig. 6 shows the position of the potential wells for contention and/or remediation.

The pumping rate parameters are 11. The discretization intervals (*NPStep*) for each parameter are 32. The range for these parameters is 0–5,000 m^3/d. The resolution of the pumping rates is (5000–0/32–1) or approximately 161 m^3/d. It means that the final pumping rates obtained with GA can differ 161 m^3/d from the optimal real rates but not to be greater than it.

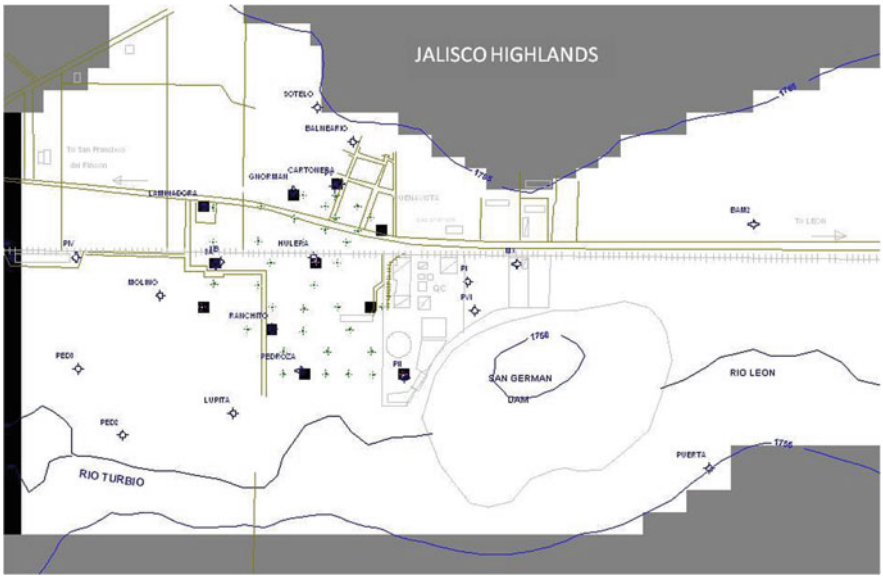

Fig. 6 Design of the capture zone. The *crossed circles* indicates the water table monitoring point (hydraulic head must be located up the aquifer *bottom*)

The number of iteration simulations, (*NSimPerIter*), or population size in GA was 100. A crossover probability of 0.5 was obtained with the uniform crossover method. The mutation probability jump is equal to 1/*NSimPerIter* or 0.01. The mutation advance option-1 was used by omission. Four cases, where all solution options were equal, were analyzed. The well quantity was varied only to compare. The objective function converges after 13 generations in all cases satisfying all restrictions. The optimized pumping rate distribution is showed in Table 1 of the different schemes tested. Results of the Case 1, for 10 candidate wells, indicated that final solution is with seven active wells. The total pumping rate for the Seven wells is 13,289 m^3/d. The rate distribution for each well is show in Fig. 7a. The solution of the four Cases presents a significant difference in the pumping rates. There is little difference in the computational efficiency, but the there is a more important difference in the remediation costs. The hydraulic head distribution, the capture zone extension and the concentrations based on the optimized pumping rates by means of MGO and the GA scheme, are showed in the Fig. 7a and b.

4 Conclusions

The modeling effort presented consisted on minimizing the groundwater pumping rate focused in the optimal containment and removal of the Cr(VI) plume, that there is migrated outside of the area source. The modeling and the

Table 1 Optimized pumping rates obtained by mean of GA

Well localization	Pumping rate (m^3/d) (− for extraction, + for injection)			
Row, column	Case 1	Case 2	Case 3	Case 4
(17,22)	−1270	−1699		−2539
(10,24)	0.000	−2209	−3261	−1862
(27,21)	0.000	−2039		
(23,18)	0.000	−1614		
(11,20)	−2624	0.000		
(14,28)	−1354	−679.7		
(17,13)	−2539	−2634		−1439
(12,12)	−1862	0.000		
(27,30)	−2201	−1444	−3763	−2285
(21,12)	−1439	0.000		−2201
(21,27)		−2124		
TOTAL	**−13,289**	**−14,442.7**	**−7,024**	**10,326**

procedure followed can determine the positions and optimal rates for a remediation system based on P&T. The constraints in pumping rates and hydraulic heads result important for the capture and containment of the Cr(VI) plume. To increase the number of wells can diminish the total pumping rate. The goal for the recovery of the system was to define an scheme of containment of the Cr(VI) plume in the area of Buenavista that was achievement in all the cases analyzed with Brute Forced and MGO, of which two schemes only present feasible application: the remediation focused with two wells, The Hulera and the Cartonera wells, and the case 4 with a system of five wells, respectively. The locations of the wells of pumping have a significant effect on the total pumping rate. This is, when extracting groundwater with the optimal rate of the selected wells considerable savings can be made in the costs, since the remediation demands the careful dimensionally of the pumping rate and the wells locations to prevent an undesirable migration or extension of the period of the remediation. A scheme of total contention of the contaminant plume with two wells, La Hulera and La Cartonera was obtained using Brute Force. The minimum obtained pumping rates were $Q = -3{,}442.76$ m^3/d and $-2{,}319.34$ m^3/d, respectively. With the results of MGO, for the domain of flow with the imposed constrains, it determines an optimal and effective solution. Five wells are only necessary with a total extraction rate of 10,326 m^3/d. With the systems provided by the codes of optimization, the contamination has reduced to located areas. With Brute Force and MGO, it was determined that the time to reduce the concentrations from the plume chromium to levels that they don't put in risk to the man and the atmosphere, it was of 365 days operating the system of the wells optimized to their maximum capacity to reach the specified goal. With the system obtained by

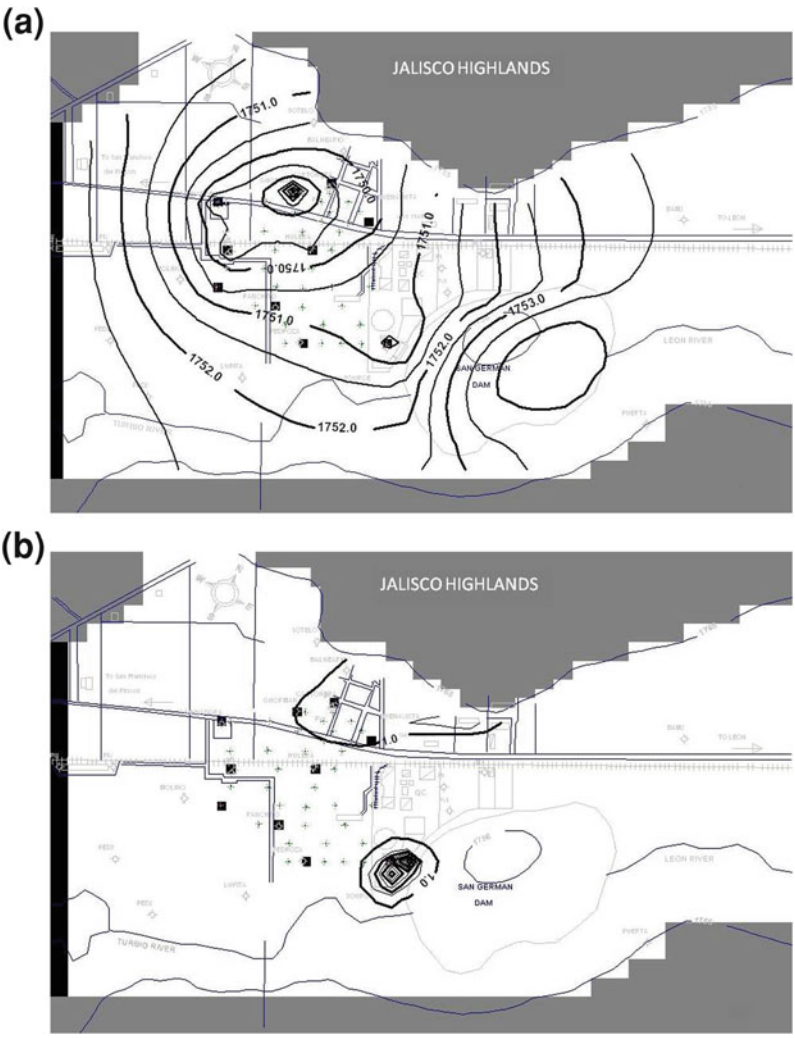

Fig. 7 **a** Distribution of the individual pumping rate for the 10 wells case and the capture zone extension. **b** Cr(VI) [mg/L] concentration distribution after one year. Isolines each 5 mg/L

Brute Forced or MGO coupled directly with GWVistas/USGS MODFLOW, it can diminish the time of cleaning and thereby indicates this approach helps in saving unnecessary costs and analyst time.

References

Ahlfeld DP, Heidari M (1994) Applications of optimal hydraulic control to ground-water systems. J Water Resour Plann Manage 120(3):350–365

Aly AH, Peralta RC (1999) Optimal design of aquifer cleanup systems under uncertainty using a neural network and genetic algorithm. Water Resour Res 35(8):2523–2532

Andricevic R, Kitanidis PK (1990) Optimization of the pumping schedule in aquifer remediation under uncertainty. Water Resour Res 26(5):875–885

Armienta MA (1992) Contribución al estudio de los Mecanismos de Transporte del Cromo en el Acuífero de León Guanajuato. Ph.D. Tesis. Universidad Nacional Autónoma de México, México DF

Armienta A, Rodríguez R (1992) Investigación del impacto ambiental de la dispersión de compuestos de cromo en el área Occidental-Central del Valle de León. Gto Rep Tec il IGF-UNAM, QC, p 107

Armienta A, Rodríguez R, Ceniceros N. Juárez F, Cruz O (1996) Distribution, Origin and Fate of Chromium in soils in Guanajuato, Mexico. Environmental Pollution, Elsevier, Gran Bretaña. 91:391–397

Environmental simulations Inc. (ESI) (2003) Guide to using groundwater vistas. Environmental Simulations Inc., p 242

Harbaugh AW, McDonald MG (1996) User's documentation for MODFLOW-96, an update to the U.S. Geological Survey modular finite-difference ground-water flow model, USGS Open-File Report, pp 96–486

McDonald MG, Harbaugh AW (1988) A modular three-dimensional finite-difference ground-water flow model. Techniques of water resources investigations of the U.S. Geological Survey, Book 6

Moridis GJ, Pruess K (1995) A package of preconditioned conjugate gradient solvers for the TOUGH2 family of codes, report LBL-36235. Lawrence Berkeley Laboratory, Berkeley, Calif

Narasimhan TN, Witherspoon PA (1976) An integrated finite difference method for analyzing fluid flow in porous media. Water Resour Res 12(1):57–64

Peralta RC (2001) Remediation simulation/optimization demonstrations. In: Seo, Poeter, Zheng, Poeter (eds) Proceedings of MODFLOW and other Modeling Odysseys. Pub. IGWMC, pp 651–657

Pollock DW (1989) Documentation of computer programs to compute and display pathlines using results from the U.S. geological survey modular 3-D finite-difference ground-water flow model. USGS Open File Report, pp 89–391

Reyes RG (1998) Parámetros que Controlan La Dispersión de Compuestos de Cromo en un Acuífero de Conductividad Hidráulica Variable. Maestría en Geofísica Tesis. Universidad Autónoma de México, México D.F

Rodríguez R, Armienta A, Villanueva S, Díaz P, González T (1991) Estudio Hidrogeoquímico y Modelación Matemática del Acuífero del Río Turbio para definir las acciones encaminadas a proteger de contaminantes la fuente de abastecimiento de la Cd. de León, Gto. Rep. Técnico il. IGF-UNAM, CNA-SARH. Jun/91, p 140

Rumbaugh JO, Rumbaugh DB (2003) Groundwater vistas V.4. environmental simulations, Inc., p 36

Zheng C (1990) MT3D: a modular three-dimensional transport model for simulation of advection, dispersion and chemical reactions of contaminants in groundwater systems. Report to the U.S. Environmental Protection Agency, p 170

Zheng C, Wang PP (1999) MT3DMS: documentation and user's guide, Report to the US Army Corps of Engineers Waterways Experiment Station. Available at http://hydro.geo.ua.edu

Zheng C, Wang PP (2002) A field demonstration of the simulation-optimization approach for remediation system design. Ground Water 40(3):258–265

Zheng C, Wang PP (2003) MGO: modular groundwater optimizer, documentation and user's guide. Groundwater Systems Research Ltd. and University of Alabama, Tuscaloosa, AL

Gas Cloud Collisions and Stellar Cluster Formation

J. Klapp and G. Arreaga-Garcia

Abstract In this paper we present computer simulations of interstellar cloud collisions that for a given range of initial conditions could favor stellar cluster formation. We first construct a single spherical molecular hydrogen cloud with the Plummer radial density distribution with rigid rotation and an $m = 2$ density perturbation. The isolated cloud collapses into a filament with no sign of fragmentation. We then place two clouds for a head-on collision, and for an oblique collision characterized by an impact parameter that depends on the initial radius of the cloud. The approaching velocity of the clouds is changed from zero up to thirty times the gas sound speed. We have found that for certain values of our parameter space fragmentation into a stellar cluster is possible.

1 Introduction

A key feature observed by astronomers is that newborn stars are clustered in well defined regions of the galaxy. These clusters are embedded in the remaining of giant gas clouds. It has also been noted that both clouds and stellar clusters acquire irregular spatial forms.

J. Klapp (✉)
Instituto Nacional de Investigaciones Nucleares, Km 36.5 Carretera México-Toluca, Ocoyoacac, 52750 Estado de México, México
e-mail: jaime.klapp@inin.gob.mx

G. Arreaga-Garcia
Centro de Investigación en Física, Universidad de Sonora, Blvd. Rosales y Blvd. Encinas, s/n, Col. Centro, Hermosillo, 83000 Sonora, México
e-mail: garreaga@cajeme.cifus.uson.mx

J. Klapp et al. (eds.), *Experimental and Theoretical Advances in Fluid Dynamics*, Environmental Science and Engineering, DOI: 10.1007/978-3-642-17958-7_14,

Giant molecular hydrogen clouds begin the star formation process by the action of several forces: gravitational, pressure, magnetic and centrifugal. The prominent attractive force of gravity is due to the weight of the cloud itself; when it exceeds the other forces the cloud collapses reducing its size and reaching higher densities and temperatures. The pressure force, due to the gas temperature, the centrifugal force caused by rotation, and in many cases the magnetic force, oppose the gravitational collapse. In addition to the mechanical forces mentioned above, the cooling and heating mechanisms play an important role as the clouds exchange energy with their environment.

A successful theoretical model should contain the fragmentation of the progenitor gas cloud during the star formation process, in such a way that the result of the gravitational collapse of the cloud will be a group of stars rather than a single newborn star in isolation. A model containing this type of fragmentation would then be closer to reproducing the results of astronomical observations.

An important question of a model is then to try to understand what physical mechanisms may promote the occurrence of fragmentation and how to capture the essence of such mechanisms in our theoretical models.

We present here the result of a set of simulations aimed to study the collision between two identical molecular gas clouds. We are interested in studying the implications of collisions on the star formation process. We have found that the presence of fragmentation in a system can be a consequence of the occurrence of a collision.

2 The Collision Model

It should be emphasized that cloud collisions may be common in the interstellar medium of a typical galaxy. For example, we know that there are a large number of these progenitor clouds located in the galaxy spiral arms. There are systems of two or more spiral galaxies forming compact groups such that they experience significant tidal forces that can make that the clouds in the same neighborhood of the spiral arm get too close or even collide.

Astrophysicists have tried to construct theoretical models describing the most important aspects of the star formation process and in particular showing fragmentation. During the last two decades, models have relied increasingly on numerical simulations, despite that it is very difficult to incorporate all observed physical elements of the actual star formation process. Then we have to resign ourselves to work with models that are not strictly realistic but rather idealized. However, due to the increasing processing power of supercomputers today, there are good chances that a theoretical model based on numerical simulations can capture some key elements of the star formation process, as we hope to show in this work.

To construct our collision models, let us consider two spherical molecular hydrogen gas clouds, which are face to face with an initial velocity which will

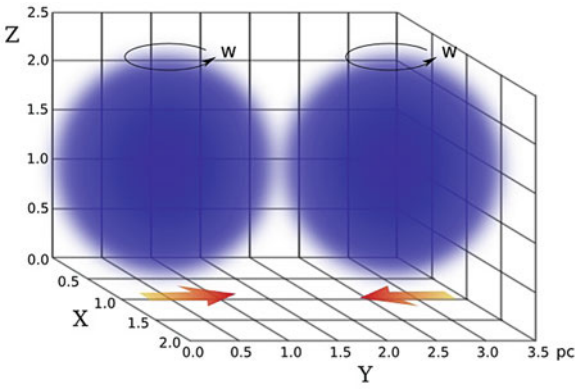

Fig. 1 The initial configuration for the two cloud collision model

make them to collide, as it is illustrated in Fig. 1. It should be noted that each separate cloud rotate as a rigid body around its own vertical axis in the opposite clockwise direction. Certainly, it is a highly idealized initial condition, given the complexity of the interstellar medium, but the advantage of this simple model is that it allows us to capture important dynamic elements such as the occurrence of turbulence in colliding gas clouds and above all, the occurrence of certain types of fragmentation, as we shall see later.

However, to better understand the nature of fragmentation that we observed in the collision models, it is necessary first to study the evolution of the cloud as an isolated system, and then to discuss the result of the two clouds collision model.

The individual spherical molecular hydrogen cloud is constructed so that the radial density follows the Plummer (1911) profile which is given by

$$\rho(r) = \rho_c \left(\frac{R_c}{\sqrt{r^2 + R_c^2}} \right)^{\eta}, \tag{1}$$

where $R_c = 3.0 \times 10^{18}$ cm is the radius of the cloud, $\rho_c = 1.3025 \times 10^{-21}$ gr/cm^3 its central density, and η is a constant. For the models of this paper the clouds are nearly uniform.

In addition we introduce the density perturbation $\rho_1(r) = \rho\,(r)\,(1 + \text{amp} \cos \text{m}\phi)$, where amp is the amplitude that we take to be 0.5 and ϕ the azimutal angle.

3 The Collapse of the Isolated Cloud

Consider a spherical gas cloud, rotating around its vertical axis with a constant angular velocity, as illustrated in Fig. 2. As we indicated, the force of gravity pulls all matter in the cloud toward the center while the pressure force pushes the gas out. The rotation of the cloud causes the appearance of a centrifugal force toward

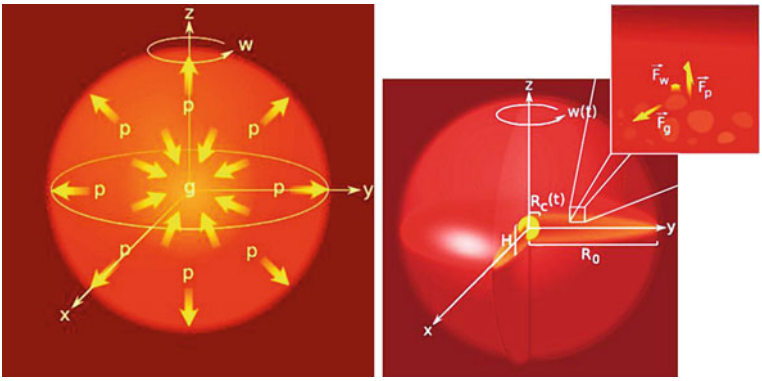

Fig. 2 The isolated cloud model (*left panel*) and accretion disk that forms in the equatorial plane of the cloud (*right panel*)

the surface at any latitude plane (any plane in the area parallel to the equatorial plane). Thus, the acceleration of every gas element is composed of two contributions: the first due to the gravitational acceleration directed towards the center of the cloud, and the second one due to the pressure of the gas and the centrifugal acceleration toward the surface.

These accelerations are co-linear only in the equatorial plane while at the poles are perpendicular. For this reason, the total acceleration is greater at the equator than in regions near the polar circles. Moreover, because there are no external forces or torques acting on the cloud, the angular momentum is conserved. Then as a consequence of the initial rotation of the cloud and the angular momentum conservation, the cloud begins to flatten at the poles toward the equator, so that it forms a flattened disk that spins faster than the rest of the gas that is still in the spherical cloud. This region is called an accretion disk because it keeps falling under the influence of the gravity force.

We use the Gadget2 computer program (Springel 2005) for solving the Navier–Stokes equations including the self gravitational interaction of the gas cloud. The Gadget2 code is based on the Smoothed Particle Hydrodynamics technique (SPH). To display the results of the simulations we use a color scale to show the density distribution of a slice of cloud parallel to the equatorial plane as seen from a high position on the axis of rotation. For example, according to this color density scale, yellow indicates high density regions, green and red intermediate densities and finally the blue correspond to low-density regions in the cloud. It should be noted that the length scale that appear in the axes of each panel are normalized with the initial radius of the cloud.

For the isolated cloud in Fig. 3 we show isodensity contour curves for a time near the beginning of the simulation and after $5.7\tau_{\text{ffc}}$, where the free fall time unit is $\tau_{\text{ffc}} = 1.84$ Myr. The dense gas is contained in about 10% of the initial radius of the cloud and is concentrated in the central region of the accretion disk. We can see that the denser gas forms a continuous elongated filament that shows no signs

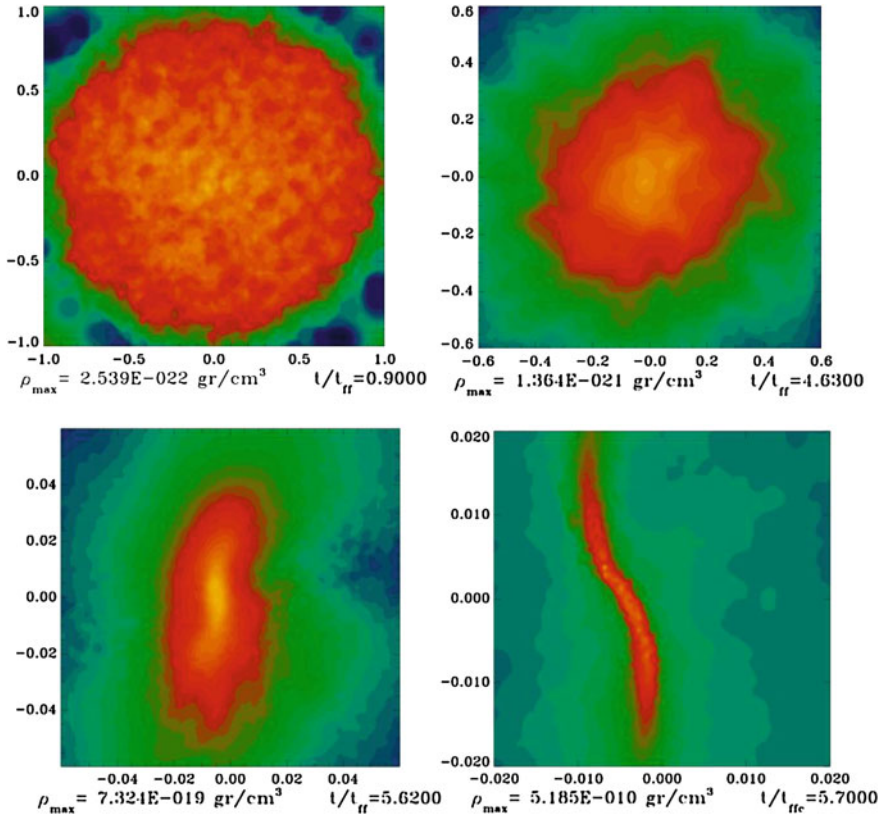

Fig. 3 Isodensity colored curves for the isolated cloud in the first and last stages of evolution, shown in the *left* and *right panels*, respectively

of being next to fragment into any part of the filament. This tendency to form needle-like thin filaments has previously been observed in simulations of gravitational collapse of clouds with a uniform radial density profile.

4 Results of the Collision

In a collision between two gas clouds the most important parameters are the impact velocity and the impact arm. The magnitude of these parameters strongly determines the collision outcome. For example, with a high impact velocity, the system ends dispersing the entire mass of the cloud because gas jets flow in directions parallel to the collision zone. On the other hand, a zero-impact arm would correspond to a purely frontal collision while a nonzero value for this parameter indicates an oblique collision.

We have explored a range of values for the magnitude of the impact velocity and the impact arm which are appropriated to avoid the total dispersion of the system, and in this way favor that the collapse occurs further and eventually lead to proto star formation. This is the kind of collision models in which we are primarily interested in this research.

The approaching velocities of our collision models vary from 2.46 to 30.78 Mach and the clouds are initially almost in contact, see Fig. 1. Then just after the start of the simulations, the clouds suffer a collision and the first effect is that they are compressed and a shock front is formed that propagates to the two clouds. The artificial viscosity transforms kinetic energy into heat that is radiated away in a very short timescale and we can assume that the shock and the clouds remain isothermal. During the collision process a slab of material is formed along the shock front. The clouds then expands but eventually collapses as will be later described. The shocked slab which is formed as a result of the supersonic collision is susceptible of having various instabilities which has been studied by Vishniac (1983) for the linear regime and by Vishniac (1994) for the non-linear case. For the present work the relevant ones are the shearing and gravitational instabilities. The shearing instability dominates at low density while the gravitational one takes over for densities above a critical density of about

$$\rho_{shear} \sim 7.86132 \times 10^{-22} \left(\frac{\eta}{pc}\right) \left(\frac{\lambda_{NTSI}}{pc}\right) \left(\frac{T}{K}\right) \mathrm{gr\,cm^{-3}},$$

where η is the amplitude of the perturbation, λ_{NTSI} is the length of the unstable mode and T the temperature (Heitsch et al. 2008). Of the shearing instabilities the main ones are the non-linear thin shell instabilities (NTSI) and the Kelvin–Helmholtz (KH) instability. The NTSI instability is expected to occur in the shocked slab just after the cloud collision, and the non-linear bending and breathing modes could also be present.

When the initial contact occurs between particles of different clouds, there is a density increase in the interface region, in which particles form knots and vortices, see Fig. 4. The magnitude of the density increase obviously depends on the impact velocity and we must mention that it is a transient behavior, because the density decreases after passing the initial impact stage. The effect of gravity is again evident by causing the clouds to begin its collapse separately in its central regions, see Fig. 5. At this time, the temporal evolution of the peak density detected in the cloud shows an increasing trend, as can be seen in Fig. 4, where we have plot the peak density against another free fall time scale, given by $\tau_{\mathrm{ffc}} = 5.22$ Myr.

It is interesting to note that one effect of the collision is to promote the occurrence of fragmentation in the central strand of each of the clouds, as seen in the Fig. 6. This observation should be contrasted with the result of the collision of the cloud as an isolated system (see Fig. 3), which never shows any tendency of fragmentation in the central filamentary region.

The result just enunciated above, that the collision favors fragmentation is very important in the area of star formation, because each of the dense knots forming

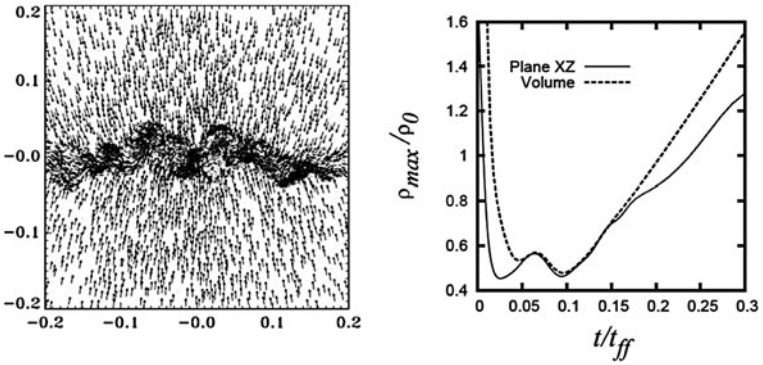

Fig. 4 Velocity field of particles located in the interface region of the two colliding clouds (*left panel*) and its transient increases of the peak density (*right panel*)

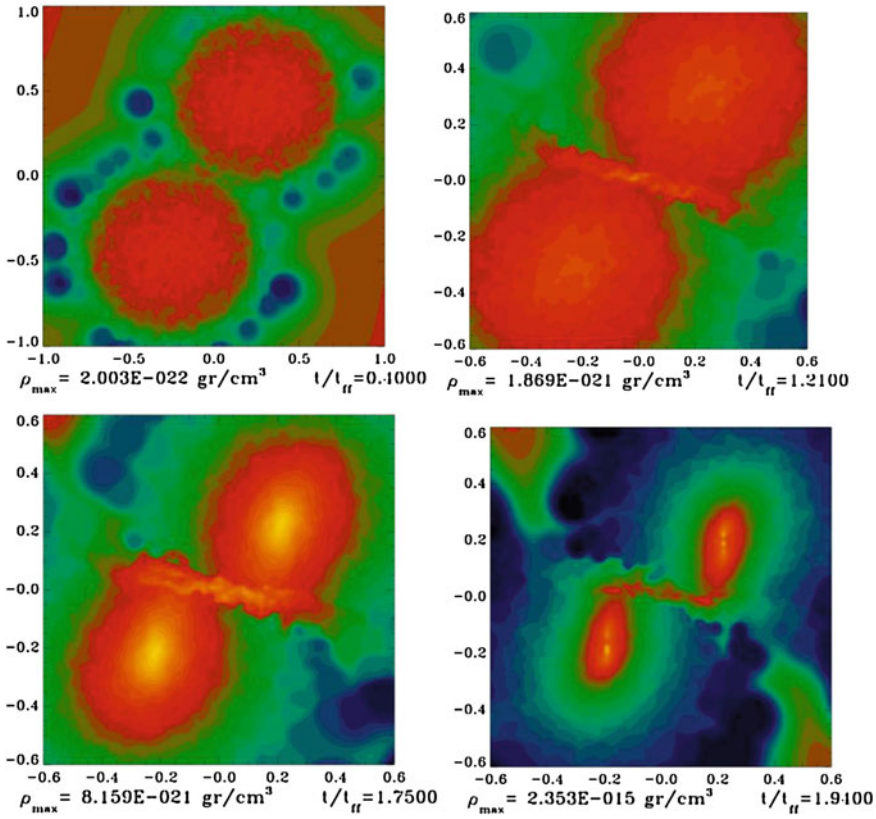

Fig. 5 Isodensity curves showing the result of one of the oblique collision model in the first (*left panel*) and last (*right panel*) states of evolution observed in the simulation

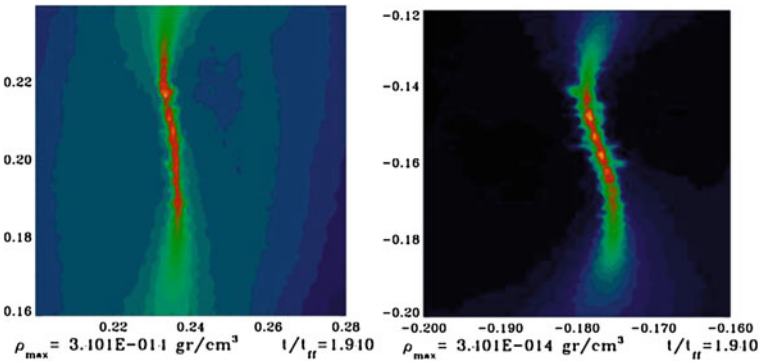

Fig. 6 Zoom in of the central region of the clouds in the collision model of Fig. 5

along filaments during cloud collisions could eventually form proto-stars. Since it is possible that more gas condensations are formed in the bridge connecting the clouds, the numerical simulation will produce a complex distribution of proto stars clustered in a binary group formed in the filaments, in addition to those proto stars formed in the bridge.

5 Conclusions

Studies using numerical simulations of gravitational collapse of clouds as isolated and colliding clouds have a long a history of nearly three decades. The early simulations predicted that the accretion of gas in the galactic disk (a collision between a gas cloud and a slab of gas) could have an enormous influence on the star formation process, and at the same time, will inherit a very peculiar physical structure for the interstellar gas. In fact, recent astronomical observations have shown some elongated gas structures in the Orion Molecular Cloud, a type of structure that appears to be common throughout the Galaxy interstellar medium.

In this paper we have considered collisions between clouds as an alternative physical mechanism for promoting the formation of complex stellar systems.

Today, we are in a position to follow the collapse of the cloud to densities in a range from 10^{-18} to 10^{-10} gr/cm^3, a peak density in which we can identify the clumps of denser gas as proto-stars. We know that some of the dynamic characteristics of a proto-star will be inherited by the real star to be formed once the process of gravitational collapse will continue further until peak densities of the order of 10^{-1} g/cm^3 are reached. Although we have been limited to consider only very idealized collision systems, we were able to capture and display some of the essential features of the collision process. For example, we must mention that we have observed some kind of fragmentation in the filaments, which is a direct

consequence of the occurrence of the collision. This result can be considered as evidence that collisions can have a major influence on the process of star formation as was thought before.

References

Heitsch F, Hartmann LW, Slyz AD, Devriendt JEG, Burkert A (2008) The Astrophysical J 674:316
Plummer HC (1911) MNRAS 71:460
Springel V (2005) MNRAS 364:1105
Vishniac ET (1983) The Astrophysical J 274:152
Vishniac ET (1994) The Astrophysical J 428:186

Collapse and Fragmentation of Gaussian Barotropic Protostellar Clouds

F. Gómez-Ramírez, J. Klapp, Jorge L. Cervantes-Cota, G. Arreaga-García and D. Bahena

Abstract We examine the problem of the collapse and fragmentation of molecular clouds with a Gaussian density distribution with high resolution, double precision numerical simulations using the GADGET-2 code. To describe the thermodynamic properties of the cloud during the collapse—to mimic the rise of temperature predicted by radiative transfer—we use a barotropic equation of state that introduces a critical density to separate the isothermal and adiabatic regimes. We discuss the effects of this critical density in the formation of multiple systems. We confirm the tendency found for Plummer and Gaussian models that if the collapse changes from isothermal to adiabatic at earlier times that occurs for the models with a lower critical density, the collapse is slowed down, and this enhances the fragments' change to survive. However, this effect happens up to a threshold density below which single systems tend to form. On the other hand, by

F. Gómez-Ramírez
Facultad de Ciencias, Universidad Autónoma del Estado de México,
El Cerrillo Piedras Blancas, C.P. 5200 Estado de México, Mexico

J. Klapp (✉) · J. L. Cervantes-Cota
Instituto Nacional de Investigaciones Nucleares,
Carretera México-Toluca S/N La Marquesa, 52750
Ocoyoacac, C.P., Estado de México, Mexico
e-mail: jaime.klapp@inin.gob.mx

J. L. Cervantes-Cota
Berkeley Center for Cosmological Physics, LBNL, Berkeley,
CA 94720, USA

G. Arreaga-García
Centro de Investigación en Física de la Universidad de Sonora, A.P. 14740,
83000 Hermosillo, C.P., Sonora, Mexico

D. Bahena
Astronomical Institute of the Academic Sciences, Bočmí II 1401,
14130 Praha 4, Czech Republic

J. Klapp et al. (eds.), *Experimental and Theoretical Advances in Fluid Dynamics*,
Environmental Science and Engineering, DOI: 10.1007/978-3-642-17958-7_15,

setting a bigger initial perturbation amplitude, the collapse is faster and in some cases a final single object is formed.

1 Introduction

The protostellar objects that begin their main sequence and pre-main sequence are mainly distributed in binary and multiple systems that suggests they were formed during the process of collapse and fragmentation of molecular clouds with dense cores and gas envelopes, see Sigalotti and Klapp (2001a), Tohline (2002) and references therein. In recent years several authors have considered different realizations of molecular clouds to study their collapse and fragmentation. Although most fragmentation calculations apply to initially uniform conditions, see for instance Bodenheimer et al. (2000), it is clear from the observations that molecular cloud cores are centrally condensed (Ward-Thompson 2002; André et al 1998; Motte et al. 1998). Thus, a number of collapse models starting from centrally condensed, Gaussian density profiles have also been made. A particular computationally demanding isothermal, Gaussian cloud model was first calculated in Boss (1991), and thereafter recalculated by other authors as a further test case to check both the likelihood of fragmentation during the isothermal collapse phase and the reliability of the numerical code results (Burkert and Bodenheimer 1996; Truelove et al. 1997; Boss 1998; Boss et al. 2000; Sigalotti and Klapp 2001b, c).

So far the great majority of this research has concentrated upon the early phases of star formation, when the collapse is dynamical, first isothermal and then non-isothermal. However, precise knowledge of the dependence of temperature on density at the transition from isothermal to nonisothermal collapse requires solving the radiative transfer problem coupled to a fully self-consistent energy equation. However, the full non-isothermal computation represents a severe computational burden imposed by solving the radiative transfer equations at high spatial resolution, even in the Eddington approximation. Therefore, it has been common to use instead a simple barotropic equation of state (Boss et al. 2000) that clearly simplifies the computational problem and it turns out to be a good approximation for the dynamical collapse of the molecular clouds, see Arreaga-García et al. (2007) and Arreaga et al. (2008). In the present work, a barotropic equation of state is assumed to simulate the transition from isothermal to adiabatic collapse. The motivation of this study is to investigate the sensitivity of fragmentation to the effects of thermal retardation by varying the value of the critical density at which nonisothermal heating is assumed to begin. In Arreaga-García et al. (2007) and Arreaga et al. (2008) it is studied the evolution of a Gaussian density profile, and found that by diminishing the critical density it enhances the fragmentation. A similar result was found for Plummer models in Arreaga-García et al. (2010).

The present work is a continuation of the analysis in Arreaga-García et al. (2007) and Arreaga et al. (2008) in which we employ a Gaussian density profile and perform the same type of numerical computations but now using double

precision in the GADGET-2 code. Particularly, we study the effect of varying the critical density of the barotropic equation of state in the collapse and fragmentation of the molecular protostar. We also analyze the effect to increasing the initial perturbation amplitude.

2 Initial Conditions and Collapse Models

According to astronomical observations, the regions from which stars are formed consist basically of molecular hydrogen clouds at a temperature of ~ 10 K. Therefore, the ideal equation of state is a good approximation to account for the thermodynamics of the gas in these clouds. The cloud models are based on the standard isothermal test case, as in the variant considered in Burkert and Bodenheimer (1993). However, once gravity has produced a substantial contraction of the cloud, the opacity increases, the collapse changes from isothermal to adiabatic and the gas begins to heat. To include this rise in temperature into our calculations, we use the barotropic equation of state proposed in Boss et al. (2000).

In order to correctly describe the non-isothermal regime, one needs to solve the radiative transfer problem coupled to the hydrodynamic equations, including a fully self-consistent energy equation to obtain a precise knowledge of the dependence of temperature on density. The implementation of radiative transfer has already been included in some mesh-based codes. In SPH, the incorporation of radiative transfer has in general not been very satisfactory, perhaps with the exception of reference (Whitehouse and Bate 2006), in which they used the f-limited diffusion approximation to model the collapse of molecular cloud cores. These authors suggested that there are important differences in the temperature evolution of the cloud when radiative transfer is properly taken into account.

However, after comparing the results of the simulations performed by Arreaga-García et al. (2007) and Arreaga et al. (2008) with those of reference Whitehouse and Bate (2006) for the uniform density cloud, it is concluded that the barotropic equation of state in general behaves quite well and that we can capture the essential dynamical behavior of the collapse. The simulations in this work are consequently carried out using the following barotropic equation of state:

$$p = c_{\mathrm{iso}}^2 \rho + K \rho^{\gamma}, \tag{1}$$

where γ is the adiabatic exponent in the opacity thick regime and K is a constant set by $K = c_{\mathrm{iso}}^2 \rho_{\mathrm{crit}}^{1-\gamma}$, where ρ_{crit} defines the critical density above which the collapse changes from isothermal to adiabatic, and for a molecular hydrogen gas the ratio of specific heats is $\gamma = 5/3$, because we only consider translational degrees of freedom.

With the above prescriptions, the local sound speed becomes

$$c = c_{\rm iso}\left[1 + \left(\frac{\rho}{\rho_{\rm crit}}\right)^{\gamma-1}\right]^{1/2}, \tag{2}$$

so that $c \approx c_{\rm iso}$ when $\rho \ll \rho_{\rm crit}$ and $c \approx C_{\rm ad} = \gamma^{1/2} c_{\rm iso}$.

The molecular cloud collapse simulations in this work begin with initial conditions in accordance to the thermodynamic model proposed in Burkert and Bodenheimer (1993). Accordingly, the models start with a spherical cloud of mass $M = 1\,M_{\odot}$, radius $R = 4.99 \times 10^{16}$ cm ~ 0.016 pc, and at a temperature $T = 10$ K. The initial model is composed by an ideal gas with an average molecular weight $\mu \sim 3$. We have chosen the initial sound speed $c_{\rm iso}$ and angular velocity ω_0 in such a way that for all models the initial ratio of thermal and rotational energies to gravitational energy are such that $\alpha = E_{\rm therm}/|E_{\rm grav}| \sim 0.26$ and $\beta = E_{\rm rot}/|E_{\rm grav}| \sim 0.16$. The gas isothermal sound speed is $c_{\rm iso} \sim 1.90 \times 10^4\,{\rm cm\,s^{-1}}$, and the average free fall time is 5.10×10^{11} s. Additionally, we impose a small perturbation to the density profile of the following form:

$$\rho = \rho_0[1 + a\cos(m\phi)], \tag{3}$$

where m is an integer number, ϕ the azimuthal angle around the z-axis, and a is the perturbation amplitude.

The chosen density profile is Gaussian with the above-mentioned initial conditions, as in Arreaga-García et al. (2007) and Sigalotti and Klapp (2001a):

$$\rho(r) = \rho_c \exp\left[-\left(\frac{r}{b}\right)^2\right], \tag{4}$$

where $\rho_c = 1.7 \times 10^{-17}\,{\rm g\,cm^{-3}}$ is the initial central density and $b \approx 0.578R$ is a length chosen such that the density is 20 times smaller there. On the other hand, solid-body rotation is assumed at the rate of $\omega_0 = 1.0 \times 10^{-12}\,{\rm s^{-1}}$.

3 Numerical Methods

The computations of this work were performed using the parallel code GADGET-2, which is described in full in Springel (2005). The code is suitable for studying isolated, self-gravitating systems with high spatial resolution. The code is based on the tree-PM methods for computing the gravitational forces and on standard SPH methods for solving the 3D Euler hydrodynamics equations. For a review on the theory and applications of SPH we refer the reader to Monagan (2005).

In order to set up the initial particle distribution, we first define a Cartesian box with sides equal to twice a specified radius $R_b \gtrsim R = 4.99 \times 10^{16}$ cm, and with its geometrical center coinciding with the origin ($x = y = z = 0$) of a Cartesian

coordinate system. The box is then subdivided into regular cubics cells of volume $\Delta^3 = \Delta x \Delta y \Delta z$ each. The spherical cloud is then copied within the box by placing an SPH particle in the center of each cell at distances $d \leq R$ from the origin, so that the region outside the sphere is empty. A little amount of disorder is added to the regular distribution of particles by shifting each particles a distance $\Delta/4$ from its cell-center location and along a specified direction, which is chosen randomly among the three Cartesian axes. We defined the mass of particle i at location (x_i, y_i, z_i) to be $m_i = \rho(x_i, y_i, z_i)\Delta^3$, where

$$\rho(x_i, y_i, z_i) = \rho_c \exp\left[-\frac{x_i^2 + y_i^2 + z_i^2}{b^2}\right]. \tag{5}$$

Solid-body rotation about the z-axis is assumed in a counter clockwise sense by assigning to particle i an initial velocity given by $v_i = (\omega_0 x_i, -\omega_0 y_i, 0)$. Finally, the bar mode density perturbation given by Eq. 3 applied by modifying the mass of particle i according to $m_i \rightarrow m_i[1 + a\cos(m\phi_i)]$, where ϕ_i denotes the azimuthal position of that particle. The computations were performed in the parallel cluster of the National Institute of Nuclear Research-Mexico, equipped with 28 AMD Quad-core (64 bits) Opteron Barcelona processors.

4 Results

In this section we present the results obtained using the GADGET-2 code of the collapse and fragmentation of Gaussian molecular clouds. The collapse of the Gaussian cloud first calculated in Boss (1991), later by other authors (Burkert and Bodenheimer 1996; Truelove et al. 1997; Boss 1998; Sigalotti and Klapp 2001b, c; Arreaga-García et al. 2007) using high spatial resolution, and in the present work we perform the same computations as in Arreaga-García et al. (2007), but adding double precision and using 10^7 SPH particles in each simulation.

We present four different cases for the barotropic collapse with the parameters as shown in Table 1. The results are illustrated with iso-density contour plots for a slide at the equatorial plane of the cloud in Figs. 1, 2, 3, and 4. The bar located at the bottom of the plots shows the $\log_{10}$ density range at a time t and normalized with the initial central density ρ_c. A color (grey) scale is then associated with the value of $\log_{10}$. For instance, the color scale uses yellow (bright) to indicate higher densities, blue (dark) for lower densities, and green and orange (grey) for intermediate densities.

The free fall time $t_{ff} \approx \sqrt{3\pi/(32G\rho_c)}$ sets a characteristic time scale for the collapse of protostellar clouds which is given in terms of the central density and it is the same for all models, see for instance (Arreaga-García et al. 2010).

The aim of the present models is to explore, using double precision variables, the sensibility of fragmentation to both the effect of thermal retardation due to nonisothermal heating that is controlled by the critical density, and the effect to increase of perturbation amplitude.

Table 1 Gaussian collapse models

Model	$\rho_{\text{crit}}(\text{g cm}^{-3})$	Amplitude a	Final outcome
G6A1	5×10^{-12}	0.1	Binary
G6B1	5×10^{-14}	0.1	Quadruple
G6C1	5×10^{-15}	0.1	Single
G6B5	5×10^{-14}	0.5	Single

The model types are explained as follows: the letter G refers to Gaussian, the number 6 refers to ten millions particles, the letters A, B, and C distinguish among the different critical densities, and finally the last digit refers to the amplitude of the initial perturbation

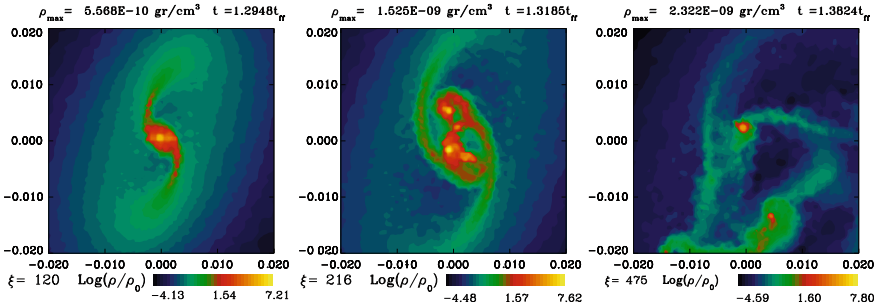

Fig. 1 Iso-density contour plots at the equatorial plane of model G6A1 for three different times

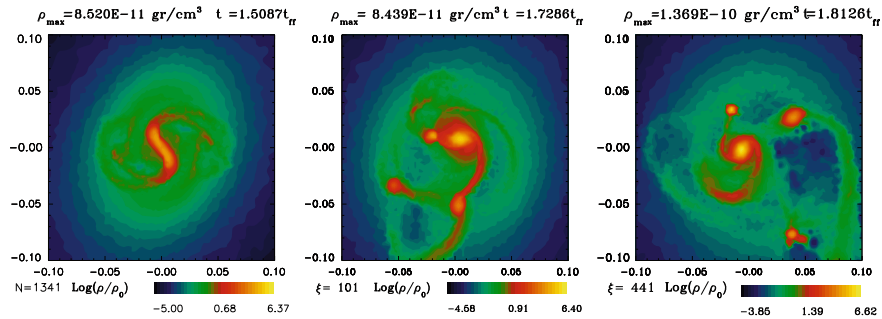

Fig. 2 Iso-density contour plots at the equatorial plane of model G6B1 for three different times

The construction of the initial conditions ensures that the collapse initial stage is similar for all models considered here. The initial phase of the collapse proceeds in such a way that the material falls down to the rotation plane, while material near the central midplane undergoes a weak expansion perpendicular to the rotation axis, causing the formation of two overdense blobs from the initial $m = 2$ perturbation seed. At about the end of the first free-fall time, the expansion stops and the middle region begins to collapse, the blobs fall toward the center and merge to form a prolate structure. By this time, the overall cloud has already been compressed into a flat disk with an inner bar that begins to rotate.

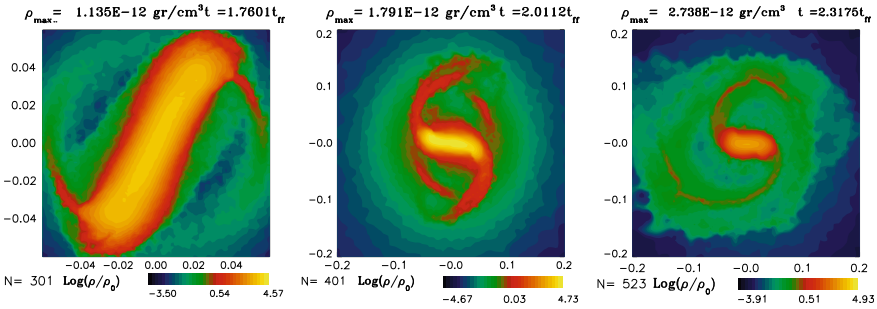

Fig. 3 Iso-density contour plots at the equatorial plane of model G6C1 for three different times

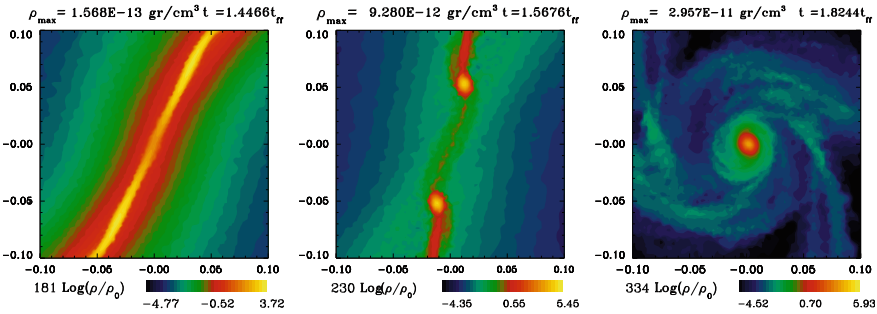

Fig. 4 Iso-density contour plots at the equatorial plane of model G6B5 for three different times

We begin the discussion with models G6A1, G6B1, seen in Figs. 1a and 2. The model G6A1 collapses faster than the corresponding single precision model reported in Arreaga-García et al. (2007), but the overall dynamics looks similar. We now proceed to decrease the critical density, as shown in model G6B1. We find however important differences in comparison to Arreaga-García et al. (2007), which reports as an end product a binary system formed by a transient quadrupole system, but we obtain as a final product a stable quadrupole system. The fact that by diminishing the critical density the fragmentation enhances, found for Gaussian (Arreaga-García et al. 2007; Arreaga et al. 2008) and Plummer models (Arreaga-García et al. 2010), seems to be reproduced for models G6A1 and G6B1. However, by diminishing even more the critical density in model G6C1, see Table 1, the collapse and fragmentation is slowed down and the fragmentation is less favored, as seen in Figs. 2 and 3.

The model G6B5, shown in Fig. 4, has a bigger initial perturbation amplitude that provokes that systems collapse earlier to form a filamentary structure, which evolves to a transient binary system that later collapses in a single system. The final system ejects significant amount of gas out of the core. In comparison the same model but with a smaller amplitude, model G6B1, forms a stable quadrupole system.

5 Conclusions

In this work, we have followed the early phases of cloud collapse and fragmentation up to the formation of the proto stellar core using the GADGET-2 code with high spatial resolution and double precision, using 10^7 SPH particles. The initial conditions for the cloud models are chosen to be the standard isothermal test case, as in the variant considered in Burkert and Bodenheimer (1993), but for a centrally condensed, Gaussian cloud, that was first treated in Boss (1991), and further considered by other authors, e.g. Arreaga-García et al. (2007). The main results are summarized as follows:

By augmenting from single to double precision, the collapse happens earlier and the number of end products augments, as seen in our simulations in comparison the same models in Arreaga-García et al. (2007).

On the other hand, we find that the effect of diminishing the critical density of the barotropic equation of state, provokes the collapse to slow down, and this enhances the fragments' change to survive. However, this effect happens up to a threshold density, as seen in our simulation G6C1, where considered a low critical density, $\rho_c = 5 \times 10^{-15}\,\mathrm{g/cm^3}$, and a single system was formed.

Moreover, models with a bigger initial perturbation amplitude provoke that systems collapse earlier, and in some cases, in the form of a filamentary structure which evolves to a transient binary system that later collapses in a single system.

Acknowledgments J.L.C.C. thanks the Berkeley Center for Cosmological Physics for hospitality, and gratefully acknowledges support from a UC MEXUS-CONACYT Grant, and a CONACYT Grant No. 84133-F.

References

André P, Bacmann A, Motte F, Ward-Thompson D, (1998) In: Ossenkopf V, Stutzki J, Winnewisser G (eds) The physics and chemistry of the interstellar medium. GCA-Verlag, Zermatt, p 241
Arreaga-García G, Klapp J, Sigalotti LD, Gabbassov R (2007) ApJ 666:290
Arreaga G, Saucedo J, Duarte R, Carmona J (2008) Rev Mex Astron Astrofis 44:259
Arreaga-García G, Klapp Escribano J, Gómez-Ramírez F (2010) A&A 509:A96
Bodenheimer P, Burkert A, Klein RI, Boss AP (2000) In: Mannings VG, Boss AP, Russell SS (eds) Protostars and planets IV. University of Arizona Press, Tucson
Boss AP (1991) Nature 351:298
Boss AP (1998) ApJ 501:L77
Boss AP, Fisher RT, Klein R, McKee CF (2000) ApJ 528:325
Burkert A, Bodenheimer P (1993) MNRAS 264:798
Burkert A, Bodenheimer P (1996) MNRAS 280:1190
Monagan JJ (2005) Rep Prog Phys 68:1703
Motte F, André P, Neri R (1998) A&A 336:150
Sigalotti LD, Klapp J (2001) Intern J Mod Phys D 10:115
Sigalotti LD, Klapp J (2001) A&A 378:165

Sigalotti LD, Klapp J (2001c) In: Macias A, Cervantes J, Laemmerzhal K (eds) Exact solutions and scalar field in gravity: recent developments. Kluwer, Dordrecht, p 223
Springel V (2005) MNRAS 364:1105
Tohline JE (2002) Annu Rev Astron Astrophys 40:349
Truelove JK, Klein RI, McKee CF, Holliman JH, Howell LH, Greenough JA (1997) ApJ 489:L179
Ward-Thompson D (2002) Science 295:76
Whitehouse SC, Bate MR (2006) MNRAS 367:32

A Hydrodynamic Model of Galactic Halos

M. A. Rodríguez-Meza, Alberto Hernández-Almada and T. Matos

Abstract The question about the existence of dark matter in the Universe is nowadays an open problem in cosmology. In this work we will present how we can build a hydrodynamic model in order to study dark matter halos of galaxies. The theoretical general idea is to start with the Einstein–Hilbert Lagrangian in which we have added a complex scalar field minimally coupled to the geometry. Then, by making variations of the corresponding action we come up with the Einstein field equations for the geometry and a Klein–Gordon equation for the scalar field. This set of coupled partial differential equations is non-linear. If we assume that dark matter halos can be described in the Newtonian limit we obtain a set of equations known as Schrödinger–Poisson equations. This set of equations can be written in the form of Euler equations for a fluid by making a Madelung transformation, where the self-interaction potential of the fluid is present. Also, there appears a quantum-like potential which depends non-linearly on the density of the fluid. We present results on the Jeans' instability of the fluid model for dark matter and show how the physical parameters of the model can be determined, in particular, we compute the mass of the scalar field.

M. A. Rodríguez-Meza (✉)
Instituto Nacional de Investigaciones Nucleares, Departamento de Física,
Apdo. Postal 18-1027, 11801 México D.F., Mexico
e-mail: marioalberto.rodriguez@inin.gob.mx

A. Hernández-Almada · T. Matos
Departamento de Física, Centro de Investigación y de Estudios Avanzados del IPN,
A.P. 14-740, 07000 México, Mexico

J. Klapp et al. (eds.), *Experimental and Theoretical Advances in Fluid Dynamics*,
Environmental Science and Engineering, DOI: 10.1007/978-3-642-17958-7_16,

1 Introduction

During the last decades we have witnessed a revolution of the human knowledge due to the appearance of two fundamental questions in modern cosmology, both related to structure formation in the Universe. One is the dark matter problem and the other is the dark energy problem. The former was made evident from several observations, in particular, from measurements of the rotation curve of spiral galaxies where the visible matter content is not enough to account for the observed rotation curves of the stars or of the gas particles in the galaxies outskirts. Also, observations tell us that the Universe appears to be expanding at an increasing rate. One way to explain this behavior is to introduce a constant in the Einstein field equations, the so called cosmological constant, that acts in opposite way to gravity. This constant has an associated constant density. General models to account for the accelerated expansion of the Universe generalize the case of the cosmological constant and consider that density is varying with time. In general, these models are known as dark energy models.

A very successful model of dark matter is called cold dark matter (CDM) where the halos of galaxies or clusters of galaxies are composed of collisionless particles that during recombination era were non-relativistic. The predictions of the CDM model are in concordance with observations at large scales ($\sim$Mpc). However, CDM fails at small scales ($\sim$kpc), for example, it predicts that the density profile in the origin of the dark matter halo diverges as $1/r$ and observations of galaxies show that the density is almost flat at the origin. This problem is called the cuspy problem. In addition, the CDM does not answer the fundamental question: What is dark matter? There are several candidates to explain dark matter in the Universe. One possibility is that dark matter is composed of one kind of supersymmetric particles called weakly interacting massive particles (WIMP's). But this particles have not been detected so far.

In this work we are proposing a hydrodynamical model to explain the dark matter component of the Universe. The model considers that a scalar field can be the dark matter in the Universe. Then by introducing this field in the corresponding terms in the Einstein field equations and taking the weak field limit —valid to study halos of galaxies—we come up with the equation that this field satisfies, this equation together with the Poisson equation that result from Einstein equations for the geometry in the Newtonian limit, are called Schrödinger–Possion equations and they govern the scalar field and the standard Newtonian potential with the source given in terms of the scalar field. This is our main set of equation that we have to solve to model dark matter halos of galaxies or cluster of galaxies. In order to obtain the hydrodynamical model, we transform this set of equations into an Euler system type of equations where the "fluid" fields are a density and a velocity field both functions of the scalar field. Then, we linearize this set of equations to study the Jeans' instability of this scalar fluid which serves us to obtain the mass of the scalar field.

This paper is organized as follows: In Sect. 2 we present the theoretical framework that starts by writing a general Einstein-Hilbert action. In Sect. 3 we present the hydrodynamical model. In Sect. 4 we study the Jeans' instability and

based on this analysis we compute the mass of the scalar field. Finally, in Sect. 5 we give our conclusions.

2 Theoretical Framework

Our hydrodynamical dark matter model is constructed starting with the Einstein–Hilbert action, where we have a complex scalar field, ϕ, coupled minimally with the geometry,

$$S[g_{\mu\nu},\phi]=\int d^4x\frac{1}{\kappa}\sqrt{-g}\mathscr{R}+\int d^4x\mathscr{L}_m, \tag{1}$$

where κ is a constant used to recover the Newtonian limit, $g=\det(g_{\mu\nu})$ is the determinant of the spacetime metric $g_{\mu\nu}$, $\mathscr{R}$ is the Ricci curvature scalar. The first term in Eq. 1 gives the usual Einstein field equations of general relativity in vacuum. The second term in the equation above is the matter term responsible to curve the spacetime. In our case we will take the Lagrangian density associated to the complex scalar field given by

$$\mathscr{L}_m=-\frac{1}{2}\sqrt{-g}\left[\gamma^2\nabla^\mu\phi\nabla_\mu\phi^*+m^2c^2\phi\phi^*\right]. \tag{2}$$

where ∇_μ is the covariant derivative compatible with the spacetime metric, γ is a constant, m is the scalar field mass and c is the speed of light. The first term in this Lagrangian is the kinetic term and the second is the contribution of the scalar field potential given by $V(\phi)=(1/2)m^2c^2\phi\phi^*$. Applying a variational principle we make the variations of Eq. 1 with respect to the metric $g_{\mu\nu}$ to obtain the field equations for the spacetime geometry,

$$\mathscr{G}_{\mu\nu}\equiv\mathscr{R}_{\mu\nu}-\frac{1}{2}g_{\mu\nu}\mathscr{R}=\frac{\kappa}{2}T_{\mu\nu}, \tag{3}$$

where $\mathscr{G}_{\mu\nu}$ is the Einstein tensor, $\mathscr{R}_{\mu\nu}$ is the Ricci tensor, and $T_{\mu\nu}$ is the energy–momentum tensor given by

$$T_{\mu\nu}=\gamma^2\nabla_{(\mu\phi\nabla_\nu)}\phi^*-\frac{1}{2}g_{\mu\nu}\left[\gamma^2\nabla^\alpha\phi\nabla_\alpha\phi^*+m^2c^2\phi\phi^*\right], \tag{4}$$

where $\nabla_{(\mu\phi\nabla_\nu)}\phi^*=(\nabla_\mu\phi\nabla_\nu\phi^*+\nabla_\nu\phi\nabla_\mu\phi^*)/2$. We should mention that the Einstein tensor and the energy–momentum tensor are symmetric, i.e., $\mathscr{G}_{\mu\nu}=\mathscr{G}_{\nu\mu}$ and $T_{\mu\nu}=T_{\nu\mu}$.

Next, in order to obtain the equation of motion of the scalar field ϕ, we take the variation of the action Eq. 1 with respect to ϕ^*,

$$\delta S[\phi^*]=\frac{1}{2}\int d^4x\sqrt{-g}\left(\gamma^2g^{\mu\nu}\nabla_\mu\phi\delta\nabla_\nu\phi^*+m^2c^2\phi\delta\phi^*\right). \tag{5}$$

Considering that the condition $\delta\partial_v\phi^* = \partial_v\delta\phi^*$ is valid and integrating by parts we obtain,

$$\begin{aligned}\delta S[\phi^*] = &-\int d^4x\nabla_v\left(\gamma^2\sqrt{-g}g^{\mu\nu}\nabla_\mu\phi\delta\phi^*\right)\\ &+\int d^4x\delta\phi^*\sqrt{-g}\left(\gamma^2\nabla_\mu(g^{\mu\nu}\nabla_v\phi) - m^2c^2\phi\right) = 0,\end{aligned} \tag{6}$$

where the first integral is a boundary term and from the second integral we obtain the equation of motion for the scalar field,

$$\nabla_\mu\nabla^\mu\phi - \left(\frac{mc}{\gamma}\right)^2\phi = 0. \tag{7}$$

This equation is known as the Klein–Gordon equation. When we take the variation of the action Eq. 1 with respect to ϕ we obtain the corresponding equation for ϕ^*, which is equivalent to calculate the complex conjugate of Eq. 7.

Now, given that, in general relativity, we associate to the curvature of the spacetime a gravitational field, then weak gravitational fields correspond to approximately flat spacetimes. In such a case we consider the following metric,

$$g_{\mu\nu} = \eta_{\mu\nu} + h_{\mu\nu}, \tag{8}$$

with $|h_{\mu\nu}| \ll 1$ y $\eta_{\mu\nu} = \text{diag}(-1, 1, 1, 1)$, i.e., the Minkowski metric. With this, we are saying that the spacetime metric $g_{\mu\nu}$ is the flat spacetime metric plus a perturbation. After a lengthly algebraic computation we arrive to the Einstein equations,

$$\partial_\alpha\partial^\alpha\bar{h}_{\beta\nu} = -\kappa T_{\beta\nu}, \tag{9}$$

where $\partial_\alpha\partial^\alpha$ is the D'Alambertian operator in the flat spacetime, i.e., is the operator in the wave equation. This equations are the field equations for a weak gravitational field in its standard form. This expression is known as the weak field limit.

A particularly important application of the weak field limit is the Newtonian limit of general relativity. This limit not only corresponds to weak fields, it also corresponds to small velocities of the sources, which implies that the energy density T^{00} is much larger than the stress density. In such a case we can consider only the $\bar{h}^{00}$ component and ignore the rest of the terms (Alcubierre 2008). For a detailed analysis of Newtonian approximation of general relativity see Bernal (2007). We have used such reference to present the results that follows. The field equations reduce to

$$\partial_\alpha\partial^\alpha\bar{h}^{00} = -\frac{16\pi G}{c^2}m^2\phi\phi^*, \tag{10}$$

where we have defined $\kappa = 32\pi G/c^4$ and $T_{00} \approx \frac{1}{2}m^2c^2\phi\phi^*$. Besides, this implies that for small velocities, the time derivative in the D'alambertian operator is much smaller than the spatial derivatives, then the equation reduces to

$$\nabla^2 \bar{h}^{00} = -\frac{16\pi G}{c^2} m^2 \phi \phi^*, \tag{11}$$

where the operator ∇^2 is the laplacian in three dimensions. Comparing this result with the field equation of Newton $\nabla^2 U = 4\pi G\rho$ we conclude that in this limit $\bar{h}^{00} = -4U/c^2$ and $\bar{h}^{i0} = \bar{h}^{ij} = 0$ (for $i \neq j,\ i,j = 1,2,3$) and $m^2\phi\phi^*$ corresponds to the source. Returning to the definition of $\bar{h}_{\alpha\beta}$ in terms of $h_{\alpha\beta}$, we have that $h^{00} = h^{ii} = -2U/c^2$. The final expression of the Newtonian limit of the Einstein field equations will be shown later in Eq. 18 because we still have to see how ϕ reduces in this limit. In the next section we will get back to this point.

The metric of spacetime in the Newtonian approximation is

$$ds^2 = -(c^2 + 2U)dt^2 + (1 - 2U/c^2)d\mathbf{r} \cdot d\mathbf{r}, \tag{12}$$

where $d\mathbf{r} \cdot d\mathbf{r} = dx^2 + dy^2 + dz^2$. Here, it is important to mention that the series expansion parameter is the dimensionless quantity $U/c^2 \ll 1$, i.e., the weak field approximation.

2.1 Schrödinger Type Equation

In this section we will show that the Newtonian approximation to the Klein–Gordon equation will give us an equation for the scalar field similar to the Schrödinger equation. To simplify notation we will use a unit system where $c = \gamma = 1$, but at the end of this section we will recover the SI units. Substituting Eq. 12 in Eq. 7

$$(1 - 2U)\partial_t^2 \phi - (1 + 2U)\nabla^2 \phi + m^2 \phi \approx 0. \tag{13}$$

As an ansatz to make the Newtonian limit of the Klein–Gordon equation let us take[1] (Greiner 1990),

$$\phi = \psi(\mathbf{x}, t)e^{-imt}. \tag{14}$$

Substituting in Eq. 13 and using that $U \ll 1$, we obtain

$$-\frac{1}{2m}\ddot{\psi} + i\dot{\psi} + \frac{1}{2m}\nabla^2\psi - mU\psi = 0 \tag{15}$$

where $\ddot{\psi} = \partial_t^2 \psi$ y $\dot{\psi} = \partial_t \psi$. For a slowly time varying field we have that $\ddot{\psi} \approx 0$, then

$$i\dot{\psi} = -\frac{1}{2m}\nabla^2\psi + mU\psi, \tag{16}$$

[1] Another way of doing the Newtonian approximation of the Klein–Gordon equation can be seen in reference Bernal (2007).

We return to SI units by making $m \to mc^2/\gamma$, $\nabla^2 \to c^2\nabla^2$ and $U \to U/c^2$ and obtain

$$i\gamma\dot{\psi} = -\frac{\gamma^2}{2m}\nabla^2\psi + mU\psi, \tag{17}$$

This is an equation of the form of the Schrödinger equation of quantum mechanics and is known as *Schrödinger type equation*.

The reason why we said that Eq. 17 is a Schrödinger type equation and not the Schrödinger equation of the quantum mechanics indeed is simple, the field ϕ in Eq. 7 is of classical nature and so is ψ, i. e., ψ is not a wavefunction of the system. However, the methods of solution that we use to solve the standard Schröndiger equation can be applied in our case.

Using the ansatz Eq. 14 the Einstein field Eq. 11 reduce to the *Poisson equation*

$$\nabla^2 U = 4\pi G\rho, \tag{18}$$

with U the gravitational potential due to the scalar field where its associated source is $\rho = m^2\psi\psi^*$. The coupled set of equations given by Eqs. 17 and 18 are known as *Schrödinger–Poisson system*. Studies of this system can be seen in Guzmán and Ureña-López (2003); Bernal and Guzman (2006); Guzmán and Ureña López (2004).

3 Scalar Field Hydrodynamic Model

We take as a motivation the hydrodynamical formulation of the Schrödinger equation of quantum mechanics as was given by Madelung (1926), and Bohm (1952), we will express Eq. 17 in a representation of hydrodynamic type. In this Madelung formulation the Schrödinger equation, which is a complex linear differential equation, is replaced by two coupled partial differential equations for the corresponding density and velocity fields.

Appliying the Madelung transformation (Madelung 1926),

$$\psi = R(\mathbf{r}, t)e^{iS(\mathbf{r},t)}, \tag{19}$$

to Eq. 17 where R y S are real functions, we obtain

$$\partial_t\rho + \nabla\cdot(\rho\mathbf{v}) = 0, \tag{20}$$

$$\partial_t\mathbf{v} + (\mathbf{v}\cdot\nabla)\mathbf{v} = -\nabla\left(U - \frac{\gamma^2}{2m^2}\frac{\nabla^2\sqrt{\rho}}{\sqrt{\rho}}\right), \tag{21}$$

where we have defined the field variables

$$\mathbf{v} = \frac{\gamma}{m}\nabla S, \tag{22}$$

$$\rho = m^2 R^2. \tag{23}$$

The Eqs. 20 and 21 are the hydrodynamic formulation of the Schrödinger type equation for the field. These equations indicate that the time evolution of the field $\psi(\mathbf{r}, t)$ is equivalent to flux of a "fluid" of density $\rho(\mathbf{r}, t)$ where its particles of mass m are moving with a velocity $\mathbf{v}(\mathbf{r}, t)$ under the action of a force derived from an external potential $U(\mathbf{r}, t)$ plus an additional force due to a potential similar to the one whose origin is of quantum nature, $Q(\mathbf{r}, t)$, that depends on the density of the fluid (Madelung 1926; Weiner and Askar 1971a, 1971b) defined as

$$Q(\mathbf{r}, t) \equiv -\frac{\gamma^2}{2m^2}\frac{\nabla^2\sqrt{\rho}}{\sqrt{\rho}}. \tag{24}$$

From Eq. 19 we see that the scalar field is invariant under a change of phase $S' = S + 2\pi n$, and therefore,

$$\oint m\mathbf{v} \cdot d\mathbf{r} = 2\pi\gamma n, \tag{25}$$

with $n = 0, \pm 1, \pm 2, \ldots$. This result is a *compatibility condition* between the hydrodynamic Eqs. 20 and 21 and the Schrödinger type equation, that is, to a solution $(\rho, \mathbf{v})$ there corresponds a unique well defined ψ.

We should mention that the "fluid" described by Eqs. 20 and 21 has an essential difference with respect to a ordinary fluid: In a rotational movement, $\mathbf{v}$ decreases when the distance to the center decreases and vice versa. This is due to the condition of compatibility Eq. 25.

As we have seen above, the dynamics of the scalar field is given by a system of equations of hydrodynamic type, this system of equations is similar to the one that describes a non-viscous fluid. Then, the set of equations in this formulation is

$$\partial_t \rho + \nabla \cdot (\rho \mathbf{v}) = 0 \tag{26}$$

$$\partial_t \mathbf{v} + (\mathbf{v} \cdot \nabla)\mathbf{v} = -\nabla\left(U - \frac{\gamma^2}{2m^2}\frac{\nabla^2\sqrt{\rho}}{\sqrt{\rho}}\right) \tag{27}$$

$$\nabla^2 U = 4\pi G\rho. \tag{28}$$

This system gives the dynamics of a self-gravitating "fluid" under the action of a potential of quantum type. By analyzing the structure of the equations we realize that if we do not have a pressure term then we may think that we are dealing with a constant "equation of state". In the literature when p = 0 is said that the system is of dust type, and although is not realist, it is a good

approximation to model some real special systems (Alcubierre 2008; Coles and Lucchin 2002).

The dust equation of state can be used to model a collection of cold collisionless particles as in cosmology. In the astrophysical context it is useful to describe the structure of the rotation of rings or discs of particles. Also it can be used to study the collapse of shell of matter initially at rest, known as the Oppenheimer–Snyder collapse. Given that there is no pressure, the movement of the fluid elements is according to the spacetime geodesics. In an scheme of particles, we can consider the dust as a set of particles that have exactly the same local velocity (known as a lamellar flux), in such a way that there is no random component (Coles and Lucchin 2002).

However, given that the force of quantum type is opposing to the self-gravitational force we can think that it is due to an effective pressure of the fluid an express it as

$$-\nabla Q = \frac{1}{\rho}\nabla p_q(\rho), \tag{29}$$

where $p_q \neq 0$ plays the role of an equation of state.

4 Jeans' Instability

In this section we present the instability analysis of the Schrödinger–Poisson system in its hydrodynamic form. This analysis is based on the study of the Jeans' instability for the gravitational collapse of protostellar gas.

Jeans (1929) showed that for a homogeneous and isotropic fluid, small fluctuations in the density and velocity fields can be generated. In particular, he shows that the fluctuations in the density can grow if the effects of instabilities due to pressure are smaller than gravity caused by a fluctuation of density. There is no surprise in the existence of such an effect because gravity is an attractive force. So pressure forces are very small, then, a region with lesser density than the background is expected to attract more matter that its surroundings, therefore that region becomes even denser. If the system is denser more matter will be attracted, resulting that the fluctuation of density will collapse producing a gravitationally bounded object. The criterion consists simply to check if the typical length of a fluctuation is larger than the Jeans' length of the fluid.

Before we compute the Jeans' length it is useful to consider an order of magnitude estimate in order to understand its physical meaning. Let us consider that in a given instant there is an spherical homogeneous fluctuation of radius λ with positive density $\rho_1 > 0$ and mass M in a medium of mean density ρ_0. The fluctuation will grow if the self-gravitating force per unit mass, F_g, exceed the opposing force per unit mass due to the pressure F_p

$$F_g \approx \frac{GM}{\lambda^2} \approx \frac{G\rho\lambda^3}{\lambda^2} > F_p \approx \frac{p\lambda^2}{\rho\lambda^3} \approx \frac{v_s^2}{\lambda}, \tag{30}$$

where v_s is the speed of sound. This relationship implies that the fluctuation will grow if $\lambda > v_s(G\rho)^{-1/2}$. This establishes the existence of the Jeans' length $\lambda_J \approx v_s(G\rho)^{-1/2}$.

4.1 Hydrodynamic Linear Equations

To study the Jeans' instability it is necessary to linearize the hydrodynamic system of Eqs. 26–28. This system of equations admits the static solution with $\rho = \rho_0$, $\mathbf{v} = 0$ and $\nabla U = 0$. However, if $\rho \neq 0$, the gravitational potential should vary spatially, i.e., an homogeneous distribution of matter cannot be stationary and should be globally expanding or contracting. The incompatibility of an static Universe with the cosmological principle seems to be in Newtonian gravity but the same effect is also the reason that the Einstein Universe is unstable. Anyhow, when we consider an expanding Universe the Jeans' results do not change qualitatively. Even though that this theory is inconsistent, it can be interpreted to give correct results. Let us look for a solution of the hydrodynamic system (26–28) that represents a small perturbation to static solution

$$\rho \approx \rho_0 + \epsilon\rho_1, \mathbf{v} \approx \epsilon\mathbf{v}_1, U \approx U_0 + \epsilon U_1, \tag{31}$$

where the perturbed variables ρ_1, $\mathbf{v}_1$ and U_1 are functions of space and time and $\epsilon \ll 1$. Substituting Eq. 31 in Eqs. 26–28 and keeping only the terms up to first order in ϵ, we obtain the linear set

$$\partial_t \rho_1 + \rho_0 \nabla \cdot \mathbf{v}_1 = 0, \tag{32}$$

$$\partial_t \mathbf{v}_1 = \nabla U_1 + \frac{\gamma^2}{4m^2} \nabla \left[\nabla^2 (\rho_1/\rho_0)\right], \tag{33}$$

$$\nabla^2 U_1 = 4\pi G \rho_1. \tag{34}$$

4.2 Jeans' Instability Analysis

Let us study the solutions to the linear system Eqs. 32–34 looking for plane wave solutions

$$\delta u_i = \delta_{i0} e^{i(\mathbf{k}\cdot\mathbf{r} + \omega t)}, \tag{35}$$

where the perturbations δu_i with $i = 1, 2, 3$ correspond to ρ_1, $\mathbf{v}_1$ and U_1, and the corresponding amplitudes δ_{0i} to D, $\mathbf{V}$ and $\mathscr{U}$, respectively. Vector $\mathbf{r}$ is the position vector, $\mathbf{k}$ is the wave vector and ω is the angular frequency of oscillation, which is in general a complex number. Using Eq. 35 in Eqs. 32–34 and defining $\delta_0 \equiv D/\rho_0$ we obtain

$$\omega\delta_0 + \mathbf{k}\cdot\mathbf{V} = 0 \tag{36}$$

$$\omega\mathbf{V} + \mathscr{U}\mathbf{k} + \frac{\gamma^2}{4m^2}\delta_0 k^2\mathbf{k} = 0, \tag{37}$$

$$k^2\mathscr{U} + 4\pi G\rho_0\delta_0 = 0. \tag{38}$$

Very briefly we consider the solutions with $\omega = 0$, i.e., the ones that do not depend on time. It is evident from Eq. 36, that the wave vector $\mathbf{k}$ is perpendicular to the velocity $\mathbf{v}_1$ and it is satisfied that $\nabla \times \mathbf{v}_1 \neq 0$. Putting together these expressions we obtain

$$k = \left(\frac{16\pi G\rho_0 m^2}{\gamma^2}\right)^{1/4}. \tag{39}$$

Now, let us find the dependent solutions, $\omega \neq 0$. We derive Eq. 32 with respect to t and consider that $\mathbf{v}_1$ is a function such that $\partial_t\nabla\cdot\mathbf{v}_1 = \nabla\cdot(\partial_t\mathbf{v}_1)$, and then we substitute the expressions Eqs. 33 and 34 to obtain

$$\partial_t^2\rho_1 - 4\pi G\rho_0\rho_1 + \frac{\gamma^2}{4m^2}\nabla^2\nabla^2\rho_1 = 0. \tag{40}$$

Substituting Eq. 35 in Eq. 40 we arrive to the dispersion relationship

$$\omega^2 = \frac{\gamma^2}{4m^2}k^4 - 4\pi G\rho_0. \tag{41}$$

This relationship is analogous to the one that Jeans found (Jeans 1929), the difference is in the quantum potential which raises the magnitude of the wave vector to the fourth power. For stable solution, we ask that $\omega > 0$, that implies

$$k > k_J \equiv \left(\frac{16\pi G\rho_0 m^2}{\gamma^2}\right)^{1/4}, \tag{42}$$

where we have defined the Jeans' wave vector k_J. This result gives us that the Jeans' wave length, $\lambda_J = 2\pi/k_J$, is given by

$$\lambda_J = \left(\frac{\pi^3\gamma^2}{G\rho_0 m^2}\right)^{1/4}. \tag{43}$$

Then, for wave lengths larger than the Jeans' wave length we have that perturbations increase or decrease exponentially. Using the Jeans' length definition, we rewrite the dispersion relationship as

$$\omega = \pm\frac{\gamma}{2m}k^2\left[1-\left(\frac{\lambda}{\lambda_J}\right)^4\right]^{1/2}. \tag{44}$$

We recall that the speed of sound in the Jeans' theory is defined as $v_s^2 \equiv dp/d\rho$. But this is not our case, so we define a quantity that we will call the speed of sound as

$$\tilde{v}_s \equiv \frac{\gamma}{2m}k. \tag{45}$$

From Eqs. 35–38 and 45 we obtain

$$\frac{\rho_1}{\rho_0} = \delta_0 e^{i(\mathbf{k}\cdot\mathbf{r}\pm|\omega|t)}, \tag{46}$$

$$\mathbf{v}_1 = \mp\frac{\mathbf{k}}{k}\tilde{v}_s\delta_0\left[1-\left(\frac{\lambda}{\lambda_J}\right)^4\right]^{1/2} e^{i(\mathbf{k}\cdot\mathbf{r}\pm|\omega|t)}, \tag{47}$$

$$U_1 = -\delta_0\tilde{v}_s^2\left(\frac{\lambda}{\lambda_J}\right)^4 e^{i(\mathbf{k}\cdot\mathbf{r}\pm|\omega|t)}. \tag{48}$$

When $\lambda > \lambda_J$ the frequency ω is imaginary

$$\omega = \pm i(4\pi G\rho_0)^{1/2}\left[1-\left(\frac{\lambda_J}{\lambda}\right)^4\right]^{1/2}. \tag{49}$$

In this case the above expressions Eqs. 46–48 become

$$\frac{\rho_1}{\rho_0} = \delta_0 e^{i\mathbf{k}\cdot\mathbf{r}\pm|\omega|t}, \tag{50}$$

$$\mathbf{v}_1 = \mp i\frac{\mathbf{k}}{k^2}\delta_0(4\pi G\rho_0)^{1/2}\left[1-\left(\frac{\lambda_J}{\lambda}\right)^4\right]^{1/2} e^{i\mathbf{k}\cdot\mathbf{r}\pm|\omega|t}, \tag{51}$$

$$U_1 = -\delta_0\tilde{v}_s^2\left(\frac{\lambda}{\lambda_J}\right)^4 e^{i\mathbf{k}\cdot\mathbf{r}\pm|\omega|t}. \tag{52}$$

They represent wave solutions, whose amplitudes increase or decrease with time. The characteristic scale time for the evolution of these amplitudes is defined as

$$\tau \equiv |\omega|^{-1} = (4\pi G\rho_0)^{-1/2}\left[1-\left(\frac{\lambda_J}{\lambda}\right)^4\right]^{-1/2}. \tag{53}$$

For scales $\lambda \gg \lambda_J$, the characteristic time τ is the same as the collapse time for free fall (the collapse time of a system under the action of its own gravity in the absence of opposing forces), $\tau_{ff} \approx (G\rho_0)^{-1/2}$, but when $\lambda \longrightarrow \lambda_J$, this time diverges.

We define the Jeans's mass as the mass that it is contained in a sphere of radius $\lambda_J/2$ and mean density ρ_0, i.e.,

$$M_J = \frac{1}{6}\pi\rho_0\left(\frac{\pi^3\gamma^2}{G\rho_0 m^2}\right)^{3/4}. \tag{54}$$

The Jeans' mass is the minimum mass a perturbation needs in order to grow.

In a work by Sikivie and Yang (2009) the cosmological case of a model of axions as a dark matter model is considered. They also used a scalar field as we do. The conclusion of this work is that this model is different to the CDM in the nonlinear regime of structure formation, and these two theories differ in the quantum potential.

4.3 Scalar Field Mass Estimation

From Eq. 43 we obtain the mass of the scalar field

$$m = \left(\frac{\pi^3\gamma^2}{G\rho_0\lambda_J^4}\right)^{1/2}, \tag{55}$$

We can make an estimation of the order of magnitude as follows

$$\gamma \sim 10^{-34}\,\mathrm{J}\cdot\mathrm{s} \rightarrow \gamma^2 \sim 10^{-68}\,\mathrm{J}^2\mathrm{s}^2, \tag{56}$$

$$G \sim 10^{-11}\,\mathrm{m}^3/\mathrm{kg}\,\mathrm{s}^2 \tag{57}$$

According to the standard theory of structure formation, a value for the Jeans' length λ_J can be fixed for the epoch in which matter and radiation were equal, when $a \simeq 1/3200$. In that time, $\rho \simeq 3 \times 10^{10} M_\odot a^{-3}/\mathrm{Mpc}^3$ (Spergel et al. 2007), and the Jeans' length $\sim \mathcal{O}(10^2)$pc (Silverman and Mallett 2002). Here $M_\odot = 1.9891 \times 10^{30}$ kg is the mass of the sun. Then, taking the density $\rho_0 \sim 10^{-14}\,\mathrm{kg}/\mathrm{m}^3$ and $\lambda_J \sim 10^2$pc we have $m \sim 10^{-57}$kg. In units of eV/c^2 the mass is $m \sim 10^{-22}\,\mathrm{eV}/\mathrm{c}^2$. Therefore, with the computation of the Jeans' instability, we obtain that the mass of the scalar field is $\sim 10^{-22}\,\mathrm{eV}/\mathrm{c}^2$, a result also obtained by Matos et al. (2002); Lee and Lim (2010). From the Jeans' mass definition we finally obtain $M_J \sim 10^{10} M_\odot$.

5 Conclusions

We have shown how a hydrodynamic model can be build to study the dark matter component of the Universe. Starting with the Einstein–Hilbert action where a term which contains a complex scalar field is added, we make the Newtonian limit to arrive to a set of equations known as Schrödinger–Poisson equations. If in addition, we use the Madelung transformation, this set of equations can be further transformed to a set of partial differential equations similar to the Euler equations of the hydrodynamics. Finaly, we used known standard techniques to analyze astrophysical fluids such as the Jeans' instability method which we have used to determine the mass of the scalar field. The value we have obtained for the mass is consistent with values obtained using other methods (Matos et al. 2002; Lee and Lim 2010).

Acknowledgments This work received financial support by CONACYT grant number CB-2007-01-84133. A.H.A. acknowledges support from CONACYT-Mexico and Instituto Nacional de Investigaciones Nucleares-Mexico through MSc grants.

References

Alcubierre M (2008) Introduction to 3+1 numerical relativity. Oxford University Press, Oxford
Bernal A (2007) Estudio Dinámico de Campos Escalares Autogravitantes. Tesis Doctoral, CINVESTAV-IPN
Bernal A, Guzman FS (2006) Scalar field dark matter: non-spherical collapse and late time behavior. Phys Rev D 74:063504
Bohm D (1952) A suggested interpretation of the quantum theory in terms of hidden variables. I Phys Rev 85(2):166–179
Coles P, Lucchin F (2002) Cosmology, the origin and evolution of cosmic structure, 2nd edn. Wiley, New York
Guzmán FS, Ureña-López LA (2003) Newtonian collapse of scalar field dark matter. Phys Rev D 68:024023
Guzmán FS, Ureña López LA (2004) Evolution of the Schrödinger-Newton system for a self-gravitating scalar field. Phys Rev D 69(12):124033
Greiner W (1990) Relativistic quantum mechanics. Springer, Heidelberg
Jeans JH (1929) Astronomy and cosmogony. Cambridge University Press, Cambrigde
Lee J-W, Lim S (2010) Minimum mass of galaxies from bec or scalar field dark matter. JCAP 1:7
Madelung E (1926) Physik 40:322
Matos T et al (2002) Scalar field dark matter. ArXiv: astro-ph/0102419v2
Sikivie P, Yang Q (2009) Bose–Einstein condensation of dark matter axions. Phys Rev Lett 103:111301
Silverman CJ, Mallett RL (2002) Dark matter as a cosmic Bose–Einstein condensate and possible superfluid. Gen Rel Grav 34:633
Spergel DN et al. WMAP collaboration (2007) Wilkinson microwave anisotropy probe WMAP three years result: implications for cosmology. Astrophys J Suppl 170:377
Weiner JH, Askar A (1971) Time-dependent perturbation calculations based on the hydrodynamics analogy to quantum mechanics. J Chem Phys 54(3):1108–1113
Weiner JH, Askar A (1971) Particle Method for the Numerical Solution of the Time-Dependent Schrödinger Equation. J Chem Phys 54(8):3534–3541

The Link Cell Method Using Compute Unified Device Architecture and the Message Passing Interface Standard

J. M. Zavala Ake, A. J. C. Crespo, M. Gómez Gesteira, J. Klapp and S. Galindo

Abstract This paper shows the parallel implementation of the Linked Cell Method using CUDA and MPI. The so called Linked Cell method is employed in particle simulations with short range interactions. The method divides the physical domain into uniform sub domains while limiting the interactions to particles occupying the same cell and the flanking ones. In CUDA the Graphic Processing Units (GPUs) can be used for general purpose calculations. In the present case, the MPI standard allows the distribution of the sub domains into the available GPUs. Achieving an optimum GPU interchange process is crucial for system scaling. Results here presented will be used in the operation of a multi-GPUs system for fluid dynamics simulations using Smoothed Particle Hydrodynamics (SPH).

1 Introduction

November 2006 marks the launching of the first GPU based computer with Compute Unified Device Architecture (CUDA) architecture, Nvidia's model GeForce 8800 GTX, a general purpose cluster. Ever since, CUDA has been enthusiastically received by the parallel processing community. An indicator of

J. M. Zavala Ake · J. Klapp (✉) · S. Galindo
Instituto Nacional de Investigaciones Nucleares, Km 36.5 Carretera México-Toluca, 52750 Ocoyoacac, Estado de México, Mexico
e-mail: jaime.klapp@inin.gob.mx

J. M. Zavala Ake
Instituto de Física, Universidad Nacional Autónoma de México, Mexico City, Mexico

A. J. C. Crespo · M. Gómez Gesteira
Grupo de Física de la Atmósfera, Universidad de Vigo, Ourense, Spain

J. Klapp et al. (eds.), *Experimental and Theoretical Advances in Fluid Dynamics*, Environmental Science and Engineering, DOI: 10.1007/978-3-642-17958-7_17,

CUDA adoption is the fact that, among the 500 most powerful supercomputers, Tianhe-IA in the National Supercomputer Center in Tiajin, China, ranks first. This system, built with 14,336 Xeon processors and 7,168 Nvidia Tesla M2050 GPUs, has an amazing 2.57 petaflop/s performance.[1]

In the following pair of sections, we will briefly overview some features of the parallel computing architecture. Then, the next two sections will describe the linked cell algorithm and how parallel processing is an adequate strategy for its use. We end up this work by giving details on the parallel implementation algorithm and finally we mention the application to SPH simulations and its performance.

2 Parallel Computer Architecture

The common feature in parallel computer architecture is the convergence of traditionally disparate approaches on a common machine structure. The simplest approach is the Symmetrical Multiprocessing Architecture (SMP) where several processors share all the system resources and all are hierarchically equivalent, each of them being capable of performing tasks indistinctly. Another different trend is the Massively Parallel Processing architecture (MPP) where several independent processing units, known as nodes, are connected by a high speed communication network. Each node is practically in itself a computer (with its own processor, memory, etc.).

A SMP system can be programed employing well known methods such as process forking which allows the parent process to spawn a subprocess and continue running both processes concurrently. Whereas in MPP architecture the independently run procedures in each node require send/receive mechanisms for data updating.

In any event either, each processor can run different instructions over different sets of data or else, data can be divided into subsets and each processor can run a single instruction simultaneously on each subset. This implies two different strategies. In the first case we have the Single Program Multiple Data (SPMD) approach where all processes run the same program, operating on different data. This approach model is particularly appropriate for problems with a regular, predictable communication pattern. These tend to be scalable if all processes read/write to files and if global communication is avoided. The second approach is the Multiple Programs Multiple Data (MPMD).

Due to its relative simplicity, the SPMD approach is frequently used in SMP systems, but this architecture present low scalability. In contrast the use of MPP systems allows a better performance by scaling the number of nodes (NVIDIA 2010).

[1] http://www.top500.org/lists/2010/11

3 CUDA FERMI

CUDA is a proprietary name given to both, hardware and software, that enables NVIDIA's GPUs to run general purpose parallel programs written in C, C++, Fortran, OpenCl and other languages (Sanders and Kandrot 2010). The NVIDIA's FERMI architecture can include up to 512 CUDA cores. Each CUDA core performs one floating point or integer instruction per clock cycle. The 512 CUDA cores are organized in 16 Multi processors (Streaming Multiprocessors or SMs). Each SM has a 64 KB configurable shared memory that can be viewed as a SMP architecture device that performs a single instruction. The set of 16 SMs are structured around a 732 KB global memory, in a similar array as that of a MPP architecture system.

In a CUDA written program, GPU calls are performed thru kernels. Each kernel runs in parallel a set of threads. The GPU instantiates a kernel program on a grid of parallel threaded blocks. A grid is a block array that runs the same kernel which manages input/output data and executes read/write operations from/to the global memory.[2] Each thread executes one kernel instruction and it has a unique identifier in its own block. A single GPU runs one grid or more and a Multiprocessor runs one or more blocks. CUDA cores in the SM run threads. SMs run threads in sets of 32, known as Warps (NVIDIA 2009).

4 The Link Cell Method

Particle models use a large number of components and their mutual interactions to model a wide variety of physical systems ranging from astrophysics, fluid mechanics, biochemistry to Solid state. Also they are amply used in video games and computer animations for collision detection (Nguyen 2007).

For a set of N interacting particles, there are $N(N-1)/2$ interactions involved, which in general, can be sorted as short and long range types. For those interactions decaying fast with distance, i.e. r^{-a}, $a > 0$, a small distance change between particles means a large alteration on their mutual interaction, but at large particle separations, effects are negligible. The threshold of this behavior is given by r_{cut}, a cutoff distance. For r smaller than r_{cut}, interactions are considered to be of short range type, whilst long range contributions are given for r larger than the cutoff value. This value is established according to the specific physical situation, and can be viewed as setting a finite particle size of the model, i.e. fixing an atomic radius in a solid state physics simulation, or the size of a star in astrophysics.

Under this approximation, the contributions to the force F on a particle i exerted by a set of j particles is given by

[2] Multiple processes run at the same time.

$$F_i = \sum_{0 < r_{ij} < r_{\text{cut}}} F_{ij} + \sum_{r_{\text{cut}} \leq r_{ij}} F_{ij}$$

where $r_{ij} = \left| r_i - r_j \right|$ is the distance between particles i and j. It is well known that the computing cost of evaluating forces are proportional to $O(N^2)$, however, costs can be reduced by choosing particle coordinates in such way that the j particle's coordinates are $r < r_{\text{cut}}$, so calculations need not to be performed including all N particles but only those within a subset N_{cut}. This can be done by dividing the system domain Ω into uniform subdomains (cells) whose cell dimensions are larger or equal than r_{cut}. In this form particle interactions will be limited to neighboring particles contained in the same cell or belonging to adjacent cells. In case of uniformly distributed particles, the number of particles per cell is $N_{\text{c}} = N/N_{\text{cells}}$, where N_{cells} is the total number of cells. Hence, for the three-dimensional case, the number of interactions is $26 \times N_{\text{c}} \times N/2$, yielding a complexity of the order $O(N)$.

The process so far described, known as the Link Cell method, is used for short range interactions where r_{cut} remains spatially constant. In case of a varying r_{cut}, a tree algorithm is the appropriate choice which is of order $O(N \log N)$ (Liu and Liu 2003).[3]

5 Parallelization

Static Domain Decomposition has proven to lead optimal parallel runs for the sequential Link Cell algorithm (Griebel 2007). The idea is to divide the domain into subdomains assigning each division to a processor. The domain is divided in such way that the subdomain limits correspond to the cell limits of the link cell algorithm.

Those particles lying in the subdomain limit are affected by particles lying in flanking cells at r_{cut} distance or nearer. For this reason is necessary to extend in all directions the size of subdomains. Regarding information on these particles must be interchanged before running force calculations. After calculation of the new particles positions it is possible that some particles may abandon their original subdomains to enter adjacent cells. If this is the case, then particles are assigned to their new subdomain.

Assuming that particles are uniformly distributed along the system domain, then the number of particles assigned to each subdomain Ω_{ip} is of the order $O(N/N_{ip})$, where N_{ip} is the number of subintervals. Consequently, the number of particles that has to be assigned to new subdomains is of the order $O((N/N_{\text{sub}})^{2/3})$.

[3] An algorithm is considered optimum if the computing complexity is of the order $\mathbf{O}(N)$. If the complexity differs from optimum by a logarithmic factor, $O(N \log^a N)$, $a > 0$, the algorithm is referred as quasi-optimum.

If we denote the simulation domain length by L_d and if $nc[d]$ represents the number of cells along the dth coordinate, then to satisfy the condition $r_{\text{cut}} \leq L_d/nc[d]$ it is necessary that

$$nc[d] = [dL_d/\, r_{\text{cut}}t],$$

where $\lfloor X \rfloor = \max\{\mathrm{m} \in \mathbf{Z} | m \leq x\}$ Now, if the Ω domain is divided into $np[d]$ intervals along the dth direction, such that $nc[d]$ is an integral multiple of $np[d]$, then the number of Ω_{ip} subdomains turns out to be

$$N_{\text{sub}} = \prod_{d=0}^{\text{DIM}-1} np[d].$$

6 Implementation

Once the system has been discretized, the next step is to cover the system domain with a uniform grid. The g_j index, labeling a cell containing an i particle, is taken from the position r_i and the grid edge length (in this case r_{cut}), so

$$g_i = \lfloor (r_i - s)/r_{\text{cut}} \rfloor,$$

where s is the grid origin. Once the cell index g_j has been obtained, a calculation is performed to find ip, an index that unequivocally labels each cell. If $d = 3$ then

$$ip = (nc[2] \times nc[1]) \times idz + (nc[0]) \times idy + idx.$$

Upto this step we have two index arrays. The first set provides a unique label for each particle ($i = 0, 1, \ldots, N_{ip}$) while the second indicates the ip cell where the particle is located. Data handling for each i particle is carried out at CUDA thread level, that is to say, the n thread belonging to block m, handles objects: $mB + m$, $mB + m + pT$, $mB + m + 2pT$, etc., where B is the number of threads per block and T is the total number of threads (Nguyen 2007). After finding the cell ip index where the i particle resides, the cj indexes of flanking cells must be identified. For this purpose, each c_{ip} cell has an index, in the index array, that corresponds to the position of the particle having the smallest index i belonging to the c_{ip} cell. From this i value, the iteration on neighbor j particles in c_j cells starts. During the iteration, it is necessary to check, for each value of j, if the value for the ip index corresponds to that found for the initial particle of that cell. The program should proceed to a succeeding adjacent cell if a different ip value is found. Finding a different value means that all particles in that cell have already been taken into account. The reader should note that the way to implement a Link Cell code in a different language from CUDA, differs from what is here described e.g. for a CPU, the proper method used is known as Linked List, see Hockney (1988) for more details.

The next step consists in the ordering of particles according to the cell where they belong. This is done by means of the function cudppSort, which belongs to the CUDPP library (CUDA Data Parallel Primitives Library).[4] The mentioned function implements the radix-sort algorithm in CUDA (Nguyen 2007). Inside the domain, each of the cells has $3^{DIM}-1$ neighbors, 26 in three dimensions. However border cells have less than 26 neighbors, i.e. seven by the corners, 17 next to the walls and 11 by the edges. The following algorithm shows the way to carry out the Link Cell method

foreach cell *c_i* of the dominion
foreach particle *i* inside cell *c_i*
Force on particle i = 0
foreach neighbor cell *c_ j* to particle *i*
foreach particle *j* inside cell *c_ j*
if (i ! = j)
if(*r_ij*<*r_cut*) calculate force between i and j

The technique employed to achieve parallelism is a multiple parallel process of the type SPMD that use multiple threads. In distributed memory architectures, Message-Passing Interface (MPI) is used to communicate with other nodes, each of which may consist of a collection of several cores and/or GPUs.

The partition of the physical domain in Ω_{ip} subdomains depends on the number of available GPUs. Information for each subdomain Ω_{ip}, is send to each GPU from a main node via the MPI protocol. As already mentioned, extended borders information needs to be interchanged by GPUs. The idea is to interchange information between a GPU and its two neighbors. All data should be delivered in a single message. As a first step, the total number of particles to be transmitted should be sent, this in order to save memory space within the core that controls the GPU. Once data has been received by the core, it in turn, transmits appropriate information to each GPU using the CUDA command cudaMemcpy( ). Then each GPU will execute the corresponding force calculations and will interchange data on bordering cells as already mentioned. The reader is referred to reference (Griebel 2007) for further details on implementing the MPI protocol.

7 DualSPHysics

The Smoothed Particle Hydrodynamic approach (SPH) (Lucy 1977) is a free grid Lagrangian method, where the fluid is numerically simulated using a discrete set of particles, each of which has an associated mass, momentum and hydrodynamic

[4] http://code.google.com/p/cudpp

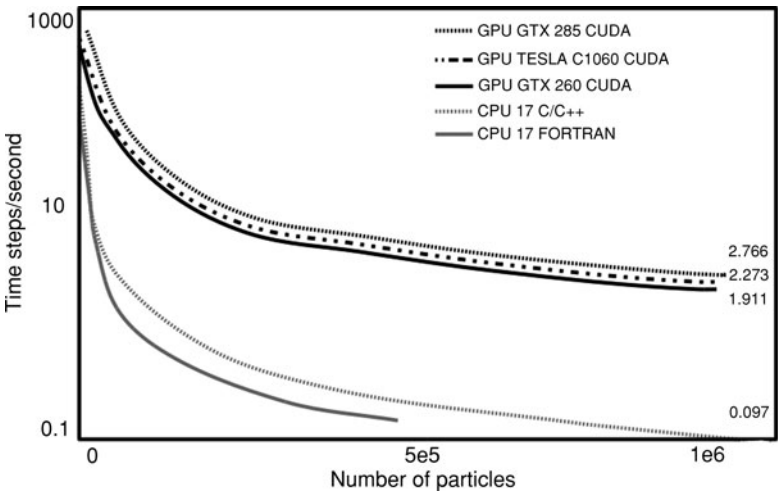

Fig. 1 Performance of SPHysics and DualSPHysics in different systems. Number of steps per second as function of the number of particles

properties (pressure, temperature, internal energy, etc.) The time evolution of the fluid is presided by Navier–Stokes equations combined with additional equations that modify the hydrodynamic properties of the particles.

Crespo et al. developed the DualSPHysics (Crespo 2010) which is a SPH CUDA code to study fluids with free surfaces. The serial version of SPHysics was written in FORTRAN and C++. Figure 1 shows the performance of SPHysics and DualSPHysics versions of a 3D example executed in different systems. The benchmark used is Dam Break (or bore in a wall) case (Gómez-Gesteira and Dalrymple 2003).

Both, DualSPHysics and Sphysics use the Link Cell method to calculate short range interactions for SPH particles. Implementation details are given in reference (Crespo 2010). This work represents the first effort to run the DualSPHysics code in distributed systems.

8 Example of Application

Figure 2 shows a simulation of water vertically falling into a glass goblet using nearly a million DualSPHysics particles (fluid particles and solid boundary) running in NVIDIA GTX 450 card. The first step of the modeling procedure comprises generating a grid. Any object of any geometrical shape, in this case the water and goblet, are created and exported, by means of a script written in Phython programming language, from Blender, a free open code used for 3D graphics. Blender subsequently generates a grid that in turn is transformed to a VTK format

Fig. 2 Simulation of water falling into a glass goblet

(Visualization ToolKit). This tool handles contours using diverse topologies (triangles in our case). Since the SPH method perform calculations only at discrete points, an algorithm, that takes into account baricentric coordinates is used to generate uniformly distributed points. Each discrete point has its own variables such as mass, momentum, and energy. Border points have their own assigned values. The temporal evolution of the system is then calculated following the Navier–Stokes equation according to the SPH formalism where the fluid is treated as weakly compressible. This temporal evolution of the system is obtained via isodensity surfaces using Paraview. Data are then reintroduced using a Python script from Blender. This allows following up the system evolution. Ray tracing techniques are used for rendering.

9 Conclusion

Simulating fluid mechanics using DualSPHysics requires the use of a parallel code to run the large number of particles needed in 3D.

The parallel code here presented using the MPI formalism implemented for CUDA architecture has proven to be a competent and efficient scheme for modeling three dimensional free surface flows.

References

Crespo AJC (2010) Development of a dual CPU-GPU SPH model. In: Proceedings of the Vth international SPHERIC workshop (Manchester), pp 401–407

Gómez-Gesteira M, Dalrymple RA (2003) Using a 3D SPH method for wave impact on a tall structure. J Waterway Port Coastal Ocean Eng ASCE 120:2

Griebel M (2007) Numerical simulation in molecular dynamics. Springer, Berlin

Hockney RW (1988) Computer simulation using particles. Adam Hilger, Bristol

Liu GR, Liu MB (2003) Smoothed particle hydrodynamics, a mesh free particle method. World Scientific Publishing, Singapore

Lucy LB (1977) Numerical approach to test the fission hypothesis. Astron J 82:1013–1024

Nguyen H (2007) GPU Gems 3. Addison-Wesley, Reading

NVIDIA (2009) Next generation CUDA compute architecture: fermi, V1.1. NVIDIA Corporation, Santa Clara

NVIDIA (2010) Nvidia Cuda C programming guide, version 3.2. NVIDIA Corporation, Santa Clara

Sanders J, Kandrot E (2010) CUDA by example an introduction to general-purpose GPU programming. Addison-Wesley, Reading

Part III
Multiphase Flow and Porous Media

Multiphase Phenomena Identification by Spectral Analysis: Electrical Impedance Sensor Signals in a Bubble Column

Juan Carlos Rodríguez and Alberto Soria

Abstract Multiphase phenomena identification in frequency domain through an electrical impedance sensor (EIS) in air–water pipes were analyzed experimentally. The electrical properties between the components were used to settle on the relative volumes of both phases. The selection of the appropriate a.c. frequency is well known to eliminate the capacitive impedance. The EIS is a device whose variable size electrodes were used to measure void fraction and its fluctuations. Measurements were carried out with six electrodes, when air was flowed into a standing water column, producing a bubble chain. Analysis in frequency domain of the electrical impedance signals allowed the spectral power density. This analysis was correlated with observed phenomena through video recording, in order to show that low frequency peaks can be associated to dynamic phenomena, while high frequency peaks could not be clearly correlated to flow particularities.

1 Introduction

Bubble columns are devices to contact two or three phases. These contactors are frequently used in chemical industry to carry out slow reaction, mass transfer between phases and multiphase flow transport. They offer many advantages over other multiphase devices: simple construction and operation, low cost and less

J. C. Rodríguez (✉) · A. Soria
Departamento de IPH, Universidad Autónoma Metropolitana-Iztapalapa,
Av. San Rafael Atlixco No. 186, Col. Vicentina, 09430 Iztapalapa, D.F., Mexico
e-mail: jcrs@xanum.uam.mx

A. Soria
e-mail: asor@xanum.uam.mx

J. Klapp et al. (eds.), *Experimental and Theoretical Advances in Fluid Dynamics*, Environmental Science and Engineering, DOI: 10.1007/978-3-642-17958-7_18,

installation space (Deckwer and Schumpe 1993). An important step in a two-phase flow study is to determine the flow regime domain; this step requires knowing some parameters such as physical properties, flow rates, volume fractions, diameter, length and angle of tubes. Some methods have been proposed to classify flow patterns using characteristic variables such as void fraction fluctuations or differential pressure, which are supposed to reflect the flow configuration (Song et al. 1995; Costigan and Whalley 1997; Cheng et al. 2002; Rodríguez 2006). Analyses of the fluctuation signal have been made by using the fast Fourier transform and statistical methods to correlate the void fluctuation signal with the observed flow phenomena. The typical values of peaks and the shape of the power spectral density function (PSD) of the measured time series have been previously utilized to identify the flow regime. However, the individual interpretation of those peaks to correlate the observed phenomena is still no clear. The void fraction parameter is very important for experimental studies in two-phase flow (Wang et al. 1991), this parameter is mainly relevant to the classification of flow patterns and its experimental estimation can be assessed by using appropriate devices (Ma et al. 1991; Micaelli 1982). The electrical impedance measurement provides an important tool to characterize components, systems and materials. Electrical impedance is a complex quantity whose real part is the resistance and whose imaginary part is the reactance. The reactance can be due to capacitive or inductive behavior. The air–water system behaves both in a resistive and a capacitive way (Micaelli 1982). The electrical properties of both components are disparate and this fact allows relating the impedance with volume fraction (Bernier 1982). Air has poor conductivity for low relative permittivity, while water has high relative permittivity owing of great concentration of ions, consequently, the measurement through electrical impedance sensors is possible. The aim of this study is to identify the main picks through estimating the PSD related to flow pattern in a bubble column utilizing the Electrical Impedance Sensor (EIS) and video at 60 frames/s.

2 Experimental Facility

Figure 1 shows the system and its components designed for this study. The system has a function generator, a bubble generator, an air supply system, a test section (EIS), and a data acquisition system. The test section used in the experiments has two cylindrical pipe made of transparent Plexiglas, its internal diameter is 0.053 m (2 in) and its height is about 1 m. The test section is filled with running water at room temperature and pressure. Air is injected into the central region through a capillary with an internal diameter of 0.005 m. The air flow injected is controlled by a regulating valve, to generate bubble chains.

The EIS has two sections of active stainless steel electrodes and two electrodes diametrically opposed 90° arcs on the circumference of the pipe. Each section has 50 active electrodes which are flush mounted to the inner wall are 1 mm in axial

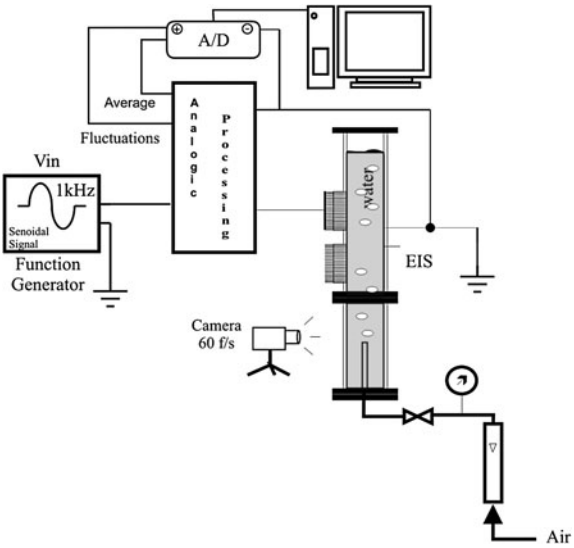

Fig. 1 Schematics of the experimental facility

length while the ground electrode opposed to each section is 75 mm in axial length. The active electrodes are set as a sandwich with insulator layers around separated by 0.5 mm each one to avoid short circuit. Figure 2 shows the electrode configuration. The EIS is specially designed so as to change the active electrode size without varying the other test conditions. Several sizes of active electrodes can be generated by connecting two or more consecutive electrodes. For example, a shielded configuration can be chosen.

The measuring principle of EIS is based upon the differences in electrical conductance between each phase in two-phase flow mixture. The measuring circuit of EIS operates with senoidal a.c. to 1 V peak to peak and 1 kHz of frequency, according to Rodríguez and Soria (2008, 2010), in this condition the EIS has a resistive behavior. Therefore, the only one factor which affects the electrical properties is the variation of gas fraction, i.e., the void fraction.

3 Experimental Procedures

Two guard electrodes were generated by connecting the electrode remainders, up and down a central measurement section made up by six active electrodes. A sine a.c. signal was provided by a function generator Insteck (GFG-3015). The voltage output was sampled through a data acquisition system Iotech Daq/3000*Series; then the void signal fluctuations were processed by a software based on the MATLAB® module. This estimation was made for stationary signals. A method to determine the stationarity of the void fraction signals was proposed by Rodríguez and Soria (2009). To avoid noise in the excitation signal (1 kHz) and its

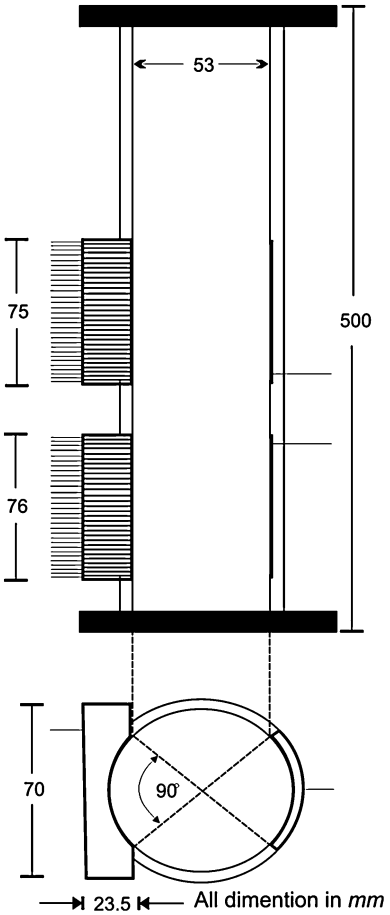

Fig. 2 Electrical impedance sensor (EIS)

Table 1 Parameters and conditions for acquisitions

Parameters	Value
Sampling frequency (f_s)	5000 Hz
Sample record length per channel	100 s
WINDOWS	f_s/0.1
NFFT	2*WINDOWS
NOVERLAP	WINDOWS/2

demodulation (2 kHz), they propose sampling to a frequency higher than two times the normal frequency, so avoiding any aliasing at low frequencies. The frequencies interval selected for this study was about 0–20 Hz. An analogical filter provided with a low-pass filter, 100 Hz cut and a digital filter with a low-pass filter, 25 Hz cut were implemented, so we can ensure that the PSD estimate is actually generated by void waves in this interval. Table 1 summarizes the

acquisition conditions and parameters for estimating the PSD (linear scaling) with a frequency resolution of 0.1 Hz.

4 Results and Discussion

In the two-phase flow, the void fraction information shows the characteristics of the structure of the discrete phase which can be correlated with flow patterns. Figure 3 shows the signal obtained by the EIS. This can be described as a set of peaks closely related to the flow of bubbles. A video-film was taken, simultaneously, to observe the relation between the EIS signals and the visualized events. A digital camera with speed of 60 frames per second was used, the video was focused on the upper end of a capillary vertical pipe (Fig. 1), provided as a bubble dispenser. The recording period was 10 s, the video shows the specific periods of time to each observable event, i.e., the time interval to generate and detach a bubble, the time interval to convey the whole bubbles chain and the time interval when no bubbles are formed (liquid plug). Voltage fluctuations are shown in Fig. 3 as a function of time. While a high signal should be associated to great water content, a decreased signal is generated as bubbles are detected by the sensor. Thus, a liquid plug gives a clear wide peak, yet with some superimposed small fluctuations, due to far away bubble chains detection. A chain of individual bubbles is detected as a set of large, well defined peaks, each one of them corresponding to the liquid bridge detection between two individual bubbles of the chain. A period of the whole bubble-chain process can be considered, therefore, as the sum of the times of the liquid plug passage plus the bubble chain passage. Both time passages were identified in Fig. 3 and marked manually with black squares and checked back with the video frames for six periods. In Table 2 the specific times for each event, according to video data are shown for the six periods, as well as its average frequency.

The void fraction signal is also shown in frequency domain as the power spectral density function (PSD) for the total time series, in Fig. 4. There are two characteristic main picks defined at low frequency, the pick at 0.65 Hz corresponds to the period of the whole bubble-chain process, while the second pick at 1.3 Hz corresponds to both the chain of bubbles and the liquid plug, these two phenomena have similar time in average, as can be established by previous analysis.

There is an interval between 1.6 and 15 Hz, which can be called the high frequency region, where some peaks with low power appear. These peaks contain information detailed processes and events difficult to extract, as well as uncontrolled noise. From the video, an important frequency corresponding to bubble generation at the capillary tip is close to 10 Hz and should appear in the spectrum. An important peak of the spectrum is 3.85, which can be associated to the third important time, the flowing time of a bubble. Since there are around five or six

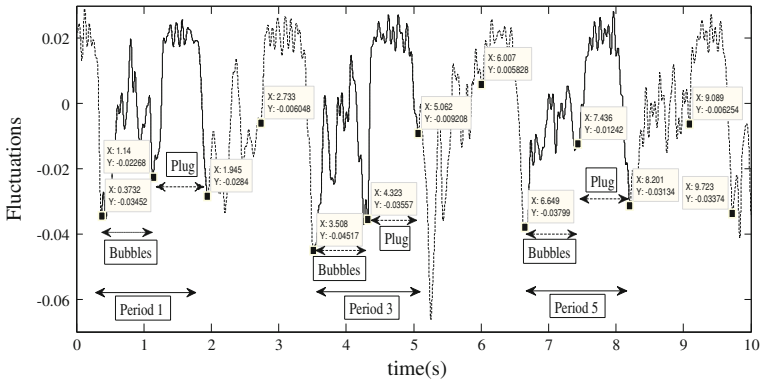

Fig. 3 Times identification for each phenomenon

Table 2 Time intervals measured through video data

Period	1	2	3	4	5	6	Average (s)	Hz (1/s)
Total	1.5	1.5	1.47	1.46	1.5	1.47	1.48	0.67
Bubble train	0.84	0.83	0.83	0.87	0.83	0.83	0.838	1.19
Plug	0.56	0.63	0.63	0.60	0.67	0.67	0.626	1.59

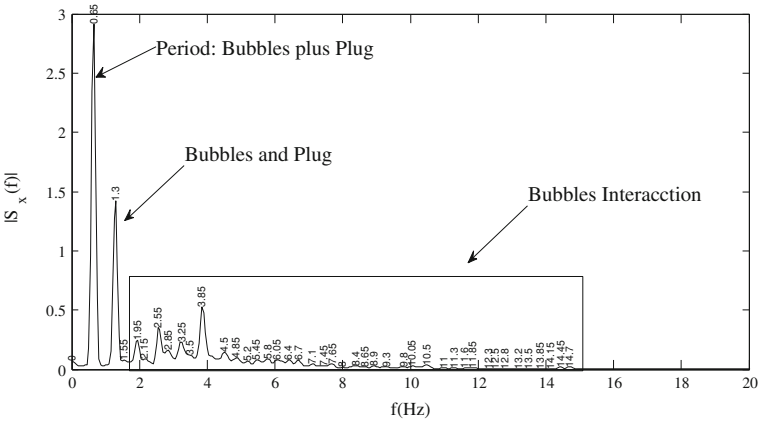

Fig. 4 Estimation of the power spectral density function (PSD)

bubbles in each train, the peak associated to this event should be around 6 Hz, far from the referred value of 3.85.

There are not straightforward explanations for high frequency peaks, aliasing is not a suitable explanation, since excitation and sampling frequencies were carefully selected with criteria developed in a previous study, as referred above. Further possible explanations should deal with the complexity of interactions.

Since the paths of bubbles are not always the same, neither their separation. Electrode size plays also an important role in the determination of the PSD.

5 Conclusion

Three confluent analyses for bubble-chain event identification in sets of bubbles, generated by a capillary tube in a bubble column were performed. The analyses through electrical impedance signal and video were correlated by finding and visualizing three main characteristic times: the whole period, the bubble chain passage and the liquid plug passage. These specific times were confirmed by the analysis of the power spectral density function obtained from the time series. The two main peaks of the spectrum of the electrical impedance signal and the video were coincident. Low frequencies were directly identified by finding their sources of generation. High frequency peaks were identified as complex interaction events, because we could not assign a particular phenomenon to each peak appearing in this frequency interval.

Acknowledgments To CONACyT, by financial support, Grant CB-2005-C01-50379-Y and Academic Scholarship No. 179552 to one of us (JCRS).

References

Bernier RJ (1982) Unsteady two-phase flow instrumentation and measurement. PhD thesis, California Institute of Technology, Pasadena, CA

Cheng H, Hills JH, Azzopardi BJ (2002) Effects of initial bubble size on flow pattern transition in a 28.9 mm diameter column. Int J Multiphase Flow 28:10473–10620

Costigan G, Whalley PB (1997) Slung flow regime identification from dynamic void fraction measurement in vertical air–water flows. Int J Multiphase Flow 23:263–282

Deckwer W, Schumpe A (1993) Improved tools for bubble column reactor design and scale-up. Chem Eng Sci 48(5):889–911

Ma Y, Chung N, Pei B, Lin W, Hsu Y (1991) Two simplifies methods to determine void fraction for two-phase flow. Nucl Technol 94:124–133

Micaelli JC (1982) Propagation d'ondes dans les écoulements diphasiques á bulles á deux constituants. Étude théorique et expérimentale, PhD thesis, L'Université, Grenoble

Rodríguez JC (2006) Ondas de presión en una columna de burbujas, MSc thesis. Universidad Autónoma Metropolitana, México

Rodríguez JC, Soria A (2008) Caracterización de un sensor de impedancia eléctrica (SIE) para la medición de la fracción volumen en una columna de burbujeo, Congreso de Instrumentación SOMI XXIII, Xalapa Veracruz, México

Rodríguez JC, Soria A (2009) Medición de ondas de fracción volumen a través de un sensor de impedancia eléctrica (SIE) en una columna de burbujeo, Congreso de Instrumentación SOMI XXIV, Mérida Yucatán, México

Rodríguez JC, Soria A (2010) Modelos para la caracterización de un sensor de impedancia eléctrica (SIE) en la medición de la fracción volumen en una columna de burbujeo, Congreso del AMIDIQ XXXI, Huatulco Oaxaca, México

Song CH, No HC, Chung MK (1995) Investigation of bubble flow developments and its transition based on the instability of void fraction waves. Int. J. Multiphase Flow 21(3):381–404
Wang Y, Pei B, Lin W (1991) Verification of using a single void fraction sensor to identify two-phase flow patterns. Nucl Technol 95:87–94

Dynamical Interaction of Bubbles in Two Dimensions

Saúl Piedra and Eduardo Ramos

Abstract We present a two-dimensional numerical study of the dynamic interaction of bubbles. The simulation is made by solving the conservation equations in a regular Cartesian coordinate system and using the front tracking technique to follow the position of the bubbles. The qualitative properties of the flow are described in terms of the Reynolds (*Re*) and Bond (*Bo*) numbers. The values explored for these parameters are $Re = 399$ and $Bo = 0.54$ which represent realistic experimental conditions. Initially, we give a brief description of the trajectory of a bubble and the flow of the liquid produced by the displacement of a single bubble. It is found that the bubble motion generates of a chain of vortices similar to a von Kármán vortex street. The details of the motion of a second bubble that interacts with the first through the surrounding liquid, critically depend on the relative initial positions of the two bubbles. In general, it can be said that in the early stages of the motion, the two bubbles follow roughly the same path, but at a certain point where the interaction is particularly strong, the paths of the two bubbles diverge.

1 Introduction

The dynamics of bubbles in liquids have been studied in the past due to its importance in chemical industry, oceanography and other applications. A classical review on the subject, written from an engineering point of view is the monograph by Clift et al. (1978).

S. Piedra (✉) · E. Ramos
Center for Energy Research, Universidad Nacional Autónoma de México,
62580 Temixco, Mor., Mexico
e-mail: sapig@cie.unam.mx

E. Ramos
e-mail: erm@cie.unam.mx

J. Klapp et al. (eds.), *Experimental and Theoretical Advances in Fluid Dynamics*, Environmental Science and Engineering, DOI: 10.1007/978-3-642-17958-7_19,

Detailed observations indicate that bubbles ascending with negligible effect of the walls of the container, undergo transitions from straight to zig-zag in a plane to spiral paths, Magnoudet and Eames (2000). Some aspects of these observations, including the instabilities, have been interpreted and explained (Mougin and Magnoudet 2006). Several models designed to describe the paths of bubbles and their shapes, are based on the concept of deformable, immersed boundary conditions that incorporate the effect of the liquid-gas interface. For a review on these algorithms see Tryggvason et al. (2001). Systematic observations of the dynamics of chains of bubbles moving in large containers have revealed complex individual and collective interactions, but a comprehensive understanding of the phenomenon is not available yet (Sanada et al. 2005). The two- dimensional models of bubble dynamics have been largely regarded as an academic exercise since in most physical situations of interest, bubbles move in three dimensional trajectories. Studies of this sort have been made by Tryggvason et al. (2001) and Hua and Lou (2007). A little studied, yet interesting physical situation that approximate the motion of bubbles in planes is when bubbles move in liquid filled Hele-Shaw cells. This phenomenon has been described by Kelley and Wu (2005), see also Ramos et al. (2007). The relevance of these studies lies on their potential application in mass exchangers, chemical reactors and mixers. Obviously, this problem can be regarded as the two dimensional case of freely moving bubbles, but as it will be discussed later, it has been found that some aspects of the bubbles shapes and vibrations and the flow patterns generated in surrounding medium are very different, from the bubble motion in large containers.

2 Physical and Mathematical Models

The physical situation of interest in the present study is the motion of bubbles in a Hele-Shaw cell, and the model described in this section, is an idealization of that phenomenon. We consider a two dimensional complex fluid composed by a liquid and gas bubbles immersed in it. The system is assumed to be in presence of the acceleration of gravity and given the density difference between the liquid and gas, the bubbles are set in motion by buoyancy forces. The surface tension that arises at the boundary between the two fluids is fully considered in the model, and the geometry of the interface is unknown a priori since it is determined by the normal and tangential stresses that arise due to the interaction of the bubbles and the surrounding liquid. We consider the interaction of bubbles through the liquid, but no break up or coalescence occur in the model. This is not a severe limitation for the most of the conditions of interest.

Considering that the two fluids are incompressible, the mass conservation is given in terms of the velocity $\mathbf{u}$, by

$$\nabla \cdot \mathbf{u} = 0. \tag{1}$$

The momentum conservation equation must take into account the different fluid properties of the two fluids and also the jump at the interface represented by the term of the surface tension. In symbols,

$$\frac{\partial \rho \mathbf{u}}{\partial t} + \nabla \cdot \rho \mathbf{u}\mathbf{u} = -\nabla p + \nabla \cdot \mu(\nabla \mathbf{u} + \nabla^T \mathbf{u}) + \int \sigma \kappa' \mathbf{n}' \delta^{\beta}(\mathbf{x} - \mathbf{x}') ds' + (\rho - \rho_l)\mathbf{g}. \quad (2)$$

The pressure is denoted by p, μ is the viscosity, $\mathbf{g}$ is the gravity vector, ρ_l is the density of the continuous phase, σ is surface tension and k is curvature. The presence of the interface is incorporated by the term $\delta^{\beta}(\mathbf{x} - \mathbf{x}') = \delta(x - x')$ $\delta(y - y')$, where $\mathbf{x}$ is the point at which the equations are evaluated and $\mathbf{x}'$ is a point in the interface. Also, the jump condition between the two fluids is a stress balance on the interface that may be expressed as:

$$[-p + \mu(\nabla \mathbf{u} + \nabla^T \mathbf{u})] \cdot \mathbf{n} = \sigma \kappa \mathbf{n}, \quad (3)$$

$$[\mu(\nabla \mathbf{u} + \nabla^T \mathbf{u})] \cdot \mathbf{t} = 0, \quad (4)$$

where $\mathbf{t}$ and $\mathbf{n}$ are the unit tangent vector and unit normal vector evaluated at the interface.

2.1 Boundary Conditions

In the present model, the physical conditions at the surface of bubbles, (3) and (4) can be regarded as internal boundaries for the liquid and an outer boundaries for the gas, thus the name of *Immersed boundary method*, but also, the boundary conditions that define the outer boundaries of the integration domain, must be given. In the present study, we considered that the vertical boundaries are periodic walls, and are separated 35 bubble diameters apart. The horizontal walls are considered periodic and are located 125 bubble diameters away from each other.

3 Numerical Solution Strategy

3.1 Front-Tracking Method

A salient feature of the physical situation considered in the present study is the determination of the position of the liquid-gas interface as a function of time. This is accomplished with the front-tracking method in which a single set of conservation equations is solved for the whole flow field, including gas and liquid, and the position of the interface or *front* is determined by the local velocity field Tryggvason et al. 2001. Thus, in the front tracking method, it is required to construct a grid covering the whole domain of integration and also a set of points that define the tracked front. The points in the front are connected by elements as indicated in Fig. 1. Each point is identified by its coordinates, but each element

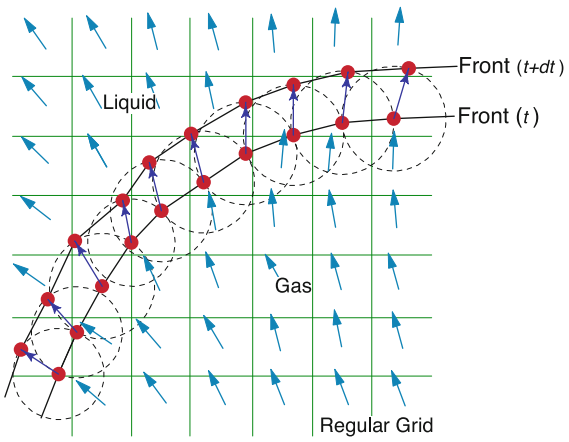

Fig. 1 The discretization of a section of the domain including a regular Cartesian grid (*green lines*) and the liquid-gas interface (*Front*) at two time snapshots. The *blue arrows* indicate the local flow velocity field that drive the motion of the front

must contain information not only by the points it is connected to, but also to its neighboring elements. This information defines the local structure of the front Prosperetti and Tryggvason (2007).

The fluid properties, such as the density and viscosity, are not advected directly since the boundary between the different fluids is moved. It is therefore necessary to reset these quantities at every time step. Generally, we first construct a marker function $I(\mathbf{x}, t)$ that is a constant in each fluid and then use the marker function to set other properties. To construct the marker function we use the fact that the front marks the jump in the density and that this jump is translated into a steep gradient on the fixed grid. The discrete form of the gradient of the density, which is used as the marker function, can be expressed as:

$$\nabla \rho_{ij} = \sum_{l} \Delta\rho \omega_{ij}^{l} \mathbf{n}_l \Delta L_l, \tag{5}$$

where ω_{ij}^{l} is the weight of grid point ij with respect to element l. The symbols $\mathbf{n}_l$ and ΔL_l are respectively, the normal vector and the length of element l. In the literature there are many weighting functions that can be used, however the one developed by Peskin (1977) is recommended in this case. Once the density gradient field has been constructed with Eq. 5, the density field can be recovered solving the resulting Poisson equation for the density Kelley and Wu (2005),

$$\nabla^2 \rho = \nabla \cdot \nabla \rho_{ij}. \tag{6}$$

The field distribution $\phi(\mathbf{x}, t)$ of other fluid properties are calculated using the marker function:

$$\phi(\mathbf{x}, t) = \frac{\phi_l(\rho(\mathbf{x}, t) - \rho_b) - \phi_b(\rho(\mathbf{x}, t) - \rho_l)}{\rho_l - \rho_b}. \tag{7}$$

The front is moved by interpolation from the velocity field in the regular grid according with the following expression,

$$\mathbf{u}_f = \sum_l \mathbf{u}_{ij}\omega_{ij}^l \frac{\Delta L_l}{h^2}, \tag{8}$$

where $\mathbf{u}_f$ is the front velocity, $\mathbf{u}_{ij}$ is the velocity at the regular grid and h is the spatial discretization interval in the regular grid. Also, the surface tension force is calculated at the front points and interpolated to the regular grid to compute the conservation equations (Tryggvason et al. 2001),

$$\mathbf{F}_{ij} = \sum_l \sigma\kappa^l\omega_{ij}^l\mathbf{n}_l\Delta L_l, \tag{9}$$

where $\mathbf{F}_{ij}$ is the surface tension force in the regular grid.

3.2 Integration in the Regular Grid

As stated in the previous subsection, the momentum equations (Eq. 3) must be integrated in the whole domain. To this end, we discretized the domain with a regular grid and applied the finite volume method. The pressure-velocity decoupling was accomplished with the SIMPLEC algorithm (Versteeg and Malalasekera 1995) which was demonstrated to be superior to the projection method for problems with markedly different densities. The integral term of the momentum equations is evaluated around the front and using the definition of the curvature in two dimensions. However, it is possible to simplify considerably the calculation using the tangent vectors of the end points of each element of the front Prosperetti and Tryggvason (2007). As part of the post processing of the data obtained, it is important to comment that the velocity of the centroid of the bubble was obtained by interpolating the velocity in the regular grid using the weighting function given by Peskin (1977).

4 Results

4.1 Preliminary

First, we describe the trajectories of the centroid of individual bubbles as well as their geometries and orientations considering external conditions that are attainable in experiments. Also, the flow generated in the liquid due to the transit of the bubbles is presented. Then, we display the corresponding information of two bubbles that may interact through the surrounding liquid. It is convenient show the numerical results in terms of the dimensionless variables:

$$x^* = \frac{x}{D}; \quad u^* = \frac{u}{(Dg)^{\frac{1}{2}}}; \quad t^* = \frac{t}{D^{\frac{1}{2}}g^{-\frac{1}{2}}}; \quad p^* = \frac{p}{\rho_f g D}, \tag{10}$$

and using the Reynolds (Re) and Bond (Bo) numbers defined by

$$Re = \frac{\rho_l U_T D}{\mu_l} \quad \text{and} \quad Bo = \frac{\rho_l D^2 g}{\sigma}. \tag{11}$$

where U_T is a characteristic velocity defined as the terminal vertical velocity and is a result of the calculation. The symbol D denotes the initial diameter of a bubble and the subscript l refers to the liquid phase. It is also useful to define the Archimedes number:

$$Ar = \frac{gD^3\rho_l(\rho_l - \rho_b)}{\mu_l^2}, \tag{12}$$

which is the rate of the buoyancy effects to the viscous effects and it represents the density difference between the two fluids.

4.2 Trajectory of the Centroid and Orientation of a Single Bubble

In Fig. 2, the trajectory of the centroid of a bubble is plotted for $Bo = 0.54$ and $Ar = 78401$; the vertical Reynolds number obtained with the simulation is $Re = 399$. It is important to note that for purposes of clarity, the abscissa has been greatly enlarged with respect to the ordinate. After an initial transient that lasts approximately $20D$, the motion is oscillatory with a fast mode that completes a cycle in $12D$ and a slow mode with a cycle of $40-50D$. The zig-zag motion is generated by the asymmetry of the pressure field in the periphery of the bubble which in turn results from the fact that the surface of the bubble deforms in response to the external field of stresses.

To further explore the dynamics, the instantaneous non-dimensional centroid velocity (Reynolds number) for the horizontal and vertical motions are given in Fig. 3. The non-dimensional vertical velocity (Re_y) oscillates around an averaged value of 399, while the horizontal non-dimensional velocity (Re_x) presents an almost periodic behavior with zero average value. The oscillation frequency of the vertical velocity is twice that of the horizontal velocity and its amplitude is approximately 150 while that of the horizontal velocity is larger than 800. Also, a crest of the horizontal velocity always correspond to a trough of the vertical velocity. The dynamical features of the motion can be interpreted in terms of the inclination of the bubble as it ascends. Incidentally, the instantaneous position of the bubble could be computed by using an ellipse fit to the bubble, since for the chosen the non-dimensional parameters it can be concluded that the bubble shape always can be accurately approximated by an ellipse since the flow regime is surface tension dominating. In Fig. 4, the inclination of the major axis of the ellipse fit with respect to the horizontal in one cycle is shown. The bubble has a positive inclination in (A) and a negative inclination in (B), the pressure field are plotted in these points and the pressure gradient between the isolines is a constant.

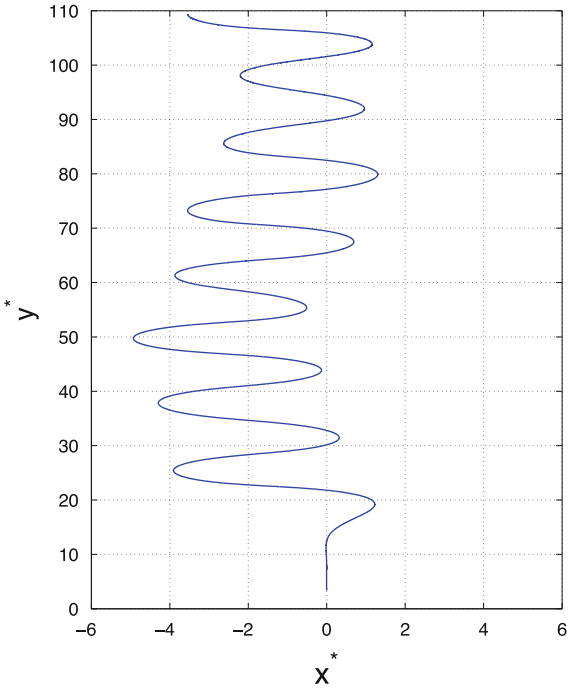

Fig. 2 Trajectory of the centroid of the bubble for $Bo = 0.54$ and $Ar = 78401$. The terminal Reynolds number is $Re = 399$

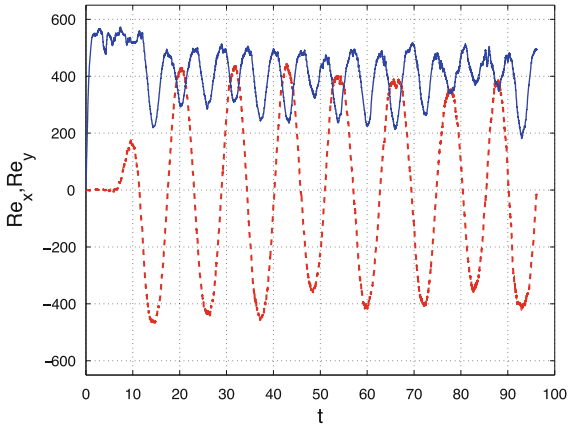

Fig. 3 Instantaneous horizontal (*dashed line*) and vertical (*continuous line*) Reynolds numbers (non-dimensional velocity) based on rising velocities of the bubble

The maximum angle of inclination of the bubble was about 45°. This tilt motion is consistent with a non-symmetric pressure field around the surface of the bubble and with an periodically varying drag.

A snapshot of the velocity, pressure and vorticity field in the wake of the ascending bubble is shown in Fig. 5. The most conspicuous feature observed in the Fig. 5 is that vortices are created on the lee side of the bubble and detach periodically from either side. This collection of vortices is similar to the Von Kármán

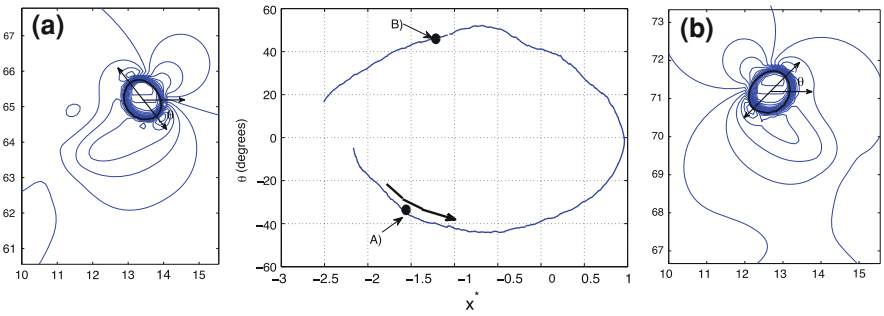

Fig. 4 Inclination of the major axis of the best elliptic fit of the bubble in one cycle. See Fig. 2. The *arrow* indicates the direction of time

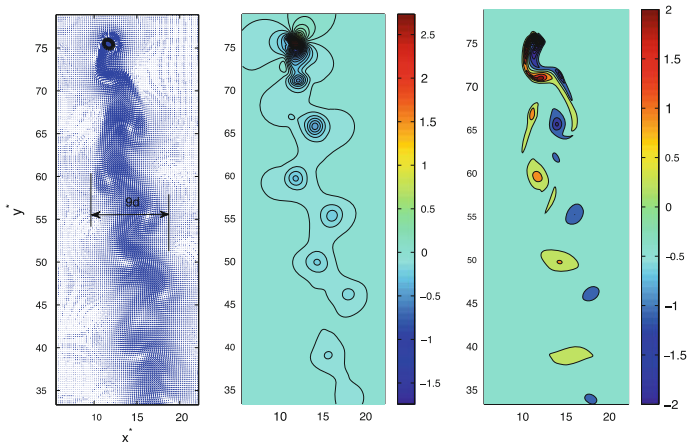

Fig. 5 Velocity, pressure and vorticity fields. The vortex shedding can be observed in the wake of the bubble similar to the Von Kármán vortex street, also in the vorticity field is shown the intensity of the vortices and the dissipation of them

vortex street generated by a rigid cylinder in relative motion with respect to a fluid. It is important to highlight that the width of the wake is about 9 diameters.

4.3 Trajectory of the Centroid and Orientation of Two Bubbles

Numerical simulations were performed to explore the interaction of two bubbles as they ascend. At the onset of the motion, the bubbles are placed near bottom of the integration area, vertically aligned and at a small distance from each other.

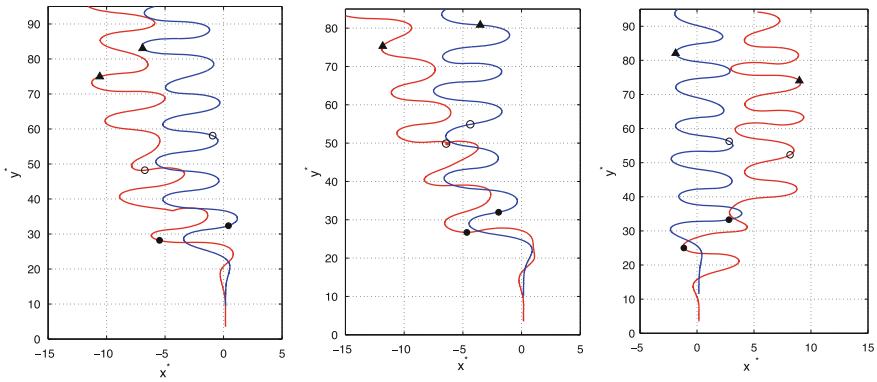

Fig. 6 Trajectories of the centroid of the two bubbles for initial distances of 5.5, 6.5 and 8 diameters ($Bo = 0.54$ and $Ar = 78401$) are shown in the *left*, *central* and *right panels* respectively. Markers indicate position of bubbles at fixed times

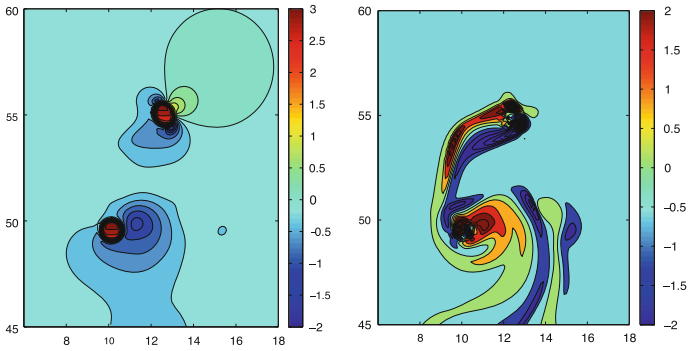

Fig. 7 *Left panel*, pressure field and *right panel*, vorticity field around the bubbles. Initial distance 6.5 diameters. These snapshots correspond to marker ○ in the central panel of Fig. 6

The interaction of the bubbles depends strongly to the initial distance, which is 5 diameters or larger. This restriction is due to the fact that smaller distances may lead to bubble coalescence which is a phenomenon that the model does not consider.

In Fig. 6, the trajectories of two bubbles (lines red and blue) are shown for different initial distances (5.5, 6.5 and 8 diameters). As it can be observed, in all three cases, the first bubble follows an approximate periodic path similar to an individual bubble (see Fig. 2), but the trajectory of the second bubble is clearly affected by the wake of the first. As discussed in the previous section, the first bubble sheds alternative vortices with low pressure zones at their centers. These structures are not fixed in space and dissipate due to viscous effects. If the path of the second bubble pass near a strong enough high vorticity, low pressure region, its path will be altered. In Fig. 7, the pressure and vorticity fields are shown at the

moment when the very strong interaction occurs and the second bubble changes its path. See marker ○ in the central panel of Fig. 6. In this particular event, the interaction is complex, with the second bubble first turning around the low pressure zone of the vortex, and then ascending again due to the ever present buoyancy force. This situation can be regarded as fresh initial conditions for the rest of the ascending path. It is interesting to observe that in the left and central panels of Fig. 6, the trajectories of the two bubbles display approximately the same phase, while in the last case, the two paths are dephased (right panel of Fig. 6).

5 Discussion and Conclusions

The numerical simulations of individual or pairs of bubbles presented in this study were obtained with a finite volume method combined with the front tracking technique to take into account the interfacial effects. The parameters chosen for the calculations are similar those of realistic experimental conditions of bubble motions in a Hele-Shaw cell, therefore they constitute potential information for comparison with experimental results. Incidentally, the shapes of individual bubbles are in qualitative agreement with the shape chart presented by Clift et al. (1978) and obtained for actual experimental observations. After an initial transient, the trajectory of the bubble centroid describe an approximately periodic zig-zag motion, and the bubble acquires an ellipsoidal shape with an inclination that oscillates between $\pm 45°$. The flow pattern around individual bubbles is closely related to the von Kármán vortex street and has similar qualitative properties to those reveled by the observations of Kelley and Wu (2005) and Ramos et al. (2007). In the numerical simulations of pairs of bubbles discussed in the final section, we analyzed, somewhat in detail the bubble-bubble interaction through the fluid in the high vorticity, low pressure zones generated by of the wake of the first bubble. We find that interaction is highly dependent on the initial conditions. In order to illustrate this effect, we present the centroid characteristics for three slightly different initial vertical distances. The simulations show that after the initial transient the second bubble follows a similar zig-zag path of the first. However, if a vortex behind the first bubble has a high enough vorticity and has low enough pressure it will be able to critically modify the motion of the second bubble.

Acknowledgments S.P. acknowledges support from CONACYT-Mexico through a MSc grant. We wish to thank Mr. José Núñez for discussions on the model and advice on the development of the code.

References

Clift R, Grace JR, Weber ME (1978) Bubbles drops and particles. Academic Press, London

Hua J, Lou J (2007) Numerical simulation of bubble rising in viscous liquid. J Comp Phys 22:769–795

Kelley E, Wu M (2005) Path instabilities of rising air bubbles in a Hele-Shaw cell. Phys Rev Lett 79:1265–1268

Magnoudet J, Eames I (2000) The motion of high-Reynolds-number bubbles in inhomogeneous flows. Annu Rev Fluid Mech 32:659–708

Mougin G, Magnoudet J (2006) Wake-induced forces and torques on a zigzagging/spiralling bubble. J Fluid Mech 567:185–194

Peskin CS (1977) Numerical analysis of blood flow in the heart. J Comput Phys 25:220–252

Prosperetti A, Tryggvason G (2007) Computatiosnal methods for multiphase flow. Cambridge University Press, New York

Ramos E, Sanchez R, Gonzalez M, Herrera JR (2007) Dynamics of chains of bubbles in a Hele-Shaw cell. 60th annual meeting of the divison of fluid dynamics, vol 52. Salt Lake City, USA

Sanada T, Watanabe M, Fukano T, Kariyasaki A (2005) Behavior of a single coherent gas bubble chain and surrounding liquid jet flow structure. Chem Eng Sci 60:4886–4900

Tryggvason G, Bunner B, Esmaeeli A, Juric D, Al-Rawahi N, Tauber W, Han J, Nas S, Jan YJ (2001) A front-tracking method for the computations of multiphase flow. J Comp Phys 169:708–759

Versteeg HK, Malalasekera W (1995) An introduction to the computational fluid dynamics, The finite volume method. Longman, Harlow

Hydrodynamic Force and Rise Velocity of an Interactive Bubble due to a Laminar Wake Effect

Sergio A. Baz-Rodríguez and Alberto Soria

Abstract The interaction between two spherical bubbles rising in-line in a stagnant Newtonian liquid was studied. A model was proposed to relate the flow structure in the wake of a leading bubble with the hydrodynamic force and the rise velocity of a trailing bubble, at separation distances of the order of its diameter ($2 \leq s/d_B \leq 14$) and moderate particle Reynolds numbers ($20 \leq Re_1 \leq 200$). To this end, a force balance on the trailing bubble was used as a starting point. The flow character in the axisymmetric laminar wake of a spherical bubble was analyzed, and an equation for the axial velocity profile was proposed in the modified form of an analytical approximation, which was fitted to numerical data. This equation, once substituted in the force balance, allowed obtaining a predictive model explaining quantitatively the in-line interaction of a pair of bubbles in terms of the average axial velocity in the leading bubble wake. The predictions of the proposed models show a good agreement with numerical and experimental data for the hydrodynamic force and the rise velocity of a trailing bubble, respectively.

S. A. Baz-Rodríguez (✉) · A. Soria
Process and Hydraulics Engineering Department,
Universidad Autónoma Metropolitana – Iztapalapa,
San Rafael Atlixco 186, Col. Vicentina,
09340 Mexico City, Mexico
e-mail: bazrodriguez@gmail.com

A. Soria
e-mail: asor@xanum.uam.mx

J. Klapp et al. (eds.), *Experimental and Theoretical Advances in Fluid Dynamics*, Environmental Science and Engineering, DOI: 10.1007/978-3-642-17958-7_20,

1 Introduction

Bubbly flows occur in different processes of nature and industry. However, the mathematical description of the hydrodynamic behavior of these flows is still difficult. This is due to a good extent to the complex interactions caused by proximity of multiple bubbles in motion. Therefore, understanding the way bubbles interact when they rise in clusters is a previous fundamental step in the development of good predictive models for the macro-scale.

Let us consider the interactions due to the proximity of a pair of bubbles moving without contact. In such a case, the incident liquid flow on each bubble is non-uniform, and its structure is the one determining the forces involved in the motion of these bubbles (Magnaudet and Eames 2000). Then, the problem consists of describing the interstitial velocity in terms of the relative position and motion of both bubbles.

Based on this, the interaction of two in-line rising bubbles is of particular interest. The leading bubble wake exerts a shield effect on the trailing bubble, which reduces the hydrodynamic force of the latter and increases its rise velocity (Yuan and Prosperetti 1994; Katz and Menevau 1996). The rise of the two in-line bubbles is the spatial configuration under which the hydrodynamic interactions are maximized (Yuan and Prosperetti 1994). Therefore, even though this is a particular case, the study of this issue is useful to understand the theoretical basis of interactions between bubble pairs.

2 Forces on the Trailing Bubble

Let us consider two spherical bubbles with the same diameter rising in-line through a stagnant Newtonian liquid. The system, with axial symmetry, is schematically depicted in Fig. 1. The framework of reference is kept fixed on the rear of the leading bubble which rises at its terminal velocity. Under this perspective, a uniform flow with constant velocity U_{B1} falls on the leading bubble. On the other hand, the trailing bubble approaches the leading bubble at a velocity $-u$, and it is affected by the wake, which generates a flow defect $w_s(r, s)$.

It is assumed that the particle Weber number (We) is low, and that the particle Reynolds number (Re) is moderate, such that the bubbles remain spherical and the wake flow is laminar. For air bubbles rising in pure water, this implies that $We < 1$ and $Re \leq 200$. The balance of forces on the trailing bubble is as follows

$$F_D + F_{IL} + F_H + F_B + F_{IB} = 0 \tag{1}$$

where F_D is the drag, F_{IL} are the inertial forces due to the liquid acceleration, F_H is the history force, F_B is the buoyancy and F_{IB} is the inertial force due to the bubble acceleration. The buoyancy force is

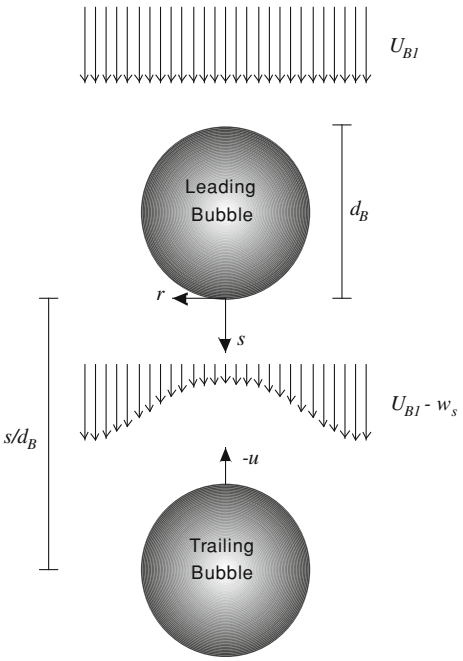

Fig. 1 In-line interaction of two spherical bubbles

$$F_B = -\frac{1}{6}\pi d_B^3(\rho - \rho_B)g \tag{2}$$

where d_B is the bubble diameter, ρ and ρ_B are the liquid and gas density, respectively, and g is the gravity acceleration. The inertial force due to the bubble acceleration is

$$F_{IB} = -\frac{1}{6}\pi d_B^3 \rho_B \frac{\partial u}{\partial t} \tag{3}$$

The drag force on the trailing bubble can be determined using known correlations for the drag coefficient, but specifying an appropriate velocity for the wake flow (Yuan and Prosperetti 1994). It is reasonable to assume that an average of the velocity profile on the projected area of the leading bubble wake is appropriate for the drag calculation. Therefore

$$F_D = C_D \frac{\pi}{8} d_B^2 \rho[(U_{B1} - \bar{w}_s) + u]^2 \tag{4}$$

where C_D is the drag coefficient on the trailing bubble, and $\bar{w}_s$ is the flow defect average of the wake. Dividing Eq. 4 by the drag force of the leading bubble and substituting equations for the drag coefficient, we have

$$F_D = \beta\left[\frac{(U_{B1} - \bar{w}_s) + u}{U_{B1}}\right] F_{D1} \tag{5}$$

If a range of Re is considered to be between 20 and 200 for spherical bubbles, β is defined as follows (Clift et al. 1978)

$$\beta = \begin{cases} Re^{0.22}/Re_1^{0.22} & \text{if } 20 \leq Re \leq 50 \\ \left(1 - 2.21Re^{-0.5}\right)/\left(1 - 2.21Re_1^{-0.5}\right) & \text{if } 50 < Re \leq 200 \end{cases} \tag{6}$$

The inertial forces due to the liquid acceleration are divided in two contributions (Magnaudet and Eames 2000): the acceleration force that is independent from the trailing bubble presence (F_{Ac}), and the added mass force (F_{Ad})

$$F_{Ac} = \frac{1}{6}\pi d_B^3 \rho \left[\frac{\partial(U_{B1} - \bar{w}_s)}{\partial t} + (U_{B1} - \bar{w}_s)\frac{\partial(U_{B1} - \bar{w}_s)}{\partial s}\right] \tag{7}$$

$$F_{Ad} = 0.5\frac{1}{6}\pi d_B^3 \rho \left[\frac{\partial(U_{B1} - \bar{w}_s)}{\partial t} + (U_{B1} - \bar{w}_s)\frac{\partial(U_{B1} - \bar{w}_s)}{\partial s} + \frac{\partial u}{\partial t}\right] \tag{8}$$

In this work, it is assumed that the leading bubble is not affected by the interaction, and thus its wake is stationary. Additionally, according to the experimental observations by Katz and Menevau (1996), the approximation of a trailing bubble to a leading bubble is of a quasi-stationary character. This results in the fact that the history force is negligible ($F_H \approx 0$), and it also implies that

$$\partial u/\partial t = -u\partial u/\partial s \tag{9}$$

Taking all of the above into account, after substituting the following dimensionless variables

$$\begin{aligned} W &= (U_{B1} - \bar{w}_s)/U_{B1} \\ U &= u/U_{B1} \end{aligned} \tag{10}$$

and dividing by the drag of the leading bubble, the substituted balance of forces (Eq. 1) finally ends up as follows

$$W\left(\beta + 2\frac{d_B}{C_{D1}}\frac{\partial W}{\partial s}\right) + U\beta - \frac{d_B}{C_{D1}}U\frac{\partial U}{\partial s}\left(\frac{2}{3} - \frac{4}{3}\frac{\rho_B}{\rho}\right) - 1 = 0 \tag{11}$$

3 Velocity Distribution in the Laminar Wake Behind the Leading Bubble

The problem at this point is to determine a velocity profile which describes the flow defect of the wake behind a bubble and which can be averaged on the projected area of the leading bubble. Due to the complexity of the flow behind a bubble, it has not been possible to find an analytical solution valid for the entire

region encompassing the wake yet. Approximate solutions have been found for the wake of an axisymmetric body, but these are valid for a region in which neither the presence of the body nor the interfacial boundary condition any longer affect the flow development (Batchelor 1967; Berger 1968). However, at downstream distances of the order of magnitude of bubble diameter, these solutions are not justified.

In view of the relevance of the flow in the wake for the in-line interaction, numerical simulations were conducted for the wake behind a spherical bubble for $20 \leq Re_1 \leq 200$, and dimensionless downstream distances of $s/d_B \geq 2$. To this end, the continuity and momentum equations were solved using the Comsol Multiphysics® 3.5a software package. A 2D geometry with axial symmetry was used, and several types of meshing were included in order for the results to be independent from the numerical parameters. The data obtained were useful to fit an equation for the axial velocity profile of a laminar wake. The equation form was based on an first analytical approach (Batchelor 1967), but incorporating an artificial origin in s dependant on Re_1. The fit was as follows

$$W_s = 1 - \frac{C_{D1}Re_1}{32}\frac{1}{\hat{s}+\hat{s}_0}\exp\left[-\frac{Re_1}{4}\frac{\hat{r}^2}{(\hat{s}+\hat{s}_0)}\right] \tag{12}$$

$$\hat{s}_0 = 0.008972Re_1 + 1.1555 \tag{13}$$

valid for $20 \leq Re_1 \leq 200$ and $s/d_B \geq 2$, and where

$$\hat{s} = \frac{s}{d_B} \qquad \hat{s}_0 = \frac{s_0}{d_B} \qquad \hat{r} = \frac{r}{d_B} \tag{14}$$

The correlation coefficient for the fit of Eqs. 12–13 was 0.983. The dimensionless velocity average in the bubble wake is

$$W = 1 - \frac{C_{D1}}{2}\left[1 - \exp\left(-\frac{Re_1}{16}\frac{1}{\hat{s}+\hat{s}_0}\right)\right] \tag{15}$$

4 Models for the Hydrodynamic Force and the Rise Velocity of the Trailing Bubble

The hydrodynamic force includes the opposing forces exerted by the liquid. Based on Eqs. 11 and 15, we have

$$\frac{F_{HD}}{F_{D1}} = W\left[\beta + \frac{Re_1}{16}\frac{1}{(\hat{s}+\hat{s}_0)^2}\exp\left(-\frac{Re_1}{16}\frac{1}{\hat{s}+\hat{s}_0}\right)\right] \tag{16}$$

For comparison purposes, in this work numerical data were obtained for the hydrodynamic force on an interactive bubble in the range of $20 \leq Re_1 \leq 200$ and

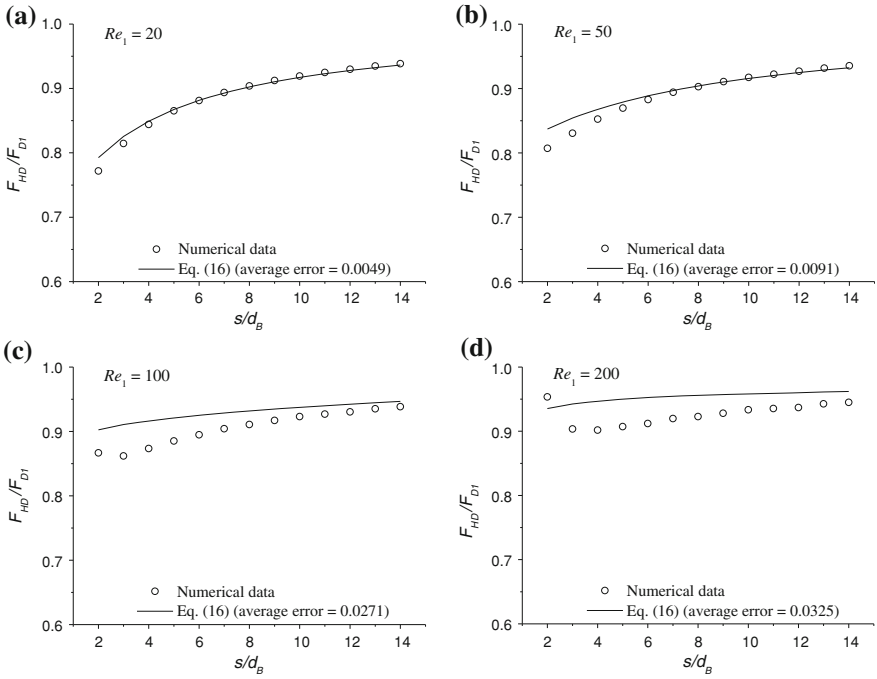

Fig. 2 Hydrodynamic force on the trailing bubble as a function of the dimensionless distance between bubbles for: **a** $Re_1 = 20$. **b** $Re_1 = 50$. **c** $Re_1 = 100$. **d** $Re_1 = 200$

$2 \leq s/d_B \leq 14$. The continuity and momentum equations were solved for a 2D geometry with axial symmetry of the problem, using the Comsol Multiphysics® 3.5a software package. The results for Re_1 at 20, 50, 100 and 200 are shown in Fig. 2.

In accordance to the numerical data, the hydrodynamic force on the trailing bubble increases with the separation distance. This is due to the fact that the flow defect in the wake drops as the downstream distance behind the leading bubble increases. Thus, the velocity average in the wake increases, and it gets closer to velocity U_{B1} of the uniform flow field, which causes an increase in the quasi-stationary drag. On the other hand, as s/d_B increases, the inertial contributions on the hydrodynamic force are to be monotonically reduced due to the fact that the wake flow is slowing down. However, because the drag is the main force, this reduction does not affect the general trend in most cases. The exceptions are Re_1 from 100 to 200, and at small s/d_B. In these cases, the numerical results suggest that the inertial forces due to the wake slowing down for $s/d_B \leq 3$ prevail in the general trend.

The hydrodynamic force also increases with Re_1. According to the numerical results for the axial velocity in the laminar wake behind a bubble, the flow defect drops slowly as Re_1 increases. This implies that the velocity average in the wake

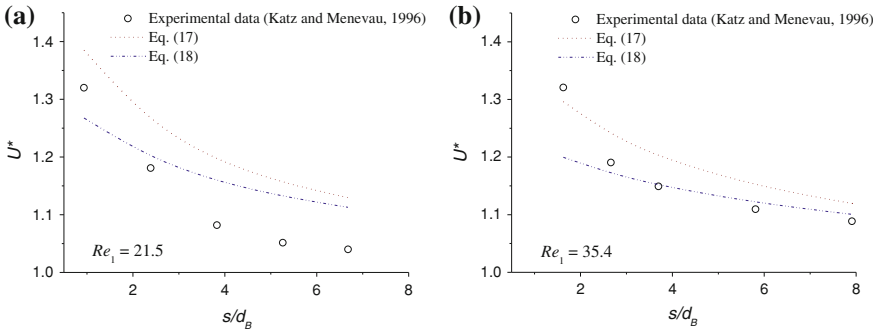

Fig. 3 Dimensionless rise velocity of the trailing bubble for: **a** $Re_1 = 21.5$. **b** $Re_1 = 35.4$

increases, and causes an increase in the drag. The increase of Re_1 should also cause an increase in the inertial contributions to the hydrodynamic force.

Figure 2 also shows the predictions of Eq. 16, and its comparison with the numerical results. The proposed equation shows a good agreement to the numerical data, particularly at low Re_1. The average relative (absolute) error of the predictions was between 0.0049 and 0.0325. The most notable discrepancies are observed at the greatest Re_1 and at reduced separation distances. In this regard, it is worthwhile mentioning that at small separation distances, the interaction among bubbles is strong (Yuan and Prosperetti 1994; Katz and Menevau 1996), and this implies that also the leading bubble is affected. The stopping effect that takes place in the wake flow generates pressure gradients upstream which affect the leading bubble. Since the proposed model does not include this effect, it is reasonable that its agreement at reduced separation distances differs slightly from the numerical results.

The balance of forces of Eq. 11 also allows determining the approximation velocity of the trailing bubble towards the leading bubble. Consider two cases: one that only takes into account the drag effects

$$U_1 = \frac{1}{\beta} - \left\{ 1 - \frac{C_{D1}}{2} \left[1 - \exp\left(-\frac{Re_1}{16} \frac{1}{\hat{s} + \hat{s}_0} \right) \right] \right\} \tag{17}$$

and another one obtained from the complete force balance

$$U_2 \frac{dU_2}{d\hat{s}} = \frac{3C_{D1}}{2} \left\{ U_2 \beta + W \left[\beta + \frac{Re_1}{16} \frac{1}{(\hat{s} + \hat{s}_0)^2} \exp\left(-\frac{Re_1}{16} \frac{1}{\hat{s} + \hat{s}_0} \right) \right] - 1 \right\} \tag{18}$$

$$U_2 = 0 \text{ at } \hat{s} \to \infty \tag{19}$$

Figure 3 shows the predictions of Eqs. 17 and 18, and their comparison with experimental data obtained by Katz and Menevau (1996) for Re_1 of 21.5 and 35.4. The dimensionless rise velocity (U^*) with respect to the terminal velocity of the leading bubble is plotted against the separation distance. The trend of experimental

data is well predicted by both equations, but the use of Eq. 17 may be advantageous if a fast approximation to the rise velocity is looked for.

5 Conclusions

Based on a force balance on a trailing bubble, in this work there was a proposal of models relating the flow in the wake of a leading bubble to the hydrodynamic force and the rise velocity of a trailing bubble, valid for $20 \leq Re_1 \leq 200$ and $2 \leq s/d_B \leq 14$. As a by-product, an equation for the axial velocity profile in the wake was proposed by adapting the form of a valid analytical approximation in the far wake. The models proposed showed a good agreement with numerical data for the hydrodynamic force (average error $\leq$0.0325), and with the trends of experimental data for the rise velocity of the trailing bubble.

References

Batchelor GK (1967) An Introduction to fluid mechanics. Cambridge University Press, Cambridge

Berger S (1968) The incompressible laminar axisymmetric far wake. J Maths Phys 47:292–309

Clift R, Grace JR, Weber ME (1978) Bubbles drops and particles. Academic Press Inc, New York

Katz J, Menevau C (1996) Wake-induced relative motion of bubbles rising in line. Int J Multiphase Flow 22(2):239–258

Magnaudet J, Eames I (2000) The motion of high-Reynolds-number bubbles in inhomogeneus flows. Ann Rev Fluid Mech 32:659–708

Yuan H, Prosperetti A (1994) On the in-line motion of two spherical bubbles in a viscous liquid. J Fluid Mech 278:325–349

Modeling of Three Phase "Bubbly Gas-Intermittent Oil" Flow in Vertical Pipes

Daniel J. Montoya-Hernández and Octavio Cazarez-Candia

Abstract In this work, a one-dimensional, thermal, transient two-fluid mathematical model for "Bubbly gas-Intermittent oil" (Bg-Io) upward flow is presented. The model was developed under the hypothesis that the Bg-Io flow pattern can be approached by two different flow patterns, each one in neighboring regions: water–gas bubbly flow through the annular region and heavy oil-gas-water bubbly flow in the slug body region. The model consists of mass, momentum and energy conservation equations for every phase whose numerical solution is based on the finite difference technique in the implicit scheme. The model is able to predict pressure, temperature, volumetric fraction and velocity profiles for each phase. For accurate modeling, a liquid slug length was proposed and used. Various oil interfacial and wall-water shear stresses correlations proposed in literature were also evaluated. The predictions are in agreement with experimental data reported in literature.

1 Introduction

In the petroleum industry, three phase flow of heavy oil-gas-water occurs often, especially in the production of hydrocarbons from heavy oil fields and also in both on-shore and offshore transporting pipelines. Knowledge of the three-phase flow

D. J. Montoya-Hernández (✉) · O. Cazarez-Candia
Eje Central Lázaro Cárdenas, Instituto Mexicano del Petróleo, Norte 152 San Bartolo Atepehuacan, Gustavo A. Madero, 07730 Mexico City, D.F., Mexico
e-mail: djmontoy@imp.mx

O. Cazarez-Candia
e-mail: ocazarez@imp.mx

J. Klapp et al. (eds.), *Experimental and Theoretical Advances in Fluid Dynamics*, Environmental Science and Engineering, DOI: 10.1007/978-3-642-17958-7_21,

characteristics, such as flow patterns, pressure drop and holdups, can have significant impact on the adeccuate design and operation of pipelines and on many flow assurance issues including hydrate formation, emulsion, wax deposition and corrosion (Zhang and Sarica 2005). Therefore the study of the three-phase flow of heavy oil, water and gas phase is in order.

Multiphase flow hydrodynamic modeling is based on flow pattern definitions, then it is virtually impossible to develop a generalized solution for all flow patterns, because each flow pattern shows a unique hydrodynamic behavior. Compared to numerous investigations of two-phase flow modeling, the gas-oil-water three-phase flow can be treated in two ways. One treatment is to combine the oil and water into a single liquid phase and then modeling the system as a two phase liquid–gas flow. In this treatment the slip between the oil and water is ignored and a homogeneous mixture is assumed for the liquid phase (Bonizzi and Issa 2003; Shi et al. 2004). For example Bonizzi and Issa (2003) simulated three-phase (liquid-liquid-gas) stratified and slug flows. They used the one-dimensional transient two-fluid model in which the continuity and momentum equations for the two liquids (light oil and water) were combined together to obtain a new equation in terms of liquid mixture quantities.

An alternative treatment consists in considering the three-phase flow as a three layer stratified flow with gas on the top, oil in the middle and water and the bottom, this can be done for immiscible liquids (Taitel et al. 1995; Zhang and Sarica 2005; Ghorai et al. 2005; Neogi et al. 1994). For example Taitel et al. (1995) developed a one dimensional model based on mass and momentum balance to calculate gas, oil, and water hold-ups. The model also evaluates the pressure drop and phase velocities. The comparison with the hold-up measurements given by Khor et al. (1997) showed a promising agreement. Most three-phase flows fit between the above mentioned treatments; however, Cazarez et al. (2009) proposed a homogeneous model of the called "Bubbly gas-Bubbly oil" flow (Bannwart et al. 2005) formed when heavy oil, gas and water flow simultaneously through a circular pipe and water forms a continuous phase. The authors considered this kind of flow as one liquid phase with mixture properties. The model predicts pressure, velocity and temperature of the mixture.

In the present investigation, a two-fluid transient, thermal, mathematical model is presented, which is able to predict pressure, volumetric fraction, temperature and velocity profiles for each phase when oil, water and gas flow simultaneously under the flow pattern known as "Bubbly gas-Intermittent oil" (Fig. 1). Similarly to Fernandes et al. (1983); Kaya (1998); Sylvester (1987) and Taitel and Barnea (1990) where the slug unit cell (air–water) is subdivided in two sections, the Bg-Io flow pattern was approached in two different flow patterns in two different regions: (1) water–gas bubbly flow through the annular region and, (2) heavy oil-gas-water bubbly flow in the slug body region.

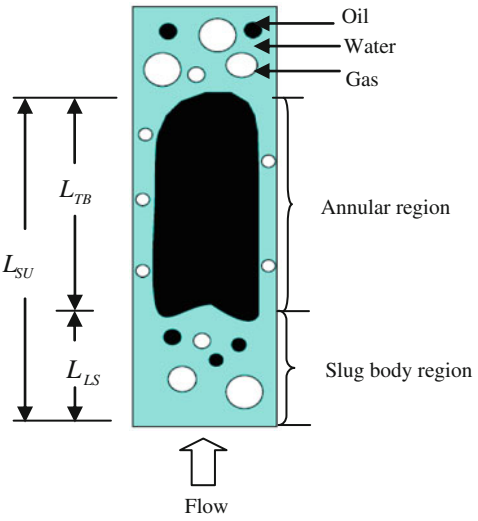

Fig. 1 "Bubbly gas-Intermittent oil" three-phase flow. The symbols L_{TB}, L_{LS}, and L_{SU} represent the Taylor bubble, the liquid slug and the slug unit lengths, respectively (modified from Bannwart et al. 2005)

2 Governing Equations

In the present model, for the gas-water bubbly flow through the annular region, the gas drag force (F_{Dg}), gas virtual mass force (F_{vmg}), water-wall (τ_{wW1}) shear stress and the interfacial heavy oil-water ($\tau_{oi} = \tau_{wi}$) shear stress were taken into account. For the heavy oil-gas-water bubbly flow in the slug body region, all forces and shear stresses used in the work of Cazarez et al. (2010) were considered. Gas is regarded as a compressible fluid obeying the ideal gas, while both liquids are incompressible. The effect of breakup and coalescence of droplets in the dispersed phases is ignored. The phase pressures are supposed to be equal within a computational cell (i.e., $P_g = P_o = P_w = P$). Mass transfer effects or chemical reactions have been neglected as well as the heat transfer among phases and between the flow and wall-pipe. Then, the conservation equations of mass, momentum and energy for the "Bubbly gas-Intermittent oil" three phase flow are as follows:

1. Gas, oil and water mass equations

$$\frac{\varepsilon_g}{\rho_g C_g^2}\left[\frac{\partial P}{\partial t} + v_g \frac{\partial P}{\partial z}\right] - \frac{\varepsilon_g}{T_g}\left[\frac{\partial T_g}{\partial t} + v_g \frac{\partial T_g}{\partial z}\right] + \left[\frac{\partial \varepsilon_g}{\partial t} + v_g \frac{\partial \varepsilon_g}{\partial z}\right] + \varepsilon_g \frac{\partial v_g}{\partial z} = 0 \quad (1)$$

$$\frac{\partial(\rho_o \varepsilon_o)}{\partial t} + \frac{\partial(\rho_o \varepsilon_o v_o)}{\partial z} = 0 \quad (2)$$

$$\frac{\partial(\rho_w \varepsilon_w)}{\partial t} + \frac{\partial(\rho_w \varepsilon_w v_w)}{\partial z} = 0 \tag{3}$$

2. Gas, oil and water momentum equations

$$\frac{\partial(\rho_g \varepsilon_g v_g)}{\partial t} + \frac{\partial(\rho_g \varepsilon_g v_g^2)}{\partial z} + \varepsilon_g \frac{\partial P}{\partial z} = -\varepsilon_g \rho_g g \sin\theta - F_{Dg} - F_{vmg} - F_{Dgo}\Lambda_2 \tag{4}$$

$$\frac{\partial(\rho_o \varepsilon_o v_o)}{\partial t} + \frac{\partial(\rho_o \varepsilon_o v_o^2)}{\partial z} + \varepsilon_o \frac{\partial P}{\partial z} = -\varepsilon_o \rho_o g \sin\theta - F_{Do}\Lambda_2 - F_{vmo}\Lambda_2 + F_{Dgo}\Lambda_2 - \frac{\tau_{oi} S_{oi}}{A}\Lambda_1 \tag{5}$$

$$\frac{\partial(\rho_w \varepsilon_w v_w)}{\partial t} + \frac{\partial(\rho_w \varepsilon_w v_w^2)}{\partial z} + \varepsilon_w \frac{\partial P}{\partial z} = -\varepsilon_w \rho_w g \sin\theta + F_{Dg} + F_{vmg} + F_{Do}\Lambda_2 + F_{vmo}\Lambda_2 - \frac{\tau_{wW1} S_w}{A}\Lambda_1 - \frac{\tau_{wW2} S_w}{A}\Lambda_2 + \frac{\tau_{wi} S_{wi}}{A}\Lambda_1 \tag{6}$$

3. Gas, oil and water energy equations

$$Cp_g \left[\frac{\partial T_g}{\partial t} + v_g \frac{\partial T_g}{\partial z}\right] + v_g \left[\frac{\partial v_g}{\partial t} + v_g \frac{\partial v_g}{\partial z}\right] - \frac{1}{\rho_g}\frac{\partial P}{\partial t} = -v_g g \cos\phi \tag{7}$$

$$\varepsilon_o \rho_o Cp_o \left[\frac{\partial T_o}{\partial t} + v_o \frac{\partial T_o}{\partial z}\right] + \varepsilon_o \rho_o v_o \left[\frac{\partial v_o}{\partial t} + v_o \frac{\partial v_o}{\partial z}\right] + \varepsilon_o v_o \frac{\partial P}{\partial z} = -\varepsilon_o \rho_o v_o g \cos\phi \tag{8}$$

$$\varepsilon_w \rho_w Cp_w \left[\frac{\partial T_w}{\partial t} + v_w \frac{\partial T_w}{\partial z}\right] + \varepsilon_w \rho_w v_w \left[\frac{\partial v_w}{\partial t} + v_w \frac{\partial v_w}{\partial z}\right] + \varepsilon_w v_w \frac{\partial P}{\partial z} = -\varepsilon_w \rho_w v_w g \cos\phi \tag{9}$$

In Eqs. 1–9 P is the averaged pressure over the cross sectional area A of the pipe, T is temperature, g is the acceleration due to gravity, ρ is density, v is velocity, ε is volumetric fraction, θ is inclination angle, $\phi = \theta + 90°$, S_w, S_{wi}, S_{oi} is water-wall, water-interfacial and oil-interfacial wetted perimeter, respectively, C_g is gas sound velocity, C_p is heat capacity, t and z are temporal and spatial coordinates, respectively, Λ_2 is liquid-slug-length−slug-unit-length ratio

(= L_{LS}/L_{SU}) and Λ_1 is Taylor-bubble-length−slug-unit-length ratio (= L_{BT}/L_{SU}). The subscripts g, o and w represent gas, oil, and water, respectively. Additionally, the following relations must be satisfied:

$$P = \rho_g R T_g \tag{10}$$

$$\varepsilon_g + \varepsilon_o + \varepsilon_w = 1 \tag{11}$$

where R is the gas constant. In order to solve the system of Eqs. 1–11, it is indispensable to formulate appropriate closure relationships that permit modeling the interaction between phases. In the present study the water-wall and the water–oil interfacial shear stresses were taken from Bannwart (2001). The rest of closure relationships were taken from Cazarez et al. (2010). Besides, information for the liquid slug and Taylor bubble lengths should be also given. Experimental observation for air–water system suggest that the stable slug-unit-length (L_{LS}) is relatively insensitive to the gas and liquid flow rates and it is fairly constant for a given tube diameter (d) (Taitel and Barnea 1990). For the vertical case the observed liquid-slug-length is about 10–20d (Moissis and Griffith 1962; Fernandes 1981; Barnea and Shemer 1989). However, for heavy oil-air-water three-phase flow a value of 35d for a liquid-slug-length is proposed and used in this study. For the Taylor-bubble-length (L_{TB}), a value of 0.04 m was taken from the work of Vieira (2004).

3 Numerical Solution

When the geometry is not complicated like the case of pipes, the finite difference method is commonly used. Discretization of Eqs. 1–11 was obtained applying a first order downstream implicit scheme for spatial derivatives and a first order upstream implicit scheme for time derivatives. The concept of donor cell is used for parameter lumping purposes. It states that the fluid exit conditions are the same as the fluid conditions in the node itself. Stability of numerical solutions is improved using this concept. The complete procedure can be consulted in Cazarez et al. (2010).

4 Results of Numerical Simulation and Discussion

The model was validated using experimental data given by Bannwart et al. (2005), whose experiments were carried out using a heavy oil of 971 kg/m^3 with a viscosity of 5040 mPa.s and a 2.84 cm i.d. and 2.5 m long glass tubing at ambient temperature and near atmospheric pressure. For nine different flow conditions,

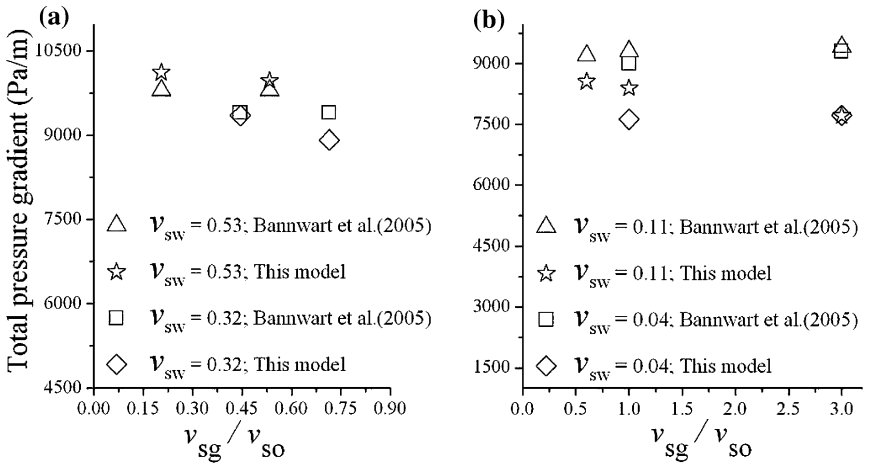

Fig. 2 Pressure gradient for the Bg-Io flow, as a function of gas-oil ratio for different water superficial velocities. **a** 0.53 and 0.32 m/s, **b** 0.11 and 0.04 m/s

Table 1 Error of pressure predictions for different flow conditions

v_{sg}	v_{so}	v_{sg}/v_{so}	v_{sw}	Error (%)
0.045	0.220	0.204	0.53	3.219
0.048	0.090	0.533	0.53	1.722
0.040	0.090	0.444	0.32	0.547
0.050	0.070	0.714	0.32	5.148
0.042	0.070	0.600	0.11	6.989
0.040	0.040	1.000	0.11	9.718
0.060	0.020	3.000	0.11	17.946
0.040	0.040	1.000	0.04	15.271
0.060	0.020	3.000	0.04	16.925
		Total average error		8.609

at which the Bg-Io flow pattern can appear, the present model was tested. In Fig. 2 the predicted and experimental pressure gradients were compared.

Predictions presented good agreement with experimental data (8.609% total average error). However, some predictions larger than the expected ones were reached when gas–oil ratios were 1.0 and 3.0 for water superficial velocities of 0.04 and 0.11 m/s (Fig. 2b), with errors of 15.2–17.9% respectively. According to the work of Bannwart et al. (2005) such conditions correspond to a transition zone; this can be the reason why the predictions do not match with experimental data. A complete error description for different flow conditions is given in Table 1.

Unfortunately, for this kind of flow pattern, neither the gas and oil volumetric fractions nor the oil and gas velocities have been reported in the literature, making it impossible to fully test the model. However, trying to demonstrate the model prediction capabilities in Fig. 3a the transient volumetric fraction profile for each

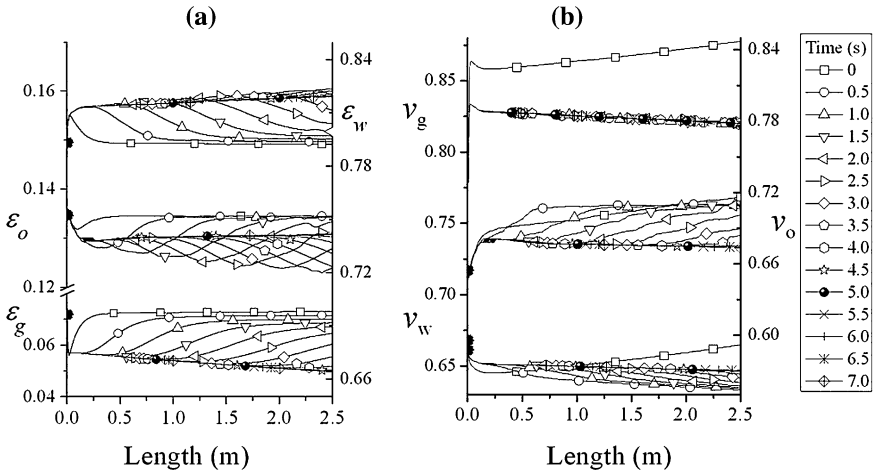

Fig. 3 Transient behavior of: **a** Volumetric fractions, **b** Velocities. ($v_{sg} = 3.5$, $v_{so} = 0.04$ and $v_{sw} = 0.53$m/s)

phase is shown. The maximum value reached of water volumetric fraction was approximately 0.82, which is greater than the gas (0.055) and oil (0.13) volumetric fractions because the water is the dominant continuous phase according to the experimental data given by Bannwart et al. (2005). Figure 3b shows the velocity profiles. As it was expected the gas velocity is the biggest one and the water velocity is the smallest one, this because their densities are different ($\rho_g = 1.18$, $\rho_o = 971$, $\rho_w = 996$ kg/m^3). Regarding to temperature profiles a constant value of 298.2 K is reached, this was an expected result because it was considered an adiabatic flow, for this reason the figure of the temperature profile was not included.

5 Influence of the Liquid Slug Length on the Predictions

An important factor for the pressure gradient predictions, when the slug flow is present, is the correct determination of parameters such liquid-slug and Taylor-bubble lengths for the estimation of Λ_1 and Λ_2. For this reason an analysis over these parameters was carried out. The liquid-slug-length was tested for 20, 30, 35 and 40d, while the Taylor-Bubble was kept constant accordingly to the experimental data of Vieira (2004). In Table2 it is shown the comparison of the error predictions with different liquid-slug lengths for different water superficial velocities, it can be seen that with $L_{LS} = 35d$ the pressure gradient prediction reached the smallest average error. Although the slug-lengths were obtained through numerical experimentation, better predictions could be reached when L_{LS} and L_{TB} are obtained from experimental data. It is important to note that for the

Table 2 Error in the predictions for different slug-liquid-lengths

v_{sg}/v_{so}	v_{sw}	Error (%)			
		$L_{LS} = 40d$	$L_{LS} = 35d$	$L_{LS} = 30d$	$L_{LS} = 20d$
0.204	0.53	3.250	3.219	7.436	3.475
0.533	0.53	0.472	1.722	1.306	3.039
0.44	0.32	5.049	0.547	6.144	4.314
0.714	0.32	6.587	5.148	4.731	3.766
0.6	0.11	7.885	6.989	8.466	7.918
1.0	0.11	7.967	9.718	8.114	7.788
3.0	0.11	13.554	17.946	11.183	23.973
1.0	0.04	15.816	15.271	19.745	21.387
3.0	0.04	18.095	16.925	26.169	28.729
Average error		8.746	8.609	10.366	11.599

Bg-Io flow, there is no experimental information about liquid-slug and Taylor-bubble-lengths. This is a topic to be investigated.

6 Conclusions

A two-fluid model for three-phase bubbly gas-intermittent oil (Bg-Io) flow in vertical pipes has been presented. The model is able to predict pressure, temperature, volumetric fraction and velocity profiles for each phase. The proposed model was developed under the assumption that the Bg-Io flow pattern can be approached by the water-gas-bubbly flow through the annular region and heavy oil-gas-water bubbly flow in the slug body region. For accurate modeling, a liquid slug length of $35d$ was proposed and used. Regarding the pressure drop predictions, it was found that the values calculated with the proposed model are in complete agreement with experimental data reported in the literature. The maximum total average error value was lower than 9.0%.

Acknowledgments The authors wish to thank the financial support provided by the Consejo Nacional de Ciencia y Tecnología (CONACyT).

References

Bannwart AC (2001) Modeling aspects of oil-water core-annular flows. J Petrol Sci Eng 32:127–143

Bannwart AC, Vieira FF, Carvalho CHM, Oliveira AP (2005) Water-assisted flow of heavy oil and gas in a vertical pipe. SPE/PS-CIM/CHOA 97875. International thermal operations and heavy oil symposium. Calgary Alberta, Canada

Barnea D, Shemer L (1989) Void fraction measurements in vertical slug flow: applications to slug characteristics and transition. Int J Multiphase flow 15:495–504

Bonizzi M, Issa RI (2003) On the simulation of three-phase slug flow in nearly horizontal pipes using the multi-fluid model. Int J Multiphase flow 29:1719–1747

Cazarez CO, Montoya D, Vital G (2009) Mathematical model for bubbly water- heavy oil–gas flow in vertical pipes. Pet Sci Technol 27:1715–1726

Cazarez CO, Montoya D, Vital G, Bannwart AC (2010) Modeling of three phase heavy oil–water–gas bubbly flow in upward vertical pipes. Int J Multiphase Flow 36(6):439–448

Fernandes RC (1981) Experimental and theoretical studies of isothermal upward gas-liquid flows in vertical tubes. PhD Thesis. University of Houston

Fernandes RC, Semiat R, Dukler AE (1983) Hydrodinamic model for gas-liquid slug flow in vertical tubes. AIChEJ 29:981–989

Ghorai S, Suri V, Nigam KDP (2005) Numerical modeling of three-phase stratified flow in pipes. Chem Eng Sci 60:6637–6648

Kaya Sendar A (1998) Comprehensive mechanistic modeling of two-phase flow in deviated wells. Ms. Thesis. University of Tulsa

Khor SH, Mendes-Tatsis MA, Hewitt GF (1997) One-dimensional modeling of phase holdups in three-phase stratified flow. Int J Multiphase flow 23(5):885–897

Moissis R, Griffith P (1962) Entrance effects in a two phase slug flow. J Heat Transfer 84:29–39

Neogi S, Lee A, Jepson WP (1994) A model for multiphase (gas–water–oil) stratified flow in horizontal pipelines. SPE 28799:553–561

Shi H, Holmes JA, Diaz LR, Durlofsky LJ, Aziz K (2004) Drift-flux parameters for three-phase steady-state flow in wellbores. SPE 89836:1–10

Sylvester ND (1987) A mechanistic model for two-phase vertical slug flow in pipes. J Energy Resour Technol 109:206–213

Taitel Y, Barnea D (1990) A consistent approach for calculating pressure drop in inclined slug flow. Chem Eng Sci 45(5):1199–1206

Taitel Y, Barnea D, Brill JP (1995) Stratified three phase flow in pipes. Int J Multiphase flow 21(1):53–60

Vieira F (2004) Escoamento trifásico vertical de óleos pesados aplicado à elevação artificial. Dissertação de mestrado. Thesis. Universidade estadual de Campinas, Brazil

Zhang HQ, Sarica C (2005) Unified modeling of gas/oil/water pipe flow-Basic approaches and preliminary validation. SPE 95749:1–9

Mathematical Model for Heavy Oil–Water–Gas Stratified Flow in Horizontal Pipes

C. Centeno-Reyes and O. Cazarez-Candia

Abstract A one-dimensional, isothermal, transient model for the stratified flow of heavy oil, water and gas, in horizontal pipelines, is presented. The two-fluid mathematical model consists of mass, momentum and energy conservation equations for every phase. The model takes into account: (1) the hydrostatic pressure, (2) wall shear stress, (3) interfacial shear stress, (4) gas–oil interfacial roughness, and (5) the non-Newtonian oil behavior. The model is able to predict pressure, volumetric fraction, temperature, and velocity profiles for every phase. The numerical solution is based on the finite differences technique in an implicit scheme. The model is validated using experimental data reported in literature, for a light oil (32°API), and a heavy oil (14°API); in both cases the pressure drop calculated by the model is reasonably close to the experimental data.

1 Introduction

The three-phase gas–oil–water flow occurs in the oil and gas industry, either in production or transportation of the produced fluids, so its study is of considerable practical importance for flow assurance in the petroleum industry. Particularly the three-phase stratified flow has been observed for light oil–water–gas flow (Ghorai et al. 2005), and also for heavy oil–water–gas flow (Bannwart et al. 2004).

C. Centeno-Reyes (✉) · O. Cazarez-Candia
Eje Central Lázaro Cárdenas, Instituto Mexicano del Petróleo, No. 152,
Col. San Bartolo Atepehuacan, 07730 México City, D.F, Mexico
e-mail: ccenteno@imp.mx

O. Cazarez-Candia
e-mail: ocazarez@imp.mx

J. Klapp et al. (eds.), *Experimental and Theoretical Advances in Fluid Dynamics*, Environmental Science and Engineering, DOI: 10.1007/978-3-642-17958-7_22,

The light oil–water–gas flow has already been mathematically modeled, either using three-fluid models (Taitel et al. 1995; Ghorai et al. 2005), or using drift-flux models (Bonizzi and Issa 2003; Tomasello 2009), in both methodologies, the treatment for three-phase flow has been to combine oil and water into a single liquid phase, and then modelling the system as a two-phase liquid–gas steady-state flow. However the heavy oil–water–gas flow has not been modeled until this work, and in contrast to the existing models, the liquid phases are not treated as a single liquid phase, and the model is not in steady-state but transitory, this implies an increase in the complexity of the equation system that is solved, but let us consider different pressures, velocities and temperatures in each phase.

2 Three-Fluid Model

The stratified flow presents the gravitational segregation of the three continuous phases. Oil is lighter than water and therefore, it flows in the middle, water at the bottom, and the gas on top of the pipe (Fig. 1). This is not the case of heavy oils with API gravity lower than 10°API, where oil is denser than water and would flow in the bottom of the pipe, not in the middle.

Due to the phases structure inside the pipe, gas-wall shear stress, oil-wall shear stress, water-wall shear stress, water–oil interfacial shear stress, and gas–oil interfacial shear stress were taken into account.

It was assumed: (1) a full-developed, one-dimensional, adiabatic flow with flat interfaces; (2) ideal gas; and (3) incompressible flow for liquid phases. The hydrostatic pressure was used to take into account the unequal phase pressure.

2.1 Pressure Gradient

The hydrostatic pressure is calculated for each phase, in terms of the gas–oil interfacial pressure. Gas pressure is related by the next hydrostatic relationship:

$$P_g = P_i - \rho_g g(D - h_L)\cos\theta \tag{1}$$

For the liquid phases, the pressure is averaged along the layer,

$$\overline{P}_o = \int_{h_w}^{h_L} [P_i + \rho_o g(h_L - y)\cos\theta] b(y) dy \Big/ \varepsilon_o A \tag{2}$$

and then it is written in terms of the angle between the centerline and the interface:

$$\bar{P}_o = P_i + \rho_o g \cos\theta h_L - \frac{2\rho_o g \cos\theta (D/2)^3}{\varepsilon_o A}\left[\frac{\theta}{4} - \frac{\text{sen}\theta}{4} - \frac{1}{3}\text{sen}^3\left(\frac{\theta}{2}\right)\right]_{\theta=\pi-2\beta}^{\theta=\pi+2\alpha} \tag{3}$$

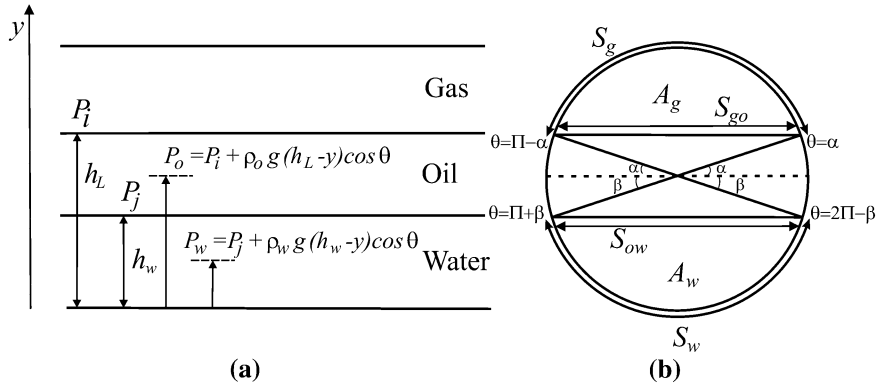

Fig. 1 **a** Hydrostatic pressure inside the liquid phases; **b** three-layer geometry

where $\bar{P}_o$ is averaged oil pressure, P_i is gas–oil interfacial pressure, ρ is density, g is acceleration due to gravity, D is pipe diameter, θ is pipe inclination angle, ε is volumetric fraction, A is the cross sectional area, h_L and h_w are liquid and water height respectively; α and β are the angles between the interfaces and the centerline (Fig. 1).

2.2 Governing Equations

Accordingly to the work of Lahey and Drew (1989) the governing averaged (space-time) equations for a one-dimensional adiabatic heavy oil–water–gas flow in a constant area duct without interfacial mass, including the averaged hydrostatic pressure, can be written as:

Gas, oil and water mass conservation equations

$$\frac{\varepsilon_g}{C_g^2 + g(D-h_L)}\left(\frac{\partial P_i}{\partial t} + U_g\frac{\partial P_i}{\partial z}\right) + \frac{\varepsilon_g \rho_g}{T_g}\left(\frac{g(D-h_L)}{C_g^2 + g(D-h_L)} - 1\right)\left(\frac{\partial T_g}{\partial t} + U_g\frac{\partial T_g}{\partial z}\right) + \varepsilon_g\rho_g\frac{\partial U_g}{\partial z} + \left(\frac{\varepsilon_g g \rho_g}{\left(C_g^2 + g(D-h_L)\right)}\frac{A}{2\sqrt{h_L(D-h_L)}} + \rho_g\right)\left(\frac{\partial \varepsilon_g}{\partial t} + U_g\frac{\partial \varepsilon_g}{\partial z}\right) = 0 \tag{4}$$

$$\frac{\partial \varepsilon_o}{\partial t} + U_o\frac{\partial \varepsilon_o}{\partial z} + \varepsilon_o\frac{\partial U_o}{\partial z} = 0 \tag{5}$$

$$\frac{\partial \varepsilon_w}{\partial t} + U_w\frac{\partial \varepsilon_w}{\partial z} + \varepsilon_w\frac{\partial U_w}{\partial z} = 0 \tag{6}$$

Gas, oil and water momentum conservation equations

$$\varepsilon_g\rho_g\left(\frac{\partial U_g}{\partial t}+U_g\frac{\partial U_g}{\partial z}\right)+\frac{\varepsilon_g C_g^2}{\left(C_g^2+g(D-h_L)\right)}\frac{\partial P_i}{\partial z}+\frac{\varepsilon_g C_g^2 g\rho_g}{\left(C_g^2+g(D-h_L)\right)}\frac{A}{2\sqrt{h_L(D-h_L)}}\frac{\partial \varepsilon_g}{\partial z}$$
$$+\frac{\varepsilon_g C_g^2 g(D-h_L)\rho_g}{\left(C_g^2+g(D-h_L)\right)T_g}\frac{\partial T_g}{\partial z}=-\frac{\tau_{gwall}S_g}{A}-\frac{\tau_{go}S_{go}}{A} \tag{7}$$

$$\varepsilon_o\rho_o\left(\frac{\partial U_o}{\partial t}+U_o\frac{\partial U_o}{\partial z}\right)+\frac{2\rho_o g R^3}{A\varepsilon_o}\Lambda\frac{\partial \varepsilon_o}{\partial z}+\varepsilon_o\frac{\partial P_i}{\partial z}+\frac{\varepsilon_o\rho_o g A}{2\sqrt{h_L(D-h_L)}}\frac{\partial \varepsilon_g}{\partial t}$$
$$=-\frac{\tau_{owall}S_o}{A}+\frac{\tau_{go}S_{go}}{A}-\frac{\tau_{ow}S_{ow}}{A} \tag{8}$$

$$\varepsilon_w\rho_w\left(\frac{\partial U_w}{\partial t}+U_w\frac{\partial U_w}{\partial z}\right)+\varepsilon_w\frac{\partial P_i}{\partial z}+\varepsilon_w g\cos\theta\left[-\frac{(\rho_w-\rho_o)A}{2\sqrt{h_w(D-h_w)}}-\frac{2\rho_w R^3}{A\varepsilon_w^2}\Theta\right]\frac{\partial \varepsilon_o}{\partial z}$$
$$+\varepsilon_w g\cos\theta\left[\frac{\rho_o A}{2\sqrt{h_L(D-h_L)}}-\frac{(\rho_w-\rho_o)A}{2\sqrt{h_w(D-h_w)}}-\frac{2\rho_w(D/2)^3}{A\varepsilon_w^2}\Theta\right]\frac{\partial \varepsilon_g}{\partial z}$$
$$=-\frac{\tau_{wwall}S_w}{A}+\frac{\tau_{ow}S_{ow}}{A} \tag{9}$$

Gas, oil and water energy conservation equations

$$\left(Cp_g-\frac{C_g^2 g(D-h_L)}{\left(C_g^2+g(D-h_L)\right)T_g}\right)\frac{\partial T_g}{\partial t}+U_g\left(\frac{\partial U_g}{\partial t}+U_g\frac{\partial U_g}{\partial z}\right)+Cp_g U_g\frac{\partial T_g}{\partial z}$$
$$-\frac{C_g^2}{\rho_g\left(C_g^2+g(D-h_L)\right)}\frac{\partial P_i}{\partial t}-\frac{C_g^2 g}{\left(C_g^2+g(D-h_L)\right)}\frac{A}{2\sqrt{h_L(D-h_L)}}\frac{\partial \varepsilon_g}{\partial t}=0 \tag{10}$$

$$\frac{\partial T_o}{\partial t}+U_o\frac{\partial T_o}{\partial z}+\frac{U_o}{Cp_o}\frac{\partial U_o}{\partial t}+\frac{U_o^2}{Cp_o}\frac{\partial U_o}{\partial z}+\frac{U_o}{Cp_o\rho_o}\frac{\partial P_i}{\partial t}$$
$$+\frac{U_o g A}{2Cp_o\sqrt{h_L(D-h_L)}}\frac{\partial \varepsilon_g}{\partial t}+\frac{2U_o g(D/2)^3}{Cp_o A\varepsilon_o^2}\Lambda\frac{\partial \varepsilon_o}{\partial t}=0 \tag{11}$$

$$\frac{\partial T_w}{\partial t}+U_w\frac{\partial T_w}{\partial z}+\frac{U_w}{Cp_w}\left(\frac{\partial U_w}{\partial t}+U_w\frac{\partial U_w}{\partial z}\right)+\frac{U_w g\cos\theta}{Cp_w\rho_w}\left[-\frac{(\rho_w-\rho_o)A}{2\sqrt{h_w(D-h_w)}}-\frac{2\rho_w(D/2)^3}{A\varepsilon_w^2}\Theta\right]$$
$$\frac{\partial \varepsilon_o}{\partial z}+\frac{U_w g\cos\theta}{Cp_w\rho_w}\left[\frac{\rho_o A}{2\sqrt{h_L(D-h_L)}}-\frac{(\rho_w-\rho_o)A}{2\sqrt{h_w(D-h_w)}}-\frac{2\rho_w(D/2)^3}{A\varepsilon_w^2}\Theta\right]\frac{\partial \varepsilon_g}{\partial z}+\frac{U_w}{Cp_w\rho_w}\frac{\partial P_i}{\partial z}=0 \tag{12}$$

where T is temperature, U is velocity, S_k is the wetted perimeter, C_g is gas sound velocity, C_p is heat capacity, t and z are temporal and spatial coordinates, respectively. The subscripts g, o and w represent gas, oil and water, respectively. Θ and Λ are defined by

$$\Theta = \frac{\pi - 2\beta}{4} - \frac{\text{sen}(\pi - 2\beta)}{4} - \frac{1}{3}\text{sen}^3\left(\frac{\pi - 2\beta}{2}\right) \tag{13}$$

and

$$\Lambda = \frac{\alpha + \beta}{2} - \frac{\text{sen}(2\alpha + 2\beta)}{4} - \frac{1}{3}\text{sen}^3(\alpha + \beta) \tag{14}$$

2.3 Shear-Stress Relationships

As was stated in Sect. 1, five shear stresses are needed to solve the equation system. The shear stresses were correlated as follows.

2.3.1 Gas-Wall and Water-Wall Shear Stresses

For the shear stresses between the water or gas and the pipe surface, the friction factors, f_w and f_g were approximated by the correlation:

$$f_k = C\,\text{Re}_k^{-n},\ \ k = w, g \tag{15}$$

where C = 0.079, n = 0.25 for turbulent flow, and C = 16, n = 1 for laminar flow. The Reynolds numbers were defined as

$$\text{Re}_w = 4U_w A_w \rho_w / S_w \mu_w \tag{16}$$

for water and

$$\text{Re}_g = 4U_g A_g \rho_g / \left(S_g + S_{go}\right)\mu_g \tag{17}$$

for the gas phase.

2.3.2 Oil-Wall Shear Stress

The crude oil was considered to exhibit a non-Newtonian behavior, using the next power law model.

$$\tau = K\gamma^n,\ n \leq 1 \tag{18}$$

where K is consistency constant and n is a measure of the non-newtonian behavior. The friction factor can be calculated analytically for laminar flow (Govier and Aziz 1972):

$$f_o = 16\,\mathrm{Re}_{oMR}^{-1} \tag{19}$$

For turbulent flow, the explicit Kawase correlation was used (Kawase et al. 1994):

$$f_o = \left\{ 3.57 \log_{10} \left[\frac{\mathrm{Re}_{oMR}^{1/n^{0.615}}}{\mathrm{Re}_{oMR}^{1/n^{0.615}} \left[10^{(3.75-8.5n)/5.756} \left(\frac{2\varepsilon}{D} \right) \right]^{1.14/n} + 6.5^{1/n^{(1+0.75n)}}} \right] \right\}^{-2} \tag{20}$$

where Re_{oMR} is Metzner-Reed Reynolds number (Metzner Reed 1955)

$$\mathrm{Re}_{oMR} = \rho_o D h_o^n U_o^{2-n} \Big/ K \left(\frac{3n+1}{4n} \right)^n 8^{n-1} \tag{21}$$

2.3.3 Water–Oil Interfacial Shear Stress

The empirical values of interfacial friction factor were taken to be same as proposed by Taitel et al. (1995).

2.3.4 Gas–Oil Interfacial Shear Stress

This interface can present waves, due to the different velocities between the phases, and can be calculated as a rough interface (Eck 1973):

$$f_{go} = 0.0625 \Big/ \left[\log_{10} \left(\frac{15}{\mathrm{Re}_g} + \frac{K}{3.715D} \right) \right]^2 \tag{22}$$

where K/D is the relative apparent roughness of the liquid interface.

3 Method of Solution

The numerical method implemented was finite differences with a first order downstream implicit scheme for spatial derivatives and a first order upstream implicit scheme for time derivatives. Equations 4–12 are discretized and then can be written in a matrix form as:

$$\mathbf{D}_i\left(\mathbf{x}_i^0\right)\mathbf{x}_i^{t+\Delta t} = \mathbf{E}_i\left(\mathbf{x}_i^0, \mathbf{x}_i^t, \mathbf{x}_{i-1}^{t+\Delta t}\right) \tag{23}$$

$\mathbf{x}$ is a column vector of dependent variables given by:

$$\mathbf{x} = \left[\varepsilon_o, \varepsilon_g, P_i, U_g, T_g, U_o, U_w, T_o, T_w\right]^T \tag{24}$$

where the superscript T indicates the transpose.

3.1 Solution Procedure

The methodology followed is similar to that of Cazarez and Vazquez (2005).

1. Assign entrance values to the first cell ($i = 1$).
2. Assign the initial conditions at $t = 0$ to the dummy variables: $\mathbf{x}_i^0 = \mathbf{x}_i^t$
3. Calculate properties (densities, viscosities, specific heats) and friction factors using the initial conditions given in step 2.
4. Each element of the coefficient matrix **D** and each element of the independent vector **E** is calculated using the initial condition given in step 2 and properties calculated in step 3.
5. Using the numerical package LINPACK, the vector solution $\mathbf{x}_i^{t+\Delta t}$ is obtained.
6. Convergence is checked. If the condition

$$\left[\mathbf{D}_i \mathbf{x}_i^{t+\Delta t} - \mathbf{E}_i\right] \leq |\text{error}| \tag{25}$$

   is not satisfied, the process is restarted from Step 2 by assigning $\mathbf{x}_i^0 = \left(\mathbf{x}_i^t + \mathbf{x}_i^{t+\Delta t}\right)/2$, until convergence.
7. The iterative process described in steps 2–6 is repeated from cell $i = 2$ to cell $i = n$. The variables calculated in cell $i = 2$ are the entrance variables to cell $i = 3$ and so on successively, until the entrance variables for cell $i = n$ are calculated at cell $i = n$-1.
8. When all cells are visited, the variables calculated at the new time $t + \Delta t$ are assigned to the variables at time t: $\mathbf{x}_i^t = \mathbf{x}_i^{t+\Delta t}$ and the process is restarted from step 2 until the total simulation time is completed.

The numerical solution was obtained using the LINPACK (Dongarra et al. 1990) package of numerical routines for solving simultaneous algebraic linear equations. The algorithm used in this study is based on the factorization of a matrix using Gaussian elimination with partial pivoting.

4 Results and Discussion

The model was validated using the experimental data given by Bannwart et al. (2004), and Trevisan (2003). The experiments took place in an acrylic tube, at ambient temperature and pressure. Heavy oil (14° API), with a density of 971 kg m^{-3}, and a viscosity of 5,040 m Pas was used. The model was also validated with the data obtained by Pan et al. (1994) whose experiments were carried out with light oil (32 API), with a density of 865 kg m^{-3}, and a viscosity of 48 m Pas.

In Fig. 2a is shown the comparison between the experimental pressure gradient and the pressure gradient calculated with the model, as can be seen there are only two points where this flow pattern is reported for heavy oil–water–air flow, in both cases the error of the model is close to 50%, however the uncertainty from the

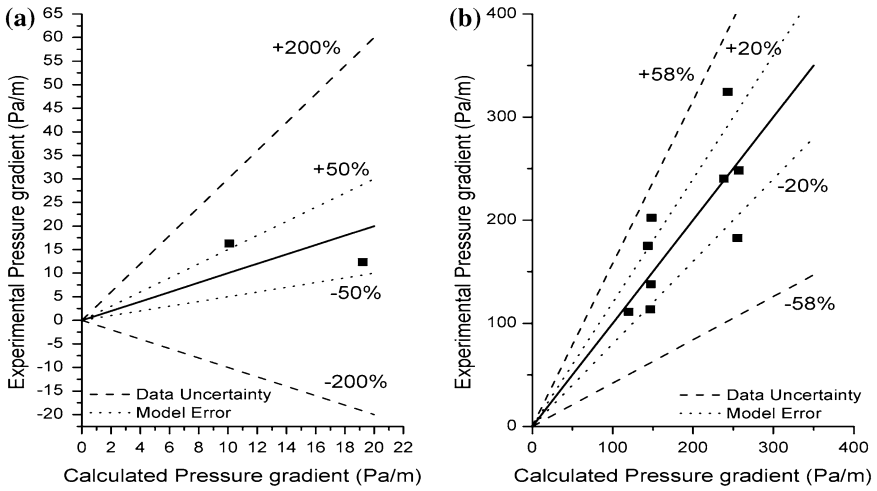

Fig. 2 Predicted pressure gradient compared with: **a** Trevisan data (Trevisan 2003), and **b** Pan data (Pan et al. 1994)

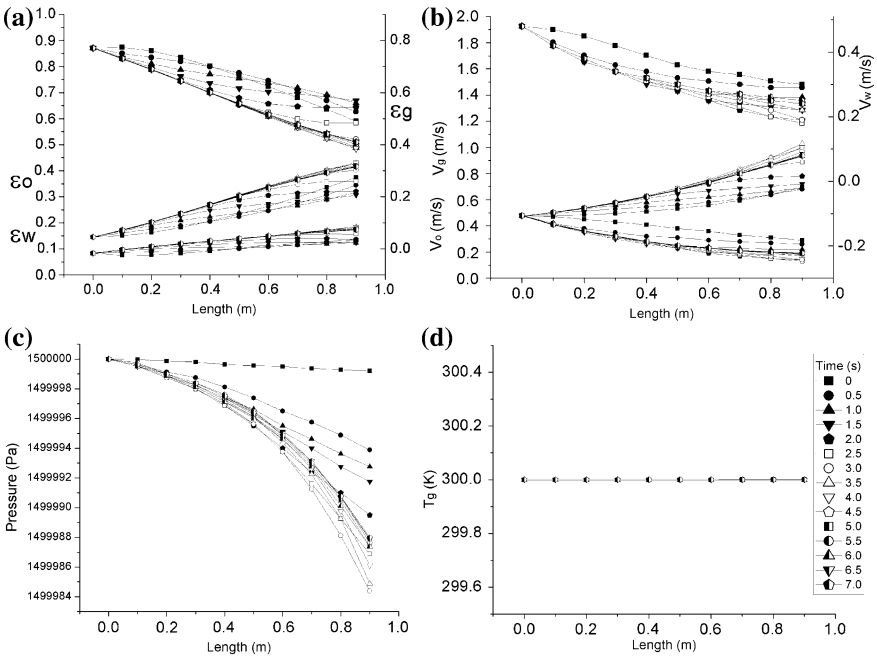

Fig. 3 Transient behavior of: **a** volumetric fractions, **b** velocities, **c** pressure, and **d** temperature

experimental data is of 200%. The corresponding analysis for a light oil–water–gas flow is shown in Fig. 2b. The huge uncertainty in the experimental data is because for horizontal pipelines the pressure drop is related only to the friction, and because of that, the pressure gradients are small, and they can be within the experimental data uncertainty.

On the other hand, Fig. 3a shows the transient volumetric fraction profiles for each phase. It can be observed that the major fraction correspond to the gas phase. Figure 3b shows the velocity profiles. As expected gas travels faster than oil and water, and the two liquids travel almost at the same velocity. Pressure profiles are show on Fig. 3c. Figure 3d shows the gas phase temperature profile; there is not any significant change, as the model was established as adiabatic flow. The same behavior was observed for the temperature of the liquid phases.

5 Conclusions

A mathematical model for the hydrodynamic of the stratified flow of heavy oil, water and gas in horizontal pipelines, was proposed. It was show that a transient three-phase stratified flow model can be solved without adding the liquid phases. The model was validated for two different oils, and in both cases, the pressure gradient predicted by the three-phase model was within the range of experimental data uncertainty. More experimental data is required for the case of heavy oil–water–gas flow to perform a better validation.

References

Bannwart AC, Rodriguez OMH, Trevisan FE, Viera FF, Carvalho CHM (2004) Flow patterns and pressure gradient in horizontal, upward inclined and vertical heavy oil–water–gas flows: experimental investigation and full-scale experiments. 3rd International Symposium on Two-phase flow modelling and experimentation

Bonizzi M, Issa RI (2003) On the simulation of three-phase slug flow in nearly horizontal pipes using the multi-fluid model. Int J Multiphase Flow 29:1719–1747

Cazarez O, Vazquez M (2005) Prediction of pressure, temperature and velocity distribution of two-phase flow in oil wells. J Petrol Sci Eng 46:195–208

Dongarra JJ, Bunch JR, Moler CB, Stewart GW (1990) LINPACK user guide. SIAM, Philadelphia, 8th printing, 1–367

Eck G (1973) Technische stromunglehre. Springer, New York

Ghorai S, Suri V, Nigam KDP (2005) Numerical modeling of three-phase stratified flow in pipes. Chem Eng Sci 60:6637–6648

Govier GW, Aziz K (1972) The flow of complex mixtures in pipes. Van Norstrand -Reinhold, New York

Kawase Y, Shenoy AV, Wakabayashi K (1994) Friction and heat and mass transfer for turbulent pseudoplastic non-newtonian fluid flows in rough pipes. Can J Chem Eng 72:798–804

Lahey RT Jr, Drew DA (1989) The three-dimensional time and volume averaged conservation equations of two-phase flow. Adv Nucl Sci Tech 20(1):1–69

Metzner AB, Reed JC (1955) Flow of non-newtonian fluids correlation of the laminar, transition, and turbulent-flow regions. AIChE J 1:434–440

Pan L, Fisher SA, Jayanti SA, Mendes-Tatsis MA, Hewitt GF (1994) High pressure three-phase flow: data bank of horizontal air–oil–water flows at 0 and 5barg(G). WASP. Imperial College

Taitel Y, Barnea D, Brill JP (1995) Stratified 3-phase flow in pipes. Int J Multiphase Flow 21(1):53–60

Tomasello A (2009) Thesis: One-dimensional modelling of mixing, dispersion and segregation of multiphase fluids flowing in pipelines. Imperial College London, England

Trevisan FE (2003) Thesis: Padrões de Fluxo e Perda de Carga em Escoamento Trifásico Horizontal de Óleo Pesado, Água e Ar. Universidade Estadual de Campinas, Brasil

Experimental Study of the Slug Flow

O. C. Benítez-Centeno, O. Cazarez-Candia and S. L. Moya-Acosta

Abstract Slug flow is the flow pattern that more often is presented in two-phase flow. It has a complex physical configuration which has not been totally understood. For decades slug flow has been modeled by mechanistic approach with the use of the slug-unity concept. For this, slug length must be known. This parameter affects the determination of shear stresses and then the pressure drop calculations. In this work data are presented from experiments carried out in a two-phase flow equipment. Equipment has a pipe of 12 m length and a diameter of 0.01905 m, which can be inclined from 0 to 90°. The measured data were: (1) angle for which the Taylor bubble breaks contact with the pipe wall, (2) the characteristic lengths of the slug-unit, (3) pressure drop, and (4) presence of bubbles by means of optical sensors. It was found that Taylor bubbles break contact with the wall pipe at 45°. With the voltage signal from optical sensors it was possible to quantify velocities, lengths and frequency for the Taylor bubbles.

O. C. Benítez-Centeno (✉) · S. L. Moya-Acosta
Centro Nacional de Investigación y Desarrollo Tecnológico,
Prolongación Av. Palmira esq. Apatzingan, Col. Palmira,
62490 Cuernavaca, Morelos, México
e-mail: omarcbc@gmail.com

O. Cazarez-Candia
Instituto Mexicano del Petróleo, Eje Central Lázaro Cárdenas 152,
07730 Col San Bartolo Atepehuacan, México
e-mail: ocazarez@imp.mx

O. C. Benítez-Centeno · O. Cazarez-Candia
Instituto Tecnológico de Zacatepec, Calzada del Tecnológico No. 27,
62780 Zacatepec, Morelos, México

J. Klapp et al. (eds.), *Experimental and Theoretical Advances in Fluid Dynamics*,
Environmental Science and Engineering, DOI: 10.1007/978-3-642-17958-7_23,

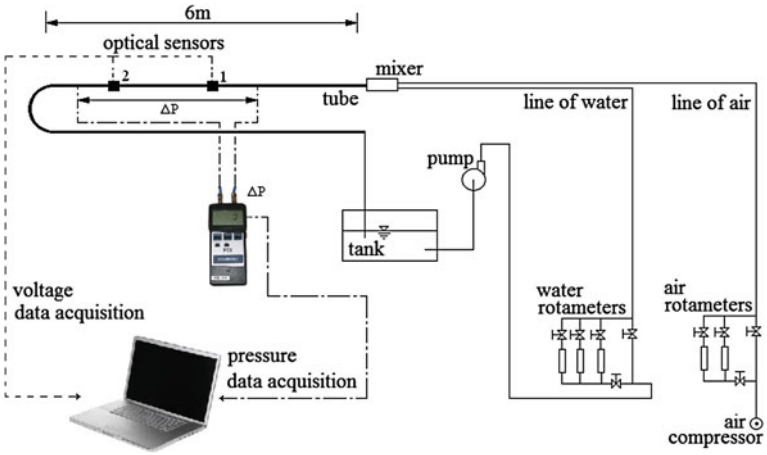

Fig. 1 Experimental equipment

1 Introduction

Slug flow is perhaps, between all the two-phase flow patterns, the one that appears with a greater incidence (Taitel and Dukler 1977). It presents a complex geometry, faults in tubes and equipment, high pressure drop and instability, and then this flow is an undesirable phenomenon. Therefore it is necessary to study it in more detail. Slug flow has been modeled using mechanistic approaches and the slug-unit concept. This work presents an experimental study about the slug flow characteristics (Taylor bubble length and velocity, pressure drop). Experiments were made in a two-phase flow equipment constituted by a tube of 12 m length and internal diameter of 0.01905 m. The equipment can be inclined from 0 to 90°. In Fig. 1 the scheme for the two-phase flow equipment is shown.

2 Experiments

Using flow patterns maps, it was determined the water and air volumetric fluxes for which the slug flow appears for 0, 3, 15 and 30° of inclination pipe. These inclinations are the four cases of tests whose parameters appear in Table 1. By means of rotameters (Fig. 1) the flow rates of each phase are introduced in the mixer. The water–air mixture goes to out from the mixer and flow through the pipe.

The detection of Taylor bubbles is made by two infrared optical sensors from which a voltage signal is obtained. Voltage varies from 4.6 to 0 volts. In Fig. 2, the physical interpretation of the obtained voltage signals from sensors 1 and 2 can be

Table 1 Test cases

Parameters	Case 1	Case 2	Case 3	Case 4
Diameter, (m)	0.01905	0.01905	0.01905	0.01905
Pressure, (Pa)	107760	110976	111321	12046
Water flow rate, (m^3/s)	2.83E-04	0.94E-04	1.80E-04	1.38E-04
Air flow rate, (m^3/s)	4.53E-05	5.66E-05	8.18E-05	7.18E-05
Water Temperature, (°C)	26.0	25.0	24.0	24.0
Air Temperature, (°C)	26.0	25.0	24.0	24.0
Inclination angle, (°)	0.0	3.0	15.0	30.0

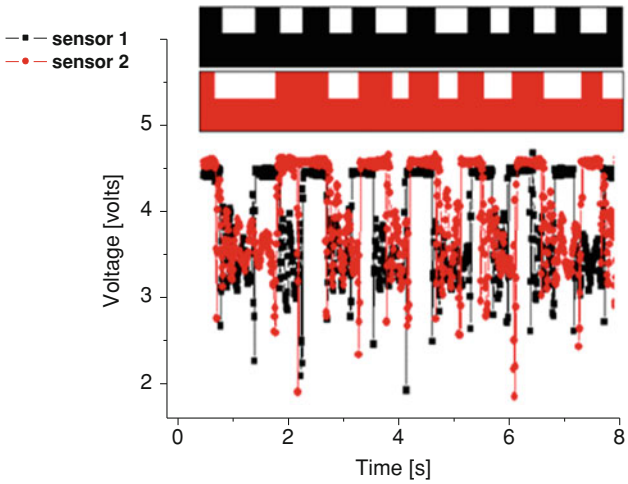

Fig. 2 Typical signals of infrared sensors

observed. When a liquid-slug is detected, a sensor obtains a voltage signal of 4.6 volts and when a bubble passes voltage diminishes.

3 Results

The voltage signals data are treated statistically, obtaining their frequency by means of Fourier transform. Slug frequency is used to calculate slug intermittence (Eq. 1), mixture velocity (Eq. 2), slug length (Eqs. 3 and 4) and Taylor bubble velocity (Eq. 5). The intermittence and mixture velocity are given by (Woods and Hanratty 1996):

$$I \cong \frac{U_{sl}}{U_{sl} + U_{sg}} \tag{1}$$

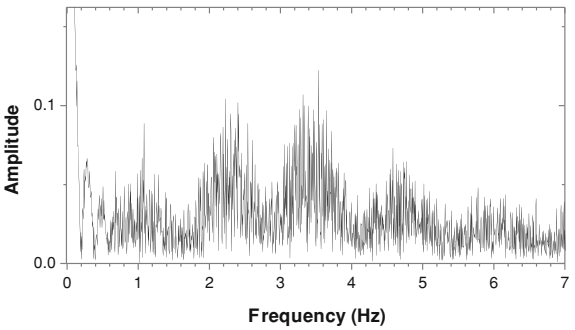

Fig. 3 Frequency for Case 3 (Frequency = 3.5 Hz, Amplitude = 0.1219)

Table 2 Slug length (m)

Angle (°)	Measured Length (Photographs)	Computed Length (Voltage Signals)
0	0.2120	0.2656
3	0.2113	0.1934
15	0.2178	0.2150
30	0.1863	0.1860

$$C = C_0 \left(U_{sl} + U_{sg}\right) \tag{2}$$

In Eqs. 1 and $2U_{sl}$ is the liquid superficial velocity, U_{sg} is the gas superficial velocity, and C_0 is a coefficient that is refered at the maximum average gas velocity in the pipe center, which has a value of 1.2 for ascending flow and 1.12 for descending flow (Hasan and Kabir 1988). The slug length can be determined by (Woods et al. 2006):

$$L_{LS} = \frac{CI}{fs} \tag{3}$$

$$L_{LS} = \frac{1.2(U_{sl} + U_{sg})}{fs}\left(\frac{U_{sl}}{U_{sl} + U_{sg}}\right) = 1.2\left(\frac{U_{sl}}{fs}\right) \tag{4}$$

The taylor bubble velocity can be determined by (Chew-Chen 2001)

$$U_{BT} = L_{LS} f_S \tag{5}$$

In Eqs. 3–5, fs is the slug frequency, I is the slug intermittence, L_{LS} is slug length, and U_{TB} is the Taylor bubble velocity. Figure 3 shows the frequency spectrum obtained by using Fourier transform on voltage signals for sensors 1 and 2 (Fig. 1). The frequency is of 3.5 Hertz. Once the slug frequency is determined, the liquid-slug length is calculated. In Table 2 the results are compared against liquid-slug lengths determined by direct readouts from 30 photography's for each case.

Table 3 Taylor bubble and slug lengths obtained by measuring

Angle (°)	0	3	15	30
L_{TB} (m)	0.4491	0.3497	0.2974	0.2651
L_{LS} (m)	0.2120	0.2113	0.2178	0.1860
L_{TB}.d	23.57	18.35	15.61	13.91
L_{LS}.d	11.12	11.09	11.43	9.76

Table 4 Slug length from literature for horizontal pipes

Author	d (mm)	Angle (°)	L_{LS} (d[a])
Dukler and Hubbard (1975)	38	0	12–30
Nicholson et al. (1978)	25.51	0	20–30
Gregory et al. (1978)	25.51	0	30
Andreussi and Bendiksen (1989)	50	0	22
Nydal (1992)	53, 90	0	15–20
Manolis (1995)	78	0	10–25
This work	19.05	0	9–11.4

[a] d is pipe diameter

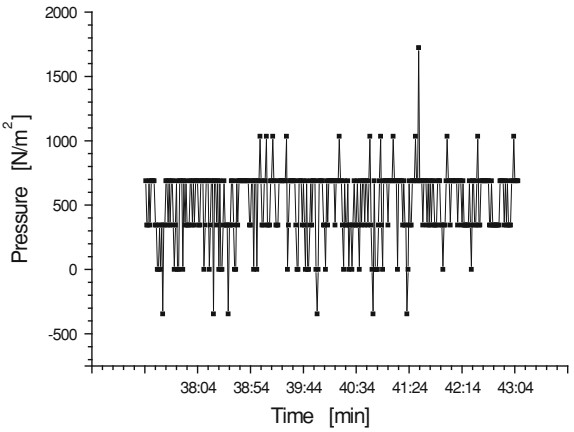

Fig. 4 Pressure drop for Case 3

In Table 3 slug (L_{LS}) and Taylor bubble (L_{TB}) average lengths are shown, d is the pipe diameter.

Table 4 shows the comparison of the slug length obtained in this work against data from literature. It is evident that it exist certain discrepancy among the data.

Another measured parameter is the pressure drop. It was measured by a digital manometer for water-to-air simultaneous flow. Figure 4 shows the behavior of pressure as function of time for Case 3 (15°). To determinate the pressure drop the median of the data (Fig. 4) was calculated. The results, for the cases stipulated in Table 1, are 344.73 Pa (Case 1), 345.79 Pa (Case 2), 689.47 Pa (Case 3) and 690.02 Pa (Case 4).

Table 5 Angle for which Taylor bubble breaks contact with the wall pipe

Author	Angle (°)
Kaya et al. (2001)	10
Gomez et al. (1999)	86
Zukoski (1966)	45
This work	45

On the other hand, experiments were done to determinate the angle for which Taylor bubble break contact with the pipe wall. In the present work it was observed that such angle is 45°. In Table 5 a comparison is shown for the angle observed in this work against data from literature.

4 Conclusions

The differential pressure drop has been measured for 0, 3, 15 and 30° of inclination for water–air slug flow. Also liquid-slug lengths were measured. It was observed that at 45° of inclination the Taylor bubble breaks contact with the pipe wall. The liquid-slug lengths and the angle of 45° measured in this work should be used into the calculation of shear stresses. This in order to obtain better predictions of pressure drop when mechanistic models are used to simulate liquid–gas two-phase slug flows.

References

Andreussi P, Bendiksen K (1989) An investigation of void fraction in liquid slugs for horizontal and inclined gas–liquid pipe flow. Int J Multiphase Flow 15(6):937–949

Chew-Chen L (2001) Slug development/dissipation in an inclined pipeline with changing pipe ID. (SPE 68827)

Dukler AE, Hubbard MG (1975) A model for gas–liquid slug flow in horizontal and near horizontal tubes. Ind Eng Chem Sci Fundm 14(4):337–347

Gomez LE, Shoham O, Schmidt Z, Chokshi RN, Zenith R, Brown A, Northug T (1999) A unified mechanistic model for steady-state two-phase flow in wellbores and pipelines. Society of Petroleum Engineers (SPE 56520)

Gregory GA et al (1978) Correlation of the Liquid volume fraction in the slug for horizontal gas–liquid slug flow. Int J Multiphase Flow 4:33–39

Hasan AR Kabir CS (1988) Predicting multiphase flow behavior in a deviated well. SPEDE 474, Trans AIME 285

Kaya AS, Sarica CY, Brill JP (2001) Mechanistic modeling of two phase flow in deviated Wells. Society of Petroleum Engineers (SPE 72998), pp 156–165

Manolis IG (1995) High pressure gas–liquid slug flow. PhD thesis, Department of Chemical Engineering and Chemical Technology, Imperial College of Science, Technology and Medicine, UK

Nicholson R et al (1978) Intermittent two phase flow in horizontal pipes: predictive models. Can J Chem Eng 56:653–663

Nydal OJ, Pintus S, Andreussi P (1992) Statistical characterization of slug flow in horizontal pipes. Int J Multiphase Flow 18(3):439–453

Taitel Y, Dukler AE (1977) A Model for slug frequency during gas–liquid flow in horizontal and near horizontal pipelines. Int J Multiphase Flow 3:585–596

Woods BD, Hanratty TJ (1996) Relation of slug stability to sheding rate. Int J Multiphase Flow 22(5):809–828

Woods BD, Fan Z, Hanratty TJ (2006) Frequency and development of slugs in a horizontal pipe at large liquid flows. Int J Multiphase Flow 2(20):902–925

Zukoski EE (1966) Influence of viscosity, surface tension, and inclination angle on motion of long bubbles in closed tubes. J Fluid Mech 25:821–837

Slug Flow Model Using the Two Fluid Approach

O. C. Benítez-Centeno, O. Cazarez-Candia and S. L. Moya-Acosta

Abstract A transient one-dimensional two fluid model to simulate slug flow through pipes was developed. It is formed by the conservation equations of mass, momentum and energy averaged in space and time for a water-air system. It was considered that water is incompressible, air is compressible and the unit-slug concept was used. For angles smaller than 45° the Taylor bubble region was modeled as a stratified flow, otherwise it was modeled as annular flow. The liquid slug region was modeled as a bubbly flow for all inclination angles. The model was solved numerically using the finite differences technique. An implicit upstream scheme was used for temporal derivatives and an implicit downstream scheme was used for spatial derivatives. The model allows predicting the profiles of pressure, liquid fraction, velocities and temperatures for the gas and liquid. The predictions present good agreement with experimental data.

O. C. Benítez-Centeno (✉) · S. L. Moya-Acosta
Centro Nacional de Investigación y Desarrollo Tecnológico,
Prolongación Av. Palmira esq. Apatzingan, Col. Palmira,
62490 Cuernavaca, Morelos, Mexico
e-mail: omarcbc@gmail.com

O. Cazarez-Candia
Instituto Mexicano del Petróleo, Eje Central Lázaro Cárdenas 152,
Col San Bartolo Atepehuacan, 07730 Mexico city, D.F., Mexico
e-mail: ocazarez@imp.mx

O. C. Benítez-Centeno · O. Cazarez-Candia
Instituto Tecnológico de Zacatepec, Calzada del Tecnológico No. 27,
62780 Zacatepec, Morelos, Mexico

J. Klapp et al. (eds.), *Experimental and Theoretical Advances in Fluid Dynamics*,
Environmental Science and Engineering, DOI: 10.1007/978-3-642-17958-7_24,

1 Introduction

Slug flow is an intermittent flow pattern characterized by elongates gas bubbles called Taylor bubbles periodically followed by liquid segments that may or may not contain small gas bubbles. In order to have a conceptual model of the slug flow the pipe inclination should be taken into account. For a horizontal pipe (Taitel and Dukler 1977; Kokal and Stanislav 1989; Fabre and Liné 1992; Woods et al. 2000), slug flow is characterized by plugs or corks of liquid that intermittently fills completely the cross-sectional pipe area, and elongated bubbles that flow at top of the pipe with a liquid film at the bottom (the form of the elongate bubble depends on the mixture speed (Grenier et al. 1995). For a vertical pipe, slug flow is performed by regions in the form of bullet that travel concentrically to the pipe wall surrounded by a liquid film (Taitel and Dukler 1977). For inclined pipes the Taylor bubble can break contact with the pipe wall around of 45°. Then for angles from 0° up to 45° the conceptual model may be the same as for a horizontal pipe.

One of the ways, to model slug flows, is by means of the mechanistic models which are based on conservation equations. In literature there are many proposals in this sense which include the use of the slug-unit concept known as unitary cell (Granados and Camacho 1998; Xiao et al. 1990; Ansari 1988; Petalas and Aziz 1998). In this work a two-fluid mathematical model is used to simulate slug flow. It is taken into account the inclination angle for which the Taylor bubble breaks contact with the pipe wall and the slug-unit concept was used.

2 Physical Model

Accordingly to the experimental work of Benítez et al. (2010), slug flow was modeled considering two cases: (1) flow for angles from 0 to 45°, and (2) flow for angles larger than 45°. Both cases were solved using the slug-unit concept (Wallis 1969; Dukler and Hubbard 1975; Kaya 1998; Taitel and Barnea 1990), which is represented by a Taylor bubble followed by a slug of liquid that may content small bubbles. For angles from 0 to 45° Taylor bubble touches the pipe wall (Fig. 1), then this region is treated as a stratified flow and the liquid-slug is treated as a dispersed bubbly flow. For an inclined pipe at angles larger than 45° Taylor bubble region is modeled as annular flow (Fig. 1).

The three-dimensional conservation equations averaged in time and space, and interfacial conditions (or jump conditions), given by Lahey and Drew (1989) and Lahey (1992), were used to simulate an adiabatic liquid–gas flow through a constant cross section duct, the following considerations and suppositions were taken into account: (1) thickness of the liquid film, in the region of the bubble, is constant; (2) Reynolds stresses are neglected; (3) viscous stresses are neglected; (4) there is not interfacial mass transfer between the phases; (5) aeration in the liquid-slug was taken into account; (6) phase pressures are equals within a given control volume.

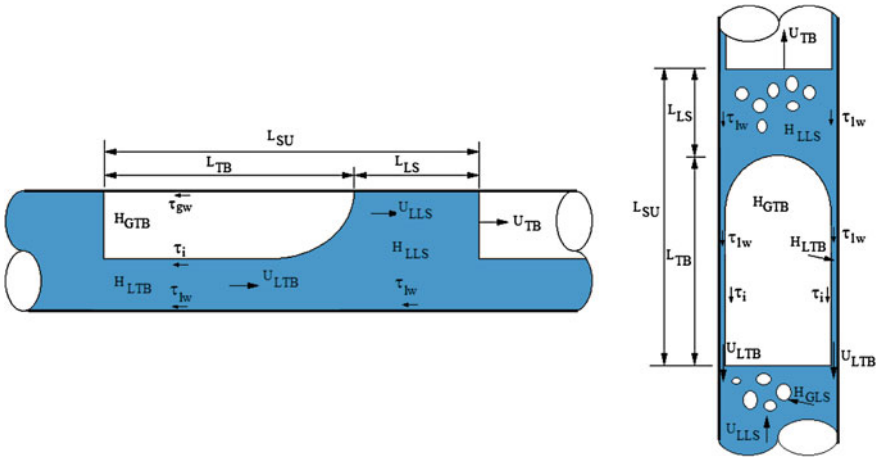

Fig. 1 Physical model

Equations 1–3 form the mathematical model for the gas–liquid slug flow. Mass equation:

$$\underbrace{\frac{\partial[\alpha_k \rho_k]}{\partial t}}_{\text{accumulation}} + \underbrace{\frac{\partial}{\partial z}[\alpha_k \rho_k \underline{U}_k]}_{\text{convection}} = 0 \tag{1}$$

Momentum equation:

$$\begin{aligned} &\underbrace{\frac{\partial[\alpha_k \rho_k \underline{U}_k]}{\partial t}}_{\text{accumulation}} + \underbrace{\frac{\partial}{\partial z}[\alpha_k \rho_k \underline{U}_k \underline{U}_k]}_{\text{convection}} = \underbrace{-\alpha_k \frac{\partial}{\partial z}[P_k]}_{\text{pressure}} \\ &\underbrace{-\frac{A\rho_l g \cos\theta}{2\sqrt{(h_l(d-h_l))}} \frac{\partial \alpha_k}{\partial z}}_{\text{correction of pressure}} + \underbrace{\alpha_k \rho_k g_k \sin\theta}_{\text{gravity}} \\ &\underbrace{-\left[\frac{\underline{\tau}_{kw}^{(slug)}}{DH_k}\left(\frac{L_{LS}}{L_{SU}}\right) + \frac{\underline{\tau}_{kw}^{(burbuja\ de\ Taylor)}}{DH_k}\left(\frac{L_{TB}}{L_{SU}}\right)\right]}_{\text{phase}-\text{wall stresses}} \\ &\underbrace{-\frac{\underline{\tau}_k}{DH_i}\left(\frac{L_{TB}}{L_{SU}}\right)}_{\text{interfacial stresses}} - \underbrace{\underline{M}_{k_i}^{nd\&d}}_{\text{interfacial forces}} \end{aligned} \tag{2}$$

Energy equation:

$$\underbrace{\frac{\partial[\alpha_k \rho_k e_k]}{\partial t}}_{\text{accumulation}} + \underbrace{\frac{\partial}{\partial z}\left[\alpha_k \rho_k e_k \underline{U}_k\right]}_{\text{convection}} = \underbrace{\frac{\partial[\alpha_k p_k]}{\partial t}}_{\text{pressure}} + \underbrace{\alpha_k \rho_k \underline{g}\, U_k}_{\text{gravity}} \tag{3}$$

$$\phi = \theta + 90 \tag{4}$$

In Eqs. 1–3 α is volumetric fraction, ρ is density, the subscript k denotes gas (g) or liquid (l), $e_k = h_k + \left(\underline{U}_k^2/2\right)$ is the specific energy, h is specific enthalpy, p is pressure, τ is shear stress, U is velocity, the subscript i denotes interface, w denotes wall, D_H is hydraulic diameter, M represents interfacial forces and θ is the inclination angle measured from the horizontal position, L_{TB} is the length of the Taylor bubble, L_{LS} is the length of the liquid slug and L_{SU} is the length of the slug unity ($L_{TB} + L_{LS}$).

3 Numerical Model

The numerical model was obtained with a discretization in finite differences of Eqs. 1–3. It was applied a first order implicit downstream scheme for spatial derivatives and a first order implicit upstream scheme for time derivatives. This technique is implemented by replacing all derivatives by difference quotients. When the geometry is not complicated (this is the case of pipes) the finite difference method is easier and faster than other methods. Equations 1–3 were discretized and written in a vector form given by Eq. 5,

$$[\underline{A}][\underline{X}] = [\underline{B}] \tag{5}$$

where the matrix of coefficients and the independent vector are given by:

$$\underline{A} = \begin{bmatrix} \frac{(1-\alpha_{lo})}{Cg^2}\left(1+U_{go}\frac{\Delta t}{\Delta z}\right) & -\rho_g\left(1+U_{go}\frac{\Delta t}{\Delta z}\right) & (1-\alpha_{lo})\rho_g\frac{\Delta t}{\Delta z} & 0 & -\frac{(1-\alpha_{lo})\rho_g}{T_{go}}\left(1+U_{go}\frac{\Delta t}{\Delta z}\right) & 0 \\ 0 & \left(1+U_{lo}\frac{\Delta t}{\Delta z}\right) & 0 & \left(\alpha_{lo}\frac{\Delta t}{\Delta z}\right) & 0 & 0 \\ \frac{\Delta t}{\Delta z} & 0 & \rho_g\left[1+U_{go}\frac{\Delta t}{\Delta z}\right] & 0 & 0 & 0 \\ \frac{\Delta t}{\Delta z} & \frac{A\rho_l g\cos\theta}{2\sqrt{(h_l(d-h_l))}}\frac{\Delta t}{\Delta z} & 0 & \rho_l\left[1+U_{lo}\frac{\Delta t}{\Delta z}\right] & 0 & 0 \\ -\left[\left(\eta Cp_g+\frac{1}{\rho_g}\right)+\eta Cp_g U_{go}\left(\frac{\Delta t}{\Delta z}\right)\right] & 0 & U_{go}\left[1+U_{go}\frac{\Delta t}{\Delta z}\right] & 0 & Cp_g\left[1+U_{go}\frac{\Delta t}{\Delta z}\right] & 0 \\ \left[\frac{U_{lo}}{\rho_l}\left(\frac{\Delta t}{\Delta z}\right)\right] & 0 & 0 & U_{lo}\left[1+U_{lo}\frac{\Delta t}{\Delta z}\right] & 0 & Cp_l\left[1+U_{lo}\frac{\Delta t}{\Delta z}\right] \end{bmatrix} \tag{6}$$

$$\underline{B} = \begin{bmatrix} \frac{(1-\alpha_{lo})}{Cg^2}\left[P^t_{(i)} + U_{go}\frac{\Delta t}{\Delta z}P^{t+\Delta t}_{(i-1)}\right] - \frac{(1-\alpha_{lo})\rho_g}{T_{go}}\left[T^t_{g(i)} + U_{go}\frac{\Delta t}{\Delta z}T^{t+\Delta t}_{g(i-1)}\right] - \rho_g\left[\alpha^t_{l(i)} + U_{go}\frac{\Delta t}{\Delta z}\alpha^{t+\Delta t}_{l(i-1)}\right] + (1-\alpha_{lo})\rho_g\frac{\Delta t}{\Delta z}U^{t+\Delta t}_{g(i-1)} \\ \left(\alpha_{lo}\frac{\Delta t}{\Delta z}\right)U^{t+\Delta t}_{l(i-1)} + \left(U_{lo}\frac{\Delta t}{\Delta z}\right)\alpha^{t+\Delta t}_{l(i-1)} + \alpha^t_{l(i)} \\ \rho_g U^t_{g(i)} + \rho_g U_{go}\frac{\Delta t}{\Delta z}U^{t+\Delta t}_{g(i-1)} + \frac{\Delta t}{\Delta z}P^{t+\Delta t}_{(i-1)} - \Delta t\rho_g g\sin\theta - \frac{\tau_{gw}S_g\Delta t}{4A_g} - \frac{\tau_{iw}S_i\Delta t}{4A_g} + \frac{M^{dkcnd}_g\Delta t}{(1-\alpha_{lo})} \\ \rho_l U^t_{l(i)} + \rho_l U_{lo}\frac{\Delta t}{\Delta z}U^{t+\Delta t}_{l(i-1)} + \frac{\Delta t}{\Delta z}P^{t+\Delta t}_{(i-1)} + \frac{A\rho_l g\cos\theta}{2\sqrt{(h_l(d-h_l))}}\frac{\Delta t}{\Delta z}\alpha^{t+\Delta t}_{l(i-1)} - \Delta t\rho_l g\sin\theta - \frac{\tau_{lw}S_l\Delta t}{4A_l} + \frac{\tau_{iw}S_i\Delta t}{4A_l} - \frac{M^{dkcnd}_l\Delta t}{\alpha_{lo}} \\ -\Delta t U_{go}g\cos\phi - \left(\eta Cp_g + \frac{1}{\rho_s}\right)P^t_{(i)} - \eta Cp_g U_{go}\left(\frac{\Delta t}{\Delta z}\right)P^{t+\Delta t}_{(i-1)} + U_{go}U^t_{g(i)} + U^2_{go}U^{t+\Delta t}_{g(i-1)}\left(\frac{\Delta t}{\Delta z}\right) + Cp_g\left[T^t_{g(i)} + U_{go}\frac{\Delta t}{\Delta z}T^{t+\Delta t}_{g(i-1)}\right] \\ -\Delta t U_{lo}g\cos\phi + Cp_l T^t_{l(i)} + Cp_l U_{lo}\frac{\Delta t}{\Delta z}T^{t+\Delta t}_{l(i-1)} - \frac{U_{lo}}{\rho_l}\left(\frac{\Delta t}{\Delta z}\right)P^{t+\Delta t}_{(i-1)} + U_{lo}U^t_{l(i)} + U^2_{lo}U^{t+\Delta t}_{l(i-1)}\left(\frac{\Delta t}{\Delta z}\right) \end{bmatrix} \tag{7}$$

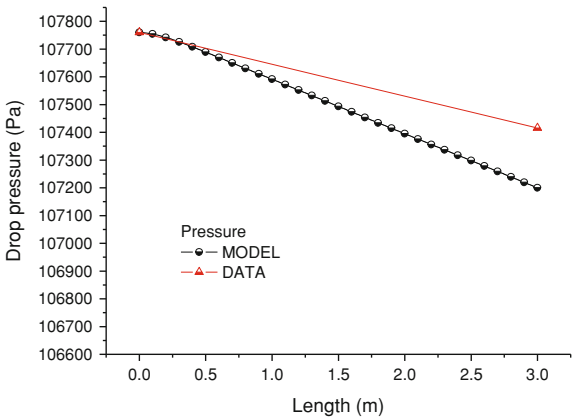

Fig. 2 Pressure drop

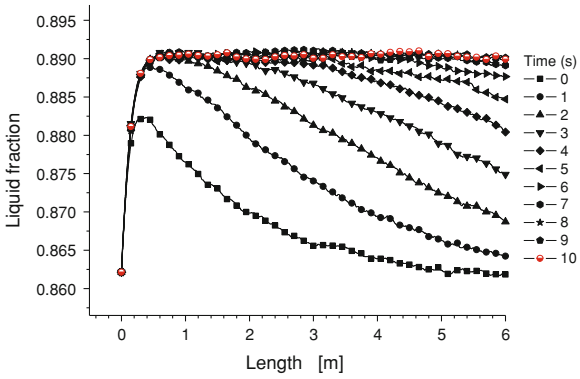

Fig. 3 Liquid fraction

The vector of unknowns is given by

$$\underline{X} = \left[\alpha_l, P, U_g, U_l, T_g, T_l\right]^T \tag{8}$$

where the superscript T represents transposed.

4 Results and Validation

The present model for slug flow was validated using data obtained in the experimental work of Benitez et al. (2010). They used a two-phase flow equipment with a horizontal tube of 3 m length and 0.01905 m internal diameter. The flow conditions were 107760 Pa, 26°C, water flow rate of 2.83E−04 m^3/s, and air flow rate of 4.53E−05 m^3/s.

More details about two phase flow equipment and experimental information appear in the work of Benítez et al. (2010).

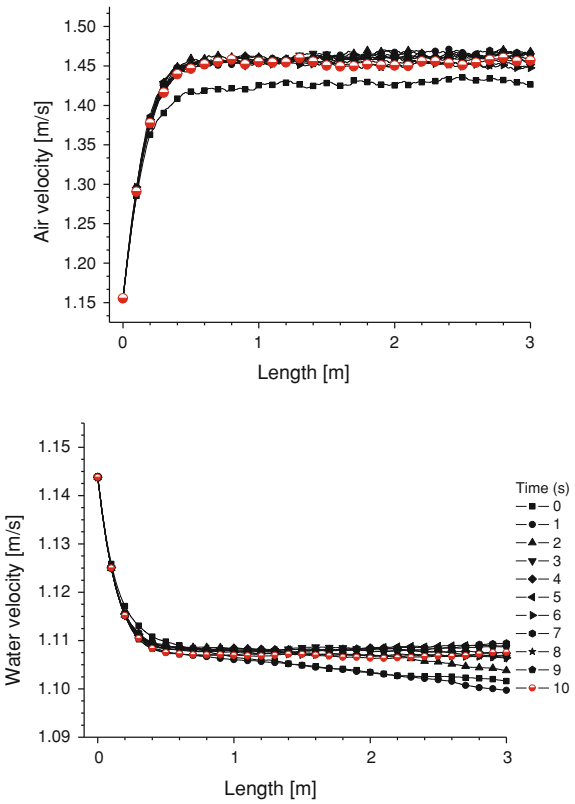

Fig. 4 Air and water velocities

The experimental and predicted pressure profiles are shown in Fig. 2. The prediction presents an absolute percent error of 0.2 with respect to experimental data. This represents a good prediction. Figures 3, 4, and 5 show the transient behaviors for others parameters.

5 Conclusions

In this work it was proposed a model that combines flow patterns for the modeling of slug flow. For angles from 0 to 45°, the Taylor bubble region was treated as stratified flow and the liquid-slug was treated as dispersed bubbly flow. For angles bigger than 45° and up to the vertical position, the Taylor-bubble region was treated as annular flow and the liquid-slug region was treated as dispersed bubbly flow. The model has a good agreement with experimental pressure data with errors smaller than 10%. The experimental pressure drop from Cases 2, 3 y 4, from the work of Benítez et al. (2010) were also simulated. For these Cases the errors obtained were 1.58, 7.3 and 10%, respectively.

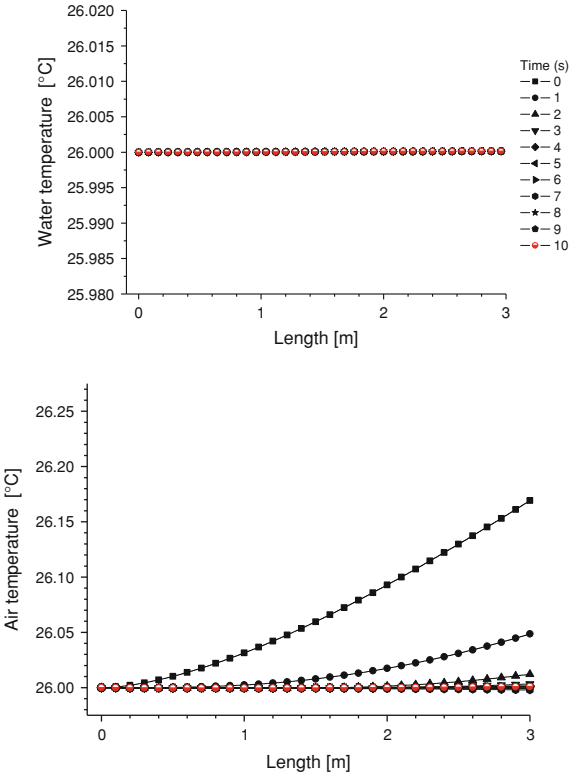

Fig. 5 Air and water temperatures

References

Ansari AM (1988) A comprehensive mechanistic model for upward two-phase flow. M.S. Thesis, The University of Tulsa

Benítez OC, Cazarez O, Moya SL (2010) Experimental study of slug flow. XVI Dynamic of fluids Congress Memories

Dukler AE, Hubbard MG (1975) A model for gas–liquid slug flow in horizontal and near horizontal tubes. Ind Eng Chem Sci Fundm 14(4):337–347

Fabre J, Liné A (1992) Modeling of two phase flow. Rev Fluid Mech 24:21–46

Granados J, Camacho R (1998) Análisis of two-phase flor in horizontal and inclined pipes uIT mechanistic models. (SPE 39857)

Grenier P, Fabre J, Fagundes Netto JR (1995) Slug flow in pipelines: recent advances and future developments. In: Proceedings of the 8th international conference on multiphase production, June 18–20, Cannes, France, Cranfield BHRG

Kaya AS (1998) Comprehensive mechanistic modeling of two-phase flow in deviated wells. Master of Science Thesis, University of Tulsa

Kokal SL, Stanislav JF (1989) An experimental study of two-phase flow in slighly inclined pipes–I flow patterns. Chem Eng Sci 44(3):665–679

Lahey RT (1992) Boiling heat transfer. Modern developments and advances. Troy, NY, USA

Lahey RT, Drew DA (1989) The three-dimensional time and volume averaged conservation equations of two-phase flow. Adv Nuclear Sci Technol 20:1

Petalas N, Aziz K (1998) A mechanistic model for multiphase flor in pipes. Annual Techinical Meeting of the Petroleum Society of the Canadian Institute of Mining, Metallurgy and Petroleum Held in Calgary, Alberta Canada., Paper No. 98–39

Taitel Y, Barnea D (1990) Two-phase slug flow. Adv Heat Transfer 20:83–132

Taitel Y, Dukler AE (1977) A model for slug frequency during gas–liquid flow in horizontal and near horizontal pipelines. Int J Multiphase Flow 3:585–596

Wallis GB (1969) One dimensional two-phase flow. Mc Graw Hill, New York

Woods BD, Hulburt ET, Hanratty TJ (2000) Mechanism of slug formation in downwardly inclined pipes. Int J Multiphase Flow 26:997–998

Xiao JJ, Shoham O, Brill JP (1990) A comprehensive mechanistic model for two-phase flow in pipelines. Presented at the annual technical conference and exhibition, New Orleans, L.A. (SPE 20631)

Mathematical Model for Pipeline Leak Simulation

Lazaro Molina-Espinosa, Cristina Verde-Rodarte and Octavio Cazarez-Candia

Abstract In this work a transient, isothermal, mixture model for one and two fluid flows through pipes is presented. The model is formed by mass, momentum and energy conservation equations, which include leak term. The model is solved numerically using the finite difference technique and allows to simulate pressure and flow rate in steady and transient state. The hydraulic grade line is experimentally obtained and compared against predictions from the model. The result shows a good agreement with experimental data. It was found that (1) leaks induce inlet pressure changes, which are directly proportional to the leak location and magnitude; and (2) the outlet flow rate diminishes directly with the leak.

1 Introduction

The aim of this study is to develop a more reliable mathematical leak model for water pipelines and further use of the model in new leak detection methodologies. Also the Hydraulic Grade Line (HGL) caused by a leak is experimentally verified. In the found literature, not all the studies agree on how leak affect the hydraulic profiles of the pipeline. Although, it is well known from fundamental fluid

L. Molina-Espinosa (✉) · O. Cazarez-Candia
Instituto Mexicano del Petróleo, 07730 México, D.F., México
e-mail: lmespino@imp.mx

O. Cazarez-Candia
e-mail: ocazarez@imp.mx

C. Verde-Rodarte
Instituto de ingeniería UNAM, 04510 México, D.F., México
e-mail: cverder@iingen.unam.mx

J. Klapp et al. (eds.), *Experimental and Theoretical Advances in Fluid Dynamics*, Environmental Science and Engineering, DOI: 10.1007/978-3-642-17958-7_25,

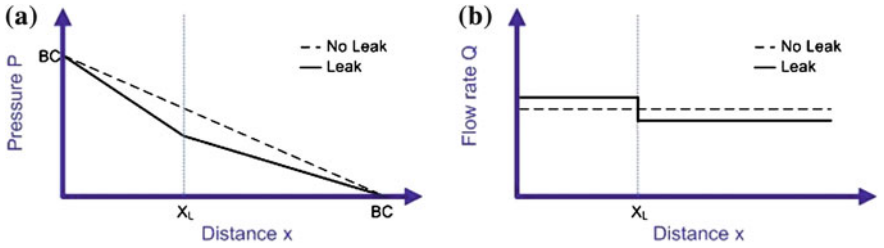

Fig. 1 Steady state schematics: **a** pressure profile and **b** flow rate profile. X_L is the leak location

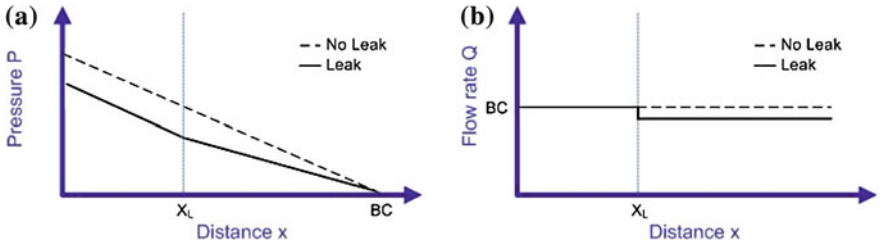

Fig. 2 Steady state schematics: **a** pressure profile and **b** flow rate profile. X_L is the leak location

mechanics (White 2005) that in a horizontal straight pipeline, with constant transversal area, the HGL or pressure profile shows a linear behavior due to friction losses. Some studies, where inlet and outlet pressures were chosen as the system boundary conditions (Emara et al. 2002; Verde et al. 2007), report a leak pressure profile which is formed by two segments (Fig. 1a). The segment ahead the leak location, shows smaller slope than the segment behind. Moreover the flow rate profile reported is divided in two segments too. The segment behind the leak shows a flow rate larger than the segment ahead of the leak (Fig. 1b).

Other studies which chose the inlet flow rate and outlet pressure as the system boundary conditions (Dinis et al. 1999; Kam 2010) report a pressure profile which is formed by two segments (Fig. 2a). However the segment behind the leak location got similar slope than no-leak condition, but with a negative offset. The segment ahead the leak shows a smaller slope. The flow rate profile shows a drop after the leak location (Fig. 2b).

2 Theoretical Development (Mathematical Model)

The mathematical model is form by mass, momentum and energy conservation equations (Eqs. 1–3). These equations form a hyperbolic partial differential equation system.

Some studies on which the leak term (Γ_L) is included within the conservation equations just consider mass and momentum analysis (Dinis et al. 1999; Emara

et al. 2002; Abhulimen and Susu 2004; Bratland 2009; Kam 2010). But inclusion of the energy equation allows to take into account the gas phase compressibility in the model.

$$\frac{\partial \rho_m}{\partial t} + \frac{\partial (\rho_m v)}{\partial x} = -\Gamma_L \tag{1}$$

$$\frac{\partial (\rho_m v)}{\partial t} + \frac{\partial (\rho_m v^2)}{\partial x} + \frac{\partial P}{\partial x} = -\rho_m g \sin\phi - \tau_w \frac{S}{A} - V_L \Gamma_L \tag{2}$$

$$\frac{\partial (\rho_m e)}{\partial t} + \frac{\partial (\rho_m v e)}{\partial x} - \frac{\partial P}{\partial t} = -\rho_m g \sin\phi - e\Gamma_L \tag{3}$$

In Eqs. 1–3, v is the one-dimensional velocity, P is the static pressure, e is the total specific convected energy (Yadigaroglu and Lahey 1976), V_L is the leak velocity, ϕ is the inclination angle from the horizontal, A is the pipe cross-sectional area, S is the wet perimeter, g is the acceleration due to gravity, and τ_w is the wall friction shear stress, which is defined as:

$$\tau_w = \frac{1}{2} F \rho_m v^2 \tag{4}$$

where F is the Fanning friction factor, which was calculated with the Blasius correlation (Taitel and Dukler 1976):

$$F = 0.0585/(Re)^{0.2} \tag{5}$$

where Re is the Reynolds number. The gas and liquid phases (air and water respectively) were treated as a pseudo-single phase. Consequently the mixture density ρ_m is defined as follows:

$$\rho_m = \varepsilon_l \rho_l + \varepsilon_g \rho_g \tag{6}$$

where subscripts g and l represent air and liquid phase respectively. And ε is the volumetric fraction, defined as:

$$\varepsilon_n = \frac{q_n}{q_t} = \frac{q_n}{q_l + q_g} \tag{7}$$

where n represents gas (g) or liquid (l) and q_t is the total volumetric flow rate. Fluids properties were calculated according to the international association of properties of water and steam (Wagner et al. 2000).

In this work the following assumptions and considerations were made: (1) constant cross-sectional pipe area; (2) adiabatic flow; (3) the flow pattern is dispersed-bubble in which velocity, pressure and temperature for gas and liquid phases are equal; (4) one-dimensional flow; (5) no chemical reactions; and (6) no mass exchange between phases.

The set of hyperbolic partial differential equations (Eqs. 1–3) was discretized by the finite difference method. First-order downstream implicit schemes are used for

spatial and time derivatives respectively. The scheme is solved for all nodes in the spatial discretization, on each time step. This task was done using the driver routine LA_GESV from the software package LAPACK95 (Barker et al. 2001).

The determination of the HGL of a straight pipeline whit no leak was carried out in the numerical model by making the leak term equal to zero ($\Gamma_L = 0$) in all nodes of the discretized space. By the case of pipeline with a leak, the HGL was obtained by placing in the leak node the leak term different of zero ($\Gamma_L \neq 0$).

3 Experimental Work

3.1 Experimental Equipment No. 1

One of the experimental equipment used in this work is shown in Fig. 3. The equipment consist of: (a) a reservoir, (b) a galvanized steel pipeline which is 132.56 m long and diameter 0.105 m, (c) pressure and flow rate sensors, (d) a pump and (e) four discharge tubes (servo-valves).

In this equipment water is pumped from a reservoir through the pipeline and finally discharged in the same reservoir. The pipeline is provided with four taped discharges tubes where leak can be performed by opening a servo-valve attached to the discharge tube. The discharges tubes are located at: 15.1, 49.46, 83.25 and 117.39 m from the inlet flow rate transmitter respectably. Also the pipeline is instrumented in order to monitor the inlet and outlet pressure as well as the corresponding flow rates. Pressures are measured with WIKA piezo-resistive transmitters and the flow rates measurements are taken with Signet 2,540 paddle wheel sensors.

At the beginning of each set of experiments pump is started and a wait period of 3,600 s is taken to let measurement to stabilize. Then flow rate and pressure measurements are logged every 1 s and recorded in spreadsheet. At 300 s from the beginning of the experiment, the servo-valve is totally open producing a leak. Measurement is recorded for 300 s more and at second 600 s measurement record is stopped. Finally servo-valve is closed and water is returned to the main reservoir before start another experiment.

Leaks were conducted in the experimental equipment 1 on the four predisposed locations given above, with constant leak size $d_L = 0.01905$ m. Figure 4a shows the inlet flow rates against time for the leaks experiment from the locations 1–4 (15.1, 49.46, 83.25 and 117.39 m, respectively). Figure 4b shows the outlet flow rates for the same set of experiments.

One can see from the Fig. 4a that leaks does not induce significant changes in the inlet flow rate trends, however the outlet flow rate trends shows important changes (Fig. 4b) due to the presence of leaks. From Fig. 4b it can be seen that the most significant change in the outlet flow rate correspond to the nearest leak to the

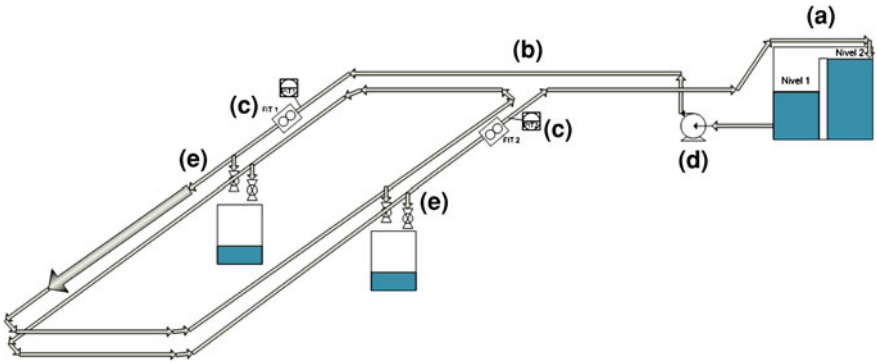

Fig. 3 Experimental equipment No. 1. **a** Reservoir, **b** pipeline, **c** pressure and flow rate transmitters, **d** pump and **e** discharge tube (servo-valves)

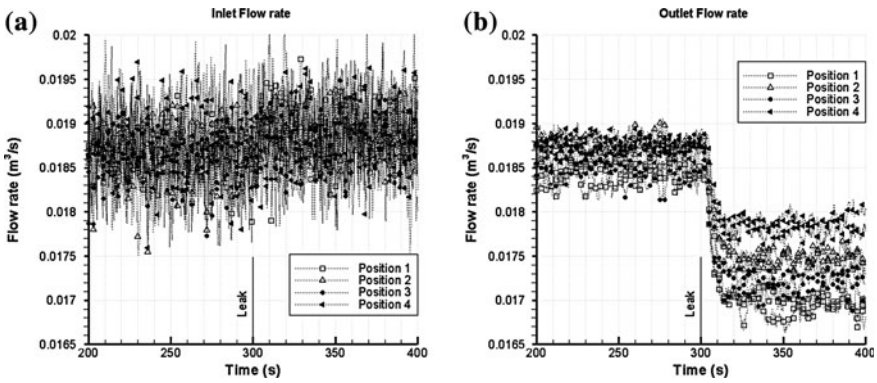

Fig. 4 Inlet flow rate trends (**a**), and outlet flow rate trends (**b**), at four leak location with constant opening size. Leak started at 300 s

pipeline entrance. The weakest changes in the outlet flow rate due to the leak correspond to the farthest leak from the pipeline entrance.

The outlet flow rate behavior observed in Fig. 4b is a direct consequence of the leak, since Eq. 8 has to be accomplished in the leak point,

$$q_{tin} = q_{tLeak} + q_{tout} \tag{8}$$

where q_{tin} is the total inlet flow rate, q_{tLeak} is the total leak flow rate and q_{tout} is the total flow just after the leak. In the case of just one leak q_{tout} is the outlet flow rate of the pipeline.

From Eq. 8 it can be directly assumed that the magnitude of the leak is the steady state difference between the inlet flow rate and the outlet flow rate

$$q_{tin} - q_{tout} = q_{tLeak} \tag{9}$$

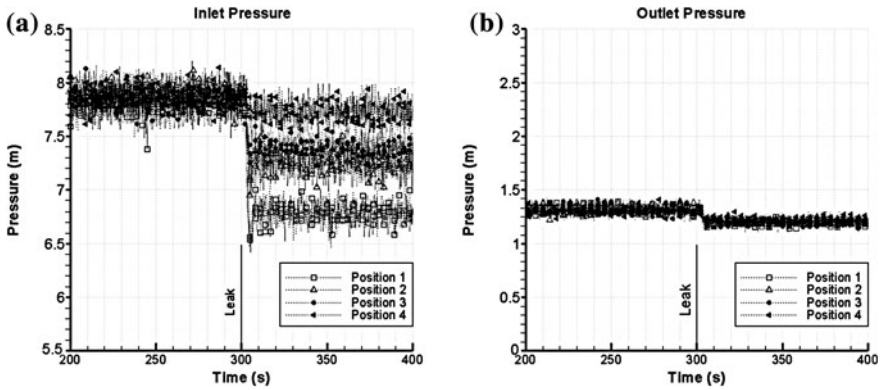

Fig. 5 Inlet pressure trend (**a**), and outlet pressure trend (**b**), at four leak location with constant opening size. Leaks started at 300 s

The pressure data for the same set of experiments are showed in Fig. 5. It can be seen from Fig. 5a that inlet pressure showed large changes due to leaks in all of the four leak locations. However, outlet pressure remains practically unchanged (Fig. 5b). Also from the Fig. 5 it can be seen that the inlet pressure is most affected by the nearest leak to the pipeline entrance. The outlet pressure shows weak changes when leak appear far from the entrance.

The inlet flow rate and outlet pressure are used as the mathematical model boundary conditions due that this measurement showed minor changes during the experiments (Figs. 4 and 5)

3.2 Experimental Equipment No. 2

The second experimental equipment used in this work is shown in Fig. 6. The equipment mainly consist of: (a) a reservoir, (b) a pipe of 2.40 m long whit a diameter of 0.0127 m, (c) seven piezometer tubes every 0.25 m (measurement point of HGL), (d) discharged to the atmosphere, (e) discharge valves and (f) a pump.

In the equipment water is pumped from the reservoir and returned to the same reservoir. The discrete measurements of the HGL are obtained from the piezometer tubes. Two experiments were carried out (Fig. 8): (1) HGL of pipe without leak. (2) HGL of pipe with a leak located at 1.02 m from the pipe inlet.

One can see from Fig. 8 that HGL caused by a leak is formed by two segments similar to the ones shown in Fig. 2a. Several experiments were carried out in the six leak location. The HGL of all experiments showed similar segmentation described above. Moreover a pressure increment was observed in the HGL caused by a leak just at leak location (Dinis et al. 1999). Such pressure behavior can be predicted from the water hammer equation

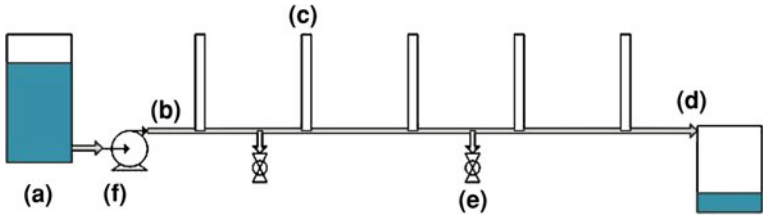

Fig. 6 Experimental equipment No. 2. **a** Reservoir, **b** pipeline, **c** piezometer tubes (diameter is exaggerated and number of piezometer tubes is diminished to simplify sketch), **d** discharge to the atmosphere, **e** discharge valves and **f** pump

$$\Delta H = -\frac{a}{g}\Delta V \tag{10}$$

where H is the piezometric head, a is the velocity of sound in the fluid and V is the velocity of the fluid. From fundamental transient analysis (Chaudhry 1987) it is well know that a decrease in the velocity produces an increases in pressure and vice versa. Such situation is exactly what happens at the leak location. This issue is important since the pressure profile is used in some leak detection methodologies.

4 Model Versus Experimental Data

The mathematical model is compared against experimental data coming from equipment 1 (Fig. 7). In the model constant inlet flow rate and constant outlet pressure were used as boundary conditions. Figure 7a shows the inlet flow rate (Qin Exp) and the outlet flow rate (Qout Exp). A leak is simulated at 300 s and located at 15.1 m from the pipeline inlet. Figure 7a shows that simulated flow rates are a very similar than the experimental data. Similarly, Fig. 7b shows simulated and experimental pressure data trends. The simulated result follows closely the experimental data.

The error between simulated and experimental flow rate is less than 6%, and the error for pressure is less than 1%. Simulated results have good agreement with experimental data not only in steady state but also in transient state.

Similar orders of magnitude of errors were obtained by comparing the simulated flow rates and pressures against experimental data for the leak locations 2–4. The experimental inlet and outlet pressure observed in Fig. 7b are actually the extreme points of the pressure profile in Fig. 2a.

The HGL were predicted for a case with and without leak (Fig. 8). The discrete points in Fig. 8 correspond to the measurements of the equipment 2 and the continuous lines correspond to the model predictions.

The experimental conditions used into the model were: flow rate of 0.0003458 m^3s^{-1}, friction factor Cn = 0.0357, leak location 1.02 m and leak diameter 0.00635 m. As a result simulation of pressure profile was obtained (Fig. 8).

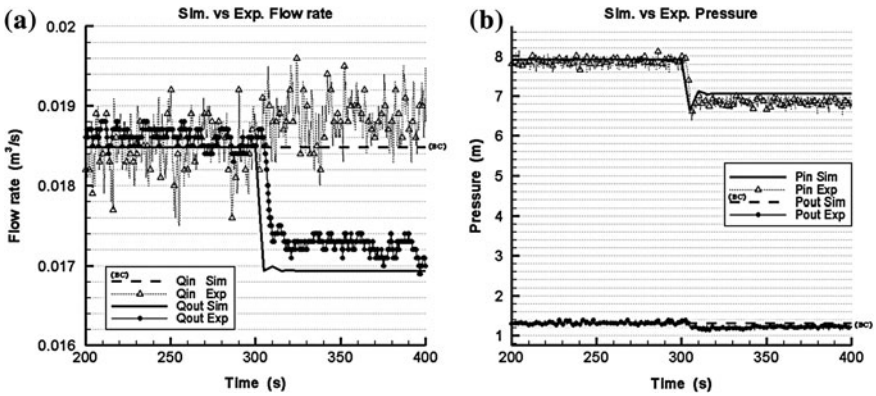

Fig. 7 Comparison between simulated data (Sim) and experimental measurements (Exp). Leaks started at 300 s. **a** Experimental and simulated flow rates and **b** experimental and simulated pressure

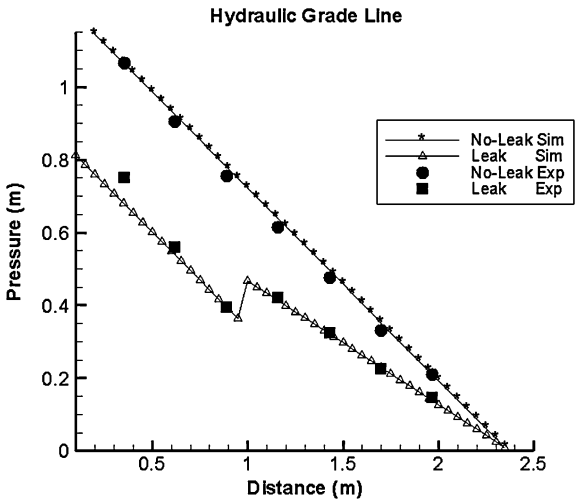

Fig. 8 HGL simulated and experimental data (Equipment 2)

5 Conclusions

The proposed model shows good agreement with experimental data not only in the steady state but also in the transient state. In this study it was observed that a leak induce several changes in the hydrodynamic of a pipeline: (1) the inlet pressure changes are directly proportional to the location and magnitude of the leak and (2) the outlet flow rate is diminishes directly with the magnitude of the leak. According to the experimental result of the present study, the behavior of the HGL in presence of a leak is more closely to the predicted by Dinis et al. (1999) and Kam (2010). The leak model proposed is considered suitable for the simulation of

leaks of different sizes and at different locations, also it can be used as a tool in leak detection methodologies.

References

Abhulimen KE, Susu AA (2004) Liquid pipeline leak detection system: model development and numerical simulation. Chem Engrg J 97(1):47–67

Barker VA, Blackford LS, Dongarra J, Du Croz J, Hammarling S, Marinova M, Wasniewski J, Yalamov P (2001) LAPACK95 users' guide, 3rd edn. Philadelphia

Bratland O (2009) Pipe flow 2: Multi-phase flow assurance, drbratland.com

Chaudhry MH (1987) Appied hydralic transients. Van Nostrand Reinhild Company Inc, New York

Dinis JM, Wojtanowicz AK, Scott SL (1999) Leak detection in liquid subsea flowlines with no record feed rate. J Energy Res Technol 121(3):161–166

Emara SHE, Khulief YA, Hussaini I (2002) Proceedings of the institution of mechanical eng, part I. J Syst Control Eng 216(6):497–512

Kam SI (2010) Mechanistic modeling of pipeline leak detection at fixed inlet rate. J Petrol Sc and Eng 70(3–4):145–156

Taitel Y, Dukler AE (1976) A model for predicting flow regime transitions in horizontal and near horizontal Gas–Liquid flow. AIChE 22(1):47–55

Verde C, Visairo N, Gentil S (2007) Two leaks isolation in a pipeline by transient response. Adv Water Resour 30(8):1711–1721

Wagner W, Cooper JR, Dittmann A, Kijima J, Kretzschmar HJ, Kruse A, Mares R, Oguchi K, Sato H, Stöcker I, Sifner O, Takaishi Y, Tanishita I, Trübenbach J, Willkommen Th (2000) The IAPWS industrial formulation 1997 for the thermodynamic properties of Water and Steam. ASME J Eng Gasturbines Power 122(1):150–182

White FM (2005) Fluid mechanics, 5th edn. McGraw-Hill, New York

Yadigaroglu G, Lahey RT (1976) On various forms of the conservation equations in two-phase flow. Int J Multiph Flow 2:477–494

On the Modeling Strategies for Hydrodynamic Slugging in Conduits of General Shapes and Layouts

J. E. V. Guzmán and R. Zenit

Abstract Some modeling aspects concerning large industrial pipelines are briefly outlined in this paper. The crucial identification of the dominant process during the model development stage is emphasized. The discussion is illustrated with examples of an application to a concrete oil-production system.

1 Introduction

Quantifying the effects produced by intermittent flows in industrial conduits is a matter of great importance. Diverse problems associated with slug flow in such systems have been reported and still motivate a continuous search for effective flow control methods (Hill and Wood 1994). Interestingly, the available models are insufficient for most practical situations and the analyses have to relay on empirical correlations tailored to specific systems.

Owing to the complexities of two-phase flows in large industrial pipelines the particular processes are considered separately (e.g. severe slugging, terrain induced slugging or slug flow in vertical tubes) and unified treatments are not usually attempted (Bergels et al. 1981).

However, sometimes a space-wise dominant flow pattern persists in the system throughout the operating cycle. Under such circumstances, any short termed

J. E. V. Guzmán (✉) · R. Zenit
Instituto de Investigaciones en Materiales, Universidad Nacional Autónoma de México, Ciudad Universitaria, C. Exterior s/n, 04510, Mexico City, D.F., Mexico
e-mail: eguzman@iim.unam.mx

R. Zenit
e-mail: zenit@servidor.unam.mx

J. Klapp et al. (eds.), *Experimental and Theoretical Advances in Fluid Dynamics*, Environmental Science and Engineering, DOI: 10.1007/978-3-642-17958-7_26,

effects may be taken into account when needed, or may even be completely disregarded. Then, it is possible to make a reasonably accurate model for the flow problem.

In this article some aspects of traditional modeling alternatives are considered for hydrodynamic slug flows in general conduits. By exploiting the resemblance of the flow pattern with a simple mechanical system (a mechanistic approach) the Euler–Lagrange method is favored.

2 Hydrodynamic Slugging in Conduits of General Shapes

Gas–liquid mixtures conveyed through arbitrarily shaped pipelines may result in an intermittent flow pattern (De Henau and Raithby 1995). The transition depends on the in situ superficial velocities and volume fractions of the phases.

Hydrodynamic slugging, in particular, is produced at some point (normally near the inlet) of the pipeline. In long conduits the slugs may continue to increase in size as they flow. Eventually, a quasi-stationary length (developed length) can be reached depending on the overall dynamical characteristics of the transport system (Guzman and Fairuzov 2009).

2.1 Conventional Modeling Strategies

In principle, the Navier–Stokes equations could be applied to each phase to produce a complete description of the flow field. In two-phase flow, however, such an application becomes challenging due to a variety of highly non-linear processes: interfacial dynamics, density fluctuations, phase transitions, etc.

To circumvent this limitation an integral formulation of the conservation laws may be used. Then, from the Reynolds transport theorem

$$\frac{d}{dt}\int\limits_{V(t)} f(\vec{r},t)\,dV = \int\limits_{V(t)} \frac{\partial f}{\partial t}dV + \oint\limits_{S(t)} (\vec{v}_s\cdot\hat{n}) f\,dS, \tag{1}$$

a local instantaneous balance can be obtained. For instance, the momentum relation for phase "k" can be written as

$$\frac{\partial}{\partial t}\langle\rho\alpha u\rangle_k + \frac{\partial}{\partial x_i}\langle\rho\alpha u^2\rangle_k = \langle\alpha\rangle_k \frac{\partial p}{\partial x_i} + \langle\rho\alpha\rangle_k g + \langle F^{\gamma}\rangle_k + \langle F^{w}\rangle_k, \tag{2}$$

once the mixed time-area averaging (indicated by the brackets) is performed. This method is normally used in general two-phase flow analyses but, for the case at hand, a better alternative is still available.

2.2 The Mechanistic Analogy

The global spatial arrangement of the liquid bodies and the gas bubbles observed in hydrodynamic slug flow resembles a series of interacting mass-spring-damper systems. This analogy with a simple "mechanism" could serve as the basis for a Lagrangian formulation. Focusing the modeling effort on such analogies proves to be useful in the mechanistic approach. To facilitate the analysis, the developed slugs are treated like idealized cylindrical bodies and the effects associated with their fronts and tails are discarded in the first approximation.

2.3 The Euler–Lagrange Method

If the kinetic and potential energies of the developed slug are considered, the corresponding Lagrangian may be expressed as (e.g. Cannon 1967)

$$\mathcal{L}_i = \frac{1}{2}\left(m_{s,i}\dot{x}_i^2\right) - g m_{s,i} x_i sin\varphi_i, \tag{3}$$

where $m_{s,i}$ is the mass of the i-th slug, g is the gravitational acceleration, φ_i is the inclination of the corresponding segment. The generalized positions and velocities are represented by x_i and $\dot{x}_i$ in a Cartesian reference frame.

Furthermore, the external forces acting on the slug can be introduced in the formulation via the generalized force terms (appearing on the right hand side) of the Euler–Lagrange equations (e.g. Lanczos 1970):

$$\frac{d}{dt}\left(\frac{\partial \mathcal{L}_i}{\partial \dot{q}_i}\right) - \frac{\partial \mathcal{L}_i}{\partial q_i} = \sum_j \vec{F}_j \cdot \frac{d\vec{r}_j}{d\dot{q}_i} \tag{4}$$

The most relevant forces are the pressures (acting at either end of the slug) and the friction. Also, during the discharge process at the outlet of the system, an intense interfacial friction produces an additional pressure drop. Therefore, the corresponding terms are written as

$$\vec{F}_{p,i} = \hat{n}(P_b A)_i;\ \vec{F}_{f,i} = \hat{n}(S\tau)_i; \vec{F}_{exit,i} = \hat{n}\left(K m_{out}\dot{x}^2\right)_i. \tag{5}$$

In these expressions, P_b is the pressure in the gas bubble, A is the area of the cross section, S is the contact area of the slug with the walls, τ is the shear stress, K is a loss coefficient (per unit length), m_{out} is the mass flowing out of the system and $\hat{n}$ is the normal unit vector on each surface. The details of the implementation of the method can be found in (Guzmán and Zenit 2011).

Figure 1 shows the agreement observed between the simulation and the experimental data. The corresponding experiments were performed in a scaled representation of an oil production system where the nominal slug size was half the length of

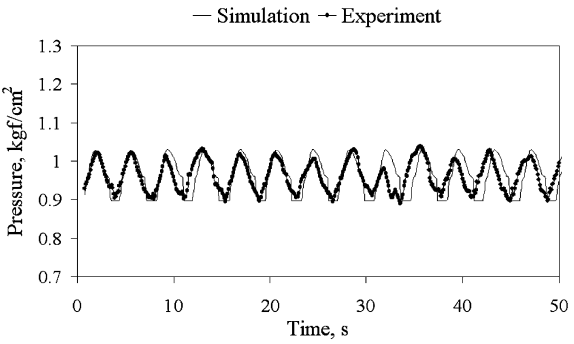

Fig. 1 Experimental and simulation pressure plots for short hydrodynamic slugs

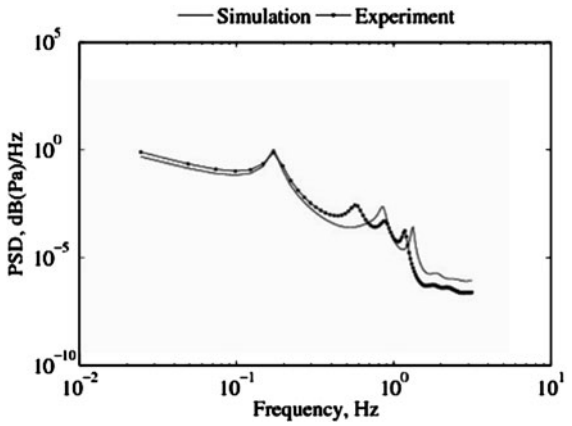

Fig. 2 Experimental and simulated PSD's for short hydrodynamic slugs

the vertical tube (Fig. 3). The validations for longer slugs and the simulation of real off-shore production systems were also satisfactory (Guzman and Fairuzov 2009).

More recently, the power spectral densities (or PSD's) related to this particular system have also been investigated (Guzmán and Zenit 2011). The information obtained from them is relevant for various design procedures (e.g. operations, structural, remediation, etc.) because the vibration modes that could be excited by the slug flow may be avoided. A comparison between the experimental and the predicted PSD's for short slugs is shown in Fig. 2.

3 Advantages of Simplified Modeling: Rapid Prototype Assessment

Frequently, the analyses of the flow characteristics in industrial systems must be accompanied by solutions which are required in real time in almost all cases. Therefore, when a control method is proposed, concerns regarding its safety and operational limits need to be addressed appropriately.

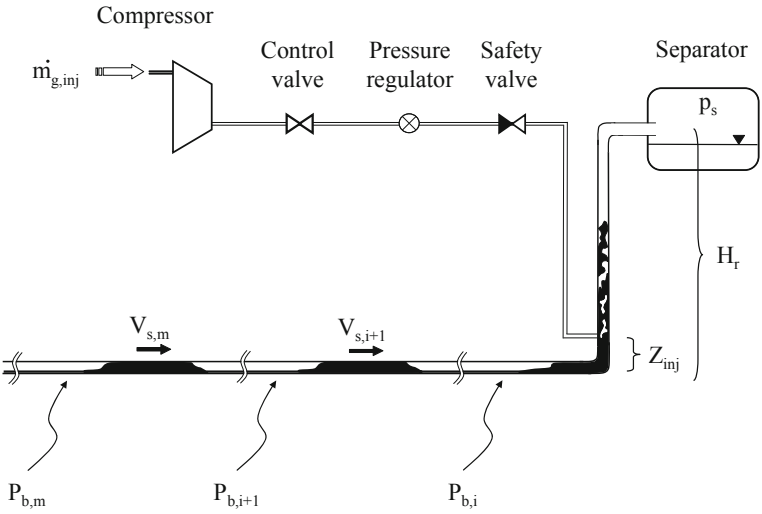

Fig. 3 Layout of the production and the gas injection systems

In the case of the oil production facility a gas injection system was suggested as a means to overcome the adverse slugging effects; in particular, the large pressure fluctuations needed to be suppressed. Both systems are schematized in Fig. 3.

By including an additional generalized force term in the Euler–Lagrange formulation, a modified equation of motion for the slug at the injection port was obtained:

$$\frac{dV_{s,i}}{dt} = \frac{\Delta P_b}{\rho_l L_{s,i}} - \frac{g z_{inj}}{L_{s,i}} - \frac{F_{friction,i}}{\rho_l L_{s,i} A} - \frac{1}{2L_{s,i}} \left(\frac{A}{A_{eff}}\right)^2 \left(\frac{\sqrt{1 - d_{eff}^4/d^4}\, V_{s,i}}{C_d}\right)^2 . \quad (6)$$

Specific parameters like the effective discharge coefficient, C_d, or the effective diameter, d_{eff}, can be modeled separately or can be determined from system-specific correlations. The simulations performed with this simple model predicted that the gas injection system would produce around a 45% reduction in the amplitude of the pressure pulses (Fig. 4). Recent experimental evidence tends to support this prediction as indicated in Fig. 5.

4 Conclusions

Simple models can be obtained for large transport systems when a dominant process governs the global dynamical response (such is the case of hydrodynamic slugging). When the fundamental mechanism has been identified, the Euler–Lagrange method becomes a powerful modeling tool. Its implementation is straightforward and allows the systematic introduction of refinements to the basic

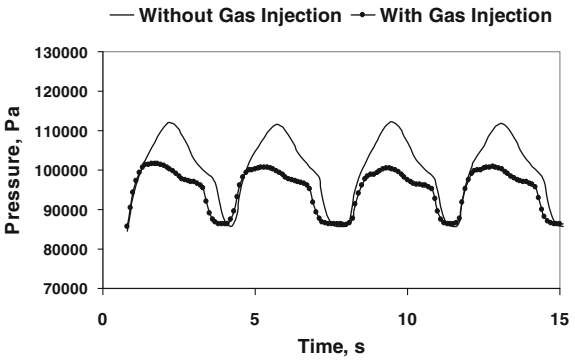

Fig. 4 Comparison of the predicted pressure signals obtained by simulating the combined production-gas injection systems

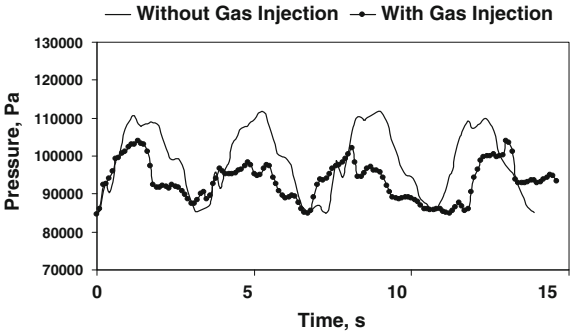

Fig. 5 Comparison of the experimental pressure signals obtained during the evaluation of the combined production-gas injection systems

problem (here represented by a flow control solution). Furthermore, the predictions provided by a simple model may guide the experimental work and may indicate where to include a more detailed analysis.

References

Bergels AE, Collier JG, Delhaye JM, Hewitt GF, Mayinger F (1981) Two-phase flow and heat transfer in the power and process industries. Hemisphere Publishing Corporation, Washington

Cannon RH (1967) Dynamics of physical systems. McGraw-Hill, New York

De Henau V, Raithby GD (1995) A study of terrain induced slugging in two-phase flow pipelines. Int J Multiphase Flow 21(3):365–379

Guzman E, Fairuzov Y (2009) A study of normal slug flow in an offshore production facility with a large diameter flowline. SPE 108752-PP, p 11

Guzmán JEV, Zenit R (2011) Application of the Euler-Lagrange method to model developed hydrodynamic slugging in conduits. J Fluids Eng 133(4)

Hill TJ, Wood DG (1994) Slug flow: occurrence, consequences and prediction. SPE 27960:53–61

Lanczos C (1970) The variational principles of mechanics. Dover Publications Inc, New York

Influence of Modifications of the Solid-Fluid Interaction by pH on the Dispersion of ^{232}Th Through a Saturated Porous Media

Estela Mayoral, Eduardo de la Cruz, Luis Carlos Longoria, Jaime Klapp and Roberto González

Abstract Migration and mass transfer of radionuclides through a saturated porous media taking into account the retention in the solid matrix as a function of the pH, is studied using the Darcy's law equation for the effective velocity, and solving the contaminant transport diffusion equation within a porous media by the finite element method. The retardation coefficient R is obtained directly from the distribution constant K_d which depends strongly on the media physicochemical characteristics such as ionic strength and pH. A logarithmic dependence of K_d with pH and its effect over the ^{232}Th transport is analyzed in two different porous media: homogeneous and heterogeneous. By means of this model we obtained the concentration for the contaminant at different positions and the retardation in the migration originated by the differences in the pH values that was analyzed. We obtain the total concentration in different substrates and the effect of the changes in the media in the final distribution of the contaminant.

E. Mayoral (✉) · E. de la Cruz · L. C. Longoria · J. Klapp
Instituto Nacional de Investigaciones Nucleares, Carretera México-Toluca s/n, La Marquesa, Ocoyoacac, 52750 Estado de México, México
e-mail: estela.mayoral@inin.gob.mx

E. de la Cruz
Instituto Tecnológico de Toluca, Av. Tecnológico S/N Ex-Rancho La Virgen, Metepec, 52140 Estado de México, México

R. González
Facultad de Ciencias, Universidad Autónoma del Estado de México, El Cerrillo Piedras Blancas, 50200 México City, Estado de México, México

J. Klapp et al. (eds.), *Experimental and Theoretical Advances in Fluid Dynamics*, Environmental Science and Engineering, DOI: 10.1007/978-3-642-17958-7_27,

1 Introduction

The study and prediction for the transport and mobility of radionuclides immersed in one or more liquid phases through a porous solid matrix, and its dependence with the changes in the medium are a key issues in assessing the future performance of nuclear waste repositories and in controlling the radionuclide migration produced by some eventuality. The dispersion rates of radionuclides in contaminated sites are significantly influenced by their distribution between liquid and solid phases. This relationship is usually expressed by a distribution coefficient represented as K_d, which is defined as the ratio of the radionuclide concentration sorbed by the solid matrix (C_s) to the radionuclide concentration in the liquid (C_l) and is expressed as $C_s = K_d C_l$. The K_d value is strongly dependent of the media (Gil-García et al. 2009; Payne et al. 2010) by example: (a) the ionic strength originated by the presence of ionic components, (b) the variation in pH values produced by the presence of acid or basic species and (c) the contribution of other chemical agents modifying the substrate surface or competing for it, are some of the phenomena that can affect the K_d value; for this reason the main purpose of this work is to understand how the complete medium modifies and affects the solid–particle–liquid interactions as well as the transport in a porous media. If we understand how the presence of the involved species and the changes in the porous media are modifying the transport properties, we will be able to design alternative materials and formulations of chemical agents with specific applications, as in the case of remediation problems, which can be studied by a macroscopic approach solving the flux fluid equations in a saturated porous media using the Darcy's law in order to obtain an effective velocity. At the same time we solve the transport equations for the solute across the media, taking into account the effect of the retention of the radionuclide in the solid matrix. In this work we solve both equations using the COMSOL Multiphysics software that is based on the finite element technique. In this approximation we introduce global properties in order to make a characterization of the media, for example: porosity, intrinsic permeability, hydraulic conductivity, retention constant and viscosity among others. In this work we present the results for the study of the transport of ^{232}Th through a saturated porous media. We study two cases: a homogeneous and heterogeneous medium constituted by stratus with different permeability and a logarithmic dependence of K_d with pH.

2 Dispersion Equations for Saturated Media

The global expression for the transport equation is (Bear 1979).

$$R\frac{\partial C}{\partial t} = \nabla \cdot (\mathbf{D} \cdot \nabla C) - \mathbf{V} \cdot \nabla C - R\lambda C \pm F \tag{1}$$

where R is the retardation coefficient which considers the retention of the contaminant in the solid, **D** is the matrix of the hydrodynamic dispersion coefficients and it is calculated as the sum of the molecular diffusion matrix and the mechanical dispersion matrix.

This transport equation describing a contaminant in a given solution expresses the variation of the concentration as a function of time considering three phenomena: (a) the hydrodynamic dispersion, represented by the first term in the right hand side of Eq. 1, which corresponds to the variation generated by the molecular diffusion and the hydrodynamic dispersion. The molecular diffusion is originated by the movement of molecules in a fluid even in steady state. The hydrodynamic dispersion in a porous medium is the spreading produced by the effect of the movement of the liquid in a medium constituted by interconnected porous; (b) the second term corresponds with the concentration change due to the water movement and it is known as advection. This phenomenon produces a transport of the contaminant in the system with no mixing; (c) the loss of mass due to radioactive decay and to the sorption on the solid matrix is expressed in the third term; (d) the source and sink possibilities are given by the forth term that represents the access or egress of the contaminant in some simulated region.

In our case, we can consider that the molecular diffusion is not fast enough and can be neglected, so we consider only the mechanical or hydrodynamic dispersion coefficients, which are calculated using the expression

$$Dij = \alpha_T |V| \delta_{ij} + (\alpha_L - \alpha_T) \frac{V_i V_j}{|V|}, \tag{2}$$

where α_L and α_T are the longitudinal and the transversal dispersion respectively, δ_{ij} is the Kronecker's delta, $|V|$ the module of the velocity vector, **V** is the effective velocity, and represents the mean displacement of a water molecule related with the medium. Its components can be calculated by the Darcy's law which considers that the flux through the soil goes from high energy to low energy levels and it depends on the pressure and depth and, as soon as the water flows, part of its energy is lost by friction. For this reason, a hydraulic pressure gradient is generated and can be expressed as a linear law where the velocity of the flux Q is proportional to the energy loss, and to a K coefficient, and inversely proportional to the length of the way of the fluid l. The K coefficient depends on the natural constitution of the soil and the hydrodynamics properties of the fluid and it is known as the permeability or hydraulic conductivity. The expression for Darcy's law is

$$Q = KA \frac{[H1 - H2]}{dl} = -KA \frac{dH}{dl} = KAS^*, \tag{3}$$

where H is known as the hydraulic head (if the fluid is water) and it is a function of the pressure and the gravitational potential. It represents the energy per unit of weight of fluid and is given by $H = z + p/\gamma + c$, where c is a constant, p is the pressure due to the fluid through the porous media and γ is the specific weight for the fluid; z is the distance at one arbitrary level respect to the surface in the vertical

direction. Darcy's law (Rives 1996; Fetter 1994) considers an effective velocity through a section in a porous media instead of a real velocity between the grains. This velocity is given by $Q/A = v = -K\,dH/dl$ or expressed in its vector form by $\mathbf{V} = -K\nabla H$.

Finally, λ is the radioactive decay constant and it only depends on the radionuclide; F is the source-sink which gives us the possibility to introduce a source with a time and position dependence, and C is the concentration of an element in the liquid phase. The retention of the solute on the solid matrix gives the retardation coefficient R and considers the physicochemical interactions between the substrate which constitutes the porous medium and the solid contaminant. These interactions depend strongly on the chemical composition of the substrate and solute and the presence of the others components in the media with the capacity to modify the sorption process. In this process several phenomena are involved such as ion interchange, chemical reaction and the adsorption–desorption process. All of them produce a global behavior which can be included in a general constant known as the distribution coefficient K_d. This coefficient gives the relationship between the amount of mass present in the solid medium and the amount of mass present in the liquid: $S = f\,(C)$, where S is the solute concentration in the solid phase. Considering that the movement of the solution through the porous medium is slow, we can assume that the system is at equilibrium, then a linear relationship between the concentration for the solute on the solid and the concentration for it in the liquid can be obtained by the expression $S = K_d C$, where K_d is known as the distribution coefficient. The retardation coefficient R is a function of K_d and can be obtained using the expression

$$R = 1 + \frac{\rho_b K_d}{\theta_t} \tag{4}$$

where ρ_b is the apparent density and θ_t is the total porosity.

3 Thorium Speciation and K_d Dependence with pH

Thorium (Th) is an element composed by 25 radioisotopes, with half-lives of seconds to 10^{10} years. These Th isotopes are mainly produced by natural disintegration of uranium isotopes (^{238}U, ^{235}U and ^{234}U) that are soluble. Usually, common Th consists almost wholly of primordial ^{232}Th ($t_{1/2} = 1.4 \times 10^{10}$ years) because of its extremely long half-life in relation with others Th isotopes. Then, when chemical equilibrium is established, ^{232}Th determines the chemical fate and speciation of all Th isotopes. The general inorganic species of Th at pH of 8 are hydroxo and carbonate complexes, other strong ligands include carbonate, humics, phosphate, ethylene-diamine-tetraacetic acid (EDTA) and diethyl-triamine-pentaacetic acid (DTPA), all of them are present in the soil natural composition. The sorption of radionuclides on soils and sediments is commonly quantified by

distribution coefficients known as K_d values. Thorium's K_d values were taking from the literature (Santschi et al. 2006) and they are significantly correlated to pH between the range of pH from 4 to 8. The pH dependence can be explained in part by taking into consideration the aqueous speciation of thorium in groundwater. Th aqueous speciation changes greatly as a function of groundwater pH; as the pH increases, the thorium complexes becomes more anionic or neutral, thereby becoming less susceptible to be electrostatically attracted to a negatively charged solid phase. This decrease in electro statically attraction would likely result in a decrease in K_d values. The regression equation for K_d and pH between the values 4–8 is

$$\log(_{Th}K_d) = -0.13 + 0.69(\mathrm{pH}). \tag{5}$$

4 The Problem Formulation

Our starting point is the physical situation of the transport of a contaminant (^{232}Th) through a homogeneous and heterogeneous saturated porous medium described by substrates with different intrinsic permeability values K characteristics of a typical clay distribution in soil. The contaminant enters at the upper boundary. The mass loading rate has a functional dependence with time given by $C_{inward} = C_o(t < 10$ years), with $C_o = 1 \times 10^{-9}$ (Kg/m^2) and is diffused along the medium with an effective porosity $\theta = 0.5$, while decaying with a first order reaction ($t_{1/2} = 1.4 \times 10^{10}$ years). The porous matrix allows diffusion in both the transversal and longitudinal directions into itself with longitudinal and transverse dispersivity constants of $\alpha_L = 2$ and $\alpha_T = 6(\mathrm{m})$, respectively. Our transport model simulates the movement and radioactive decay of ^{232}Th as it moves through the subsurface, we simulate the movement of the contaminant by advection, diffusion and dispersion, considering the contaminant sorption or desorption on soil or rock using a logarithmic dependence of the K_d value with the pH expressed by Eq. 5, and the corresponding alteration in the retardation constant R by changes in pH in the media. The simulation of transport processes requires characterization of horizontal and vertical distribution of average groundwater velocity (direction and magnitude) obtained by solving Darcy's equations considering a constant mean inward flux of 8×10^{-8} mm/year. Using numerical models based on finite element methods, we solve the Darcy's equation for saturated water flow and the convection–dispersion type equations for solute transport (Eq. 1). In the discretization, the domain is represented by a network of grid cells or elements and the time of the simulation is presented by time steps. The accuracy of the numerical models depends on the model input data, the size of the space, the time discretization, and the numerical method used to solve the model equations. We tested different parameters in order to obtain the most accurate results.

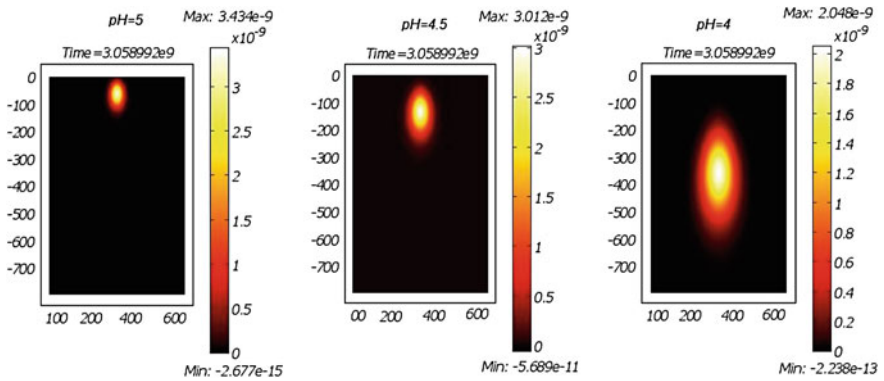

Fig. 1 Concentration for the migration of ^{232}Th at different pHs in a homogeneous clay type medium

5 Results

5.1 Migration of ^{232}Th in Homogeneous Media as a Function of pH

In this study we consider the logarithmic dependence of K_d regarding the pH and its consequences in the migration of ^{232}Th in a saturated homogeneous porous medium with an intrinsic permeability of 5×10^{-6}. The pH dependence for the K_d was taken from the literature and it is represented by Eq. 5. Using numerical models based in the finite element method, we solve the Darcy's equation for saturated water flow and the solute transport equations for ^{232}Th. The changes in the concentration at $t = 1 \times 10^8$ years for this contaminant at different pH values in homogeneous media is presented in Fig. 1 where we can observe a very regular form in the plume because of the homogeneous medium but with a delay in its evolution.

The next plots show the relative concentration of ^{232}Th versus y (the vertical position) at different times for pH = 4.5, 5.5, 7 (Fig. 2).

The next plot shows the total concentration in the first substrate for different pH values. We can observe a regular form in the migration of the contaminant and the delay produced by the pH changes. We also observe the delay in the migration of the contaminant when the pH is increased (Fig. 3).

5.2 Migration of ^{232}Th in Heterogeneous Media as a Function of pH

The next system that we studied was the migration of ^{232}Th in a heterogeneous medium with 18 different substrates each one with a different intrinsic

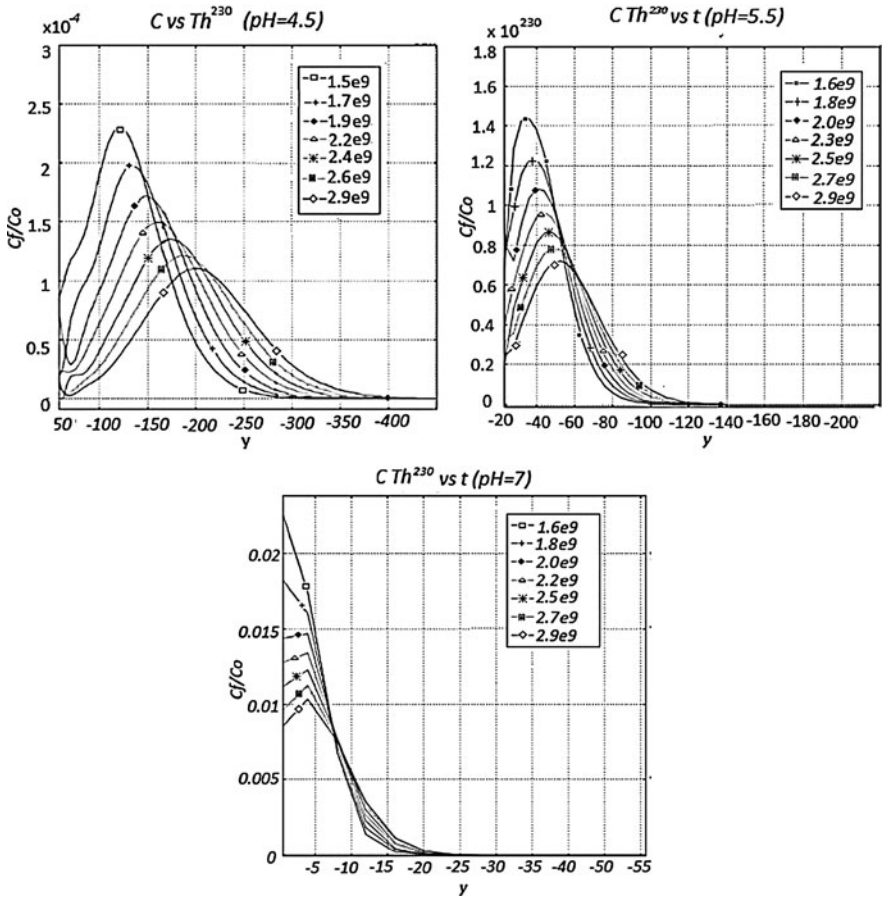

Fig. 2 Relative concentration of ^{232}Th versus y at different times for pH = 4.5, 5.5, 7

permeability value showed in Fig. 4. The Figure also shows the velocity field and pressure distribution for the different stratum obtained by solving Darcy's law considering a saturated porous media.

The migration of ^{232}Th across this medium for different pH is shown in Fig. 5 where we have plotted the concentration at $t = 10^8$ years. We can observe a very irregular form in the plume originated for the heterogeneity in the media. Also a delay in the migration is observed due to the difference in retention originated by pH changes.

The changes in the concentration as a function of time in the first substrate for different pH are presented in the next figure. We can observe that the form of the plot becomes irregular due to the heterogeneity in the media. The delay in the rate of migration of the contaminant is evident for different pHs.

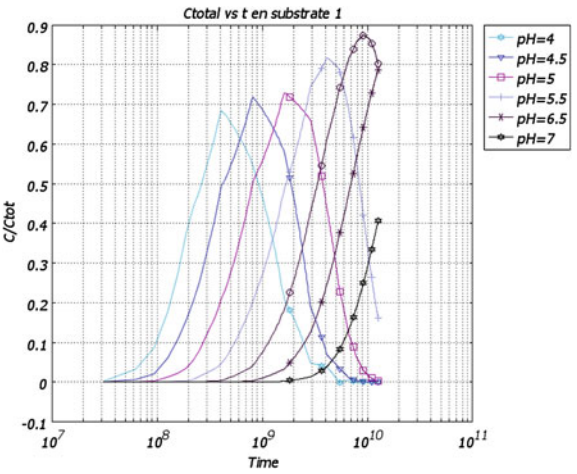

Fig. 3 Comparison of the total concentration of ^{232}Th in the first substrate for different pH values

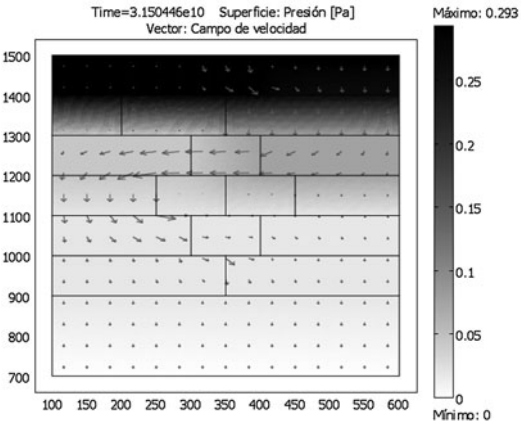

Fig. 4 Velocity field and pressure distribution for the different stratus

6 Conclusions

We simulated the migration of ^{232}Th in homogeneous and heterogeneous media. Our model is able to describe the behavior of the contaminant and to obtain its final distribution through the porous media. The heterogeneity of the media was analyzed obtaining a regular or irregular form for the plume. By means of this model we also obtained the concentration for the contaminant at different positions and the retardation in the migration originated by the differences in the pH values

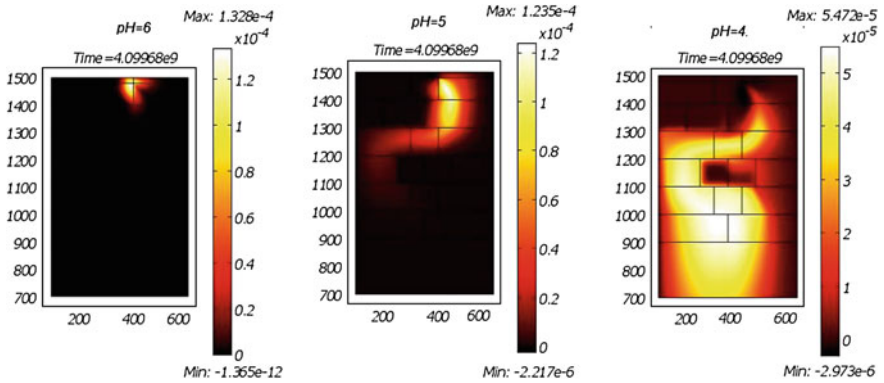

Fig. 5 Concentration for the migration of ^{232}Th at different pHs in a heterogeneous clay type medium

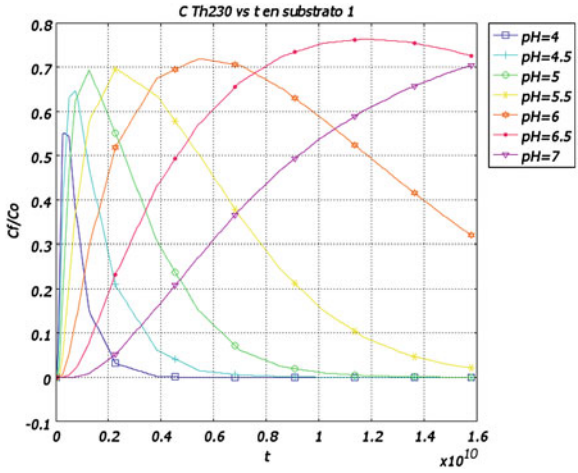

Fig. 6 Comparison of the total concentration of ^{232}Th in the first substrate for different pH values in a heterogeneous media

that was analyzed. We obtain the total concentration in different substrates and the effect of the changes in the media in the final distribution of the contaminant (Fig. 6).

References

Bear J (1979) Dynamic in porous Media. Dover, New York

Fetter CW (1994) Applied hydrogeology. Prentice Hall, New Jersey

Gil-García C, Tagami K, Uchida KT, Rogol A, Vidal M (2009) New best estimates for radionuclide solid-liquid distribution coefficients in soils. Part 3: miscellany of radionuclides (Cd, Co, Ni, Zn, I, Se, Sb, Pu, Am, and others). J Environ Radioact 100:704–715

Payne TE, Brendler V, Comarmond MJ, Nebelung C (2010) Assessment of surface area normalisation for interpreting distribution coefficients (K(d)) for uranium sorption. J Environ Radioact 1–8

Rives DE (1996) Manual del usuario del modelo de dispersión de radionúclidos en acuíferos freáticos. Comisión Regulatoria Nuclear

Santschi PH, Murray JW, Baskaran M, Benitez-Nelson CR, Guo LD, Hung CC, Lamborg C, Moran SB, Passow U, Oy-Barman M (2006) Thorium speciation in seawater. Mar Chem 100:250–268

Volume Average Transport Equations for In Situ Combustion

A. G. Vital-Ocampo and O. Cazarez-Candia

Abstract In this work a volume average mathematical model for multiphase flow of oil, water and gas through a homogeneous, isotropic and rigid porous media was developed, and proposed to simulate an in situ combustion problem. Such model consists of mass, momentum and energy equations. The gas is considered ideal and incompressible and the following processes were taken into account: (1) the formation of coke due to an oil chemical reaction, (2) formation of gas due to a combustion reaction between coke and oxygen, and (3) mass transfer due to oil and water phase change. The closure relationships for the water phase change, the formation of coke and the combustion of coke, were taken from the work of Gottfried and Mustafa (1978). However, the oil phase change equation, presented by Chu (1964), was modified as function of the partial pressure of the oil vapor in the gas phase and the vapor pressure of oil. The model is solved using the finite differences technique with explicit scheme for the mass equations and the Crack-Nicholson scheme for energy equation. The model allows predicting the profiles of: (1) temperature, (2) pressure, (3) oil, water and gas saturations, (4) oxygen, oil vapor, and steam mass fractions, and (5) cumulative oil recovery. The predictions are in agreement with experimental data reported in literature.

A. G. Vital-Ocampo (✉)
Depto. de Mecánica, Centro Nacional de Investigación y Desarrollo Tecnológico, Interior Internado Palmira s/n, Col. Palmira, C.P., 62490 Cuernavaca, Morelos, Mexico
e-mail: agvital@yahoo.com

O. Cazarez-Candia
Instituto Mexicano del Petróleo, Eje central Lázaro Cárdenas No. 152, Col. San Bartolo Atepehuacan, 07730 Mexico City, D.F., Mexico
e-mail: ocazarez@imp.mx

J. Klapp et al. (eds.), *Experimental and Theoretical Advances in Fluid Dynamics*, Environmental Science and Engineering, DOI: 10.1007/978-3-642-17958-7_28,

1 Introduction

Recently one of the techniques used for hydrocarbons recovery in oil reservoirs is the in situ combustion technique. When this technique is used, the common way to determine the amount of fuel that could be burned, the temperature profiles as well as other important parameters (pressure, oil recovery, etc.) is by experimentation in combustion tubes. However, carrying out experimentation under different operating conditions is very expensive. Therefore, the necessity arises for mathematical models able to predict the main thermal and hydrodynamic phenomena observed in laboratory.

One of the main approaches to multiphase flow modeling, which is presented when the in situ combustion technique is applied in oil reservoirs, is to average (in time, space or in some combination of these) the local instantaneous conservation equations. Specifically the volume averaging method has been widely used to develop the transport equation for multiphase flow (Whitaker 1986; Soria and De lasa 1991). For this reason, in this work it is shown that such a method can be used to solve an in situ combustion problem.

In order to model the in situ combustion, many researches have proposed mathematical models that involve mass, momentum and energy equations for multiphase flow that permit a significant improvement on the oil recovery (Gottfried 1965; Penberthy and Ramey 1965; Verma et al. 1978 and Lu and Yortsos 2001). Those models have been also used to simulate combustion tube experiments. In the present work, the volume average mass and energy equations for oil (o), water (w), gas (g), and coke (c) are obtained and used to simulate in situ combustion in experimental tubes.

The equations are developed taking into account: (1) the generation of coke due to the chemical reaction of oil, (2) the generation of gas due to the combustion reaction between coke and oxygen, and (3) mass transfer due to the phase change of oil and water. The closure relationships for the water phase change, the formation of coke and the combustion of coke, were taken from the work of Gottfried and Mustafa (1978). However, the oil phase change equation, presented by Chu (1964), was modified as a function of the partial pressure of the oil vapor in the gas phase and the vapor pressure of oil. The mathematical model is able to predict the profiles of: (1) temperature, (2) pressure, (3) oil, water and gas saturations, and (4) oxygen, oil vapor, and water steam mass fractions.

2 Study System

The system under consideration consists of a multiphase flow of oil, water and gas interacting among them, and with the porous media (Fig. 1). During the movement of phases through the porous media coke combustion can occur. The gas phase consists of air that is injected, combustion gases, and oil and water vapors. When

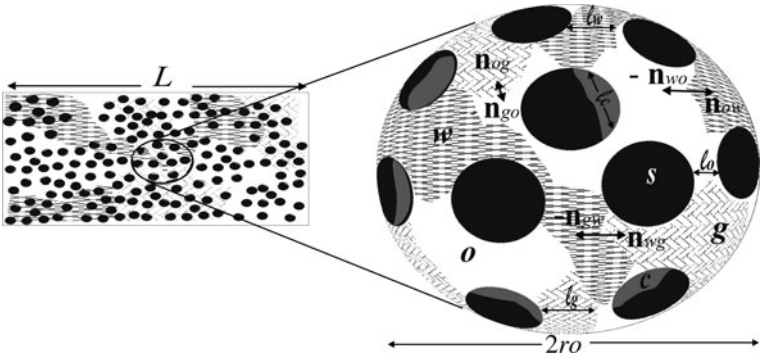

Fig. 1 Averaging volume (V).$\mathbf{n}_{og} = -\mathbf{n}_{go}$, $\mathbf{n}_{wg} = -\mathbf{n}_{gw}$, and $\mathbf{n}_{wo} = -\mathbf{n}_{ow}$ are the oil–gas, water–gas, and water–oil normal vectors

the combustion occurs, heat and oil can be cracked, and coke is formed (which is supposed that does not affect the porosity). Water and oil have phase change (condensation and evaporation).

3 Volume Averaging

The system under consideration is illustrated in Fig. 1 in which the averaging volume selected is constant, smaller than the characteristic macroscopic length of the porous media (L) and larger than the characteristic lengths of coke, oil, water and gas (ℓ_o, ℓ_w, ℓ_g, ℓ_c). The characteristic length of the averaging volume (r_o) must satisfy the following inequality:

$$\ell_o,\ \ell_w,\ \ell_g,\ \ell_c << r_o << L \tag{1}$$

4 Averaged Equations

When the averaging theorems (Whitaker 1986) and the interface jump conditions are applied on the local equations (Vital-Ocampo and Cazarez-Candia 2010), the following averaged mass, momentum and energy equations are obtained:

Averaged mass equation:

$$\begin{aligned}\frac{\partial \varepsilon_k \langle \rho_k \rangle^k}{\partial t} + \nabla \cdot \varepsilon_k \langle \rho_k \rangle^k \langle \mathbf{v}_k \rangle^k + \nabla \cdot \varepsilon_k \langle \mathbf{j}_k \rangle^k - \varepsilon_k \langle \Phi_k \rangle^k \\ = -\sum_{\substack{km \\ k \neq m}}^{N} \frac{1}{V} \int_{A_{km}(t)} \{\rho_k (\mathbf{v}_k - \mathbf{w}_{km}) + \mathbf{j}_k\} \cdot \mathbf{n}_{km}\, dA\end{aligned} \tag{2}$$

Averaged momentum equation:

$$\begin{aligned}
&\frac{\partial \varepsilon_k \langle \rho_k \rangle^k \langle \mathbf{v}_k \rangle^k}{\partial t} + \nabla \cdot \left(\varepsilon_k \langle \rho_k \rangle^k \langle \mathbf{v}_k \rangle^k \langle \mathbf{v}_k \rangle^k \right) + \nabla \cdot \left(\varepsilon_k \langle \rho_k \rangle^k \langle \tilde{\mathbf{v}}_k \tilde{\mathbf{v}}_k \rangle^k \right) \\
&\quad + \varepsilon_k \nabla \langle p_k \rangle^k - \mu_k \varepsilon_k \nabla^2 \langle \mathbf{v}_k \rangle^k - \varepsilon_k \langle \rho_k \rangle^k \mathbf{g}_k \\
&\quad = -\sum_{\substack{km \\ k \neq m}}^{N} \frac{1}{V} \int\limits_{A_{km}(t)} \rho_k \mathbf{v}_k (\mathbf{v}_k - \mathbf{w}_{km}) \cdot \mathbf{n}_{km} \, dA \\
&\qquad + \sum_{\substack{km \\ k \neq m}}^{N} \frac{1}{V} \int\limits_{A_{km}(t)} (-\tilde{p}_k + \mu_k \nabla \tilde{\mathbf{v}}_k) \cdot \mathbf{n}_{km} \, dA + \mu_k \nabla \cdot \left(\sum_{\substack{km \\ k \neq m}}^{N} \frac{1}{V} \int\limits_{A_{km}(t)} \tilde{\mathbf{v}}_k \cdot \mathbf{n}_{km} \, dA \right)
\end{aligned} \tag{3}$$

Averaged energy equation:

$$\begin{aligned}
&\frac{\partial C p_k \langle \rho_k \rangle^k \varepsilon_k \langle T_k \rangle^k}{\partial t} + \nabla \cdot \varepsilon_k \langle C p_k \rangle^k \langle \rho_k \rangle^k \langle \mathbf{v}_k \rangle^k \langle T_k \rangle^k + \beta_k \varepsilon_k \frac{\partial \langle p_k \rangle^k}{\partial t} \\
&\quad + \beta_k \nabla \cdot \varepsilon_k \langle \mathbf{v}_k \rangle^k \langle p_k \rangle^k + \nabla \cdot \left\langle \tilde{C} p_k \tilde{\mathbf{v}}_k \tilde{T}_k \right\rangle \langle \rho_k \rangle^k + \beta_k \langle \nabla \cdot \tilde{\mathbf{v}}_k \tilde{p}_k \rangle \\
&\quad + \sum_{km}^{N} \frac{1}{V} \int\limits_{A_{km}(t)} C p_k \rho_k T_k (\mathbf{v}_k - \mathbf{w}_{km}) \cdot \mathbf{n}_{km} \, dA \\
&\quad + \beta_k \left(\sum_{\substack{km \\ k \neq m}}^{N} \frac{1}{V} \int\limits_{A_{km}(t)} p_k (\mathbf{v}_k - \mathbf{w}_{km}) \cdot \mathbf{n}_{km} \, dA \right) \\
&\qquad = \nabla \cdot \left[K_k \left(\varepsilon_k \nabla \langle T_k \rangle^k + \sum_{\substack{km \\ k \neq m}}^{N} \frac{1}{V} \int\limits_{A_{km}(t)} \tilde{T}_k \cdot \mathbf{n}_{km} \, dA \right) \right] \\
&\qquad + \sum_{\substack{km \\ k \neq m}}^{N} \frac{1}{V} \int\limits_{A_{km}(t)} K_k \nabla T_k \cdot \mathbf{n}_{km} \, dA + \varepsilon_k \langle \Phi_k \rangle^k
\end{aligned} \tag{4}$$

In Eqs. 2–4, ρ the mass density, $\mathbf{v}$ the flow velocity, $\mathbf{j}$ the diffusive flux, p the pressure, μ the viscosity, $\mathbf{g}$ the gravity acceleration, Cp the heat capacity, T the temperature, K the thermal conductivity, $\Phi_k = \varepsilon_k \langle \Phi_k \rangle^k$ is mass generation of the kth-phase, $\langle \rangle^k$ represents the intrinsic averaged value, $\varepsilon_k \ (= V_k / V)$ is the volume fraction of the kth-phase, $V_k \, (t)$ is the volume of the kth-phase contained within the averaging volume V, which is independent of space and time, $A_{km} \, (= A_{mk})$ is the interfacial area formed by the k and m phases $(k \neq m)$, $\tilde{\mathbf{v}}_k, \tilde{p}_k$ and $\tilde{T}_k$ are the spatial

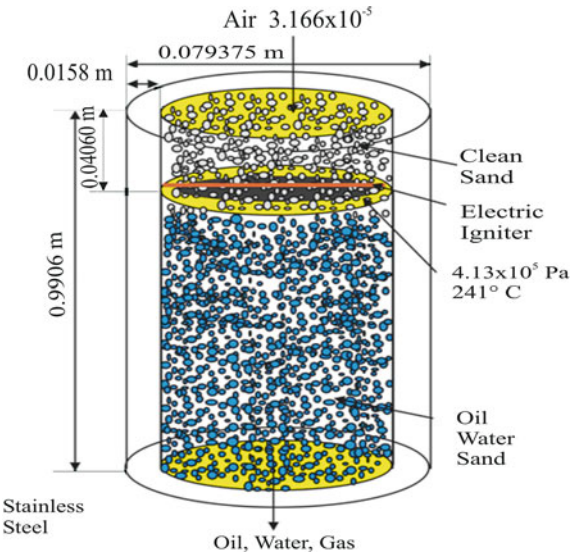

Fig. 2 Combustion tube

deviation of velocity, pressure and temperature of the kth-phase, $\sum_{km(k\neq m)}^{N}$ defines the summation of all the interfaces km that surround the phase k, the subscript k represents the phase, o, w, g, c and s which represents oil, water, gas, coke and solid, respectively, and t is the temporal coordinate.

5 Physical Model

To test the mathematical model developed, the physical model (Fig. 2) and the experimental data (Table 1) were taken from Cazarez-Candia et al. (2010).

In such work two experiments were done in a combustion tube of stainless steel with an external diameter of 0.079375 m, a width of 0.015875 m and a length of 0.9906 m, which contains about 0.94996 m of a uniform mixture of sand, water and oil (see Fig. 2). In the experiments an insulation band was placed along the tube. The oil used had activation energy of 1.56×10^7 J/kg mol and 27 API. The space formed from the sample to the top of the tube, was filled with clean sand, and an electric igniter was placed on this place. Electric current was gradually introduced into the igniter until the temperature in the combustion tube at the igniter level reached about 241°C and air injection was initiated. The production pressure was maintained constant. After the ignition, the combustion front moved from the igniter to bottom of the combustion tube. The combustion gases and liquids went out from the bottom of the tube. The end of the phenomenon occurred when the sand pack was burned all the way to the bottom flange of the combustion tube.

Table 1 Experimental parameters

Parameter	Experiment 1	Experiment 2
Water saturation (s_w)	0.23	0.275
Oil saturation (s_o)	0.325	0.383
Porosity (Φ)	0.41	0.41
Ignition temperature	427°C	462°C
Production pressure	4.13×10^5 Pa	4.20×10^5 Pa
Air injection	3.166×10^{-5} m^3/s	3.166×10^{-5} m^3/s

6 Equations for In Situ Combustion

To apply the averaged Eqs. 2–4, for an in situ combustion tube it is necessary to do the next considerations and suppositions: (1) non-permeable solid phase, (2) Newtonian fluids, (3) oil and water phase change occur, (4) there is mass generation, (5) liquid phases are mono-component ($\mathbf{j}_k = 0$ in A_{km}), incompressible and immiscible, (6) gas is ideal and incompressible, (7) gas is a mixture composed by nitrogen, oxygen, oil vapor, steam, and combustion gases, (8) momentum equation is reduced and expressed using the Darcy velocity definition, (9) all the dispersive terms are neglected, (10) local thermal equilibrium, (11) heat is transferred from the system to the environment by convection, and (12) the study is done in one dimension. Therefore Eqs. 2–4 can be re-written as:

Gas, oil water and coke averaged mass equations:

$$\frac{\partial \varepsilon_g \langle \rho_g \rangle^g}{\partial t} + \frac{\partial \varepsilon_g \langle \rho_g \rangle^g \langle \mathrm{v}_g \rangle^g}{\partial x} = -\frac{1}{V} \int_{A_{go}(t)} \rho_g (\mathbf{v}_g - \mathbf{w}_{go}) \cdot \mathbf{n}_{go} dA - \frac{1}{V} \int_{A_{gw}(t)} \rho_g (\mathbf{v}_g - \mathbf{w}_{gw}) \cdot \mathbf{n}_{gw} dA - \varepsilon_g \langle \Phi_g \rangle^g \quad (5)$$

$$\frac{\partial \varepsilon_o \langle \rho_o \rangle^o}{\partial t} + \frac{\partial \varepsilon_o \langle \rho_o \rangle^o \langle \mathrm{v}_o \rangle^o}{\partial x} = -\frac{1}{V} \int_{A_{og}(t)} \rho_o (\mathbf{v}_o - \mathbf{w}_{og}) \cdot \mathbf{n}_{og} dA - \varepsilon_o \langle \Phi_o \rangle^o \quad (6)$$

$$\frac{\partial \varepsilon_w \langle \rho_w \rangle^w}{\partial t} + \frac{\partial \varepsilon_w \langle \rho_w \rangle^w \langle \mathrm{v}_w \rangle^w}{\partial x} = -\frac{1}{V} \int_{A_{wg}(t)} \rho_w (\mathbf{v}_w - \mathbf{w}_{wg}) \cdot \mathbf{n}_{wg} dA \quad (7)$$

$$\frac{\partial \varepsilon_c \langle \rho_c \rangle^c}{\partial t} = \varepsilon_c \langle \Phi_c \rangle^c \quad (8)$$

Gas, oil and water momentum equations:

$$\langle \mathrm{v}_g \rangle = -\frac{k_g}{\mu_g} \left(\frac{\partial p}{\partial x} \right); \langle \mathrm{v}_o \rangle = -\frac{k_o}{\mu_o} \left(\frac{\partial p}{\partial x} \right); \langle \mathrm{v}_w \rangle = -\frac{k_w}{\mu_w} \left(\frac{\partial p}{\partial x} \right) \quad (9)$$

where $\langle \mathrm{v}_k \rangle \left(= \varepsilon_k \langle \mathbf{v}_k \rangle^k \right)$ is the averaged velocity of the k-phase and k_k is the permeability of the k-phase.

As a consequence of averaging the local equations additional terms arose, which are known as closure terms: interfacial mass transfer, dispersion, interfacial flux, interfacial forces, etc.

The interfacial mass transfer between w and g and o and g is expressed according to the work of Duval et al. (2004) as:

$$\frac{1}{V}\int\limits_{A_{gw}(t)} \rho_g(\mathbf{v}_g - \mathbf{w}_{gw}) \cdot \mathbf{n}_{gw} dA = -\frac{1}{V}\int\limits_{A_{wg}(t)} \rho_w(\mathbf{v}_w - \mathbf{w}_{wg}) \cdot \mathbf{n}_{wg} dA$$
$$= \dot{m}_{gw} = -\dot{m}_{wg} \tag{10}$$

$$\frac{1}{V}\int\limits_{A_{go}(t)} \rho_g(\mathbf{v}_g - \mathbf{w}_{go}) \cdot \mathbf{n}_{go} dA = -\frac{1}{V}\int\limits_{A_{og}(t)} \rho_o(\mathbf{v}_o - \mathbf{w}_{og}) \cdot \mathbf{n}_{og} dA$$
$$= \dot{m}_{go} = -\dot{m}_{og} \tag{11}$$

The mass generation of coke and gas, due to chemical reactions, are written according to the work of Gottfried and Mustafa (1978) as:

$$\Phi_o = -S_l;\ \Phi_g = (1 - M_c)\, S_l + S_c;\ \Phi_c = M_c S_l - S_c \tag{12}$$

where M_c is the ratio between the mass of formed coke and the mass of consumed oil, S_l is the coke deposition term and S_c is the coke reaction rate term.

For Eq. 10, Gottfried (1965) presented a mass transfer equation for water as:

$$\dot{m}_{gw} = -\dot{m}_{wg} = h\, a\, (p_{lw} - p_{gw}) \tag{13}$$

where h is the evaporation or condensation coefficient, a is the gas–water interfacial area per unit of volume, p_{lw} is the vapor pressure of water and p_{gw} is the partial pressure of the water vapor in the gas phase.

The Eq. 11, is presented by Vital-Ocampo and Cazarez-Candia (2010) as function of the vapor partial pressure of oil in the gas phase (p_{go}) and vapor pressure of oil (p_{lo}). Such expression is:

$$\dot{m}_{go} = -\dot{m}_{og} = \omega M_o (k_e p_{lo} - p_{go}) \tag{14}$$

where ($\omega = k_{mo}/RT$; k_{mo} is the oil mass transfer coefficient, R is the ideal gas constant and T is the system temperature), M_o is the oil molecular weight, and k_e is the vaporization equilibrium constant.

In the in situ combustion phenomenon, it was assumed that the following two reactions occur in the vicinity combustion zone:

$$\text{Heat} + \text{Oil} \rightarrow \text{Coke} + \text{Hydrocarbon vapor} \tag{15}$$

$$\text{Coke} + \text{Oxygen} \rightarrow \text{CO},\ \text{CO}_2,\ \text{H}_2\text{O} \tag{16}$$

The above two reactions represent an idealized simplification of the actual coking process, since effects such as low-temperature oxidation are not considered. However these mechanisms offer a reasonable approximation to the true process.

If the coking reaction described by Eq. 15 depends only upon temperature, then the reaction rate can be expressed as a zero order Arrhenius reaction:

$$S_l = \mathrm{Z}\ \mathrm{e}^{-\mathrm{E}/\mathrm{R}(\mathrm{T}+460)} \tag{17}$$

where Z is the Arrhenius rate coefficient for coke formation, E is the Arrhenius activation energy for coke formation, R is the ideal gas constant and T is the system temperature.

The combustion reaction described by Eq. 16 is written as:

$$S_c = \mathrm{Z_c}\ (\phi f_a \rho_g s_g)\ \mathrm{F}\ \mathrm{e}^{-\mathrm{E_c}/\mathrm{R}(\mathrm{T}+460)} \tag{18}$$

where Z_c is the Arrhenius rate coefficient for combustion, f_a is the mass fraction of oxygen in the gas phase, ρ_g is the gas density, s_g is the gas saturation, F is the accumulated coke concentration and E_c is the Arrhenius activation energy for combustion.

Substituting Eq. 9 and the closure terms given by Eqs. 12–14 into Eqs. 5–8, and then applying the volume fraction $\varepsilon_k\,(= s_k\phi)$ and Darcy velocity $\langle \mathrm{v}_k \rangle \left(= s_k \phi \langle \mathbf{v}_k \rangle^k \right)$ definitions, the next mass equations in terms of variables from the oil industry are obtained:

Mass equations:

Gas

$$\frac{\partial\, s_g\, \phi\, \rho_g}{\partial t} + \frac{\partial}{\partial x}\left(- \frac{\rho_g k_g}{\mu_g}\frac{\partial p}{\partial x}\right) = (1 - M_c)\, S_l + S_c \ + \ \dot{m}_{go} \ + \ \dot{m}_{gw} \tag{19}$$

Oil

$$\frac{\partial\, s_o\, \phi\, \rho_o}{\partial t} + \frac{\partial}{\partial x}\left(- \frac{k_o \rho_o}{\mu_o}\frac{\partial p}{\partial x}\right) = \ - \ \dot{m}_{og} - \ S_l \tag{20}$$

Water

$$\frac{\partial\, s_w\, \phi\, \rho_w}{\partial t} + \frac{\partial}{\partial x}\left(- \frac{k_w \rho_w}{\mu_w}\frac{\partial p}{\partial x}\right) = \ -\dot{m}_{w\,g} \tag{21}$$

Coke

$$\frac{\partial\, F}{\partial t} = M_c \ \ S_l \ - S_c \tag{22}$$

The Eq. 19 can be written for oxygen, oil vapor, and steam as:
Oxygen

$$\phi \frac{\partial}{\partial t}\left(f_a \rho_g s_g\right) - \frac{\partial}{\partial x}\left(\frac{f_a \rho_g k_g}{\mu_g}\frac{\partial p}{\partial x}\right) = -M_a S_c \tag{23}$$

Water vapor

$$\phi \frac{\partial}{\partial t}\left(f_s \rho_g s_g\right) - \frac{\partial}{\partial x}\left(\frac{f_s \rho_g k_g}{\mu_g}\frac{\partial p}{\partial x}\right) = M_s S_c + \dot{m}_{gw} \tag{24}$$

Oil vapor

$$\phi \frac{\partial}{\partial t}\left(f_o \rho_g s_g\right) - \frac{\partial}{\partial x}\left(\frac{f_o \rho_g k_g}{\mu_g}\frac{\partial p}{\partial x}\right) = M_{vo} S_l + \dot{m}_{go} \tag{25}$$

where s_k is the saturation $(s_k = V_k/V_H)$ of the k-phase, ϕ is the porosity $(\phi = V_H/V)$ of the k-phase, V_H is the hole volume, $F(= \rho_c s_c\, \phi)$ is known as the accumulated coke concentration, f_s is mass fraction of steam in the gas phase, f_o is the mass fraction of the oil vapor in the gas phase, M_a, is the ratio between the mass of consumed oxygen and the mass of consumed coke, M_s is the ratio between the mass of produced steam and the mass of consumed coke, M_s is the ratio between the mass of produced oil vapor and the mass of consumed oil, $\dot{m}_{gw} = -\dot{m}_{wg}$ and $\dot{m}_{go} = -\dot{m}_{og}$ are terms of evaporation for the water and oil, S_l is the coke deposition term, and S_c is the coke reaction rate term. The subscripts s, o, a, g, w represents steam, oil vapour, oxygen, gas and water, respectively.

Energy equation:

It was considered that there is thermal equilibrium among the phases then the energy equation can be written as:

$$\begin{aligned}
&\frac{\partial \varepsilon_g \langle Cp_g\rangle^g \langle \rho_g\rangle^g \langle T\rangle}{\partial t} + \frac{\partial \varepsilon_o \langle Cp_o\rangle^o \langle \rho_o\rangle^o \langle T\rangle}{\partial t} + \frac{\partial \varepsilon_w \langle Cp_w\rangle^w \langle \rho_w\rangle^w \langle T\rangle}{\partial t} \\
&+ \frac{\partial \varepsilon_c \langle Cp_c\rangle^c \langle \rho_c\rangle^c \langle T\rangle}{\partial t} + \frac{\partial \varepsilon_s \langle Cp_s\rangle^s \langle \rho_s\rangle^s \langle T\rangle}{\partial t} + \frac{\partial \varepsilon_o \langle \rho_o\rangle^o \langle \lambda_o\rangle}{\partial t} + \frac{\partial \varepsilon_w \langle \rho_w\rangle^w \langle \lambda_w\rangle}{\partial t} \\
&+ \frac{\partial \varepsilon_c \langle \rho_c\rangle^c \langle \lambda_c\rangle}{\partial t} + \frac{\partial \varepsilon_o \langle \rho_o\rangle^o \langle \mathrm{v_o}\rangle^o \langle \lambda_o\rangle}{\partial x} + \frac{\partial \varepsilon_w \langle \rho_w\rangle^w \langle \mathrm{v_w}\rangle^w \langle \lambda_w\rangle}{\partial x} \\
&+ \frac{\partial \varepsilon_g \langle Cp_g\rangle^g \langle \rho_g\rangle^g \langle \mathrm{v_g}\rangle^g \langle T\rangle}{\partial x} + \frac{\partial \varepsilon_o \langle Cp_o\rangle^o \langle \rho_o\rangle^o \langle \mathrm{v_o}\rangle^o \langle T\rangle}{\partial x} + \frac{\partial \varepsilon_w \langle Cp_w\rangle^w \langle \rho_w\rangle^w \langle \mathrm{v_w}\rangle^w \langle T\rangle}{\partial x} \\
&+ h' a' (\langle T\rangle - T_r) = \frac{\partial}{\partial x}\left[\left(K_g \varepsilon_g + K_o \varepsilon_o + K_w \varepsilon_w + K_c \varepsilon_c + K_s \varepsilon_s\right)\frac{\partial \langle T\rangle}{\partial x}\right]
\end{aligned} \tag{26}$$

where λ_w is the water heat of vaporization, λ_o is the latent heat associated with coke formation, λ_c is the heat of combustion, h' is the external heat loss coefficient, a' is the external heat loss area per unit of volume, T_r is the initial (ambient) temperature, and $\langle T\rangle \left(= \varepsilon_g \langle \mathrm{T}_g\rangle^g + \varepsilon_o \langle \mathrm{T}_o\rangle^o + \varepsilon_w \langle \mathrm{T}_w\rangle^w + \varepsilon_c \langle \mathrm{T}_c\rangle^c + \varepsilon_s \langle \mathrm{T}_s\rangle^s\right)$ is the space average temperature.

To simplify the nomenclature it is assumed that $\langle\psi\rangle = \psi$ and $\langle\psi_k\rangle^k = \psi_k$ where ψ is a property, and ψ_k is any function associated with the k-phase.

If Eqs. 19–25, are substituted into Eq. 26, the energy equation can be written as:

$$\alpha\frac{\partial^2 T}{\partial x^2} + \beta\frac{\partial T}{\partial x} - \gamma T + \delta = \frac{\partial T}{\partial t} \tag{27}$$

where

$$\alpha = \frac{k_{ef}}{\theta} \tag{28}$$

$$\theta = \{(1-\phi)Cp_s\rho_s + \phi[s_g\rho_g Cp_w f_s + s_g\rho_g Cp_a f_o + s_g\rho_g Cp_g(1-f_s-f_o) + s_w Cp_w\rho_w + s_o Cp_o\rho_o] + FCp_c\} \tag{29}$$

$$\beta = \frac{1}{\theta}\left[\left(\frac{k_g\rho_g}{\mu_g}(f_s Cp_w + f_o Cp_o + Cp_g(1-f_s-f_o)) + \frac{k_w\rho_w Cp_w}{\mu_w} + \frac{k_o\rho_o Cp_o}{\mu_o}\right)\frac{\partial p}{\partial x}\right] \tag{30}$$

$$\gamma = \frac{1}{\theta}\{[(Cp_w - Cp_g)M_s + Cp_g - Cp_c]S_c + [(Cp_c - Cp_g)M_c + Cp_g - Cp_o + (Cp_o - Cp_g)M_{vo}]S_l + h'a'\} \tag{31}$$

$$\delta = \frac{1}{\theta}[(\lambda_c - \lambda_w M_s)S_c - \lambda_w\dot{m}_{gw} - \lambda_o\dot{m}_{go} - (\lambda_o M_{vo} + \lambda_c M_c)S_l + h'a'T_r] \tag{32}$$

where $K_{ef}\left(= K_g\varepsilon_g + K_o\varepsilon_o + K_w\varepsilon_w + K_c\varepsilon_c + K_s\varepsilon_s\right)$ is the effective thermal conductivity.

7 Numerical Solution

For solving the Eqs. 19–25 and 27 a finite differences technique was used; an explicit scheme for the mass equations while a Crank–Nicholson scheme for the energy equation (for more details see the work of Cazarez-Candia and Vital-Ocampo 2010).

8 Results

Figure 3 shows the comparison between experimental temperature (Experiments 1 and 2, from Cazarez-Candia et al. 2010), and the results from the model. The front velocity and the temperature profiles obtained with the model are in agreement with experimental data. It can be also seen in the figure that due to the injected air,

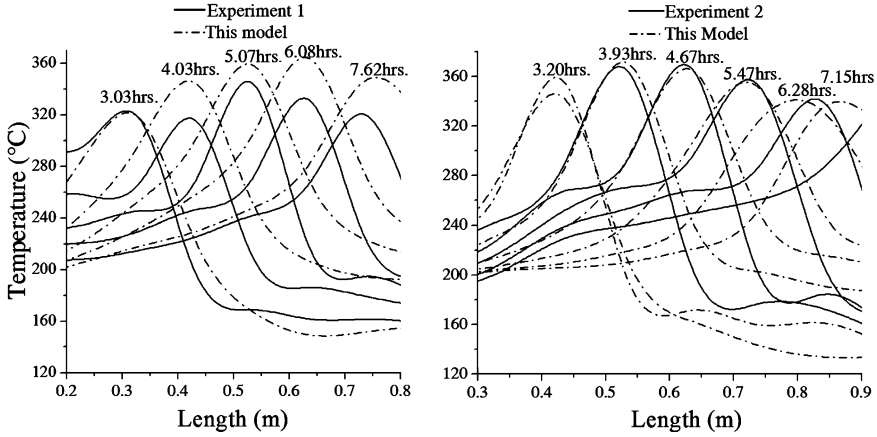

Fig. 3 Temperature profiles. Experiments 1and 2 vs. the present model

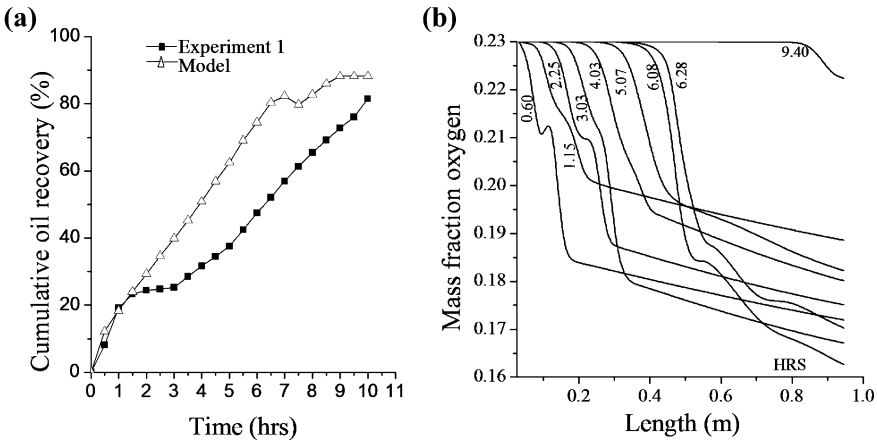

Fig. 4 **a** Comparison between experimental cumulative oil recovery and the results from the model, and **b** Mass fraction of oxygen for experiment 1

the temperature profiles grow until the combustion front temperature (maximum temperatures in the profiles) is attained, ahead of it temperature falls quickly (coke formation zone) and finally it remains almost constant. The maximum average error between Experiment 1 vs. model and Experiment 2 vs. model are 11% and 10%, respectively.

The accumulated oil recovery and the mass fraction of oxygen are shown in Fig. 4a and Fig. 4b, respectively. In Fig. 4a the total oil recovery from experiment 1 was 82% while the total oil recovery from the model was 88%. The differences are possibly due in experiment 1, to the fact that the fluids recuperation is done every 15 min and this is not considered in the model.

In Fig. 4b at the beginning, the oxygen concentration falls abruptly in the combustion zone. However, it does not disappear which indicates that the oxygen is not entirely consumed by the combustion reaction.

9 Conclusions

In this work a set of averaged mass, momentum and energy equations for a multiphase flow of gas, of two immiscible liquids (water and oil) and coke into a homogeneous, isotropic and rigid porous media was developed and written for an in situ combustion application.

The simulation of a combustion tube was done using the averaged mass, momentum and energy equations. It was found that: (1) predictions for temperature are in agreement with experimental data, the maximum average error found for the Experiment 1 was 11% while the Experiment 2 was 10%, (2) predictions for the accumulated oil recovery shown a difference of 6% respect to experimental data.

References

Cazarez-Candia O, Vital-Ocampo AG (2010) Average model for in situ combustion II: numerical solution. V congreso internacional de Métodos numéricos Del 3 al 5 de Octubre, Gto. Gto. México

Cazarez-Candia O, Cruz-Hernández J, Islas-Juárez R, Márquez RE (2010) Theoretical and experimental study of combustion tubes. Pet Sci Technol 28:1186–1196

Chu C (1964) The vaporization-condensation phenomenon in a linear heat wave. Soc Petrol Eng J 680:85–95

Duval F, Fichot F, Quintard M (2004) A local thermal non-equilibrium model for two-phase flow with phase change in porous media. Int J Heat Mass Transfer 47:613–639

Gottfried BS (1965) A mathematical model of thermal oil recovery in linear systems. SPE 1117, SPE production research symposium. Tulsa Okla. May 3–4:196–210

Gottfried BS, Mustafa K (1978) Computer simulation of thermal oil recovery processes. Soc Pet Eng J 7824:1–42

Lu C, Yortsos YC (2001) A pore-network model of in situ combustion in porous media. SPE 69705, SPE International thermal operations and heavy oil symposium. Margarita. Venezuela, March 12–14

Penberthy WL, Ramey HJ (1965) Design and operation of laboratory combustion tubes. SPE 1290, SPE Annual fall meeting. Denver Colo. Oct 3–6

Soria A, De Lasa HI (1991) Averaged transport equations for multiphase systems with interfacial effects. Chem Eng Sci 46(8):2093–2111

Verma VB, Reynolds AC, Thomas GW (1978) A theoretical investigation of forward combustion in a one-dimensional system. SPE 7526, SPE-AIME 53rd annual fall technical conference and exhibition. Houston, Oct 1–3

Vital-Ocampo AG, Cazarez-Candia O (2010) Average model for in situ combustion I: transport equations. V congreso internacional de métodos numéricos Del 3 al 5 de Octubre, Gto. Gto. México

Whitaker SA (1986) Flow in porous media II: the governing equations for immiscible, two-phase flow. Trans Porous Media 1:105–125

Migration and Decay of ^{226}Ra in a Saturated Porous Media

Eduardo de la Cruz, Roberto González, Jaime Klapp, Luis Carlos Longoria and Estela Mayoral

Abstract This work presents the mathematical formalism of a numerical model used for the simulation of ^{226}Ra migration and decay in saturated porous layers. The simulation methodology employs Darcy's law for calculating the velocity field; it is subsequently used as input data for solving the transport equation. The latter includes advection, diffusion and hydrodynamic dispersion processes. The interactions with the medium are represented by a retention coefficient of the solid matrix, and a term associated to the radioactive decay. For the computational system we consider a vertical cross section composed of five saturated porous stratums. The hydrodynamic system of equations is solved by the finite element numerical technique.

E. de la Cruz (✉) · R. González · J. Klapp · L. C. Longoria · E. Mayoral
Instituto Nacional de Investigaciones Nucleares, Apartado Postal 18-1027, 11801 Mexico city, D.F., Mexico
e-mail: eduardo.delacruz@inin.gob.mx

R. González
e-mail: rgonzalez470@yahoo.com.mx

E. de la Cruz
Instituto Tecnológico de Toluca, Av. Tecnológico S/N Ex-Rancho La Virgen, 52140 Metepec, Mexico

R. González
Universidad Autónoma del Estado de México, El Cerrillo Piedras Blancas, 50200 Mexico city, Estado de Mexico, Mexico

J. Klapp et al. (eds.), *Experimental and Theoretical Advances in Fluid Dynamics*, Environmental Science and Engineering, DOI: 10.1007/978-3-642-17958-7_29,

1 Introduction

The aim of this work is to study soil migration of the ^{226}Ra radionuclide, a common radionuclide originated by the radioactive disintegration of ^{238}U present in uranium mine wastes (Rojas 1996). Soil mobility studies of radioactive contaminants dragged by the underground water flow to deep underground areas, is of central importance to assess pollution and irradiation in areas of human interest, aquifers in particular.

The main mechanism by which radionuclides migrate is by being dissolved in groundwater. The water chemistry (salinity, pH, complexing agents) is the main parameter that controls the aqueous speciation of the radionuclide and its mobility. It is well know that water moves across a porous saturated media driven by the hydraulic gradient; we compute the underground flow using the Darcy's law (Rives 1996). The main mechanisms involved in the solute transport are: (a) advection, (b) molecular diffusion, and (c) mechanical dispersion (Bear 1979); additionally, for solutes who suffer degradation and/or radioactive decay processes, it is necessary to incorporate these processes in the transport equation. In a radioactive decay chain the initial radionuclide, called father, decays into a daughter radionuclide that then becomes the father for a subsequent decay. This process continues until the daughter is stable and the chain ends. The desintegration of a father radionuclide is independent of the instability of the daughter and its behavior is given by the exponential law of radioactive disintegration. We can specify the decay probability per unit time, which is normally expressed in terms of the half-life timescale. Additionally, a valid approximation could be done if we consider the global disintegration from ^{226}Ra (radioactive) to ^{206}Pb (stable).

The radionuclide transport depends upon the type of geologic formation and on the existing physical–chemical condition, and this makes the modeling of this kind of systems quite complicated. This work presents a numerical simulation of contaminant migration and decay through a porous saturated stratum, for which we consider hydrogeological conditions similar to those existing in Northern Mexico's soils (Rojas 1996). For calculating the solute diffusion through the geological heterogeneous medium, we use the COMSOL numerical software.

2 Methodology

The soil is a heterogeneous system formed by a solid matrix or skeleton composed of an assembly of mineral grains separated and surrounded by a complex system of voids, pores or interstices, which may be filled with water, gas or organic matter. Liquid with a certain concentration of pollutant solute flows through the system. We assume a macroscopic approach which avoids a detailed

physical–chemical description of the system, so that we introduce properties that depend upon the morphology and constitution of the medium. These "bulk" properties are inserted into the Darcy and other flow equations giving an excellent estimate of the phenomenon over short and long space dimensions. The groundwater flow and solute transport equations are coupled to the Darcy's diffusion formalism that assumes the diffusion velocity is $\mathbf{V} = -K\nabla H$, where K is the permeability and H the hydraulic head. The fluid flow velocity $\mathbf{V}$ from an infinitesimal surface corresponds to both the solid and the pore spaces. We first calculate the Darcy's velocity field $\mathbf{V} = (u, w)$, where u and w are the velocities in the x and z directions, respectively. Then, assuming that the pollutant follows the previously obtained velocity field, we solve the pollutant transport equation. The diffusion simulation of the pollutant dissolved in water, flowing through the underground implies at least two types of physical analysis, and for our case we first obtain a cuasi-static solution for the hydrogeological system; then the velocity field in particular is used to determine the behavior of the fluid through the stratum.

2.1 Groundwater Flow: Darcy's Law

According to Darcy, the fluid discharge rate through a porous material is proportional to the hydraulic load loss. Based on the mass conservation principle (Fetter 1994) we can express the local balance equation as

$$\frac{\partial(\varphi\rho)}{\partial t} + \nabla \cdot (\rho \mathbf{V}) = g(x,t) + \tau(x,t), \tag{1}$$

where $\mathbf{V}$ is the Darcy's velocity, $g(x, t)$ is the amount of fluid created or destroyed inside the domain, $\tau(x, t)$ is the amount of fluid created or destroyed in the boundary of the domain, and both $\rho = \rho\,(p)$ (the density of the fluid) and $\phi = \phi\,(p)$ (the porosity of the medium) depends on the pressure p, so we can write

$$\frac{\partial(\phi\rho)}{\partial t} = \phi\frac{d\rho}{dp}\frac{\partial p}{\partial t} + \rho\frac{\mathrm{d}\phi}{\mathrm{dp}}\frac{\partial p}{\partial t}. \tag{2}$$

Defining $\alpha = d\phi/dp$ and $\beta = (1/\rho)(d\rho/dp)$ we arrive to the expression

$$\frac{\partial(\phi\rho)}{\partial t} = \rho(\alpha + \beta\phi)\frac{\partial p}{\partial t}. \tag{3}$$

Substituting the specific storage coefficient $S_s = \rho g(\alpha + \beta\phi)$ into (3), dividing by ρ and developing the divergence term we obtain that

$$S_s\frac{\partial H}{\partial t} + \nabla \cdot \mathbf{V} + \mathbf{V} \cdot \nabla \ln\rho = Q_s, \tag{4}$$

where we have defined $Q_s = (g(x, t) + \tau(x, t))/\rho$. Considering that $|\nabla \ln\rho| << 1$, we can ignore this term and finally write

$$S_s \frac{\partial H}{\partial t} + \nabla \cdot \mathbf{V} = Q_s. \tag{5}$$

If we consider the stationary case, $S_s \partial H/\partial t = 0$ and inserting the Darcy's velocity we finally obtain that

$$\nabla \cdot (-K \nabla H) = Q_s. \tag{6}$$

2.2 Solute Transport

The local balance equation for the solute concentration c is given by

$$\frac{\partial \varphi c}{\partial t} + \nabla \cdot (\varphi c \mathbf{V}) = g + \nabla \cdot \tau, \tag{7}$$

where $\mathbf{V} = -K\nabla H$ is Darcy's velocity, φ is the porosity and in our study case $g(\boldsymbol{x}, t) = -\lambda(\mathbf{x}, t)c(\mathbf{x}, t)$ is given by the presence of radioactive decay for the solute, where λ is the semi-disintegration constant. The dispersion is given by $\tau(\mathbf{x}, t) = \mathbf{D}\cdot\nabla c$. The components for the dispersion hydrodynamic tensor are given by

$$D_{ij} = vD_T\delta_{ij} + (D_L - D_T)\frac{v_i v_j}{v} + D_d\delta_{ij}, \tag{8}$$

where D_{ii} are the components of the dispersion tensor based on Darcy's velocity, D_T is the transversal dispersivity coefficient and D_L is the longitudinal dispersivity coefficient, d_{ij} are delta of Kronecker, is "1" for $i = j$ and "0" when $i \neq j$, $v = (v_i^2 + v_j^2)^{1/2}$ is the magnitude of the Darcy's velocity vector, and D_d represents the effective molecular diffusion in a saturated porous media. Substituting this expression for the dispersion into Eq. 7 we finally obtain that

$$\frac{\partial c}{\partial t} = \nabla \cdot (\mathbf{D}\nabla c) - \mathbf{V} \cdot \nabla c - \lambda c. \tag{9}$$

The first right hand side term originates from the molecular diffusion and hydrodynamic scattering considered together as a hydrodynamic dispersion. The second term is the transport due to the "drag" of pollutant particles by the groundwater flow because of the hydraulic gradient, and it is driven by Darcy's law. Finally, the third term is due to the radioactive decay expressed by $\partial c/\partial t = -\lambda c$, where λ is the ^{226}Ra decay constant (equal to the reciprocal of the ^{226}Ra mean decay lifetime).

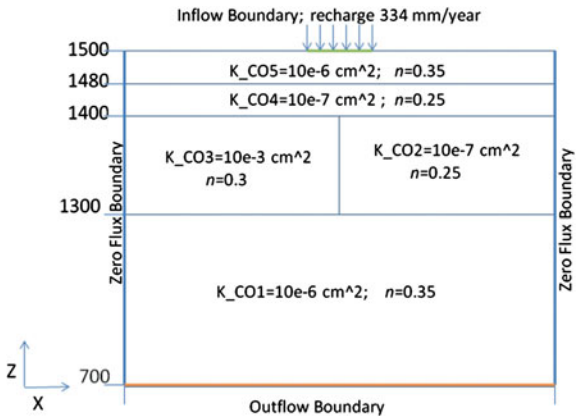

Fig. 1 The five layers computational system. The permeability coefficient of each layer is denoted by the constant K and the porosity by *n*

3 The Input Model

The system configuration is shown in Fig. 1. It is constituted by five layers with different lithology and hydrological properties originated by the geological formation characteristic of the region chosen.

Each layer has different composition and is characterized by a specific porosity in the range 0.25–0.35. The molecular diffusion coefficient in each stratum is 1.34×10^{-9} m^2/s and the transverse and longitudinal dispersivity are 2 and 5 m respectively. The studied system has 500 m length in the x-direction and 800 m depth in the z-direction.

The boundary zero-flow Neumann condition is imposed at the left and right boundaries along the z-axis. The vertical borders are located at $x = 100$ and 600 m, respectively, and satisfy the condition $\mathbf{n} \cdot (K\nabla H) = 0$, where $\mathbf{n}$ is a unitary vector normal to the boundary. This condition implies that at the boundary, the velocity is parallel to the z-axis and that the x-component of the velocity $V_x = 0$, i.e. there is no fluid flow across the left and right boundaries.

In the top boundary located at $z = 1500$ m there is an inflow water flow $R = \mathbf{n}\cdot(K\nabla H)$ with a recharge rate of 334 mm/year, which is a characteristic pluvial precipitation in the region. In the bottom boundary at $z = 700$ m, we have imposed an outflow boundary condition, assuming that the time derivatives of the variables that characterize the fluid are zero at the boundary.

For the pollutant concentration transport, the initial and boundary conditions are given by the Dirichlet condition $c(x, 1500, t) = 0$ in the upper border, except in the segment $300 < x < 400$, where the solute initial concentration is $c_0 = -\mathbf{n}\cdot(-\phi D_L\nabla c + \mathbf{V}c)$.

The Dirichlet condition at the right and left boundaries is $c(100, z, t) = 0$ and $c(600, z, t) = 0$, respectively. The Neumann zero flow condition is $-\mathbf{n} \cdot (-\theta s D_L \nabla c) = 0$.

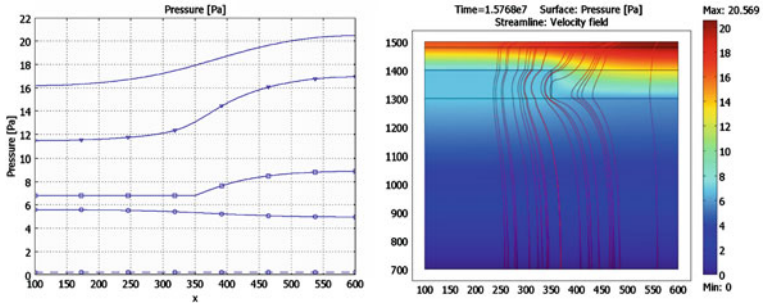

Fig. 2 *Left side*: pressure along the x-direction for the regions CO1 (*circles*), CO2 and CO3 (*squares*), CO4 (*triangles*) and CO5 (*top line*). *Right side*: pressure field and velocity streamlines in the system at time 0.5256 years

Finally, the initial condition indicating that the subsoil on the site is free of pollutants at the beginning of the simulation is $c(x, z, 0) = 0$.

4 Results and Discussion

In the simulation model we assume that ^{226}Ra enters the system at a constant rate from the uppermost superficial layer during the first 50 years, and then the source is removed. The ^{226}Ra radioactive decay constant is $\lambda = 1.4653 \times 10^{-11}$ 1/s.

In Fig. 2 we present the pressure field in each layer at time 0.5256 years which is near the start of the calculation. We observed that the pressure is higher on the right side of each region except for layer CO1, which has a higher pressure in its left; this is because the fluid goes faster in layers with higher permeability causing an accumulation of the fluid and its consequent pressure increase in the upper left part of layer CO1. At the level $z = 1340$ m there is an abrupt pressure change in the horizontal direction, for the region $100 < x < 350$ the pressure is 6–8 Pa, while for $350 < x < 600$ it is higher. This is due to the subdivision of stratum two between layers CO2 and CO3 which have a very different permeability that differ by a factor of 10^4, Fig. 1. The shape of the velocity streamlines is given by the particular pressure distribution. The ^{226}Ra distribution concentration is shown in Fig. 3, which is consistent with the estimated flow field. The main transport direction is in the vertical direction except for layers CO3 and CO2 that as we have already described is in the horizontal direction. The time evolution of the ^{226}Ra concentration in the different substrates is shown in Fig. 4. For early times the ^{226}Ra concentration is higher in the top layer CO5, but as the simulation progresses the ^{226}Ra moves to the lower substrates. The highest ^{226}Ra concentration is reached in each layer after a time of 63, 138, 634 and 1100 years, for layers CO5, CO4, CO3 and 2, and C01, respectively.

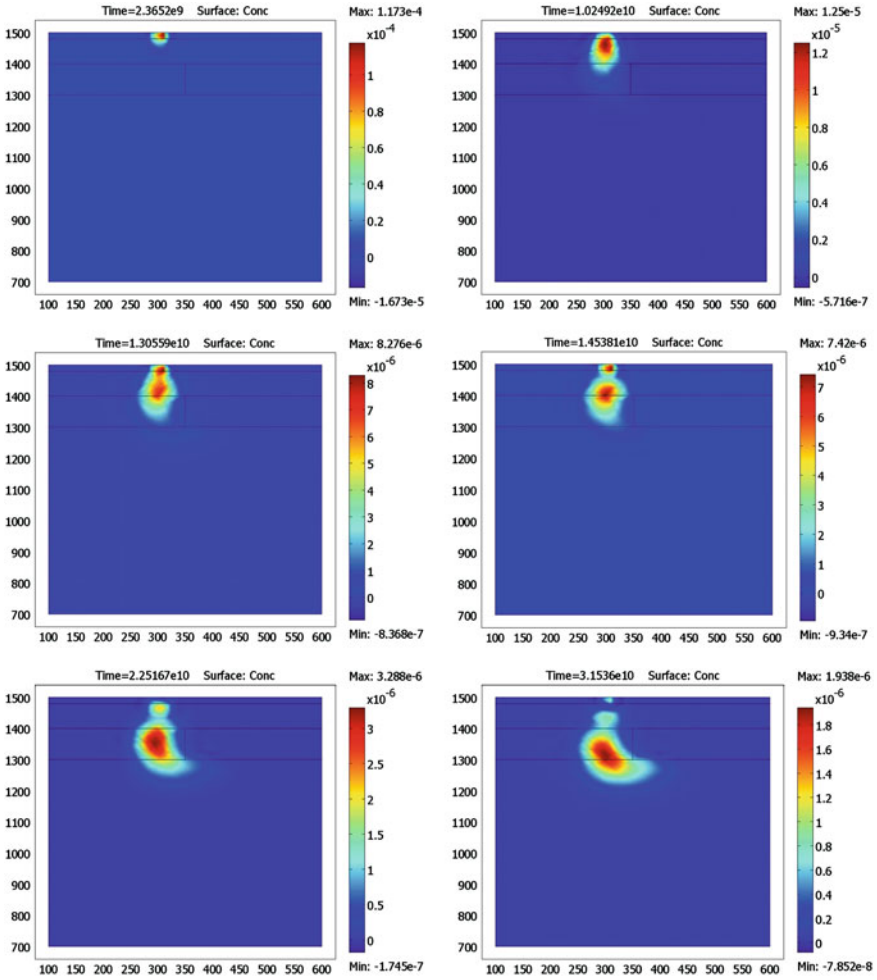

Fig. 3 Time evolution of the ^{226}Ra concentration plume

5 Conclusions

The simulation presented in this work is aimed to study the transport and decay of ^{226}Ra in a soil of the type found in the North of Mexico. The results of this investigation allow a better understanding of the mechanisms involved in underground contaminant migration. We estimated the time required by the contaminant to reach the bottom of the lower stratum, which was found to be about one thousand years. We identified that the particular flow obtained in our numerical experiment is due to the physical and chemical properties of the soil layers, the pressure distribution in the system and the interaction of the contaminant with the

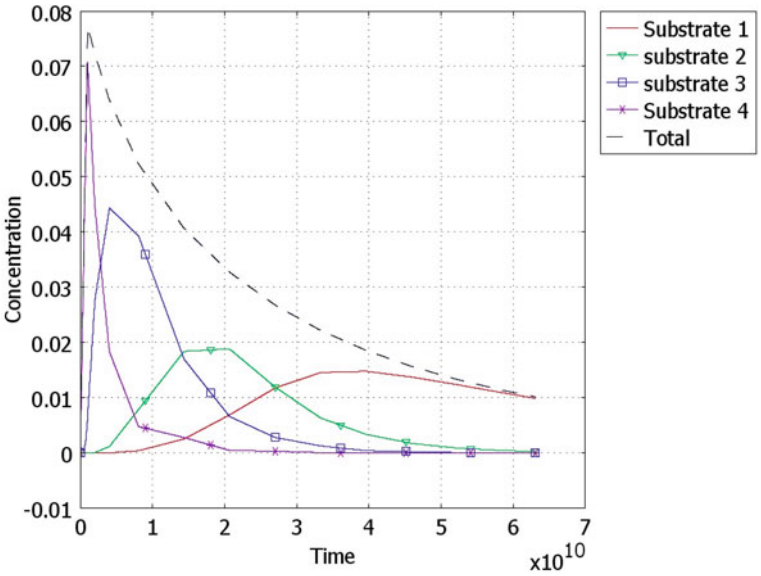

Fig. 4 Concentration profiles of ^{226}Ra in each substrate given in arbitrary unit

medium. The simulation of this type of phenomena will allow the adoption of preventive soil protection measures and decision-making support for mitigation or environmental impact risk remediation actions.

References

Bear J (1979) Dynamics of fluids in porous media. Dover, New York

Fetter CW (1994) Applied hydrogeology. Prentice Hall, New Jersey

Rives DE (1996) Manual del usuario del modelo de dispersión de radionúclidos en acuíferos freáticos. Comisión Regulatoria Nuclear

Rojas VPM (1996) Un enfoque biológico sobre la migración del ^{226}Ra en los estratos someros subyacentes en el depósito de estériles en Peña Blanca Chihuahua. Tesis de Licenciatura, FES-Zaragoza

Dispersion and Sorption of Arsenic in a Biofilter with a not Living Biomass (*Eicchornia crassipes*): Comparison of Experimental and Numerical Results

Carlos Enrique Alvarado-Rodríguez, Ricardo Duarte-Pérez, Jaime Klapp-Escribano, Elizabeth Teresita Romero-Guzmán, Zayre Ivonne González-Acevedo and María de Jesus Marín Allende

Abstract Experiments in natural porous media such as *Eicchornia crassipes* biomass for determining the sorption of arsenic are compared with numerical simulations done with the COMSOL Multiphysics code. The close agreement between the experimental and numerical results suggest that the theoretical model of hydrodynamic dispersion can be used to model the transport of arsenic in unsaturated porous media composed of *Eichhornia crassipes* biomass. The aim of this work was to find the best fitting between the experimental breakthrough curve and the simulated curve, during the arsenic sorption through the biomass.

1 Introduction

Dispersion plays a critical role in numerous processes and practical applications, including contaminant transport in groundwater, filtration, etc. Hydrodynamic dispersion in a porous medium occurs as a consequence of two different processes:

C. E. Alvarado-Rodríguez (✉) · R. Duarte-Pérez · J. Klapp-Escribano · E. T. Romero-Guzmán · Z. I. González-Acevedo
Instituto Nacional de Investigaciones Nucleares, Carretera México-Toluca s/n, La Marquesa, 52750 Ocoyoacac, Estado de México, Mexico
e-mail: q_l_o@hotmail.com

C. E. Alvarado-Rodríguez
Campus Guanajuato, División de Ciencias Naturales y Exactas, Universidad de Guanajuato, Noria Alta s/n, Guanajuato, Gto, Mexico

María de Jesus Marín Allende
Universidad Autónoma del Estado de México, Paseo Tollocan esq, Paseo Colon, Mexico

J. Klapp et al. (eds.), *Experimental and Theoretical Advances in Fluid Dynamics*, Environmental Science and Engineering, DOI: 10.1007/978-3-642-17958-7_30,

(1) molecular diffusion, which is caused by the random molecular motion of solute molecules, and (2) mechanical dispersion, which is caused by non-uniform velocities and the flow path distribution. Both processes cannot be separated in a flow regime (Nützman et al. 2002; Gaganis et al. 2005). The biosorption of the metalloid arsenic by *Eichhornia crassipes* biomass was simulated using experimental data. The aim of this work is to evaluate the behavior of the arsenic sorption in natural porous media such as *Eicchornia crassipes* biomass through the experimental and simulated breakthrough curves.

2 Experimental

The working model consists of a cylindrical container in three dimensions (3D), using porous biomass of *Eicchornia crassipes* as fixed bed column, and 0.1 M arsenic solution as eluents for the sorption studies. The simulation is performed assuming the biomass is a porous and permeable material. The speed of the water flow into the cylindrical container was obtained by solving the Navier Stokes and continuity equations. The speed of the porous media was obtained by solving the Brinkman and continuity equations. The dispersion, convection and sorption on biomass were obtained by solving the transport equation. The equations were solved by the finite element method. The COMSOL Multiphysics postprocessing was used to analyze the simulation results. The analysis is performed by the generation of images of the process and its animation.

2.1 Equations

The flow in the interstitial access from the biomass is calculated by solving the Navier Stokes and continuity equations which are written in the form:

$$\rho \frac{Dv}{Dt} = -\nabla p + \mu \nabla^2 \boldsymbol{v} + \rho \mathbf{g}, \tag{1}$$

$$\frac{\partial \rho}{\partial t} = -(\nabla \cdot \rho \boldsymbol{v}), \tag{2}$$

Where ρ in the density [M/L^3], v is the velocity [L/t], t is the time [t], p is the pressure [M/Lt^2], μ is the viscosity [M/Lt] and $\mathbf{g}$ is the gravity [L/t^2]. The equation used for the free flow in this simulation is obtained from Eq. 1, which is written as follows:

$$\left(-\nabla \cdot \mu(\nabla \boldsymbol{v} + (\nabla \boldsymbol{v})^T)\right) + \rho \boldsymbol{v} \cdot \nabla \boldsymbol{v} + \nabla p = 0, \tag{3}$$

where the density is considered constant and for the steady state equation the time dependent terms are eliminated (Bird et al. 2003). For the flow through the biomass (porous system), the Brinkman and the modified continuity equations for the porous systems are

$$-\nabla p - \frac{\mu}{k}\boldsymbol{v} + \mu\nabla^2\boldsymbol{v} + \rho\mathbf{g} = 0, \tag{4}$$

$$\varepsilon\frac{\partial p}{\partial t} = -(\nabla\cdot\rho\boldsymbol{v}), \tag{5}$$

Where ρ is the density [M/L^3], v is the velocity [L/t], t is the time [t], p is the pressure [M/Lt^2], μ is the viscosity [M/Lt], $\mathbf{g}$ is the gravity [L/t^2], k is the permeability [L/t], ε is the porosity (the ratio between porous volume and total container volume). The equation used for the porous media flow in this simulation is obtained from Eq. 4, which is written as follows:

$$\left(-\nabla\cdot\frac{\mu}{\varepsilon}(\nabla\boldsymbol{v} + (\nabla\boldsymbol{v})^T)\right) - \left(\frac{\mu}{k}\boldsymbol{v} + \nabla p\right) = 0, \tag{6}$$

where the density is considered constant and for steady state equation the time dependent terms has been eliminated. The steady state Eqs. 2, 3, 5 and 6 are solved according with the experimental methodology. Arsenic transport and its sorption through the biomass are calculated by solving the transport equations. The Freundlich isotherm solution is written in the following form:

$$\varepsilon\frac{\partial c}{\partial t} + \rho_b\frac{\partial c_p}{\partial c}\frac{\partial c}{\partial t} + \nabla\cdot[-\varepsilon D_L\nabla c + \boldsymbol{v}c] = \mathrm{R_L} + \mathrm{R_P} + \mathrm{S_c}, \tag{7}$$

$$c_p = K_F c^N,\ \frac{\partial c_p}{\partial c} = NK_F c^{N-1}, \tag{8}$$

Where ε is the porosity, c is the solute concentration [M/L^3], t is the time [t], ρ_b is the density of the porous medium [M/L^3], c_p is the concentration of the solute sorbed in the biomass (the mass amount of solute sorbed per unit of biomass), v is the velocity [L/t], D_L is the hydrodynamic dispersion tensor, K_F and N are constants of Freunlich isotherms (COMSOL 2008). The equation used for flow in the porous medium in this simulation is obtained from Eq. 7 (COMSOL 2008; Fetter 1999), which is written as follows:

$$\varepsilon\frac{\partial c}{\partial t} + \rho_b\frac{\partial c_p}{\partial c}\frac{\partial c}{\partial t} + \nabla\cdot[-\varepsilon D_L\nabla c + \boldsymbol{v}c] = 0, \tag{9}$$

where the reaction terms are removed if there are no chemical reactions.

2.2 Constants

The values of the constants were obtained from the physicochemical characterization of the biomass and the interaction between the arsenic as a solute-biomass to determine the sorption rate, see Table 1.

Table 1 Values of the constants obtained by experimental procedures (Marín 2010)

Constants		Value
ρ_s	Biomass density	570 kg/m^3
ε	Porosity	15%
k_s	Permeability	1.4e–3 m/s
K_F	Freundlich constant	1.1007 mg/g
N	Freundlich isotherms exponent	0.7578
$\alpha 1$	Longitudinal dispersivity	0.05 m
$\alpha 2$	x Transversal dispersivity	0.005 m
$\alpha 3$	y Transversal dispersivity	0.005 m
C_{in}	Feed concentration	1e–4 kg/m^3
V_{max}	Feed velocity	1.909 cm/min

2.3 Problem Solution

The solution of the model was obtained with the COMSOL Multiphysics software version 3.5a. This software uses the finite element method for the discretization of the partial differential equations. The mesh elements are prisms and we use for the Navier Stokes equation a total of 161,764 elements with 711,345 degrees of freedom and for the transport equation 227,123 elements.

3 The Input Model

The geometry is based on the characteristics of the system used in the laboratory, in which the biomass is deposited in a cylindrical container with the dimensions indicated in Fig. 1a. The system is divided into three zones, see Fig. 1b. Zone 1 is the feed injection zone, in this area there is no biomass and the feed flow is constant. In zone 2 the biomass is present and this is where the interaction between the biomass and the arsenic solution occurs; it is considered a saturated porous system. In zone 3 there is no biomass; it is here where the arsenic concentration value in the eluates is measured to determine the concentrations of arsenic sorbed in the biomass.

3.1 Initial and Boundary Conditions

The initial and boundary conditions are the following: for $t = 0$, $c = 0$ and $c_p = 0$ and the boundary conditions are shown in Fig. 2, where $r = (x^2 + y^2 + z^2)^{1/2}$, R is the radius of the cylinder (see Fig. 1), v is the velocity, n is a unit vector normal to the plane, N is the total flux of As, V_{max} is the feed velocity (see Table 1), U_{chns} is the velocity calculated by the Navier Stokes equation, C_{in} is the initial

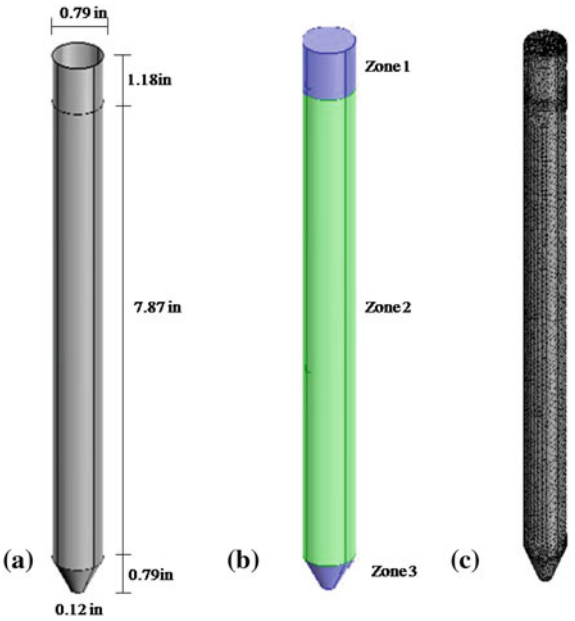

Fig. 1 Geometry used for the simulation, **a** System dimensions, **b** zone subdomains, and **c** computational mesh

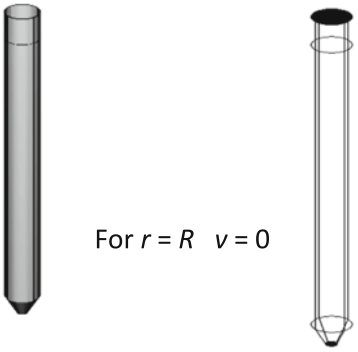

For $r = R$ $v = 0$

For $r = R$ $\boldsymbol{n}N = 0$

Upper limit

For $z = 0.25$ mt

$$v = V\max * \left(1 - \frac{r^{30}}{R^{30}}\right)$$

$\boldsymbol{n}N = U\_chns * C\_in$

Lower limit

For $z = 0$

$p = 0$

$\boldsymbol{n}N = -U\_chns * c$

Fig. 2 Boundary conditions for the arsenic sorption simulation

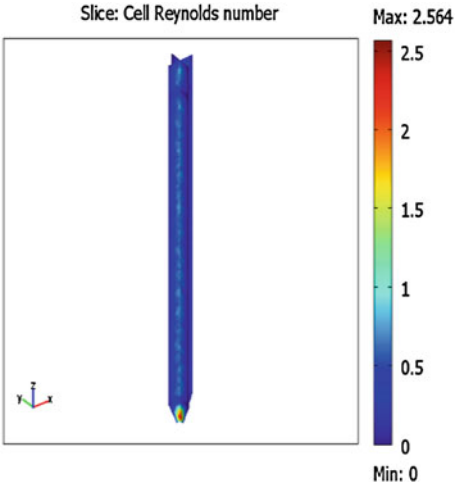

Fig. 3 Reynolds numbers

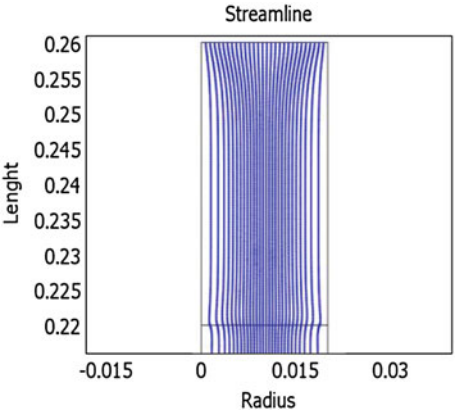

Fig. 4 Flow lines simulation on column

concentration of As (see Table 1), p is the pressure, c is the arsenic concentration in the solution, c_p is the solute concentration sorbed in the biomass, z is the coordinate in the xyz plane and t is the time.

4 Results and Discussion

The Reynolds number values are shown in Fig. 3, which were obtained by solving the fluid flow equations. The values indicate that the flow is in the laminar regime as also reported by Basak (1977). In Fig. 4 we present the velocity field at the entrance of the system and in the region occupied by the biomass represented as a porous system. The velocity field deviates when the arsenic solution gets in contact with the biomass because the porosity change and the permeability are modified.

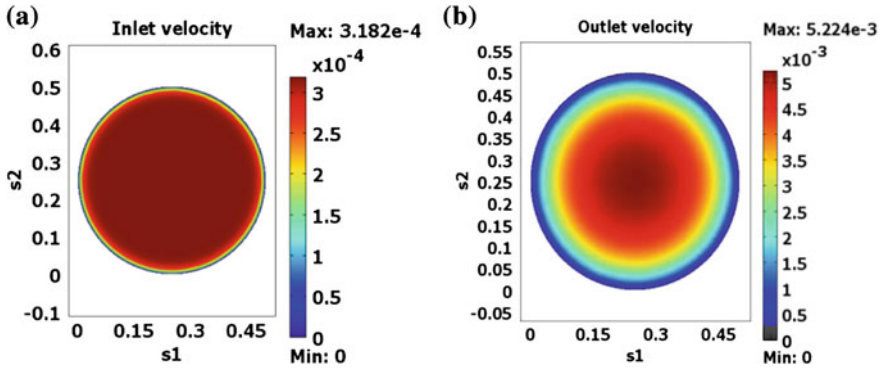

Fig. 5 **a** Input velocity field, **b** output velocity field

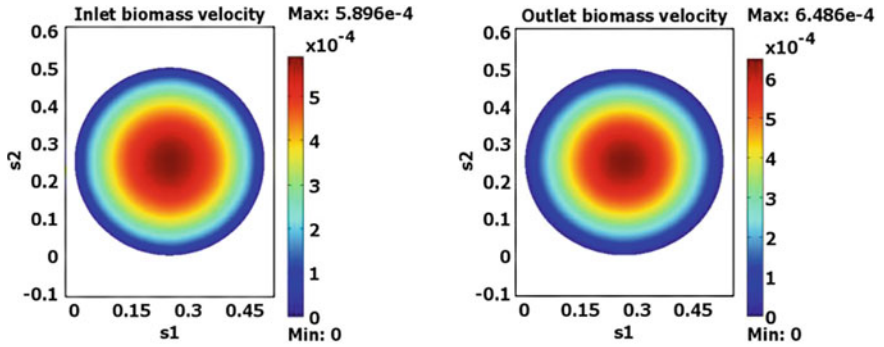

Fig. 6 Arsenic solution input and output velocities in biomass

The input and output speed are shown in Fig. 5. The results indicate that the velocity is greater in the center and zero on the walls. In the first case, the velocity field is uniform; the arsenic solution is injected at a constant rate around the entire surface.

Figure 5b shows speed values larger than the maximum speed entry value due to the decrease in the cross-sectional area, as well as a more uniform profile. The multiple core measurements at the outlet column allowed an estimation of the velocity fluctuations. Due to different steady state infiltration rates, the water content distribution in the biomass column varied with depth. In the central region the velocity is greater than near the walls, this behavior is correlated with Fig. 4 that indicates that in the core the velocity is greater and so the arsenic sorption is probably lower due to the lower arsenic-biomass interaction time. On the other hand, on the walls, the biomass has more interaction time with the solute, because the velocity of interaction is lower or the interstitial water is saturating the pores.

The input and output velocity field of the porous biomass are shown in Fig. 6a and b, respectively. These results indicate that the pores of the biomass were

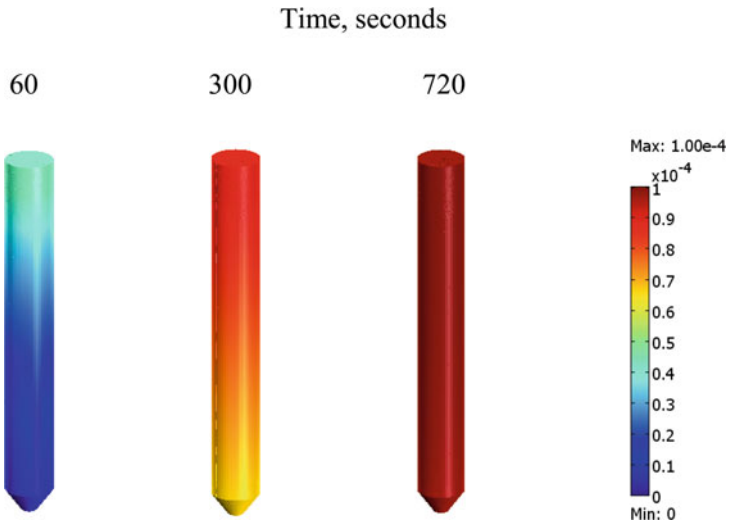

Fig. 7 Transport of the arsenic solution in biomass, through the time, (kg/m^3)

saturated by the arsenic solution, and then the fluid velocity diminishes through the biomass column, causing the outlet velocity to decrease. Thus, higher values are obtained at the fluid outlet due of the pressure difference between the input and output of the porous medium.

Solving the transport equation using the velocity field obtained previously, the arsenic transport system and its sorption onto *Eichhornia crassipes* biomass was simulated. Figure 7 shows the biomass saturation time evolution during the arsenic solution transport through the system at 60, 300 and 720 s. In the same Fig. 7 it was observed that the arsenic concentration is not present at the bottom of the column, but it increases when it is transported through the *Eichhornia crassipes* biomass. At 300 s the arsenic transport is observed, the arsenic is sorbed on the biomass, in the upper of the biomass column; the system is getting saturated depending upon arsenic transport. The arsenic concentration in the solution increases because the biomass is reaching its arsenic saturation or the arsenic concentration in the solution decreases through the biomass because it is sorbed by the biomass. Finally, at 720 s the biomass reaches its arsenic saturation, the concentration is constant; the biomass is saturated and does not sorb arsenic from solution.

Various mathematical models have been developed to predict the dynamic behavior of sorption column studies (Volesky 2003; Naja and Volesky 2006). In this case, the experimental and simulated breakthrough curves for arsenic sorption are shown in Fig. 8. Comparison between experimental and simulated breakthrough curves showed good agreement with predicted software COMSOL values, which indicates that the chosen models are suitable for explaining arsenic sorption during the interaction between the biomass and the arsenic solution.

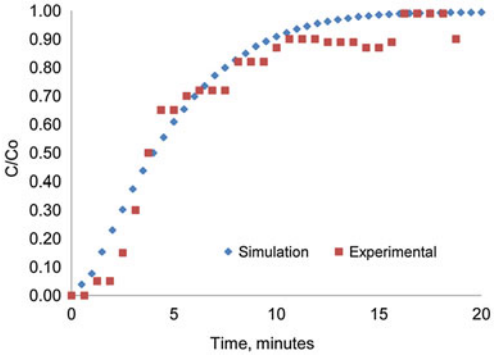

Fig. 8 Experimental and predicted breakthrough curves of As(V) sorption in a fixed column of biomass (*Eicchornia crassipes*) in vertical flux

Table 2 Transport of the arsenic solution through the biomass (kg/m^3)

Aquatic plant	Process	Procedure	Breakthrough point time, minutes	Saturation point time, minutes
Eichhornia crassipes	Sorption	Experimental	2.2	12
		Simulated	1.2	12

According to breakthrough curves obtained with *Eichhornia crassipes* biomass, the point of rupture and saturation in the vertical flow is reached at 2.2 and 1.2 for experimental and simulated system and 12 min. This indicates a greater capacity of sorption in vertical flow and that the COMSOL simulation is able to represent the dynamic conditions observed in a biomass-column test Table 2.

5 Conclusions

Arsenic concentration measurements, as obtained from experiments during the solute-biomass interaction, were used for the simulation of the hydrodynamic dispersion. The method gives an accurate estimate of the breakthrough curve using the experimental data. At 720 s the biomass was arsenic satured.

References

Basak P (1977) Non-darcy flow and its implications to seepage problems. J Irrigation and Drainage Div Am Soc of Civil Eng 103:459

Bird RB, Stewart WE, Lightfoot EN (2003) Fenómenos de transporte. Editor reverte 3–11(3–5): 4–29

COMSOL, Earth Science Module User's Guide, ©1998–2008 by COMSOL AB

Fetter CW (1999) Contaminant hydrogeology. Prentice Hall, Englewood Cliffs, NJ

Gaganis P, Skouras ED, Theodoropoulou MA, Tsakiroglou CD, Burganos VN (2005) On the evaluation of dispersion coefficients from visualization experiments in artificial porous media. J Hydrol 307:79–91

Marín Allende MJ (2010) Remoción de Arsénico en solución empleando biomasas no vivas de malezas acuáticas, Tesis, Universidad Autónoma del Estado de México

Nützmann G, Maciejewski S, Joswig K (2002) Estimation of water saturation dependence of dispersion in unsaturated porous media: experiments and modelling analysis. Adv Water Res 25:565–576

Naja G, Volesky B (2006) Behavior of the mass transfer zone in a biosorption column. Environ Sci Technol 40:3996–4003

Volesky B (2003) Biosorption: application aspects—process simulation tools. Hydrometallurgy 71:179–190

Part IV
Convection, Diffusion and Heat Transfer

Inverse Heat Transfer Using Particle Swarm Optimization Methods for Heat Source Estimation

Obed Cortés-Aburto, Rafael Rojas-Rodríguez and Rita Marina Aceves-Pérez

Abstract This work uses Particle Swarm Optimization (PSO) for estimating the heat generation function of a Guarded Hot-Plate Apparatus (GHPA). The device is used for the determination of thermal conductivity of insulating materials. The problem is one-dimensional in cylindrical coordinates. The geometry includes a disc (Hot-Plate) and an annulus (Guard). The heat generation function is estimated from a one to five parameters polynomial series. The capability of the method for recovering the analytical function is tested. Results are good enough for this kind of problem.

1 Introduction

Heat transfer inverse problems have no fully specified conditions, and rely on temperature and/or heat flux measurements to estimate the unknown quantities appearing in the mathematical formulation of the physical problem (Alifanov 1994; Ozisik and Orlande 2000).

The use of inverse analysis techniques is a recent research paradigm. The results obtained from numerical simulations and from experiments are not simply compared a posteriori, but a close synergism exists between experimental and theoretical researchers during the course of the study, in order to obtain the maximum of information regarding the physical problem under picture (Colaco et al. 2004). Therefore, in the recent past, inverse problems have evolved from a specific theoretical research topic to an important practical tool of engineering analysis.

O. Cortés-Aburto (✉) · R. Rojas-Rodríguez · R. M. Aceves-Pérez
Departamento de Ingeniería Mecatrónica, Universidad Politécnica de Puebla, Tercer Carril del Ejido Serrano S/N, San Mateo Cuanalá, 72640 Juan C. Bonilla, Puebla, México
e-mail: obedca@uppuebla.edu.mx

J. Klapp et al. (eds.), *Experimental and Theoretical Advances in Fluid Dynamics*, Environmental Science and Engineering, DOI: 10.1007/978-3-642-17958-7_31,

Inverse problems can be solved either using a parameter estimation approach or a function estimation approach. Inverse problems are mathematically classified as ill-posed, whereas standard heat transfer problems are well-posed. A successful solution of an inverse problem generally involves its reformulation as an approximate well-posed problem, and makes use of some kind of regularization (stabilization) technique.

In this paper, Particle Swarm Optimization as a technique to solve inverse heat transfer problems is tested. The test problem involves the recovery of the heat generation function in one-dimensional cylindrical coordinates. Two geometries are used, a disc and an annulus. Results exhibit a good agreement with experiments.

2 Direct Problem

Measured temperatures are taken into account from a device for determining thermal conductivity of insulating materials for buildings which are generally manufactured in Mexico. This device is called Guarded Hot-Plate Apparatus (GHPA). The problem is as follows:

Hot Plate has a resistance $g(t)$ placed in $r_1 = 0.0538$ m, initial temperature $T_0 = 302.378$ K for time $t = 0$ s and lose heat by convection to a medium with temperature $T_{\text{amb}} = 302.378$ K in a boundary placed in $r = b = 0.0762$ m for times $t > 0$. Guard has a resistance $g(t)$ placed in $r_2 = 0.0983$ m, initial temperature $T_0 = 300.39$ K for time $t = 0$ s and for times $t > 0$ lose heat by convection to a medium with temperature $T_{\text{amb}} = 300.39$ K in both boundaries placed in $r = b = 0.0762$ m and $r = d = 0.15245$ m. Both diagrams, Hot Plate and Guard, are shown in Fig. 1a, b.

The mathematical formulation of these direct heat conduction problems is given by (Cortés 2004):

$$\begin{aligned} \frac{\partial^2 T}{\partial r^2} + \frac{1}{r}\frac{\partial T}{\partial r} + \frac{g(t)\cdot\delta(r-r_1)}{2\pi k r} &= \frac{1}{\alpha}\frac{\partial T}{\partial t} \quad 0<r<b, \quad t>0 \\ k\frac{\partial T}{\partial r} + hT &= hT_{\text{amb}} \quad r=b, \quad t>0 \\ T &= T_0 \quad 0\le r\le b, \quad t=0 \end{aligned} \tag{1}$$

and

$$\begin{aligned} \frac{\partial^2 T}{\partial r^2} + \frac{1}{r}\frac{\partial T}{\partial r} + \frac{g(t)\cdot\delta(r-r_2)}{2\pi k r} &= \frac{1}{\alpha}\frac{\partial T}{\partial t} \quad b<r<d, \quad t>0 \\ -k\frac{\partial T}{\partial r} + hT &= hT_{\text{amb}} \quad r=b, \quad t>0 \\ k\frac{\partial T}{\partial r} + hT &= hT_{\text{amb}} \quad r=d, \quad t>0 \\ T &= T_0 \quad b\le r\le d, \quad t=0 \end{aligned} \tag{2}$$

where $\delta(\cdot)$ is the Dirac delta function.

The solution to this problem is obtained by means of the integral transform method (Cortés 2004). For this inverse problem, the time varying strength $g(t)$ of

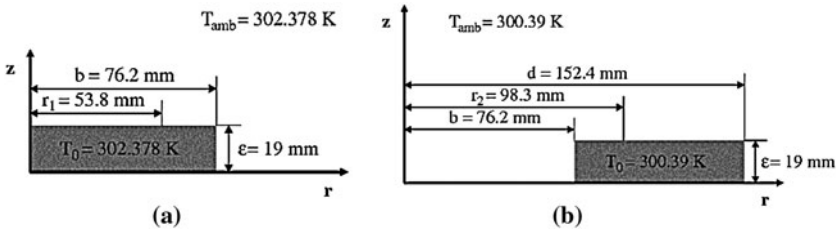

Fig. 1 Physical model for **a** the hot-plate and **b** the guard

the heat source is regarded as unknown. The additional information obtained from transient temperature measurements taken at a location $r = r_{\text{meas}}$ at times t_i, $i = 1, 2, \ldots, I$, is then used for the estimation of $g(t)$.

For this work, it will be considered a polynomial approximation from one to five parameters, expressed in the following form (Cortés 2004):

$$g(t) = P_1 + P_2 t + P_3 t^2 + P_4 t^3 + P_5 t^4 \tag{3}$$

The solution of this inverse heat conduction problem for the estimation of the unknown parameters is based on the minimization of the ordinary least squares norm given by:

$$S(\mathbf{P}) = \sum_{i=1}^{I} [Y_i - T_i(\mathbf{P})]^2 \tag{4}$$

where Y_i are the measured temperature at time t_i, $T_i(\mathbf{P})$ are estimated temperature at time t_i, $\mathbf{P}^{\mathrm{T}}$ is the vector of unknown parameters, N is the total number of unknown parameters and I is total number of measurements, where $I \geq N$.

The estimated temperatures $T_i(\mathbf{P})$ are obtained from the solution of the direct problem at the measurements location, r_{meas}, by using the current estimate for the unknown parameters. To minimize the least squares norm given by Eq. 4, it is needed to equate to zero the derivatives of $S(\mathbf{P})$ with respect to each of the unknown parameters.

The whole solution for this problem (Cortés 2004) is given by:

$$\begin{aligned} T(r,t) = {} & \frac{hbT_0}{\beta^2 kN} R_0(\beta,r) R_0(\beta,b) e^{-\alpha\beta^2 t} + \frac{hbT_{\text{amb}}}{\beta^2 kN} R_0(\beta,r) R_0(\beta,b) \left(1 - e^{-\alpha\beta^2 t}\right) \\ & + \frac{\alpha}{2\pi kN} R_0(\beta,r) R_0(\beta,r_1) \left\{ \frac{P_1}{\alpha\beta^2} \left(1 - e^{-\alpha\beta^2 t}\right) + \frac{P_2}{\alpha^2\beta^4} \left[\alpha\beta^2 t - \left(1 - e^{-\alpha\beta^2 t}\right)\right] \right. \\ & + \frac{P_3}{\alpha^3\beta^6} \left[\alpha^2\beta^4 t^2 - 2\alpha\beta^2 t + 2\left(1 - e^{-\alpha\beta^2 t}\right)\right] \\ & + \frac{P_4}{\alpha^4\beta^8} \left[\alpha^3\beta^6 t^3 - 3\alpha^2\beta^4 t^2 + 6\alpha\beta^2 t - 6\left(1 - e^{-\alpha\beta^2 t}\right)\right] \\ & + \frac{P_5}{\alpha^5\beta^{10}} \left[\alpha^4\beta^8 t^4 - 4\alpha^3\beta^6 t^3 + 12\alpha^2\beta^4 t^2\right) \\ & \left. - 24\alpha\beta^2 t + 24\left(1 - e^{-\alpha\beta^2 t}\right)\right] \Bigg\} \end{aligned} \tag{5}$$

where

$$N = \frac{\left(h^2 + \beta^2 k^2\right) b^2 R_0^2(\beta, b)}{2\beta^2 k^2}$$
$$R_0(\beta, r) = J_0(\beta r) \tag{6}$$

and

$$\begin{aligned} T(r,t) = {} & [bR_0(\beta,b) + dR_0(\beta,d)]\frac{hT_0}{\beta^2 kN}R_0(\beta,r)e^{-\alpha\beta^2 t} + [bR_0(\beta,b) \\ & + dR_0(\beta,d)]\frac{hT_{\text{amb}}}{\beta^2 kN}R_0(\beta,r)\left(1 - e^{-\alpha\beta^2 t}\right) + \frac{\alpha}{2\pi kN}R_0(\beta,r)R_0(\beta,r_2) \\ & \left\{\frac{P_1}{\alpha\beta^2}\left(1 - e^{-\alpha\beta^2 t}\right) + \frac{P_2}{\alpha^2\beta^4}\left[\alpha\beta^2 t - (1 - e^{-\alpha\beta^2 t})\right]\right. \\ & + \frac{P_3}{\alpha^3\beta^6}\left[\alpha^2\beta^4 t^2 - 2\alpha\beta^2 t + 2(1 - e^{-\alpha\beta^2 t})\right] \\ & + \frac{P_4}{\alpha^4\beta^8}\left[\alpha^3\beta^6 t^3 - 3\alpha^2\beta^4 t^2 + 6\alpha\beta^2 t - 6(1 - e^{-\alpha\beta^2 t})\right] \\ & \left. + \frac{P_5}{\alpha^5\beta^{10}}\left[\alpha^4\beta^8 t^4 - 4\alpha^3\beta^6 t^3 + 12\alpha^2\beta^4 t^2 - 24\alpha\beta^2 t + 24(1 - e^{-\alpha\beta^2 t})\right]\right\} \end{aligned} \tag{7}$$

where

$$N = \frac{\left(h^2 + \beta^2 k^2\right)\left[d^2 R_0^2(\beta,d) - b^2 R_0^2(\beta,b)\right]}{2\beta^2 k^2}$$
$$R_0(\beta, r) = \frac{J_0(\beta r)}{-\beta k J_1(\beta d) + h J_0(\beta d)} - \frac{Y_0(\beta r)}{-\beta k Y_1(\beta d) + h Y_0(\beta d)} \tag{8}$$

3 Particle Swarm Optimization

Natural creatures sometimes behave as a swarm. One of the main streams of artificial life research is to examine how natural creatures behave as a swarm and reconfigure the swarm models inside a computer. Kennedy and Eberhart (1995) developed particle swarm optimization (PSO) based on the analogy of swarms of birds and fish schooling. Each individual exchanges previous experiences in PSO. These research efforts are called swarm intelligence (Kennedy and Eberhart 2001).

Kennedy and Eberhart (2001) developed PSO through simulation of bird flocking in a two-dimensional space. The position of each agent is represented by its x, y axis position and by its velocities expressed by v_x (the velocity of x axis) and v_y (the velocity of y axis). Modification of the agent position is realized by the position and velocity information. This modification can be represented by the concept of velocity (modified value for the current positions). The velocity of each agent can be modified by the following equation:

$$v_i^{k+1} = wv_i^k + c_1 \text{rand}_1 \times \left(pbest_i - s_i^k\right) + c_2 \text{rand}_2 \times \left(gbest - s_i^k\right) \tag{9}$$

where v_i^k is the velocity of agent i at iteration k, w is the weighting function, c_j is the weighting coefficients, rand is a random number between 0 and 1, s_i^k is current position of agent i at iteration k, $pbest_i$ is $pbest$ of agent i, and $gbest$ is $gbest$ of the group.

Namely, velocity of an agent can be changed using three vectors. The velocity is usually limited to a certain maximum value. PSO using (9) is called the *Gbest* model.

The following weighting function is usually utilized in (9):

$$w = w_{\max} - \frac{w_{\max} - w_{\min}}{\text{iter}_{\max}} \times \text{iter}, \tag{10}$$

where $w_{\max}$ is the initial weight, $w_{\min}$ is the final weight, $\text{iter}_{\max}$ is the maximum iteration number, and iter is the current iteration number.

As shown below, for example, $w_{\max}$ and $w_{\min}$ are set to 0.9 and 0.4, respectively (Fukuyama 2008). Therefore, at the beginning of the search procedure, *diversification* is heavily weighted, while *intensification* is heavily weighted at the end of the search procedure such like simulated annealing (SA). Namely, a certain velocity, which gradually gets close to *pbest* and *gbest*, can be calculated. PSO using (9), (10) is called *inertia weights* approach (IWA).

The current position (searching point in the solution space) can be modified by the following equation:

$$s_i^{k+1} = s_i^k + v_i^{k+1} \tag{11}$$

Figure 2 shows a concept of modification of a searching point by PSO. Shi and Eberhart (1998a, b) tried to examine the parameter selection of the above parameters. According to their examination, the following parameters are appropriate and the values do not depend on problems:

$$c_i = 2.0, \qquad w_{\max} = 0.9, \qquad w_{\min} = 0.4.$$

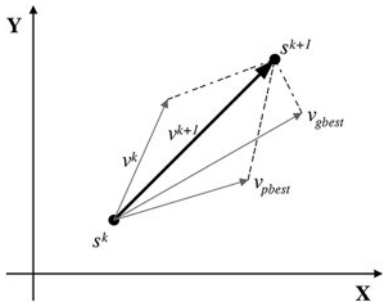

Fig. 2 Concept of modification of a searching point by PSO

Table 1 Minimum ordinary least squares norm for hot plate and guard

Parameters	Hot-Plate		Guard	
	LMM	PSO	LMM	PSO
1	1891.6394	1891.6394	200.6026	200.5644
2	1132.1777	1132.1777	29.1051	28.4137
3	865.1679	919.9884	21.5268	13.5919
4	758.5913	758.6564	17.3220	13.5064
5	733.9622	751.0625	17.5800	13.3632

4 Results

In the Hot-Plate of the GHPA an electrical heat generation of 5 W was used. The temperature measurements were taken every 1 min (624 time steps) at position $r_{\text{meas}} = 0.0762$ m. The heat generation used in the Guard was 3 W. The measurements were taken every 30 s (345 time steps) at position $r_{\text{meas}} = 0.1524$ m. The number of particles used for optimization was 20. Results are compared with Levenberg-Marquardt method (LMM) because it is a very stable and fast convergence method.

Table 1 shows the ordinary least squares norm for LMM and PSO for the Hot Plate. LMM has a best performance when the number of parameters is growing. For one and two parameters it can be seen that PSO is slightly better than LMM. Table 2 shows the parameters estimated for each case with both methods.

For the guard, Table 1 also shows the ordinary least squares norm for LMM and PSO for the Guard. It is seen that PSO has the best performance for all cases because its ordinary least squares norm is less than LMM. In Table 2 the parameters estimated for each case with both methods are listed.

Table 2 Values estimated for the parameters of the heat generation function of the hot plate and guard for each case and method

Case	Par.	Hot-Plate		Guard	
		LMM	PSO	LMM	PSO
I	1	261.4209	261.4209	390.4734	390.4734
II	1	279.9517	279.9517	467.4291	467.4386
	2	−0.001074	−0.001074	−0.01795	−0.01795
III	1	299.1446	295.4970	513.7841	515.4850
	2	−0.004133	−0.003186	−0.04634	−0.04733
	3	8.68571×10^{-8}	5.7683×10^{-8}	3.0314×10^{-6}	3.1345×10^{-6}
IV	1	318.7107	319.2394	499.5220	510.4633
	2	−0.009961	−0.01011	−0.03001	−0.04152
	3	4.8308×10^{-7}	4.9293×10^{-7}	-1.1185×10^{-6}	1.6476×10^{-6}
	4	-7.3747×10^{-12}	-7.5533×10^{-12}	2.8613×10^{-10}	1.0297×10^{-10}
V	1	332.9782	321.2141	500.4345	505.5068
	2	−0.01670	−0.01182	−0.03065	−0.03395
	3	1.2784×10^{-6}	7.7478×10^{-7}	-1.2106×10^{-6}	-1.3086×10^{-6}
	4	-4.0981×10^{-11}	-2.1763×10^{-11}	3.4898×10^{-10}	5.2527×10^{-10}
	5	4.6357×10^{-16}	2.1672×10^{-16}	-5.2327×10^{-15}	-2×10^{-14}

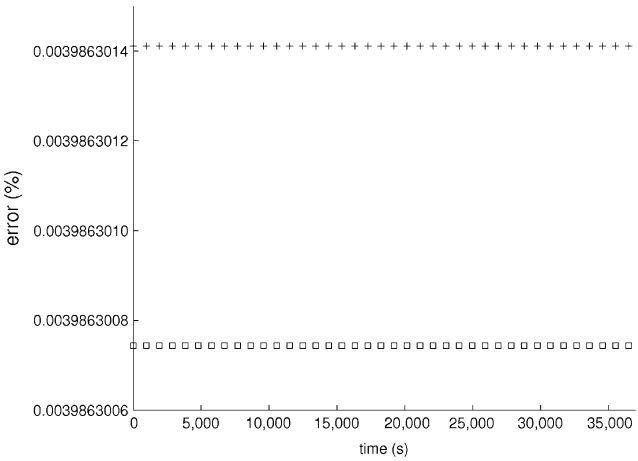

Fig. 3 Errors for heat source estimation for LMM (□) and PSO (+) in the hot-plate

Figure 3 shows the errors for the cases with minimum errors in the heat source estimation for each case with LMM and PSO for the hot-plate. Figure 4 shows the same results for the guard.

Figures 5 and 6 show the temperature fields for the cases with minimum values of ordinary least squares norm for hot-plate and guard, respectively.

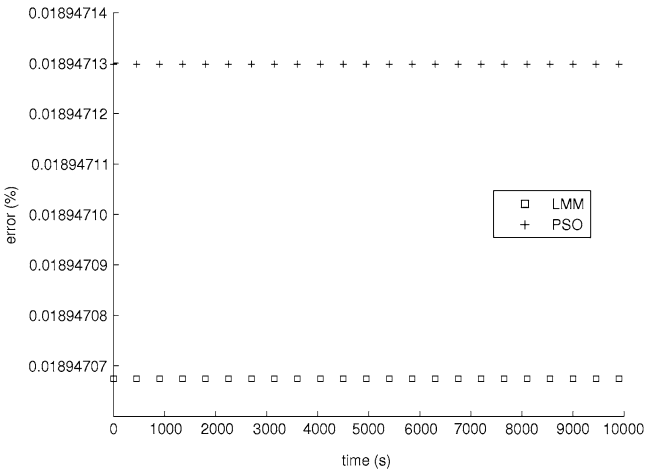

Fig. 4 Errors for heat source estimation for LMM (□) and PSO (+) in the guard

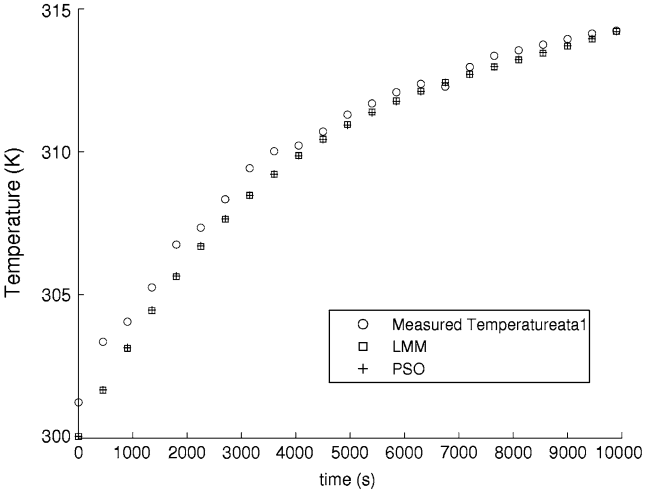

Fig. 5 Temperature field for best ordinary least squares norm with LMM (□) and PSO (+) for guard compared against measured temperature (○)

5 Conclusion

One strategy for inverse heat transfer problems has been applied. Particle Swarm Optimization is a new method with good performance. This method was compared with the Levenberg–Marquardt method, a method used for a long time for this kind of problem. In the case of the guard, PSO has shown a better performance than LMM.

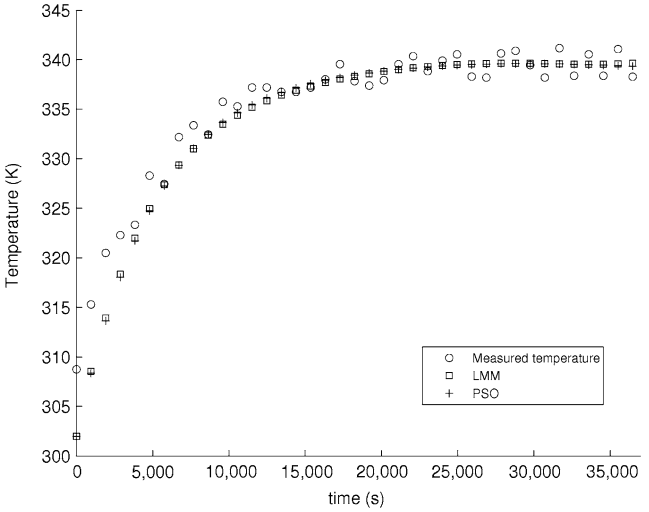

Fig. 6 Temperature field for best ordinary least squares norm with LMM (□) and PSO (+) for hot-plate compared against measured temperature (○)

In the guard case, it can be seen that PSO is slightly better than LMM. However, both methods are good enough to optimize the source term. More applications for inverse problems to demonstrate PSO capability are needed. Results are encouraging to do more work in this direction.

References

Alifanov OM (1994) Inverse heat transfer problems. Springer, New York

Colaco MJ, Orlande HRB, Dulikravich GS (2004) Inverse and optimization problems in heat transfer. In: Proceeding of the 10th Brazilian congress of thermal sciences and engineering, ENCIT 2004, Rio de Janeiro, Brazil

Cortés O (2004) Aplicación del Método de Levenberg-Marquardt y del Gradiente Conjugado en la estimación de la generación de calor de un Aparato de Placa Caliente con Guarda. M.Sc. thesis, CENIDET, Cuernavaca, Mor., México

Fukuyama Y (2008) Fundamentals of particle swarm optimization techniques. In: Lee KY, El-Sharkawi MA (eds) Modern heuristic optimization techniques. Wiley, New York

Kennedy J, Eberhart R (1995) Particle swarm optimization. In: Proceedings of IEEE international conference on neural networks (ICNN'95); vol IV. IEEE Press, Perth, pp 1942–1948

Kennedy J, Eberhart R (2001) Swarm intelligence. Morgan Kaufmann, San Mateo

Ozisik MN, Orlande HRB (2000) Inverse heat transfer: fundamentals and applications. Taylor and Francis, New York

Shi Y, Eberhart R (1998a) A modified particle swarm optimizer. In: Proceedings of IEEE International Conference on Evolutionary Computation (ICEC'98). EEE Press, Anchorage, pp 69–73

Shi Y, Eberhart R (1998b) Parameter selection in particle swarm optimization. In: Proceedings of the seventh annual conference on evolutionary programming. MIT Press, San Diego

Microbubble Generation Using Carbon Nanostructures Deposited onto Optical Fibers

Reinher Pimentel-Domínguez and Juan Hernández-Cordero

Abstract We present an easy, fast and inexpensive method to produce micron-sized bubbles using a low power laser diode operating in CW mode. The technique is based on light absorption by a thin layer of carbon nanostructures (nanotubes and nanoparticles) deposited on the tip of an optical fiber. Through flow visualization techniques and thermal imaging, we have observed evidence of the thermal and pressure gradients that appear in this process. With this method, micron-sized bubbles can be generated. These effects might be of significance for cavitation studies as well as for laser surgery.

1 Introduction

Generation of sub-picosecond pulses with optical fiber lasers has lead to the development of carbon nanotube-based fiber devices to achieve mode-locked operation. A variety of techniques have been demonstrated for incorporating carbon nanotubes in fiber laser systems (Nicholson et al. 2007; Kashiwagi et al. 2007; Set et al. 2004; Chow et al. 2009). The simplest way to achieve this is by dipping an optical fiber in a solution of nanotubes dispersed in ethanol (Nicholson et al. 2007) or DMF (Kashiwagi et al. 2007). This novel and simple technique results in the deposition of carbon nanotubes on the ends of the fibers owing to the

R. Pimentel-Domínguez (✉) · J. Hernández-Cordero
Instituto de Investigaciones en Materiales, UNAM, Ciudad Universitaria,
Apartado Postal 70-360, 04510, México, D.F., México
e-mail: vetuasaber@ciencias.unam.mx

J. Hernández-Cordero
e-mail: jhcordero@iim.unam.mx

J. Klapp et al. (eds.), *Experimental and Theoretical Advances in Fluid Dynamics*, Environmental Science and Engineering, DOI: 10.1007/978-3-642-17958-7_32,

pressure and thermal gradients generated by laser light guided in the core of the waveguide. Deposition on the tip of the fibers is attained from the "optical force" exerted on the nanotubes moving them towards the fiber core. We have recently extended this technique to incorporate other types of nanostructures onto fiber tips and fiber optic connector. To date, we have successfully deposited nanostructured materials such as graphite, iron, iron–graphite and various types of carbon nanotubes (Pimentel-Domínguez et al. 2010). Other materials that have also been incorporated on fibers include tungsten oxide nanospheres and titania nanotubes (Zaca-Morán et al. 2010).

In spite of its simplicity, the physical principles underlying this "dipped fiber" technique have not been fully elucidated yet. Different mechanisms such as the optical tweezers effect and thermophoresis caused by localized heating of the solution and nanotubes due to optical absorption have been noted to play a role in this process (Nicholson et al. 2007; Kashiwagi et al. 2007). Furthermore, it has been shown that for particles between 10 nm and 1 μm in diameter various degrees of thermophoresis and Brownian motion may contribute to particle deposition (Zahmatkesh 2008). In an attempt to gain a better insight of the possible mechanisms behind the "optical force" driving the nanostructures, we have been using flow visualization techniques during the deposition process. Remarkably, we have observed other interesting effects such as micro-bubble generation that have not yet been reported.

Bubbles and bubbly flows are important in fields as diverse as geophysics, chemistry, biology, medicine and physics. Generation of bubbles with laser light usually involves high-power pulsed laser sources so as to generate cavitation effects (Frenz et al. 1996). In this paper, we show that a low-power laser diode can be used for generating micron-sized bubbles in a non-absorbing liquid by means of an optical fiber coated with nanostructures.

2 Experiments

The experimental setup used for the optically driven deposition of nanostructured materials onto optical fibers is very simple. As shown in Fig. 1a, it involves three basic elements: a laser light source, an optical fiber for guiding the laser light, and the nanostructures to be deposited on the fiber. The nanostructures are dissolved in a liquid that must be chosen so as to avoid optical absorption at the laser wavelength. In our experiments, we use a CW fiber-coupled laser diode (JDSU, 975 nm, 70 mW max. Output power), standard single-mode optical fiber (SMF-28e) for laser guiding and as the deposition target; the nanostructures are dissolved in an ethanol solution. The tested nanostructures were fabricated in our Institute and these included carbon nanotubes, nanoparticles (graphite, iron–graphite, and silica) as well as micron-sized iron particles. Prior being immersed in the solution, the fibers were cleaved to obtain a flat end face; the laser output power varied depending on the type of nanostructure used in the

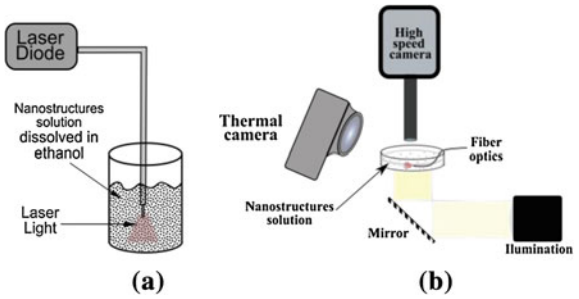

Fig. 1 **a** Experimental setup for nanostructure deposition onto optical fibers. **b** Arrangement for the visualization of bubble generation

deposition process (Pimentel-Domínguez et al. 2010). Deposition onto the fiber end faces occurs when the laser diode is turned on when the fiber end is immersed in the solution containing the nanostructures. The fiber end faces were subsequently observed with a scanning electron microscope (SEM) in order to verify the successful deposition of nanostructures.

Bubble generation was observed by means of a high-speed camera (Redlike, 1108–0014) with a zoom imaging lens (TECHSPEC® VZM, 1000i). A thermal imaging camera (Fluke Ti45 FlexCam) was also used for monitoring thermal gradients around the location of the fiber end faces. The sample was illuminated with a high intensity white LED spot lamp (Fig. 1b).

3 Results and discussion

Deposition of the nanostructures was readily achieved after immersing the fibers in the solution for 5 min. Laser diode powers ranging from 35 to 70 mW were used for successfully depositing carbon nanotubes (multi-wall), graphite nanoparticles as well as iron–graphite, silica, and iron micro particles (3 μm). Figure 2 shows side views of optical fibers with coatings of different nanostructured materials. As seen in the figure, the thickness of the coatings varies for all the different samples. Once deposited, the coatings are very stable and remain attached to the tip of the fiber even after the laser is turned off. Although we have not performed experiments to optimize the thickness of the deposited material, we believe that the main factors involved in this process include laser power, immersion time and the distribution of nanostructures within the solution. In this sense, more detailed experiments are necessary so as to achieve deposition of thin films or single layer coatings of nanostructures on the fiber end faces.

We have previously observed that during deposition, when the laser diode is turned on, a flow of nanostructures is generated around the tip of the fiber (Pimentel-Domínguez et al. 2010). The light emerging from the optical fiber generates a gradient force (optical tweezers effect) driving the particles towards the tip of the fiber.

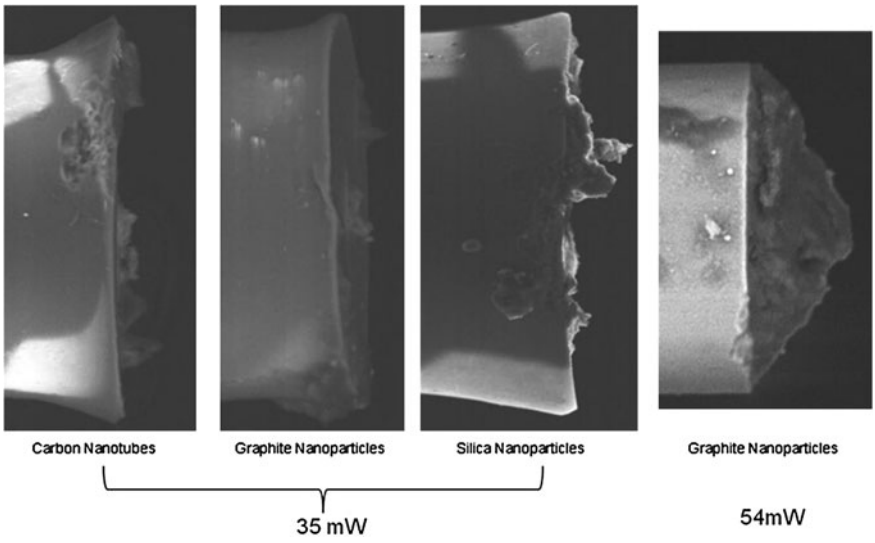

Fig. 2 Side view of optical fiber end faces after deposition of different nanostructures

After deposition of the nanostructures, the fiber tips were immersed in clean ethanol and the laser diode was turned on. By means of the high-speed camera, bubble formation was readily observed at the tip of the optical fiber. Figure 3 shows a series of photographs taken over 20 ms intervals showing the process of bubble formation and growth in ethanol using a carbon nanotube coated optical fiber. Similar results were obtained using the other nanostructured materials, with the exception of silica that did not yield bubble formation. Aside from ethanol, bubbles were also generated in water using the coated optical fibers. An optical power as low as 35 mW was adequate to generate bubbles either in water or ethanol; the bubble sizes ranged from 10 μm to 1.5 mm in diameter.

Bubble formation in the vicinity of the fiber tip may be attributed to thermal effects. Once deposition of nanostructures on the fiber end faces has been achieved, a temperature gradient produces thermophoresis due to optical absorption by the nanostructures. Micron-sized bubbles can thus be generated on the tip of the fiber and they keep increasing in size until reaching a maximum diameter. The bubble remains attached to the optical fiber until the laser is turned off, at which point it is released and the flow around the tip of the fiber disappears. As seen in Fig. 4, bubble formation clearly modifies the flow pattern around the optical fiber.

The fact that bubbles can be formed in our experiments suggests that temperature gradients become extremely relevant when nanostructures are present in the solution. Optical absorption by the nanostructures causes localized heating and subsequently produces explosive vaporization of the liquid, resulting in microbubble formation. The role of optical absorption by the nanostructures was verified experimentally repeating the same set of experiments using a clean optical fiber

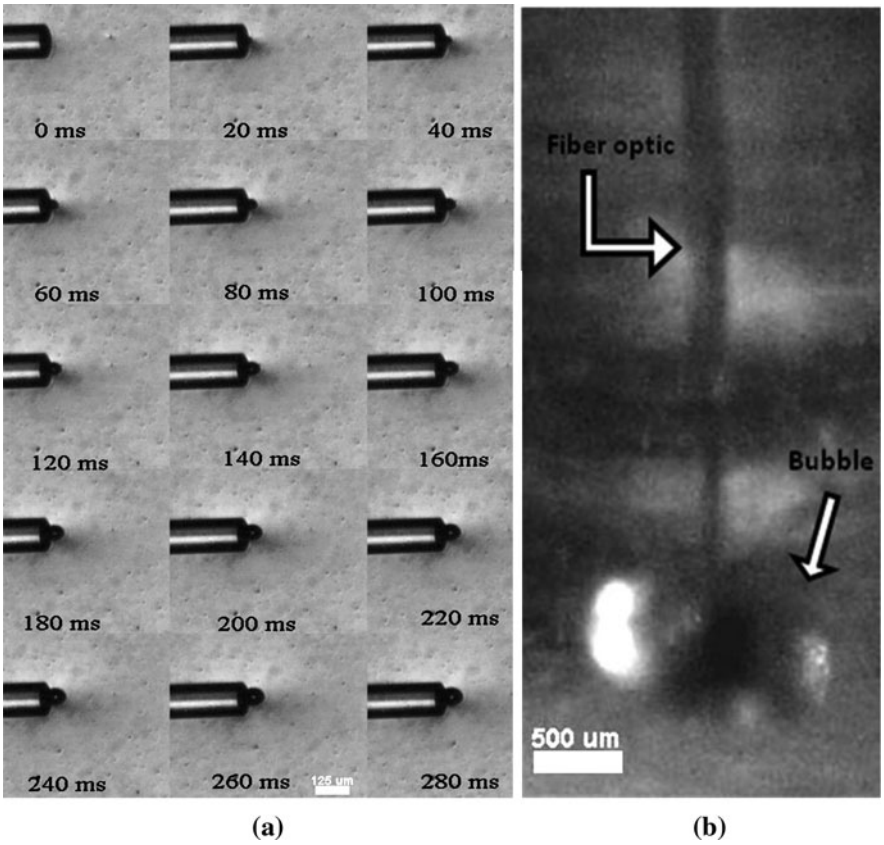

Fig. 3 Bubble generation with an optical fiber coated with carbon nanotubes (ethanol, 35 mW optical power). Bubble maximum diameter: **a** 70 μm and **b** 1500 μm

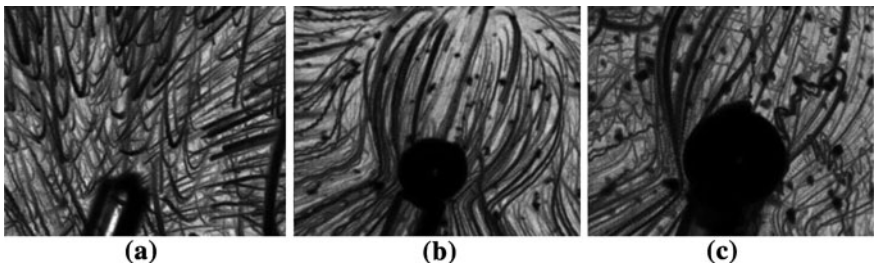

Fig. 4 Flow patterns around the optical fiber tip: **a** early bubble formation after turning the laser diode on; **b** after 120 s of bubble growth; **c** after turning the laser off. Solution: graphite-iron nanoparticles in ethanol; laser diode output power: 34 mW

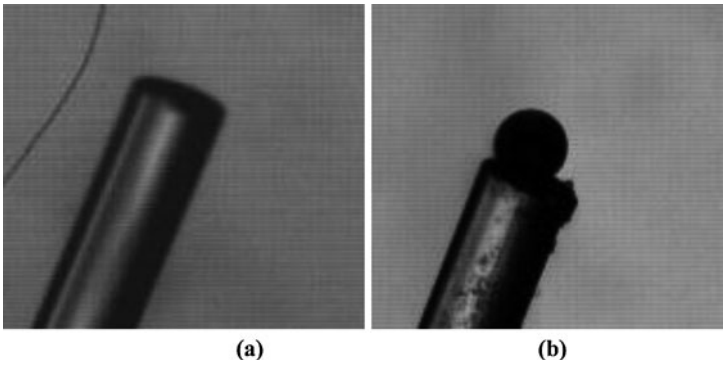

Fig. 5 Optical fiber immersed in ethanol: **a** without nanostructures and **b** with a coating of graphite nanoparticle

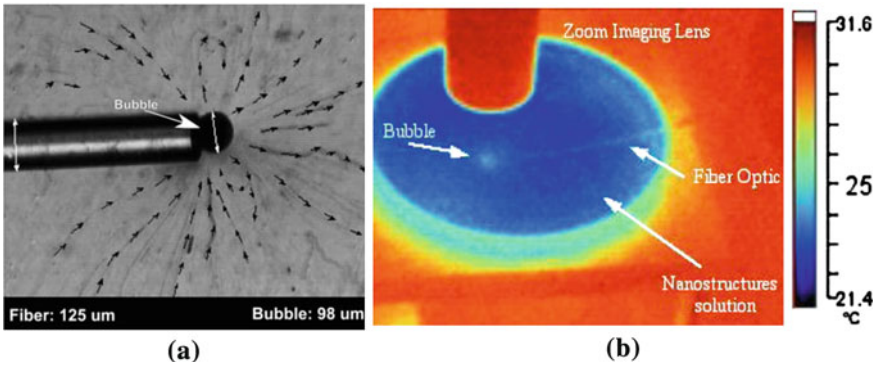

Fig. 6 Graphite nanoparticles in ethanol: **a** flow pattern around the fiber tip; **b** thermal image of the experiment (notice the temperature gradient due to microbubble formation)

immersed in ethanol. As shown in Fig. 5a, a fiber without a nanostructured coating did not lead to bubble formation. For comparison, Fig. 5b depicts the same fiber after being coated with graphite nanoparticles. Clearly, the coated fiber does provide the necessary effect for microbubble generation. Further evidence of this localized heating was observed with the thermal camera (see Fig. 6). Albeit resolution limitations of the camera, the thermal image shows a temperature gradient in the vicinity of the tip of the optical fiber.

It is interesting to note that, in contrast to reports demonstrating bubble formation in liquids due to laser absorption (Frenz et al. 1996; Paltauf et al. 1998; Vogel et al. 2008; Kröninger et al. 2010; Ramirez-San-Juan et al. 2010), our results were obtained using a low power CW laser diode (<70 mW). While we have observed in our experiments bubbles with lifetimes ranging from seconds to minutes, cavitation generated bubbles have an average lifetime of micro or milliseconds. In addition, cavitation bubbles typically implode intensely at the end of

their lifetime; in contrast, bubbles obtained with our technique remain attached to the fiber until being released to the surface upon turning the laser off.

4 Conclusions

We have demonstrated the formation of micron-sized bubbles due to optical absorption of nanostructures deposited on an optical fiber end face. In contrast with the bubbles obtained from cavitation experiments, our method to produce microbubbles offers advantages such as using CW laser light, low optical power, and does not require dyes dissolved in the liquid to enhance light absorption. In addition, the generated bubbles are stable; they also show a longer lifetime and do not seem to implode intensely thereby avoiding potential secondary damage in the surroundings.

In spite of its simplicity, there are several questions to answer regarding this technique. Work is underway in order to obtain a better understanding of all the physical phenomena associated with bubble formation using nanostructures. This novel and inexpensive technique could render useful for developing microbubble generators and mixers for micron sized structures, convective flow studies, as well as optical fiber sensors and photonic devices. Cavitation studies and laser surgery with low optical powers may also benefit from the proposed technique.

Acknowledgments We thank R. Zenit and C. García-Segundo for invaluable technical support and useful discussions. Technical support from Omar Novelo with the SEM images is also duly appreciated. This work was supported by DGAPA-UNAM through grant PAPIIT-IN116509.

References

Chow K et al (2009) A widely tunable wavelength converter based on nonlinear polarization rotation in a carbon-nanotube-deposited D-shaped fiber. Opt Express 17(9):7664–7669

Frenz M et al (1996) Laser-generated cavitation in absorbing liquid induced by acoustic diffraction. Phys Rev Lett 76(19):3546–3549

Kashiwagi K et al (2007) Optically manipulated deposition of carbon nanotubes onto optical fiber end. Jpn J Appl Phys 46(40):L988–L990

Kröninger D et al (2010) Particle tracking velocimetry of flow field around a collapsing cavitation bubble. Exp Fluids 48(3):395–408

Nicholson JW et al (2007) Optically driven deposition of single-walled carbon-nanotube saturable absorbers on optical fiber end-faces. Opt Express 15(15):9176–1983

Paltauf G et al (1998) Photoacoustic waves excited in liquids by fiber-transmitted laser pulses. J Acoust Soc Am 104(2):890–897

Pimentel-Domínguez et al (2010) Optically driven deposition of nanostructures on optical fiber end faces. 2nd Workshop on Specialty Optical Fibers, Proceedings of SPIE, pp 7839–56

Ramirez-San-Juan JC et al (2010) Time-resolved analysis of cavitation induced by CW lasers in absorbing liquids. Opt Express 18(9):8735–8742

Set SY et al (2004) Laser mode locking using a saturable absorber incorporating carbon nanotubes. J Lightwave Technol 22(1):51–56

Vogel A et al (2008) Femtosecond-laser-induced nanocavitation in water: implications for optical breakdown threshold and cell surgery. Am Phys Soc 100(3)

Zaca-Morán P et al (2010) Comparative analysis of WO_3 nanospheres and TiO_2 nanotubes as saturable absorber for applications in passive mode-locked laser. 2nd Workshop on specialty optical fibers, proceedings of SPIE, pp 7839–56

Zahmatkesh I (2008) On the importance of thermophoresis and Brownian diffusion for the deposition of micro- and nanoparticles. Int Commun Heat Mass Transfer 35:369–375

Natural Convective Heat Transfer in a Box Filled With a Participating Medium

Manuel A. Ramírez-Cabrera and Eduardo Ramos

Abstract We present a model for calculating the heat transfer by convection and radiation inside a cubic box with high density thermal radiation incident on a small window. The box is filled with a participating fluid and thermal radiation is absorbed by the bulk of the fluid. The numerical method used to integrate the resulting system of integro-differential equations is described and a particular example is discussed. The system analyzed is proposed as the fundamental concept of a heat exchanger that is specifically designed to absorb and store efficiently high density radiation as required in solar energy absorption in Central Receiver Systems.

1 Introduction

One of the most successful technologies in solar energy utilization is the Central Receiver Systems where the sunlight reflected from hundreds or thousands of mirrors is concentrated at a single spot with a small area where it is absorbed and converted into useful energy (Romero 2002). A big challenge posed by this technology, is capturing the energy in the form of high density thermal radiation and prevent it from being radiated back to the atmosphere. The long term objective of the project that embodies the present investigation is the design of a heat

M. A. Ramírez-Cabrera (✉) · E. Ramos
Center for Energy Research, Universidad Nacional Autónoma de México,
62580 Temixco, Mor., Mexico
e-mail: marac@cie.unam.mx

E. Ramos
e-mail: erm@cie.unam.mx

J. Klapp et al. (eds.), *Experimental and Theoretical Advances in Fluid Dynamics*, Environmental Science and Engineering, DOI: 10.1007/978-3-642-17958-7_33,

exchanger that should work efficiently under conditions similar to those found in Central Receiver Systems. We propose an idea based on the use of a participating medium as a working fluid of the heat exchanger. In contrast to the conventional designs where the radiating energy hits the external wall of the heat exchanger and heat is transferred to the interior through the wall by conduction, in the design proposed, the heat exchanger will absorb the radiating heat in the bulk of the fluid. In the present report, we analyze a heat transfer situation closely related to that occurring in the proposed heat exchanger. We consider the radiation and convection heat transfer process in a box with a small window on one side and filled with a participating fluid. This system can be interpreted as a blackbody filled with a material that absorbs radiating energy.

2 Physical Model

The physical situation analyzed in the present report is sketched in Fig. 1, left. We consider a cubic container of side L filled with a material that absorbs and emits heat radiation in presence of gravity force. On one vertical wall, a centered small window (area $L/7 \times L/7$) made of a material with perfect transmittance allows the incident radiation to enter into the volume and to be absorbed by the participating medium. Once absorbed, the working fluid is set in motion due to natural convection, continuously refreshing the material exposed to the maximum radiation intensity. This situation is sketched in Fig. 1, right. Our objective is to develop a model to calculate the heat transfer processes occurring inside the container.

3 Governing Equations

3.1 Energy Balance in a Radiation Beam

The classical analysis of heat transfer by thermal radiation is based on the evaluation of the intensity I of a radiation beam (power per cross sectional area, $\mathrm{W/m^2}$) as it travels through a participating medium. A beam attenuates due to absorption and by scattering away energy from its direction of travel $\hat{s}$. Simultaneously, its intensity increases by the emission and scattering from other material points into the direction of the beam propagation.

The absolute amount of absorption is directly proportional to the magnitude of the incident energy as well as to the distance the beam travels through the medium,

$$dI_{abs} = -\kappa I ds. \tag{1}$$

The subscript *abs* indicates that the change in intensity is due to absorption, the proportionality constant κ is the absorption coefficient, and the negative sign is

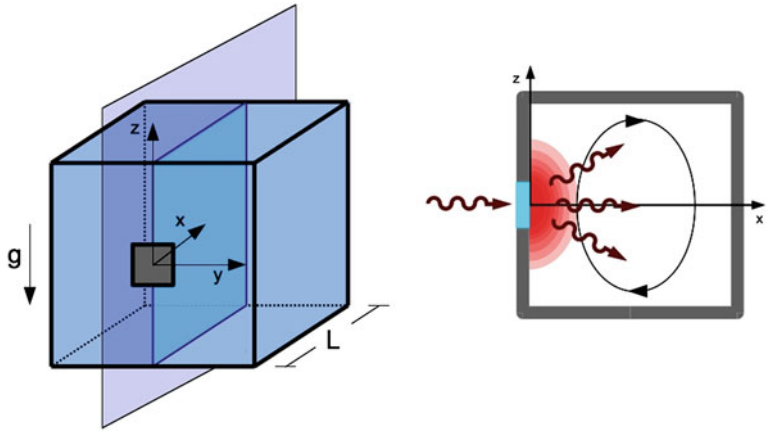

Fig. 1 *Left*, geometry of the cubic container indicating the axis of coordinates. *Right*, sketch of the central vertical plane. A horizontal beam of radiation energy is transmitted through the window and interacts with the material filling the box transferring energy by radiation, conduction and convection

introduced since the intensity decreases by absorption as the beam progresses. Beam attenuation by scattering energy away from the direction under consideration, is very similar to absorption, i.e., part of the incoming intensity is removed from the direction of propagation. The only difference between the two phenomena is that absorbed energy is converted into internal energy, while scattered energy is simply redirected and appears as augmentation along another direction. Thus, we may write,

$$dI_{sca} = -\sigma_s I ds, \tag{2}$$

where the proportionality constant σ_s is the scattering coefficient for energy deflected from the beam under consideration into all other directions. The subscript *sca* indicates that the change in intensity is due to scattering.

The total attenuation of intensity by absorption and scattering is known as extinction and thus, the extinction coefficient β is defined as

$$\beta = \kappa + \sigma_s. \tag{3}$$

As it was described previously, a heat radiation beam traveling through a participating medium in direction $\hat{s}$ loses energy by absorption and by scattering energy away from the direction of travel, but it also gains energy by emission as well as by scattering from other directions into the direction of the beam propagation.

The change of the beam intensity due to emission is proportional to the intensity itself, and in thermodynamic equilibrium, the intensity everywhere must be equal to the blackbody intensity. i.e.

$$dI_{em} = -\kappa I_b ds. \tag{4}$$

The subscripts *em* and *b* indicate emission and blackbody, respectively. It should be emphasized that in equilibrium, the proportionality constant for emission is equal as that for absorption (compare Eqs. 1 and 4).

Augmentation by scattering, has contributions from all directions and must be calculated by integrating over all solid angles. The energy flux scattered into the direction of the beam $\hat{s}$ from all incoming directions $\hat{s}_i$ is given by

$$dI_{sca}(\hat{s}) = ds \frac{\sigma_s}{4\pi} \int_{4\pi} I(\hat{s}_i)\Phi(\hat{s}_i \cdot \hat{s}) d\Omega_i. \tag{5}$$

The function $\Phi(\hat{s}_i \cdot \hat{s})$ is called the scattering phase function and describes the probability that a ray from one direction $\hat{s}_i$, will be scattered into the direction $\hat{s}$.

The total change in intensity of the radiative energy traveling in direction $\hat{s}$ is found by summing up the contributions from emission, absorption, and scattering, both away and into the direction $\hat{s}$. Considering Eqs. 1, 2, 4 and 5 the expression becomes

$$\begin{aligned} I(s + ds, \hat{s}, t + dt) - I(s, \hat{s}, t) = &- \kappa I(s, \hat{s}, t) ds - \sigma_s I(s, \hat{s}, t) ds + \kappa I_b(s, t) ds \\ &+ \left(\frac{\sigma_s}{4\pi} \int_{4\pi} I(\hat{s}_i)\Phi(\hat{s}_i \cdot \hat{s}) d\Omega_i \right) ds. \end{aligned} \tag{6}$$

Upon using truncated Taylor series, the outgoing intensity may be written as

$$I(s + ds, \hat{s}, t + dt) \approx I(s, \hat{s}, t) + dt \frac{\partial I}{\partial t} + ds \frac{dI}{ds}. \tag{7}$$

With this expression interpreted as an equality, Eq. 6 may be simplified to

$$\frac{1}{c}\frac{\partial I}{\partial t} + \frac{dI}{ds} = -\kappa I - \sigma I + \kappa I_b + \frac{\sigma_s}{4\pi} \int_{4\pi} I(\hat{s}_i)\Phi(\hat{s}_i \cdot \hat{s}) d\Omega_i. \tag{8}$$

We have used the fact that $c = ds/dt$, where c is the propagation velocity . The first term on the left hand side is negligible as compared to the second and will not be further used in the analysis.

After introducing the extinction coefficient defined in (3), the previous equation becomes

$$\frac{dI(\hat{s})}{ds} = \hat{s} \cdot \nabla I = -\beta I + \kappa I_b + \frac{\sigma_s}{4\pi} \int_{4\pi} I(\hat{s}_i)\Phi(\hat{s}_i \cdot \hat{s}) d\Omega_i. \tag{9}$$

Equation 9 is the radiation energy balance for an infinitesimal beam, and in order to calculate a volume balance, this expression should be integrated over all solid angles,

$$\int_{4\pi} \hat{s} \cdot \nabla I d\Omega = \nabla \cdot \int_{4\pi} I \hat{\mathbf{s}} d\Omega$$

$$\int_{4\pi} \hat{s} \cdot \nabla I d\Omega = -\int_{4\pi} \beta I d\Omega + 4\pi\kappa I_b + \frac{\sigma_s}{4\pi} \int_{4\pi} I(\hat{s}_i) \left(\int_{4\pi} \Phi(\hat{s}_i \cdot \hat{s}) d\Omega_i \right) d\Omega. \quad (10)$$

Since the beam direction and space coordinates are independent variables, we can change the order of the integral and differential operators on the left hand side of Eq. 10. Also, on the right hand side the order of integration has been inverted, applying the Ω-integration to the only part depending on it, the scattering phase function Φ. This last integration can be carried out using the condition $\int_{4\pi} \Phi(\hat{s}_i \cdot \hat{s}) d\Omega_i = 4\pi$. It is convenient to introduce the definition

$$\mathbf{q} = \int_{4\pi} I \hat{\mathbf{s}} d\Omega, \quad (11)$$

in Eq. 10 to write

$$\begin{aligned} \nabla \cdot \mathbf{q} &= 4\pi\kappa I_b - \beta \int_{4\pi} I(\hat{\mathbf{s}}) d\Omega + \sigma_s \int_{4\pi} I(\hat{s}) d\Omega \\ &= \kappa \left(4\pi I_b - \int_{4\pi} I(\hat{\mathbf{s}}) d\Omega \right) \\ &= \kappa \left(4\sigma T^4 - \int_{4\pi} I(\hat{\mathbf{s}}) d\Omega \right) \end{aligned} \quad (12)$$

In the last equality, we have used the expression for the black body heat radiation in terms of the temperature, $I_b = \sigma T^4/\pi$, where T is the temperature and σ is the Stefan–Boltzmann constant.

The integration domain and boundary conditions are naturally defined in Cartesian coordinates (see Fig. 1), thus, in order to integrate Eq. 9, it is convenient to express the general direction s in this set of coordinates. For this procedure, we have used the method proposed in reference (Mishra 2007) with small modifications. Consider a Cartesian coordinate system and integrate over the elemental solid angle $\Delta\Omega^m$ and associate the direction of propagation $\hat{\mathbf{s}}$ with its perpendicular elemental solid angle Ω^m as defined in Fig. 2.

Equation 9 can be written as

$$\frac{\partial I^m}{\partial x} D_x^m + \frac{\partial I^m}{\partial y} D_y^m + \frac{\partial I^m}{\partial z} D_z^m = -\beta I^m \Delta\Omega^m + S_b \Delta\Omega^m, \quad (13)$$

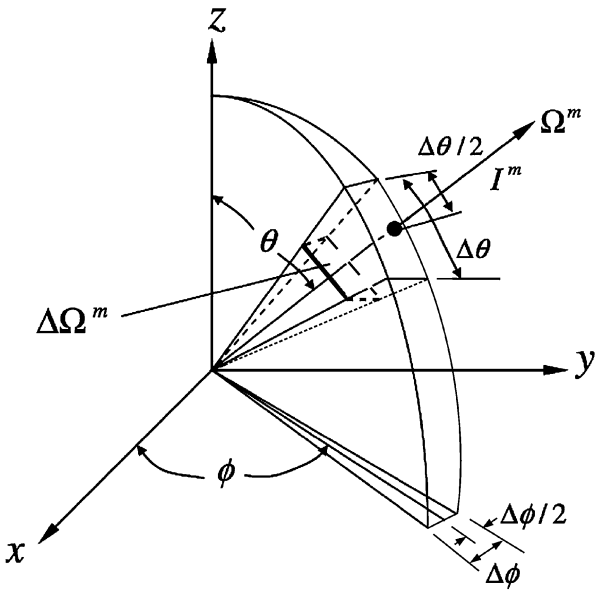

Fig. 2 Definition of angles for the calculation of heat radiation

with

$$S_b = \kappa\left(\frac{\sigma T^4}{\pi}\right) + \frac{\sigma_s}{4\pi}\int_{4\pi} I(\Omega')\Phi(\Omega,\Omega')d\Omega'. \tag{14}$$

Note that Ω^m represents an arbitrary direction, and for each Ω^m direction corresponds a pair of θ^m and ϕ^m. See Fig. 2.

If $\hat{n}$ is the outward normal to a surface, then D^m is given by

$$D^m = \int_{\Delta\Omega^m} (\hat{n}\cdot\hat{s}^m)d\Omega, \tag{15}$$

where $\hat{s}^m = (\sin\theta^m\cos\phi^m)\hat{i} + (\sin\theta^m\sin\phi^m)\hat{j} + (\cos\theta^m)\hat{k}$. When $\hat{n}$ is pointing towards one of the positive coordinate directions, D_x^m, D_y^m and D_z^m are given by

$$\begin{aligned} D_x^m &= \int_{\phi^m-\frac{\Delta\phi}{2}}^{\phi^m+\frac{\Delta\phi}{2}}\int_{\theta^m-\frac{\Delta\theta}{2}}^{\theta^m+\frac{\Delta\theta}{2}} \sin^2\theta\cos\phi\, d\theta\, d\phi \\ &= \cos\phi^m \sin\left(\frac{\Delta\phi}{2}\right)[\Delta\theta - \cos 2\theta^m \sin\Delta\theta] \end{aligned} \tag{16}$$

$$D_y^m = \int_{\phi^m - \frac{\Delta\phi}{2}}^{\phi^m + \frac{\Delta\phi}{2}} \int_{\theta^m - \frac{\Delta\theta}{2}}^{\theta^m + \frac{\Delta\theta}{2}} \sin^2\theta \sin\phi \, d\theta \, d\phi$$
$$= \sin\phi^m \sin\left(\frac{\Delta\phi}{2}\right)[\Delta\theta - \cos 2\theta^m \sin\Delta\theta] \tag{17}$$

$$D_z^m = \int_{\phi^m - \frac{\Delta\phi}{2}}^{\phi^m + \frac{\Delta\phi}{2}} \int_{\theta^m - \frac{\Delta\theta}{2}}^{\theta^m + \frac{\Delta\theta}{2}} \cos\theta \sin\theta \, d\theta \, d\phi$$
$$= \sin\theta^m \cos\theta^m \sin(\Delta\theta)\Delta\phi \tag{18}$$

For $\hat{n}$ pointing towards the negative coordinate directions, the signs of D_x^m, D_y^m and D_z^m are opposite to those obtained from Eqs. 16, 17 and 18. In Eq. 13

$$\Delta\Omega^m = \int_{\Delta\Omega^m} d\Omega = \int_{\phi^m - \frac{\Delta\phi}{2}}^{\phi^m + \frac{\Delta\phi}{2}} \int_{\theta^m - \frac{\Delta\theta}{2}}^{\theta^m + \frac{\Delta\theta}{2}} \cos\theta \, d\theta \, d\phi = 2\sin\theta^m \sin\left(\frac{\Delta\theta}{2}\right)\Delta\phi \tag{19}$$

Using expressions (16–19), Eq. 13 is integrated in the Cartesian domain.

3.2 *Energy Conservation Equation Including Radiative Heat Transfer*

The energy conservation equation for a homogeneous medium, including conduction, convection, and radiative heat transfer, is given by

$$\rho C_v \left(\frac{\partial T}{\partial t} + \mathbf{v} \cdot \nabla \mathbf{T}\right) = k\nabla^2 T - \nabla \cdot \mathbf{q}, \tag{20}$$

where ρ, C_v and k are the density, heat capacity and conductivity of the medium and $\mathbf{v}$ is the velocity. For future reference, the diffusivity is defined by $\alpha = k/\rho C_v$. The radiative term $\mathbf{q}$ is a heat source (or sink, depending on whether the beam transfers energy to the material or the opposite) whose expression in terms of the beam intensity is given by Eq. 12. The physical properties of the medium are assumed to be known and constant.

3.3 Mass and Momentum Conservation Equations

We assume that the Boussinesq approximation is valid in the present analysis and thus, the mass conservation equation can be written as

$$\nabla \cdot \mathbf{v} = 0, \tag{21}$$

and the momentum conservation is equation is

$$\rho_o \left(\frac{\partial \mathbf{v}}{\partial t} + (\mathbf{v} \cdot \nabla)\mathbf{v} \right) = -\nabla p + \mu \nabla^2 \mathbf{v} + \rho \mathbf{g}. \tag{22}$$

In this equation, p is the pressure, μ is the dynamic viscosity, and the $\mathbf{g}$ is the gravity acceleration vector. The state equation $\rho = \rho_o(1 + \beta_o(T - T_C))$ was used to eliminate the variable density from Eq. 22. In the last expression, β_o is the volumetric expansion coefficient and T_C is a reference temperature.

3.4 Initial and Boundary Conditions

Initial and boundary conditions corresponding to Eqs. 9, 20, 21 and 22 must be specified and since the mathematical nature of the equations is different, it is important to guarantee that conditions for the whole set are consistent and reflect the physical situation of interest. We consider the geometry sketched in Fig. 1.

Relation (9) is a first order, ordinary differential equation, and we need to specify the intensity at one fixed point on s, considering all possible directions. Equivalently, we may establish initial conditions on the Cartesian coordinates corresponding to all six walls (see Eq. 13). From an energy balance at a boundary, the intensity can be expressed as:

$$I^m = \frac{\varepsilon_o \sigma T_o^4}{\pi} + \left(\frac{1 - \varepsilon_o}{\pi} \right) I^m_{ref} + I^m_{ext}, \tag{23}$$

where ε is the emissivity and the subscript o refers to properties and temperature on the boundary. I^m_{ref} is the intensity reflected in the m direction, which is described by Snell's law and I^m_{ext} is an externally imposed intensity. The variable I^m_{ext} is zero except at the window (see Fig. 1), T_o is a prescribed temperature as described in the next paragraph. The energy conservation equation is a partial differential equation, parabolic in time and elliptic in space, and therefore we need to specify the initial temperature, and the temperature at all boundaries of the integration domain. We assume that the temperature at the whole boundary except at a window, is T_C. At the window, the condition on the temperature is

$$k \frac{dT}{dx} = I_{ext} \Delta\Omega + \varepsilon_w \sigma (T^4_{amb} - T^4(x = 0)), \tag{24}$$

where T_{amb} is an external, ambient temperature and ε_w is the emissivity of the window. Non-slip boundary conditions are considered for all boundaries, including the window.

4 Numerical Integration

The beam intensity equation and the mass, momentum and energy conservation equations were discretized and solved with numerical methods. Equation 9 is expressed as Eq. 13 and discretized with the finite volume method. The pressure decoupling in the momentum equation was accomplished with the SIMPLEC algorithm. This method is essentially a guess-and-correct procedure for the calculation of pressure on a staggered grid arrangement of the system. Since this is a explicit method the contribution of velocity and pressure suggests solve work like a non-coupled system (Versteeg 1995). In all calculations, we used a regular discretization mesh of $40 \times 40 \times 40$ volumes for the cube, and the number of directions used in the angular discretization for the calculation of the radiation effects is 53 in direction θ and 100 in direction ϕ, which leads to a total of 5300 directions of beam propagation. We make the integration using SI units and the time step is 0.05 s.

We used the following sequence to integrate the set of coupled Eqs. 9, 12, 20, 21 and 22,

(a) Initially ($t = 0$), the velocity $\mathbf{v}$ and the heat source $\mathbf{q}$ are assumed to be zero and the initial temperature is T_C.
(b) With a known temperature field, integrate (9) in the form of Eq. 13, considering (23) to obtain the intensity in any direction and at all points of the θ^m and ϕ^m mesh.
(c) Calculate $\nabla \cdot \mathbf{q}$ for each control volume using Eq. 12.
(d) Solve Eq. 20, to determine the temperature field. Except at the window, the temperature at all boundaries is prescribed. The boundary condition at the window is Eq. 24.
(e) Determine velocity and pressure field, solving Eqs. 21 and 22.
(f) Return to step (b) using updated values to find the solution at time $t + \Delta t$.
(g) Stop when the maximum time has been attained.

5 Results

In Figs. 3, 4 and 5, we display sample calculations of the dynamic and thermal behavior of the system using the following parameters. The temperatures at the walls of the box are $T_C = 473\,\text{K}$ and $T_H = 973\,\text{K}$, while the ambient temperature is $T_{amb} = 296\,\text{K}$. The results are expressed in terms of a normalized temperature $T^* = (T - T_C)/(T_H - T_C)$. The radiation beam is assumed to enter horizontally

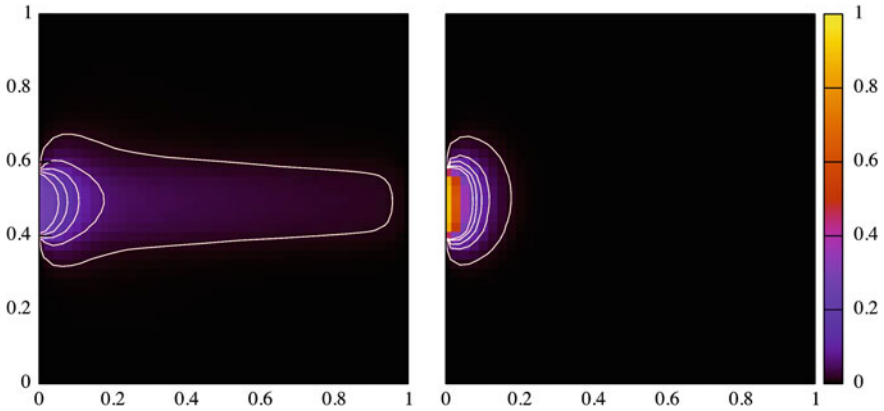

Fig. 3 Temperature field in the central cross section of the cube (see Fig. 1) at an early time $t = 0.05$ s. *Left panel*: temperature field for a container with a participating medium. *Right panel*: temperature field for a container with a non-participating material. The color code is the same for the two figures and the isotherms correspond to 0.01, 0.06, 0.11, 0.16 and 0.21 scaled temperature units

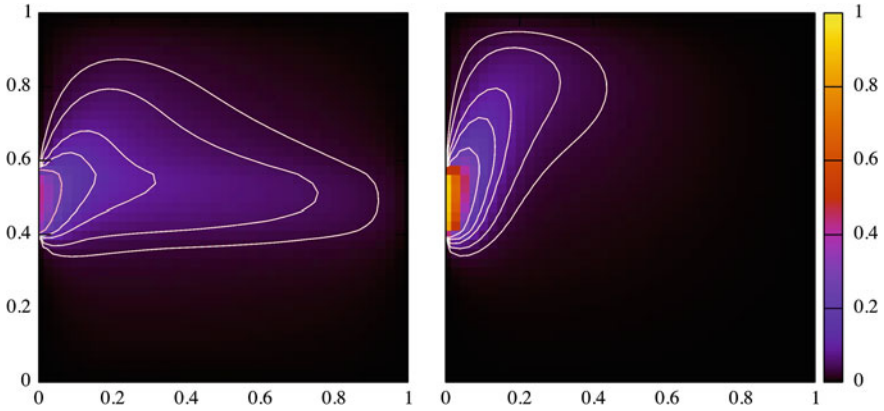

Fig. 4 Temperature field on the central cross section of the box (see Fig. 1) at time $t = 4.0$ s. *Left panel*: Participating material. *Right panel*: Non-participating material. The color code is the same for the two figures, and the lines correspond to isotherms 0.025, 0.045 and 0.085, 0.125 and 0.225 scaled temperature units

through the window (x-direction) and has an intensity of $I_{ext} = 5 \times 10^6\,\mathrm{W/m^2}$, the emissivity of the wall and the window are set equal to one, $\varepsilon_o = \varepsilon_w = 1.0$. The side L of the cubic container is taken as 1 m and the working fluid is assumed to be a hypothetical material with the following physical properties: $\kappa = 1.5$, $\sigma = 0$, $\beta_o = 0.0033\,\mathrm{K}^{-1}$ and $k = 2\,\mathrm{W/mK}$. These parameters correspond to a Rayleigh number $Ra = g\beta\Delta TL^3/(\alpha\nu) = 10^5$, and a Prandtl number $Pr = \nu/\alpha = 0.7$.

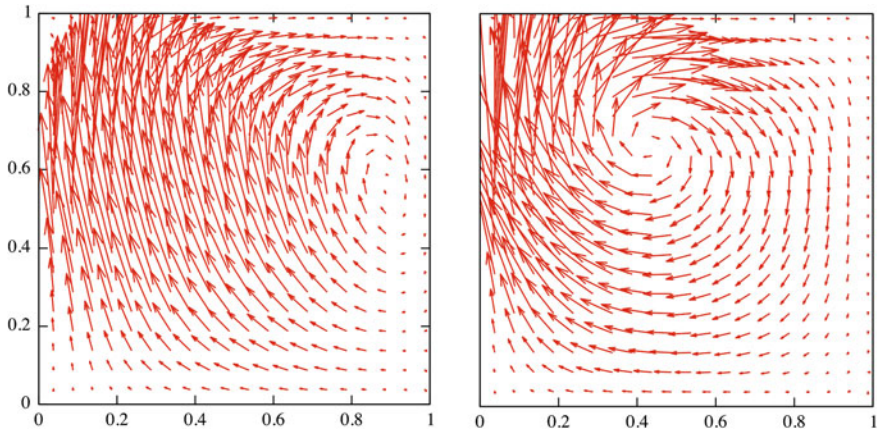

Fig. 5 Velocity field on the central cross section of the box (see Fig. 1) at time $t = 4.0$ s. *Left panel*: Participating material. *Right panel*: Non-participating material

The normalized temperature field at the mid vertical plane of the cube is shown in Fig. 3 left, for an early time ($t = 0.05$ s, which is equivalent to 0.0004 diffusive times). For purposes of comparison, Fig. 3 right, shows the temperature field in a cavity with the same dimensions and with a small heated zone located at the same position of the window but assuming that the medium is not participating and that the temperature of the heated zone is $T_H = 973$ K. The different distribution of the temperature is evident from the figure; for the participating medium, the path of the radiation beam is clearly shown by a temperature rise in a horizontal region starting at the window. In contrast, in the cavity filled with a non participating material, heat is transferred only by diffusion from the heated zone close to the heated wall. Another important difference between the two processes is that in the first case (participating material), the highest temperature in the vicinity of the window, is smaller than the corresponding for the cavity filled with a non-participating material, potentially reducing the radiation energy losses.

In Fig. 4, the temperature field in the mid vertical plane and at $t = 4.0$ s is shown for a container filled with a participating (left) and non-participating (right) materials. In the first case, high temperature region shows two zones, a radiative dominated horizontal. In the two temperature fields, an ascending convective plume can be identified, but in the participating material case, plume is much wider and a horizontal zone heated mostly by radiation is present. In the non participating material, a typical (detached) boundary layer is formed. The region transferring heat is clearly larger and the temperatures are lower for the box with a participating material.

The dynamic behavior corresponding to the temperature fields of Fig. 4 are displayed in Fig. 5. For purposes of clarity, we have only plotted every other vector in the two directions. In the left image (participating medium), the velocity field shows a larger ascending area, indicating that more mass participates in the

heat evacuation fluid. The image on the right hand side displays a typical velocity distribution of a detached dynamic boundary layer.

6 Conclusions

A numerical model for the heat transfer process that includes conduction, convection and radiation has been constructed. This tool can be used to assess the merits of the design of a heat exchanger with a participating medium as the working fluid. Exploratory calculations indicate that the material active in the heat exchange process is much larger when the container is filled with a participating material as it absorbs heat in the bulk of the working fluid.

Acknowledgments M.A.R.C. acknowledges support from CONACYT-Mexico through an MSc grant. We wish to thank Mr. José Núñez for discussions on the model and advice on the development of the code.

References

Mishra SC, Roy HK (2007) Solving transient conduction and radiation heat transfer problems using the lattice Boltzmann method and the finite volume method. J Comp Phys 223:89–107

Romero M, Buck R, Pacheco J (2002) An update on solar central receiver systems, projects, and technologies. ASME J Solar Energy Eng 124:98–108

Versteeg HK, Malalasekera W (1995) An introduction to computational fluid dynamics. Longman Scientific and Technical, New York

Analysis of the Oberbeck-Boussinesq Approximation as a First Step to its Applications to the Czochralski Process

A. C. Pérez-Guerrero N, R. Chicharro S, I. Camarillo R and E. Vázquez L

Abstract We derive the Oberbeck-Boussinesq approximation using a rigorous thermodynamic approach, within the framework of one of the simplest implicit constitutive theories.

1 Introduction

The proposed work is part of a larger project on the growth of crystals by the badly named technique Czochralski. Here our attention is focused on the study of the behavior of the melt in the crucible. It has been known that convective flow plays an important role in material processing such as crystal growth systems. Changes in the flow pattern such as the onset of convective flow and transition to oscillatory flow cause inhomogeneous doping, and therefore macroscopic defects such as the

A. C. Pérez-Guerrero N (✉)
Área de Mecánica Estadística, Departamento de Física,
Universidad Autónoma Metropolitana, Iztapalapa, Mexico
e-mail: acpgn@yahoo.com

R. Chicharro S · E. Vázquez L
Laboratorio de Fluidos, Departamento de Física, Facultad de Ciencias,
Universidad Nacional Autónoma de México, Coyacan, Mexico

I. Camarillo R
Laboratorio de Crecimiento de Cristales, Departamento de Física,
Universidad Autónoma Metropolitana, Iztapalapa, Mexico

A. C. Pérez-Guerrero N
On sabbatical year at the Laboratorio de Fluidos, Departamento de Física, Facultad de Ciencias, Universidad Nacional Autónoma de México, Coyacan, Mexico

J. Klapp et al. (eds.), *Experimental and Theoretical Advances in Fluid Dynamics*, Environmental Science and Engineering, DOI: 10.1007/978-3-642-17958-7_34,

segregation in the crystal. Literature on the subject indicates that changes in the geometry of the crucible generate changes in the flow of the melt (Xu et al. 2007). However, few experimental works and their respective simulations take into account this effect. This review lead us to the Oberbeck-Boussinesq (O-B) approximation (Mokthari et al. 2009).

In this search we find that there are different points of view to the formulation of Boussinesq equations, which we call the attention, so for example, Barletta (2009) points out the discrepancy between the different equations for the balance of energy. He mentions at least three or more different ways to define the equation for the rate of change of internal energy in the (O-B) equation, (a) Chandrasekhar (1981) and White, (b) Enthalpy representation and (c) Landau and Lifshitz, Bejan, Kundu-Cohen. On the development of the approximation of (O-B) for the momentum equation there are two main investigations, one by Spiegel and Veronis (1960), and a more recent one presented by Rajagopal et al. (2009).

Spiegel and Veronis (1960) determine under what conditions the geometric approach of O-B can be applied. They argue that the equations are formally equivalent to those for an incompressible system when the static temperature gradient is replaced by its excess over the adiabatic, and c_v is replaced by c_p. Rajagopal et al. (2009) try to obtain the same approach from a hierarchy with respect to the Froude's number.

In this work we verify that by considering the density as a function of pressure and temperature as independent variables, as noted by Rajagopal et al. (2009) and Spiegel and Veronis (1960), throughout the deduction of the balance equations, one has to impose certain conditions to achieve the set of (O-B) approximate equations. Taking into consideration the case of a buoyant force, and considering a multicomponent fluid (Faghri et al. 1969), the Gibbs' energy as a function of temperature, pressure and concentrations was used instead of the internal energy, obtaining a set of generalized equations of the (O-B), such that, when considering constant pressure, they are reduced to the balance equations already mentioned.

In order to analyze from a thermodynamic point of view, temperature $\theta(x, t)$ and pressure $p(x, t)$ are considered the independent variables and as independent variables and the density $\rho(\theta, p)$. It is obvious that the density depends implicitly on x and t. Although it seems redundant to write the equations denoting the explicit dependence on temperature and pressure from a thermodynamic point of view, we believe that this notation is needed. We consider a mass element $m \in M$ where M is the total system mass. The mass $m(x, t)$ is contained in a geometric volume element $d\vartheta(x, t)$. When $\lim \Delta\vartheta \to 0$, then $\rho(\theta, p) = \Delta m/\Delta\vartheta$. Also $\rho(\theta(x, t), p(x, t))$, thus ρ depends on x and t.

2 Mass Balance

The principle of conservation of mass for an element of mass $m \in M$, volume $\vartheta(x, t)$ and density $\rho(\theta, p)$ can be expressed as,

$$\frac{d\mathrm{m}}{dt} = \frac{d}{dt}\int_{\vartheta} \rho(\theta,p)d\vartheta$$
$$= \int_{\vartheta}\left[\left[\frac{\partial\rho(\theta,p)}{\partial\theta}\right]_p \frac{d\theta}{dt} + \left[\left[\frac{\partial\rho(\theta,p)}{\partial p}\right]_\theta \frac{dp}{dt} + \rho(\theta,p)\nabla\cdot\mathbf{u}\right]\right]d\vartheta \quad (1)$$

Since $d\vartheta \neq 0$, the kernel of the integral must be zero and therefore

$$\left[\frac{\partial\rho(\theta,p)}{\partial\theta}\right]_p \frac{d}{dt}\theta + \left[\frac{\partial\rho(\theta,p)}{\partial\theta}\right]_\theta \frac{d}{dt}p + \rho(\theta,p)\nabla\cdot\mathbf{u} = 0 \quad (2)$$

Taking into account the definitions of the volumetric expansion coefficient α and compressibility κ, written in terms of the density,

$$\alpha(\theta,p) = -\frac{1}{\rho(\theta,p)}\left[\frac{\partial\rho(\theta,p)}{\partial\theta}\right]_p,\ \kappa(\theta,p) = \frac{1}{\rho(\theta,p)}\left[\frac{\partial\rho(\theta,p)}{\partial p}\right]_\theta \quad (3)$$

We can finally express the mass balance as,

$$-\alpha(\theta,p)\frac{d}{dt}\theta(x,t) + \kappa(\theta,p)\frac{d}{dt}p(x,t) = -\nabla\cdot\mathbf{u}(x,t) \quad (4)$$

Equation 4 corresponds to a local state equation, whose state variables, $\rho(x, t)$, $\theta(x, t)$ and $p(x, t)$ change with time. If the process is isobaric then $\kappa\frac{d}{dt}p = 0$, and the divergence of the velocity is proportional to $\alpha\frac{d\theta}{dt}$, that is, $\nabla\cdot\mathbf{u} = -\alpha\frac{d}{dt}\theta$ as shown by Rajagopal. If the process is isothermal, then $\alpha\frac{d}{dt}\theta = 0$, and $\nabla\cdot\mathbf{u} = \kappa\frac{d}{dt}p$ is proportional to the product of the compressibility coefficient and the pressure change with time. On the other hand, the volumetric expansion and the isothermal compressibility will be functions of temperature and pressure only, when the density is the initial density ρ_0. Obviously, if the fluid is incompressible, then the density remains constant and the divergence of velocity is zero.

3 Momentum Balance

The local equation of the linear momentum balance is also slightly different when considering the density dependence with temperature and pressure. This can be expressed for a mass element $\mathrm{m} \in \mathrm{M}$ as,

$$\frac{d}{dt}\vec{p}(\mathrm{m},\mathrm{t}) = \int_{\vartheta}\frac{d}{dt}[\rho(\theta,p)\mathbf{u}(x,t)d\vartheta] = \int_{\vartheta}\rho(\theta,p)\frac{d}{dt}\mathbf{u}(x,t)d\vartheta \quad (5)$$

And the forces are,

$$\mathcal{F}(m,t) = -\int_{\vartheta} \rho(\theta,p)\mathbf{g}\, d\vartheta + \int_{\vartheta} \rho'(\theta,p)\mathbf{b} d\vartheta - \int_{\partial\vartheta} p(x,t)\, d\mathbf{a} + \int_{\partial\vartheta} \tau(x,t)\, d\mathbf{a} \tag{6}$$

where surface forces are considered through the pressure $p(x, t)$ and the stress tensor $\tau(x, t)$. Body forces are gravity and buoyancy. The buoyancy term is necessary to understand the origin of Rayleigh-Benard instabilities. In order to take into account the effects of buoyancy, we can write Eqs. 5 and 6 in their local form, and rewrite the terms associated with body and surface forces as follows

$$\frac{d}{dt}\mathbf{u}(\mathrm{x,t}) = \frac{1}{\rho(\theta,p)}[-\nabla p(x,t) + \nabla\cdot\tau(x,t) + \rho'(\theta,p)\mathbf{b} - \rho(\theta,p)\mathbf{g}] \tag{7}$$

By the Archimedes principle we replace $\rho'(\theta, p)\mathbf{b}$ by $\mathbf{g}$ and the density $\rho' = \rho + \delta\rho$ is considered a small aproximation. Then, if $\theta(x, t)$ or $p(x, t)$ change, then $\delta\rho(\theta, p)/\rho(\theta, p)$ can be approximated as,

$$\begin{aligned}\frac{\delta\rho(\theta,p)}{\rho(\theta,p)} &= \frac{1}{\rho(\theta,p)}\left[\left(\frac{\partial\rho(\theta,p)}{\partial\theta(x,t)}\right)_p \Delta\theta(x,t) + \left(\frac{\partial\rho(\theta,p)}{\partial p(x,t)}\right)_\theta \Delta p(x,t) + \cdots\right] \\ &\approx -\alpha(\theta,p)\Delta\theta(x,t) + \kappa(\theta,p)\Delta p(x,t)\end{aligned} \tag{8}$$

In (8) we take κ and α were defined in (3). Then, introducing (8) in the (7) we get

$$\begin{aligned}\frac{d}{dt}\mathbf{u}(x,t) = &-\nabla\frac{p(x,t)}{\rho(\theta,t)} - p(x,t)(\alpha(\theta,p)\nabla\theta(x,t) - \kappa(\theta,p)\nabla p(x,t)) \\ &+\nabla\cdot\frac{\tau(x,t)}{\rho(\theta,p)} + \tau(x,t)(-\alpha(\theta,p)\nabla\theta(x,t) + \kappa(\theta,p)\nabla p(x,t)) \\ &-(\alpha(\theta,p)\Delta\theta(x,t) - \kappa(\theta,p)\Delta p(x,t))\mathbf{g}\end{aligned} \tag{9}$$

This equation can be considered as a generalization of the equation (O-B) for linear momentum, taking into consideration that the thermodynamic variables temperature and pressure are independent. If the density does not change with respect to changes in pressure, then (9) is reduced to,

$$\frac{d}{dt}\mathbf{u}(x,t) = \frac{1}{\rho(\theta,p)}(-\nabla p(x,t) + \nabla\cdot\tau(x,t)) - \alpha(\theta,p)\Delta\theta\mathbf{g} \tag{10}$$

corresponding to the Oberbeck-Boussinesq expression, generally used in fluids.

4 Energy Balance

The next step is to check the energy balance equation, obtained from the principle of conservation of energy. Here we try to verify that the fact of taking c_p rather than c_v is correct since, as stated in the references, there are at least three ways to represent the term associated to the internal energy.

The total energy balance is the sum of the energies contained in the volume ϑ of the body $\mathrm{m} \in \mathrm{M}$ and it has to be balanced with the power flow. Then the energy balance can be expressed as $\frac{d}{dt}E(m,\mathrm{t}) = \Theta(m,\mathrm{t}) + \wp(m,\mathrm{t})$ where $\frac{d}{dt}E(m,\mathrm{t})$ is the change of total energy, $\Theta(\mathrm{m}, t)$ the heat applied per unit of time, and $\wp(\mathrm{m},\mathrm{t})$ the mechanical power. The total energy $\mathcal{E}(\mathrm{m}, t)$ is defined in terms of the kinetic $\mathcal{K}(\mathrm{m}, t)$ and the internal $\mathcal{U}(\mathrm{m}, t)$ energies. The change in time of the total energy can be expressed as,

$$\begin{aligned}\frac{d}{dt}\mathcal{E}(m,t) &= \frac{d}{dt}\Big[\mathrm{K}(m,t)+\mathrm{U}(m,t)\Big] \\ &= \int_{\vartheta}\rho(\theta,p)\frac{d}{dt}\mathbf{u}(x,t)\mathbf{u}(x,t)d\vartheta + \int_{\vartheta}\rho(\theta,p)\dot{u}(x,t)d\vartheta\end{aligned} \tag{11}$$

Here we use Eq. 4. It is obvious that the first term within the square brackets correspond to the kinetic energy of the mass, $\mathrm{m} \in \mathrm{M}$. Here $\mathbf{u}(x,t)$ and $\frac{d}{dt}\mathbf{u}(x,t)$ are respectively the velocity and acceleration of m. The second term inside the parentheses corresponds to the internal energy associated with the mass m where u is the specific internal energy density. We denote the energy supply (or heat supply) of m by $\Theta(m, t)$ and assume that it can be given by

$$\Theta(m,t) = \int_{\partial\vartheta} h(x,t,\partial m)da + \int_{\vartheta}\rho(\theta,\mathrm{p})r(x,t)d\vartheta \tag{12}$$

where $\mathrm{h}(x, t, \partial\mathrm{m})$ is the contact heat supply and $\mathrm{r}(x, t)$ is the energy supply density due to external sources. Also by Fourier-Stokes, we can write the heat flux as

$$h(\mathrm{x},\mathrm{t},\partial m) = h(\mathrm{x},\mathrm{t},\mathbf{n}) = \mathbf{q}(\mathrm{x},\mathrm{t})\cdot\mathbf{n} \tag{13}$$

where $\mathbf{q}(x, t)$ is called the heat flux vector, and $\mathbf{n}$ is the exterior unit vector normal to $\partial\mathrm{m}$ at time t in x. Finally the mechanical power $\wp(m, t)$ for the mass $\mathrm{m} \in \mathrm{M}$ can be written as,

$$\wp(m,t) = \int_{\partial\vartheta}\mathbf{u}(x,t)\cdot(\tau(x,t)+p(x,t))\mathbf{n}da + \int_{\vartheta}\mathbf{u}(x,t)\delta\rho(\theta,p)\mathbf{g}\mathrm{d}\vartheta \tag{14}$$

With (11), through (14), the equation of energy balance becomes,

$$\int_{\vartheta}\left[\rho(\theta,p)\frac{d}{dt}\mathrm{u}(\theta,p)+\nabla\cdot\mathbf{q}(\mathrm{x,t})+p(\mathrm{x,t})\nabla\cdot\mathbf{u}-\tau(\mathrm{x,t}):\nabla\mathbf{u}-\rho\mathrm{r}(\mathrm{x},t)\right]d\vartheta \quad (15)$$

Thus for all $d\vartheta$ the kernel of the integrand must be zero, i.e.

$$\begin{aligned}\rho(\theta,p)\frac{d}{dt}u(\theta,p) = &-\nabla\cdot\mathbf{q}(x,t)-p(x,t)\nabla\cdot\mathbf{u}(x,t)\\ &+\tau(x,t):\nabla\mathbf{u}(x,t)+\rho(\theta,p)r(x,t)\end{aligned} \quad (16)$$

In this expression $u(\theta,p)$ corresponds to the change of internal energy of the mass m. We also know that, if we take the temperature $\theta(x,t)$ and the pressure $p(x,t)$ as independent state variables, it is better to use the enthalpy or Gibbs free energy. The Gibbs free energy $g(\theta(x,t),p(x,t),c_i(x,t))$ per unit mass is defined as

$$g(\theta(x,t),p(x,t),c_i(x,t)) = u(\theta,p) - \theta(x,t)\eta(\theta,p) + v(\theta,p)p(x,t) \quad (17)$$

where $\eta(\theta,p)$ is the entropy density. Replacing $\dot{u}(\theta,p)$ in Eq. 16 as a function of $g(\theta,p,c_i)$ and $\eta(\theta,p)$ we get

$$\begin{aligned}\dot{u}(\theta,p) = &\left(\frac{\partial g(\theta,p,c_i)}{\partial\theta(x,t)}\right)_{p,c_i}\frac{d\theta(x,t)}{dt}+\left(\frac{\partial g(\theta,p,c_i)}{\partial p(x,t)}\right)_{\theta,c_i}\frac{dp(x,t)}{dt}\\ &+\left(\frac{\partial g(\theta,p,c_i)}{\partial c_i(x,t)}\right)_{\theta,p}\frac{dc_i(x,t)}{dt}-\theta(x,t)\left(\frac{\partial\eta(\theta,p)}{\partial p(x,t)}\right)_{\theta}\frac{dp(x,t)}{dt}\\ &-\left[\theta(x,t)\left(\frac{\partial\eta(\theta,p)}{\partial\theta(x,t)}\right)_{p}+p(x,t)v^2(\theta,p)\left(\frac{\partial\rho(\theta,p)}{\partial\theta(x,t)}\right)_{p}+\eta(\theta,p)\right]\frac{d\theta(x,t)}{dt}\\ &-\left[p(x,t)v^2(\theta,p)\left(\frac{\partial\rho(\theta,p)}{\partial p(x,t)}\right)+v(\theta,p)\right]\frac{dp(x,t)}{dt}\end{aligned} \quad (18)$$

Taking into consideration Maxwell relations, using (4) and rearranging terms we obtain

$$\begin{aligned}\frac{d\mathrm{u}(\theta,p)}{dt} = &\,c_p(\theta)\frac{d\theta(x,t)}{dt}-p(x,t)v(\theta,p)\nabla\cdot\mathbf{u}(x,t)\\ &+\mu(\theta,p,c_i)\frac{dc_i(x,t)}{dt}+(v(\theta,p)-\theta(x,t)\alpha(\theta)v(\theta,p))\frac{dp(x,t)}{dt}\end{aligned} \quad (19)$$

We know that, $v(\theta,p)-\theta(x,t)\alpha(\theta)v(\theta,p) = \left(\frac{\partial h}{\partial p}\right)_{\theta}$ where h is the enthalpy function. Substituting this term in (19), we obtain

$$\begin{aligned}\dot{u}(\theta,p) = &\,c_p(\theta)\frac{d\theta(x,t)}{dt}-p(x,t)v(\theta,p)\nabla\cdot\mathbf{u}(x,t)\\ &+\mu(\theta,p,c_i)\frac{dc_i(x,t)}{dt}+\left(\frac{\partial h}{\partial p}\right)_{\theta}\frac{dp(x,t)}{dt}\end{aligned}$$

Introducing this results into (16) we obtain,

$$\rho(\theta,p)\left[c_p(\theta)\frac{d\theta(x,t)}{dt}+\mu(\theta,p,c_i)\frac{dc_i(x,t)}{dt}+\left(\frac{\partial h(\theta,p)}{\partial p(x,t)}\right)_\theta\frac{dp(x,t)}{dt}\right]$$
$$=-\nabla\cdot\mathbf{q}(x,t)+\tau(x,t):\nabla\mathbf{u}(x,t)+\rho(\theta,p)r(x,t) \tag{21}$$

If the pressure and concentration are constants, and there is no heat supply r(x, t), Eq. 21, is reduced to the equation of energy of the Oberbeck-Boussinesq model, that is

$$\rho(\theta,p)c_p\frac{d\theta(x,t)}{dt}=-\nabla\cdot\mathbf{q}(\mathbf{x},\mathbf{t})+\tau(x,t):\nabla\mathbf{u}(x,t) \tag{22}$$

So then, the set of main equations for the balances of mass, momentum and energy equations are established in (4), (9) and (22).

5 Conclusions

First, at this stage of research we have taken into account the thermodynamic formalism to describe mass, momentum and energy balance. In this description, temperature, pressure and velocity play the role of independent variables. The first important result is that through mass balance, we find a relationship that may be considered as an equation of state for pressure, temperature and velocity through the density.

Second, we found a direct way to obtain the general equation of motion taking into account the strength of buoyancy. This allowed us to obtain directly a competitive term between weight and buoyancy through the change in the temperature and in the thermal expansion. The mathematical expression so obtained is called the approximation of Oberbeck-Boussinesq. While the isothermal compressibility factor, is not important for liquids, it may be so for gases.

Third, regarding the balance of the rate of energy, it is clear that if a liquid made up of different components is considered, then the heat capacity at constant volume is not the most convenient. So in the case of a thermodynamic process where the temperature and pressure are variable independent, it is much better to use the thermodynamic potential and consider the description through Gibbs' energy. This potential leads to a more general expression of the balance of power, which ultimately reduces to the Oberbeck-Boussinesq expression when the pressure is considered constant. The introduction of the chemical potential is important for the description of the Marangoni's effect (Irvin 1986), while the introduction of the buoyancy force is important for the study of the instabilities of Rayleigh-Benard-Marangoni.

Acknowledgments We appreciate the suggestions of Dr. Marcos Ley Koo.

References

Barletta A (2009) Local energy balance, specific heats, and the Oberbeck-Boussinesq approximation. Int J Heat Mass Tran. arXiv:0904.3968v1. (physics.flu-dyn)

Chandrasekhar S (1981) Hydrodynamic and Hydro magnetic stability. Dover publications, New York

Faghri A, Zhang Y (1969) Transport phenomena in multiphase system. Academic Press, New York

Irvin BR (1986) Energetics of the Marangoni instability. Langmuir 2:79–82

Mokthari F, Bouabdallah A, Zizi M, Hanchi S, Alemany A (2009) Combined effects of crucible geometry and Marangoni convection on silicon czchrolaski crystal growth. Cryst Res Technol 44(8):787–799

Rajagopal KR, Saccomandi G, Vergori L (2009) On the Oberbeck-Boussinesq approximation for fluids with pressure dependent viscosities. Nonlinear Anal 10:1139–1150

Spiegel EA, Veronis G (1960) On the Boussinesq approximation for a compressible fluid. American astronomical society. Astrophys J 131:442

Xu B, Ai X, Li BQ (2007) Rayleigh-Benard-Marangoni instabilities of low-Prandtl-number fluid in a vertical cylinder with lateral heating. Numer Heat Transf Part A 51:1119–1135

Forced Oscillations of a Membrane

Rocío Fabiola Arellano Castro, María Ester Mejía Marin and Anne Cros

Abstract This paper focuses on the resonance frequencies in a membrane. We plot the amplitude response of the cantilever when it is subjected to a sinusoidal force in its clamped extreme. We took into account the presence of air and a damping coefficient to quantify the resonant frequency shifts and the quality factors of the resonant peaks. Theoretical calculations were also developed. Despite this, the experimental results did not correlate well with the theoretical results. We therefore infer that other energy dissipations must be taken into account.

1 Introduction

It is well known that any structure has resonant frequencies. In the field of civil engineering, it is important to take them into account to avoid catastrophic disasters. These frequencies depend upon both the elastic properties and geometry of the material.

Several studies describe how to determine the Young's modulus with dynamical methods (Wilson and Lord 1973; Turvey 1990; Ganci 2009). These authors, however, omit the dissipation effects and the consequences of the presence of fluid. They measure the resonant modes "only" by sight. In our study, we present a more quantitative study since we measure the vibration amplitude caused by a driven

R. F. Arellano Castro · M. E. Mejía Marin · A. Cros (✉)
Departamento de Física, Universidad de Guadalajara, Av. Revolución 1500, Col. Olímpica, 44430 Guadalajara, Jalisco, Mexico
e-mail: anne_cros@yahoo.com

J. Klapp et al. (eds.), *Experimental and Theoretical Advances in Fluid Dynamics*, Environmental Science and Engineering, DOI: 10.1007/978-3-642-17958-7_35,

force applied to the clamped extreme of our sheet. We plot the amplitude as a function of the driven frequency.

Various studies deal with the frequency shift and quality factor of cantilevers (Blom et al. 1992; Yasumara et al. 2000). Nevertheless, they concern cantilevers in the scale of micrometers. These studies have a direct application with the atomic force microscope (AFM). This system has a resolution of the order of nanometers. The probe of this microscope consists of a microscopic silicon cantilever that "scans" the studied material surface. In the dynamic mode, the cantilever is externally excited near the fundamental resonant frequency. The contact between the cantilever and the material leads to an interaction that modifies the mode amplitude, phase and frequency. These changes provide the required information about the sample's characteristics.

This study focuses on the response of an acetate sheet to an external sinusoidal force. Theoretical preliminaries will be presented in Sect. 2. In Sect. 3, we will describe the experimental set-up. The results will be presented in Sect. 4 followed by the discussion in Sect. 5. The conclusion will be made in Sect. 6.

2 Theoretical Preliminaries

We present in Sect. 2.1 how the equation of motion for a cantilever is resolved, taking into account a damping ratio. In Sect. 2.2, we introduce a sinusoidal forcing and show how the resonance peaks are affected. In Sect. 2.3 we express the quality factor in the case of a damped cantilever.

2.1 Equation of Motion and Solutions

The equation of motion for a membrane with internal dissipation is written as:

$$EI\frac{\partial^4 y}{\partial x^4} + B\frac{\partial y}{\partial t} + m\frac{\partial^2 y}{\partial t^2} = 0 \tag{1}$$

where y is the membrane transversal displacement at longitudinal coordinate x and time t. EI is the membrane flexural modulus (Nm^2), B the damping coefficient (kg/ms) and m membrane mass by unit length (kg/m).

In order to solve this equation, we take solutions in the form of:

$$y(x,t) = \Psi(x)\theta(t) \tag{2}$$

If we substitute (2) into (1) the ordinary differential equation is easily resolved (Hodges and Pierce 2002; Ganci 2009; Turvey 1990). The solution for Ψ is written as:

$$\Psi(x) = A_1\cosh(kx) + A_2\sinh(kx) + A_3\cos(kx) + A_4\sin(kx) \tag{3}$$

Furthermore, solutions must verify the following limit conditions:

$$at\ x = 0, \begin{cases} y = 0 \\ \dfrac{\partial y}{\partial x} = 0 \end{cases} \tag{4}$$

$$at\ x = L, \begin{cases} \dfrac{\partial^2 y}{\partial x^2} = 0 \\ \dfrac{\partial^3 y}{\partial x^3} = 0 \end{cases} \tag{5}$$

The conditions (4) lead to:

$$\begin{cases} A_1 + A_3 = 0 \\ A_2 + A_4 = 0 \end{cases} \tag{6}$$

The addition of the limit conditions (5) at $x = L$ leads to:

$$1 + \cosh(kL)\cos(kL) = 0 \tag{7}$$

This equation can be solved numerically. The first three first values which verify Eq. 7 are: $k_i L = \{1.87510;\ 4.69409;\ 7.85476\}$.

On the other hand, the solution for θ is given by:

$$\theta(t) = G\, e^{-\frac{B}{2m}t} \cos(\omega_{d,i} t + \varphi) \tag{8}$$

where

$$\omega_{d,i} = \sqrt{\frac{k_i^4 EI}{m} - \left(\frac{B}{2m}\right)^2} \tag{9}$$

The damped angular frequencies $\omega_{d,i}$ are slightly different from the no-damped harmonic frequencies $\omega_{0,i} = \sqrt{k_i^4 EI/m}$. Constants G and φ depend upon initial conditions. Finally, the general solution is written as:

$$\begin{aligned} y(x,t) = \sum_{i=1}^{\infty} & A_i e^{-\frac{B}{2m}t} \cos(\omega_{d,i} t + \varphi_i) \\ & [\cosh(k_i x) + C_i \sinh(k_i x) - \cosh(k_i x) - C_i \sin(k_i x)] \end{aligned} \tag{10}$$

where A_i, φ_i and C_i are integration constants.

2.2 Forced Oscillations: Resonant Peaks

Now let us consider a membrane that is excited by a sinusoidal force with angular frequency ω. The forced motion equation for a membrane is written as:

$$EI\frac{\partial^4 y}{\partial x^4} + B\frac{\partial y}{\partial t} + m\frac{\partial^2 y}{\partial t^2} = F\,\cos(\omega t) \tag{11}$$

As seen in the previous subsection, we can look for solutions of type (2). Now, it does lead to the same spatial solutions (3), but the time differential equation is slightly modified. The membrane will oscillate with the same frequency ω as the driven frequency. Moreover, the amplitude A of the sinusoidal solution $\theta(t)$ varies with the driven frequency as:

$$A = \frac{F}{m\sqrt{(\omega_0^2 - \omega^2)^2 + (\omega B/m)^2}} \tag{12}$$

which represents the same evolution $A(\omega)$ as for damped harmonic oscillator.

2.3 Quality Factor

The quality factor Q is defined as (2π) multiplied by the ratio between the stored vibration energy with respect to the dissipated energy. Clearly, the higher the energy dissipation, the lower the Q and the narrower the resonant peak. For a large Q, as for the damped harmonic oscillator, it can be shown that

$$Q = \frac{\omega_d}{\Delta\omega} \tag{13}$$

where ω_d is the angular resonance frequency and $\Delta\omega$ the bandwidth.

The theoretical expression for Q for a cantilever material is described as the stored vibration energy being equal to the maximum kinetic energy of the system. Following Blom et al. (1992):

$$\begin{aligned} E = (E_{kin})_{\max} &= \int_0^L \frac{1}{2}(mL)\left[\left|\frac{\partial y(x,t)}{\partial t}\right|^2\right]_{\max} dx \\ &= \frac{1}{2}mL\omega^2 \int_0^L \Psi^2(x)dx \end{aligned} \tag{14}$$

On the other hand the dissipated energy per period E_d corresponds to the energy dissipated by the force by unit of length $B\ \partial y/\partial t$. So that:

$$E_d = \int_0^L \left(\int_0^T B\frac{\partial y}{\partial t}\cdot\frac{\partial y}{\partial t}dt\right) dx$$

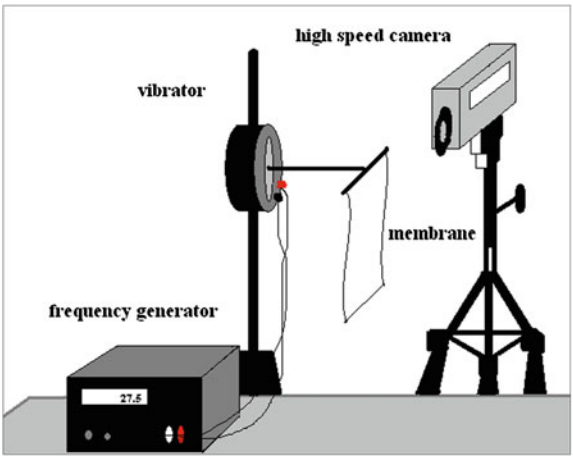

Fig. 1 Experimental set-up for the determination of the eigenmodes of the acetate sheet

$$= \int_0^L \left(\int_0^T B\omega^2 \theta^2(t) dt \right) \Psi^2(x)\, dx$$

$$= B\omega^2 \left(\frac{\pi}{\omega}\right) \int_0^L \Psi^2(x)\, dx \tag{15}$$

The spatial integral $\int_0^L \Psi^2(x)dx$ varies with the considered mode. But as the quality factor is the ratio of Eq. 14 with respect to Eq. 15, this term is eliminated. Finally the quality factor is equal to:

$$Q = (2\pi)\frac{E}{E_d} = \frac{m\omega_d L}{B} \tag{16}$$

where ω_d is the resonant frequency given by Eq. 9.

3 Experimental Set-Up

The experimental set-up is shown in Fig. 1. An acetate sheet is clamped between two stainless steel plates in its top extreme. One of these plates is perpendicularly fixed to an axis whose other extreme is fixed to a vibrating system. This system is controlled via a frequency generator. A high-speed video camera is placed in the acetate sheet plane in order to record the membrane dynamics.

The acetate rectangular sheet has got the geometrical dimensions shown in Table 1.

Table 1 Physical dimensions for the acetate sheet used in this study

Length L (m)	Width H (m)	Thickness e (mm)	Gramage $\rho_s(kg/m^2)$
0.200 ± 0.001	0.100 ± 0.001	0.183 ± 0.003	0.242 ± 0.005

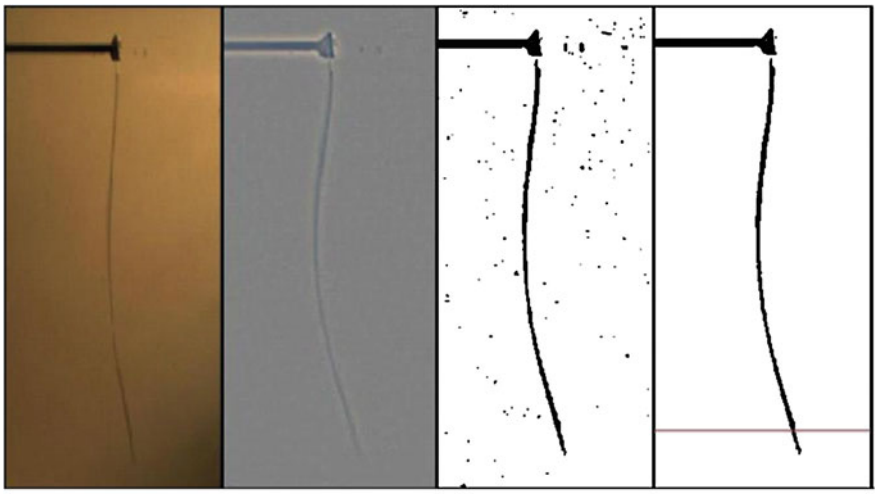

Fig. 2 Different steps for the image analysis. **a** Picture extracted from the video. **b** Image after a high-pass filter. **c** Binarized picture. **d** "Cleaned" picture with Photoshop routine "dust & noise scratches"

We estimated the acetate flexural modulus by measuring the sheet deflection generated by its own weight for several sheet lengths (Belendez et al. 2001). We found: $EI = (3.3 \pm 0.2) \times 10^{-4}$ Nm^2.

The experimental procedure is as follows. We begin with a frequency equal to 1 Hz and increase f by increments of 0.2 Hz, until we reach $f = 31$ Hz. For each frequency value, a video is recorded with the high-speed camera. We use an acquisition frequency equal to 100 Hz for $f = 1$–10 Hz, and then equal to 200 Hz for $f > 10$ Hz.

Then we extract a sequence of 300 pictures from each video. We use Photoshop software to filter the pictures. Figure 2 shows the different steps.

The original picture is seen on the left-hand (Fig. 2a). We apply a high-pass filter to eliminate the light inhomogeneity and we obtain the Fig. 2b. Then we binarize the picture. As there are black unwanted isolated pixels as it can be seen in Fig. 2c, we remove them using the tool of Photoshop routine "dust & noise scratches". The final picture is shown in Fig. 2d.

Finally using Matlab, we measure for each picture of each sequence the membrane transversal deflection y near the membrane extreme free. The horizontal line in Fig. 2d shows the coordinate x_0 at which we chose to measure the

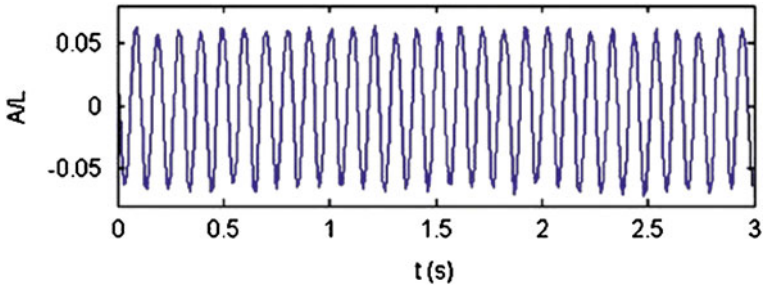

Fig. 3 Time evolution of transversal deflection $y(x_0, t)$ for $f = 9.8$ Hz

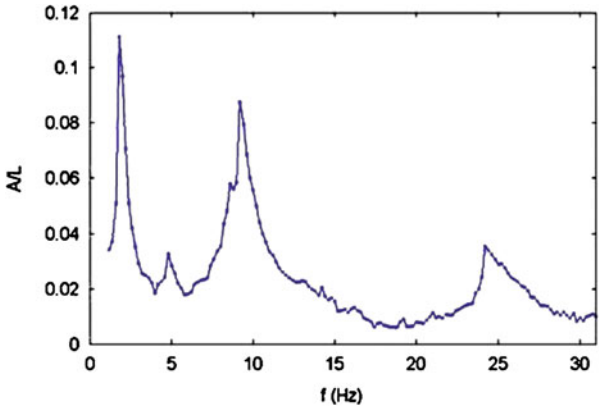

Fig. 4 Response curve of the acetate sheet to the sinusoidal excitation. In x: driven frequency f (Hz). In y: normalized amplitude A/L, where A is amplitude of signal $y(x_0, t)$ shown in Fig. 3, and L is the acetate length

transversal deflection. An example of time evolution $y(x_0, t)$ for the driven frequency $f = 9.8$ Hz is shown in Fig. 3.

4 Results

The amplitude A is extracted from the signal shown in Fig. 3. The quantity A/L as a function of the driven frequency f is shown in Fig. 4.

Table 2 shows in the first column the theoretical resonant frequencies (without damping) in vacuum. The second column shows the resonant frequencies, taking into account that the membrane must displace a surrounding fluid volume when it vibrates. We used the formula given by Chu (1963):

$$f_f = f_v \left(1 + \frac{\pi \rho_f H}{4\rho_s}\right)^{-1/2} \tag{17}$$

Table 2 Comparison between experimental results and theoretical frequencies

Theoretical resonant frequencies in vacuum f_v (Hz)	Theoretical resonant frequencies in air f_f (Hz)	Experimental resonant frequencies (Hz)
1.63	1.39	1.8 ± 0.1
10.24	8.69	9.2 ± 0.2
28.67	24.32	24.2 ± 0.5

First column: theoretical frequencies given by Eq. 9 with $B = 0$. Second column: resonant frequencies in air (Eq. 17). Third column: experimental resonant frequencies

Table 3 Damping coefficient deduced from the resonance curve (Fig. 4)

	Δf (Hz)	Q	B (kg/ms)	$\zeta = B/(2\ m\omega_d)$
1	0.62 ± 0.05	2.9 ± 0.4	0.030 ± 0.006	0.05 ± 0.01
2	1.6 ± 0.1	5.8 ± 0.5	0.08 ± 0.01	0.027 ± 0.004
3	2.4 ± 0.2	10.3 ± 1.1	0.11 ± 0.02	0.015 ± 0.002

First column: mode numbers. Second column: peak bandwidths Δf (Hz). Third column: quality factors Q deduced from Eq. 13. Fourth column: damping coefficient deduced via Eq. 16. Fifth column: damping ratio

where f_v is the theoretical frequency in vacuum, f_f is the frequency in the surrounding fluid, H the membrane depth (see Table 1) and ρ_f the fluid density. The third column of Table 2 shows the measured resonance frequencies.

Table 3 shows the bandwidth for each peak. This bandwidth was measured at half path between the peak basis and the peak top. Quality factors are calculated via formula (13), and damping coefficient B via formula (16). The fourth column shows the damping ratio ζ defined by $\zeta = B/(2\ m\omega_d)$.

5 Discussion

We plotted the amplitude response of an acetate sheet with respect to the driven frequency. We found that the first experimental resonant frequency is higher than both the theoretical ones. The second resonant frequency is between f_f and f_v, whereas it should be lower than f_f if we take into account an internal dissipation (Eq. 9). Finally the third frequency is slightly lower than f_f. This experimental value is the one that most closely fits the theoretical one. We did not find any explanation for the discrepancies of the two first resonant modes. These resonant frequencies were found to be roughly equal in three different experiments performed with the same acetate sheet. We observed the vibration of the support structure for frequencies around 8 Hz.

On the other hand, the estimation of the damping ratio ζ via the quality factor leads to different values (see Table 3). We found in Adams and Askenazi (1999)

that the damping ratio for the rubber is $\zeta \sim 0.05$. For other materials, the damping ratio values vary between 0.01 and 0.08. The order of magnitude changes only for reinforced concrete structures and aluminum, for which $\zeta < 0.01$. So our results are in agreement with values found in literature.

Nevertheless, the values for the damping ratio were not constant in our experiment. There may be other sources of energy dissipation that could be taken into account. We mention them in the following.

1. We could, like Yasumara et al. (2000), write a complex valued-Young's modulus to take into account the internal friction of the material, where the imaginary part plays a dissipative role.
2. Blom et al. (1992) include in the membrane motion equation a term proportional to the membrane velocity like in our study. But their coefficient is complex. The imaginary part is an inertial term which is equivalent to an added mass. We could consider this added mass (Eq. 16) directly in the motion equation.
3. Prak et al. (1991) studied the vibration of silicon diaphragms with typical lengths a few millimeters. These authors neglected viscous damping and supposed that the main source of dissipation was the acoustic radiations. We could include this mechanism in the analysis of our system.

6 Conclusion

We presented the response curve of a periodically excited cantilever. The cantilever consists of an acetate sheet clamped in its top extreme. We measured the oscillation amplitude as a function of the driven frequency and we observed three resonant peaks. The resonant frequencies are close to the theoretical ones taking into account the effects of the air. The quality factors permitted to us to determine the damping ratio of our acetate sheet. We found a good agreement with values found in literature.

References

Adams V, Askenazi A (1999) Builing better products with finite element analysis. OnWord Press, Santa Fe, NM

Beléndez A, Neipp C, Beléndez T (2001) Estudio experimental de la flexión de una viga en voladizo. Revista Española de Física 15(3):42–45

Blom FR, Bouwstra S, Elwenspoek M, Fluitman JHJ (1992) Dependence of the quality factor of micromachind silicon bean resonators on pressure and geometry. J Vac Sci Technol B 10(1):19–26

Chu WH (1963) Tech Rep No. 2, DTMB, contract NObs-86396(X). Southwest Research Institute, San Antonio, Texas

Ganci S (2009) A simple experiment on flexural vibrations and Young's modulus measurement. Phys Edu 44(3):236–240

Hodges DH, Pierce GA (2002) Introduction to structural dynamics and aeroelasticity. Cambridge Aerospace Series

Prak A, Blom FR, Elwenspoek M, Lammerink TSJ (1991) Q-factor and frequency shift of resonating silicon diaphragms in air. Sens Actuators A 25–27:691–698

Turvey K (1990) An undergraduate experiment on the vibration of a cantilever and its application to the determination of Young's modulus. Am J Phys 58(5):483

Wilson F, Lord AE Jr (1973) Young modulus determination via simple, inexpensive static and dynamic measurements. Am J Phys 41(5):653–656

Yasumara KY, Stowe TD, Chow EM, Pfafman T, Kenny TW, Stipe BC, Rugar D (2000) Quality factors in micron- and submicron-thick cantilevers. J Microelectromech Syst 9(1):117–125

Part V
Rheology and Granular Media

Visualization of Vorticity Banding in a Shear Thickening Micellar Solution in Couette Flow

Benjamín M. Marín-Santibáñez, José Pérez-González, Rodrigo Sánchez and Francisco Rodríguez-González

Abstract The shear thickening behavior and flow instabilities of an equimolar semidilute aqueous solution of cetylpyridinium chloride and sodium salicylate were studied in this work by using rheometry coupled with flow visualization. The experiments were conducted at 25°C in a stress controlled Couette rheometer with a transparent flow cell. A detailed flow curve was obtained for this solution, which includes five different regimes. At very low shear rates a Newtonian behavior was found, followed by a shear thinning one in the second regime. In the third regime, a strong orientation of the micelles consistent with shear banding served as a precursor of the shear induced structures (SIS) and shear thickening. The fourth and fifth regimes in the flow curve were separated by a spurt-like behavior, and they clearly evidenced the existence of shear thickening accompanied by stick–slip oscillations at the rotating cylinder. The use of the combined method allowed the detection of SIS. The visualization of this solution in the shear thickening regime showed the build-up of SIS (turbid fluid) in the shear banding regime followed by large variations in shear rate and viscosity, corresponding to the oscillation of clear and turbid bands stacked in the vorticity direction. These alternating bands and shear rate variations are in agreement with the presence of the vorticity banding instability as well as with the creation and destruction of SIS.

B. M. Marín-Santibáñez (✉) · F. Rodríguez-González
Escuela Superior de Ingeniería Química e Industrias Extractivas,
Instituto Politécnico Nacional U.P.A.L.M. C.P, Col. S. P. Zacatenco,
Del. Gustavo A. Madero, 07738 México City, D.F., México
e-mail: bmarin@ipn.mx

J. Pérez-González · R. Sánchez
Laboratorio de Reología, Escuela Superior de Física y Matemáticas,
Instituto Politécnico Nacional U.P.A.L.M. C.P, Col. S. P. Zacatenco,
Del. Gustavo A. Madero, 07730 México City, D.F., México
e-mail: jpg@esfm.ipn.mx

J. Klapp et al. (eds.), *Experimental and Theoretical Advances in Fluid Dynamics*,
Environmental Science and Engineering, DOI: 10.1007/978-3-642-17958-7_36,

1 Introduction

Surfactants in aqueous solutions can form molecular aggregates known as micelles, whose morphology depends on the concentration and ionic strength of the solution. In the semi-dilute regime, solutions of cylindrical wormlike micelles may be formed, which have a complex viscoelastic behavior that includes the presence of flow instabilities such as shear banding and spurt, flow induced phase transitions, and shear thickening resulting from shear induced structures (SIS) (Lerouge and Berret 2010).

One issue that has attracted particular attention is the shear thickening occurring in some dilute and semi-dilute surfactant solutions. This behavior has been studied by different techniques including rheometry (Fischer et al. 2002; Azzouzi et al. 2005; Herle et al. 2005; Marín-Santibáñez et al. 2006), birefringence and flow visualization (Fischer et al. 2002; Herle et al. 2008), light and neutron scattering (Herle et al. 2005, 2007) as well as by velocimetry (Marín-Santibáñez et al. 2006; Herle et al. 2008). In general, the flow behavior of semi-dilute micellar solutions at low deformation rates is Newtonian, it may change to shear thinning one, and then to shear thickening shear induced structures (SIS) that may be parallel or perpendicular to the flow direction at high shear rates. Sánchez and coworkers (2008) carried out a study of the shear thickening equimolar 40 mMol/l cetylpyridinium chloride and sodium salicylate aqueous solution by using electrical measurements and concluded that the SIS were oriented in the flow direction. At still higher shear rates, the solutions may eventually exhibit a shear thinning behavior, but the high shear regime has received limited attention.

The formation of SIS has been attributed to micellar association that may occur by side to side or end to end collisions under shear or extensional flow. In the shear thickening regime large fluctuations of shear rate and viscosity are observed if the shear stress is controlled. These fluctuations have been attributed to the formation and breakage of SIS (Lerouge and Berret 2010).

SIS dynamics in the shear thickening regime have been recently associated with a flow instability observed in the vorticity direction of a Couette flow cell, called *vorticity banding* (Dhont and Briels 2008 and Fielding 2007). Vorticity banding in wormlike micellar solutions has been described by flow visualization experiments as alternating clear (isotropic) and turbid (anisotropic) bands of fluid stacked in the vorticity direction (Fischer et al. 2002; Azzouzi et al. 2005; Herle et al. 2007, 2008; Kang et al. 2008 and Fardin et al. 2009). This type of flow instability is manifested in a similar way to Taylor vortexes (1923) in Newtonian fluids, whose physical origin is completely attributed to inertial effects. However, in contrast to Newtonian fluids, the origin of vorticity banding in micellar solutions is still not completely understood. Several authors have reported that local velocity gradients may cause local disturbances in wormlike concentration that may initiate the build-up of SIS (Dhont and Briels 2008).

In the present work, a detailed investigation of the shear thickening semi-dilute equimolar 40 mMol/L cetylpyridinium chloride and sodium salicylate aqueous

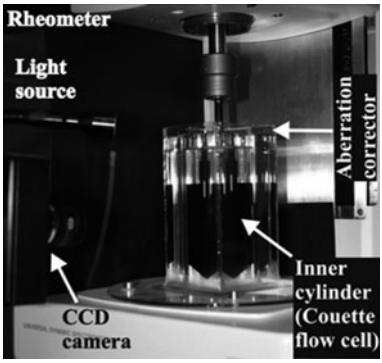

Fig. 1 Experimental set up. Rotational rheometer, Couette flow cell, CCD camera, light source and aberration corrector

solution is carried out by using rotational rheometry and flow visualization. The use of the combined method allowed the detection of SIS stacked in the vorticity direction and accompanied by fast spatial and temporal variations in the flow, which are consistent with the description of vorticity banding.

2 Experimental Procedure

The system studied was the equimolar 40 mMol/l CPyCl/NaSal aqueous solution, which has been recently studied by Marín-Santibáñez et al. (2006), and Herle and coworkers (2005, 2007, 2008). The CPyCl and NaSal (from Aldrich) had a purity of 98 and 99% respectively, and were used as received. Solutions were prepared following the procedure described by Marín-Santibáñez et al. (2006). Flow measurements were carried out at 25°C, which is above the Kraft temperature for this system. Fresh samples were used in each experiment to prevent pre-shear history.

Rheological measurements were performed in a stress-controlled Paar Physica UDS 200 rotational rheometer with a Couette flow cell (inner cylinder radius of 0.0225 m and a gap of 0.0019 m). Visualization experiments were carried out by coupling a transparent borosilicate outer cylinder and an aberration corrector to the rheometer as is shown in Fig. 1. Scattered light images were acquired by using a CCD camera for different stresses in each flow regime and further analyzed to describe the changes induced by the flow field.

3 Results and Discussion

3.1 Rheological Characterization

The flow curve of the equimolar wormlike micellar solution was divided into five different regions as shown in Fig. 2a. Specifically, at low shear stresses (region I),

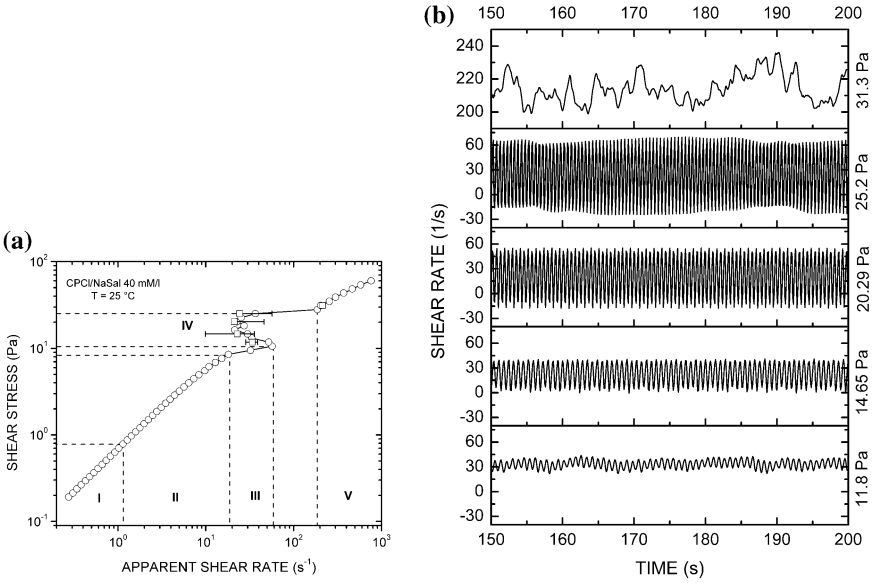

Fig. 2 **a** Flow curve of the shear thickening micellar solution at 25°C. The horizontal error bars indicate the shear rate variations in the thickened state. **b** Shear rate as a function of time for different shear stresses in IV ($11 < \tau < 26$ Pa) and V ($\tau > 26$ Pa) regimes

a Newtonian flow regime was found, followed by a slightly shear thinning behavior given by the power-law model $\tau = m\dot{\gamma}^n$, where n and m are the shear thinning index (0.914) and the consistency index (0.73 Pas^n), respectively. In the third regime, a strongly shear thinning behavior ($n = 0.189$) was observed, consistent with a strong orientation of micelles in the flow direction. This prominent shear thinning has been attributed to shear banding for other types of surfactant solutions, namely, the coexistence of both, a homogeneous and a structured phase (Lerouge and Berret 2010).

At higher shear stresses, between 10.5 and 25.3 Pa (region IV), a shear thickening behavior was clearly observed; error bars indicate shear rate fluctuations occurring under stress-controlled flow. The evolution of these fluctuations is shown in Fig. 2b for different stresses lying in this flow regime. It is clear that the amplitude of the oscillations increases along with the shear stress and then decreases once the flow sets in region V. Fourier analysis of the shear rate *versus* time data indicated different oscillation modes with increasing frequencies for each shear stress, until a the shear rate evolution ceases to be periodic. Some authors have reported a chaotic behavior for high shear rates (Ganapathy et al. 2008), such flow regimes however, were not reached in this work.

The shear rate fluctuations in this flow regime are related to stick–slip oscillations of the solution at the rotating cylinder and prevailed up to the highest shear stresses in the fourth regime. On the other hand, stick–slip oscillations arise from changes in the viscosity of the solution due to the dynamic creation and breakage

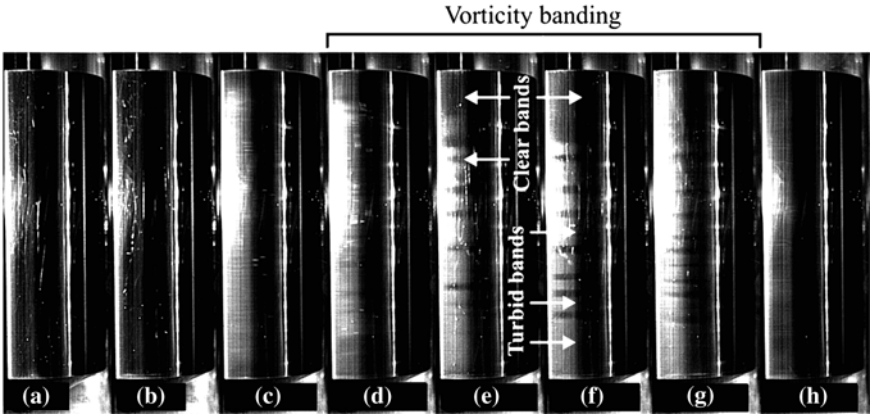

Fig. 3 Flow visualization of the shear thickening micellar solution at 25°C for different shear stress values: **a** rest, **b** 4 Pa (region II), **c** 10.5 Pa (Region III, shear banding regime), **d** 11.5 Pa, **e** 15.5 Pa, **f** 18.8 Pa, **g** 22.8 Pa (Region IV, shear thickening regime) and **h** 54.4 Pa (Region V, high shear rate branch)

of SIS. The stick–slip behavior referred to in this paragraph is clearly observed in video one at http://esfm.ipn.mx/reologia/videos.php. Finally, region V is separated from the IV by a spurt discontinuity. At the end of the fifth regime, the Weissenberg effect was observed, indicating the influence of normal stresses on the flow stability.

3.2 Flow Visualization

Figure 3a–h show the structural changes in the micellar solution under flow for different shear stresses as compared with the solution at rest. At rest and for low shear stresses in region II (Fig. 3a–b), the micellar solution is completely transparent, suggesting that the solution is fully isotropic. However, in the shear banding regime (III, 10.5 Pa, Fig. 3c), the solution becomes turbid suggesting a flow induced physical change. This low viscosity phase has been associated with a strong orientation of the micelles in the flow direction, as explained above, (Lerouge and Berret 2010) and is considered to be the precursor of the SIS.

On the other hand, in the shear thickening regime, Fig. 3d–g show alternating bands of anisotropic (turbid) and isotropic (clear) material stacked in the vorticity direction, and whose vertical positions change with time and shear stress (see video two at http://esfm.ipn.mx/reologia/videos.php). The variation of the structure of the stacked bands along with the shear stress is shown in Fig. 4, in which the light intensity is plotted as a function of the position along the cylinder. The appearance of two different phases, represented by peak and valleys is evident in the plots. Some relationship of these bands is expected with the shear rate

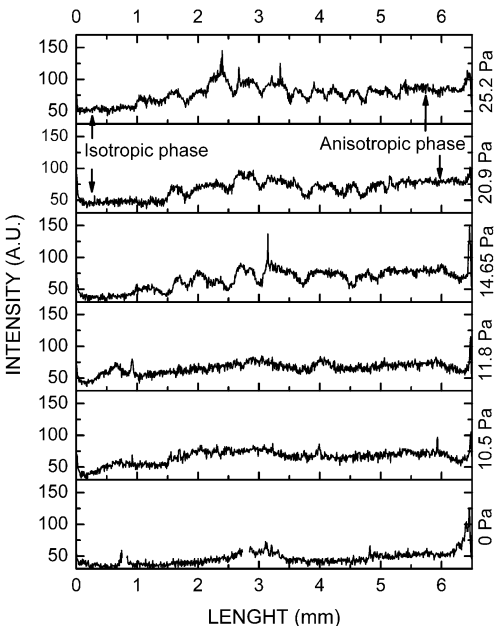

Fig. 4 Light intensity variations as a function of the position along the cylinder at rest, 10.5 Pa (Region III, shear banding regime), 11.5, 14.65, 20.9 and 25.5 Pa (Region IV, shear thickening regime)

oscillations, but it is not clear how to establish such a connection from the data in this work.

The alternating bands have been related with a new type of instability called *vorticity banding*, which consists of rolls of structured (turbid) and isotropic (clear) fluid, with a non-zero velocity component in the vorticity direction (Dhont and Briels 2008). The results in this work conform to this description. However, there is always the question regarding the origin of the instability; in other words, is this instability different from the Taylor one? In order to address this point we provide a series of data that may help in making a distinction. Taylor instability has its origin in inertial effects, i.e., it occurs at high Reynolds numbers. The Reynolds numbers corresponding to the data at the onset of the shear thickening regime are of the order of one, which is much lower than the critical value reported for inelastic fluids ($\sim$ decades). Also, the instability might be considered as a purely elastic one, as those reported in some polymeric solutions (Larson 1992). The critical modified Weissenberg number $\left(\Sigma = (e/R_i)^{1/2} Wi\right)$ for a purely elastic instability is around 6; here (e/R_i) is the ratio of the rheometer gap and the radius of the rotating cylinder, Wi is the well known Weissenberg number. The calculated value for the data at the onset of the shear thickening regime in this work is 1.7, which is well below the value mentioned above, although it should be noted that some degree of elasticity, that is evident by the appearance of the Weissenberg effect, is necessary for the instability to be triggered. Thus, in the present case, we suggest that the instability observed is consistent with vorticity banding, which is

preceded by a shear or gradient banding. An analysis of the details of the kinematics of the unstable flow by using velocimetry is currently underway.

4 Conclusions

A combined method of rheometry and flow visualization was used in this work to study the shear thickening behavior and flow instabilities of an equimolar semidilute aqueous solution of cetylpyridinium chloride and sodium salicylate. The present results show that shear banding serves as a precursor of the SIS and shear thickening. Stick–slip oscillations in the inner cylinder produce shear rate fluctuations under stress-controlled flow and prevailed up to the highest shear stresses used in this work. Flow visualization of this solution showed the build-up of SIS (turbid fluid) in the shear banding regime followed by the appearance of bands of clear and turbid fluid stacked in the vorticity direction. These bands and their fluctuations were linked to the vorticity banding instability, which has been suggested as an elastic instability produced by local velocity and concentration gradients that occur during the shear banding regime.

Acknowledgments This work was supported by SIP-IPN (20101435, 20111119). J. P.-G. is COFAA-EDI-IPN fellow. B. M. M.-S. has a fellowship under the CONACyT program for Consolidación Institucional de grupos de Investigación (Sol. 147970).

References

Azzouzi H, Decruppe JP, Lerouge S, Greffer O (2005) Temporal oscillations of the shear stress and scattered light in a shear banding-shear thickening micellar solution. Eur Phys J E 17:507–514

Dhont JKG, Briels WJ (2008) Gradient and vorticity banding. Rheol Acta 47:257–281

Fardin MA, Lasne B, Cardoso O, Grégoire G, Argentina M, Decruppe JP, Lerouge S (2009) Taylor-like vortices in shear-banding flow of giant micelles. Phys Rev Lett 103:028302

Fielding S (2007) Vorticity structuring and velocity rolls triggered by gradient bands. Phys Rev E 76:016311

Fischer P, Wheeler EK, Fuller GG (2002) Shear-banding structure orientated in the vorticity banding direction observed for equimolar micellar solution. Rheol Acta 41:35–44

Ganapathy R, Majumdar S, Sood AK (2008) Spatiotemporal nematodynamics in wormlike micelles en route to rheochaos. Phys Rev E 78:021504

Herle V, Fischer P, Windhab E (2005) Stress driven shear bands and the effect of confinement on their structures-A rheological, flow visualization, and rheo-SALS study. Langmuir 21:9051–9057

Herle V, Kohlbrecher J, Pfister B, Fischer P, Windhab E (2007) Alternating vorticity bands in a solution of wormlike micelles. Phys Rev Lett 99:158302

Herle V, Manneville S, Fischer P (2008) Ultrasound velocimetry in a shear-thickening wormlike micellar solution: evidence of coexistence of radial and vorticity shear bands. Eur Phys J E 26:3–12

Kang K, Lettinga MP, Dhont JKG (2008) Is vorticity banding due to an elastic instability? Rheol Acta 47:499–508

Larson RG (1992) Instabilities in viscoelastic flows. Rheol Acta 31:213–263
Lerouge S, Berret J-F (2010) Shear-induced transitions and instabilities in surfactant wormlike micelles. Adv Polym Sci 230:1–71
Marín-Santibáñez BM, Pérez-González J, de Vargas L, Rodríguez-González F, Huelsz G (2006) Rheometry-PIV of shear thickening wormlike micelles. Langmuir 22:4015–4026
Sánchez R, Pérez-González J, de Vargas L (2008) Study of flow-induced structures in a shear thickening micellar solution by simultaneous rheometrical and electrical current measurements. J Non-Newton Fluid Mech 149:71–79
Taylor GI (1923) Stability of a viscous liquid contained between two rotating cylinders. Trans Royal Soc A 223:289–343

New Experiments on the Kaye Effect

José Eduardo Ochoa, Catalina Ramírez Guerra and Catalina Stern

Abstract When a jet of a thinning fluid is poured over a perpendicular surface covered with the same fluid, under certain circumstances it is observed that a small jet seems to bounce out of the surface very close to the incident jet. This phenomenon was first described by Kaye in 1963. In this work, the same type of fluid was used but the surface of incidence was inclined between 10 and 45 degrees. To better visualize the flow, the fluid was seeded with metallic flakes and illuminated with a sheet of light. The speed of the incident jet was kept constant. For each angle of incidence several videos at 240 frames per second were captured. It was observed that initially, a column of the falling liquid is formed. When the column breaks down, a jet comes out of it. The length of contact between the surface and the jet gets longer as the angle of inclination is increased. A critical angle θc was found for which the terminal speed is larger than the falling speed of the incident jet. This cannot be explained by any of the mathematical models that have been proposed. The thinning characteristic of the fluid is not taken into account in any of the models.

1 Introduction

When a thinning fluid is poured over a surface covered with the same fluid, an interesting phenomenon is observed. First a column is formed (Fig. 1) and, when it breaks down (Fig. 2), a small jet comes out (Fig. 3). This phenomenon was first

J. E. Ochoa · C. R. Guerra · C. Stern (✉)
Facultad de Ciencias, Universidad Nacional Autónoma de México,
Ciudad Universitaria, C. Exterior s/n, Coyoacán,
04510 México, D.F., México
e-mail: catalina@ciencias.unam.mx

J. Klapp et al. (eds.), *Experimental and Theoretical Advances in Fluid Dynamics*,
Environmental Science and Engineering, DOI: 10.1007/978-3-642-17958-7_37,

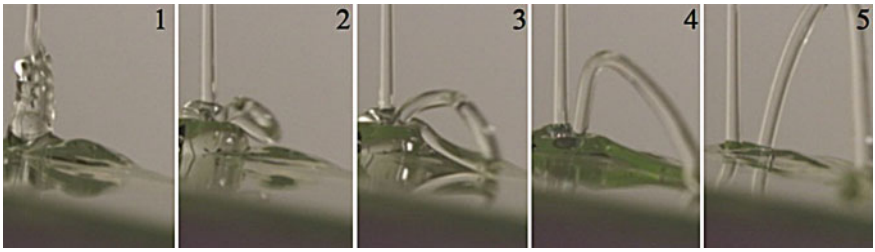

Fig. 1 The Kaye effect

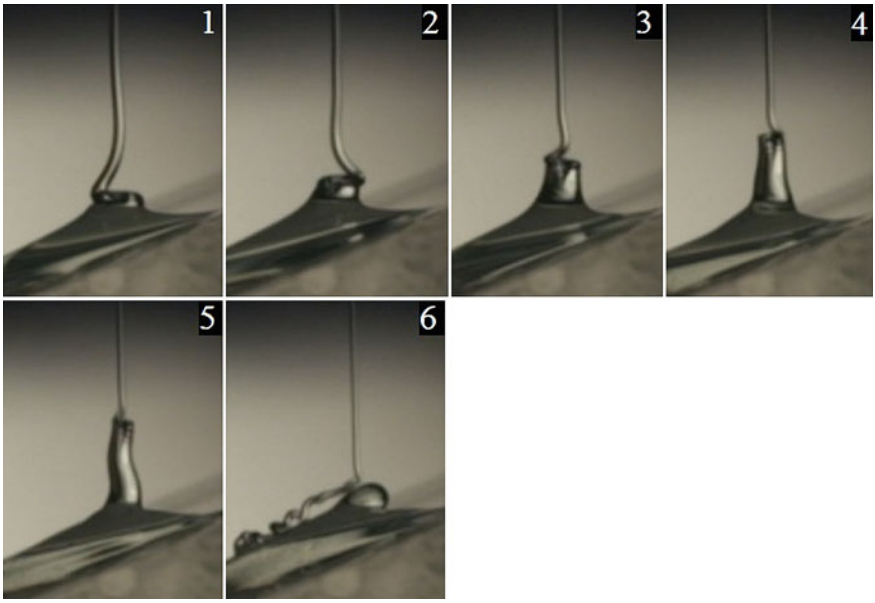

Fig. 2 When the speed is low, the viscous column is wide and small, as the speed increases, the column gets wider until it becomes unstable and collapses

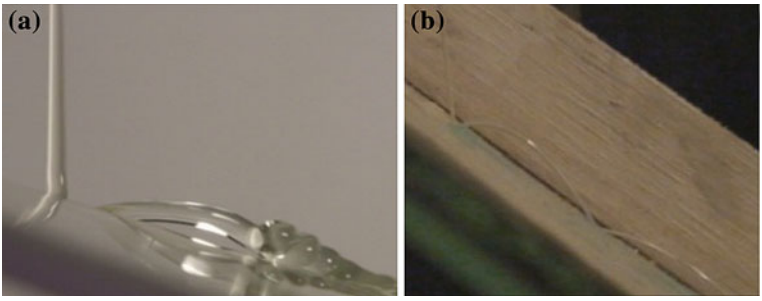

Fig. 3 **a** The exiting jet merges into the fluid layer or **b** rebounds producing the effect again

described by Kaye in 1963. Since then some theories have been suggested to understand its nature (Verluis 2006; Binder 2009).

The Kaye effect can be observed in various fluids like shampoo, liquid soap and detergent, blood, synovial liquid, yogurt, catsup, some gels, creams, cement and certain paints. All of them are thinning in the presence of shear stress.

2 Qualitative Description

When the jet impinges on the flat surface, a spiral column of fluid appears (Fig. 2). Inside the column a tiny vortex is formed, and bubbles are entrained by its motion at the bottom of the column. The height and the width of the column start to oscillate depending on the speed of the impinging jet, becoming more and more unstable, until it collapses.

The phenomenon is produced only for certain widths of the layer of fluid on the flat surface. Besides, for every angle of the surface, there is a minimum and a maximum speed of the impinging jet at which the secondary jet is formed. For such speed interval, the column appears first, and after it collapses, the secondary jet is formed. The impinging jet creates a vertical force that makes a curved indent in the fluid layer through which the jet passes and comes out at another direction. As the indent becomes deeper, the exiting angle changes.

After bouncing, the fluid in the secondary jet can merge into the fluid layer (Fig. 3a), or behave like a primary jet and reproduce the effect (Fig. 3b). This can happen several times producing a cascade of jets.

The effect can be interrupted in different ways. As the indent becomes deeper, the amount of energy dissipated increases, and the exiting jet disappears. Sometimes there is a perturbation that makes the exiting jet wander in several directions and eventually stop. For small angles of inclination of the flat surface, the exiting jet, as it wanders, can collide with the incoming jet, ending the effect.

3 Theoretical Model

Two different models, based on the conservation of energy, have been made to explain the Kaye effect. Both models correspond to an angle of incidence of 90 degrees. Binder and Landing consider a layer of air between the impinging jet and the layer of fluid in the surface (Fig. 4), but they do not give an analytical solution. In the Verluis model, the layer of air between the surface layer and the jet is not considered. In this work, an analytical solution is obtained following suggestions from Binder and Landing. None of them take into account the thinning characteristics of the fluid.

As shown in Fig. 4, a thin layer of air is supposed to exist between the jet and the surface layer of fluid. Even though the thin layer is not observed in the pictures,

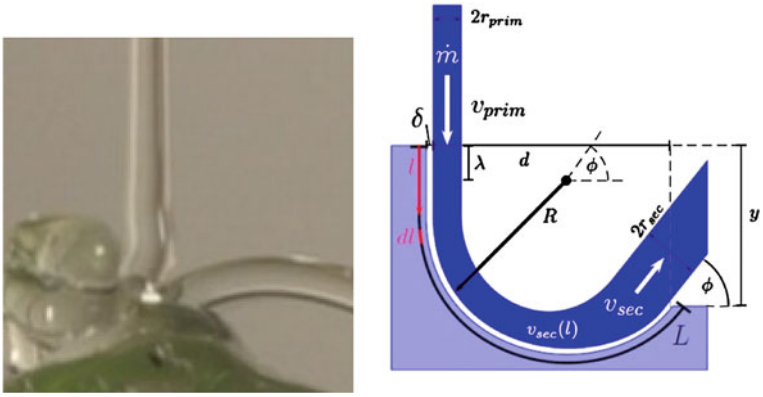

Fig. 4 **a** Observation of the point of incidence and **b** theoretical model of Binder and Landig

it can be seen in the videos that the primary jet curves in the indent, and comes out again becoming what appears to be a secondary jet. It is really the same jet. One way of explaining the curvature of the jet without it mixing with the shampoo in the flat plate, is to consider the presence of a layer of air between them. The loss of energy by friction in a differential area dA between the moving jet and the layer of air will be considered.

By conservation of mass

$$\pi r^2 V(l) = \frac{\dot{m}}{\rho} \Rightarrow r = \sqrt{\frac{\dot{m}}{\rho \pi V(l)}}$$

where $V(l)$ is the instantaneous speed and l is the length of the arc in the indent, it goes from zero to L, as shown in Fig. 4. $V(0)$ is then the incident speed and $V(L)$ the speed of the secondary jet. The width of the jet increases as it looses speed due to friction; r is the radius of the jet. The force due to viscosity in an area dA is

$$dF_r = \eta\tau = \eta dA\dot{\gamma} = \eta dA\frac{V}{\delta}$$

with δ the width of the layer of air, η the viscosity and $\dot{\gamma}$ the shear rate between the fluid and the air.

If

$$dA = \pi r\ dl = \sqrt{\frac{\pi\dot{m}}{\rho V}}dl$$

The force of Friction in a distance dl is:

$$dF_r = \eta\sqrt{\frac{\pi\dot{m}}{\rho V}}\frac{V}{\delta}dl$$

and the dissipated power.

$$VdF_r = \eta\sqrt{\frac{\pi\dot{m}}{\rho V}}\frac{V}{\delta}dl \tag{1}$$

The amount of power coming in is:

$$\dot{E} = \frac{1}{2}\dot{m}V^2 \Rightarrow d\dot{E} = \frac{1}{2}\dot{m}\left(V^2(l+dl) - V^2(l)\right) = \dot{m}V\,dV$$

$$d\dot{E} = \dot{m}V\,dV$$

By conservation of energy,

$$\dot{m}V\,dV = \eta\sqrt{\frac{\pi\dot{m}}{\rho V}}\frac{V}{\delta}V\,dl$$

And a differential equation is obtained

$$dV = \frac{\eta}{\delta}\sqrt{\frac{\pi}{\rho m}}\sqrt{V}dl \tag{2}$$

Equation 2 can be expressed in terms of a dimensional parameters if the following scales are introduced: $\beta = \frac{\eta}{\delta\rho}$ for the speed and $\Delta^2 = \frac{\delta\dot{m}}{\eta\pi}$ for the length. The adimensional parameters are then $U = \frac{V}{\beta}$ and $\xi = \frac{l}{\Delta}$, so Eq. 2 can be written as

$$dU = \sqrt{U}d\xi \tag{3}$$

Solving

$$2\left(\sqrt{U_{pri}} - \sqrt{U_{\text{sec}}}\right) = \xi_L \Rightarrow U_{\text{sec}} = \left(\sqrt{U_{pri}} - \frac{1}{2}\xi_L\right)^2$$

so

$$V_{\text{sec}} = \left(\sqrt{V_{pri}} - \frac{1}{2}\frac{\eta L}{\delta}\sqrt{\frac{\pi}{\rho\dot{m}}}\right)^2 \tag{4}$$

Equation 4 predicts the existence of a minimal critical speed ($V_c = \frac{\eta^2 L^2 \pi}{4\delta^2\rho\dot{m}}$) from which the Kaye effect starts, showing that the speed of the exiting jet is always smaller than the speed of the incident jet. Parameters L and δ, are left free; they have to be measured experimentally.

One way of changing L, is by changing the angle of inclination of the flat surface.

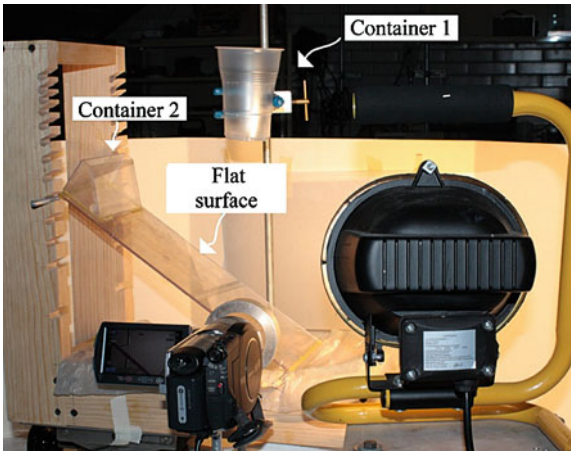

Fig. 5 Experimental set-up that allows changes in the angle of the flat surface

4 Experimental Set-up and Procedures

The flat surface is set at an initial angle of 10°, and is varied by 5° steps up to 45°. Underneath the support, the fluid is received in a jug through a hose (Fig. 5).

Two containers are filled with the same fluid. Container one will create the impinging jet. By filling the container more or placing it higher in the support, the speed of the jet can be increased. Container two will create the dynamic layer of fluid on the flat surface, accelerated by gravity. Several tests of the position of container one and of the height of the fluid column inside it were made, to determine a minimal speed at which the Kaye effect takes place. This initial speed was kept constant for the rest of the experiments. Another parameter that was kept constant is the height of the fluid column in container two. All experiments were filmed at 250 frames per second.

5 Results

In general, the following observations were made for all angles of inclination of the flat surface:

- The length of contact L increases as the angle between the surface and the impinging jet is increased.
- A column is formed by the spiral motion of the incident fluid. The height and width of the column vary with the speed of the impinging jet.
- There are critical maximum and minimum velocities of the incident jet that produce the Kaye effect.
- The range of speeds favorable to the effect depends on the angle of the flat surface.

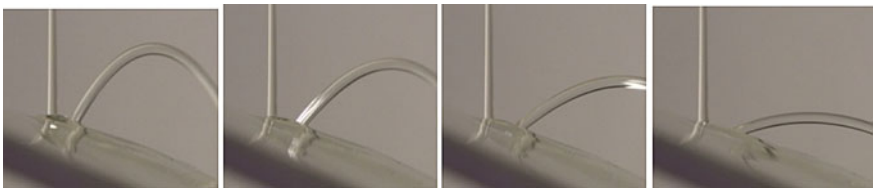

Fig. 6 Evolution of the secondary jet as a function of time. The inclination diminishes, the speed increases and the jet gets thinner, until it arrives at a state of equilibrium

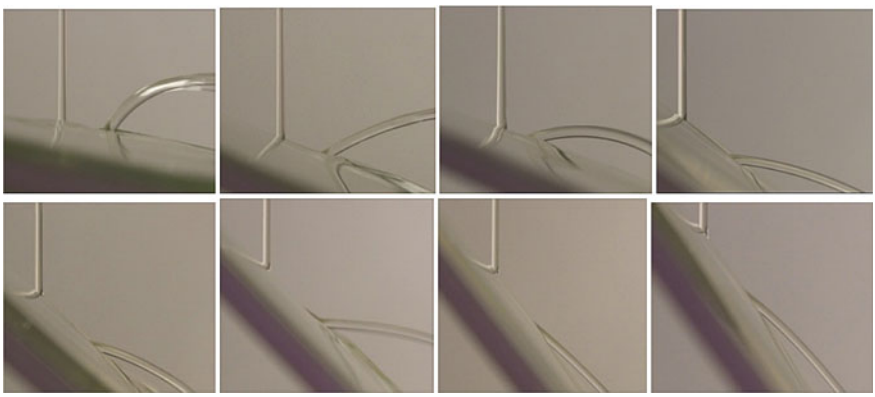

Fig. 7 When the angle between the flat plate and the incident jet increases, the angle of the secondary jet is smaller and its width diminishes

- When the flat plate is perpendicular to the incident jet, the secondary jets wanders in many directions until the effect disappears. When the flat plate is inclined, the jet stabilizes at a preferred direction that depends on the angle.
- The speed of the secondary jet increases until it reaches a state of equilibrium (Fig. 6).
- The bouncing angle with respect to the flat plate decreases as the inclination of the flat plate increases (Figs. 7 and 8).
- There is a critical angle of inclination for which the speed of the secondary jet is larger than the speed of the incident jet, contradicting Eq. 4 (Fig. 9).

6 Conclusions

Several differences were observed in the Kaye effect when the impinging jet is not perpendicular to the flat plate. In the perpendicular case there is no preferred direction for the secondary jet, it wanders around the impinging point. When the angle is different to ninety degrees, there is a preferred direction at which the

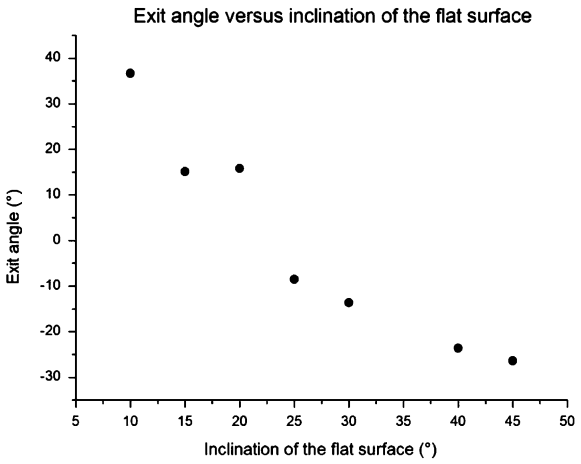

Fig. 8 Exit angle versus angle of inclination of the flat surface

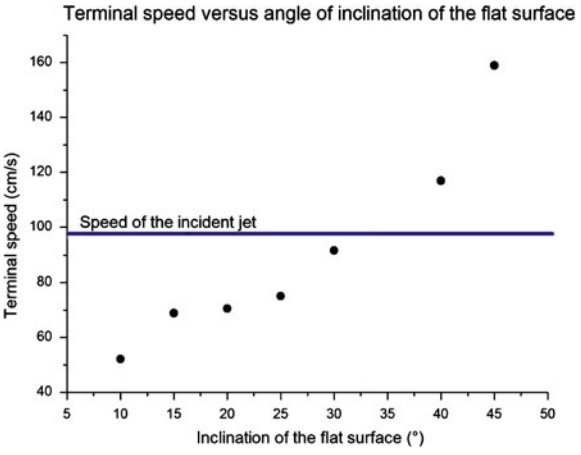

Fig. 9 Terminal speed versus angle of inclination of the flat surface. The speed of the incident jet is always 100 cm/s

exiting jet stabilizes. This direction depends on the angle of inclination of the flat plate. There is a maximum speed of the primary jet for which the Kaye effect can take place, that changes with the angle of inclination of the flat surface. There is also a critical angle for which the speed of the secondary jet is larger than the speed of the primary jet. None of these results can be explained by the models that consider only dissipation of energy.

The experiments in this work show the need of better models that take into account the motion of the fluid layer on the flat surface due to the acceleration of gravity.

Acknowledgments The authors thank Yadira Salazar for her help in the experiments. The authors acknowledge support from DGAPA UNAM through project PAPIME PE104907.

References

Binder JM, Landing AJ (2009) The Kaye effect. Eur J Phys 30:S115–S132
Verluis M, Blom C, van der Meer D, van der Weele K, Lohse D (2006) Leaping shampoo and the stable Kaye effect. J Stat Mech P07007

Traction Forces on Rods in Cylindrical Silos

Carlos A. Vargas, Abraham Medina and Abel López-Villa

Abstract In this work we present a theoretical study, based on the continuum approach, of the traction forces on the wall of the silo and on a cylindrical rod located at its center when the silo is filled with a dry, non cohesive granular material. We derive expressions for the traction forces by using the Janssen model and the modified, two-parameter Janssen model in order to take into account the existence of dead zones, i.e., the existence of zones without traction occurring during the incipient filling of the silos. Comparison between both models allow understand important aspects observed in experiments.

1 Introduction

Contrary to the case of liquids where the hydrostatic pressure, p_h, in a reservoir is independent on its shape and it only depends on the depth respect to the free surface z, i.e., $p_h \sim z$, the *pressures* in silos, measured at the position z respect to the free surface, have different values if they are measured along the horizontal or vertical direction. Moreover, pressure depends non-linearly on z and this dependence is dictated mainly by the friction among grains and the friction between grains and the silo walls. The more accepted law that describes this dependence

C. A. Vargas · A. Medina (✉)
Laboratorio de Sistemas Complejos, Departamento de Ciencias Básicas, UAM Azcapotzalco, Avenue San Pablo 180 C.P., 02200 Mexico City, D.F., Mexico
e-mail: abraham_medina_ovando@yahoo.com

A. López-Villa
SEPI ESIME Azcapotzalco, Instituto Politécnico Nacional, Avenida de las Granjas 682, Col. Sta. Catarina, C.P., 02250 Mexico, D.F., Mexico

J. Klapp et al. (eds.), *Experimental and Theoretical Advances in Fluid Dynamics*, Environmental Science and Engineering, DOI: 10.1007/978-3-642-17958-7_38,

was initially proposed by Janssen a century ago (Janssen 1895), but still now there is no conclusive correlation for the pressure.

In this work we will mainly discuss the nature of the tangential force on the inner wall of a cylindrical silo and on a cylindrical rod located at the center of the silo. This force is known as traction and occurs when granular material is stored in silos. In liquids this force is null. The aim of the work is to analyze how this force acts when a dry, non cohesive granular material fills a cylindrical silo. Theory here developed is not valid for cohesive granular materials and in non cylindrical (e.g., conical) silos. Here we are going to incorporate, in calculations, the two-parameter Janssen model which appears to describe better very accurate measurements of the pressures and the traction force on silos and rods. A more detailed discussion of the Janssen model and of the modified Janssen model will be given in next section.

The paper is organized as follows in the next section a brief discussion of how pressures act in silos is given. After, we derive formally the pressure in a cylindrical silo through the Janssen model and by using the corresponding two-parameter modification. In Sect. 3, the force compressing the wall is computed for both cases. In Sect. 4 we give a series of plots to compare the validity of each of these approaches. Finally, in Sect. 5 the main conclusions of the work are summarized.

2 Pressures and Traction Force on the Silo Wall

2.1 How Pressures Act in a Silo

Pressures in quiescent liquids and in non cohesive granular materials at rest are quite different. Consider a vertical cylindrical silo filled with a granular material. The vertical pressure on a horizontal plane at a certain depth below the surface of the material does not increase linearly with depth, as occurs for a normal liquid. Instead, the Janssen's model predicts that this pressure tends to a constant value independent of depth. The origin of this behavior is in the static friction between the grains and the walls of the container. Due to this friction, the container walls can support part of the weight of the material.

The validity and possible shortcomings of the simple theory underlying the original Janssen model have been extensively tested experimentally and numerically. Janssen himself carried out experiments to measure the pressure on the base of a silo, and apparently he found good agreement with the predictions of his model. However, careful laboratory observations have revealed serious difficulties in the measurements of this vertical pressure (Brown and Richards 1970; Boutreux et al. 1997; Bratberg et al. 2005; Shaxby and Evans 1923; Ovarlez and Clément 2005; Vanel and Clément 1999; Vanel et al. 2000), with the results depending on the method of filling and even on the jamming of the displacement of the piston often used to measure the pressure (Bratberg et al. 2005; Brown and Richards 1970; Boutreux et al. 1997; Shaxby and Evans 1923; Vanel and Clément 1999;

Vanel et al. 2000). Precise and reproducible pressure profiles have been measured in some carefully designed experiments (Bratberg et al. 2005; Vanel and Clément 1999; Vanel et al. 2000), and molecular dynamics simulations which rely on the notion that the grains have settled to a final state (Landry et al. 2003) have reproduced these measurements. Comparison shows that the predictions of Janssen model are reasonable over most of the granular material but degrade in a region around the top of the column where the pressure varies nearly linearly with vertical distance. This discrepancy has led to modifications of Janssen's model. Among these, a two-parameter modification, which suppresses friction with the wall in an upper slice of the column, improves the agreement with the experimental and numerical vertical pressure profiles in that region (Vanel and Clément1999).

The purpose of this work is to explore which are the main changes between the pressure distributions and traction forces due to the use of Janssen model and the modified Janssen model. In a recent work (Vargas et al. 2010) we have shown that measurements of the traction force that the granular material exerts on the wall overcomes the difficulties often encountered in the direct measurements of the vertical pressure on a piston, which are due to jamming of the piston displacement induced by the compression force. Measurements of the traction force give further evidence of the existence of a region not predicted by the original Janssen model.

2.2 Computation of the Pressure and Traction Force

Consider a vertical, cylindrical tube of radius r_0 filled with a dry granular material up to a certain height H (Fig. 1). Take a horizontal section of the tube at a depth z respect to the free surface of the granular material. According to Janssen's model, the force exerted per unit area of this section by the material above it on the material below is a vertical pressure $p_z(z)$. This pressure is not equal to the horizontal pressure $p_r(z)$ of the material on the wall of the cylinder at the same depth, but the two pressures are linearly related (Janssen 1895; Brown and Richards 1970; Pitman 1994; Schulze 2008; McGlinchey 2008; Shaxby and Evans 1923; Boutreux et al. 1997):

$$p_r(z) = Kp_z(z), \tag{1}$$

where K, named the Janssen parameter, is a constant independent of z that characterizes the conversion of vertical stress into horizontal stress within the granulate.

The horizontal pressure acting on the wall of the tube causes a vertical friction stress τ between the wall and the granular material. A simple balance of the vertical forces acting on a slab of the granular material gives

$$\pi r_0^2 \frac{dp_z}{dz} = \pi r_0^2 \rho g - 2\pi r_0 \tau, \tag{2}$$

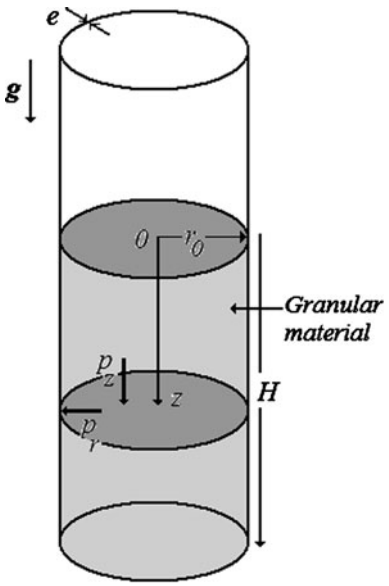

Fig. 1 Schematic of a cylindrical silo of radius r_0 and thickness e. It is assumed that the silo has been filled up to the height $z = H$

where ϱ is the bulk density of the granular material, assumed to be independent of z, and g is the acceleration due to gravity.

In the original Janssen's model, the vertical friction stress is assumed to be given by Coulomb's law, $\tau = \mu_w p_r$, with a constant static friction coefficient μ_w. The solution of Eq. 2 with the condition $p_z(0) = 0$ is then (Janssen 1895; Schulze 2008; Brown and Richards 1970; Pitman 1994)

$$p_z(z) = P_J(z), \tag{3}$$

with

$$P_J(z) = \rho g \lambda \left[1 - \exp\left(-\frac{z}{\lambda}\right)\right] \quad \text{and} \quad \lambda = \frac{r_0}{2\mu_w K}. \tag{4}$$

Equation 4 shows that the vertical pressure increases linearly with z, as $p_z(z) \approx \rho g z$, for $z/\lambda \ll 1$ and tends to the limiting value $\lambda \rho g$ for $z/\lambda \gg 1$. The length λ is the characteristic size of the region where the pressure undergoes this transition. In laboratory columns $\lambda \approx 0.1$ m (Boutreux et al. 1997), so that the wall of the container supports most of the weight of the grains when $H \gg 0.1$ m.

As aforementioned, the two-parameter Janssen model suppresses friction with the wall for very small filling levels. It suggest that the pressure will be a linear function of z for $z < a$ and $\tau = 0$, where a, the thickness of the frictionless slice, is the second parameter of the model. In terms of the traction force these results imply that for small filling levels the traction will be null. To support these facts Fig. 2 shows experimental plots of the traction force as a function of the level of filling, H, when a silo, 2.48 cm diameter, was filled with glass beads, 1 mm diameter. Incidentally, we shall comment

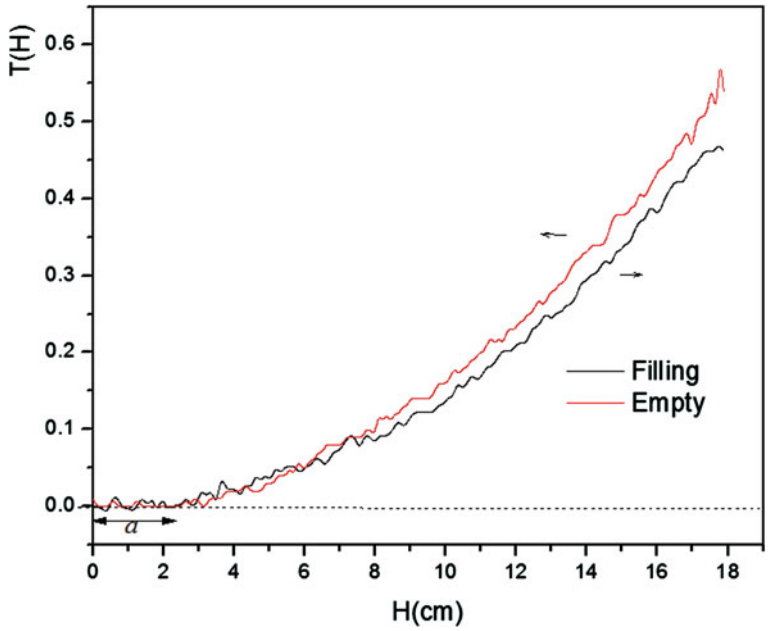

Fig. 2 Actual measurements of the traction force on the wall of a cylindrical silo as a function of height, H. The *black curve* corresponds to the filling of the silo and the red curve is for the silo empty. *Arrows* indicate the direction of evolution of H. Notice that, in both cases, there is a "dead zone" (of size a), i.e., a zone where traction force do not is detected. These results will be useful to introduce the modified Janssen model

that Atkinson et al. (1983) did experiments on traction on a rod during the emptying of cylindrical silos but in their case was not detected the dead zone, perhaps this fact was due to the very coarse measurements. The plot for the traction under the empty process is also show. In both cases is appreciated the existence of the "dead zone" where traction is null. The solution of Eq. 2 is then

$$p_z(z) = \begin{cases} \rho g z & \text{for } z < a \\ \rho g a + (1 - \frac{a}{\lambda}) P_J(z - a) & \text{for } z > a. \end{cases} \tag{5}$$

The maximum vertical force acting on the wall of a tube filled to a height H is the traction, given by

$$T(H) = 2\pi r_0 \int_0^H \tau(z)\, dz = T_J(H), \tag{6}$$

with

$$T_J(H) = \pi r_0^2 \rho g \left\{ H - \lambda \left[1 - exp\left(-\frac{H}{\lambda} \right) \right] \right\}, \tag{7}$$

according to the original Janssen model. By the way

$$T(H) = \begin{cases} 0 & \text{if} \quad H < a \\ \pi r_0^2 \rho g \frac{a}{\lambda}(H-a) + (1-\frac{a}{\lambda})\, T_J(H-a) & \text{if} \quad H > a. \end{cases} \tag{8}$$

according to the modified Janssen model.

The function T_j (H) increases quadratically with H, as $T_J \approx \pi r_0 \rho g \mu_w K H^2$, for H $\ll \lambda$, and linearly, as $T_J \approx \pi r_0^2 \rho g H$, for H $\gg \lambda$, when most of the weight of the granular material is supported by the wall of the silo. The maximum vertical stress due to the granular material is $T(H)/(2\pi r_0 e)$ where e is the thickness of the wall of the silo. In a conventional silo standing on its base, this maximum stress is a compression at the lower part of the wall, which makes of buckling a critical factor in the design of tall silos.

3 Traction Force on a Rod

Consider now the presence of a rod of radius r_1 located at the center of the silo of radius r_0. See Fig. 3. In this case the balance of the vertical forces acting on a slab of the granular material is

$$\pi\left(r_0^2 - r_1^2\right) \frac{dp_z}{dz} = \pi\left(r_0^2 - r_1^2\right) \rho g - 2\pi(r_0\tau_0 - r_1\tau_1), \tag{9}$$

where the vertical shear stress on the rod is $\tau_0 = \mu_{w_0} p_r$ and on the inner wall is $\tau_1 = \mu_{w_1} p_r$. Using the previous relations in Eq. 9, it allows finding that

$$\pi\left(r_0^2 - r_1^2\right) \frac{dp_z}{dz} = \pi\left(r_0^2 - r_1^2\right) \rho g - 2\pi\left(r_0\mu_{w_0} - r_1\mu_{w_1}\kappa\right) K p_z, \tag{10}$$

where $\kappa = \mathrm{K_1/K}$. This differential equation has the solution

$$P_J(z) = \frac{\left(r_0^2 - r_1^2\right)\rho g}{2K\left(r_0\mu_{w_0} - r_1\mu_{w_1}\kappa\right)} \times \left\{1 - exp\left[\left(-\frac{2K\left(r_0\mu_{w_0} - r_1\mu_{w_1\kappa}\right) z}{\left(r_0^2 - r_1^2\right)}\right)\right]\right\}, \tag{11}$$

or in a simpler form

$$P_J(z) = \rho g \lambda \left\{1 - exp\left[-\frac{z}{\lambda}\right]\right\}, \tag{12}$$

the screening parameter λ is now

$$\lambda = \frac{\left(r_0^2 - r_1^2\right)}{2K\left(r_0\mu_{w_0} - r_1\mu_{w_1}\kappa\right)}. \tag{13}$$

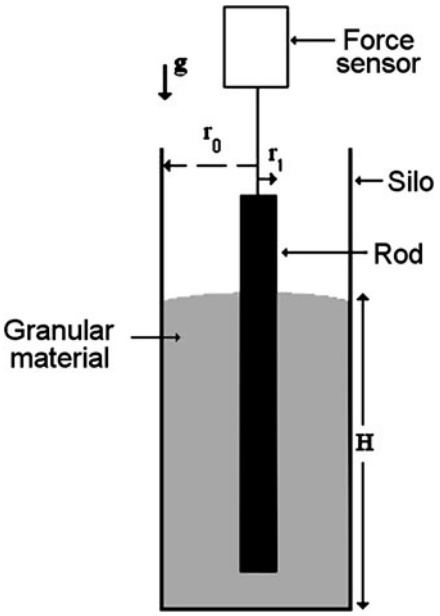

Fig. 3 Schematic of a cylindrical silo or radius r_0 filled up to the height $z = H$. In this case the *inner rod* has a radius r_1. In experiments the rod is sustained by a force meter in order to quantify the traction force which is detected during the filling process

If the inner rod is absent, $r_1 = 0$, immediately the Janssen pressure for a silo is obtained.

In accordance with the Janssen model, the traction force on the wall of the rod is

$$T(H) = 2\pi r_1 \int_0^H \tau_1(z)\, dz = T_{Jr}(H), \tag{14}$$

where $\tau_1 = \mu_{w_1} p_r = \mu_{w_1} K_1 p_z$, thus this traction force is finally

$$T_{Jr}(H) = 2\pi \mu_{w_1} K_1 \rho g \lambda r_1 \left\{ H - \lambda \left[1 - exp\left(-\frac{H}{\lambda} \right) \right] \right\}. \tag{15}$$

The traction on the wall of the silo is

$$T(H) = 2\pi r_0 \int_0^H \tau_0(z)\, dz = T_{Jw}(H), \tag{16}$$

$$T_{Jw}(H) = 2\pi \mu_{w_0} K_0 \rho g \lambda r_0 \left\{ H - \lambda \left[1 - \exp\left(-\frac{H}{\lambda} \right) \right] \right\}. \tag{17}$$

It is clear that the traction force on the wall of the silo, when there is a rod in itself, Eq. 17, is different from the traction when there is not a rod in the silo, Eq. 7. It will be discussed in next section.

Finally, we again use the two-parameters Janssen model: making $\tau = 0$ for $z < a$ and $\tau_1 = \mu_{w1}\ p_r$ and $\tau_0 = \mu_{w_0}\ p_r$ for $z > a$, where a, the thickness of the frictionless slice, is the second parameter of the model

$$p_z(z) = \begin{cases} \rho g z & \text{for } z < a \\ \rho g a + \left(1 - \frac{a}{\lambda}\right) P_j(z - a) & \text{for } z > a \end{cases} \tag{18}$$

according to the original Janssen model, and

$$T_r(H) = \begin{cases} 0 & \text{if } H < a \\ 2\pi\mu_{w_1} K_1 \rho g \lambda r_1 & \\ \times\left[(H - a) - \lambda\left(1 - \frac{a}{\lambda}\right)\left[1 - exp\left(-\frac{H-a}{\lambda}\right)\right]\right] & \text{for } H > a \end{cases} \tag{19}$$

according to the modified model,

$$T_w(H) = \begin{cases} 0 & \text{if } H < a \\ 2\pi\mu_{w_0} K_0 \rho g \lambda r_0 & \\ \times\left[(H - a) - \lambda\left(1 - \frac{a}{\lambda}\right)\left[1 - exp\left(-\frac{H-a}{\lambda}\right)\right]\right] & \text{for } H > a \end{cases} \tag{20}$$

It is clear that the traction force on the wall of the silo, when there is a rod in it Eqs. 17 and 20, is different from the traction when there is not a rod in the silo Eq. 7. It will be discussed in the next section.

4 Discussion of Results

In this part of the work we will show the behavior of the vertical pressure as a function of depth and the traction force on the wall of the silo and on the rod when this later object is absent or present during the filling. These plots will be useful to understand the role of the rod on the traction. We suppose the next conditions for the calculations: silo's inner radius $r_0 = 2.5$ cm, radius of the rod $r_1 = 0.75$ cm and a height of filling $H = 20$ cm. It was assumed that the friction coefficient between the wall and the granular material is $\mu_w = \mu_{wo} = 0.5$ and that the friction coefficient between the rod and the granular material is $\mu_{w1} = 0.3$. The bulk density was that of the glass spheres, $\rho = 1{,}600$ kg/m^3, we also assume that $K = 0.63$ and $a = 0.04$ m.

4.1 Traction Force on the Wall of the Silo

Employing those data in the equations derived in the previous sections we have made a series of plots that allow understanding the results here found for the pressures and tractions.

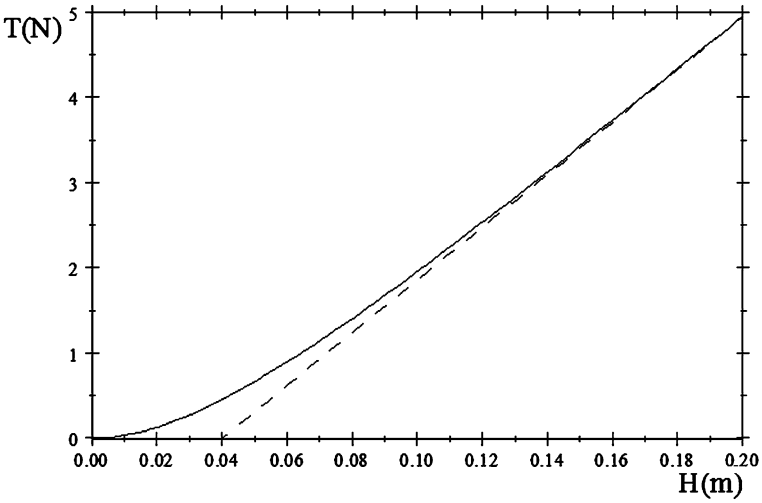

Fig. 4 Plot of the traction force on the wall of the silo: *continuous curve* corresponds the traction given by the Janssen model (Eq. 7) and the *dashed curve* corresponds to that given by the two-parameter Janssen model (Eq. 8)

In Fig. 4 we plot the traction on the wall of the silo where the rod is absent. The continuous curve corresponds to the Janssen model and the dashed curve corresponds to the traction obtained thought the modified Janssen model. The main aspect in this plot is that in the dashed curve appears a "dead" zone which is indicative of null traction for very small levels of filling, $H < a$ as is observed in experiments (Vargas et al. 2010).

4.2 Traction Forces on Rod and on the Wall of the Silo

We now suppose that there is a rod at the center of the silo and that its lower edge is very close to the bottom of the silo but it does not touches it. In a first instance the silo is filled with the glass beads. In Fig. 5 we plot the vertical pressure, p_z, as a function of z under the filling conditions assumed initially. The continuous curve describes the behavior of this pressure in accordance with the Janssen model, Eq. 12, and the dashed curve describes the pressure derived from the two-parameter Janssen model, Eq. 18. A very similar behavior of that for the dashed curve in Fig. 5 was reported by Landry et al. (2003) when a two-parameter Janssen model is assumed.

In Fig. 6 we plot the traction force on the wall of the silo and on the rod by using the Janssen model, i.e., the continuous curve of the pressure given in Fig. 5. In this plot is evident that traction on the silo wall is larger than on the rod but, additionally, in this case the traction force on the wall is larger than the traction

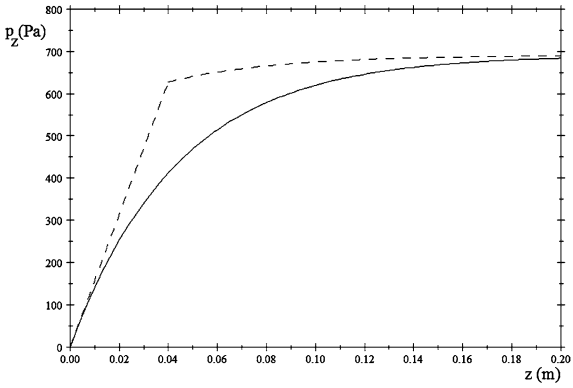

Fig. 5 Plot of the vertical pressure as a function of z when the rod is in the silo, the *continuous curve* corresponds to p_z given by the Janssen model, Eq. 12 and the *dashed curve* corresponds to p_z given by the two-parameter Janssen model, Eq. 18

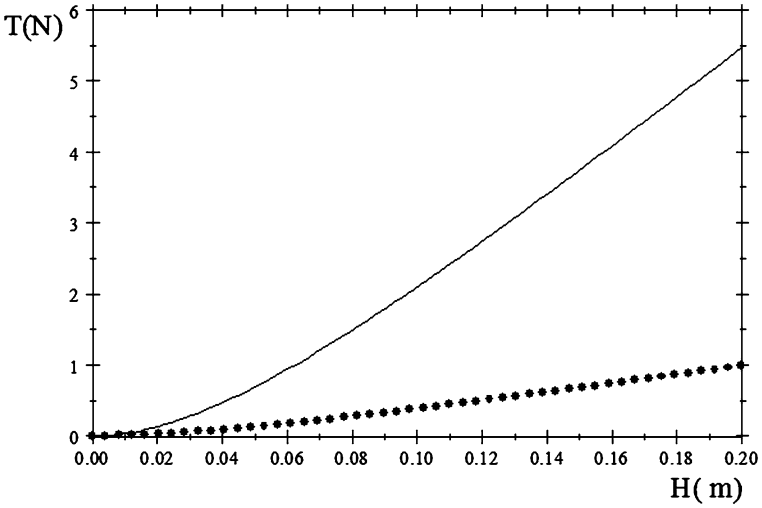

Fig. 6 Traction forces predicted through the Janssen model on the wall of the silo (*continuous curve*, Eq. 17) and on the rod (*dotted curve*, Eq. 15)

when the rod is absent (Fig. 3). Thus, the presence of the rod in the silo may increases the traction on the wall.

This result do not is general and it depends on the relative values of the friction coefficients, the Janssen constants and the radii.

In plot 7 we have plotted the traction force on the silo wall and on the rod by using the pressure obtained from the two-parameter Janssen model (dashed curve in Fig. 5). There is noted the dead zones of the tractions which are associated with the hydrostatic (linear) behavior of the dashed plot in Fig. 5.

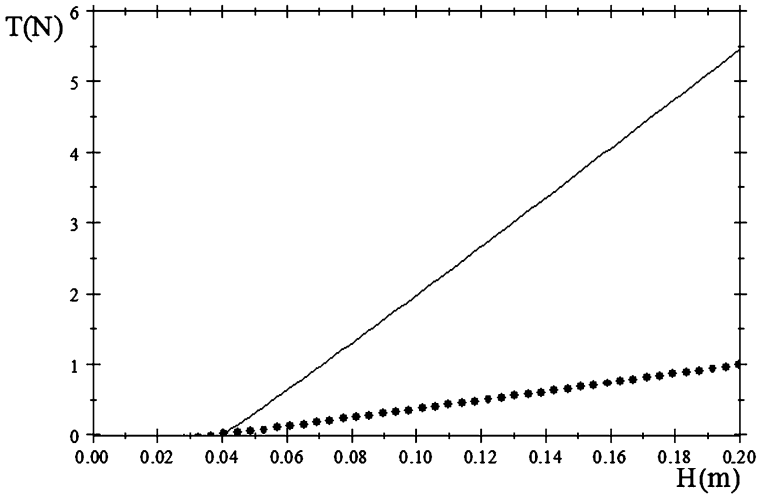

Fig. 7 Traction forces predicted through the two-parameter Janssen model on the wall of the silo (*continuous curve*, Eq. 19) and on the rod (*dotted curve*, Eq. 20)

Therefore, the dead zone in the traction occurs due to a hydrostatic behavior of the vertical pressure in the silo and such a behavior appears in silo with or without rods (Fig. 7).

5 Conclusions

In this work has been presented a theoretical study of the traction force on the wall of a cylindrical silo when it is filled with a non cohesive, dry granular material. Also the traction force on a rod and, simultaneously, on the wall of the silo were estimated following the same conditions. In both cases were plotted the tractions for all these cases when are used the Janssen model and the two-parameter (modified) Janssen model. It was found that both model give very similar results but the existence of the dead zone in the measurements of the traction it is adequately described by the modified Janssen model. Experimental studies yield similar results for the case of silos and more studies for the cases of silos with rods are now in process.

Acknowledgments A. M. thanks UAM Azcapotzalco for the support to this research through the Carlos Graef-Fernández chair.

References

Atkinson TD, Butcher JC, Izard MJ, Nedderman RM (1983) Chem Engng Sci 38:91
Boutreux TE, Raphael E, de Gennes PG (1997) Phys Rev E 55:5759
Bratberg I, Malloy KJ, Hansen A (2005) Eur Phys Jour E 18:245
Brown RL, Richards JC (1970) Principles of powder mechanics. Pergamon, New York
McGlinchey D (ed) (2008) Bulk solids handling: equipment selection and operation. Blackwell Publishing Ltd, Oxford
Janssen HA (1895) Zeitschr d Vereines deutcher Ingenieure 39:1045
Landry JW, Grest GS, Silbert LE, Plimpton SJ (2003) Phys Rev E 67
Ovarlez G, Clément E (2005) Eur Phys Jour E 16:421
Pitman EB (1994) Math Mtly Am 101:28–35
Schulze D (2008) Powders and bulk solids. Springer, Berlin
Shaxby JH, Evans JC (1923) Trans Faraday Soc 19:60
Vanel L, Clément E (1999) Eur Phys Jour B 11:525
Vanel L, Claudin P, Bouchaud JP, Cates M, Clément E, Wittmer JP (2000) Phys Rev Lett 84:1439–041303
Vargas CA, Medina A, Gutierrez, GJ (2010) Submitted Phys Lett A

The Collision of a Deformable Particle with a Corner Formed by Two Perpendicular Walls

J. Federico Hernández-Sánchez and Roberto Zenit

Abstract Squash is a highly competitive racquet sport. Professional players can answer most shots, regardless of how near the ball is to the wall. Only one shot is unanswerable. When the ball collides against the 'nick' formed by a vertical and a horizontal wall, under certain conditions, it rolls instead of bouncing, loosing most of its vertical momentum; hence, a reply is impossible. In this investigation, we study the conditions for this process to occur. We conducted visualizations with a high speed camera, throwing a squash ball to a corner to reproduce the nick shot in a controlled manner. Balls were thrown with a sling shot at different positions and angles in the vicinity of the corner. We determined the conditions for which a ball can loose all of its vertical bouncing motion. In this paper, we present some results, and a simple model to explain the phenomenon.

1 Introduction

The game of squash, a racquet sport, is played in a walled court. The ball is bounced off the walls, and points are scored when the opponent is not able to hit the ball back to the front wall before it bounces a second time against the floor. Experienced players are able to develop skills such that most shots can be answered regardless of the closeness to the walls or the position in the court (near

J. F. Hernández-Sánchez (✉) · R. Zenit
Instituto de Investigaciones en Materiales, Universidad Nacional Autónoma de México, 04510 México, D.F., Mexico
e-mail: fedejher@gmail.com

R. Zenit
e-mail: zenit@servidor.unam.mx

J. Klapp et al. (eds.), *Experimental and Theoretical Advances in Fluid Dynamics*, Environmental Science and Engineering, DOI: 10.1007/978-3-642-17958-7_39,

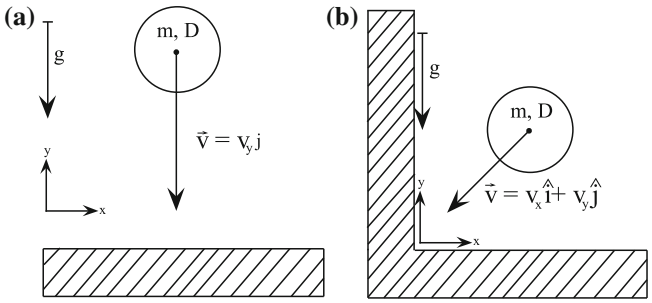

Fig. 1 Scheme of the experimental setup: **a** a ball thrown vertically against the floor, used to measure the coefficient of restitution; **b** the ball was launched at a certain angle in the vicinity of the nick formed by a vertical wall and the floor

the front or back). The only needed condition is that the ball bounces with sufficient vertical height. There is only one shot that cannot be answered at all: the nick shot. In this case, the ball collides with the corner formed between a vertical wall and the floor (literally, the nick); the ball does not bounce vertically, instead it rolls or moves horizontally very near the floor. Professional players, of course, aim to hit the nick on purpose while the rest of us simply hope for it. Although there are some serious studies of the mechanics of bouncing sport balls (Cross 2005), including squash balls (Chapman and Zuyderhoff 1986), to our knowledge, a mechanical analysis of the nick shot does not exist. Even in more specialized literature, where elastic and elasto-plastic collisions are studied (Johnson 1985), an analysis of the collision against two walls simultaneously has not been addressed to date. It is our purpose to investigate the conditions for which the vertical momentum is annihilated after a nick shot.

2 Experimental Setup

Experiments were conducted throwing a green dot squash ball (World Squash Federation 2010) against one or two walls as shown schematically in Fig. 1. The properties of the balls used here are listed in Table 1. The speed and angle of incidence were modified using an elastic band mounted on a base (a sling). Firstly, balls were made to collide normally against the floor to measure the coefficient of restitution (Fig. 1a). The coefficient of restitution was defined as

$$e = -\frac{U_2}{U_1} \tag{1}$$

where U_1 y U_2 are the wall-normal velocity components before and after the collision, respectively. This coefficient measures the global energy dissipation that occurs as a result of the collision.

Table 1 Properties of the squash ball; a green dot ball was considered (World Squash Federation 2010)

Property	Value
Diameter (d)	40 ± 0.4 mm
Mass (m)	24 ± 1 g
Rigidity (k)	3.2 ± 0.4 N/m
Restitution coefficient (e)	0.26 ± 0.33

Figure 1b shows the arrangement used to study the collision of the ball against the nick formed by a vertical wall and the floor. By slightly varying the contact point, we determined the conditions for which the ball left the corner with negligible vertical momentum. The process was filmed using a high speed camera with a framing rate of up to 1,500 frames per second. The obtained images were digitally processed to determine the center of gravity of the ball at each instant; for a given frame rate, the velocity components in each direction were calculated as the ratio of the displacement between frames and the time step, throughout the entire collision process.

3 Results

Figure 2 shows an image in which the profile of the ball was over-imposed for several instants before and after the collision. For this case, the ball bounced off against a horizontal wall to measure the restitution coefficient. The ellipses show the shape and position of the ball at different times; for each case, the center of the ellipse denotes the position of the geometric center of the ball and the ratio of long to short radius shows the deformation. Considering the definition of the coefficient of restitution (Eq. 1), we measured $e = 0.319 \pm 0.03$, for the range of velocities considered in this study $(U_1 \sim O(1)\,\mathrm{m/s})$. This value is in agreement to what is required by professional squash rules (World Squash Federation 2010).

Figures 3 and 4 show image sequences of two typical collisions aimed at the nick. Figure 3 shows the case for which the ball collided very near the nick, touching both vertical and horizontal walls nearly at the same time. However, the ball is observed to bounce significantly in the vertical direction. On the other hand, when the ball collides first with the vertical wall, in the close vicinity of the nick, the bounce trajectory is almost parallel to the horizontal wall, as shown in Fig. 4. It is important to closely observe the ball during the contact in this case: as the ball deforms colliding with the vertical wall, its lower edge appears to slightly touch the horizontal wall. We believe that during this instant there is a complex energy transfer process; the vertical momentum cannot be dissipated simply from the normal contact (as shown below), so there must be a transfer of momentum from the horizontal translational direction to rotational momentum.

Figure 5 shows the trajectories of the two experiments shown above (Figs. 3, 4). Clearly, the trajectory for which the nick shot is observed shows a bouncing trajectory which is nearly parallel to the horizontal wall. For the other case, the ball

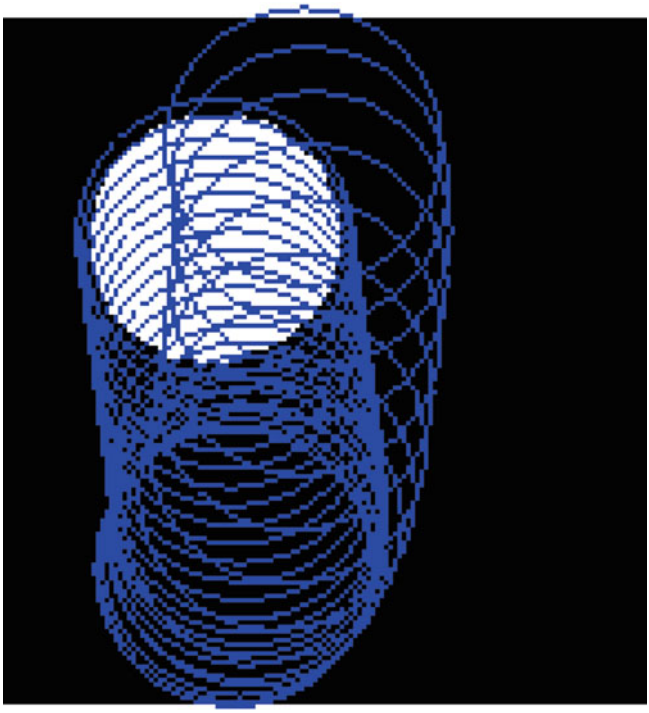

Fig. 2 The image shows the binarized image of a squash ball bouncing off a horizontal wall. The ball corresponds to the filled region. The geometric center of this region was measured for different instants during the collision. The empty ellipses (fitted to the filled regions) show the position and shape of the ball during the process

bounces back with a trajectory which is, in fact, slightly more elevated that the incoming one.

4 Discussion

Let us consider a simple model to infer the energy loss resulting from a collision. If we consider that the kinetic energy of the ball is given by $E_k = \frac{1}{2}m|\mathbf{v}|^2$, where m is the mass of the ball and $\mathbf{V}$ its velocity, we can calculate the energy dissipation as:

$$\Pi = \frac{E_{k2}}{E_{k1}} \tag{2}$$

where E_{k2} and E_{k1} are the kinetic energies after and before the wall contact, respectively. Therefore,

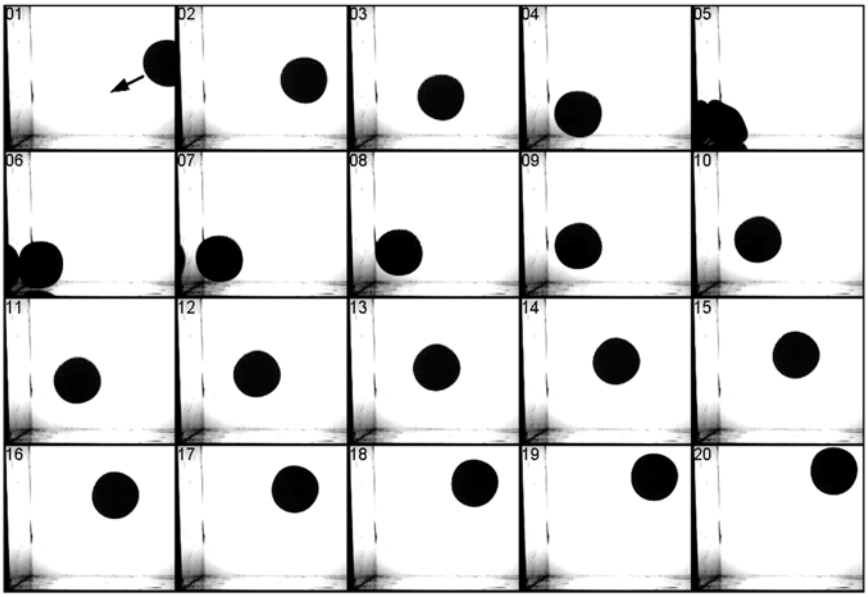

Fig. 3 Image sequence of the collision of a ball very near the nick formed by the vertical and horizontal walls. The time interval between images is 2 ms. In this case, the contact with both walls is nearly simultaneous; however, the ball bounces off vertically. The nick shot did not occur

$$\Pi = \frac{U_2^2 + V_2^2}{U_1^2 + V_1^2} \tag{3}$$

where U and V are the velocity components in the horizontal and vertical directions, respectively. If we assume that the collision of a ball with two walls can be modeled as the succession of two separate normal collisions, as illustrated in Fig. 6, and considering the definition of the restitution coefficient (Eq. 1), the loss of kinetic energy can simply be expressed as:

$$\Pi = e^2 \tag{4}$$

Hence, if the restitution coefficient is known, the energy dissipated during a collision can be evaluated.

Moreover, we can calculate the dissipation of kinetic energy in each separate direction independently considering

$$\Pi_H = \frac{U_2^2}{U_1^2} = e^2 \tag{5}$$

$$\Pi_V = \frac{V_2^2}{V_1^2} = e^2 \tag{6}$$

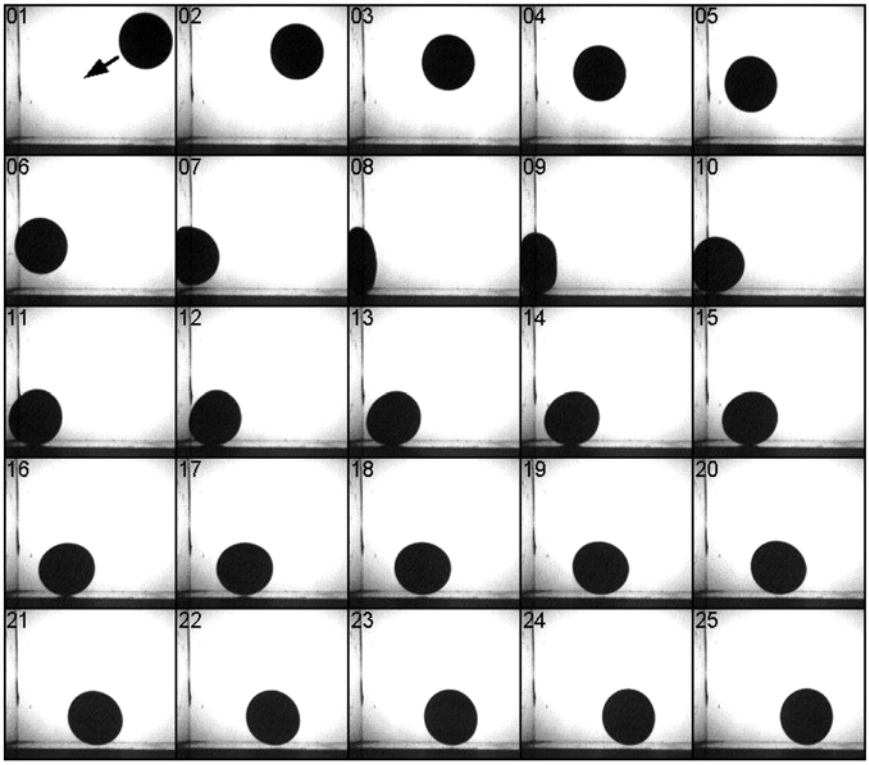

Fig. 4 Image sequence of the collision of a ball very near the nick formed by the vertical and horizontal walls. The time interval between images is 2 ms. In this case, the nick shot is observed. The contact occurs first with the vertical wall; note that when the ball deforms, its lower edge touches the horizontal wall. As a result, the ball leaves the wall with a negligible vertical motion nearly rolling over the floor

In Table 2 the measurements obtained for two typical collisions (those shown in Figs. 3 and 4) are shown. The measurements are compared with the predictions of the simple model shown above.

For all cases, the collisions are very dissipative processes. Even for the single wall collision, only 8% of the initial kinetic energy is preserved. For the two-wall contacts, the energy lost is even larger. For the nick shot case, the kinetic energy in the vertical direction is almost completely annihilated: only 1% of the initial energy in that direction remains (this is the essence of a successful nick shot). The model correctly predicts the amount of energy dissipation for a single wall collision (within 20%). However, for collisions with two walls the predicted energy loss is greatly underestimated, even for the case in which the nick shot was not observed.

The model is rather simple, and it only gives us an estimation of the energy loss that occurs as a result of the normal contact. Hence, the difference between the

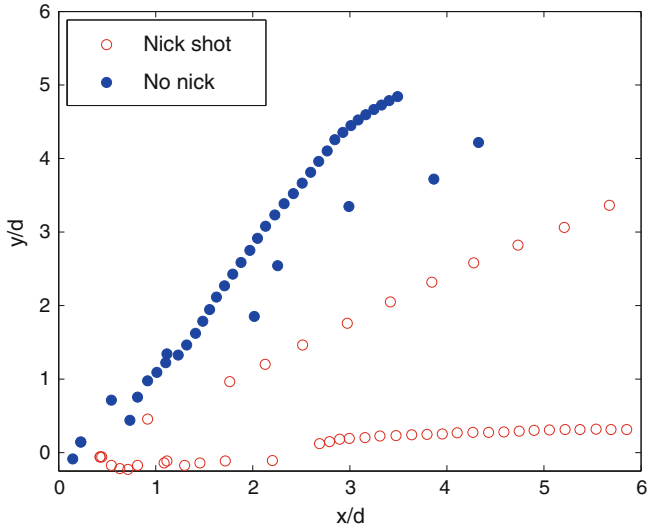

Fig. 5 Collision trajectory. Two typical cases are shown: a contact near the nick with bounce (filled circles) and a collision slightly above the nick (empty circles) for which no vertical bounce is observed, a successful nick shot

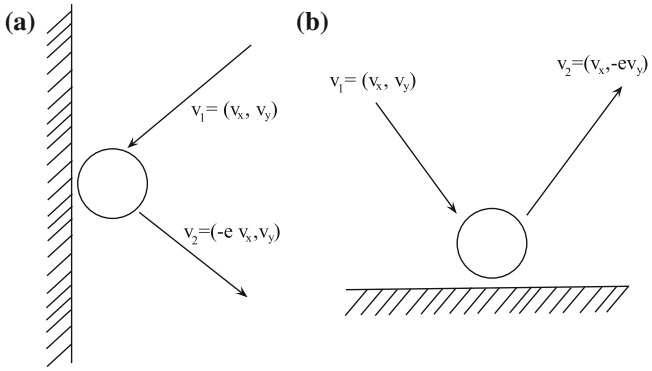

Fig. 6 Simplification of the collision with two walls **a** first, the impact with the vertical wall is considered: the vertical velocity component is unaffected by the process while the horizontal velocity changes sign and is damped by factor *e* (the coefficient of restitution). **b** Similarly, for the contact with the horizontal wall, the horizontal velocity component of the ball remains the same after the contact. The vertical velocity changes sign and is reduced in magnitude by a factor *e*

predictions and the measurements result from other effects (other than normal contacts). We believe that, when a nick shot occurs, the bouncing ball acquires rotational momentum. That is to say, some of the linear momentum is transformed into rotational momentum; hence, some momentum is not dissipated but instead is transformed into rotation. However, with the present experimental technique we

Table 2 Energy dissipation during a collision

	Π		Π_H		Π_V	
Condition	Measurement	Model	Measurement	Model	Measurement	Model
One wall	0.073	0.090	-	-	0.073	0.090
Two walls, no nick	0.058	0.090	0.040	0.090	0.132	0.0090
Two walls, nick	0.063	0.090	0.080	0.090	0.001	0.090

Measurements and model results. For all cases $e = 0.3$ was considered

cannot determine the amount of rotation acquired by the ball resulting from the collision. We intend to incorporate a more general definition of the coefficient of restitution to account for rotational motion, like that proposed by Cross (1999):

$$e_x = \frac{v_{y2}}{v_{y1}} \tag{7}$$

$$e_y = \frac{v_{x2} - R\omega_2}{v_{y1} - R\omega_1} \tag{8}$$

where R is the ball radius and ω is the angular velocity.

Another factor which is not taken into account by the model is the fact that the ball attains very large deformations during the contact. Such deformation can cause other non linear effects which could not be captured by the superposition of normal contacts. To fully elucidate the process, numerical simulations could be conducted. There are techniques available (Tsuji 1992) to account for large deformation effects. We plan to continue this investigation in this direction in the future.

5 Conclusion

Experiments were conducted to investigate the collision of squash balls against walls in typical game conditions. In particular, we investigated the reasons for the complete dissipation of vertical kinetic energy during the bounce of a ball which hits the nick formed by the floor and a vertical wall (the nick shot). To calibrate our experimental technique, we measured the normal coefficient of restitution by throwing balls vertically towards the floor. We found very good agreement between the measured coefficient of restitution and that reported nominally ($e = 0.3$). For the case of collisions aimed at the nick, we found that the vertical momentum during the bounce is significantly reduced if the ball collides first with the vertical wall. If during the deformation caused by collision, the lower edge of the ball graces the floor, the outgoing trajectory is almost horizontal with negligible vertical momentum. By considering a simplified normal contact model, we inferred that rotation and large deformation effects are very important in this process. Yet, a more in depth investigation is needed to

fully elucidate this process. Although we now understand this shot better, our squash skills remain rather modest!

References

Chapman AE, Zuyderhoff RN (1986) Squash ball mechanics and implications for play. Can J Appl Sport Sci 11:47–54
Cross R (2005) Bounce of a spinning ball near normal incidence. Am J Phys 173:914–920
Cross R (1999) The bounce of a ball. Am J Phys 67:222–227
Johnson KL (1985) Contact mechanics. Cambridge University Press, Cambridge
World Squash Federation (2010) World Squash Singles Rules
Tsuji Y, Tanaka T, Ishida T (1992) Lagrangian numerical simulation of plug flow of cohesionless particles in a horizontal pipe. Powder Technol. 71:239–250

Part VI
Viscous Flow

Numerical Simulation of Vortex Formation Inside a Cavity with Two Cross Jet Flows

Guillermo E. Ovando-Chacon, Sandy L. Ovando-Chacon, Juan C. Prince-Avelino and Alberto Servin-Martínez

Abstract Simulations of steady state fluid dynamics and heat transfer in a two-dimensional flow inside a channel with main and secondary inlet flows were carried out in this work for a Reynolds number of $Re = 1{,}562$. The main cool jet was injected by a submerged inlet at the top while the secondary hot jets were injected at the vertical walls. The analysis was done by the finite element method for three different positions of the lateral entrance and three different velocities ratios of the main and secondary jets. The vortex formation and heat fluxes were analyzed and the temperature, streamline and velocity fields were obtained. The simulations have shown that is possible to control the dynamics and formation of vortices inside a channel with the variation of the secondary jet position.

G. E. Ovando-Chacon (✉) · S. L. Ovando-Chacon · J. C. Prince-Avelino · A. Servin-Martínez
Depto.de Metal Mecánica y Mecatrónica, Instituto Tecnológico de Veracruz, Calzada Miguel A. de Quevedo 2779, Col. Formando Hogar, 91860 Veracruz, Mexico
e-mail: geoc@itver.edu.mx

S. L. Ovando-Chacon
e-mail: ovansandy@hotmail.com

J. C. Prince-Avelino
e-mail: jcpa@itv.edu.mx

A. Servin-Martínez
e-mail: alser@hotmail.com

J. Klapp et al. (eds.), *Experimental and Theoretical Advances in Fluid Dynamics*, Environmental Science and Engineering, DOI: 10.1007/978-3-642-17958-7_40,

1 Introduction

The fluid dynamic analysis inside a channel has been the subject of several studies due to the fact that is present in many practical situations and natural processes. The mixing of two jets at different temperature is important due to the number of technical applications, such as separation process in industries, dispersion of contaminants through fluids, solidification of liquid metals, etc. An indepth knowledge of the flow behavior generated by the interaction between two jets may help in designing and optimizing many engineering problems. Arruda et al. (2006) and (Lawson and Davidson 2001) studied the oscillation of a submerged jet inside a cavity with secondary flow that represented a scale model of a typical mould of a thin slab steel casting. (Chiang et al. 1999) investigated numerically the vortex formation and the reattachment lengths in a channel with a backward-facing step for laminar flows. (Martínez and Esperanza 2007) simulated a two-dimensional viscous incompressible flow generated as fluid passes over a backward-facing step and they obtained the separation point and the velocity profiles for Reynolds numbers up to 875. Barbosa et al. (2007) studied numerically the laminar flow in a three dimensional horizontal forward facing step channel. The reattachment lines, separation lines, velocity profiles and pressure contours were presented. Bilir and Ates (2003) analyzed the heat transfer in tick walled pipes for thermally developing laminar flows. The heat by convection from the ambient fluid with a heat transfer coefficient was imposed along the outer wall surface in the downstream region. Sivasamy et al. (2010) studied the jet impingement cooling of a constant heat flux surface immersed in a fluid and they obtained the streamlines, the isotherms and the Nusselt number. They found that the heat transfer rate is increased when the distance from the jet exit to the heat source is reduced. The objective of this numerical investigation is to study the effect of the secondary jet position on the vortex formation over a channel with a submerged main jet. The interaction of two jets generates vortices in the flow field, which control the transport process inside the channel.

2 Problem Formulation

In this work, it is considered a moderate Reynolds number where the vortex formation occurs and the flow is assumed to be two-dimensional because the major changes only occur in the axial and transversal directions. The simulations were carried out inside an axial symmetric channel with a submerged main flow inlet at the top and two secondary flow inlets at the vertical walls. The main flow moves downward and the secondary flows move horizontally, see Fig. 1. The diameter and the velocity of the main jet is denoted by D_m and U_m, respectively. The diameter and the velocity of the secondary jet is denoted by D_s and U_s, respectively. No slip boundary conditions were established in all the walls of the channel.

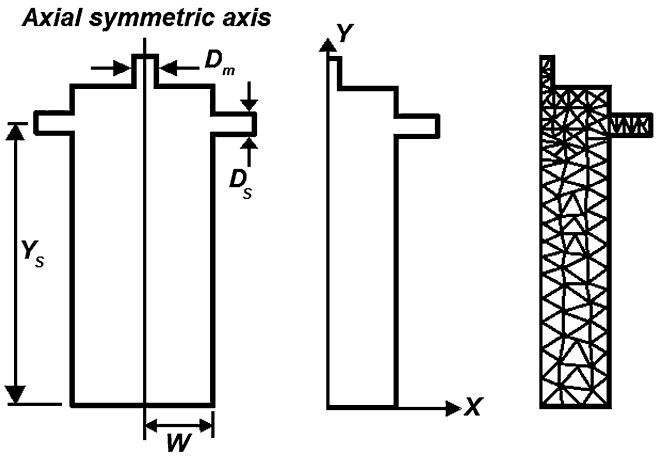

Fig. 1 Geometry of an axial symmetric channel with a main jet entrance and two laterals secondary jet entrances

The Reynolds number ($Re = U_m\ W/\nu$), based on the velocity of the main jet, studied in this investigation was of $Re = 1{,}562$, and the semi width of the channel (W) was of 0.125 m. This analysis consider a diameter ratio of the main and secondary jets entrances of $D_m/D_s = 1.4$ for three velocity ratios of the main and secondary flows of $U_m/U_s = 2, 5, 1.25$. The entrances of the secondary jets were located at three different positions of $Y_s = 0.555, 0.425, 0.196$ m. Due to the symmetry of the channel only the middle part of the domain was simulated. The top wall of the channel was supposed adiabatic, while the main and secondary entrances conduits were also considered adiabatic. In the vertical boundaries, the convection heat flux condition was imposed with $h = 5$ W/m^2.°C and $T_\infty = 303.5$ K. The main jet temperature was of $T_m = 303.15$ K and the secondary jet temperature was fixed at $T_s = 333.15$ K. The Navier–Stokes equation coupled with the energy equation and the Boussinesq approximation, for a non-isothermal incompressible steady state flow, was solved with the finite element method combined with the operator splitting scheme, see Glowinski (2003).

3 Results

The left panel of Fig. 2 shows the details of the streamlines and the temperature field for a flow inside a channel with a lateral secondary jet inlet at $Y_s = 0.555$ m for a speed ratio of the main and secondary jets of $U_m/U_s = 2$. For this arrangement, it was observed a clockwise, small and strong vortex at the top of the channel. This vortex formation was due to the interaction between the horizontal secondary jet and the submerged wall of the main jet entrance. The secondary jet emerges horizontally, but as moves forwards its vertical component is increased

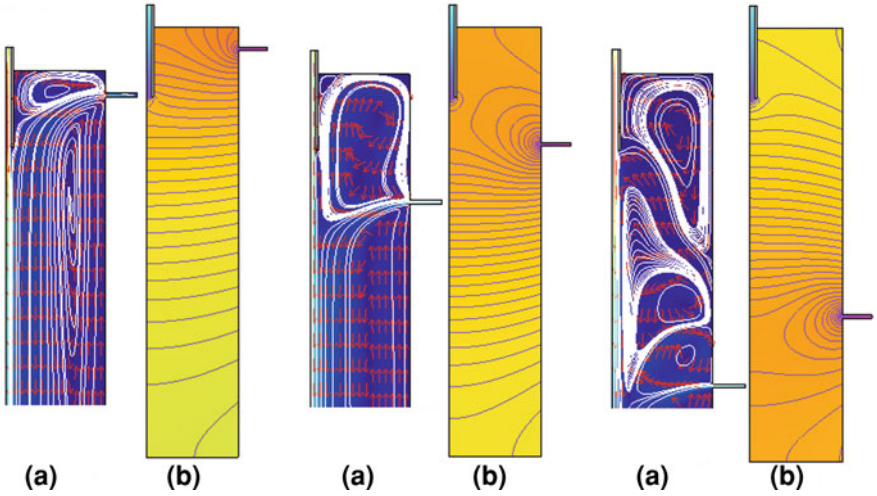

Fig. 2 **a** Details of the streamlines. **b** Temperature field for $Re = 1{,}562$ and $U_m/U_s = 2$. *Left* $Y_s = 0.555$ m. *Middle* $Y_s = 0.425$ m. *Right* $Y_s = 0.196$ m

downward, however the perturbation due to the impingement of this jet against the wall generates fluid recirculation and part of the secondary jet is projected upward. At the central part of the domain, an anti-clockwise vortex of less intensity and extended in the axial direction was observed, which was formed due to the interaction between the downward high-speed stream of the main jet and the upward stream on the vertical wall driven by shedding of boundary layer. As the secondary flow exits from its entrance conduit and it is injected to the channel, the fluid experiments an abrupt change of transversal section generating recirculation zones up and down of the secondary jet. The parcels of fluid located at the top of the secondary stream tend to produce a clockwise rotation; while the parcels of fluid located at the bottom of the secondary stream tend to produce an anti-clockwise rotation, which is perturbed by the strong stream of the main jet generating the axial vortex. Below of the secondary jet entrance, the behavior of the fluid is more uniform and it can be observed a downward stream at the center of the channel and a weak upward stream near of the vertical wall.

The main flow was injected at the surrounding temperature while the secondary flow was injected at higher temperature. The mixing of the two jets kept the fluid inside the channel with a uniform temperature of 323 ± 2 K. As it was expected, the fluid temperature at the neighborhood of the secondary entrance was slightly hotter 325 K, while in the outlet of the channel the fluid temperature was slightly cooler 321 K. The above behavior implies that convective effects dominate the fluid dynamics of the jets due to the fact that the hot fluid is kept above and the cool fluid is kept below. Middle panel of Fig. 2 shows the details of the streamlines and temperature field for a fluid inside a channel with a lateral secondary jet inlet at $Y_s = 0.425$ m for a speed ratio of the main and secondary jets of $U_m/U_s = 2$. For this arrangement, it was observed a clockwise and large vortex above of the

secondary jet entrance, which occupies all the semi width of the channel domain. This vortex formation is driven by the horizontal stream of the secondary jet and its interaction with the stream of the main jet which moves downward. For this case, the secondary jet exits horizontally and then part of this fluid moves downward carried away by the stream of the main jet, while the rest of the fluid changes abruptly its direction upward impinging against the corner formed by the wall of the submerged entrance and the top wall of the channel where it can be seen a small zone of secondary vorticity with an opposite rotation in regard to the main vortex, as a consequence of its high velocity gradients. Below of the secondary entrance, it is observed two zones, one of them is characterized for a downward stream near the symmetry axis where the main jet effect dominates. The other one is characterized for an upward flow due to the recirculation effect at the entrance of the secondary jet where viscous effects are high. Above of the secondary entrance, the fluid is kept at a temperature of 324 K, while the fluid reduces its temperature until reaching a temperature of 322 K at the bottom end of the channel, that is, the hot fluid moves upward and the cool fluid moves downward. The right panel of Fig. 2 shows details of the streamlines and the temperature field for a fluid inside a channel with a lateral secondary jet inlet at $Y_s = 0.196$ m for a speed ratio of the main and secondary jets of $U_m/U_s = 2$. In this case the vortex formation is more complex and it can be observed that three vortices locate above the secondary jet entrance. The upper vortex has a clockwise rotation, below appears other vortex with anti-clockwise rotation. On the other hand, just above of the secondary jet entrance one-third vortex appears which has a clockwise rotation due to the impulse of the secondary jet, which moves horizontally leftward and impinges against the stream of the main jet. For this case the fluid is kept at a cooler temperature of 322 K on the top and a hotter temperature of 324 K at the exit of the channel, this implies that jets effects dominate over the convective effects inside the channel provoking that cool fluid is placed above and the hot fluid sets below.

Figure 3 shows the streamlines, the velocity and the temperature fields for Re = 1,562 with $U_m/U_S = 5$ and $U_m/U_S = 1.25$ for three different positions of the secondary jet entrance. If the velocity of the secondary flow is reduced ($U_m/U_S = 5$), the intensity of the vortices is reduced and for $Y = 0.555$ m the vortices practically disappear, while the temperature fields remain with small changes. For $Y_s = 0.196$ m the intensity of the superior and inferior vortices is reduced while the central vortex increases its intensity when the secondary jet velocity is increased ($U_m/U_S = 1.25$). In order to analyze in detail the perturbation of the main jet due to the secondary jet, the axial velocity profiles were obtained at $y = 0.485$ m.

In order to get insight of the effect of the secondary jet in the fluid dynamic, we simulated the case without secondary jet for $Re = 1562$; see panel (b) of Fig. 4, observing that when there is no secondary jet, only a small weak vortex is formed at the corner between the submerged entrance and the top wall of the channel. On the other hand, from the comparison of panels b of Fig. 1, it can be established that the position of the secondary jet can control the formation and distribution of

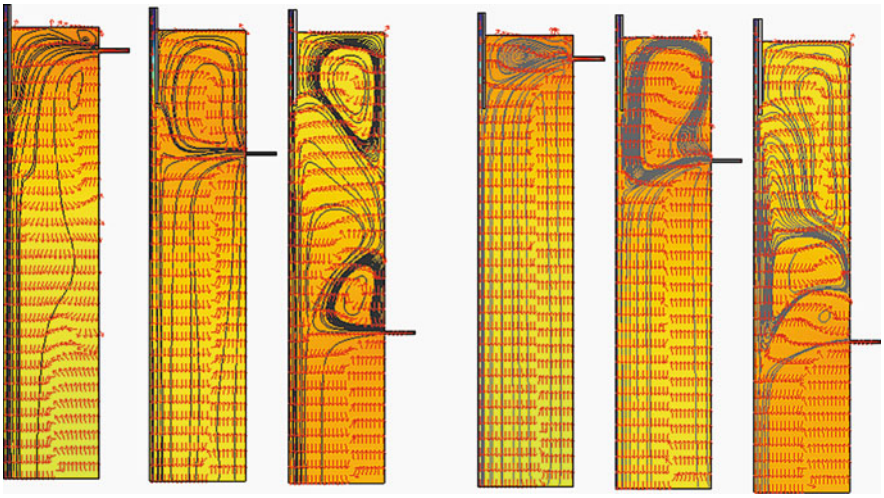

Fig. 3 Streamlines, velocity and temperature fields for $Re = 1{,}562$ and three different position of the secondary jet. *Left*: $U_m/U_s = 5$. *Right*: $U_m/U_s = 1.25$

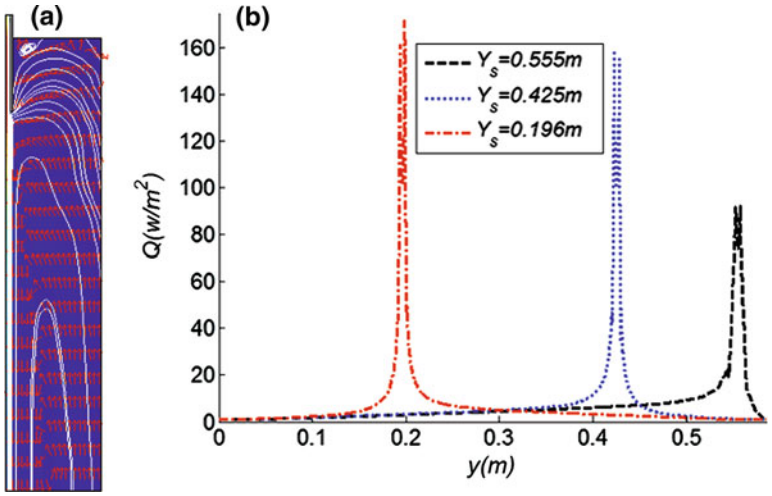

Fig. 4 **a** Streamlines and velocity field for the case without a secondary jet with $Re = 1{,}562$. **b** Axial velocity profiles as a function of the transversal coordinate at $y = 0.485$ m. *Left* $Y_s = 0.555$ m. *Right* $Y_s = 0.425$ m

the vortices inside the channel, which suggests that a secondary jet can enhance the mixing process, transport and dispersion of particle in the flow.

The panel (b) of Fig. 4 shows the heat flux along the vertical boundary for three different positions of the secondary jet with $U_m/U_s = 2$, observing that the heat flux tends to zero far away of the secondary jet, due to the fact that in this zone the

fluid reaches thermal equilibrium with the surroundings. The heat flux peak corresponds to the zone where the secondary jet starts to mix with the rest of the fluid. For $Y_s = 0.196$ m, it was observed the maximum heat flux peak.

4 Conclusions

Heat transfer and fluid dynamics simulations of the flow inside a channel fed by a main jet and two axial symmetrically secondary jets are presented in this work. It was found that for a channel without secondary jet, only one vortex appears beside of the submerged entrance of the main jet, which becomes stronger and bigger as the *Re* is increased, this agrees with the simulation reported by Arruda et al. (2006). On the other hand, the results demonstrate that the size and the position of the vortices can be perturbed by a secondary jet in the channel due to the interaction of the jets shear layers. This instability involves the break-up and shedding of the cross-flow boundary layer associated with the deformation of the secondary jet fluid sheets. The streamline patterns reveal that when the secondary jet impinges directly with the main jet, the number of vortices increases given as a result a more uniform temperature of the fluid inside the channel. For the studied cases, always appears one clockwise vortex at the top of the channel and below of this one anti-clockwise was formed when the secondary jet is located at $Y_s = 0.196$ m. Furthermore, as the secondary jet is locate far away from the main jet entrance the vortices are elongated axially. The heat flux peaks along the vertical boundary occur when the secondary jet meets the fluid inside the channel. The model implemented in this work, captures the effect of the secondary jet in the vortex formation process and in the heat transfer phenomena. So far, this study is limited by the Reynolds number of 1,562, the fluid dynamic behavior beyond this value is the subject of ongoing research, but it is useful to understand the secondary jets effect on flows and it is considered that the results can have significant implications in practical process such as mixing of solutes or solid particles in the fluid, the control of the material final properties of continuous casting and the dispersion of pollutants.

References

Arruda MP, Lawson NJ, Davidson M (2006) Control of an oscillatory rectangular cavity jet flow by secondary injection. JSME Int J Serie B 49:1105–1110

Barbosa JG, Quinto P, Sánchez F, Carbajal I (2007) Numerical simulation for the flow structures following a three-dimensional horizontal forward-facing channel. Rev Mexi Fís 53:87–95

Bilir S, Ates A (2003) Transient conjugated heat transfer in thick walled pipes with convective boundary conditions. Int J Heat Mass Transfer 46:2701–2709

Chiang TP, Sheu TWH, Fang CC (1999) Numerical investigation of vortical evolution in a backward-facing step expansion flow. Appl Math Model 23:915–932

Glowinski R (2003) Numerical methods for fluids. Part 3, Handbook of Numerical Analysis, vol IX, Garlet PG, Lions JL (eds), North-Holland, Amsterdam

Lawson NJ, Davidson MR (2001) Self-sustained oscillation of a submerged jet in a thin rectangular cavity. J Fluids Struct 15:59–81

Martínez JJ, Esperanza PT (2007) A chebyshev collocation spectral method for numerical simulation of incompressible flow problems. J Braz Soc Mech Sci Eng XXIX 3:317–328

Sivasamy A, Selladurai V, Rajesh Kanna P (2010) Mixed convection on jet impingement cooling of a constant heat flux horizontal porous layer. Int J Therm Sci 49:1238–1246

Numerical Study of Water Flow in a Channel Output with Periodic Forcing

Erick Javier López-Sánchez and Gerardo Ruiz-Chavarría

Abstract In this work a numerical solution for the flow in a system of two basins connected by a channel is presented. The flow rate is assumed to be time dependent. With this assumption we intend to model the effect of tides in coastal systems. Our results show the formation of a vortex dipole at the channel outlet. Evolution of dipole depends strongly on the period of flow rate, as already noted by previous works. Using the velocity field obtained with the numerical method we calculate trajectories of fluid particles and show that dipole has an effect of suction in the region it pass. On the other hand the process of vortex formation and further evolution are well described.

1 Introduction

Vortex formation near a solid wall is a fact well known in fluid dynamics. Von Karman Street in a fluid past a cylinder is a typical example. At a different scale, vortex formation also occurs at the outlet of a river or a channel, as we can see in Fig. 1, where a satellite image is shown. In the figure a vortex street evolves near the coastal line.

Wells and Van Heijst modeled this kind of flow with the introduction of a dipole and a sink (Wells and Van Heijst 2003). The model is based on potential theory and consequently vorticity creation or destruction are not allowed.

E. J. López-Sánchez (✉) · G. Ruiz-Chavarría
Facultad de Ciencias, UNAM, Circuito exterior s/n, Ciudad Universitaria,
04520 México City, D.F., Mexico
e-mail: lsej@ciencias.unam.mx

G. Ruiz-Chavarría
e-mail: gruiz@servidor.unam.mx

J. Klapp et al. (eds.), *Experimental and Theoretical Advances in Fluid Dynamics*, Environmental Science and Engineering, DOI: 10.1007/978-3-642-17958-7_41,

Fig. 1 Vortex street in the sea. Image was taken from a satellite. Vorticity is produced by the shear in the channel (picture taken from Google Earth 5.1)

According to them, when translation velocity of the vortex dipole exceeds velocity induced by the sink, the dipole escapes. Model is validated in a laboratory experiment with shallow waters.

The main result of this work is set forth in terms of a dimensionless parameter $S = H1/UT$, where $H1$ is the channel width, U is the maximum velocity and T is the forcing period. According to them dipole escapes when $S < 0.13$.

More recently Lacaze et al. (2010) present experimental results on the dynamics of a vortex dipole evolving in a shallow fluid layer and show the existence of three dimensional effects. A span wise vortex is formed in front of dipole and then vertical motion is generated.

The problem we address is the calculation of fluid particle paths in a system of two rectangular domains connected by a channel when flow rate has sinusoidal time dependence. To this end we solve in a first stage vorticity and stream function equations in two dimensions. Then particle displacement is calculated provided the velocity field is known.

Attention is devoted among other things to the vortex formation and eventually to the process of destruction of dipole. Moreover, suction effect is highlight by the fact that distances traveled by some particles are greater than the distance traveled by the dipole.

2 Theoretical Framework and Methodology

In this work the system of two basins connected by a channel is intended to represent for example a coastal lake flushing into the sea. The basins and the channel are assumed to be rectangular. Two-dimensional solution is carried out by the use of a Chebyshev pseudo spectral code for spatial variables and second order finite difference for the time.

The system is decomposed in seven domains as shown in Fig. 2. This decomposition is made so that the collocation points of any two domains coincide in their intersections.

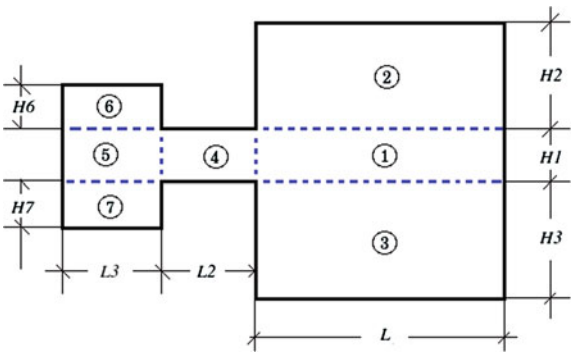

Fig. 2 System of two basins connected by a channel. In order to obtain numerical solution, system is decomposed in seven domains. The purpose of such decomposition is to match collocation points in the intersections

In a two dimensional incompressible flow, we can introduce the stream function ψ, which is related to velocity field $\vec{u} = (u, v)$ through the two relations:

$$u = \frac{\partial \psi}{\partial y},\ v = -\frac{\partial \psi}{\partial x} \tag{1}$$

On the other hand, the vorticity $\vec{\omega} = \omega \hat{k} = curl(\vec{u})$ can be written in terms of stream function:

$$\omega = -\nabla^2 \psi \tag{2}$$

If curl operator is applied to Navier–Stokes equation we obtain the vorticity equation:

$$\frac{\partial \omega}{\partial t} + \left(\frac{\partial \omega}{\partial x}\frac{\partial \psi}{\partial y} - \frac{\partial \omega}{\partial y}\frac{\partial \psi}{\partial x} \right) = v \nabla^2 \omega \tag{3}$$

where v is the kinematical viscosity.

The system (2), (3) is equivalent to Navier–Stokes and continuity equations. The main advantage of this system lies in the fact that the number of equations is reduced from 3 to 2.We introduce a variable flow rate:

$$\alpha = \alpha_0 \, sin(\omega_f t) \tag{4}$$

where ω_f is the forcing frequency. This choice allows periodical reversal in the flow and is intended to mimic the effect of tides. Before solving equations we write them in non-dimensional form. To this end the width of channel ($H1$) is selected as the characteristic length while the representative velocity is taken as $U = \alpha_0 / H1$, that is, the velocity attained when flow rate is maximum. The dimensionless equations are:

$$\nabla^2 \psi = -\omega \tag{5}$$

$$\frac{\partial \omega}{\partial t} + \left(\frac{\partial \omega}{\partial x}\frac{\partial \psi}{\partial y} - \frac{\partial \omega}{\partial y}\frac{\partial \psi}{\partial x} \right) = \frac{1}{Re} \nabla^2 \omega \tag{6}$$

here $Re = U\, H1/v$ is the Reynolds number.

In order to solve system (5), (6), boundary conditions must be imposed. First at all velocity vanish in solid walls: $\vec{u} = 0$. When velocity is decomposed in normal and tangential components, conditions for Eq. 5 are easily recovered. $u_n = 0$ is equivalent to put $\psi =$ constant. Due to the fact that ψ is defined up to an undetermined constant we select $\psi = 0$ on the solid boundaries situated on the lower part of Fig. 2. On the other side, value of ψ in the upper wall is the flow rate: $\psi = \alpha_0 sin(\omega t)$. At this stage vanishing of tangential velocity has not been invoked, but this condition must be accomplished. The key to impose $u_t = 0$ comes from the fact that we don't have boundary conditions for vorticity Eq. 6. Considering that ψ and ω depend on each other, values of vorticity in solid boundaries are selected in a such manner that $u_t = 0$ is satisfied. This procedure is well known in the vorticity- stream function formulation (Peyret 2002). Finally, conditions for remaining boundaries are of Neumann kind, that is vanish of normal derivative is imposed either for ψ or ω.

As initial condition, we assume that flow is at rest. In order to test numerical method in different conditions, some simulations were made with constant flow rate. In this circumstance a parabolic profile for velocity is set initially for domains 1, 4 and 5, and velocity equal 0 on other domains. This condition can be approximated in experiments if solid plates are put in the intersection of domains 1–2, 1–3, 5–6 and 5–7. At $t = 0$, plates are removed and flow evolves over all domains.

3 Numerical Method

Spectral methods for solving differential equations are based in the principle that the solution is approximated with a sum of orthogonal functions. Two types of spectral methods are mostly used, based respectively on trigonometric (Fourier) or polynomial (Chebyshev) functions. The choice between them is made according to the characteristic of the problem under study. In our case Chebyschev method is used. Instead of calculating coefficients appearing in the sum, solution is obtained in a set of points (collocation points). This procedure is known as pseudo spectral method. In the Chebyshev method, collocation points lie in the interval $[-1, 1]$ according to the Gauss–Lobatto formula:

$$x_i = cos\left(\frac{i\pi}{N_x}\right),\ y_j = \cos\left(\frac{j\pi}{N_y}\right),\ i = 0, \ldots, N_x,\ j = 0 \ldots, N_y \tag{7}$$

In order to fit rectangular domains of arbitrary size, some linear transformations that relate the interval [–1, 1] and a interval $[a, b]$ are performed. Collocation method can be considered as a global polynomial approximation (Peyret 2002).

Solution of Eqs. 5 and 6 gives the stream function and the vorticity. The process of dipole formation when flow evolves from rest is well recovered, as we can see in the next section.

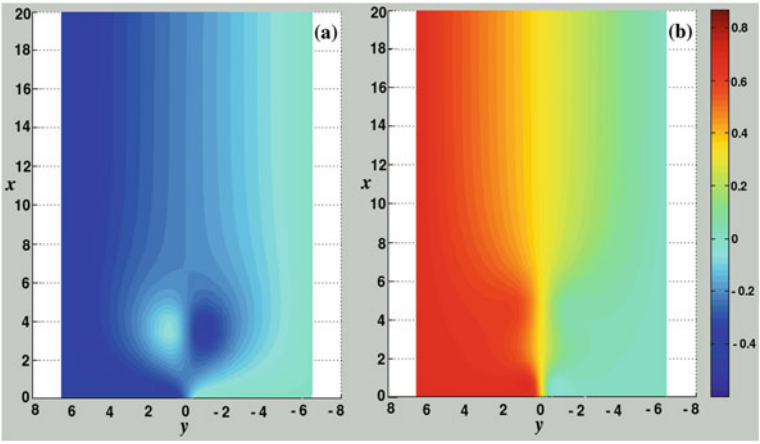

Fig. 3 Stream function with $S = 0.62$. **a** $t = 0.88T$, sink velocity is negative; dipole stay near the channel. **b** $t = 1.24T$, dipole has been destroyed

4 Numerical Results

Vorticity (ω) and stream function (ψ) were calculated for different values of parameter S. The results presented in this paper correspond to three values of S: 0.09, 0.24 and 0.62. This choice was made to cover cases ranging from configurations when dipole returns to configurations when dipole escapes. The velocity field, which is necessary to determine trajectories of fluid particles, is obtained with relations given in Eq. 1. In all cases $Re = 100$. The results presented in this section are given in terms of stream function because this quantity provides a good picture of dipole evolution. In Fig. 3 two colored plots of ψ in the $x-y$ plane are shown for $S = 0.62$ at two different times. In the first graph dipole was already created by the shear occurring in the channel. It persists even when flow rate becomes negative. The subsequent evolution of flow leads to the destruction of the vortex approximately after a forcing period, as we can see in the second graph. It is interesting to note that the dipole remains until its destruction in the vicinity of channel output.

In Fig. 4 two colored plots of ψ in the x–y plane are shown for two different times and $S = 0.09$. Process of dipole formation is shown in the first graph (4a) which corresponds to $t = 0.25T$ (T is the forcing period). In the second graph (4b) vortex has moved away from the channel output. Dipole persists even when flow rate is negative. It is interesting to note that the time elapsed in the second graph is less than a forcing period. Finally vortex escapes.

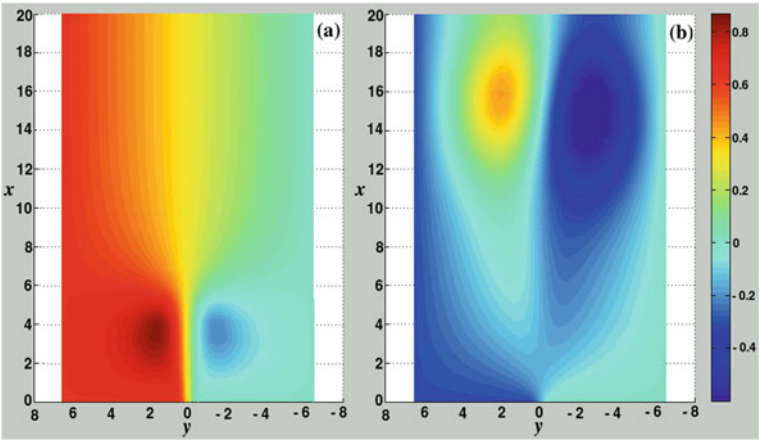

Fig. 4 Stream function with $S = 0.09$. **a** $t = 0.25T$, dipole is forming. **b** $t = 0.7T$, dipole goes away before first period ends

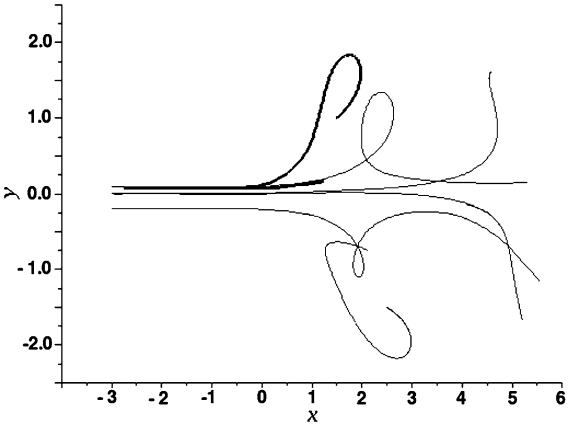

Fig. 5 Trajectories for $S = 0.62$, Initial time $t = 0$. Final time $t = 1.24T$, when the dipole is destroyed. Coarse line shows how fluid particle, starting in (1.5, 1) goes into the channel and after a while it goes out. Paths do not go beyond $x = 6$

5 Fluid Particle Transport

Using the velocity field obtained with the numerical method we can calculate the trajectories of fluid particles, according to the equation:

$$q_{i+1} = q_i + u_q \Delta t \tag{8}$$

where q_i is the particle position at time i, u_q is the velocity of particle and Δt is the time increment. In Fig. 5 some trajectories are plotted for the case $S = 0.62$. Starting at $t = 0$, initial position of fluid particles are either inside or outside the channel.

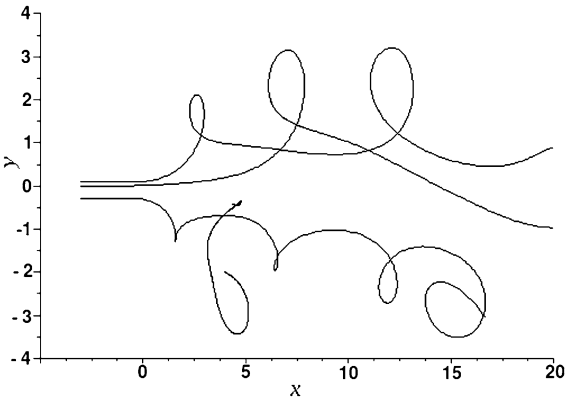

Fig. 6 Trajectories for $S = 0.09$ Initial time is $t = 0$ and final time is $0.88T$. Distance traveled by some particles exceeds that traveled by vortex. This is a signature of the suction effect of the dipole, because they move in a time interval between two vortex

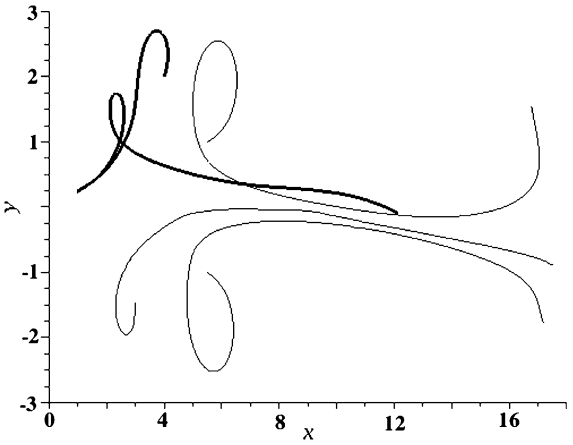

Fig. 7 Trajectories drawn since $t = 0.22T$ until $t = 1.66T$, the dipole already was formed. The dipole reaches $x = 17$ at the final time

Due to the fact that a dipole remains in the vicinity of the channel outputs, we can expect that particles near the centerline move to the right and after a while they return. If distance to the centerline increases, motion in y direction becomes important when particles leave the channel and after they follow curves paths. Some of these particles do not return to the channel.

Figure 6 shows some trajectories corresponding to the case $S = 0.09$. Time interval begins at $t = 0$ and ends at $t = 0.88T$. However, for two fluid particles that leave the integration domain at $x = 20$, path was calculated until $t = 0.5T$ (upper) and $t = 0.7T$ (lower) respectively. In the first case dipole was approximately at $x = 11$ whereas in the second case position of dipole was approximately $x = 15$. Then these fluid particles move faster than dipole and in fact part of the paths lie in the space between the vortex. That illustrates that dipole sucks fluid particles.

An intermediate case between those of Figs. 5 and 6, with a value $S = 0.24$, is shown in Fig. 7. Initial time is $0.22T$, whereas final time is $1.66T$. Coarse line is the trajectory of fluid particle begins in (4, 2) and ends in (12, 0). Some particles are sucked by the vortex and some other particles go into the channel and after they return to the basin.

6 Conclusions

In this paper we show some numerical results concerning the velocity field and the paths of fluid particles for moderate Reynolds number in a system consisting of two basins separated by a channel. A variable flow rate was introduced with the purpose to simulate effect of tides.

The solution of vorticity and stream function equations gave us a more realistic picture with respect to models based on potential theory. In particular, a detailed description of vortex creation and further evolution is obtained. Moreover, trajectories of fluid particles have been determined, giving a picture of the suction effect produced by the vortex dipole. This phenomenon is well revealed by the fact that fluid particles move ahead the dipole in some cases. Cases described in this work are in agreement with the fact that S is the parameter governing evolution of vortex dipole.

A more complete study requires the introduction of three dimensional effects and if transport of sand or pollutants are being considered, it is necessary to solve the equation of motion for solid particles.

References

Batchelor GK (2000) An introduction to fluid dynamics. Cambridge University Press, UK

Gill A (1982) Atmosphere ocean dynamics. Academic Press, USA

Lacaze L, Brancher P, Eiff O, Labat L (2010) Experimental characterization of the 3D dynamics of a laminar shallow vortex dipole. Exp Fluids 48:225–231

Landau LD, Lifschitz EM (2001) Mecánica de Fluidos, Curso de Física Teórica. vol 6, 2da Ed. Reverté, Barcelona, España

Peyret RG (2002) Spectral methods for incompressible viscous flows. Springer, USA

Pozrikidis C (1997) Introduction to theoretical and computational fluid dynamics. Oxford University Press, NY

Wells MG, Van Heijst GJF (2003) A model of tidal flushing of an estuary by dipole formation. Dyn Atmos Oceans 37:223–244

Super Free Fall of Liquids in Conical Containers

Abraham Medina and Carlos A. Vargas

Abstract The motion of the upper free surface of a liquid column released from rest in a vertical container, whose cross-section opens slowly in the downward direction, is analyzed theoretically. An inviscid, one-dimensional model, for a slightly expanding pipe's radius, describes how the recently reported super free fall of liquids occurs in liquids of very low viscosity.

1 Introduction

Consider a chain of uniform mass and length L initially attached at both ends to a horizontal support. As one end is suddenly released, the chain begins to fall in the gravitational field. Moreover, "if the initial distance between the ends of the chain is very close to L, that is, when the chain is initially stretched to its maximum length, the vertical motion of the chain tip becomes identical with the motion of a freely falling body" (Tomaszewski et al. 2006). However, when the horizontal separation Δl between the ends of the chain is shorter than L, that is, the chain is tightly folded, the falling chain tip will attain an acceleration that is larger than the gravity acceleration, g, i.e., there is a super free fall. All these results have been confirmed both in experiments and numerical simulations (Tomaszewski et al. 2006 and Calkin and March 1989).

In this work the problem of the free fall of a mass of low viscosity liquid in a vertical, open on top, weakly expanding (conical) pipe (Villermaux and Pomeau

A. Medina (✉) · C. A. Vargas
Departamento de Ciencias Básicas, UAM Azcapotzalco, Laboratorio de Sistemas Complejos, Av. San Pablo 180, 02200 México City, D.F., Mexico
e-mail: abraham_medina_ovando@yahoo.com

J. Klapp et al. (eds.), *Experimental and Theoretical Advances in Fluid Dynamics*, Environmental Science and Engineering, DOI: 10.1007/978-3-642-17958-7_42,

2010) is revisited. In this case, it has recently been found that the motion of the free surface of liquid in this system has an effective acceleration that overcomes the acceleration due to the gravity (Villermaux and Pomeau 2010). They have argued that this motion in a conical pipe super accelerates downward due to a force originated by a positive pressure gradient at the upper interface. Thus, it appears that the pressure force added to the pure gravitational body force induces this type of motion.

The theoretical model here developed, also based on the slender slope approximation, allows showing that the argument of the positive pressure is unnecessary. Instead, appears that the relative levels of filling are crucial to get a super free fall in this geometry.

The division of this work is as follows. In next section the formulation of the governing equations for the one-dimensional motion of an inviscid liquid in a vertical cone is given. Next, in Sect. 3 are discussed the numerical results concerning the super accelerated motion of the free surface for several initial levels of filling. Finally, in Sect. 4 the main conclusions and perspectives of this work are presented.

2 Theory

When an ideal liquid is in a vertical, cylindrical pipe and suddenly the lower part of the cylinder is opened, the gravity will accelerate the liquid. The main flow is one-dimensional and the conservation equations of mass and momentum are, respectively,

$$\frac{\partial u}{\partial z} = 0, \tag{1}$$

$$\rho \frac{\partial u}{\partial t} = -\frac{\partial p}{\partial z} + \rho g. \tag{2}$$

In the previous equations u is the downward velocity, z is the vertical velocity pointing downward, p is the pressure, ρ is the liquid density and t is the time. The solution of Eq. 1 allows finding that

$$u = u(t).$$

Now consider the same liquid in a vertical, conical pipe where the initial level of the free surface measured from its apex is $H_2(0)$ and the position of the bottom exit is H_1 (see Fig. 1). When the bottom exit is suddenly opened the liquid falls due to the gravity action. The continuity and momentum equations, in the slender

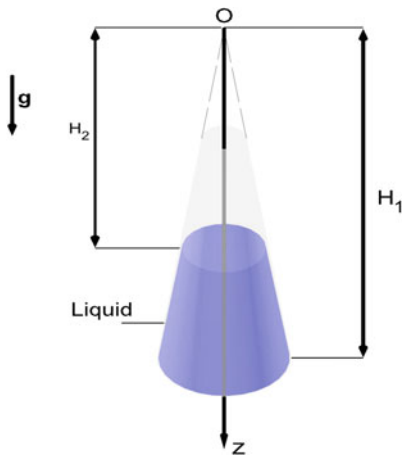

Fig. 1 Two-dimensional projection of a vertical conical pipe filled with an inviscid liquid. In the figure are shown the system of coordinates and the position of the upper free surface ($z = H_2(0)$) and the lower free surface ($z = H_1$), which appears when the pipe is suddenly opened. The region $z < H_2$ is open to the atmosphere

slope approximation, i.e., when the angle of aperture α is small, which is valid for a smoothly expanding tube, are now

$$\frac{1}{z^2}\frac{\partial}{\partial z}\left(z^2 u\right) = 0, \tag{3}$$

$$\rho\left(\frac{\partial u}{\partial t} + u\frac{\partial u}{\partial z}\right) = -\frac{\partial p}{\partial z} + \rho g. \tag{4}$$

Equations 3 and 4 will be solved under the initial conditions: at $t = 0$, $p(H_1) = p(H_2(0)) = p_a$. In this case the velocity can be obtained from Eq. 3, in the form $z^2 u = A(t)$ and therefore

$$u = \frac{A(t)}{z^2}. \tag{5}$$

Using this last result in Eq. 4, it is obtained that

$$\frac{\rho}{z^2}\left(\frac{dA}{dt} - 2\frac{A^2}{z^3}\right) = -\frac{\partial p}{\partial z} + \rho g. \tag{6}$$

If Eq. 6 is integrated from H_2 to H_1 the resulting height-averaged momentum equation is

$$\frac{dA}{dt}\left(\frac{H_1 - H_2}{H_1 H_2}\right) - \frac{A^2}{2}\left(\frac{H_1^4 - H_2^4}{H_1^4 H_2^4}\right) = g(H_1 - H_2). \tag{7}$$

By the way, the liquid velocity is given also by

$$u = \frac{dH_2}{dt},$$

Using the later equation in Eq. 5 it is easy to show that

$$\frac{dH_2}{dt} = \frac{A(t)}{H_2^2}, \tag{8}$$

or

$$\frac{dH_2^3}{dt} = 3A(t). \tag{9}$$

A second derivative of the previous equation gives

$$\frac{d^2H_2^3}{dt^2} = 3\frac{dA}{dt}. \tag{10}$$

Substitution of Eq. 10 in Eq. 7 yields

$$\frac{1}{3}\left(\frac{d^2H_2^3}{dt^2}\right)\left(\frac{H_1 - H_2}{H_1 H_2}\right) - \frac{1}{18}\left(\frac{dH_2^3}{dt}\right)^2\left(\frac{H_1^4 - H_2^4}{H_1^4 H_2^4}\right) = g(H_1 - H_2). \tag{11}$$

Rearranging terms and using the identity

$$\left(\frac{d^2H_2^3}{dt^2}\right) = 3H_2^2\frac{d^2H_2}{dt^2} + 6H_2\left(\frac{dH_2}{dt}\right)^2,$$

in Eq. 11 it is finally found that

$$\frac{d^2H_2}{dt^2} = \frac{H_1}{H_2}g + \frac{1}{2}\left(\frac{dH_2}{dt}\right)^2\left\{\frac{1}{H_1} + \frac{H_2}{H_1^2} + \frac{H_2^2}{H_1^3} - \frac{1}{H_2}\right\}. \tag{12}$$

In this later differential equation it should be noted that the term on the left hand side is the acceleration of the upper free surface of the liquid, H_2. On the right hand side appears the term $(H_1/H_2)g$ which can be much larger than g if $H_2 << H_1$. The second term has acceleration units but is related to the kinetic energy (per unit mass) $(dH_2/dt)^2/2$ of the free surface. This highly nonlinear equation should be solved numerically giving the conditions of the free fall: at $t = 0$ the upper surface is at $H_2(0)$ and there is no initial velocity, $(dH_2/dt)_{t\,=\,0} = 0$.

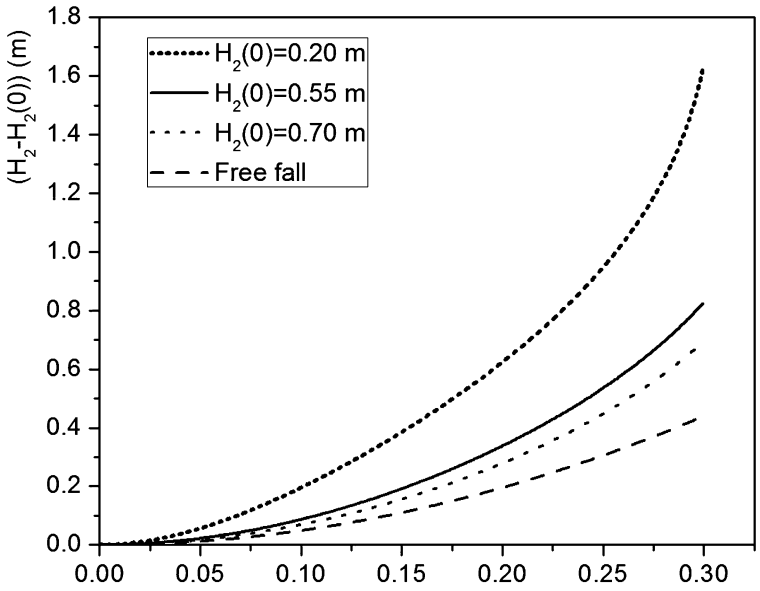

Fig. 2 Plots of the evolution of the position of the upper free surface, $H_2-H_2(0)$, as a function of time. It is assumed that initially the upper free surface was at the position $H_2(0)$. Three different initial positions are assumed, as can be seen in the box in the plot. In all cases the lower free surface was at $H_1 = 1$ m

3 Numerical Solutions

In the numerical computations we assumed that $H_1 = 1$ m. The solution of Eq. 12 was obtained by using a Runge–Kutta method of fourth-order. In order to show the effect of the level of filling, $H_2(0)$, on the overall motion of the liquid, three values of this quantity were chosen: $H_2(0) = 0.20$ m, 0.55 m and 0.70 m. The first value corresponds to a high level of filling, whereas $H_2(0) = 0.70$ m indicates that the level of filling is close to the bottom exit.

As a result, in Fig. 2 are plotted the free surfaces, $H_2-H_2(0)$, as a function of time for the three different values of $H_2(0)$. There, also is plotted the free fall case. It is noted that for these three cases the rate of change of the position of the free surface as a time function is faster than that corresponding to the free fall. This is confirmed through Figs. 3 and 4 where we plotted the corresponding instantaneous velocities and the accelerations of the free surfaces.

From Fig. 3 it is possible to conclude that, for $H_2(0) = 0.55$ and 0.70 m, the velocities behave as linear functions of t. Thus, the motions occur following relations of the form $u = dH_2/dt = g^* t$, where g^* is the effective acceleration and, in this case, it can be computed as $g^* = du/dt$, which is the slope of the straight lines in Fig. 3. This behavior is the mark of the uniformly accelerated motion and

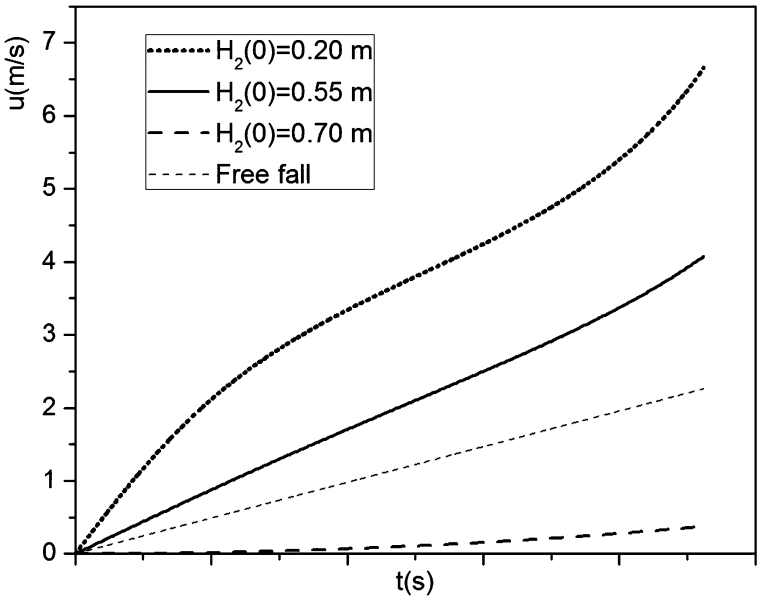

Fig. 3 Instantaneous velocities of the upper free surfaces, $u = dH_2/dt$, as functions of time. The different curves correspond to the initial positions, $H_2(0)$ of Fig. 2

the respective accelerations are: $g^* = 13.92$ m/s^2 for $H_2(0) = 0.55$ m and $g^* = 15.15$ m/s^2 for $H_2(0) = 0.70$ m. For the value $H_2(0) = 0.20$ m the behavior of the instantaneous velocity of the interface is non linear and the motion is non uniformly accelerated.

In Fig. 4 are given the plots of the non dimensional accelerations, g^*/g, as functions of time. In Mexico City $g = 9.779$ m/s^2. There the plots show, in a more accurate way, that the kinematics of the free surface when $H_2(0) = 0.20$ m is complex. In a first stage the motion is fast, it has a high acceleration, after the acceleration of this motion decreases but even is super accelerated and finally the acceleration increases again. This behavior is similar to that occurring to the tip of a chain (Tomaszewski et al. 2006) in the sense that at the final stages of motion strong inertial forces, equivalent to the gravity forces, are added to the motion. In this case the description of the motion can be made through the time-averaged acceleration which is defined as $\langle g^* \rangle = \int_{\Delta t} g^* dt / \int_{\Delta t} dt$, where Δt is the time interval during which the motion occurs. Computations allow us to find that for the case with $H_2(0) = 0.20$ m the average acceleration of the overall motion is $\langle g^* \rangle = 28.83$ m/s^2 or $\langle g^* \rangle / g = 2.94$. The estimation of the average acceleration for the other two values of $H_2(0)$ yield essentially the same values obtained through the estimation of the slope of the straight lines of Fig. 3.

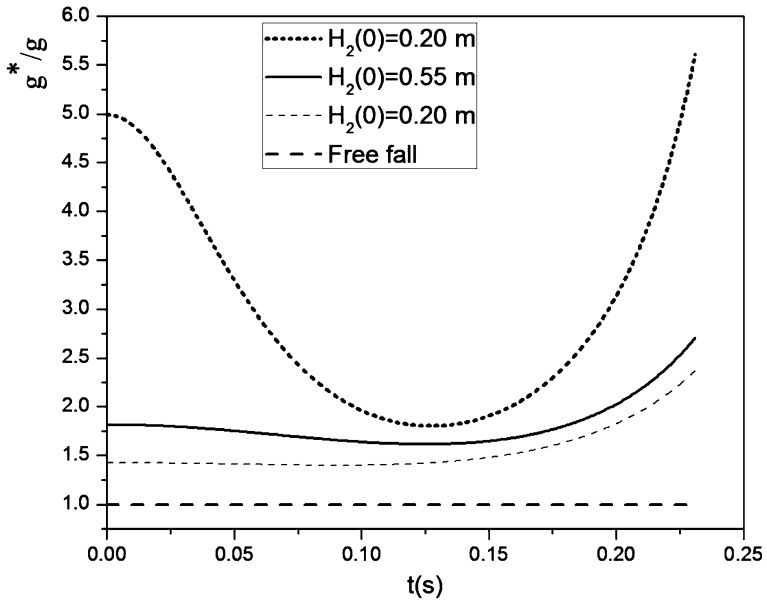

Fig. 4 Plots of the non dimensional instantaneous accelerations of the upper free surfaces, g^*/g, as functions of time. Plots correspond to cases given in Fig. 2

In order to compare the goodness of the results here derived with the results given by Villermaux and Pomeau (2010) it is convenient to remember that they give the initial acceleration in the form $g^* = g/(1 - \beta)$, where in the present context, $\beta = 1 - (H_2(0)/H_1)$. Villermaux and Pomeau (2010) studied two cases. In case 1: $\beta = 0.33$, $\alpha = 1.71^o$, $H_1 = 1.1$ m and $H_2(0) = 0.737$ m. For case 2: $\beta = 0.52$, $\alpha = 4^o$, $H_1 = 0.52$ m and $H_2(0) = 0.25$ m. Using this values, in Fig. 5 are plotted the time-averaged accelerations by assuming the two constant values of H_1 and taken into account several values of $H_2(0)$, i.e., several levels of filling. In such a plot also were plotted the instantaneous accelerations computed by using the model here developed. Both models give very similar results for levels of filling very close to the respective value of H_1. Moreover, the experiments discussed by Villermaux and Pomeau (2010) are two square points in the plots.

Figure 5 shows that different sizes of the conical containers and different levels of filling produce different regimes of super free fall. Notice that when $H_2(0)$ is close to the apex, the ratio $\langle g^* \rangle/g$ increases its value and, logically, when $H_2(0) \to H_1$, $\langle g^* \rangle/g \to 1$. It means that the greater level of filling the larger value of the average acceleration. The substantial difference between the curves given by the Villermaux et al. (2010) model and the model developed here for small values of $H_2(0)$, may be due to the acceleration in the first case that corresponds to an instantaneous acceleration at short times whereas the average acceleration in the model here discussed is for the overall flow.

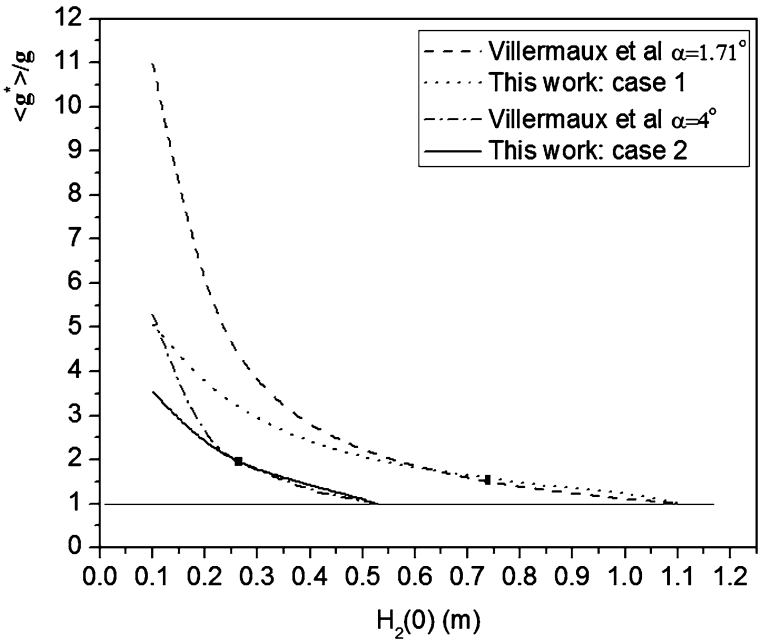

Fig. 5 Plots of the average non dimensional acceleration of the upper free surface, $\langle g^* \rangle/g$, as a function of the initial position of the upper free surface, $H_2(0)$. The two square symbols correspond to the experimentally analyzed cases in the work of Villermaux et al. (Villermaux and Pomeau 2010)

4 Conclusions

It is apparent that the theoretical model here developed predicts the super free fall in the motion of the upper interface of a liquid in a conical container when it falls only during the action of the gravity field. Moreover, it has been shown that the effective acceleration depends strongly on the level of filling, $H_2(0)$ and on the length of the container, H_1. Experiments reported (Villermaux and Pomeau 2010) show that during the free fall it has been observed the formation of nipples at the middle part of the free surface. The simple model here presented does not allow quantifying the properties of this structure, but surely their increase as the flow occurs, is due to the increase of cross-section. Theoretical and experimental studies in this direction are now conducted.

Acknowledgments A. M. thanks UAM Azcapotzalco for supporting this research through the *Carlos Graef Fernández chair*. He also acknowledges Profs. PD Weidman and FJ Higuera for their useful discussions about this topic.

References

Calkin MG, March RH (1989) Am J Phys 57:154–157
Tomaszewski W, Pieranski P, Geminard JC (2006) Am J Phys 74:776–783
Villermaux E, Pomeau Y (2010) J Fluid Mech 642:147–157

The Saline Oscillator: Visualization Using Shadowgraphs and Particle Image Velocimetry

Yadira Salazar Romero and Catalina Stern

Abstract A saline oscillator is a device that consists of a small container with salt water and a tiny hole in the bottom. The small container is partially submerged into a larger container with distilled water. First, as expected, a jet of salt water falls into the larger container, but after a certain time the jet becomes unstable, a jet of distilled water starts going up, and an apparently periodic motion is installed. The global structure of the flow has been visualized using a technique sensitive to the density gradients, called shadowgraph. The velocity fields have been measured using particle image velocimetry (PIV). The flow rate has been measured as a function of time. Not all instabilities lead to a change of direction of the flow, so different flow patterns can be observed. With a pair of electrodes inserted in each container, a voltage signal with the same period of oscillation as the flow has been obtained. The interval of time when the flow goes down is always larger than the interval of time going up. Some experimental results that do not agree with other authors are presented.

1 Introduction

A saline oscillator is a device that consists of a small container with salt water and a tiny hole in the bottom that is originally blocked. The small container is partially submerged into larger container with distilled water. When the orifice is

Y. Salazar Romero (✉) · C. Stern
Facultad de Ciencias, Universidad Nacional Autónoma de México,
Ciudad Universitaria, C. Exterior s/n, 04510 Coyoacán, D.F., Mexico
e-mail: yayafisica@gmail.com

C. Stern
e-mail: catalina@ciencias.unam.mx

J. Klapp et al. (eds.), *Experimental and Theoretical Advances in Fluid Dynamics*, Environmental Science and Engineering, DOI: 10.1007/978-3-642-17958-7_43,

unblocked, a jet of salt water falls into the larger container. After a certain time, the jet becomes unstable, the process stops and is inverted, a jet of distilled water starts going up, and an apparently periodic oscillation is installed.

The saline oscillator was first described by Seely Martin in 1970 (Martin 1970), who built the first device using the piston of a syringe and a very small container. He believed the oscillation was due to the density difference between the liquids.

It has been shown that the changes in the voltage between two electrodes, one in each solution, occurs at the same time than the changes in the direction of the flow. The period of the oscillation is independent of the molar concentration of salt. However, the amplitude of the voltage increases with the concentration, due to an increase in the number of ions (Rincon and Fajardo 2006).

In other type of studies, simulations have been made using an algorithm called Cubic-Interpolated pseudo-Particle (CIP), where the parameters were obtained from an experiment with small dimensions. Navier–Stokes and the continuity equations were used to describe the dynamics of the flow. The period in the simulation is 15 s larger than in the experiment, but the rest of the experiment is well reproduced (Takemoto et al. 2000). The same authors show, in another paper, that the oscillator can be described by Rayleigh's equation, which is a second order differential equation. In this case, they obtain that the period is twice as long as in the experiment. They predict the existence of a limit cycle (Okamura et al. 2000).

There is also a mathematical model proposed by Kenji Aoki (Aoki Kenji 2000), based on the experimental results of Yoshikawa. This model uses the Navier–Stokes equations in cylindrical coordinates and considers that near the hole there is a Poiseuille flow. It predicts a Hopf bifurcation and discusses under which circumstances a limit cycle can appear.

Until now, the mechanism that produces the oscillation is not understood, and there are no equations that describe the dynamics accurately. One of the interesting characteristics of the system shows the same dynamics as heart pulses under certain conditions. These observations were made in the Laboratory of Excitable Systems at the Physics Department of the School of Sciences at UNAM. Electrodes were used to determine the form of the pulses, and to measure the period of oscillation (González et al. 2008). In the same Department, Dr. Málaga and his collaborators are working on a numerical model of the oscillator (Hubard Aline 2009). In the Hydrodynamics Laboratory, the Saline oscillator has been studied through shadowgraph and Particle Image Velocimetry (PIV).

2 Experimental Set-Up

The experimental set-up consists of three parts. First a saline oscillator large enough to be visualized has to be built. Then, a shadowgraph system has to be mounted to visualize the flow. Finally, the optics as well as the data acquisition and analysis for PIV have to be assembled.

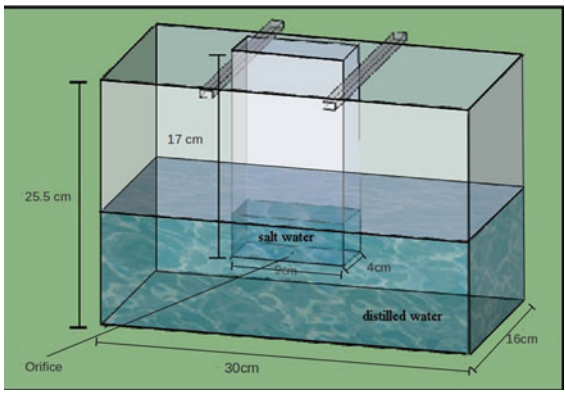

Fig. 1 The saline oscillator

2.1 Saline Oscillator

A saline oscillator with the proper conditions for visualization was built as shown in Fig. 1. 2.980 L of distilled water with a density $\rho_1 = 1{,}000$ kg/m^3 were introduced in the large container and 102 ml of salt water with $\rho_2 = 1.128 \times 10^3$ kg/ml in the small container. The hole in the small container remains blocked. When both liquids are in equilibrium, the hole is opened and salt water starts flowing into the large container. After a few minutes, the process is reversed.

2.2 Shadowgraphy

Our eyes, as well as photographic cameras, cannot distinguish the phase differences of light, only the differences in intensity and color, contrasts, and with the help of some filters, we can determine the polarization. The technique known as Shadowgraph, transforms the differences in phase o differences in intensity, and sometimes in color, which are characteristics that our eyes can detect (Settles 2001).

To understand how the technique works it is necessary to understand first, the relationship between the index of refraction and the density, and second, how the density gradients transform into variations in the intensity of light and the formation of an image.

The electromagnetic theory explains how the index of refraction changes with density, $n(\rho)$. In the medium, the light is polarized and scattered. Using Maxwell equations and some approximations when the index of refractions is close to one, the Gladstone-Dale equations (Goldstein 1996) can be obtained

$$n - 1 = k\rho \tag{1}$$

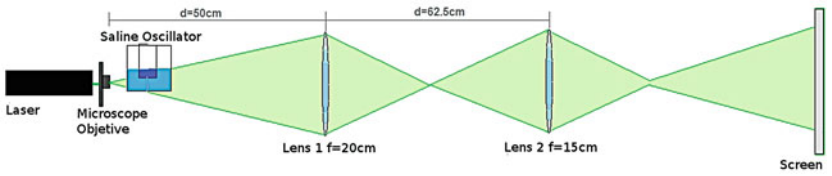

Fig. 2 Optical set-up for shadowgraphs

where ρ is the medium's density, n the index of refraction and k the Gladstone-Dale coefficient that depends on the properties of the material. From (1), the gradients of n can be related to the gradients of ρ through:

$$\frac{\partial \rho}{\partial y} = \frac{1}{K}\frac{\partial n}{\partial y} = \frac{\rho_0}{n_0 - 1}\frac{\partial n}{\partial y} \tag{2}$$

where y is the depth. The values with sub index zero correspond to a stationary state with constant ρ.

The derivative of Eq. 2 gives the equation used in Shadowgraphy:

$$\frac{\partial^2 \rho}{\partial y^2} = \frac{1}{K}\frac{\partial^2 n}{\partial y^2} = \frac{\rho_0}{n_0 - 1}\frac{\partial^2 n}{\partial y^2} \tag{3}$$

The gradients of n are responsible for the changes in the phase. When Shadowgraphy is used, the waves that have gone through the medium are sent to an optical system made out of lenses or mirrors, that works as a Fourier transformer, and converts the differences in phase into variations in the intensity of light.

The set-up to obtain a shadowgraph is shown in Fig. 2. Light from a 532 nm crystalaser is sent to a 40 objective with a focal distance f = 20 cm, then to a second lens with f = 15 cm and finally a screen.

2.3 Particle Image Velocimetry

PIV is based on a simple idea. If the distance traveled by a particle and the time between two successive pictures are known, the mean velocity at which the particle moves can be determined (Dantec Dynamics 2002).

Small particles, called seeds, that follow the motion of the flow, are introduced into the medium, in such a way as to not change the density. These particles are covered with silver to reflect light, and have a bubble of air inside to make sure that they do not sink or float. A sheet of light is used to illuminate the seeded flow, and two pictures are taken at a known interval of time. By measuring the distance between the positions of the same seed in two pictures, the velocity of the particle can be detected.

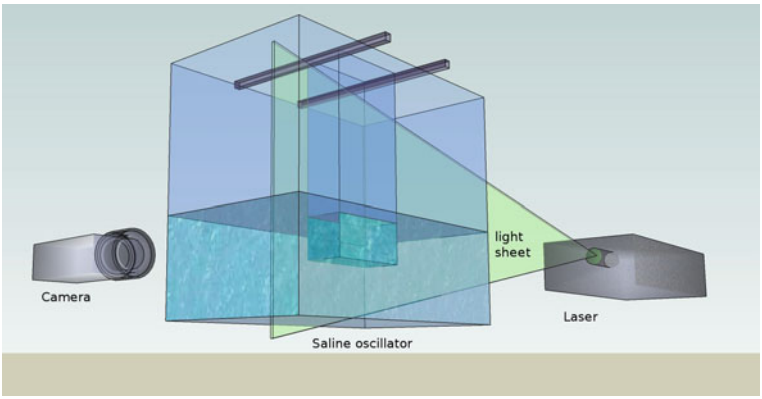

Fig. 3 Optical set-up for PIV measurements

To do this work, a Dantec Dynamics system with a pulsed New Wave 532 nm laser and 100 mW exit Power is used. The optics is already integrated to create a thin sheet of light. A CCD fast camera Megaplus ESI.0 captures the images. Each sensor corresponds to a cell in a spatial matrix, and all the cells together are the interrogation area. It would be impossible to identify the motion of each particle, so a statistical approach is taken. A cross correlation is applied to each pair of images, obtaining a mean displacement for each cell; and consequently a mean velocity. If the process is repeated in a sequence of pairs of photos, the video of the velocity field is obtained. The cross correlation can lead to errors. The commercial software Flow Manager is used to capture the data, analyze it and validate all the vectors in the velocity fields (Raffel et al. 1998). The experimental set-up is shown in Fig. 3.

First the camera was focused on the container with salt water 80 cm away. Later the lower part with distilled water was focused. Finally, the area near the hole was focused. In a second round, the camera was placed 35 cm away from the containers.

3 Results and Analysis

A series of shadowgraph images are shown in Figs. 4 and 5. Different structures can be observed as the flow goes up or down. In this case, it goes down for 173.6 s and goes up for 169.

The structure that is formed when the jet bounces from the bottom is seen in Fig. 4b; 4a is a close-up of the same image. Figure 4c shows a diffraction pattern produced by the jet. It was taken two days after the oscillation started. The jet seems to be pulsating in time and space.

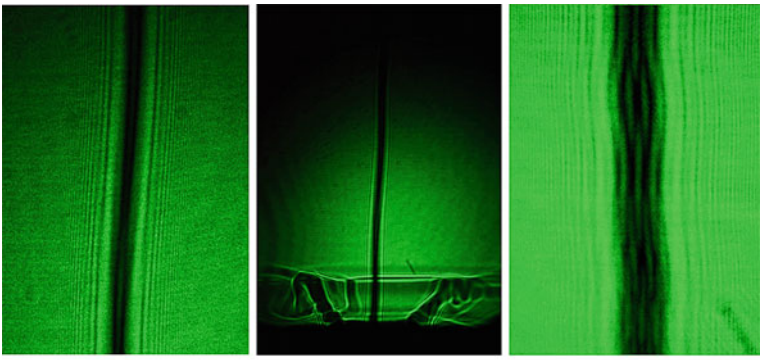

Fig. 4 Shadowgraphs of the jet going down

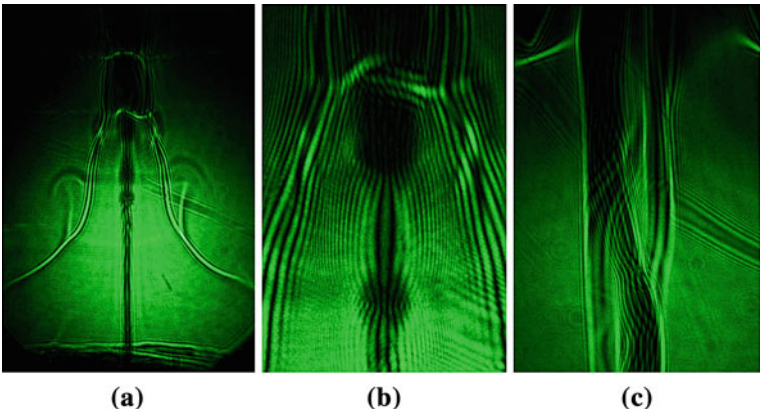

Fig. 5 Shadowgraphs of the jet going up

The jet becomes unstable and the direction of the flow changes. A jet of distilled water goes up for 169 s. Figure 5a shows the structure that is formed when it arrives at the free surface and bounces. The jet is narrow enough to form a diffraction pattern. Figure 5b is a close-up of the same image. Figure 5c was taken two days later. The structure has changed, the jet is wider and the pattern formed at the free surface is completely different.

Once the oscillation starts, the system can go on for many days. The period varies during the first hour and a half, but after that, it stabilizes.

Close to the hole, there seems to be a change in the width instants before the change of direction.

So far, all observations have been qualitative. Eventually a relationship of the intensity in the image as a function of density is hoped to be found, and the changes in density will be quantified.

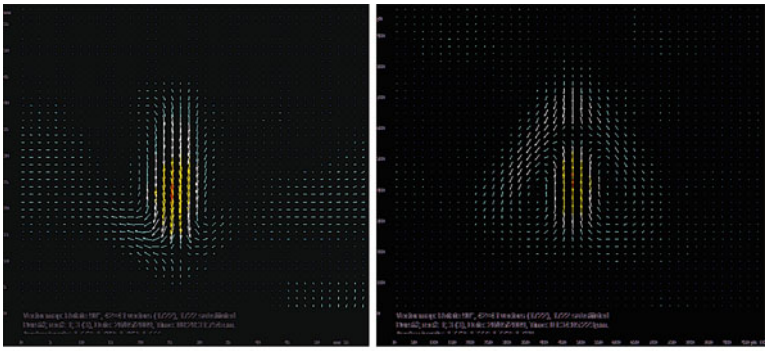

Fig. 6 **a** Flow field going down. **b** Flow field going up

The velocity fields will be obtained from the images that have been taken with the PIV system. However, contrary to what is expected, a change in the period of oscillation was observed when the flow was seeded. The first discharge was particularly long, 120 min versus fourteen in the unseeded case. Afterwards, the oscillator behaved in an unusual manner. A jet going up and another going down appeared simultaneously for a few minutes. Then the oscillation started going down for 180.0 s and going up for 193.0 s (Fig. 6).

The jet seems wide but actually only the four centerlines correspond to it. The other arrows are due to the motion of the fluid surrounding the jet. It is interesting to note that the flow seems to go faster away from the hole. The images show a jet that accelerates and creates a recirculation area. The recirculation is probably due to the lower boundary.

With the PIV data and Matlab, the flow rate close to the hole was calculated. The regions considered for these calculations (small opaque circles) and the acrylic interface where the hole is, are shown in Figs. 7 and 8. The resolution in the figure does not allow to see that several lines of data are included.

Figure 8 shows the change in the velocity vector in the center of the jet, as a function of time. When the data was taken the oscillation was already stabilized. Between 0 and 45 s, the speed values are maintained between 2.1×10^{-3} m/s and 3.2×10^{-3} m/s, at 48 s the flow changes its direction. At 55 s the flow seems to pulsate, it becomes unstable and the peak in the speed appears.

Figure 9 shows the whole period for the flow rate. A jet goes up at 55 s and another goes down at 238 s. At 440 s it starts going up and another peak is observed at 550. Every time there is a change in the direction, an instability occurs and it appears as a peak in the graph.

To complete the experiment, two electrodes were inserted in the flow without seeds, one in the small and the other in the big container. The signal that was obtained is shown in Fig. 10. The interval of time of the flow going down is 12.6 s longer than the time interval going up, and this is perfectly consistent with the

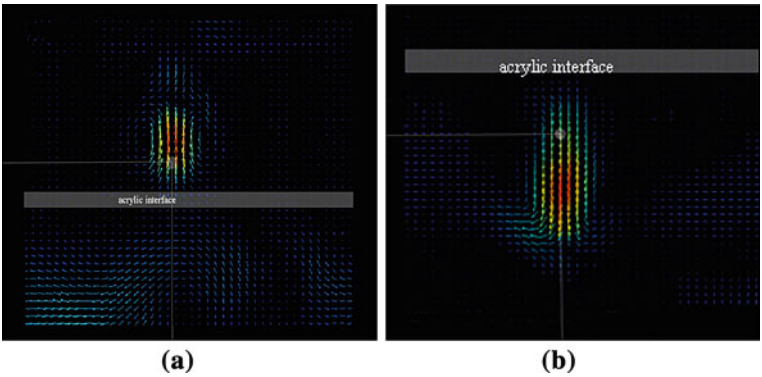

Fig. 7 Regions considered for the calculation of the flow rate (**a**), above the hole (**b**), below the hole

Fig. 8 Half period, speed vs time

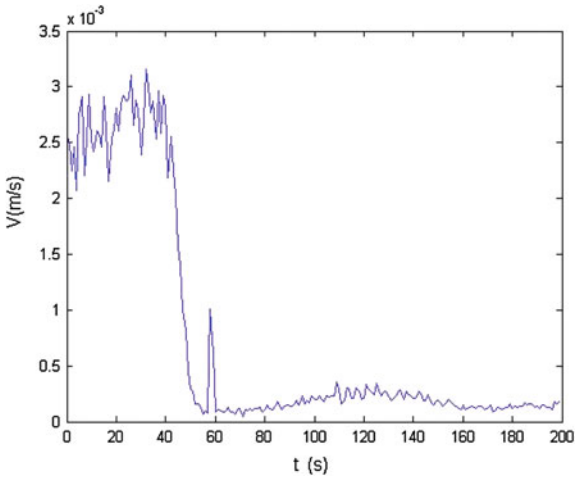

signal, that is the change in the voltage is directly related to the change in direction of the flow.

4 Conclusions

- The changes in the structure of the flow due to changes in salt concentration are qualitatively observed in shadowgraphs.
- The shadowgraphs show that sometimes the jet gets thinner and starts pulsating.
- The relationship between intensity in the image and density is being studied in order to quantify results.

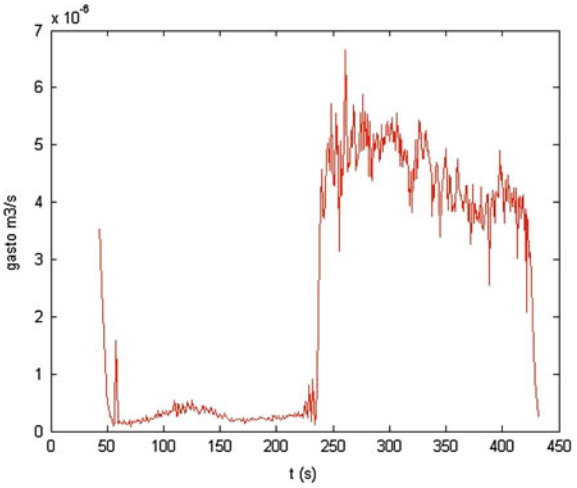

Fig. 9 Whole period flow rate vs time

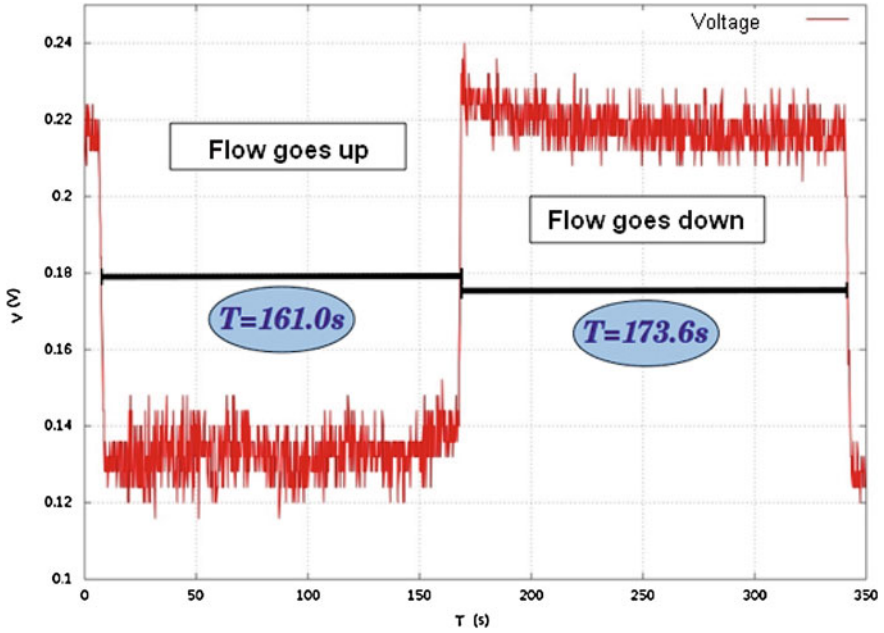

Fig. 10 Voltage as a function of time in a saline oscillator

- Seeds affect the behavior of the oscillator. This can be observed in the time of the first discharge and in the duration of the intervals of the flow going up or down.

- The two techniques used in this article provide different but complementary information. Shadowgraphs detect gradients in the index of refraction related to gradients in the density. PIV gives the velocity field.
- Peaks in the graph of speed as a function of time can be related to changes in the width of the jet going up that can be observed in the shadowgraph. However, big changes are always related to changes in the direction of the flow.
- The time for the flow going down is always longer than when it is going up. The total period becomes longer and longer so it doesn't seem to stabilize in a limit cycle.
- The change in the voltage given by the electrodes is always related to a change in the direction of the flow.
- Important parameters that can change the period of the oscillation are the area of the hole in the small container, the ratio of areas between both containers, the amount of water in each container and changes in temperature.

Acknowledgments The authors thank Dr. Zenit and his collaborators for their help in some of the experiments, also Cesar Aguilar and Dr. Alvarado. We acknowledge the support of DGAPA UNAM through project PAPIME PE104907.

References

Aoki Kenji (2000) Mathematical model of a saline oscillator. Phys D 147

Dantec Dynamics A/S, Flow manager software and introduction to PIV instrumentation. Software, user's guide, Publication no. 9040U3625. September 2002. Copyright 2000–2002 All rights reserved

Goldstein RJ (1996) Fluid mechanics measurements. In: Goldstein RJ (ed) Copyright (1996). Taylor and Francis, copyright 1983 by Hemisphere Publishing Corporation, pp 451–463

González H et al (2008) Phase resetting, phase locking, and bistability in the periodically driven saline oscillator. Experiment and model. Phys Rev E 78

Hubard Aline (2009) Model of a saline oscillator. Undergraduate thesis, Universidad Nacional Autónoma de México

Martin S (1970) Geophys Fluid Dyn 1(143):197

Okamura M et al (2000) Rhythm in a saline oscillator. Phys Rev 61(3):2445–2452

Raffel M, Villert C, Kompenhans J (1998) Particle image velocimetry. Springer-Verlag, Berlin

Rincon NE, Fajardo F (2006) Study of a density oscillator by electrical potential measurements. Revista Brasileña de Ensino de Física 28(1):67–76

Settles GS (2001) Schlieren and shadowgraph techniques. Springer-Verlag, Berlin

Takemoto Y, Yokkaichi CS, Okamura M, Yoshikawa K (2000) Numerical simulation on simple saline oscilatory flows with free surfaces. Phys Rev 61(3):82–97

Part VII
Gallery of Fluids

Main Facts of the Oil Spill in the Gulf of Mexico

Hermilo Ramírez-León and Angelica Guerrero-Zúñiga

This a review of the main issues involving the oil spill that occurred on April 20, 2010 in the Deepwater Horizon platform owned by British Petroleum.

A general description of the main facts that occurred, supported by images and a brief description, since the spill began to the date when it was finally controlled on July 15. It contains brief comments on future consequences.

First images of the accident (April 20–22)

H. Ramírez-León (✉) · A. Guerrero-Zúñiga
Mexican Petroleum Institute, Mexico city, Mexico
e-mail: hrleon@imp.mx

A. Guerrero-Zúñiga
e-mail: aguerrer@imp.mx

J. Klapp et al. (eds.), *Experimental and Theoretical Advances in Fluid Dynamics*, Environmental Science and Engineering, DOI: 10.1007/978-3-642-17958-7_44,

1 Deepwater Horizon Spill Response

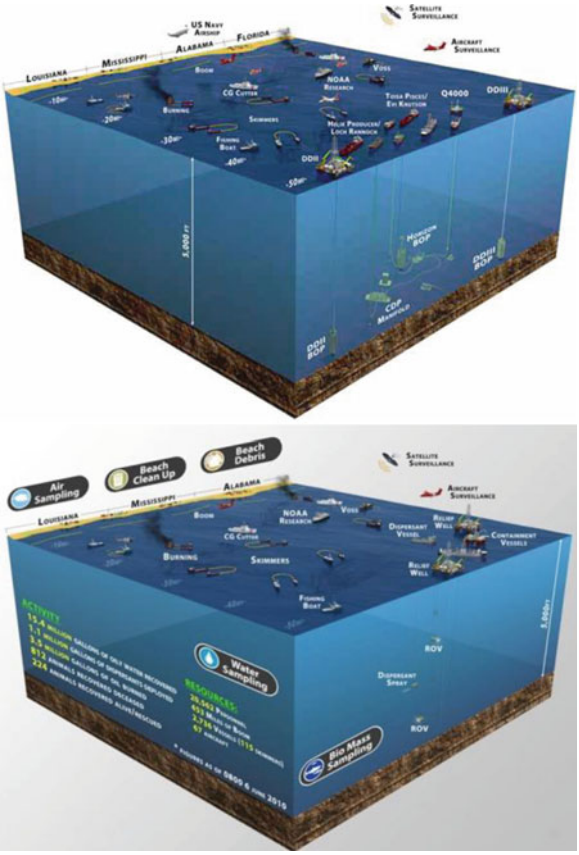

Deepwater Horizon Spill control strategies on surface and the bottom

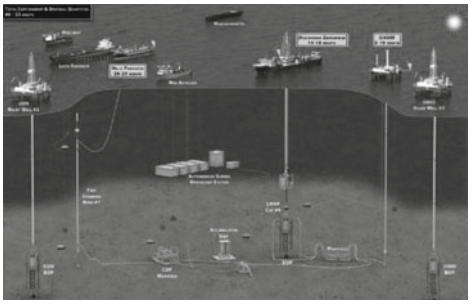

The three recovery systems (June 30)

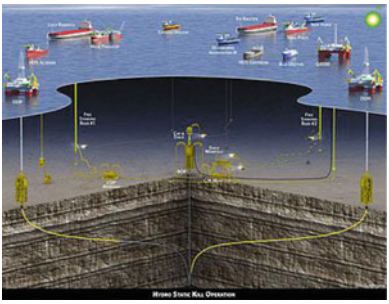

Static kill completed (July 15)

2 The Black Oil Tide Dispersion

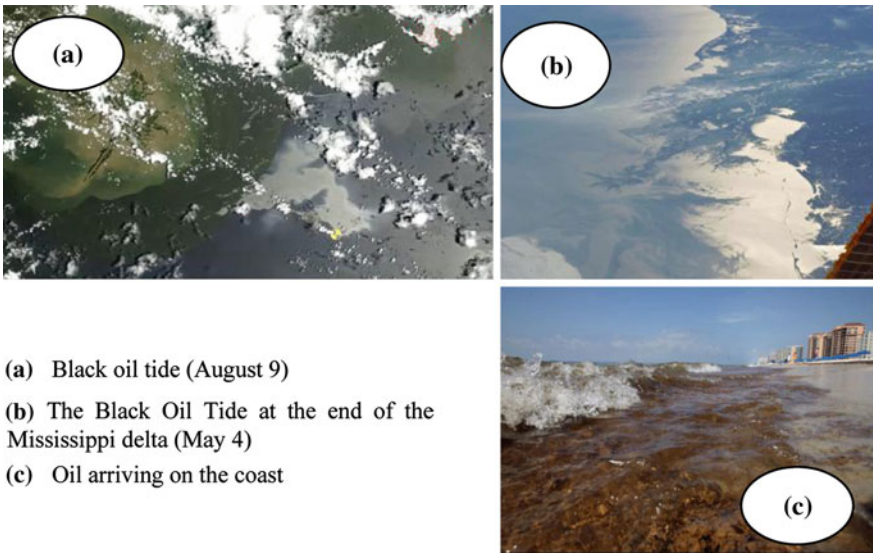

(a) Black oil tide (August 9)

(b) The Black Oil Tide at the end of the Mississippi delta (May 4)

(c) Oil arriving on the coast

3 Surface Strategies Used to Contain Oil Spillage

(a) Aerial dispersant applications
(b) Oil collecting runs from the surface
(c) Controlled burning

Protection works around shores and islands

4 Tracking the Gulf Oil Spill

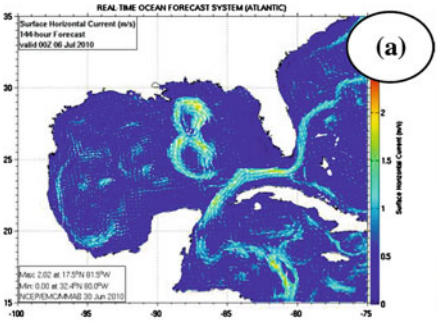

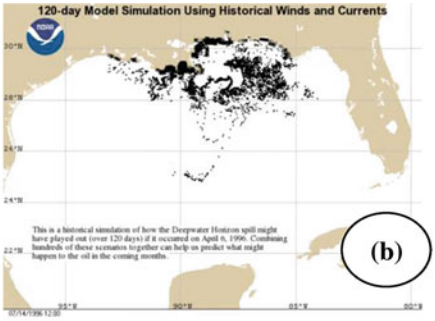

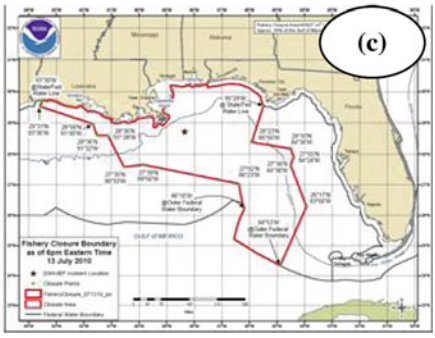

(a) Circulation estimated and predicted with de HYCOM model. **(b)** Dispersion patterns using particles as tracers **(c)** Restricted area implemented by EPA/NOAA

5 Environmental Impact

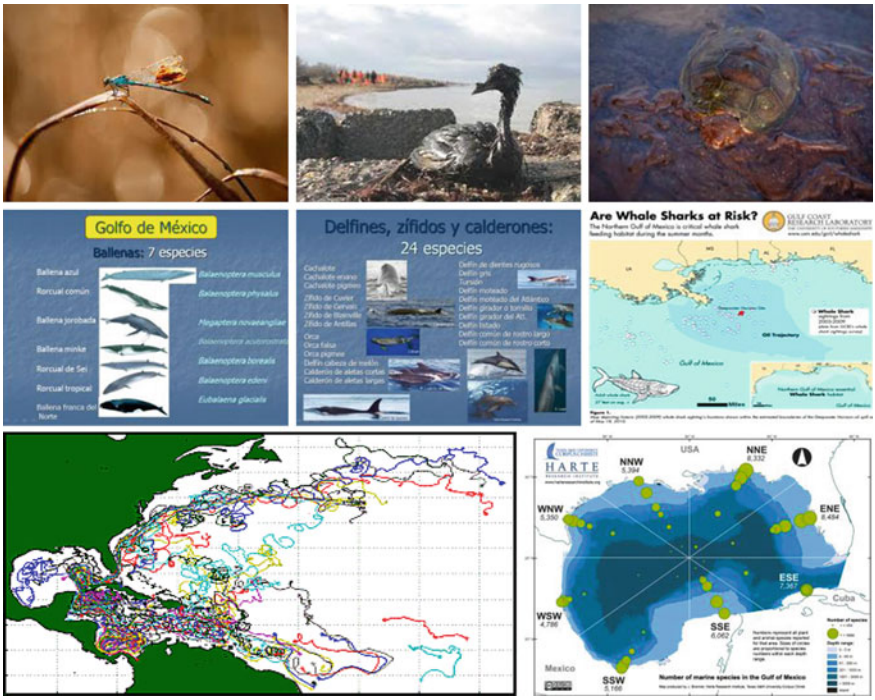

Connectivity in benthic larvae. Estimation of marine species distribution in GOM

6 Possible Consequences on the Mexican Side

(a) (b)

a Hydro-meteorological intensity (September 15). **b** Possible affectation areas in Mexican coast

7 Where is it the Oil Spill?

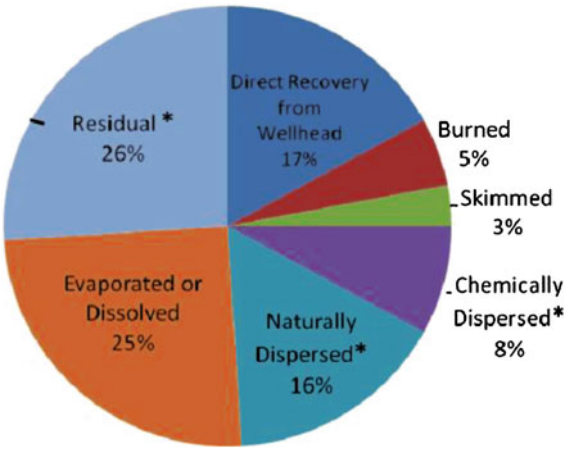

Deepwater Horizon oil budget. Based estimated release of 4.9 million barrels of oil

8 Final Note

All references of the images and facts from the oil spill are contained in the paper presented by the first author in this volume.

Bubble Clusters in Associative Polymers

J. R. Vélez-Cordero, D. Sámano and Roberto Zenit

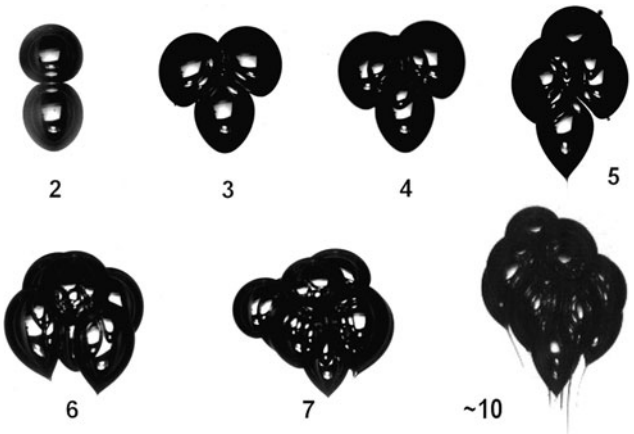

Groups of bubbles were collected and released in an associative polymer (HASE 1.5%, **H**ydrophobically modified **A**ssociative **S**oluble Polym**E**r). The bubbles (volume $\approx$18 mm^3) rising in this highly viscous fluid tend to form clusters. The images show clusters formed by different number of bubbles; the number below each image indicates the number of individual bubbles (N) in each cluster. In agreement with what has been observed in the case of settling particles (Jayaweera et al. 1964; Hocking 1964), the bubbles form regular polyhedrons for $N < 7$.

J. R. Vélez-Cordero · D. Sámano · R. Zenit (✉)
Instituto de Investigaciones en Materiales, Universidad Nacional Autónoma de México, México City, México
e-mail: Zenit@servidor.unam.mx

J. Klapp et al. (eds.), *Experimental and Theoretical Advances in Fluid Dynamics*, Environmental Science and Engineering, DOI: 10.1007/978-3-642-17958-7_45,

Surprisingly, the bubble clusters do not experience the velocity jump (Soto et al. 2006) observed for the case of single bubbles having an equivalent total volume. However, the appearance of the characteristic cusped tail is observed on the bubbles near the trailing edge of the cluster.

References

Hocking LM (1964) The behavior of clusters of spheres falling in a viscous fluid, Part 2. J Fluid Mech 20:129

Jayaweera KOLF, Mason BJ, Slack GW (1964) The behavior of cluster of spheres falling in a viscous fluid. J Fluid Mech 20:121

Soto E, Goujon C, Zenit R, Manero O (2006) A study of velocity discontinuity for single air bubbles rising in an associative polymer. Phys Fluids 18:121510

Flow of Air Bubbles in a Packed Bed

Enrique Soto, Alicia Aguilar-Corona, Amós Benjamín Domínguez Gómez and Roberto Zenit

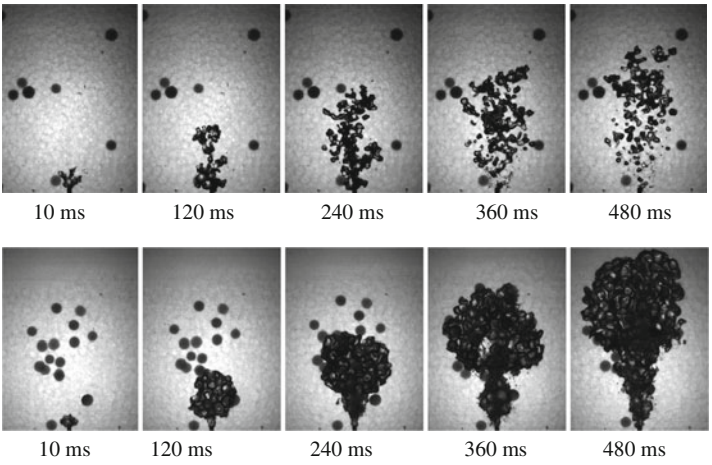

E. Soto
Centro de Ciencias Aplicadas y Desarrollo Tecnológico, Universidad Nacional Autónoma de México, México City, México

A. Aguilar-Corona (✉)
Universidad Michoacana de San Nicolás de Hidalgo, Morelia, Michoacán, México
e-mail: aliac77@hotmail.com

A. B. D. Gómez
Instituto Tecnológico de Ciudad Madero, Ciudad Madero, Tamaulipas, México

R. Zenit
Instituto de Investigaciones en Materiales, Universidad Nacional Autónoma de México, México City, México

J. Klapp et al. (eds.), *Experimental and Theoretical Advances in Fluid Dynamics*, Environmental Science and Engineering, DOI: 10.1007/978-3-642-17958-7_46,

An air stream is injected into a packed bed immersed in water. The refractive index of the water and the packed bed is closely matched; yet, the edges of the spherical particles can be seen. Two distinctive regimens can be observed. The first one, for low air flow rates, is characterized by the percolation of the air through the interstitial spaces among particles, which remain fixed in space. The second one, for high air flow rates, is characterized by the accumulation of air inside the packed bed without percolation; in this case the bubble causes significant agitation of the surrounding particles.

Dipolar Vortex in a Rotating System

Luis Zavala Sansón and Ana C. Barbosa Aguiar

Abstract Dipolar vortex in an anticlockwise rotating platform. The mean depth is 0.85 m and the rotating period of the system is 30 s. The radius of the visible cyclonic part is 0.80 m. The anticyclonic part is formed due to potential vorticity conservation as fluid columns are squeezed over an obstacle at the bottom (not visible). The flow is visualized with small particles floating on the free surface and illuminated with a horizontal laser sheet. The experiments were performed at the Coriolis platform (CNRS/LEGI, Grenoble, France).

L. Zavala Sansón (✉)
Departamento de Oceanografía Física, Centro de Investigación Científica y de Educación Superior de Ensenada, Carretera Ensenada-Tijuana 3918, 22860 Ensenada, Baja California, México
e-mail: lzavala@cicese.mx

A. C. Barbosa Aguiar
Instituto de Oceanografia, Faculdade de Ciências da Universidade de Lisboa, Campo Grande, 1749-016 Lisbon, Portugal

J. Klapp et al. (eds.), *Experimental and Theoretical Advances in Fluid Dynamics*, Environmental Science and Engineering, DOI: 10.1007/978-3-642-17958-7_47,

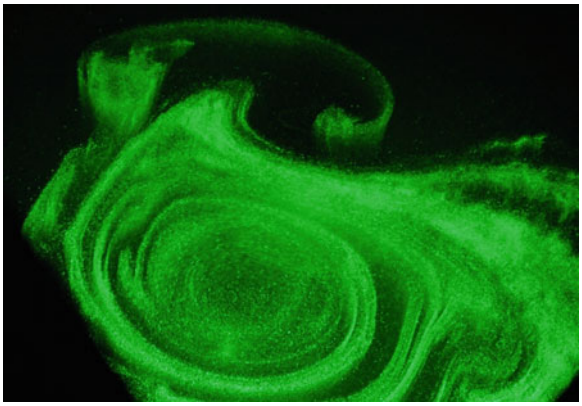

Dipolar vortex in an anticlockwise rotating platform. The mean depth is 0.85 m and the rotating period of the system is 30 s. The radius of the visible cyclonic part is 0.80 m. The anticyclonic part is formed due to potential vorticity conservation as fluid columns are squeezed over an obstacle at the bottom (not visible). The flow is visualized with small particles floating on the free surface and illuminated with a horizontal laser sheet. The experiments were performed at the Coriolis platform (CNRS/LEGI, Grenoble, France).

Hurricanes at Landfall Over the Baja California Peninsula

Luis M. Farfán

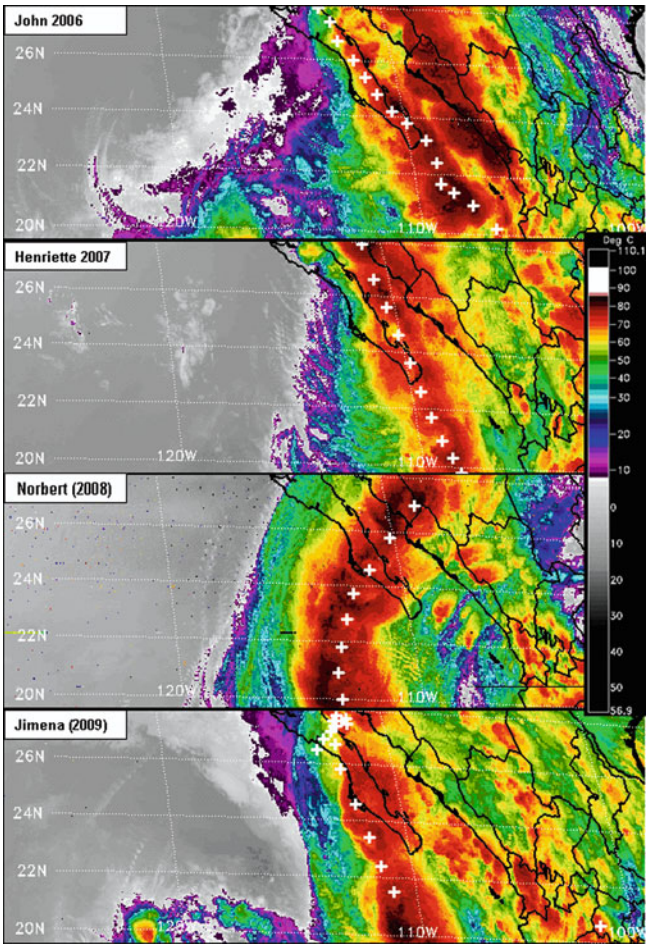

L. M. Farfán (✉)
Centro de Investigación Científica y de Educación Superior de Ensenada, B.C., Miraflores 334, 23050 La Paz, B.C.S., Mexico
e-mail: farfan@cicese.mx

J. Klapp et al. (eds.), *Experimental and Theoretical Advances in Fluid Dynamics*, Environmental Science and Engineering, DOI: 10.1007/978-3-642-17958-7_48,

Composites from Hurricanes John (1–3 September 2006), Henriette (1–4 September 2007), Norbert (9–12 October 2008), and Jimena (1–4 September 2009). Plus signs are circulation center positions. Images indicate minimum temperatures (maximum cloud tops) from 30-min infrared imagery. The coldest (below –60°C, highest) clouds appear in black, red, and yellow tones. These images are derived from the GOES-11 satellite and indicate the location of deep convection and likelihood of heavy rainfall prior to and during the landfall of each hurricane. This is an excellent tool to determine areas that were strongly impacted by direct hits.

Fiber Optic Micro-Bubble Generator

Reinher Pimentel-Domínguez, Juan Hernández-Cordero and Roberto Zenit

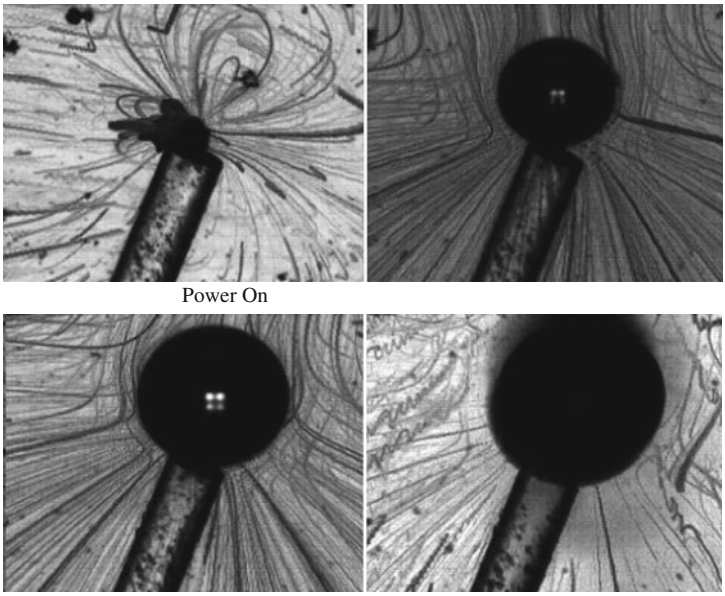

A simple method to incorporate carbon nanotubes onto optical fibers is to immerse its tip in a solution of nanostructures dispersed in ethanol. Laser light guided by the fiber attracts the nanostructures thus forming deposits on the optical fiber tip. After deposition, micron-sized bubbles can be formed on the tips of the optical fibers owing to light absorption by the nanostructures.

R. Pimentel-Domínguez (✉) · J. Hernández-Cordero · R. Zenit
Universidad Nacional Autónoma de México, Instituto de Investigaciones en Materiales, México City, D.F., México
e-mail: vetuasaber@ciencias.unam.mx

J. Klapp et al. (eds.), *Experimental and Theoretical Advances in Fluid Dynamics*, Environmental Science and Engineering, DOI: 10.1007/978-3-642-17958-7_49,

Pressure Behavior and Evolution of the Bubbles Inside the Pipes of an Experimental Installation of Centrifugal Pump During the Occurrence of Cavitation

Jorge Luis Reyes de la Cruz, Gerardo Ruiz Chavarría and Sergio Hernández Zapata

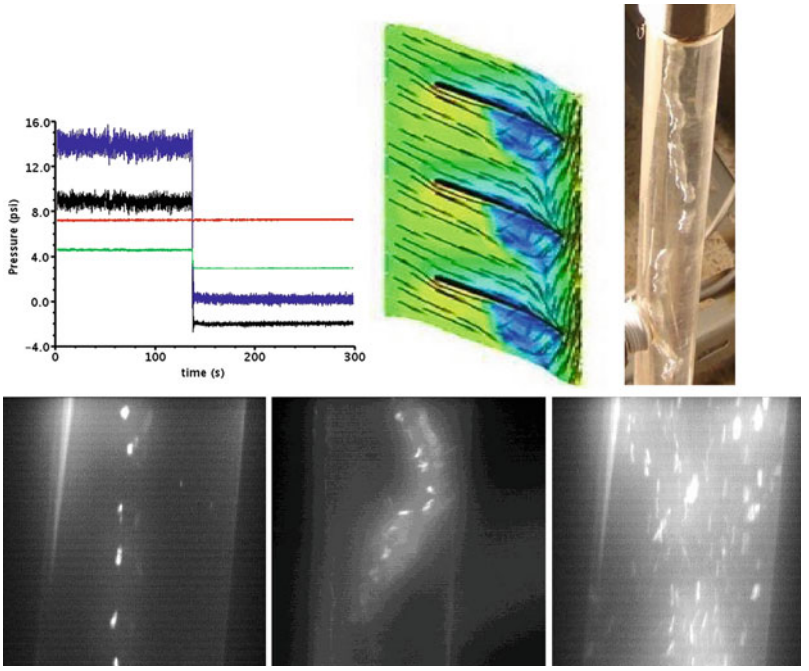

J. L. Reyes de la Cruz
Departamento de Ingeniería Mecánica, Instituto Superior Minero Metalúrgico, Moa, Cuba

G. Ruiz Chavarría (✉) · S. Hernández Zapata
Departamento de Física, Facultad de Ciencias, 04510 México City, D.F., México
e-mail: gruiz@servidor.unam.mx

J. Klapp et al. (eds.), *Experimental and Theoretical Advances in Fluid Dynamics*, Environmental Science and Engineering, DOI: 10.1007/978-3-642-17958-7_50,

Pressure drop inside a hydraulic installation was measured by piezoelectric transducers when cavitation begins. Bubbles appear in the vicinity of blades of the centrifugal pump and after they moves through the outlet pipe following, in some cases, a line. The three last figures (second row) show different cavitation regimes. On the other side bubbles reveal regions of vorticity concentration both near the blades and in the outlet pipe.

Oil Filaments Produced in a Stirred Tank

Rene Sanjuan-Galindo, Enrique Soto, Gabriel Ascanio and Roberto Zenit

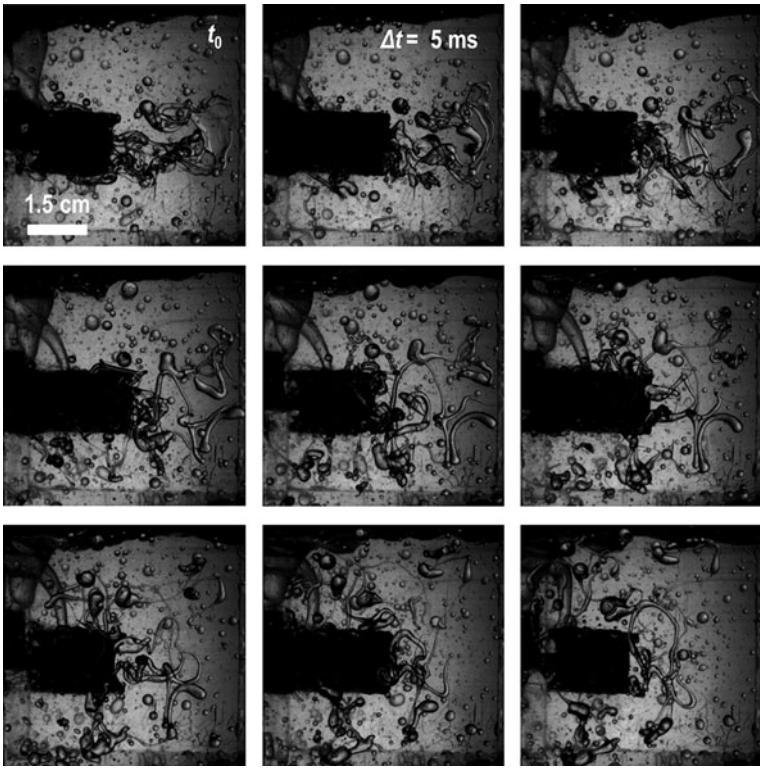

R. Sanjuan-Galindo · E. Soto · G. Ascanio
Centro de Ciencias Aplicadas y Desarrollo Tecnológico, Universidad Nacional Autónoma de México, Apdo. Postal 70-186, 04510 México City, D.F., México

R. Zenit (✉)
Instituto de Investigaciones en Materiales, Universidad Nacional Autónoma de México, Apdo. Postal 70-360, 04510 México City, D.F., México
e-mail: zenit@servidor.unam.mx

J. Klapp et al. (eds.), *Experimental and Theoretical Advances in Fluid Dynamics*, Environmental Science and Engineering, DOI: 10.1007/978-3-642-17958-7_51,

In the process to disperse a viscous oil in water in a stirred tank, filaments are produced before droplets appear. The impeller blades drive the oil and pushed it radially into the liquid bulk. The process is followed by an elongation of the filaments due to the fluid forces that make them thinner. This set of photographs was obtained with a high speed camera. Note that filaments are highly unstable and deformed, which causes the breakage to occur unexpectedly. The broken filaments recoil and finally droplets are produced.

Thermal Plume and Stratification

J. Antonio Castillo, Ramón Tovar, Jorge Rojas, Luis Thomas and Beatriz Marino

Visualization by synthetic schlieren of the filling box process with fluid heated by a thermal source located on the floor. A constant power of 73 W is released in a 25 cm tall, closed, insulated box filled with water. The initial temperature of the fluid is uniform and equal to the environment.

When the heater is turned on, warm fluid rises as a turbulent buoyant plume (**a**).

J. Antonio Castillo · R. Tovar (✉) · J. Rojas
Centro de Investigación en Energía, Universidad Nacional Autónoma de México, Privada Xochicalco S/N Col. Centro, AP 34, CP 62580 Temixco, Morelos, México
e-mail: rto@mazatl.cie.unam.mx

L. Thomas · B. Marino
Instituto de Física Arroyo Seco, Facultad de Ciencias Exactas, Universidad Nacional del Centro de la Pcia de Buenos Aires, Pinto 399, B7000GHG Tandil, Argentina

J. Klapp et al. (eds.), *Experimental and Theoretical Advances in Fluid Dynamics*, Environmental Science and Engineering, DOI: 10.1007/978-3-642-17958-7_52,

The rising plume mixes with the interior fluid causing a decrease in its temperature until it reaches the ceiling where it spreads out (**b**).

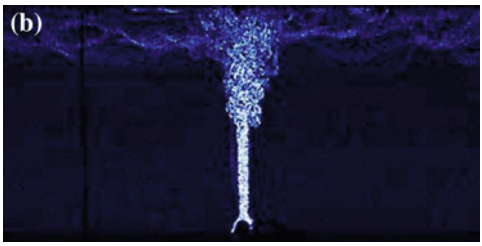

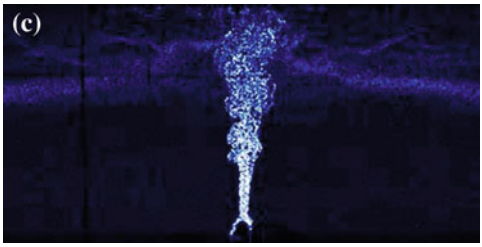

This produces a top warm layer limited by a lower thermal front that descends as more warm fluid is added by the plume (**c**).

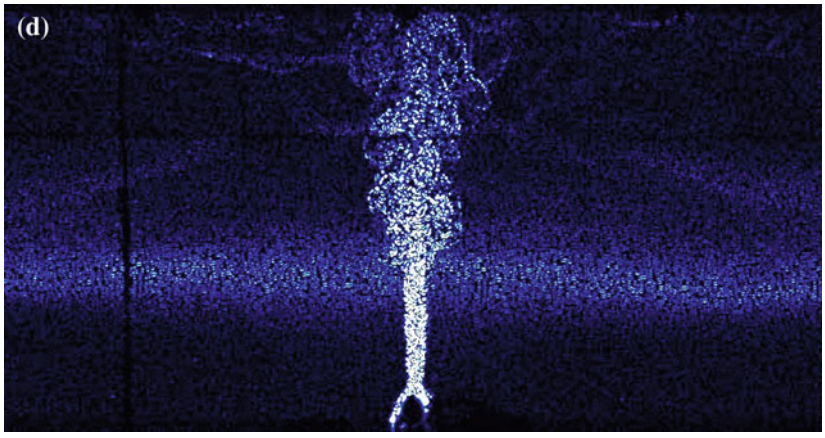

Then a stable stratification is established (**d**). This is the filling box process that was described by Tovar et al. (2007). The filling box time scale is $t_f = V\lambda^{-1}B^{-1/3}H^{-5/3}$, where V and H are the volume and height of the space, B is the buoyancy flux and $\lambda = 0.1$. This is the time required for the thermal front to reach the floor and all the fluid within the space to be entrained by the plume.

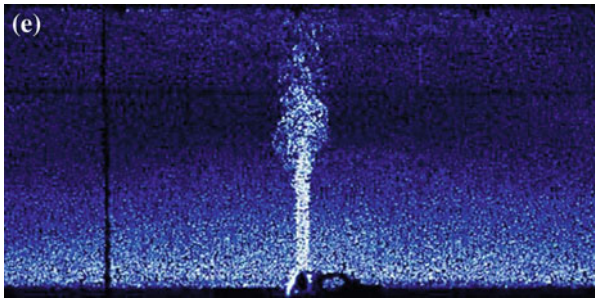

After the filling box process ends the plume continues passing through and recirculating warm fluid from the space, thus the fluid temperature increases linearly with time as long as the heat source is maintained (**e**).

References

Tovar R, Linden PF, Thomas LP (2007) Hybrid ventilation in two interconnected rooms with a buoyancy source. Sol Energy 81:683–691

Visualization of Structures in Non Homogeneous Flows

Yadira Salazar Romero, César Aguilar Espinosa and Tikva Karen Levy C

A container with salt water is introduced into a larger container with distilled water. A quasi-periodic oscillation is induced when the small hole in the bottom of the small container is opened. The difference in the level of water is negligible. Initially, as expected, salt water starts flowing down. However, after a certain time the process is inverted and distilled water starts flowing up.

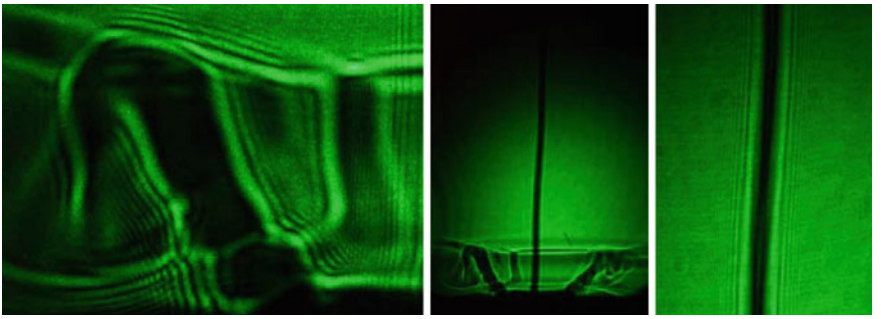

Structure formed when the salted jet goes down, and impinges the bottom of the large container.

Y. Salazar Romero (✉)
Facultad de Ciencias, Ciudad Universitaria 3000, Col. Copilco Universidad, Del. Coyoacán, CP 04360, México City, D.F., Mexico
e-mail: yayafisica@gmail.com

C. A. Espinosa · T. K. Levy C
Colegio de Ciencias Humanidades, UNAM Cataratas y Llanura S/N, Jardines del Pedregal, Coyoacán, CP 04500, México City, D.F., Mexico

J. Klapp et al. (eds.), *Experimental and Theoretical Advances in Fluid Dynamics*, Environmental Science and Engineering, DOI: 10.1007/978-3-642-17958-7_53,

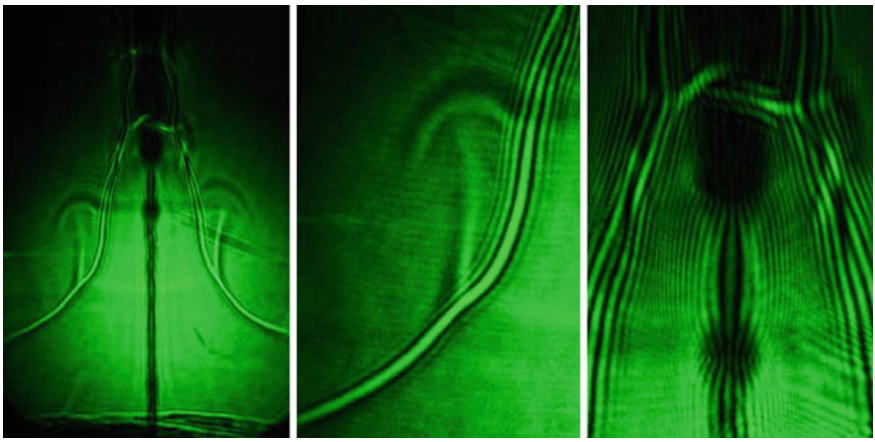

Structure formed when the distilled water jet goes up and touches the free surface. The pictures to the *right* correspond to an enlargement of the *left* side and to the jet structure respectively.

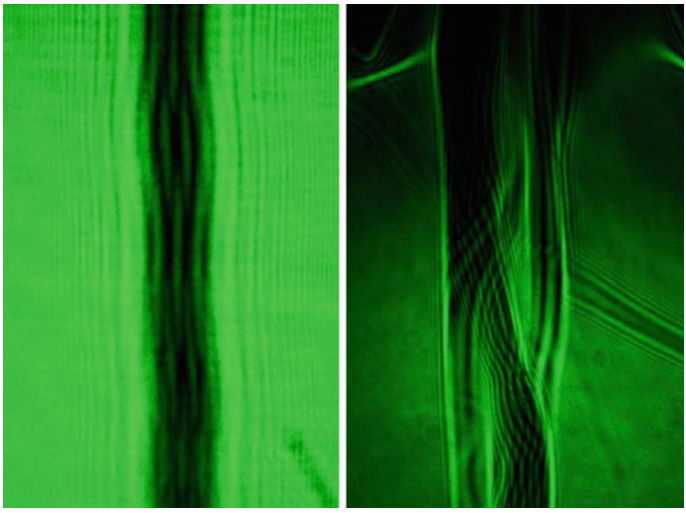

Left: Structure of the jet going down. It is so thin that light is diffracted and its structure can be observed. *Right*: Structure of the jet 24 h after it started to oscillate.

Images of an axisymmetric supersonic air jet produced by a nozzle with a diameter of 1.6 mm.

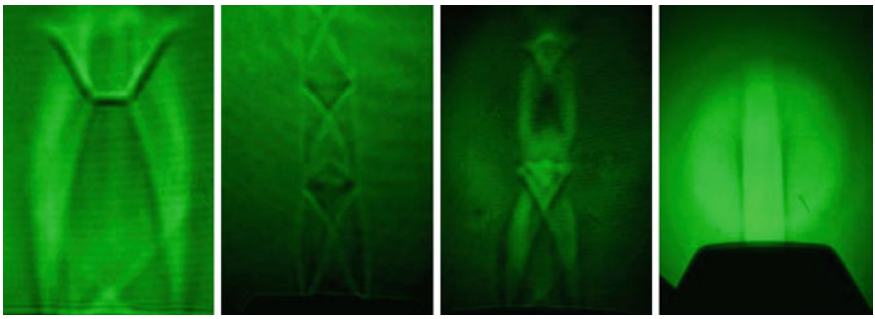

From left to right images of structures formed at decreasing pressures. The picture to the *left* shows a Mach disk at exit pressure of 6.137×10^5 Pa. The two pictures in the *middle* correspond to shock waves at 3.585×10^5 Pa. The difference between them is the distance between the nozzle and the laser source. The image to the *right* shows a subsonic jet at 1.379×10^5 Pa, no shock structure is observed.

Acknowledgments The authors acknowledge support from DGAPA UNAM through project PAPIIT IN119509.